

AD-A229 588



VOLUME 158

In-Situ Patterning: Selective Area Deposition and Etching

EDITORS

Anthony F. Bernhardt

Jerry G. Black

Robert Rosenberg

DISTRIBUTION STATEMENT A

Approved for public release;
Distribution Unlimited

DTIC FILE COPY

DTIC
ELECTE
NOV 15 1990
S E D

REPORT DOCUMENTATION PAGE			Form Approved OMB No. 0704-0188	
<small>Public reporting burden for this collection of information is estimated to average 1 hour per response, including the time for reviewing instructions, searching existing data sources, gathering and maintaining the data needed, and completing and reviewing the collection of information. Send comments regarding this burden estimate or any other aspect of this collection of information, including suggestions for reducing this burden, to Washington Headquarters Services, Directorate for Information Operations and Reports, 1215 Jefferson Davis Highway, Suite 1204, Arlington, VA 22202-4302, and to the Office of Management and Budget, Paperwork Reduction Project (0704-0188), Washington, DC 20503.</small>				
1. AGENCY USE ONLY (Leave blank)	2. REPORT DATE	3. REPORT TYPE AND DATES COVERED		
		Final Report 22 Nov 89-21 Nov 90		
4. TITLE AND SUBTITLE		5. FUNDING NUMBERS		
1989 Materials Research Society Fall Meeting		2306/A2		
6. AUTHOR(S)				
Dr John Ballance				
7. PERFORMING ORGANIZATION NAME(S) AND ADDRESS(ES)		8. PERFORMING ORGANIZATION REPORT NUMBER		
Material Reserach Society 9800 McKnight Road, Suite 327 Pittsburgh, PA 15237-6005		AFOSR-TR 90 1058		
9. SPONSORING/MONITORING AGENCY NAME(S) AND ADDRESS(ES)		10. SPONSORING/MONITORING AGENCY REPORT NUMBER		
AFOSR/NE Bldg 410 Bolling AFB DC 2033206448		AFOSR-90-0081		
11. SUPPLEMENTARY NOTES				
12a. DISTRIBUTION/AVAILABILITY STATEMENT			12b. DISTRIBUTION CODE	
UNLIMITED				
13. ABSTRACT (Maximum 200 words)				
<p>CONFERENCE WAS HELD ON THE FOLLWING AREA</p> <p>(158) In Situ Patterning: Selective Area Deposition and Etching</p> <p>(161) Properties of II-VI Semiconductors: Bulk Crystals, Expitaxial Films, Quantum Well Structures, and Dilute Magnetic Systems</p> <p>(163) Impurities, Defects and Diffusion in Semiconductors: Bulk and Layered Structures</p> <p>(168) Chemical Vapor Deposition of Refractory Metals and Ceramics</p> <p>(170) Tailored Interfaces in Composite Materials.</p>				
14. SUBJECT TERMS			15. NUMBER OF PAGES	
17. SECURITY CLASSIFICATION OF REPORT			18. SECURITY CLASSIFICATION OF THIS PAGE	
UNCLASS			UNCLASS	
19. SECURITY CLASSIFICATION OF ABSTRACT			20. LIMITATION OF ABSTRACT	
UNCLASS			UNLIMITED	

In-Situ Patterning:
Selective Area Deposition and Etching

Accession For	
DTIC GRA&I	<input checked="" type="checkbox"/>
DTIC TAB	<input type="checkbox"/>
Unannounced	<input type="checkbox"/>
Justification	
By	
Distribution/	
Availability Codes	
Dist	Avail and/or Special
A-1	



In-Situ Patterning: Selective Area Deposition and Etching

Symposium held November 29-December 1, 1989, Boston,
Massachusetts, U.S.A.

EDITORS:

Anthony F. Bernhardt

University of California, Lawrence Livermore National Laboratory,
Livermore, California, U.S.A.

Jerry G. Black

Massachusetts Institute of Technology, Lincoln, Massachusetts, U.S.A.

Robert Rosenberg

IBM T.J. Watson Research Center, Yorktown Heights, New York, U.S.A.



MATERIALS RESEARCH SOCIETY
Pittsburgh, Pennsylvania

This work was supported by the Air Force Office of Scientific Research, Air Force Systems Command, USAF, under Grant Number AFOSR 90-0081.

Single article reprints from this publication are available through University Microfilms Inc., 300 North Zeeb Road, Ann Arbor, Michigan 48106

CODEN: MRSPDH

Copyright 1990 by Materials Research Society.
All rights reserved.

This book has been registered with Copyright Clearance Center, Inc. For further information, please contact the Copyright Clearance Center, Salem, Massachusetts.

Published by:

Materials Research Society
9800 McKnight Road
Pittsburgh, Pennsylvania 15237
Telephone (412) 367-3003
Fax (412) 367-4373

Library of Congress Cataloging in Publication Data

In-situ patterning : selective area deposition and etching : symposium held November 29-December 1, 1989, Boston, Massachusetts, U.S.A. / editors, Anthony F. Bernhardt, Jerry G. Black, Robert Rosenberg.

p. cm. -- (Materials Research Society symposium proceedings : ISSN 0272-9172 ; v. 158)

Includes bibliographical references.

ISBN 1-55899-046-1

1. Semiconductors—Etching—Congresses. 2. Semiconductor doping—Congresses. 3. Lasers—Industrial applications—Congresses 4. Plasma etching—Congresses. I. Bernhardt, Anthony. II. Black, Jerry G. III. Rosenberg, R.
IV. Series: Materials Research Society symposium proceedings : v. 158.

TK7871.85.I49 1990
621.381'52—dc20

90-34801
CIP

Manufactured in the United States of America

Contents

PREFACE	xi
MATERIALS RESEARCH SOCIETY SYMPOSIUM PROCEEDINGS	xiii
PART I: SURFACE SCIENCE	
*NOVEL PHOTOIMAGING SCHEMES AT POLYMER SURFACES: THEIR ROLE IN HIGH RESOLUTION LITHOGRAPHY Gary N. Taylor, Omkaram Nalamasu, and Richard S. Hutton	3
SURFACE CHEMISTRY OF DIMETHYLALUMINUM HYDRIDE AND TRIMETHYLALUMINUM ON ALUMINUM Daniel R. Strongin and Paul B. Comita	21
MECHANISM OF CHROMIUM DEPOSITION FROM $\text{Cr}(\text{CO})_6$ BY UV LASER LIGHT R. Nowak and P. Hess	27
SELECTIVE SURFACE MODIFICATION OF FLUOROCARBON RESIN USING EXCIMER LASER M. Okoshi, M. Murahara, and K. Toyoda	33
DIRECT EVIDENCE FOR THE CREATION OF MICROPORES IN UV-IRRADIATED POLY(METHYL METHACRYLATE) J.A. Moore and Jin-O Choi	39
UV LASER-INDUCED ETCHING OF THE FIRST-ROW TRANSITION METALS George W. Tyndall	47
PHOTOCHEMICAL AREA-SELECTIVE ETCHING OF Si AND SiO_2 USING SYNCHROTRON RADIATION Jun-Ichi Takahashi, Yuichi Utsumi, and Tsuneo Urisu	53
PART II: LASER DEPOSITION I	
*LASER-BASED AREA-SELECTIVE PROCESSING TECHNIQUES FOR HIGH-DENSITY INTERCONNECTS Y.S. Liu and H.S. Cole	61
TIME-RESOLVED STUDIES OF SURFACE MELTING DURING LASER-INDUCED CHEMICAL VAPOR DEPOSITION WITH LASER INTENSITY MODULATION Paul B. Comita, Peter E. Price, Jr., and Toivo T. Kodas	73

*Invited Paper

VISIBLE-WAVELENGTH LASER PHOTODEPOSITION OF COBALT INTERCONNECTS	79
M. Rothschild, J.H.C. Sedlacek, D.C. Shaver, D.J. Ehrlich, S.N. Bittenson, D. Edwards, Jr., and N.P. Economou	
LASER CHEMICAL VAPOR DEPOSITION OF W ON Si AND SiO ₂ /Si	85
Jian-Yang Lin and Susan D. Allen	
LASER INDUCED CHEMICAL VAPOR DEPOSITION OF GaN	91
A. Kobayashi, T. Asai, S. Kawai, and P.J. Chong	
LASER DIRECT WRITING OF OPTICAL INTERCONNECTS IN POLYIMIDES AND SiO ₂ :TiO ₂ COATINGS	97
D.W. Hewak and H. Jerominek	
SELECTIVE AREA DEPOSITION OF CONDUCTING PALLADIUM FILMS ON POLYIMIDE RESINS	103
Yoon-Gi Kim, S. Bialy, R.W. Miller, J.T. Spencer, P.A. Dowben, and Saswati Datta	
UV EXCIMER LASER-INDUCED DEPOSITION OF PALLADIUM FROM PALLADIUM ACETATE FILMS	109
Hilmar Esrom and Georg Wahl	
PART III: LASER DEPOSITION II	
IN SITU CHARACTERIZATION OF METALLORGANIC CHEMICAL VAPOR DEPOSITION	121
R. Scarmozzino, T. Cacouris, and R.M. Osgood, Jr.	
LASER WRITING OF HIGH PURITY GOLD LINES	129
M. Jubber, J.I.B. Wilson, J.L. Davidson, P. John, and P.G. Roberts	
WAVELENGTH-DEPENDENT AREA SELECTIVITY IN PHOTOCHEMICAL VAPOR DEPOSITION OF ALUMINUM FILMS	135
Mitsugu Hanabusa and Masashi Ikeda	
KrF EXCIMER LASER DEPOSITION OF TITANIUM FROM TiCl ₄	141
R. Izquierdo, C. Lavoie, and M. Meunier	
SELECTIVE RAPID THERMAL CVD OF GERMANIUM	147
D.T. Grider, M.C. Öztürk, J.J. Wortman, M.A. Littlejohn, Y. Zhong, D. Batchelor, and P. Russell	
LASER INDUCED LOCAL DECOMPOSITION OF ADSORBED TUNGSTEN FLUORINE MOLECULES FOR METAL DEPOSITION ON SILICON	155
Geoffroy Auvert, Yves Pauleau, and Didier Tonneau	
EXCIMER LASER INDUCED DEPOSITION OF TUNGSTEN FROM W(CO) ₆ AND WF ₆	161
Berthold Rager and Friedrich Bachmann	
DIRECT WRITING OF COPPER LINES FROM COPPER FORMATE PRECURSORS USING A Nd:YAG-LASER	169
Heinrich G. Müller and Siegfried Schuler	

ROLES OF GAS PHASE AND SURFACE PHOTOLYSIS IN LASER CHEMICAL VAPOR DEPOSITION FROM $\text{Fe}(\text{CO})_5$ Xin Xu and J.I. Steinfeld	175
--	-----

PHOTO-OXIDATION OF HYDROGENATED AMORPHOUS SILICON-CARBON ALLOYS P. John, I.M. Odeh, A. Qayyum, and J.I.B. Wilson	181
--	-----

METAL DEPOSITION WITH INCOHERENT EXCIMER RADIATION Hilmar Esrom and Ulrich Kogelschatz	189
---	-----

PART IV: E-BEAM AND ION BEAM PROCESSING

*ELECTRONIC EXCITATION-INDUCED SURFACE CHEMISTRY AND ELECTRON-BEAM-ASSISTED CHEMICAL VAPOR DEPOSITION F. Bozso and Ph. Avouris	201
--	-----

PATTERNING OF GaAs/AlGaAs WAFERS BY FOCUSED ELECTRON-BEAM INDUCED CHLORINE ETCHING AND SUBSEQUENT MBE GROWTH M. Taneya, Y. Sugimoto, H. Hidaka, and K. Akita	211
--	-----

DEEP STRUCTURES PRODUCED IN III-V MATERIALS BY COMBINED FOCUSED ION BEAM IRRADIATION AND DRY ETCHING L.R. Harriott, Y.L. Wang, B.H. Chin, and H. Temkin	217
---	-----

MASKLESS FORMATION OF TUNGSTEN FILMS BY ION BEAM ASSISTED DEPOSITION TECHNIQUE Zheng Xu, Toshihiko Kosugi, Kenji Gamo, and Susumu Namba	223
--	-----

THE ROLE OF ADSORPTION AND VAPOR PRESSURE IN FOCUSED ION BEAM INDUCED DEPOSITION OF CARBON FILMS S.J. Kirch and D.E. Seeger	229
---	-----

SELECTIVE CHEMICAL VAPOR DEPOSITION OF TUNGSTEN FILMS ON TITANIUM-ION-IRRADIATED SILICON DIOXIDE H. Okuhira, S. Nishimatsu, and K. Ninomiya	235
---	-----

PART V: LASER DOPING, ANNEALING AND PLANARIZATION

*NANOSECOND THERMAL PROCESSING FOR ULTRA-HIGH-SPEED DEVICE TECHNOLOGY Thomas W. Sigmon, Anthony M. McCarthy, Kurt H. Weiner, and Paul G. Carey	241
---	-----

IN SITU MEASUREMENT OF PULSED LASER INDUCED CARRIER GENERATION IN DOPED SILICON FILMS T. Sameshima, M. Hara, and S. Usui	255
--	-----

LASER PROCESSED SILICIDES FOR GaAs HEMTS W.T. Anderson, A. Christou, P.E. Thompson, J.L. Davis, C.R. Gossett, J.M. Eridon, C. Michelakis, G. Kiriakidis, Z. Hatzopoulos, T. Ethimiopoulos, M. Kudumas, and D.V. Morgan	261
--	-----

*Invited Paper

SUBSTRATE HEATING EFFECTS IN EXCIMER LASER PLANARIZATION OF ALUMINUM Robert J. Baseman and Joseph C. Andreshak	267
LOW TEMPERATURE INTERLEVEL SiO ₂ LAYERS BY PHOTOINDUCED PROCESSING H. Sigmund, A. Klumpp, and G. Springholz	273
PHOSPHORUS DOPING INTO SILICON USING ArF EXCIMER LASER Abdelilah Slaoui, Francois Foulon, Eric Fogarassy, and Paul Siffert	281

PART VI: PHOTO-ETCHING

THE INTERACTION OF LASER GENERATED METHYL RADICALS WITH Cd, Te, AND CdTe SURFACES J.J. Zinck, G.L. Olson, P.D. Brewer, and J.E. Jensen	289
HOLOGRAPHIC PATTERN ETCHING OF SILICON-CARBIDE BY EXCIMER LASER M. Murahara, M. Yonekawa, and K. Shirakawa	295
CONTROL OF ETCHING IN LASER-CHEMICAL REACTION OF Mn-Zn FERRITE BY MeV ION IMPLANTATION Y.F. Lu, M. Takai, H. Sanda, A. Chayahara, M. Satou, T. Minamisono, and S. Namba	301
X-RAY PHOTOEMISSION INVESTIGATION OF EXCIMER LASER INDUCED ETCHING OF InP R. Matz, J. Meiler, and D. Haarer	307
SELECTIVE ETCHING AND PHOTO-BLEACHING IN THIN AMORPHOUS Ge-Sb-S FILMS Evdokia B. Savova and B.I. Pashmakoff	313
COPPER VAPOR LASER USED IN ETCHING AND DEPOSITION Belgacem Haba, Brian W. Hussey, Arunava Gupta, and Robert J. Baseman	319
EXCIMER LASER-ASSISTED ETCHING OF SILICON USING CHLOROPENTAFLUOROETHANE S.D. Russell and D.A. Sexton	325
LOCAL LASER INDUCED ETCHING OF COPPER FILMS BY CHLORINE Hua Tang and Irving P. Herman	331

PART VII: EPITAXY I

*SELECTIVE SILICON EPITAXY FOR ADVANCED DRAM STRUCTURES Gary B. Bronner	339
SELECTIVE EPITAXY OF Al _x Ga _{1-x} As AND Al _x Ga _{1-x} As BASED STRUCTURES M.S. Gorsky, T.F. Kuech, and R. Potemski	351

*Invited Paper

SURFACE REACTION MECHANISMS IN SELECTED AREA EPITAXY OF II-VIs Stuart J.C. Irvine, H. Hill, J.E. Hails, A.D. Pitt, and J.B. Mullin	357
NOVEL STACKED CMOS PROCESS BY LOCAL OVERGROWTH P. Zingg, B. Höflinger, and G.W. Neudeck	365
OPTIMIZED MOLECULAR BEAM EPITAXY STRUCTURES FOR GaAs ON SILICON PHOTODETECTORS A. Christou, N.A. Papanicolaou, and G.W. Anderson	371
LASER SELECTIVE AREA EPITAXY FOR THE POTENTIAL OF OPTOELECTRONIC INTEGRATION H. Liu, J.C. Roberts, J. Ramdani, and S.M. Bedair	377
LASER INDUCED SURFACE CHEMICAL EPITAXY OF II-VI MATERIALS Charter D. Stinespring and Andrew Freedman	381
PART VIII: ETCHING II	
XPS STUDIES OF CHLORINE ETCHING INTERACTIONS WITH GaAs(100) Andrew Freedman and C.D. Stinespring	389
A PROCESS MODEL FOR REACTIVE ION ETCHING AND STUDY OF THE EFFECTS OF MAGNETRON ENHANCEMENT M. Meyyappan and R.C. Buggeln	395
ETCHING OF GaAs ON AlGaAs IN RIE-MODE Gudrun Kaufel and Elfriede Olander	401
DOWNSTREAM ETCHING OF GaAs AND InP USING MOLECULAR CHLORINE AND CHLORINE RADICALS David G. Lishan and Evelyn L. Hu	407
HOLLOW COLD CATHODE ION SOURCE FOR REACTIVE ION-BEAM ETCHING A.I. Stognij and V.V. Tokarev	413
REACTIVE ION ETCHING OF In-BASED III-V SEMICONDUCTORS - COMPARISON OF Cl AND C ₂ H ₆ CHEMISTRIES S.J. Pearton, U.K. Chakrabarti, F.A. Baiocchi, and W.S. Hobson	417
ELEVATED TEMPERATURE REACTIVE ION ETCHING OF GaAs AND AlGaAs IN C ₂ H ₆ /H ₂ S.J. Pearton, W.S. Hobson, and K.S. Jones	425
CHARACTERIZATION OF SIDEWALL RESIDUE FILM AND ATOMIC STRUCTURE OF THE TRENCH FORMED BY BCl ₃ /Cl ₂ REACTIVE ION ETCHING Sun Jin Yun, Young-Jin Jeon, and Jeong Y. Lee	431

PART IX: ABLATION

*GENERATION OF BLIND VIA-HOLES FOR A HIGH DENSITY MULTI-CHIP-MODULE USING EXCIMER LASERS Friedrich G. Bachmann	439
*LASER DEPOSITION AND PATTERNING OF HIGH-TEMPERATURE SUPERCONDUCTORS D. Bäuerle, J. Heitz, W. Ludorf, P. Schwab, and X.Z. Wang	451
PRECURSORS TO THE PHOTO-ABLATION OF SODIUM TRISILICATE GLASS DUE TO UV EXCIMER IRRADIATION P.A. Eschbach, J.T. Dickinson, S.C. Langford, L.C. Jensen, L.R. Pederson, and D.R. Baer	463
ULTRAFast IMAGING OF ULTRAVIOLET LASER ABLATION AND ETCHING OF POLYMETHYL METHACRYLATE Bodil Braren, R. Srinivasan, Kelly G. Casey, and Mildred Yeh	471
LOW TEMPERATURE LASER PHYSICAL VAPOR DEPOSITION OF MULTILAYERED THIN FILMS N. Biunno, J. Krishnaswamy, S. Sharan, L. Ganapathi, and J. Narayan	477
LASER PATTERNING AND ELECTRICAL PROPERTIES OF SUBMICRON LINES OF Y-Ba-Cu-O J.P. Zheng, Q.Y. Ying, H.S. Kim, D. Bhattacharya, D.T. Shaw, and H.S. Kwok	485
AUTHOR INDEX	491
SUBJECT INDEX	493
MATERIALS RESEARCH SOCIETY SYMPOSIUM PROCEEDINGS	497

*Invited Paper

Preface

The MRS symposium on In-Situ Patterning: Selective Area Deposition and Etching brought together a wide selection of microfabrication technologies and detailed studies of their enabling mechanisms. The 85 accepted papers included many contributions from academic institutions, and strong representation of industrial research laboratories, many of whom have made major investments towards the commercialization of the techniques resulting from their research. Those researchers who, like us, are dedicated to applied research are encouraged by this demonstration of long-term commitment and support.

The common thread through the invited and contributed papers is the chemical and/or physical alteration of surfaces by the actions of ion, electron, or photon energy. The applications ranged from state-of-the-art lithographic techniques, to direct processing of semiconductor surfaces, aiming to obviate lithography in device fabrication. This direct processing encompasses patterned deposition of metallic conductors and insulating films, as well as local etching and doping of device structures. The work demonstrated in this symposium ranged from the detailed atomic behavior of treated surfaces, to nuts-and-bolts packaging techniques for the high-density descendants of today's printed circuit boards.

The organizers of this symposium wish to thank all of the dedicated people whose work made it possible. Firstly, the participants who presented their work in Boston last Fall, and whose papers follow, have spent innumerable hours to prepare their results for their colleagues; the MRS staff for their continuing logistical support; and the symposium participants who "volunteered" to referee and edit the papers. Finally, we thank those institutions who provided essential financial support for the symposium: The Air Force Office of Scientific Research, Amoco Technology Company, IBM Corporation, Lambda-Physik, Inc., and Newport Corporation.

May 1990

Jerry G. Black
Anthony F. Bernhardt
Robert Rosenberg

MATERIALS RESEARCH SOCIETY SYMPOSIUM PROCEEDINGS

Recent Materials Research Society Symposium Proceedings

- Volume 145—III-V Heterostructures for Electronic/Photonic Devices, C.W. Tu, V.D. Matterna, A.C. Gossard, 1989, ISBN: 1-55899-018-6
- Volume 146—Rapid Thermal Annealing/Chemical Vapor Deposition and Integrated Processing, D. Hodul, J. Gelpey, M.L. Green, T.E. Seidel, 1989, ISBN: 1-55899-019-4
- Volume 147—Ion Beam Processing of Advanced Electronic Materials, N.W. Cheung, A.D. Marwick, J.B. Roberto, 1989, ISBN: 1-55899-020-8
- Volume 148—Chemistry and Defects in Semiconductor Heterostructures, M. Kawabe, T.D. Sands, E.R. Weber, R.S. Williams, 1989, ISBN: 1-55899-021-6
- Volume 149—Amorphous Silicon Technology-1989, A. Madan, M.J. Thompson, P.C. Taylor, Y. Hamakawa, P.G. LeComber, 1989, ISBN: 1-55899-022-4
- Volume 150—Materials for Magneto-Optic Data Storage, C.J. Robinson, T. Suzuki, C.M. Falco, 1989, ISBN: 1-55899-023-2
- Volume 151—Growth, Characterization and Properties of Ultrathin Magnetic Films and Multilayers, B.T. Jonker, J.P. Heremans, E.E. Marinero, 1989, ISBN: 1-55899-024-0
- Volume 152—Optical Materials: Processing and Science, D.B. Paker, C. Ortiz, 1989, ISBN: 1-55899-025-9
- Volume 153—Interfaces Between Polymers, Metals, and Ceramics, B.M. DeKoven, A.J. Gellman, R. Rosenberg, 1989, ISBN: 1-55899-026-7
- Volume 154—Electronic Packaging Materials Science IV, R. Jaccodine, K.A. Jackson, E.D. Lillie, R.C. Sundahl, 1989, ISBN: 1-55899-027-5
- Volume 155—Processing Science of Advanced Ceramics, I.A. Aksay, G.L. McVay, D.R. Ulrich, 1989, ISBN: 1-55899-028-3
- Volume 156—High Temperature Superconductors: Relationships Between Properties, Structure, and Solid-State Chemistry, J.R. Jorgensen, K. Kitazawa, J.M. Tarascon, M.S. Thompson, J.B. Torrance, 1989, ISBN: 1-55899-029
- Volume 157—Beam-Solid Interactions: Physical Phenomena, J.A. Knapp, P. Borgesen, R.A. Zuhr, 1989, ISBN 1-55899-045-3
- Volume 158—In-Situ Patterning: Selective Area Deposition and Etching, R. Rosenberg, A.F. Bernhardt, J.G. Black, 1989, ISBN 1-55899-046-1
- Volume 159—Atomic Scale Structure of Interfaces, R.D. Bringans, R.M. Feenstra, J.M. Gibson, 1989, ISBN 1-55899-047-X
- Volume 160—Layered Structures: Heteroepitaxy, Superlattices, Strain, and Metastability, B.W. Dodson, L.J. Schowalter, J.E. Cunningham, F.H. Pollak, 1989, ISBN 1-55899-048-8
- Volume 161—Properties of II-VI Semiconductors: Bulk Crystals, Epitaxial Films, Quantum Well Structures and Dilute Magnetic Systems, J.F. Schetzina, E.J. Bartoli, Jr., H.F. Schaake, 1989, ISBN 1-55899-049-6
- Volume 162—Diamond, Boron Nitride, Silicon Carbide and Related Wide Bandgap Semiconductors, J.T. Glass, R.F. Messier, N. Fujimori, 1989, ISBN 1-55899-050-X
- Volume 163—Impurities, Defects and Diffusion in Semiconductors: Bulk and Layered Structures, J. Bernholc, E.E. Haller, D.J. Wolford, 1989, ISBN 1-55899-051-8
- Volume 164—Materials Issues in Microcrystalline Semiconductors, P.M. Fauchet, C.C. Tsai, K. Tanaka, 1989, ISBN 1-55899-052-6
- Volume 165—Characterization of Plasma-Enhanced CVD Processes, G. Lucovsky, D.E. Ibbotson, D.W. Hess, 1989, ISBN 1-55899-053-4
- Volume 166—Neutron Scattering for Materials Science, S.M. Shapiro, S.C. Moss, J.D. Jorgensen, 1989, ISBN 1-55899-054-2

MATERIALS RESEARCH SOCIETY SYMPOSIUM PROCEEDINGS

- Volume 167—Advanced Electronic Packaging Materials, A. Barfknecht, J. Partridge, C-Y. Li, C.J. Chen, 1989, ISBN 1-55899-055-0
- Volume 168—Chemical Vapor Deposition of Refractory Metals and Ceramics, T.M. Besmann, B.M. Gallois, 1989, ISBN 1-55899-056-9
- Volume 169—High Temperature Superconductors: Fundamental Properties and Novel Materials Processing, J. Narayan, C.W. Chu, L.F. Schneemeyer, D.K. Christen, 1989, ISBN 1-55899-057-7
- Volume 170—Tailored Interfaces in Composite Materials, C.G. Pantano, E.J.H. Chen, 1989, ISBN 1-55899-058-5
- Volume 171—Polymer Based Molecular Composites, D.W. Schaefer, J.E. Mark, 1989, ISBN 1-55899-059-3
- Volume 172—Optical Fiber Materials and Processing, J.W. Fleming, G.H. Sigel, S. Takahashi, P.W. France, 1989, ISBN 1-55899-060-7
- Volume 173—Electrical, Optical and Magnetic Properties of Organic Solid-State Materials, L.Y. Chiang, D.O. Cowan, P. Chaikin, 1989, ISBN 1-55899-061-5
- Volume 174—Materials Synthesis Utilizing Biological Processes, M. Alper, P.D. Calvert, P.C. Rieke, 1989, ISBN 1-55899-062-3
- Volume 175—Multi-Functional Materials, D.R. Ulrich, F.E. Karasz, A.J. Buckley, G. Gallagher-Daggitt, 1989, ISBN 1-55899-063-1
- Volume 176—Scientific Basis for Nuclear Waste Management XIII, V.M. Oversby, P.W. Brown, 1989, ISBN 1-55899-064-X
- Volume 177—Macromolecular Liquids, C.R. Safinya, S.A. Safran, P.A. Pincus, 1989, ISBN 1-55899-065-8
- Volume 178—Fly Ash and Coal Conversion By-Products: Characterization, Utilization and Disposal VI, F.P. Glasser, R.L. Day, 1989, ISBN 1-55899-066-6
- Volume 179—Specialty Cements with Advanced Properties, H. Jennings, A.G. Landers, B.E. Scheetz, I. Odler, 1989, ISBN 1-55899-067-4

MATERIALS RESEARCH SOCIETY MONOGRAPH

Atom Probe Microanalysis: Principles and Applications to Materials Problems, M.K. Miller, G.D.W. Smith, 1989; ISBN 0-931837-99-5

Earlier Materials Research Society Symposium Proceedings listed in the back.

PART I

Surface Science

NOVEL PHOTOIMAGING SCHEMES AT POLYMER SURFACES: THEIR ROLE IN HIGH RESOLUTION LITHOGRAPHY

GARY N. TAYLOR, OMKARAM NALAMASU AND RICHARD S. HUTTON
AT&T Bell Laboratories, Murray Hill, New Jersey 07974

ABSTRACT

Polymer surfaces play essential roles in many technical arenas, but their importance in imaging science and technology has only recently been established. As optical lithography for integrated circuit applications pushes below $0.5\mu\text{m}$ feature sizes, ever shorter wavelengths and lenses with larger numerical apertures are required. These narrow the depth-of-focus to such a degree that it eventually becomes less than the substrate topography, resist film thickness and wafer nonuniformity contributions to focus placement. Thick single-layer, surface-conforming resists will not be able to record the aerial image accurately.

Surface imaging of planarized single-layer or bilayer organic films offers a means for minimizing the depth-of-focus constraints. This paper outlines this general concept which includes radiation-induced chemical changes in the surface and near-surface regions, amplification of these events by gas-solid reactions with inorganic and organometallic agents and plasma development using an oxygen plasma. Two approaches to surface imaging are discussed. The first employs Plasmask® resist, a very absorbing diazonaphthoquinone-functionalized novolac resin which is exposed and functionalized in the topmost several hundred nm of film. According to Coopmans, Roland and coworkers [14] and Pierrat, et al., [22] two tones are possible depending upon the processing. The present study reports results obtained for both processing modes using 248.4 nm lithography.

The second approach involves imaging at the surface and utilizes one of the oldest polymer photoreactions, photo-oxidation, in the imaging step. Hydrophobic aromatic polymers are first irradiated in air to give hydrophilic groups. These sorb water selectively on the hydrophilic areas. The water is reacted in a separate step with an inorganic or organometallic compound such as TiCl_4 to give a metal oxide film (TiO_2) on the exposed areas. Development with an oxygen plasma gives negative tone patterns because TiO_2 reduces the etching rate by a factor of ~ 500 in the exposed regions. Imaging is dependent upon the polymer structure, among other things, and is optimized at shorter wavelengths likely to be used in future exposure systems. From the present results we feel that surface imaging resists may realize $0.25\mu\text{m}$ resolution at 193 nm and that $<0.10\mu\text{m}$ resolution may be achieved using x-ray radiation.

1. INTRODUCTION

Over the past thirty years the role of polymer surfaces in science and technology has become an integral part of a number of classical fields of study including adhesion [1], membrane science [2], aging and wear of protective films [3], sorption and diffusion science [4] and corrosion science [5]. In contrast, until recently [6] there has only been one application of polymer surfaces to imaging science, photosensitive electroless deposition, which had its origins in the early 1970's [7]. A recent version of this technique [8] may eventually be employed to selectively activate photopatterned surfaces to the electroless deposition of Cu, Ni, etc., used in electronic interconnection technology.

Electroless deposition technology has been very successfully applied to thick film ($>10\text{ }\mu\text{m}$), low resolution ($>25\text{ }\mu\text{m}$) interconnection technology, but has not been successful for high resolution patterning ($<0.5\text{ }\mu\text{m}$) of $1\text{--}2\text{ }\mu\text{m}$ thick polymer films used in ultra large scale integrated circuits (ULSIC) manufacturing. Unfavorable factors may be the isotropic nature of metal film growth and the localized deposition of the metal catalyst which often results in discontinuous electroless deposition of very thin ($<0.1\text{ }\mu\text{m}$) metal films. Another problem is the accessibility of surface sites and the question of what constitutes the "surface".

Until 1983 the importance of the polymer or "resist" surface in high resolution imaging was not evident. Until that time all resists for IC manufacturing were exposed completely through their thickness ($1\text{--}3\text{ }\mu\text{m}$) and developed with aqueous base (positive tone) or solvent (negative tone) liquid developers. The former method is employed widely today to provide $\leq 0.5\text{ }\mu\text{m}$ resolution patterns in $>1.0\text{ }\mu\text{m}$ thickness films [9] using 248.4 nm light. However, this approach is becoming increasingly more difficult because the depth-of-focus is on the order of the sum of the topographic and resist film thicknesses and will be even less when smaller features are exposed at shorter wavelengths. In addition, such resists are subject to reflectance and bulk (diffraction) effects which degrade resolution.

Surface and even near-surface imaging eliminate the latter two difficulties and substantially minimize depth-of-focus problems especially when true surface imaging is used [6]. These points are summarized in Fig. 1 which includes other issues such as wafer "bow" and device topography. The means for optimizing resolution is clear; employ a planarizing surface-sensitive resist having other desirable characteristics such as resistance to plasmas used to etch device substrate films, a high T_g and reasonable sensitivity of $<100\text{ mJ/cm}^2$ ($<30\text{ }\mu\text{C/cm}^2$ for e-beam lithography).

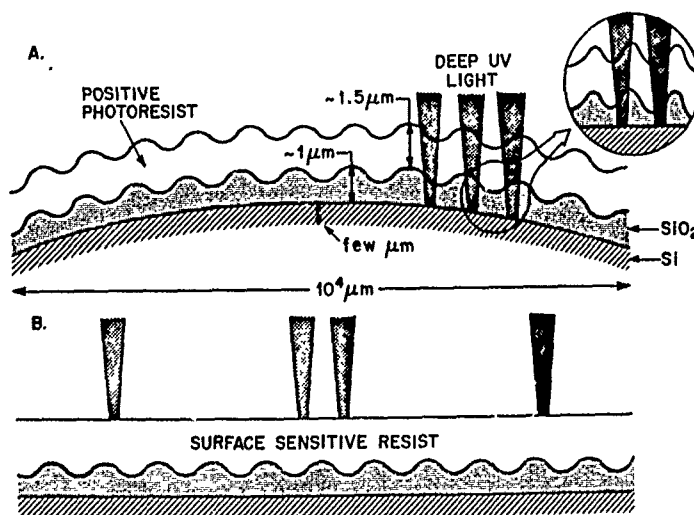


Figure 1. Diagram depicting (A) the influence of wafer curvature, substrate film topography and resist thickness on the focus required for optimum imaging and (B) a means for minimizing focus variations by employing a planarizing, surface-sensitive resist.

A general scheme [10] for accomplishing this is presented in Fig. 2 for both positive and negative tone patterns. In this instance radiation-sensitive groups A in the polymer are converted to product groups B. The conversion of A to B is restricted to the near surface

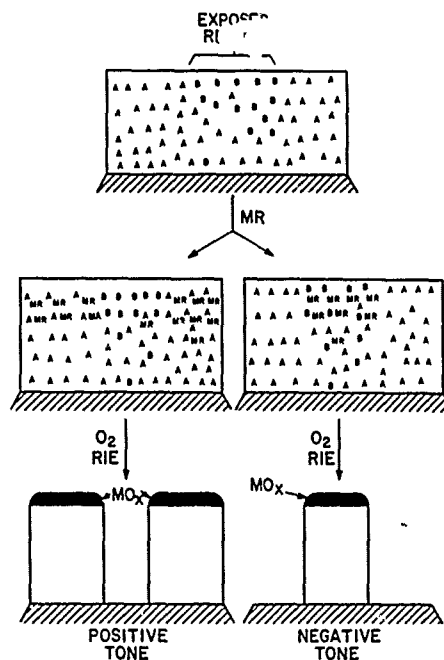


Figure 2. Gas-phase functionalized resist process using a polymer with highly absorbing radiation-sensitive groups A affording product groups B, gas-phase functionalization by organometallic or inorganic reagent MR to give selective reaction in the near-surface region and plasma development to give either positive or negative tone patterns depending on whether A or B reacted respectively, with MR.

region of the film by its extremely high absorption cross section that is optimized by using the appropriate radiation, low energy electrons (<5 keV) and ions (<200 keV) and high energy photons (100-2500Å) or by incorporating highly absorbing chromophores for longer wavelengths of light. The radiochemical conversion is amplified by the gas-solid reaction of an inorganic or organometallic compound MR with either A or B, thus locking the metal atoms M into selective regions of the film. Oxidative plasma development then converts M to its refractory oxide MO_x, which is an excellent barrier, or mask, for anisotropically removing unfunctionalized polymer.

Restriction of MR to the near-surface region also can be achieved, even in the case of exposure through the entire film thickness, by confining the permeation of MR to this region [10] (Fig. 3). So far, this method has achieved the highest resolution imaging in conventional optical lithography as we shall see in a later section. Si is the most commonly used metal atom because its organometallic compounds are readily available and undergo selective reactions with a variety of organic functional groups; also SiO₂, the masking species during development, is an effective etching mask for anisotropic oxygen reactive ion etching (RIE).

2. SYSTEMS USING Si MASKING

MacDonald and coworkers [11] first reported the reaction of hexamethyldisilazane (HMDS) with polymeric phenolic groups, generated by direct or catalytic photolysis

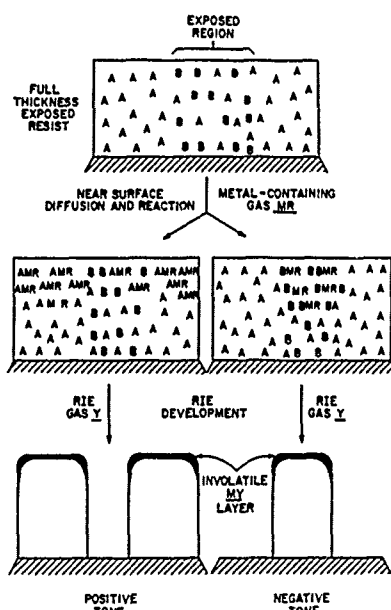


Figure 3. Gas phase functionalization as in Fig. 3 except for exposure through the film. Near-surface functionalization in this instance is obtained by limiting permeation of the reagent MR to the near-surface region.

techniques, to give plasma-developed resist images. The use of Si in plasma-developed resists was pioneered several years before by workers at AT&T Bell Laboratories [12,13]. However, neither of these groups used surface or near-surface selective incorporation of Si in the imaging process.

A joint effort by Coopmans and coworkers at IMEC and Roland, et al. at UCB Electronics, both in Leuven, Belgium, resulted in the first production worthy process using Si functionalization and near-surface imaging [14]. Called DESIRE[®] it employs a diazonaphthoquinonesulfonyl ester derivative (DNQ) of a phenol formaldehyde novolac as the photoactive resin which is called Plasmask[®] resist. In the presence of water the absorbing DNQ group photodecomposes with loss of nitrogen to give a ketene which reacts with water to give an indenecarboxylic acid that is thermally stable at temperatures up to $\sim 180^{\circ}\text{C}$. Heat ($>120^{\circ}\text{C}$) also produces the same ketene intermediate, which in the absence of water reacts with the phenolic hydroxyl groups on the resin to give a resin ester. Since the DNQ derivatized resin is multifunctional, crosslinking occurs readily upon heating and many reactive phenol groups are converted to ester groups which can not be silylated. In a typical DESIRE[®] process outlined in Fig. 4 the resist is heated after exposure. This causes a considerable difference in the permeation rate for trimethylsilylating agents, such as HMDS, in the exposed (high rate) versus the unexposed (low rate) regions. With proper control of the post-exposure heating and silylation conditions permeation can be restricted to a depth of $\sim 3000\text{\AA}$ in exposed regions and $<1000\text{\AA}$ in the crosslinked unexposed regions. The different Si concentrations and permeation profiles afford a much lower O_2 RIE rate in exposed regions and negative tone images upon development. However, the low Si concentration in the unexposed areas leads to the formation of residue (grass) in these nominally clear areas. This is minimized by using the post-exposure bake, but usually other techniques are employed to assure grass-free patterns. These include freon plasma

etching [15] or high bias oxygen plasma etching [16] prior to development or extensive overetching (~30%) after development.

The DESIRE[®] process is complex and requires specific (silylation and etching) equipment and processes. It has afforded superior patterning in quite thick films using 436 and 365 nm light and 5X demagnification step-and-repeat exposure tools. Lines and spaces as small as 0.5 μm were fabricated with 436 nm light while 0.4 μm patterns over 1 μm Al metalization patterns were made with 365 nm light [14-16].

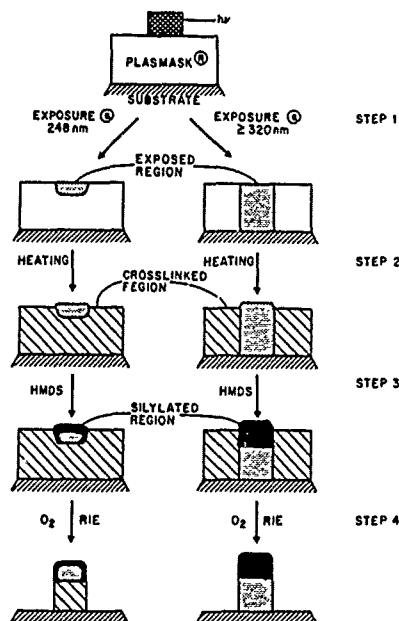


Figure 4. Schematic of the DESIRE[®] plasma-developed resist process using the Plasmask[®] resist and showing the exposure, heating, silylation, and O₂ RIE development steps for both UV and DUV exposure.

Extrapolation to short wavelength, deep-UV exposures at 248.4 nm and 193 nm should afford even higher resolution patterns. Using Lin's equations [17] to estimate resolution (ω) and depth-of-focus (Δ_z) as a function of resist and optical system parameters, values for ω and Δ_z at these shorter wavelengths may be estimated for an NA = 0.45 projection system as

$\lambda(\text{nm})$	$\omega(\mu\text{m})$	$\Delta_z(\mu\text{m})$
365	0.40	1.50
248.4	0.30	0.96
193	0.22	0.73

Several groups [18,19] including that of these authors [20] have investigated the predictions for 248 nm exposure. At this wavelength the Plasmask[®] absorption is more intense than at the longer wavelengths (Fig. 5) and ~15% of the incident light is absorbed in the topmost 1000Å of the film. This should limit exposure to a narrower surface region than the longer wavelength exposures and afford better permeation control (of HMDS),

better depth-of-focus than expected and perhaps slightly better resolution.

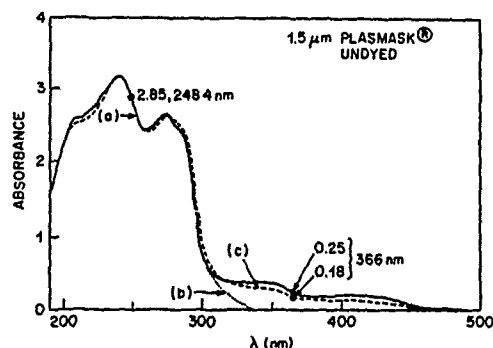


Figure 5. The absorption spectrum of 1.5 μm thick Plasmask[®] resist on quartz showing the sample as coated (a), exposed by 1 J/cm^2 of UV light (b) and exposed by 1 J/cm^2 of 248 nm light (c).

The results [18-20] do not agree with this hypothesis and the resist is quite insensitive at 248 nm ($\sim 300 \text{ mJ}/\text{cm}^2$) versus 365 nm ($150 \text{ mJ}/\text{cm}^2$). Grass-free, high-aspect-ratio patterns are obtained by overetching, but only for $0.40 \mu\text{m}$ and larger line and space patterns. $0.30 \mu\text{m}$ lines and spaces can be obtained using new dry processing methods, but still exhibit some line edge roughness and profile degradation while $0.25 \mu\text{m}$ features are discontinuous and ragged (Fig. 6) [20]. Apparently the etching selectivity between exposed and unexposed regions is not as high as in the longer wavelength exposures. One possible cause may be deep-UV induced side reactions such as crosslinking which have been observed by Yamashita and coworkers with the LMR resist [21] and also by Pierrat, et al. [22] with Plasmask[®] resist exposed by deep-UV contact printing.



Figure 6. Fine line patterns of (a) 0.30 and $0.25 \mu\text{m}$ lines and spaces and (b) $0.3 \mu\text{m}$ lines and spaces in 1.5 μm thick Plasmask[®] resist exposed to $300 \text{ mJ}/\text{cm}^2$ of 248 nm light on a DUV stepper.

Recently, there have been attempts to obtain positive tone near-surface functionalized, plasma-developed resists. The work of the Grenoble group [22] is particularly interesting for the scheme outlined in Fig. 7. They exposed Plasmask[®] under water free conditions in an e-beam exposure system (high vacuum) which gave highly crosslinked exposed regions entirely through the resist film. Then they exposed the entire sample to 1 J/cm^2 of 365 nm light, thus increasing the HMDS permeability in the initially unexposed regions. Silylation under more discriminating (lower temperature) conditions than usual selectively incorporated Si, as $\text{Si}(\text{CH}_3)_3$ from HMDS, into the unexposed regions, but not in the initially exposed and crosslinked areas. O_2 RIE development afforded high-aspect-ratio,

positive tone 0.3 μm lines and spaces with e-beam doses of $190 \mu\text{C}/\text{cm}^2$ at 50 keV and 750Å lines and spaces with doses of $500 \mu\text{C}/\text{cm}^2$ in a somewhat thinner film.

The Grenoble group also showed 0.2 μm line and space patterns exposed at 248 nm with a Karl Süss contract printer and claimed analogous results for deep-UV stepper exposures. We have tried to reproduce their results using a 0.38 NA, GCA 4200 5X stepper [20], using processing conditions as close to those reported [22] as possible, but without success. Only partial development occurred as shown by the SEMs of samples overdeveloped by at least 100% (Fig. 8).

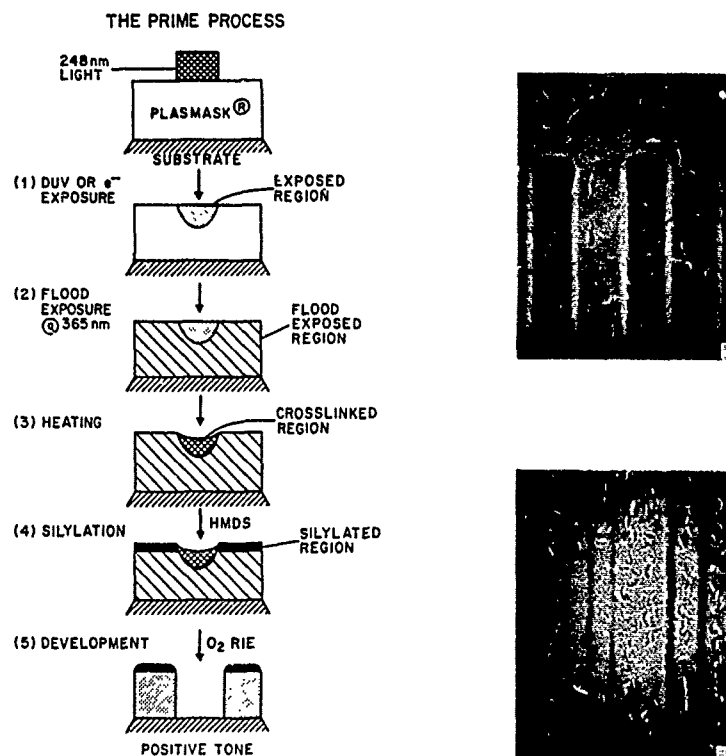


Figure 7.

Tone inversion scheme for Plasmask® resist.

Figure 8. SEMs of patterns obtained as in Fig. 6, but using 5X, 248 nm stepper exposures in an ambient environment of 2 μm (A) and 0.5 and 0.45 μm lines and spaces (B).

Another approach based on photogenerated acid that induces crosslinking of the phenolic resin to other acid-labile multifunctional reagents such as melamine methyl ethers [23] and benzylic alcohols and acetates [24] has been applied more successfully to deep-UV lithography. Silylation of phenolic groups with HMDS is used to induce etch resistance in unexposed areas while thermal crosslinking after exposure amplifies the initial photolysis step and minimizes HMDS permeation in exposed regions. In both cases near-surface (topmost 5000Å) Si-functionalization is used and some residue is observed in the exposed regions. This imaging scheme is summarized in Fig. 9a and has afforded $\sim 0.5 \mu\text{m}$

resolution, positive tone patterns thus far. Such schemes become very tenuous when silylation or the exposure depth is limited to the upper 1000Å of the resist. In the first instance there is too little Si present to adequately mask the unexposed regions during development, while in the latter case the requisite deeper permeation of HMDS, an isotropic process, intrudes beneath the crosslinked upper region as depicted in Fig. 9b, and restricts resolution. None of the above approaches using Si functionalization is a true surface imaging process. Therefore they are limited in their ultimate resolution under the poor depth-of-focus exposure conditions expected at $\lambda < 200$ nm. Even thin SiO_2 layers (several hundred Angstroms) have inadequate resistance to O_2 RIE conditions to act as good etching masks (selectivity versus aromatic polymers is $\sim 1:100$) for organic planarizing layers. Transition metal oxides have better etching selectivity (300-2000) and should adequately protect organic materials during O_2 RIE pattern transfer [25]. The presence of traces of such materials (Fe_2O_3 , TiO_2 and Co_2O_3) as contaminants during trilayer resist processing often leads to unwanted residue in unmasked areas. Because of this tenacious etch resistance in O_2 RIE we have sought to develop processes that utilize such materials. Thus far three metals (Al, Ti, W) and thin films of their metal oxides (Al_2O_3 , TiO_2 , WO_3) are particularly promising with TiO_2 exhibiting the best combination of properties.

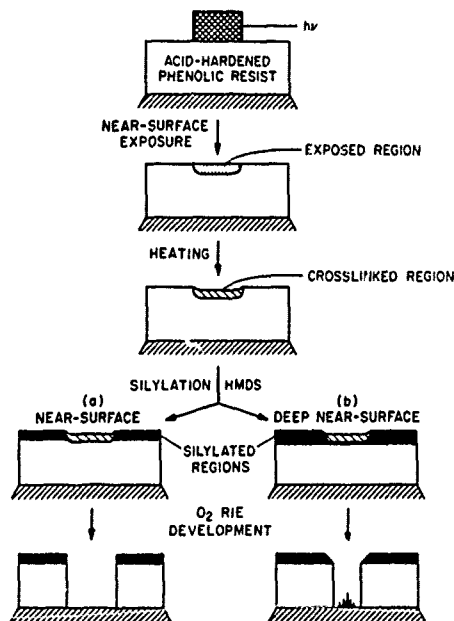


Figure 9. Scheme showing near-surface exposure of a resist, crosslinking of the exposed region by heating, silylation in the near-surface region (a) or even deeper into the film (b) and development by O_2 RIE.

We found that gaseous TiCl_4 is readily converted to a thin continuous TiO_2 film at hydrophilic polymer surfaces by reaction with sorbed water [26]. Initially, we employed this reaction to selectively coat hydrophilic polymers with TiO_2 , while their hydrophobic counterparts exhibited no similar reactions. First we employed this selective coating technique in bilayer resist processing [26] and later extended it to submicrometer trilayer pattern transfer techniques with reasonable defect densities [27]. Recently, the bilayer process was extended to other organic-on-organic bilayer applications by Kodak workers [28] and other groups [29] who silylated the exposed and developed topmost positive

photoresist layers with HMDS and transferred the silylated patterns into the lower layer by O_2 RIE. Fine patterns were obtained, but dimensional control of the relief image during processing was complicated by volumetric expansion of the silylated layer and inadequate masking in large silylated features. Analogous liquid silylation methods recently reported by Shaw and coworkers [30] may provide alternate solutions to these problems and require exact process control during the functionalization step.

3. SURFACE-SENSITIVE SYSTEMS USING A TiO_2 MASKING LAYER

We have focused our efforts on finding true surface-sensitive imaging processes using single layer or organic-on-organic bilayer resists. Starting from the observation that thin TiO_2 , WO_3 and Al_2O_3 films are excellent O_2 RIE etching masks we searched for ways to selectively deposit them on polymer surfaces. Extensive structure-property studies with nearly 100 polymers showed that polymer surface reactions with Ti or W and Al compounds were dominated by the water sorbed on the polymer surfaces [26]. We found that hydrophilic polymers containing polar hydrogen bonding groups (OH, $-NH_2$, etc.) readily reacted with $TiCl_4$ to give O_2 RIE resistant materials. Hydrophobic polymers such as poly(styrene) and poly(α -methylstyrene) did not react similarly with $TiCl_4$ and were very rapidly removed by O_2 RIE. A detailed surface analytical study using Rutherford backscattering spectrometry (RBS) and depth profiling X-ray photoelectron spectroscopy revealed that a very thin (30-100Å) TiO_2 film was deposited on the hydrophilic polymer surfaces, whereas Ti was incorporated at low atomic percentages throughout the hydrophobic aromatic polymers [31]. The latter apparently results from permeation of $TiCl_4$ into these polymers where it forms a weak charge transfer complex with the aromatic groups. This complex is relatively stable at room temperature. Thus $TiCl_4$ does not diffuse out of the film rapidly. Rather, water diffuses into the film when the wafer is brought into the ambient environment and TiO_2 is formed dispersed throughout the film. Because the TiO_2 is dispersed, the hydrophobic polymers are still rapidly removed by O_2 RIE with rates about $\frac{1}{4}$ those of the untreated polymers. In contrast, hydrophilic polymers treated with $TiCl_4$ etch at rates as low as 7×10^{-4} times that of the untreated polymer because of a continuous protecting TiO_2 layer on the polymer surface.

Based on these results a scheme was developed for imaging at polymer surfaces [6] (Fig. 10) which utilized the change in surface hydrophilicity, or a corresponding change in hydrophobicity, induced by radiation absorbed at the polymer surface. The scheme outlined in Fig. 16 shows how both resist tones can result, the crucial steps being selective sorption of water only on hydrophilic regions and selective metal oxide deposition on them.

Our initial idea for surface imaging was to use photosensitive, moderately or weakly hydrophilic polymers such as polyesters, polyethers and polycarbonates as precursors for the generation of very hydrophilic, strongly hydrogen bonding OH groups. Thus, we studied [32] a wide variety of polymers containing different types and amounts of oxygen containing groups. These included poly(4-methoxystyrene), poly(4-*t*-butylcarbonatostyrene), a number of aliphatic and aromatic methacrylates and copolymers of vinyl acetate and vinyl alcohol, copolymers of methyl methacrylate and methacrylic acid, *m*-cresol novolac resins having various degrees of acetylation, several polysulfones, and two aliphatic poly(ketones). Some of the results are collected in Table 1. The Ti concentrations were measured by x-ray fluorescence spectroscopy (XRFS) after $TiCl_4$ treatment and O_2 RIE.

Polymers 1-7 in the Table all have oxygen containing groups with varying hydrogen bonding and acidity characteristics. Entries 1, 2, 4, and 6 are strongly hydrogen bonding while 4 also is quite acidic. In comparison, polymers 3, 5 and 7 are non-acidic, mildly hydrogen bonding esters. However, all seven react readily with $TiCl_4$ to give extremely etch resistant films. The amount of Ti reacted ranges from a low value of 1×10^{16} Ti

atoms/cm² to a high of twice that amount. The etching rates are extremely low even though as much as 50% of the Ti was lost during etching. Even very weakly hydrogen bonding groups such as $-\text{SO}_2$, $-\text{NO}_2$, $-\text{OR}$ are sufficiently active to afford highly etch resistant films upon TiCl_4 treatment. Thus, the hydrogen bonding properties of polymers appear to determine the degree of water sorption and surface reaction to form TiO_2 .

Only very hydrophobic polymers such as poly(styrene) PS (Table 1) behave differently. More Ti is present in PS than on all other films, but less Ti is lost upon etching and the etching rate is still high. We tested copolymers of styrene and allyl alcohol having various compositions to determine the minimum amount of the strongly hydrogen bonding OH group needed to convert polystyrene to a water sorbing polymer. Surprisingly, as little as ~0.3 atom % OH was sufficient to give TiO_2 functionalized polymers with very low etching rates.

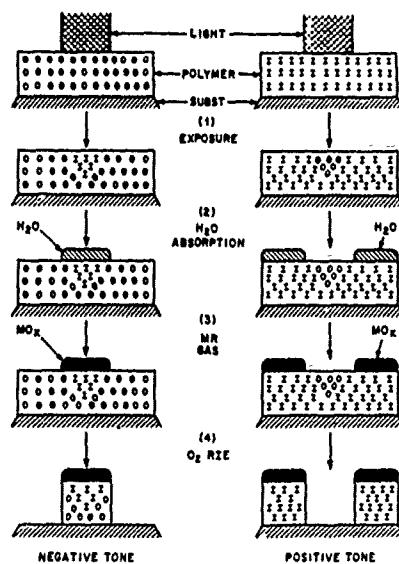


Figure 10. Photo-oxidative and photoreductive imaging schemes in which (1) hydrophobic, strongly absorbing groups O are converted to hydrophilic groups I and the converse (2). Subsequent steps involve sorption of water, reaction with a readily hydrolyzed inorganic or organometallic compound MR and O_2 RIE development.

These results prompted us to develop a new photooxidative [6,32] surface-sensitive imaging process shown in Fig. 11. It is modeled on the well known photooxidation of polystyrene [33,34] that has garnered considerable interest over the past 25 years and recent mechanistic studies of photooxidized surfaces as well [35,36]. It is generally agreed that 254 nm initiated photooxidation occurs primarily via free radical intermediates that first cleave the methyne C-H bond and react further by thermal processes to give more oxygen bearing functional groups such as OH , $>\text{C}=\text{O}$ and $-\text{CO}_2\text{H}$.

Since surface photoreactions are favored by high absorption cross-sections, we selected 193 nm ArF excimer laser light in our initial experiments with the aromatic hydrophobic polymers listed in Table 2. All have high absorption while three have readily abstracted methyne hydrogens. However, only the monobenzenoid systems are photoactive while the most sensitive one has no readily abstracted hydrogen. The sensitivity curves are highly

Table 1 Ti Present In or On Various Polymer Films Upon Treatment' with TiCl_4 at 10 Torr for 2 Minutes

Polymer	Ti ($\times 10^{-15}$ atoms/ cm^2) in 1 μm Thickness Films		O_2 RIE Rate ^c ($\text{\AA}/\text{min}$)	ΔTi Upon Etching (%)
	After Treatment	After Etching ^b		
1. Hard Baked Positive Photoresist HPR-206	20.3	16.4	0 (580)	19
2. <i>m</i> -Cresol Novolac	13.0	6.2	15 (660)	52
3. 100% Acetylated <i>m</i> -Cresol Novolac	12.4	9.8	10	21
4. Poly(methyl methacrylate-co-methacrylic acid) (75:25 mole %)	12.9	8.1	10 (1560)	37
5. Poly(methyl methacrylate)	14.0	7.4	20 (1500)	47
6. Poly(vinyl alcohol)	12.8	11.3	27 (1800)	17
7. Poly(vinyl acetate)	9.9	7.4	6	26
8. Poly(styrene)	26.2	24.0	300 (610)	8

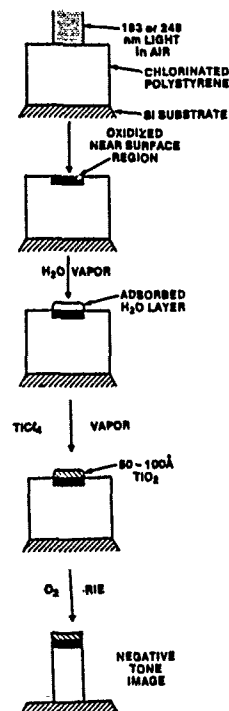
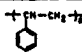
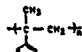
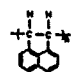



Figure 11. Photo-oxidative imaging process for hydrophobic aromatic polymers via an hydrophilic oxidized surface layer which selectively sorbs H_2O , reaction with TiCl_4 to give TiO_2 on the polymer surface and O_2 RIE development to give negative tone patterns.

Table 2 Lithographic Results for Various Aromatic Polymers at 193 nm

	Polymer	ϵ_{193} (l/mole-cm)	Image Type, Thickness	Incident Dose (mJ/cm ²)
1.	 Poly(styrene)	54,000	Negative, Full	6-30
2.	 Poly(alpha-methylstyrene)	80,000	Negative, Full	4-10
3.	 Poly(acenaphthylene)	6,500	None	≤6000
4.	 Poly(N-vinylcarbazole)	14,000	None	≤6000

dependent on radiation fluence as depicted by the plots presented in Fig. 12. Better sensitivity is achieved for higher fluence which suggests the role of two photon processes and slow radiationless decay of excited state intermediates in the monobenzenoid systems having excited states with considerable energy differences. Note that the two polybenzenoid aromatics, which have smaller energy differences between excited states, are not active.

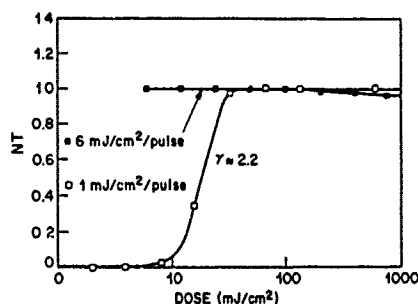


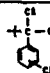
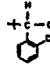
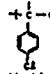
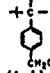
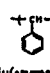
Figure 12. Influence of 193 nm light flux on the sensitivity curves for poly(styrene) where NT is normalized thickness.

We attempted to obtain patterns with 193 nm light using a Leitz IMS 36X demagnification exposure system, but were plagued by system problems [37]. Thus, we directed our attention to the 248.4 nm wavelength employed in a 0.38 NA, KrF excimer laser, 5X demagnification step-and-repeat exposure apparatus. We quickly found that poly(styrene), and even the 100 fold more absorbing polymer poly(4-vinylbiphenyl), barely afforded traces of an image at 500 mJ/cm² dose. Since the fluences are nearly equivalent at 248 and 193 nm (0.2 and 1 mJ/cm²/pulse, respectively) the differences can be ascribed to lower absorption and perhaps lower quantum yields for oxidation at the longer wavelengths.

To increase the probability for photolytic cleavage we investigated a variety of hydrophobic polystyrenes containing halogen and halomethyl groups. Poly(bromostyrene) and poly(iodostyrene) were unreactive, but several chlorine-containing polystyrenes proved quite responsive despite their weak absorption ($\epsilon_{248} < 400$ l/mole-cm). Results for these polymers are summarized in Table 3. Chlorinated poly(styrene) CPS with ring and

methyne carbon chlorination was most sensitive followed closely by chloromethylated polystyrene (CMPS). For CPS the sensitivity increased with the degree of chlorination and was optimum at 1.15 Cl/monomer unit. Performance also was dependent on O₂ RIE time. Sensitivity decreased with etching time while contrast initially increased, but latter decreased when most of the TiO₂ protecting layer had been removed by sputtering (Fig. 13). High resolution patterns were resolved at the optimum dose (250-300 mJ/cm²) and etching time (21 min) as shown by the SEMs for 0.8 and 0.4 μm lines and spaces in 1.2 μm thick films (Fig. 14). The widths of both sets of lines were not changed when the dose was increased by 20% indicating a wide process window. However, considerable residue was evident in the unexposed regions.

Table 3
Lithographic Results for Several
Chlorine-Containing Poly(styrenes)
Exposed at 248 nm

	Polymer	Cl/C	Image Type, Thickness	Dose (mJ/cm ²)
1.	 Chlorinated Poly(styrene)	0.143	Negative, Full	200
2.	 Poly(2-chlorostyrene)	0.125	Negative, Fair	500
3.	 Poly(4-chlorostyrene)	0.125	Negative, Moderate	500
4.	 Poly(4-chloromethylstyrene)	0.111	Negative, Full	300
5.	 Poly(styrene)	0.0	Negative, Trace	500

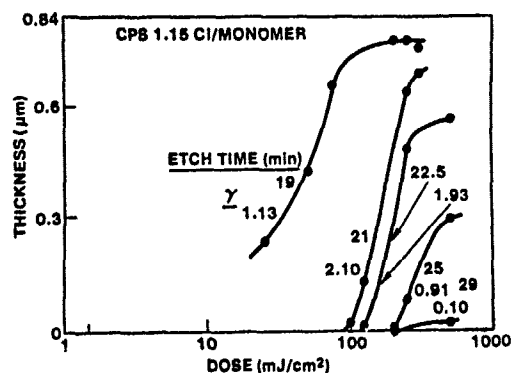


Figure 13. Normalized thickness versus dose plots for CPS with 1.15 Cl/monomer unit after 248 nm exposure, treatment with TiCl₄ and O₂ RIE development for various times.

The residue results from permeation of TiCl_4 into unexposed regions during the gas-polymer metalization step and is independent of the exposure wavelength and process. We employed XRFs to measure the amount of Ti present as a function of exposure dose for 193 nm exposures and found very high concentrations at low doses where the film is completely developed by O_2 RIE and 3 times lower concentrations at higher doses where

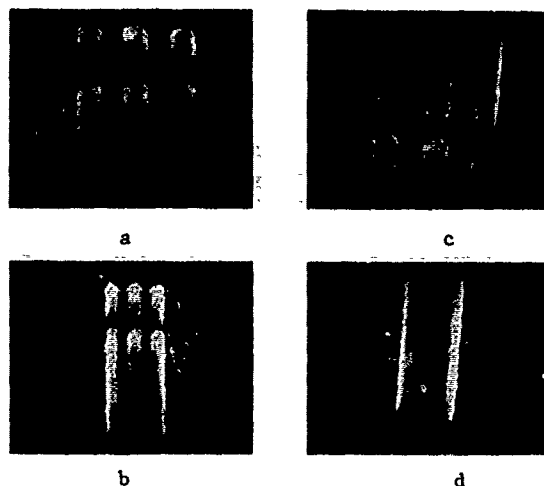


Figure 14. SEMs of 0.8 and 0.4 μm lines and spaces in 1.2 μm of CPS resist for 248 nm doses of 250 (a,b) and 300 mJ/cm^2 (c,d).

masking was very effective during development (Fig. 15). Using polymers such as chlorinated poly(4-vinylbiphenyl) CPVB, which has a 100 fold stronger absorption at 248 nm, we obtained patterns with even greater residue, but at somewhat lower dose (150 mJ/cm^2). In this instance the greater residue formed may result from the greater solubility of TiCl_4 in this polymer since the charge-transfer complex is expected to be more stable. It also may result from partial autooxidation of the surface after spin coating and during the baking step that must be done at temperatures approaching the high T_g of this polymer ($\sim 200^\circ\text{C}$).

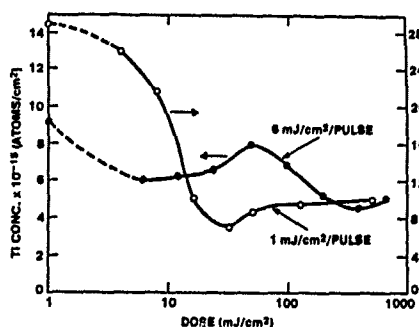


Figure 15. Effect of 193 nm light dose and fluence on the amount of Ti reacted with polystyrene films.

Residue formation presently prevents consideration of this technology for device manufacturing. There are several approaches for eliminating it including using a very dilute 1:30 buffered $\text{HF}:\text{H}_2\text{O}$ liquid etch after development. Other methods would involve

preventing or at least severely limiting permeation perhaps by means of thermal or photochemical crosslinking, use of more bulky reagents whose steric requirements severely impede diffusion or development of new processing methods. In this latter category we have intensely investigated the role of temperature in retaining water sorbed on polymer surfaces and TiCl_4 sorption throughout the hydrophobic polymer films. Above 35°C no TiCl_4 is found in poly(styrene) after a 2 minute TiCl_4 treatment and the subsequent pump down in our standard process (Table 1). Unfortunately, only small amounts of Ti ($<10^{15}$ atoms/ cm^2) were found on hydrophilic polymers (HB HPR-204) under the same conditions. Thus, at 35°C no films were functionalized while at 25°C considerable selectivity was observed.

Control of permeation appears to be more promising. In studying this we have used two organic layers, a thin chlorinated poly(styrene) topmost imaging layer $0.4\ \mu\text{m}$ thick and a $1.2\ \mu\text{m}$ thick lower layer of hydrophobic crosslinked PCMS. The latter was crosslinked by exposure to $5\ \text{J}/\text{cm}^2$ of broad band deep-UV radiation prior to over-coating with CPS. Alternatively a lower crosslinked hydrophilic layer, $1.2\ \mu\text{m}$ of hard-baked HPR-204, was employed. For each bilayer resist, the scheme outlined in Fig. 16 was followed. With a hydrophilic lower layer patterns were formed, but were highly distorted and contaminated by large circular defects reaching above the film surface. The hydrophobic bilayer film gave high resolution patterns with much less "grass" than in a $1.2\ \mu\text{m}$ thick single layer CPS film (Fig. 17). Although this result is in the right direction it still is not sufficient for device patterning. Other problems are the somewhat poor sensitivity and the line edge roughness which may result from the weak poly(styrene) absorption. We are presently seeking solutions to these problems by investigation of new highly absorbing polymeric materials (at $248\ \text{nm}$) and new organometallic or inorganic reagents that have low or zero permeation rates.

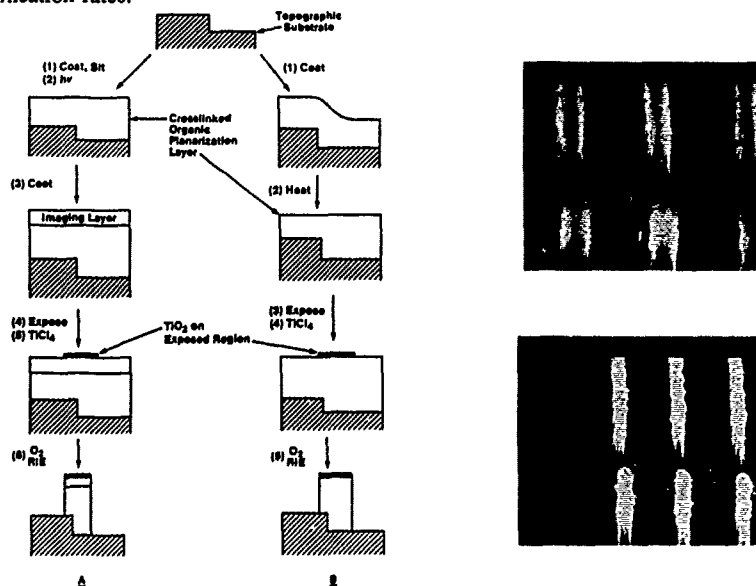


Figure 16. Organic-on-organic photooxidized bi-layer resist scheme with a thin, absorbing imaging layer on a thick, crosslinked organic planarizing layer and processing analogous to Fig. 11.

Figure 17. SEMs of 0.8 and $0.4\ \mu\text{m}$ line and space patterns in $0.4\ \mu\text{m}$ CPS on $1.2\ \mu\text{m}$ of DUV crosslinked poly(chloromethyl styrene). Note the reduced residue relative to that in Fig. 14.

4. CONCLUSIONS

We strongly believe that surface imaging will be the dominant photolithographic process for resolution $\leq 0.35 \mu\text{m}$. At least three methods appear to be useful in this regime: (1) near-surface exposure and functionalization with Si-containing reagents to a controlled depth (2) surface exposure altering surface hydrophobicity and functionalization with more etch resistant inorganic species than Si (3) surface exposure, functionalization with metallic catalytic species and electroless deposition of ultrathin highly etch resistant metal layers.

From our present experiments with the first and second options we can estimate the resolution which might be attained using future shorter-wavelength lithography systems. The wavelengths we choose are 193 nm, which is being intensely investigated at Lincoln Laboratories [38], and 13.0 nm which was recently postulated for a new reflective optic [39] imaging system [40] by Wood, Silfvast and Jewell for x-ray lithography. For the former an NA = 0.40 is assumed, whereas an NA = 0.10 is used for the latter [40]. A k_1 value of 0.50 is used to calculate resolution ω based on the contrast of the Plasmask[®] and CPS resists, while a more standard value of 0.35 is used for k_2 to calculate Δ_z . The results presented in Table 4 predict that imaging with 130Å light will define sub 0.1 μm features with a depth of focus comparable to that for vacuum and deep-UV light where only 0.25 μm patterns are feasible. Depth of focus is sufficiently low such that device planarization or resist planarization would be required. Overall, the coupling of surface-sensitive resist technology with planarization and new optical lithographic exposure systems seems to be a good approach to ultrasmall pattern fabrication and we expect that work in this area will be intense over the next several years.

Table 4
Resolution and Depth of Focus
Values for Surface-Sensitive
Resists with $k_1 = 0.50$ and
 $k_2 = 0.35$

λ (nm)	NA	ω (μm)	Δ_z (μm)
248.4	0.40	0.31	0.54
193.0	0.40	0.24	0.42
13.0	0.10	0.065	0.46

References

- [1] H. Schonhorn in "Polymer Surfaces", D. T. Clark and W. J. Feast, Ed., John Wiley and Sons, Inc., New York, 1978, pp. 213-233; S. Affrossman, J. M. R. MacAllister, R. A. Pethrick, B. Thomson, N. M. D. Brown and B. J. Meehan, in "Polymer Surfaces and Interfaces", W. J. Feast and H. S. Munro, Eds., John Wiley and Sons, Inc., New York, 1987, pp. 99-117.
- [2] U. B. Sletyr, M. Sara and D. Pum, *Microelectronic Eng.*, 9, 13 (1989).
- [3] Papers in "Advances in Polymer Friction and Wear", L.-H. Lee, Ed., Vol. 5A and 5B in the "Polymer Science and Technology Series", Plenum Press, New York, 1974; "Polymer Wear and Its Control", L.-H. Lee, Ed., ACS Symp. Series 287, Amer. Chem. Soc., Washington, DC, 1985.
- [4] E. J. Kramer in "Electronic Packaging and Materials Science", E. A. Giess, K.-N. Lu and D. R. Uhlmann, Eds., *Mat'ls Res. Soc. Symp. Proc.*, 40, 227 (1985).

- [5] K. N. Somasekharan and R. V. Subramanian in "Modification of Polymers", C. E. Carraher, Jr. and M. Lauda, Eds., ACS Symp. Series 121, Amer. Chem. Soc., Washington, DC, 1980, pp. 165-181.
- [6] G. N. Taylor, O. Nalamasu and L. E. Stillwagon, *Microelectronic Eng.*, **9**, 513 (1989).
- [7] S. L. Chow, N. E. Hedgecock, M. Schlesinger and J. Rezek, *J. Electrochem. Soc.*, **119**, 1013 (1972).
- [8] J. Finter, U. S. Patent 4677155 (1987).
- [9] K. J. Orvek, C. M. Garza and R. R. Doering, *Proc. SPIE*, **1086**, 615 (1989).
- [10] G. N. Taylor, L. E. Stillwagon and T. N. R. Venkatesan, *J. Electrochem. Soc.*, **131**, 1654 (1984).
- [11] S. A. MacDonald, H. Ito, H. Hiraoka and C. G. Willson, "Proc. Reg. Tech. Conf.", Mid-Hudson Sect., Soc. Plast. Eng., Ellenville, New York, Oct. 28-30, 1985, pp. 177-196.
- [12] G. N. Taylor and T. M. Wolf, *Polym. Eng. and Sci.*, **20**, 1087 (1980).
- [13] G. N. Taylor and T. M. Wolf and J. M. Moran, *J. Vac. Sci. and Technol.*, **19**, 872 (1980).
- [14] F. Coopmans and B. Roland, *Solid State Technol.*, **30**, 6, 93 (1987).
- [15] F. Coopmans and B. Roland, *Proc. SPIE*, **631**, 34 (1986).
- [16] P. Lombaerts, B. Roland, A. Selino, A. M. Goethals and L. van den Hove, *Proc. Microcircuit Eng.* **88**, Cambridge, England, Sept. 26-28, 1989, Abst. P-29.
- [17] B. J. Lin, *Microelectronic Eng.*, **6**, 31 (1987).
- [18] S. Das, H. Gaw and R. Hollman, "Proc. 1988 KTI Conf. on Microlithography", San Diego, Calif., Nov. 10-11, 1988.
- [19] C. M. Garza, G. R. Misium, R. R. Doering and B. Roland, *Proc. SPIE*, **1086**, 583 (1989).
- [20] R. S. Hutton, R. A. Kostelak, O. Nalamasu, A. Kornblit, S. McNevin and G. N. Taylor, in press.
- [21] Y. Yamashita, R. Kawazu, K. Kawamura and S. Ohno, *J. Vac. Sci. and Technol.*, **B3**, 314 (1985).
- [22] C. Pierrat, S. Tedesco, F. Vinet, M. Lerme and B. Dal' Zotto, "Proc. 33rd Int'l Symp. on Electron, Ion and Photon Beams", Monterey, Calif., May 30-June 2, 1989, Abst. L-39.
- [23] J. W. Thackeray, G. W. Orsula, E. K. Pavelchek, L. E. Bogan, Jr., A. K. Berry and K. A. Graziano, *Proc. SPIE*, **1086**, 324 (1989).
- [24] B. Reck, R. D. Allen, R. J. Twieg, C. G. Willson, S. Matuozczak, H. D. H. Storer, N. H. Ti and J. M. J. Fréchet, "Proc. Reg. Tech. Conf.", Mid-Hudson Sect., Soc. Plast. Eng., Ellenville, New York, Oct. 30-Nov. 2, 1988, pp. 63-72.
- [25] S. K. Gupta and C. G. Audein, *Proc. SPIE*, **469**, 179 (1984) and references therein.
- [26] L. E. Stillwagon, P. J. Silverman and G. N. Taylor, *Proc. Reg. Tech. Conf.*, Mid-Hudson Sect., Soc. Plast. Eng., Ellenville, New York, Oct. 28-30, 1985, pp. 87-103.
- [27] L. E. Stillwagon, A. Kornblit and G. N. Taylor, *J. Vac. Sci. and Technol.*, **E5**, 2229 (1988).

- [28] W. C. McColgin, R. C. Daley, J. Jech, Jr. and T. B. Brust, *Proc. SPIE*, 920, 253 (1988).
- [29] H. Hiraoka, A. Patloch and C. Wade, "Proc. 33rd Int'l Symp. on Electron, Ion and Photon Beams", Monterey, Calif., May 30-June 2, 1989, Abst. L-34.
- [30] J. Shaw, M. Hatzakis, E. Babieh, J. R. Paraszczak, D. Witman and K. Stewart, *ibid*, Abst. H-2.
- [31] G. N. Taylor, L. E. Stillwagon, F. A. Baiocchi and M. J. Vasile, *Microelectronics Eng.*, 6, 381 (1987).
- [32] O. Nalamasu, F. A. Baiocchi and G. N. Taylor, "Proc. ACS Divis. Polym. Mat'ls: Sci. and Eng.", Vol. 60, Amer. Chem. Soc., Wash., DC, 1989, pp. 381-384.
- [33] G. Grassi and N. A. Weir, *J. Appl. Polym. Sci.*, 9, 963, 987, 999 (1965).
- [34] G. Geuskens, D. Balyens-Volant, G. Delaernois, Q. Lu-Vinh, W. Piret and C. David, *Eur. Polym. Journal*, 14, 291, 298 (1978).
- [35] J. Peeling and D. T. Clark, *Polym. Degrad. and Stabil.*, 3, 97 (1981).
- [36] D. T. Clark and H. M. Munro, *ibid*, 8, 213 (1984); *ibid*, 9, 63, 185 (1984).
- [37] O. Nalamasu and G. N. Taylor, *Proc. SPIE*, 1086, 186 (1989).
- [38] M. Rothschild and D. J. Ehrlich, *J. Vac. Sci. and Technol.*, B6, 1 (1988).
- [39] A. M. Hawryluk and L. G. Seppala, *ibid*, B6, 2162 (1988).
- [40] O. R. Wood, II, W. T. Salvast and T. Jewell, *ibid.*, B7, 1989, to be published.

SURFACE CHEMISTRY OF DIMETHYLALUMINUM HYDRIDE AND TRIMETHYLALUMINUM ON ALUMINUM

Daniel R. Strongin* and Paul B. Comita
IBM Corporation, Almaden Research Center, 650 Harry Road, San
Jose, California 95120

*Permanent address: Department of Chemistry, State University
of New York, Stony Brook, New York 11794

ABSTRACT

The surface chemistry of dimethylaluminum hydride (DMAH) and trimethylaluminum (TMA) on aluminum has been investigated with temperature programmed desorption (TPD), and Auger electron spectroscopy (AES). The TPD spectra of TMA shows a single desorption peak with a peak maximum which shifts from 190 to 200 K for surface coverages of 0.5 and 2.0 monolayers (ML) respectively. DMAH desorbs from an aluminum surface between 198 and 236 K at surface coverages ranging from 0.1 to 4.0 ML. A second DMAH desorption peak is observed at about 200 K (2.0 ML) when the aluminum surface is contaminated with carbonaceous species, resulting from the decomposition of DMAH. Both DMAH and TMA yield methane as a reaction product on the aluminum surface. The surface reactions of DMAH on aluminum also yield TMA as a reaction product.

INTRODUCTION

Interest in the surface reactions of alkylaluminum compounds on aluminum surfaces has been intensified by the discovery of reactive aluminum species which produce pure metal films [1-4]. The nature of the ligands bonded to aluminum can influence the reaction channels available to the alkylaluminum molecule, and can therefore influence the metal formation reactions. For example, DMAH has been reported to produce aluminum[2], in contrast to the fully alkylated species TMA, which produces predominantly aluminum carbide [5]. We have investigated the reactions of DMAH and TMA on a clean aluminum surface in an attempt to understand the elementary surface reactions which underly these experimental observations. We report here that the production of methane is a reaction product (during TPD experiments) resulting from surface decomposition of DMAH and TMA. DMAH decomposition on the aluminum surface yields about an order of magnitude more methane product than does an equivalent initial surface concentration of TMA. It is also suggested by the TPD results that TMA is a reaction product, formed by DMAH surface reactions. The production of TMA from surface DMAH might provide a reaction channel for the removal of carbon

and the deposition of pure aluminum. However, AES shows that the carbon coverage on the aluminum substrate is approximately equivalent after either DMAH or TMA temperature programmed desorption experiments.

EXPERIMENTAL

TPD experiments were performed by adsorbing either DMAH or TMA (Alfa, electronic grade > 99.99% purity) on an aluminum foil (Aldrich >99.99% purity) which was held at about 90 K. The sample was resistively heated at 8 K/sec, and the sample temperature was monitored with a chromel - alumel thermocouple, and the desorbing species were detected with an Extrel (model C50) mass spectrometer.

Due to the electron deficiency of aluminum in both DMAH and TMA bonding between the monomeric species is found experimentally [5,6]. Under our experimental conditions DMAH exists primarily in its trimeric form, linked by aluminum - hydrogen bridges [5]. TMA exists in a dimeric form, linked by aluminum - methyl bonds [6]. Thus, in the experiments presented later the aluminum surface is being primarily dosed with either DMAH trimer or TMA dimer. The cracking pattern for each species was obtained by aligning the dosing source directly with the mass spectrometer. The cracking pattern obtained in this manner was identical to the pattern obtained from the desorbing species during the TPD experiments indicating that DMAH trimer and TMA dimer accounted for the desorbing alkylaluminum compounds. The m/e 159 intensity ($\text{H}_3\text{Al}_3(\text{CH}_3)_5^+$) was used to monitor DMAH trimer desorption and m/e 129 ($\text{Al}_2(\text{CH}_3)_5^+$) was monitored for TMA dimer desorption.

Static secondary ion mass spectrometry (SIMS) experiments were carried out with 2 keV Ar^+ ions. Coverages of DMAH and TMA quoted in this paper were estimated by using static SIMS and are indicated in monolayers (ML). The m/e 57 signal ($(\text{CH}_3)_2\text{Al}^+$) was monitored during the SIMS experiment as a function of TMA or DMAH exposure. One ML is defined, in this study, as the adsorbate coverage which produces no further increase in the m/e 57 signal intensity. Coverages are also assumed to vary linearly with dose time. Sample cleaning was achieved by repeated Ar^+ ion bombardment and anneal cycles. Surface cleanliness was monitored by AES, using a single pass cylindrical mirror analyzer. Carbon coverages quoted in the text were determined by using the sensitivity factors for aluminum and carbon in ref. [7].

RESULTS AND DISCUSSION

Figure 1 shows TPD spectra for DMAH adsorbed on atomically clean aluminum as a function of surface coverage. At DMAH coverages between 0.1 and 0.5 ML only one desorption

peak is evident, shifting in temperature from 198 K to 220 K. This rapid increase in the temperature at peak maximum at low DMAH coverages suggests that there are strong attractive interactions between neighboring DMAH molecules on the aluminum surface. At higher DMAH coverages (1 ML) an additional desorption state at about 200 K appears, while the high temperature peak shows fractional order kinetics (an increasing peak maximum with adsorbate coverage), suggesting that this high temperature peak is due to the desorption of DMAH which had been molecularly adsorbed in a condensed state on the aluminum surface.

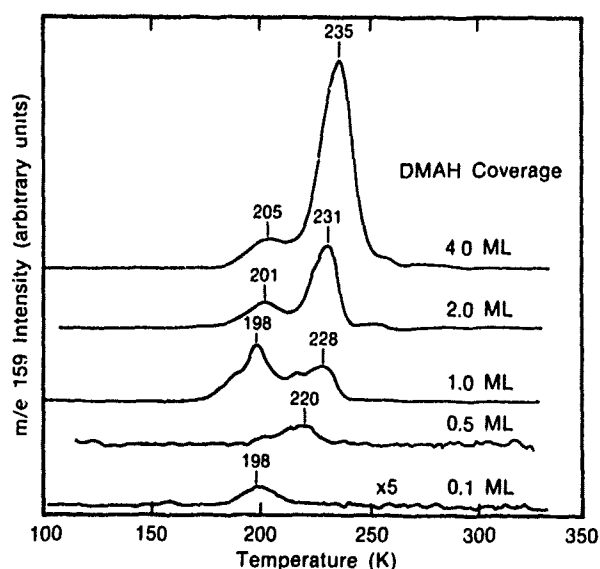


Figure 1. DMAH/Al TPD spectra for various DMAH coverages.

It is important to note that each TPD spectrum shown in figure 1 was performed after the aluminum surface was cleaned of any carbon contamination. It was found that after DMAH TPD experiments (where the DMAH coverage was greater than 1 ML) a carbon surface concentration of 0.25 was left on the aluminum surface after a single DMAH adsorption - desorption cycle. If the surface was not cleaned the carbon surface concentration increased and then plateaued at 0.5 after three more TPD experiments. This carbon buildup altered the DMAH TPD profiles by decreasing the intensity of the high temperature peak and increasing the intensity of the low temperature DMAH desorption peak. For example, after four 2.0 ML DMAH adsorption - desorption cycles the intensity

of the high temperature peak decreases by about a factor of 5, while the low temperature peak increases by a factor of 5. These results suggest that the high temperature desorption peak results from DMAH desorbing from clean aluminum and the low temperature TPD peak results from DMAH desorbing from carbon contaminated aluminum.

TMA temperature programmed desorption spectra are shown in figure 2 as a function of coverage. As is the case with DMAH the adsorbed TMA produces a carbon coverage of about 0.5, but this carbon contamination did not affect the TPD profile for TMA.

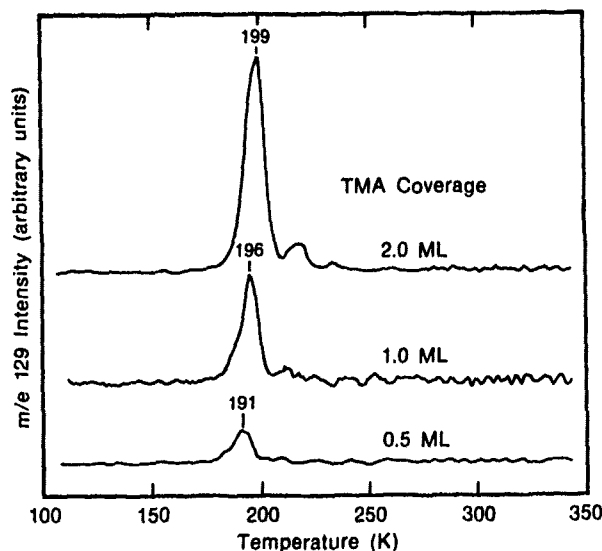


Figure 2. TMA/Al TPD spectra for various TMA coverages.

Product formation from DMAH and TMA

Figures 3 a and b show gas phase products detected during TPD experiments for both DMAH and TMA reactants respectively. In the case of DMAH, both methane (m/e 15) and a product with a cracking fragment having a m/e - 129 are observed. The contribution to m/e 129 by DMAH has been deconvoluted from the spectrum. Cracking fragments with a m/e greater than 174 (DMAH parent ion) were not detected in the TPD experiments suggesting that the m/e 129 peak is due to a compound with a molecular weight less than DMAH.

The presence of TMA dimer as a product would account for the m/e 129 peak and is just the reverse reaction of a known synthetic route to DMAH from TMA and hydrogen [6]. The production of TMA also would allow the production of pure aluminum from the reaction of DMAH on aluminum ($\text{DMAH} = 2/3\text{TMA} + 1/2\text{H}_2 + 1/3\text{Al}$), which has been found experimentally [5].

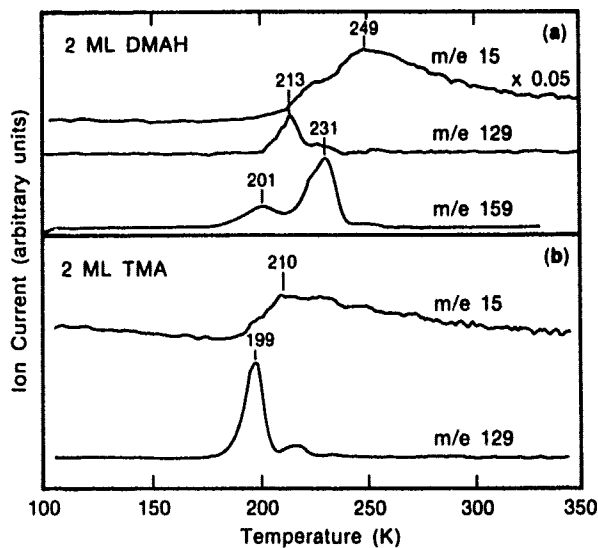


Figure 3. a) DMAH reaction products, b) TMA reaction products.

The production of methane product is also found from the surface reactions of both DMAH and TMA as shown in figures 3 a and b. The yield of methane is an order of magnitude greater when DMAH is the reacting surface species than when TMA is the adsorbed species on the aluminum surface. The presence of atomic hydrogen bound closely to the methyl group on DMAH might account for this observation. It has been shown in previous work [8] that methyl groups deposited on clean aluminum by methylhalides were not stable beyond 150 K. In this research we observe the production of methane between 200 and 300 K implicating the existence of methyl groups at temperatures higher than 150 K. This observation suggests that methyl groups are stabilized in the DMAH and TMA molecule (or in the decomposition fragments of DMAH and TMA) on the aluminum surface. This stabilization of the methyl

group might allow hydrogenation to occur producing methane product and avoiding decomposition which probably results in the carbonaceous overlayer.

SUMMARY

Temperature programmed desorption and secondary ion mass spectroscopy experiments have been presented for the DMAH/Al and TMA/Al systems. The results of this research are summarized as follows:

- 1) DMAH is found to desorb from an aluminum surface in its trimeric form and TMA in its dimeric structure.
- 2) Both DMAH and TMA leave residual carbon (surface coverage of about 0.5) on the surface after the TPD experiments.
- 3) DMAH is found to produce about four times as much methane product as TMA.
- 4) The research suggests that the surface reactions of DMAH produce TMA as a reaction product and this pathway may offer a pathway for the deposition of pure aluminum.

REFERENCES

1. B.E. Bent, R.G. Nuzzo, and L.H. Dubois, J. Am. Chem. Soc. 111 (1989).
2. T. Cacouris, G. Scelsi, P. Shaw, R. Scarmozzino, R.M. Osgood, and R.R. Krchnavek, Appl. Phys. Lett. 52, 1865 (1988).
3. M.L. Green, R.A. Levy, R.G. Nuzzo, and E. Coleman, Thin Solid Films 114, 367 (1984).
4. H.O. Pierson, Thin Solid Films 45, 257 (1977).
5. J.P. Oliver, in Advances in Organometallic Chemistry, Vol. 15, edited by F.G.A. Stone and R. West (Academic Press, New York, 1977), p. 239.
6. G.E. Coates in Organometallic Compounds, Methuen's Monographs on Chemical Subjects, edited by G.J. Emeleus and D.W.G. Style (Methuen and Co., London, 1956), p.72.
7. L.E. Davis, N.C. MacDonald, P.W. Palmberg, G.E. Riach, and R.E. Weber, Handbook of Auger Electron Spectroscopy, (Physical Electronics Div., Perkin - Elmer Corp., MN, 1976), p.13.
8. J.G. Chen, T.P. Beebe, J.E. Crowell, and J.T. Yates, J. Am. Chem. Soc. 109, 1726 (1987).

MECHANISM OF CHROMIUM DEPOSITION FROM $\text{Cr}(\text{CO})_6$ BY UV LASER LIGHT

R. NOWAK AND P. HESS

Institute of Physical Chemistry, University of Heidelberg,
Im Neuenheimer Feld 253, D-6900 Heidelberg, F. R. G.

ABSTRACT

The mechanism of metal film deposition from carbonyls as precursors is discussed in detail. It is shown that different species produced by UV laser irradiation in the gas phase contribute to film growth. Highly reactive species such as metal atoms may be important during the nucleation phase, whereas more stable carbonyls are responsible for the main growth process. This indicates that the main decarbonylation effect occurs at the surface. The higher level of impurity incorporation in chromium films in comparison with nickel films is explained by the relative position of the Fermi level in the d-band of Ni and Cr with respect to the $2\pi^*$ level of CO, which favors CO bond dissociation in the case of chromium.

INTRODUCTION

Laser-induced chemical vapor deposition (LICVD) is a rapidly expanding field. This is mainly due to the unique new possibilities in materials processing and microelectronics fabrication. Chemical vapor deposition of metals using carbonyls as film precursors has been studied carefully in recent years. For example, detailed results are available for nickel [1-3] and for chromium [4-15].

Carbonyls possess a relatively high vapor pressure and strong absorption bands in the UV spectral region. Thus, according to their spectroscopic and thermodynamic properties, carbonyls are well suited as film precursors. The simplest mechanism for deposition of a pure metal film from the metal carbonyl with UV laser radiation would be selective excitation and photodissociation of the weak metal ligand bond in the gas phase and/or at the surface. The CO ligands should be desorbed quantitatively from the surface. This simple concept fails, if the strong CO bond dissociates in an autocatalytic process on the growing film, because the highly reactive O and C atoms form oxides and carbides, which are incorporated into the growing network.

The deposition of relatively pure films containing more than 90% metal was reported for nickel [2,3] as well as chromium [6]. However, in the case of chromium this first result never was confirmed. Careful experiments by different groups showed that the typical chromium content is between 50% and 60% for deposition from the hexacarbonyl using a pulsed KrF laser at 248 nm [8,12,15] and between 20% and 40% employing a frequency doubled cw Ar⁺ laser at 257 nm [10,11] (see Fig. 1).

A more detailed discussion of the differences between the nickel and chromium system, based on a better understanding of the reaction dynamics and surface chemistry involved, is the purpose of this paper.

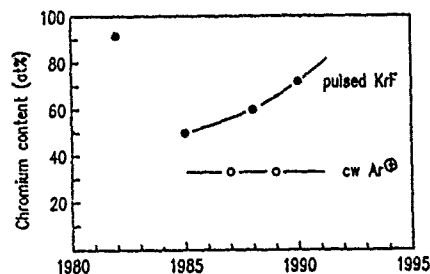


Fig. 1: Chromium content of Cr(O,C) films deposited by pulsed KrF laser radiation [6,8,12,15] and by frequency doubled Ar⁺ laser radiation [10,11].

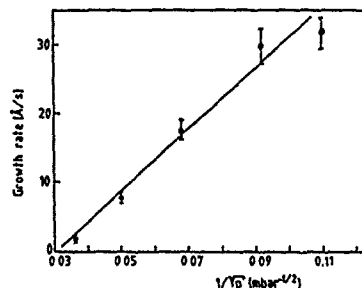


Fig. 2: Growth rate versus reciprocal square root of hydrogen partial pressure for chromium film deposition from Cr(CO)₆ at 248 nm.

EXPERIMENTAL

The deposition of the chromium films was performed with a KrF excimer laser at maximum fluences of about 100 mJ/cm² and pulse repetition rates in the range between 5 and 80 pps. The chromium hexacarbonyl was supplied to the deposition cell by saturating a carrier gas (e.g. argon, carbon monoxide) in a gas saturator with the vapor pressure of the Cr(CO)₆ (about 0.2 torr) at variable flows of up to 50 sccm. The total pressure in the deposition cell was varied between 60 and 900 mbar. The film deposition was performed on quartz substrates (Suprasil I) at a laser beam spot diameter of about 3 mm or 1.5 mm.

The film growth was studied in situ by measuring the transmission of a HeNe laser probe beam passing through the growing deposit. Monitoring the film growth in situ with the HeNe laser at 633 nm revealed that under the conditions of the present experiments the change of the optical density with time was nearly constant for film thicknesses greater than approximately 200 Å. Therefore, a calibration of the optical transmission curves with mechanically measured film thicknesses was possible (Talystep profilometer). In all cases the film growth could be monitored up to a film thickness of about 4000 Å using a sensitive photodiode for probe beam detection. More details on the experimental setup can be found elsewhere [12-15].

RESULTS

Growth rate and nucleation time

The dependence of the deposition rate on laser fluence, pulse repetition rate, buffer gas pressure, gas flow rate and substrate temperature was studied for film growth on the entrance window [12] and the exit window [13,14] of the deposition cell. The results suggest that the kinetics is dominated by gas phase processes under the conditions employed. A simple gas phase diffusion model gives a reasonable description of most measured dependences in terms of a diffusion length [13]. For a simple diffusion model a linear dependence of the

deposition rate on the reciprocal square root of the pressure is expected. Figure 2 shows such a plot for hydrogen as the buffer gas. These results were obtained for a repetition rate of 20 pps, a flow rate of 25 sccm and a fluence of 87 mJ/cm^2 . It is interesting to note that the corresponding deposition rate for hydrogen is a factor 3-4 higher than for argon, probably due to the higher value of the diffusion constant. A diffusion limited process is also indicated by the $1/\sqrt{p}$ dependence of the nucleation rate, as shown in Fig. 3. In addition, this figure illustrates the increase of the nucleation time with hydrogen pressure. This analysis, however, gives no further information on the nature of the species involved in the growth process.

It is well known that unsaturated chromium carbonyls can be obtained in the gas phase by a one photon process and Cr atoms can be formed either by multi-photon excitation or sequential absorption of 248 nm photons. The addition reaction of unsaturated chromium carbonyls with CO is very fast and occurs within an order of magnitude of the gas kinetic collision process. This points to a small influence of Cr atoms formed in the gas phase on the deposition rate. This conclusion

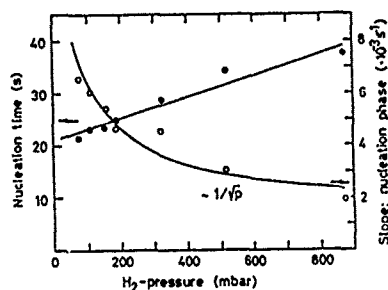


Fig. 3: Nucleation time and nucleation rate versus hydrogen partial pressure for chromium film deposition from $\text{Cr}(\text{CO})_6$ at 248 nm.

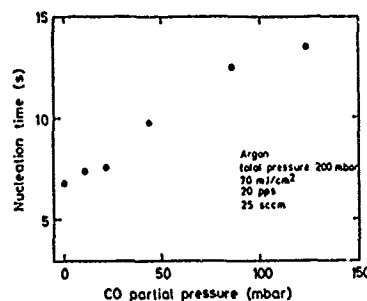


Fig. 4: Nucleation time versus CO partial pressure for chromium film deposition from $\text{Cr}(\text{CO})_6$ at 248 nm.

is supported by experiments using CO instead of rare gases as the buffer gas. In these measurements the in situ detection of the growth rate allowed the separation of the nucleation time from the main phase of film growth. The nucleation time increased by less than a factor of two, when the CO partial pressure was changed from zero to about 200 torr in the deposition gas as shown in Fig. 4. The decrease of the deposition rate was very small as shown in Fig. 5 for different buffer gases, repetition rates and flow rates. This finding indicates that only chromium atoms and unsaturated chromium carbonyls located within a few mean free path lengths from the surface have a chance to reach the surface before recombination. These highly active species may contribute to a larger extent to nucleation, but cannot explain the measured growth rates. This points to an important contribution of more stable carbonyl molecules and possibly clusters to the deposition process. At the highest CO pressures studied (200 torr) a brown material was deposited, which was no longer metallic.

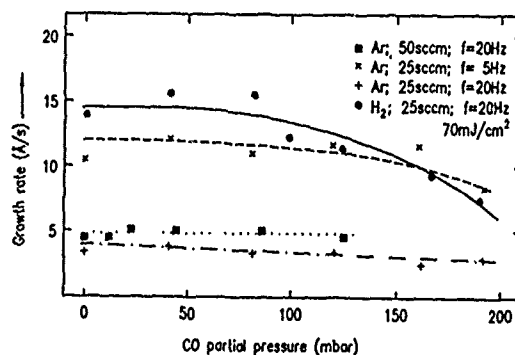


Fig. 5: Growth rate versus CO partial pressure for chromium film deposition from $\text{Cr}(\text{CO})_6$ at 248 nm.

Film composition

The influence of buffer gases and pressure on the chemical composition of the chromium films was investigated in detail by X-ray photoelectron spectroscopy [15]. Films deposited using argon or helium as the buffer revealed a typical Cr concentration of about 60 at% and O and C contents of about 20 at% each. In these films oxygen was bonded predominantly as Cr_2O_3 and carbon was bonded as Cr_3C_2 [15]. A second carbon and oxygen compound was found, which might be inserted CO. For hydrogen as the buffer gas the highest Cr content of 72 at% was obtained, connected with a reduction of the carbon concentration by about 10at%. The presence of additional CO during film deposition showed that gaseous CO is a considerable source of film contamination.

DISCUSSION

For pulsed UV laser deposition of chromium from $\text{Cr}(\text{CO})_6$ at 248 nm the following scenario can be extracted from the recent data. The kinetics is mainly determined by the diffusion of active species to the surface. Depending on the deposition conditions and the stage of film growth these can be Cr atoms, unsaturated or saturated carbonyls. However, larger carbonyl molecules such as polykernel chromium carbonyl complexes and clusters cannot be excluded for certain deposition conditions as direct film precursors. The results are consistent with a mechanism where highly reactive species such as Cr atoms may contribute predominantly to the nucleation phase and more stable species are responsible for the main film growth process.

As a consequence, the laser pulses will induce decarbonylation, responsible for film growth, predominantly in the adsorbed and chemisorbed phase. Dissociation of carbonyls in the gas phase has an indirect influence on the growth process. The final decarbonylation process at the surface, however, is not quantitative. Dissociation of CO molecules occurs on the surface, presumably by dissociative chemisorption through a parallel π -bonded chemisorbed state as already detected on a

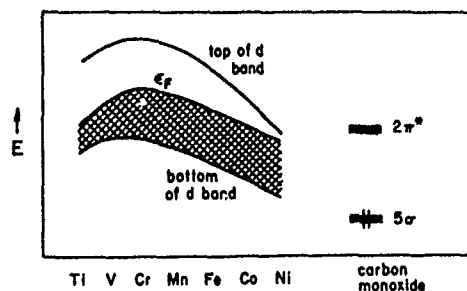


Fig. 6: Comparison of the position of the 5σ and $2\pi^*$ levels of CO with the shift of the Fermi level in the d-band of transition metals.

Cr(110) surface [16]. Figure 6 shows a comparison of the position of the CO 5σ and $2\pi^*$ levels with the position of the Fermi level in the d-band of transition metals [17]. In the case of nickel the $2\pi^*$ level lies above the d-band leading to an interaction as required for chemisorption. For Cr, however, the Fermi level rises above the $2\pi^*$ level. This causes a stronger interaction and increases the population of the $2\pi^*$ level. This effect allows the CO molecule to stretch and tilt toward the surface and finally may be responsible for dissociation. Figure 6 explains why in the case of chromium the strong CO bond can be broken by heterogenous catalysis, whereas in the case of nickel this process is less pronounced.

In a similar way the effect of hydrogen as the buffer gas could be hydrogenation of carbon compounds or intermediates at the surface, leading to a reduction in the carbon content of the film. The XPS analysis shows that mainly the smaller C-peak in the XPS spectrum tentatively assigned to incorporated CO disappears [15]. Thus, the effect of hydrogen is consistent with a Fischer-Tropsch type catalytic mechanism.

ACKNOWLEDGEMENTS

We would like to thank Professor Schmidt and Dr. Oetzmann from Corporate Research of ABB in Heidelberg for the XPS analysis of the films and valuable discussions. Financial support of this work by the German Ministry of Research and Technology (BMFT) under contract No. 13N5363 8 and the Fonds der Chemischen Industrie is gratefully acknowledged.

REFERENCES

- [1] T.R. Jervis, J. Appl. Phys. **58**, 1400 (1985)
- [2] H. Schröder, S. Metev, W. Robers and B. Rager, E-MRS Proceedings, Strasbourg (1986) 71
- [3] D. Tonneau, G. Auvert and Y. Pauleau, J. Appl. Phys. **64**, 5189 (1988)
- [4] D.J. Ehrlich, R.M. Osgood Jr. and T.F. Deutsch, J. Electrochem. Soc. **128**, 2039 (1981)

- [5] R. Solanki, P.K. Boyer, J.E. Mahan and G.J. Collins, Appl. Phys. Lett. 38, 572 (1981)
- [6] R. Solanki, P.K. Boyer and G.J. Collins, Appl. Phys. Lett. 41, 1048 (1982)
- [7] T.M. Mayer, G.J. Fisanick and T.S. Eichelberger, J. Appl. Phys. 53, 8462 (1982)
- [8] H. Yokoyama, F. Uesugi, S. Kishida and K. Washio, Appl. Phys. A 37, 25 (1985)
- [9] D.K. Flynn, J.I. Steinfeld and D.S. Sethi, J. Appl. Phys. 59, 3914 (1986)
- [10] N.S. Gluck, G.J. Wolga, C.E. Bartosch, W. Ho and Z. Ying, J. Appl. Phys. 61, 998 (1987)
- [11] K.A. Singmaster, F.A. Houle and R.J. Wilson, Appl. Phys. Lett. 53, 1048 (1988)
- [12] L. Konstantinov, R. Nowak and P. Hess, Appl. Phys. A 47, 171 (1988)
- [13] R. Nowak, L. Konstantinov and P. Hess, Appl. Surf. Sci. 36, 177 (1989)
- [14] R. Nowak, L. Konstantinov and P. Hess, MRS Symp. Proc. Vol. 129 (1989)
- [15] R. Nowak, P. Hess, H. Oetzmänn and C. Schmidt, Appl. Surf. Sci., to be published
- [16] N.D. Shinn and T.E. Madey, Phys. Rev. Lett. 53, 2481 (1984)
- [17] R. Hoffmann, Solids and Surfaces, (VCH Verlagsgesellschaft mbH, Weinheim, 1988) p. 111

SELECTIVE SURFACE MODIFICATION OF FLUOROCARBON RESIN USING EXCIMER LASER

M. Okoshi, Graduate Student of Faculty Eng. Tokai University.
M. Murahara, Faculty of Engineering, Tokai University, 1117 Kitakaname,
Hiratsuka, Kanagawa, 259-12, JAPAN.
K. Toyoda, RIKEN, The Institute of Physical and Chemical Research, 2-1
Hirokawa, Wako, Saitama, 351-01, JAPAN.

ABSTRACT

The fluorocarbon resin (Teflon) which is a very stable material chemically, has chemical resistance. Because of this property, it has no affinity for oil or water. Therefore, we have tried selective area modification of the resin surface by using an excimer laser.

Fluorocarbon resin is a polymer of C-F bonds. In our experiment, the resin surface was irradiated by an ArF excimer laser, of which the photon energy is higher than that of the C-F bond, to excite the strong C-F bonds. B radicals, the best combination for F atoms, were formed simultaneously. Consequently, F atoms of C-F bonds were pulled out by B radicals. $B(CH_3)_3$ with absorption in agreement with the wavelength of the ArF laser were used as raw materials of the B radicals. By irradiating the gas by the ArF laser beam, the photodecomposed B radicals functioned by pulling out F atoms, and the other methyl radicals ($-CH_3$) substituted for F atoms. As the result, this resin surface turned out to be oleophilic exclusively on the areas exposed to the light.

Introduction

Development of functional materials employing a specificity of a generating material and modifying its surface as well has been studied extensively in recent years. Especially, fluorocarbon resin has taken much of our notice as a material due to its superiority of weatherability for use in medical, chemical industries, and so on [1,2,3]. Accordingly, given a function, fluorocarbon resin can be used in many ways and expected to be a sensor and a catalyst.

There are two well-known modification methods for fluorocarbon resin surfaces; one is a chemical modification to be done in a Na atmosphere, and another is modification using RF plasma. In addition to the existing methods, we propose here a method of selective surface modification by using a laser [4,5,6,7]. The advantage of using a laser is that surface modification can be done selectively. The surface of the sample is irradiated perpendicularly by a laser beam in pattern form through a mask screen. In this experiment, we adopted the ArF excimer laser which has high photon energy. The C-F bonds, the main structure of fluorocarbon resin, were cut by this beam, and the F atoms were substituted by other radicals. Then, the surface of this resin was found to be oleophilic. In the photochemical reaction, this functional resin would be utilized as a medical macromolecule, especially artificial blood vessels and medical sensors. If the absent positions of F atoms could be occupied by a metal or semiconductor films, it would open up one approach to sensors and new materials.

In this paper, accordingly, we would like to report how the surface of the fluorocarbon resin was changed to oleophilic as a foothold of that approach.

Photochemical Reactions

In general, in order to get a photochemical reaction by a laser effectively, two conditions have to be satisfied. Firstly, absorption of a material must agree with the wavelength of the laser; secondly, the laser's photon energy must be higher than the dissociation energy of the molecules or atoms of the material. UV spectra of the fluorocarbon resin and $B(CH_3)_3$ gas are shown in Fig. 1. They indicated that both the resin and the gas possess strong absorption at the 193nm wavelength of the ArF excimer laser. Furthermore, the ArF laser's photon energy is 147 kcal, and the C-F bond of this resin is 128 kcal/mol. The above two conditions, hence, are met. In this way, an effective photochemical reaction is induced on the surface of the fluorocarbon resin which is a chemically stable material.

On the other hand, as shown in Fig. 2, the fluorocarbon resin is composed

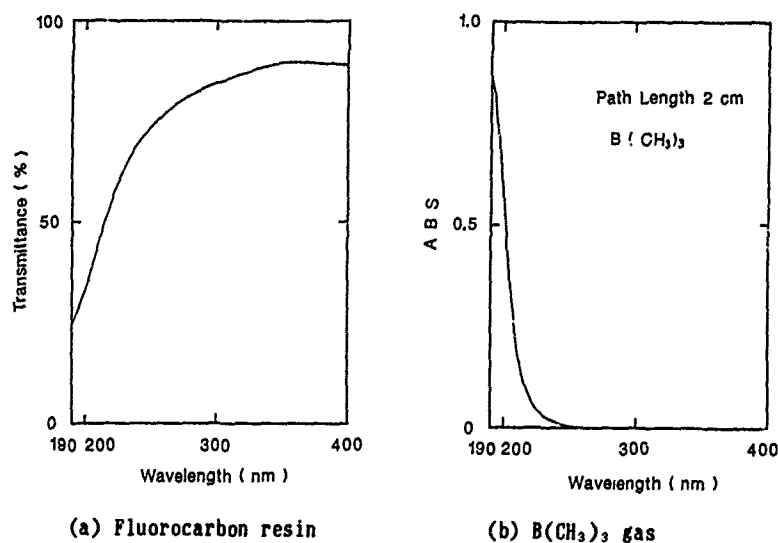


Fig.1 UV spectra of fluorocarbon resin and $B(CH_3)_3$ gas

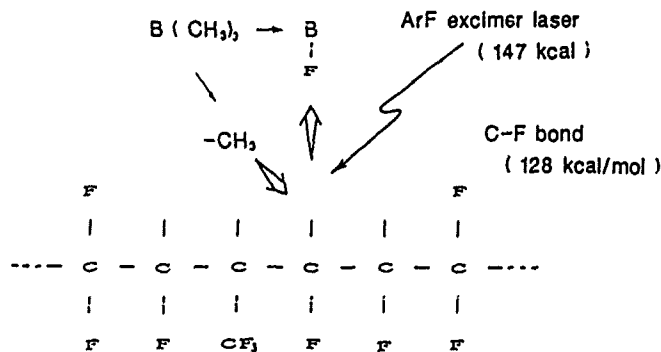


Fig.2 Illustration of photochemical reaction.

of C-C bond, which is a main chain of carbon. The dissociation energy of this C-C bond is 104 kcal/mol, lower than the ArF laser's photon energy of 147 kcal. Still, it is lower than the C-F bond of 128 kcal/mol. Consequently, the C-C bond is easier to cut than C-F bond by the ArF irradiation. And in this case, it is impossible to achieve the aim of this experiment. The essential aim is to cut selectively the C-F bond only. Even if the bond could be cut, C and F atoms would be immediately coupled because of the high electronegativity of fluorine. Under this situation, we have taken up the fact that B atoms are easier to bond with F atoms than C atoms. The F atoms were pulled out by B atoms, being substituted for by the other $-CH_3$ photodecomposed from $B(CH_3)_3$. In this photochemical reaction, the surface of this resin was selectively turned to oleophilic.

Experimental set-up

Schematic diagram of the experimental system is shown in Fig. 3. The reaction cell was produced from stainless steel containing a fused silica glass window. The fluorocarbon resin sample, sizing in $10 \times 20 \text{ mm}^2$ was housed in the cell. The reaction cell was vacuumed and then the $B(CH_3)_3$ gas was sealed in. An image-pattern mask was set on the beam pass, and the ArF laser of 193 nm was projected on the surface of the sample. The experimental conditions were as outlined below: The $B(CH_3)_3$ gas possess strong absorption at 193 nm, therefore, between the incident window and the sample was 2 mm, of which was obtained experimentally. When the oleophilic of the modified sample become eminent, the contact angle with oil become small. Accordingly, on laser fluence in three different gas pressures and shot number in three different pulse repetitions, dependence of the contact angle are measured to find the best conditions for modification. The parameter of these values were as following: the laser fluence, $12.5 \sim 50 \text{ mJ/cm}^2$; the gas pressure, $5 \sim 40 \text{ Torr}$; the shot number, $500 \sim 3000 \text{ shots}$; the pulse repetition, $5 \sim 50 \text{ pps}$; The chemical structure which were reformed were measured by XPS and IR analysis spectrum.

Results and Discussion

The fluorocarbon resin (NEOFLON FEP) was used as specimen. The sample was put in the reaction cell. When the patterned ArF laser beam was irradiated onto the Teflon surface, a changeing was not visible with the unaided eye. But the oil were attached onto the sample surface only irradiated parts. So we carried out XPS analysis for the purpose of investigating the molecules' bonding of the modified surface. The

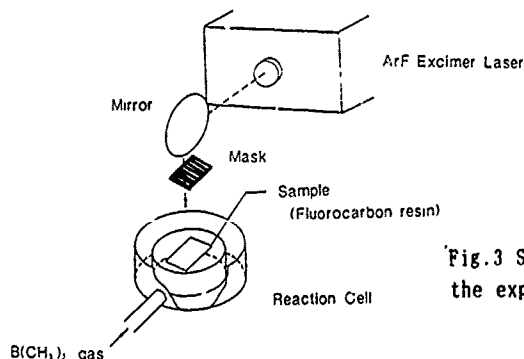


Fig.3 Schematic diagram of the experimental apparatus.

results are shown in Fig. 4. The analysis of deep layer was carried out by Ar ion etching. The peak of F 1s was not observed on the surface, and it appeared gradually while the surface being etched deeper. The figure shows that fluorine at the surface was certainly pulled out by B atoms. Measurement of IR spectra, then, was conducted to confirm whether the substitution of methyl-radicals was completed on the surface. Especially, considering that the modified surface was an extremely shallow layer, it was done by ATR (Attenuated Total Reflection) method. The result is shown in Fig. 5. As shown there, the two absorptions of methyl-radicals were exhibited in vicinity of 2900 cm^{-1} , which certified that the surface of the fluorocarbon resin was substituted by oleophilic radicals.

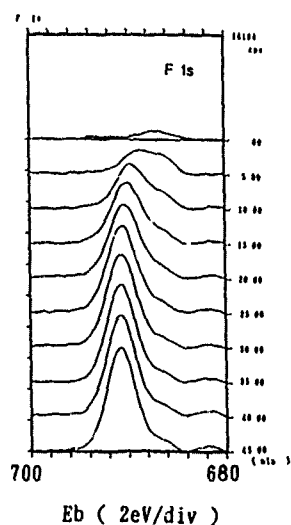


Fig.4 Result of XPS analysis as to F 1s

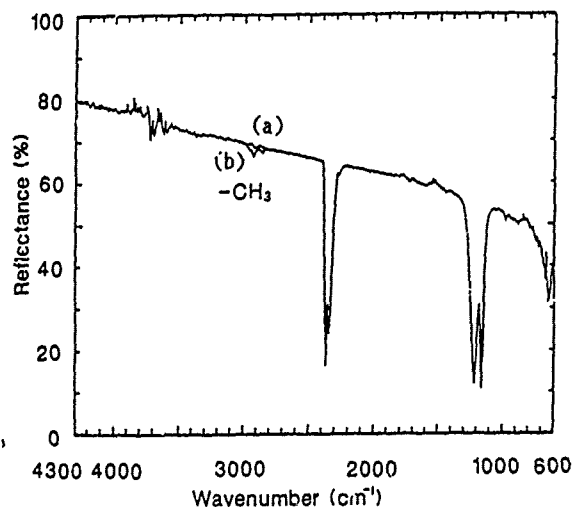


Fig.5 IR spectra of fluorocarbon resin with (a) and without (b) ArF excimer laser

Next, the modified samples were soaked in acid and alkali to inspect if the samples were chemically stable materials. The result is shown in Fig. 6. The measurement of contact angle indicated in the vertical line is a general evaluation method of oleophilic property: the smaller the contact angle is, the stronger the property is. It is also shown that the contact angle was little changed when the samples were soaked in H_2SO_4 and NaOH , and they were chemically stable materials as well.

The experiment was performed under the constant gas pressure of 40 Torr. The laser fluence dependence of the contact angle in three different gas pressures is shown in Fig. 7. It indicates that the contact angle was quite large with the gas pressure at 5 Torr. When the pressure was, however, increased gradually, the angle became smaller. Consequently, the angle reached almost 0 degree at 40 Torr, and the surface of the resin was modified effectively. However, when the pressure went up over 40 Torr, the intermediate products were deposited on the window. It means that no effective modification on the surface was achieved [7].

Next experiment was carried out under variable laser pulse repetition. Then, the shot number dependence of the contact angle in three different pulse repetitions is seen in Fig. 8. This figure shows, the value of the

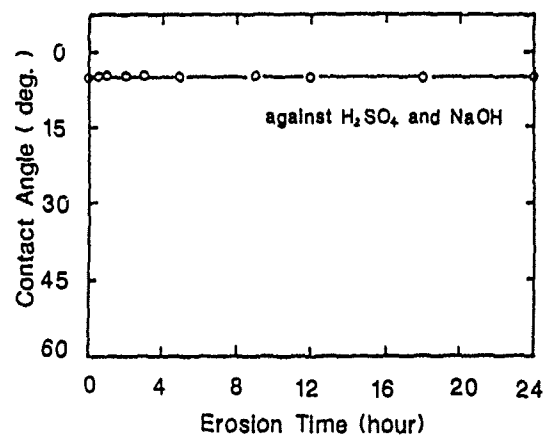


Fig. 6 Erosion time dependence of the contact angle for acid and alkali.

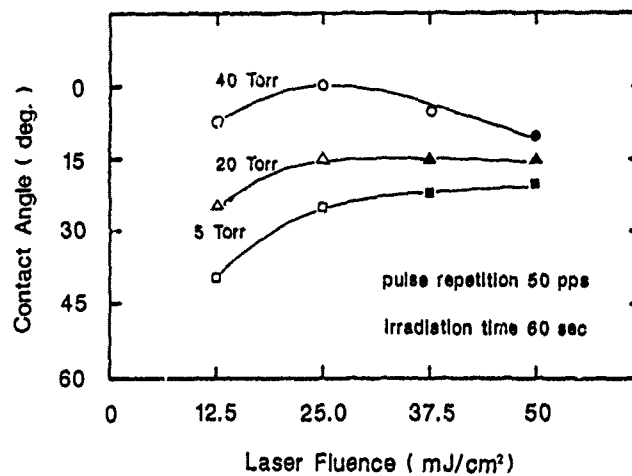


Fig. 7 Laser fluence dependence of the contact angle in three different gas pressures.

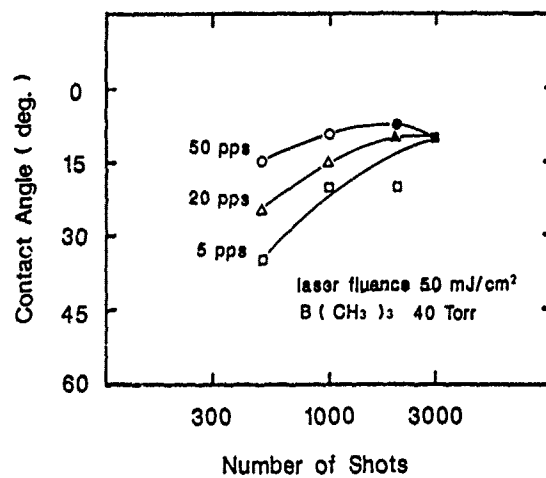
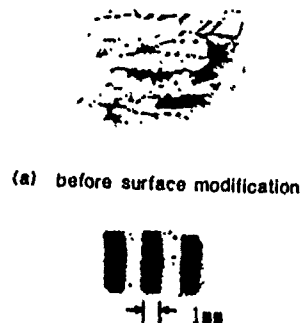


Fig. 8 Shot number dependence of the contact angle in three different pulse repetitions.

contact angle became smaller when the pulse repetition was increased [7].

An example of the selective surface modification is shown in Fig. 9. Photograph (a) was before surface modification, and (b) was after surface modification. As this photograph, the selective surface modification of fluorocarbon resin by using excimer laser was, thus, successfully achieved.



Conclusion

Selective surface modification of the fluorocarbon resin was carried out by ArF excimer laser. $B(CH_3)_3$ gas was used to achieve the study, and XPS analysis indicates that fluorine of the resin were certainly pulled out by B atoms photodecomposed from the $B(CH_3)_3$. IR spectra shows that being pulled out, the fluorine were substituted by the other methyl-radicals ($-CH_3$); consequently, it was clear that the resin surface was exclusively turned to oleophilic. And then, modified samples were chemically stable materials against acid and alkali. Accordingly, based on these successful results, we would like to carry out further the study to medical sensors and new materials.

References

1. J.M. Burkstrand, J.Appl.Phys. 52, 1981
2. S. Küper and M. Stuke, Appl.Phys.Lett. 54, 4 (1989)
3. R. Srinivasan and V. Mayne-Banton, Appl.Phys.Lett. 41, 576(1982)
4. M. Okoshi, N. Sugawara, T. Shigeeda, M. Murahara and K. Toyoda, Extend Abstract (The 36th Spring Meeting, 1989) The Japan Society of Applied Physics No.2, 593 (1989)
5. N. Sugawara, R. Takahashi, M. Okoshi and M. Murahara, Extend Abstract (The 36th Spring Meeting, 1989) The Japan Society of Applied Physics No.2, 593 (1989)
6. M. Hayashi, M. Okoshi, T. Shigeeda, M. Murahara and K. Toyoda, Extend Abstract (The 50th Autumn Meeting, 1989) The Japan Society of Applied Physics No.2, 511 (1989)
7. M. Okoshi, K. Tanaka, M. Murahara, Extend Abstract (The 50th Autumn Meeting, 1989) The Japan Society of Applied Physics No.2, 511 (1989)

DIRECT EVIDENCE FOR THE CREATION OF MICROPORES IN UV-IRRADIATED POLY(METHYL METHACRYLATE)

J. A. MOORE* and JIN-O CHOI*

*Rensselaer Polytechnic Institute, Polymer Science and Engineering
Program, Troy, New York 12180-3590.

ABSTRACT

Films of PMMA containing azobenzene were prepared by casting from polymer solutions containing the probe or by exposing pre-irradiated films to the vapor of azobenzene. These materials were irradiated at 335 nm and the amount of trans azobenzene which had been photoisomerized was monitored spectrophotometrically. The largest amount of photoisomerization was observed for the pre-irradiated samples which had been penetrated by azobenzene from the vapor, indicating that the created free volume allowed the isomerization to proceed more easily.

INTRODUCTION

When polymers are exposed to ultraviolet and high energy radiation, changes of chemical properties (scission or crosslinking) can be detected experimentally and should be associated with changes in the physical properties such as the local free volume [1-3] and glass transition temperature [4, 5]. These changes of chemical and physical properties affect the solubility characteristics in the irradiated area of polymer films and play a major role in lithographic materials [1-3].

Degradation of PMMA by various types of radiation such as ultraviolet, x-ray, γ -ray, electron and proton beams has been of interest both from the basic and practical point of view [6, 7]. Exposure of PMMA films to these radiation sources results in reduced molecular weight, the generation of unsaturated bonds by the scission of side chains, the evolution of gaseous products, and the appearance of the characteristic electron spin spectra of propagating [8] and peroxy radicals [9]. These chemical changes should be associated with the increase of local free volume (creation of micropores) in the irradiated PMMA.

A detailed study of the factors affecting the dissolution rate of PMMA film showed that the magnitude of the increase in the dissolution rate of irradiated film could not be entirely attributed to the reduction of the molecular weight [1, 2]. The evolution of gaseous products, i. e., CO, CO₂, HCO₂CH₃, CH₄, and CH₃OH, would cause an increase in local free volume in the irradiated film. Ouano observed indirect evidence of micropore formation in the irradiated PMMA from a study of changes in the dissolution rate (S) based on the solvent molecular weight (M_s) of a homologous series of n-alkyl acetate solvents. As the micropores become more numerous and larger with increasing radiation dose, the diffusion process of butyl acetate and the higher acetate homologs becomes less hindered, thus the break in

the $\log S$ vs. $\log M_s$ becomes less pronounced. When PMMA films were prepared containing Meldrum's diazo as a dopant, the dopant acted as a mild retarder of film dissolution [10]. Upon irradiation at 254 nm, CO, N₂ and acetone as photoproducts diffused quickly out of the film leaving microvoids in the PMMA films. This process led to a pronounced acceleration of dissolution in the irradiated areas.

The presence of micropores in the polymer matrix permits increased diffusion compared to the homogenous polymer - penetrant system [11]. Therefore, the formation of micropores should affect the sorption of penetrants in the irradiated PMMA film. There are a variety of methods for measuring the sorption of a penetrant in polymers [11, 12]. However, these methods are not easily employed for the determination of sorption in a microthin film on a silicon wafer substrate. On the other hand, the sorption of a species, which has a very high extinction coefficient ($\approx 10^4$ l/mol-cm) compared to PMMA film, can penetrate PMMA film and the amount of a reporter molecule such as naphthalene absorbed in the irradiated PMMA films can be easily determined spectrophotometrically.

In recent reviews [13, 14], the dominant factor in the photoisomerization of labels in polymeric solids is the local free volume in the vicinity of the label, because photoisomerization is strongly dependent on the rotational mobility of the label in the matrix. Analyses of the photoisomerization behavior of photochromic labels allows the study of processes such as physical aging, plasticization, and volume dilation caused by glassy deformation to be monitored sensitively. The free volume and the size distribution of free volumes in polymeric systems have been probed by the use of photochromic labels [15, 16]. In this work, azobenzene was used as a molecular label to study the formation of micropores in irradiated PMMA film. Trans azobenzene located in a PMMA matrix is photoisomerized when exposed to UV light of appropriate wavelength. The amount of photoisomerization (trans to cis) of azobenzene irradiated for a specific time was used to probe the formation of micropores in PMMA films by UV irradiation.

EXPERIMENTAL

Sorption of Naphthalene and Azobenzene in Irradiated PMMA Films

An irradiated PMMA film on a quartz disk was placed in a chamber containing naphthalene or trans azobenzene crystals, which were used in commercial grade. The sample disks were positioned at about 5 cm from the bottom of the container to avoid contact between the crystals and the films. The closed container was stored in an oven at 50 ~ 60 °C to increase the rate of sublimation of naphthalene or azobenzene. Immediately after the sample was removed from the sorption chamber, its UV absorption spectrum was measured.

Photoisomerization (Trans to Cis) of Azobenzene in PMMA Films

PMMA films containing trans azobenzene were exposed to a flash UV light from a PRA flash lamp (Model 6199A) by using a narrow band interference filter (335 ± 10 nm). The UV spectra of samples changed photochemically were measured with a Perkin Elmer UV spectrophotometer immediately after a given number of flashes.

RESULTS AND DISCUSSINS

There are a variety of methods for measuring the sorption of a penetrant in polymer films. The most general procedures involve gravimetric and volumetric determinations. However, these methods are not easily employed for the determination of sorption in an ultra-thin film on a silicon wafer. On the other hand, sorption in PMMA films can be measured spectrophotometrically by using aromatic compounds as a probe. Naphthalene (solubility parameter, $\delta = 9.9$ [cal/cm³]^{1/2}) was chosen as the sorption species because its vapor does not dissolve PMMA films at 60 °C and it is sublimed at a rate slow enough to be disregarded with respect to the loss of naphthalene during the spectroscopic measurement.

UV-irradiated and unexposed PMMA films were exposed to naphthalene vapor sublimed at 60 °C in the same vessel. The difference spectra of UV-irradiated PMMA films before and after naphthalene sorption are shown in Figure 1.

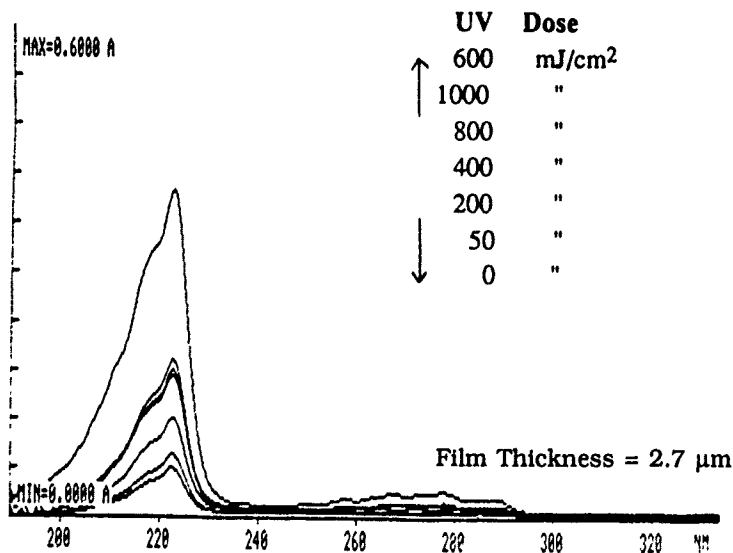


Figure 1. UV Difference Spectra of UV-Irradiated PMMA Films before and after Naphthalene Sorption at 60 °C for 3 Hours.

The amount of naphthalene imbibed by these samples was dependent on the incident dose. Under the same conditions, irradiated films imbibed more azobenzene than unirradiated films or irradiated films which had been annealed above T_g . PMMA films irradiated with electron and proton beams showed a similar trend of naphthalene sorption. The concentration of absorbed material was calculated from the UV difference spectra by using Beer's equation and is plotted in Figure 2. The absorption of naphthalene in PMMA films increases with longer exposure to radiation, then decreases beyond a certain dose. The azobenzene sorption in UV-irradiated PMMA films showed the same trend as naphthalene. These data indicate that the creation of micropores in PMMA film by radiation could be indirectly determined by the sorption. Further, the creation of the micropores may have been limited by recombination of polymeric fragments beyond a certain dose.

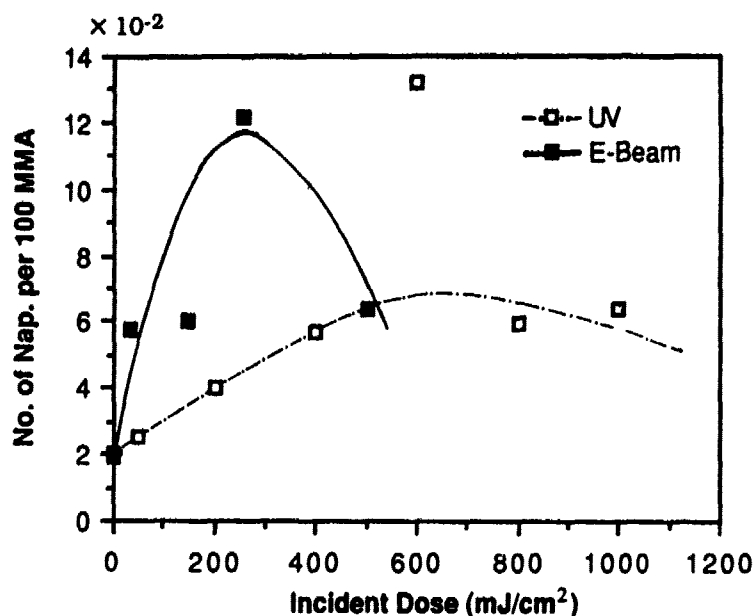


Figure 2. Plot of Naphthalene Sorption vs. Incident Dose in PMMA Film ($\approx 3 \mu\text{m}$) at 60°C for 3 Hours.

It was reported that the free volume in the polymer matrix could be probed by the use of photochromic labels [13-16]. Analysis of the photoisomerization behavior of photochromic labels within local free volume should be applicable to the study of the creation of micropores in a PMMA film irradiated with UV light. In this work, azobenzene was used to monitor the creation of micropores spectrophotometrically. Azobenzene exists as the extended trans isomer under normal conditions, but upon irradiation at 335 nm it is isomerized to the compact cis isomer by rotation about the weakened $\text{N}=\text{N}$ bond in the excited state. Clearly this isomerization process will be affected by the amount of space (local free volume or microporosity) available on the molecular level as long as it is small compared to the

molecular dimensions of the probe. The amounts of photoisomerization (trans to cis) were compared in the various samples prepared by different methods. Figure 3 shows changes in the UV spectra of azobenzene in PMMA film upon exposure to UV light at 335 nm.

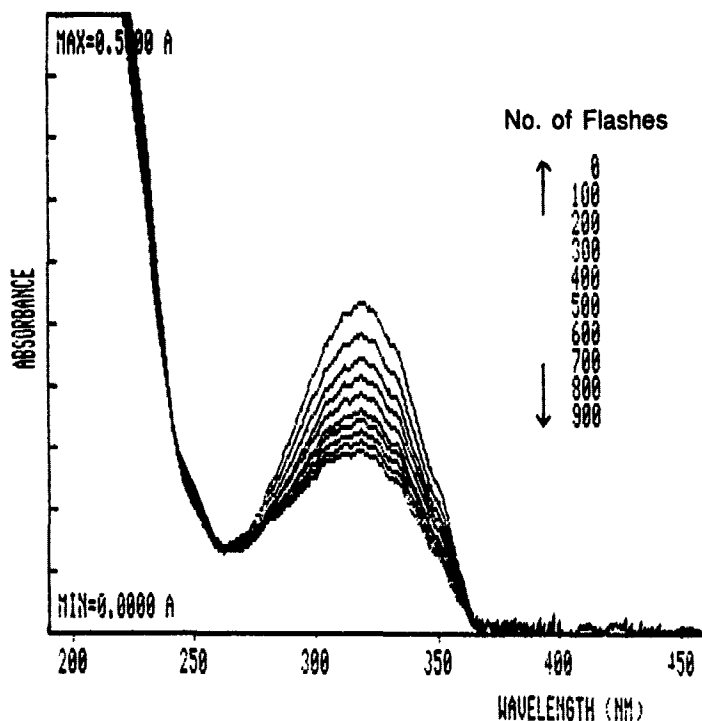


Figure 3. Changes of the UV Spectrum of Azobenzene in Irradiated PMMA Film by Exposure to UV Light (335 ± 10 nm).

The amount of photoisomerization of azobenzene can be determined from the changes in the UV spectrum, assuming that the thermal and photochemical re-isomerization (cis to trans) is negligible in the early stages. Four PMMA samples, where azobenzene would be located in different amounts of free volume, were prepared as described below.

- (A) irradiated PMMA film was exposed to azobenzene vapor at 55 °C for 24 hours. Most of the azobenzene would enter micropores created by degradation of PMMA by UV light.
- (B) A benzene solution of PMMA containing azobenzene was used for spin-coating. When the resulting thin film was baked at 130 °C for 30 minutes, only azobenzene remained in the PMMA film.
- (C) Azobenzene was sorbed in PMMA film by exposing unirradiated films to azobenzene vapor at 120 °C.
- (D) Irradiated PMMA film was exposed to azobenzene vapor at 55 °C and annealed at 120 °C in the presence of excess

azobenzene to prevent its loss during the annealing process. The micropores should be collapsed and azobenzene would be contained in the original (before irradiation) free volume of PMMA film.

The concentration of azobenzene in PMMA was in the range of 0.3 ~ 1.3 molecules per 100 MMA repeating units. The extent of photoisomerization of azobenzene in Table I clearly shows the dependence on the method of sample preparation.

Table I. Photoisomerization of Azobenzene from Trans to Cis by 335 ± 10 nm UV Light.

Samples		Photoisomerization (trans to cis)		Concentration of azobenzene per 100 repeating units
		100 flashes	200 flashes	
A	AZB diffused into irradiated PMMA film	12.9 %	30.0 %	0.5 AZB/100 MMA
		13.8 %	25.0 %	0.3 AZB/ "
B	AZB co-cast in PMMA film	7.4 %	10.8 %	0.6 AZB/ "
		8.4 %	15.3 %	1.3 AZB/ "
C	AZB diffused into PMMA film	7.5 %	13.7 %	1.1 AZB/ "
		7.5 %	15.2 %	0.5 AZB/ "
D	AZB diffused and annealed in irradiated PMMA film	9.9 %	13.2 %	0.6 AZB/ "
		9.3 %	18.2 %	0.5 AZB/ "

The largest amount of photoisomerization was observed for the pre-irradiated samples (A) which has been penetrated by azobenzene from the vapor, indicating the created free volume allowed the isomerization to proceed more easily. This result is direct evidence that a larger local free volume was created in PMMA films after UV-irradiation.

ACKNOWLEDGEMENTS

We thank Mr. Y.-S. Kim and Prof. C. S. P. Sung at the University of Connecticut for their willingness to assist and advise us on the photoisomerization experiments with their flash lamp.

REFERENCES

1. A. C. Ouano, Polym. Engr. Sci. **18** (4), 306 (1978).
2. A. C. Ouano, in Materials for Microlithography: Radiation

Sensitive Polymers, edited by L. F. Thompson, C. G. Willson and M. J. Frechet (ACS Symposium Series **266**, Washington, D. C., 1984), pp. 79 ~ 90.

3. W. M. Moreau, *Optical Engr.* **22** (2), 181 (1983).
4. J. W. Martin, *J. Appl. Poly.* **29**, 777 (1984).
5. A. R. Schultz, P. Frank, B. F. Griffing, and A. L. Young, *J. Polym. Sci., Polym. Phys.* **23**, 1749 (1985).
6. J. -O. Choi, J. A. Moore, J. C. Corelli, J. P. Silverman, and H. Bakhru, *J. Vac. Sci. Technol. B* (6), 2286 (1988).
7. J. A. Moore, and J. -O. Choi, *Polym. Preprints* **30**, 335 (1989).
8. H. Hiraoka, *IBM J. Res. Dev.*, **21**, 121 (1977).
9. R. M. Tarro, J. T. Warden, J. C. Corelli, J. A. Moore, A. J. Steckl, and, S. Kumar, *Microcircuit Engineering 84*, edited by A. Heuberger and H. Beneking (Academic Press, London), 1985, p. 537.
10. W. Limm, and M. A. Winnik, *Proceedings of Photopolymers: Processes and Materials* (Society of Plastics Engineers, Inc., Mid-Hudson Section, 1988), pp. 215-233.
11. D. Machin and C. E. Rogers, *Encyclopedia of Polymer Science and Technology*, Vol. 12 (Interscience Publishers, New York, 1964), pp. 679-685.
12. S. Matsuoka, and T. K. Kwei, in *Macromolecules: An Introduction to Polymer Science*, edited by F. A. Bovey and F. H. Winslow (Academic Press, New York, 1979), pp. 398-406.
13. J. L. R. Williams, and R. C. Daly, *Prog. Polym. Sci.* **5**, 61 (1977).
14. K. Horie, and I. Mita, *Advances in Polymer Science* **88**, *Specialty Polymers/ Polymer Physics*, (Springer-Verlag, Berlin, 1989), pp. 106-128.
15. L. Lamarre, and C. S. P. Sung, *Macromolecules* **16**, 1729 (1983).
16. W.-C. Yu, and C. S. P. Sung, *Macromolecules* **21**, 365 (1988).

UV LASER-INDUCED ETCHING OF THE FIRST-ROW TRANSITION METALS

GEORGE W. TYNDALL, IBM Almaden Research Center, 650 Harry Rd., San Jose, CA 95120.

ABSTRACT

The 248 nm excimer laser-induced etching of Ti, Cr, Fe, Co, Ni, and Cu by Br₂ has been studied. The experiment consists of focusing the pulsed UV laser beam at normal incidence onto the surface of a quartz crystal microbalance (QCM) coated with 1 μ m of polycrystalline metal. Absolute etch rates are determined as a function of the Br₂ pressure and the laser fluence. On the basis of the kinetic information, four mechanisms are proposed to explain the etching of these transition metals.

INTRODUCTION

Laser processing of materials in the microelectronics industry has become widespread in recent years. The ability to promote localized chemical reactions with laser light is currently used for the deposition of metals with submicron resolution. In addition to depositing materials, lasers are also suitable sources for inducing localized chemical etching processes. Metals are in general difficult to etch via dry processes, which makes the laser-induced chemical etching technique particularly appealing. Because laser etching can potentially lead to improvements in the spatial resolution of etched features and a decrease in the number of defects, this process is an attractive alternative to the wet lithographic techniques currently employed for microcircuit patterning.

EXPERIMENTAL

The kinetic measurements reported in this work were performed using a quartz crystal microbalance (QCM) as the substrate. The experimental apparatus has been described previously [1]. We used 6 Mhz quartz crystals onto which the metal films were evaporated. The QCM frequency was monitored with a frequency counter interfaced to an IBM PC. The quartz crystals were mounted in a vacuum cell which was typically pumped to a base pressure of 10^{-3} torr with a 14 l-sec⁻¹ mechanical pump. Br₂ was introduced to the cell through a molecular leak valve, and the pressure measured with a capacitance manometer. The excimer laser was operated at 10 Hz. A uniform portion of the beam was focused onto the surface of the microbalance at normal incidence. The amount of metal removed per laser pulse was determined from the change in the frequency of the quartz crystal.

RESULTS AND DISCUSSION

We find that all of the metals studied can be etched in a bromine atmosphere at moderate laser fluences. Representative data illustrating the typical changes observed in the crystal frequency vs time are shown in Fig. 1 for the case of a titanium coated QCM. The decrease in the QCM frequency upon addition of Br₂ to the vacuum cell shown in Fig. 1(a) (no laser present), corresponds to adsorption of approximately three to four monolayers of Br₂ onto the crystal surface. Upon evacuation of the cell, the QCM frequency increases by an amount equivalent to the removal of less than one monolayer, indicating that the remaining Br₂ is chemisorbed on the titanium surface. Similar results were obtained on Cr, Co, Fe, and Ni coated QCMs. The results obtained for the adsorption onto a Cu coated QCM suggest a much greater quantity of bromine can be adsorbed by Cu (see below). Fig. 1(b) shows the effect of irradiating the microbalance surface with the laser in the absence of Br₂. The dramatic increase in the frequency of the QCM is due to the transient heating of the metal surface induced by the laser. After approximately 10 seconds, the

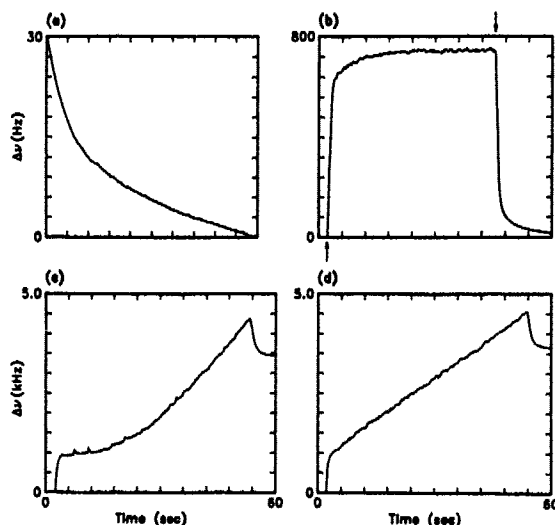


Figure 1. Frequency response of a titanium coated quartz crystal to: (a) addition of 0.100 Torr Br₂ to the vacuum cell (no laser present); (b) 300 mJ-cm⁻² of 248 nm laser radiation incident on the surface of the QCM (no etchant present), the arrows denote the time at which the laser beam is admitted (up) and blocked (down); (c) etching of an "air exposed" titanium sample using 0.100 Torr of Br₂, and a laser fluence of 300 mJ-cm⁻²; (d) etching of a "clean" titanium sample using 0.100 Torr of Br₂ and a laser fluence of 270 mJ-cm⁻².

frequency of the QCM stabilizes at a constant value. Upon blocking the beam, the frequency drops to its original value. While heating of the QCM surface obscures the first few seconds of the etching process, it does not prohibit measurement of the etching rate. Fig. 1(c) shows the results of an etching experiment performed on an "air exposed" titanium surface. The non-linear dependence of the frequency change with time results from the presence of the native oxide layer. Initially the oxide covers the entire surface and the frequency change in time reflects the etching of the oxide by Br₂. As the oxide is removed, clean titanium is exposed and etched concurrently with the oxide. At the end of the run, the oxide layer is completely removed, and the frequency change with time reflects the etching of a "clean" titanium surface. In Fig. 1(d) the results from an etching run in which the oxide layer was etched prior to data collection are shown to be constant on the time scale of the experiment. The etch rates reported in this work correspond to experiments performed on "clean" metal surfaces.

The QCM was used to measure the rates of the 248 nm laser-induced etching of these transition metals by Br₂ as a function of the incident laser fluence, and the Br₂ pressure. Over the range of laser fluences used, no net change in the QCM frequency is found in the absence of Br₂. Thus the material is not removed by ablation of the pure metal surface, but requires interaction of the metal with either Br₂, photochemically produced Br radicals, or both (see below).

A. Titanium Etching

The dependence of the Ti etch rate on Br₂ pressure is shown in Fig. 2. The etch rate increases rapidly over the pressure range of 0.005 - 0.090 torr as Br₂ adsorbs on the titanium surface. Above 0.090 Torr the etch rate is independent of Br₂ pressure up to the highest pressures studied suggesting that the uptake of bromine by the titanium surface saturates at this pressure.

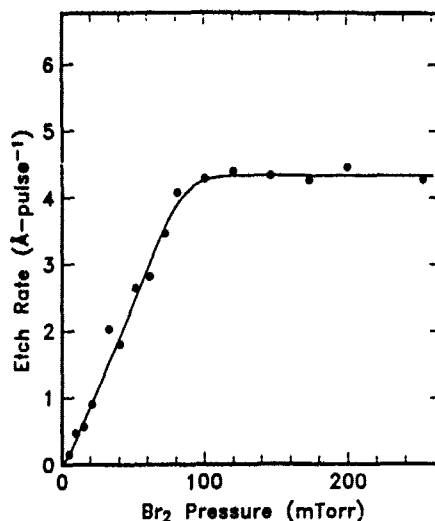


Figure 2. Dependence of the titanium etch rate on Br₂ pressure. The laser fluence was 275 mJ-cm⁻².

The laser fluence dependence of the titanium etch rate was measured from 100 - 400 mJ-cm⁻² and is shown in Fig. 3. The laser fluence threshold for obtaining etching is 180 mJ-cm⁻². Above this threshold the etch rate increases very rapidly with laser fluence up to 320 mJ-cm⁻². Above 320 mJ-cm⁻² the etch rate is independent of the laser fluence. Qualitatively, the observed dependence of the etch rate on laser fluence is typical of a laser-induced thermal desorption (LITD) process. The threshold laser fluence needed to observe etching arises from the formation of an etch product that is involatile at room temperature, but which desorbs as the temperature of the surface increases. The observed invariance of the etch rate on laser fluence at fluences greater than 320 mJ-cm⁻² results from the fact that all of the product has been removed from the surface. Quantitatively, one can model the fluence dependence of the etch rate to determine the desorption energy of the etch product [2]. A good fit to the etch rate vs. laser fluence (shown as the solid line in Fig. 3) is obtained for a desorption energy of 172 kJ-mole⁻¹. These results are consistent with the desorption of TiBr₂ from the surface, i.e. $\Delta H_{\text{sub}}(\text{TiBr}_2) = 168 \text{ kJ-mole}^{-1}$ [3].

Based on the above kinetic measurements we propose that the etching of Ti by Br₂ occurs via two independent steps: (1) formation, between laser pulses, of a TiBr₂ layer via the dissociative chemisorption of Br₂ and (2) sublimation of this product via laser-induced thermal desorption.

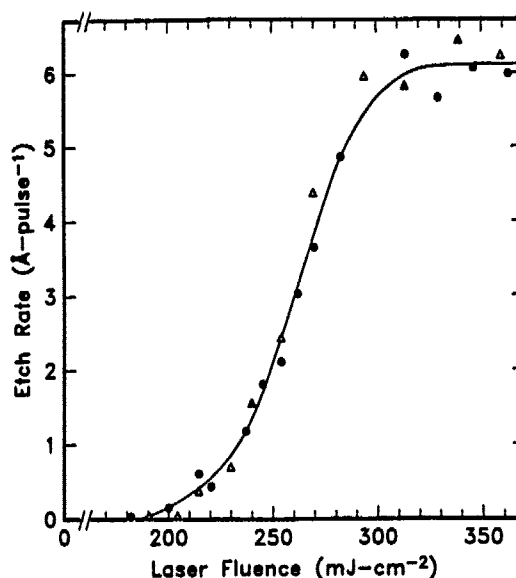


Figure 3. Dependence of the titanium etch rate on laser fluence. The Br₂ pressure was 0.100 Torr and the laser repetition rate was 10 Hz.

B. Chromium, Cobalt and Nickel Etching

We find that the etching of each of these metals increases with increasing Br₂ pressure over the range of 0.005 – 0.100 Torr. Above approximately 0.100 Torr, the etch rate is independent of the Br₂ pressure. We interpret these results in terms of the formation of a monolayer of dissociatively chemisorbed Br₂. Above 0.100 Torr the etch rate is constant because the metal surface is saturated with chemisorbed Br, and no further adsorption occurs.

The dependence of the etch rate on laser fluence for Cr, Co, and Ni are shown in Fig. 4. The dependence of the etch rate on laser fluence for each of these metals is qualitatively similar to the fluence dependence observed in the etching of Ti. In each case a threshold laser fluence is found which is dependent of the metal being studied. Above the threshold, the etch rate increases rapidly with increasing laser fluence up to a certain laser fluence, above which the etch rate is independent of any further increase in the fluence. By fitting the observed laser fluence dependence, we obtain desorption energies of 79, 67, and 88 kJ-mole⁻¹ for the products formed in the etching of Cr, Co and Ni with Br₂ respectively. We note that these values are significantly lower than the sublimation enthalpies of any of the potential metal halide products [3].

We propose that the etching of Cr, Co, and Ni by Br₂ occurs via the following mechanism: (1) formation, between laser pulses, of a chemisorbed Br monolayer, (2) reaction of the chemisorbed Br with the metal surface, during the laser pulse, to form the metal dihalide, and (3) sublimation of the metal dihalide, where the energy required for the sublimation is supplied by both the laser induced temperature increase at the surface, and the exothermicity of reaction (2).

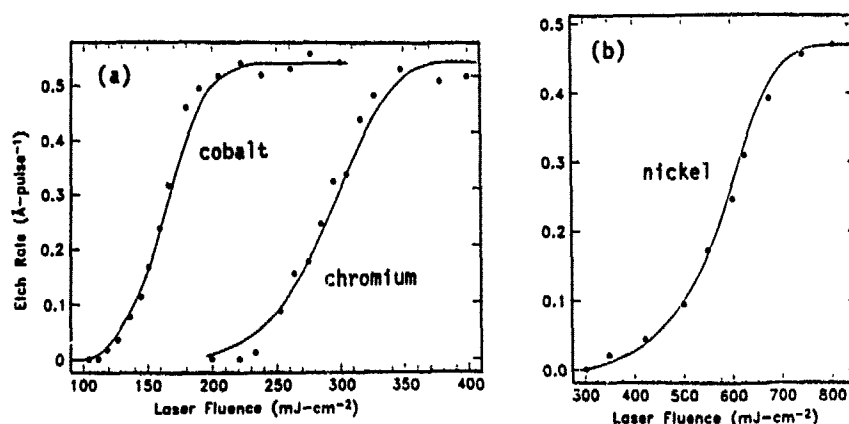


Figure 4. Laser fluence dependence of the etching of: (a) chromium and cobalt, and (b) nickel. The Br_2 pressure was 0.100 Torr in each case.

C. Iron Etching

In the etching of iron by Br_2 , we find evidence of a third type of mechanism. The Br_2 pressure dependence of the etch rate indicates that bromination of the surface occurs between laser pulses via the dissociative chemisorption of Br_2 . In this respect, the mechanism for the etching of Fe by Br_2 is similar to those reported above. The difference between this system and the etching of the other transition metals studied is that product removal does not proceed via a thermal mechanism. The 248 nm laser fluence dependence of the etch rate is shown in Fig. 5. We observe a threshold laser fluence of $100 \text{ mJ}\cdot\text{cm}^{-2}$. Above this threshold, the etching increases linearly with laser fluence. No maximum in the etch rate was observed over the range of laser fluences studied. The 193 nm laser fluence dependence of the etching of Fe is also shown in Fig. 5. Again a threshold is observed ($70 \text{ mJ}\cdot\text{cm}^{-2}$) and the etch rate increases linearly with laser fluence above this threshold. The slope of the 193 nm fluence dependence is less than that obtained at 248 nm. Since iron absorbs more strongly at 193 nm, the removal of the reaction product is inconsistent with a thermal desorption mechanism. The linear dependence on laser fluence is suggestive of a photon stimulated desorption process. The exact nature of this process is unclear, but we note that the presence of the threshold eliminates a number of otherwise plausible explanations, i.e. photodesorption, and photodissociation of the reaction product. A similar dependence on laser fluence has been observed in the 308 nm etching of GaAs by Cl_2 [4], and in the laser sputtering of semiconductors and insulators [5]. In these systems material removal most likely occurs from the formation of electron-hole pairs via photon absorption. In the present case, it is possible that a semiconductor layer of $\text{Fe}^{2+}/\text{Fe}^{3+}$ forms on the Fe surface via formation of FeBr_2 and FeBr_3 .

D. Copper Etching

Copper can be etched by Br_2 at 248 nm. While the etching is extremely fast, i.e. greater than $100 \text{ \AA}\cdot\text{pulse}^{-1}$, this process is plagued by bromine diffusion into the bulk of the copper film. For example, exposure of a room temperature crystal to Br_2 at 0.100 Torr results in the absorption of greater than 100 monolayers of Br_2 in 60 seconds. These results are very similar to those obtained in the etching of Cu with Cl_2 [6]. Since this diffusion (and hence corrosion) makes this process of little practical use, this system was not studied further.

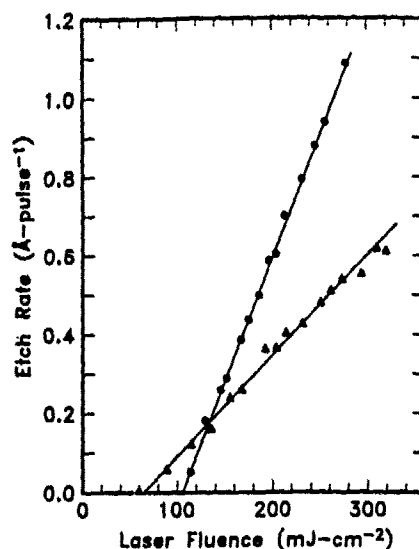


Figure 5. Laser fluence dependence of the etching of iron at 248 nm (●), and 193 nm (Δ). The Br₂ pressure was 0.100 Torr.

CONCLUSIONS

The results of this work are summarized below.

Etching System	Laser Threshold (mJ-cm ⁻²)	Maximum Etch Rate (Å-pulse ⁻¹)	Metal Layers Removed	Desorption Energy (kJ-mole ⁻¹)
Ti + Br ₂	190	6.2	2.7	172
Cr + Br ₂	220	0.53	0.35	79
Co + Br ₂	115	0.54	0.27	67
Ni + Br ₂	300	0.46	0.26	88
Fe + Br ₂	100 (248 nm) 70 (193 nm)	> 1.1 (248 nm) > 0.6 (193 nm)	> 0.78 > 0.43	—
Cu + Br ₂	---	> 100	---	---

We have demonstrated that each of the metals studied can be etched by bromine at 248 nm. We have quantified both the laser fluence dependence and the Br₂ pressure dependence of the etch rate for each metal. These measurements have provided insight into the mechanisms by which these first-row transition metals are etched by Br₂.

REFERENCES

1. G.W. Tyndall and C.R. Moylan, Appl. Phys. A, submitted.
2. D. Burgess, P.C. Stair, and E. Weitz, J. Vac. Sci. Technol. A **4**, 1362 (1986).
3. R. Colton and J. H. Canterford, Halides of the First Row Transition Metals (Wiley-Interscience, London, 1969).
4. G. Koren and J. E. Hurst Jr., Appl. Phys. A **45**, 301 (1988).
5. T. Nakayama, Surf. Sci. **133**, 101 (1983).
6. J. J. Ritsko, F. Ho, and J. Hurst, Appl. Phys. Lett., **53**, 78, (1988).

PHOTOCHEMICAL AREA-SELECTIVE ETCHING OF Si AND SiO₂ USING SYNCHROTRON RADIATION

JUN-ICHI TAKAHASHI, YUICHI UTSUMI, AND TSUNEO URISU
NTT LSI Laboratories, 3-1, Morinosato Wakamiya, Atsugi-Shi,
Kanagawa, 243-01 Japan

ABSTRACT

Photochemical etching of Si and SiO₂ using synchrotron radiation (SR) is carried out. The etching rate of SiO₂ is much higher than those of poly-Si and single crystal Si. The etching rate of poly-Si increases as dopant concentration decreases. These material selectivities are quite different from those for plasma- or laser-excited etching. These new phenomena in SR-stimulated etching can be explained by a reaction model that contains reaction centers that are produced by both core and binding electronic excitation of Si and fluorinated Si in the surface layers. These centers are quenched by majority carriers.

INTRODUCTION

The synchrotron radiation (SR) excited process has many unique characteristics compared with conventional plasma- or laser-excited processes. Concerning SR-stimulated etching of silicon and silicon dioxide, we have already reported that the surface reaction mechanism is dominant and that area-selective, anisotropic etching can be achieved due to this reaction scheme [1,2,3]. These characteristics suggest that material surface photo-excitation plays an important role in SR-stimulated etching. One of the most interesting etching characteristics is material selectivity, not only because of its practical applicability to the fabrication process but also for investigation for surface reaction mechanism. From these standpoints, we studied the material selectivity, including the doping effect on silicon etching and also studied wavelength dependence of the reaction to specify the surface excitation process. On the basis of these results, a reaction model for SR-stimulated etching was proposed.

EXPERIMENT

The experimental setup is shown in Fig.1. A radiation beam with a horizontal acceptance angle of 2 mrad from a 2.5 GeV storage ring at the Photon Factory of National Laboratories of High Energy Physics (KEK-PF) in Tsukuba was bent by 8° and focused at the reaction chamber using a Pt-coated toroidal mirror. The spectrum of the incident light beam ranged from about 20 to 1000 Å in wavelength. For the purpose of wavelength selection a pair of Pt-coated plane mirrors was set between the toroidal mirror and the reaction chamber [3]. This method is based on the principal that a spectrum of the vacuum ultraviolet (VUV) light reflected on the mirror surface varies depending on a grazing incidence angle. In our system, the grazing incident angles to

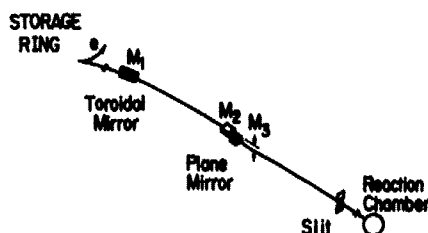


Fig.1. Experimental setup for SR-stimulated etching.

the mirrors were varied simultaneously from 0° to 30° . In the case of 0° angle, the mirrors can be moved aside the beam pass so that the SR white beam can be utilized. The incident beam was introduced perpendicular to the sample surface. The average beam spot size at the sample surface was about $3 \times 4 \text{ mm}^2$. Reaction gas, 100% SF_6 , was fed into the reaction chamber. Total pressure of the reaction chamber ranged from 0.05 to 0.13 Torr. A large amount of pressure difference between the beam line and the reaction chamber was sustained by differential vacuum pumping.

The samples we used for the investigation of material selectivity were SiO_2 and Si. The SiO_2 samples were thermally oxidized films of single crystal Si wafer, vitreous quartz and crystalline quartz plates. The Si samples used were single crystal Si wafers and two kinds of CVD films; sample groups A and B. Sample group A was silicon films formed by using low pressure chemical vapor deposition (LPCVD) at 500°C , in which phosphorous atoms were in-situ doped from PH_3 gas to a concentration of $2 \times 10^{20} \text{ atoms/cm}^3$. Two of them were annealed for impurity activation at 650, and 800°C . It is confirmed by using Raman scattering measurement that the unannealed sample was amorphous and 650 and 800°C annealed ones were polycrystalline. Sample group B was silicon films formed by using LPCVD at 625°C , in which boron or phosphorous was ion-implanted to a concentration of $10^{19} - 10^{20} \text{ atoms/cm}^3$ after deposition. The implanted samples and undoped one were separately annealed at 900°C in a nitrogen atmosphere. These samples were confirmed to be polycrystalline with Raman scattering. The dopant concentration and resistance of the samples were measured by using secondary ion mass spectroscopy (SIMS) and four point probe method, respectively.

RESULTS

The etching rates of Si sample group A and SiO_2 are shown in Table I. The etching rates are presented as etched volume per dose (storage ring current \times etching time) under the equivalent condition (total pressure 0.13 Torr, substrate temperature 300K, Pt mirror angle 3°) in all cases. The etched volume was estimated on the basis of etched depth distribution, which was obtained by using a stylus step profiler. The Si etching rate drastically decreases above the annealing temperature 650°C at which crystallization and activation of dopants occur. The etching rates for SiO_2 are larger than for Si and there is not a

Table I. SR-stimulated etching rate of Si and SiO₂ on the condition of SF₆ total pressure 0.13 Torr, substrate temperature 300K, and Pt mirror angle 3°.

MATERIAL	ETCHING RATE (10 ⁻⁸ cm ³ /A min*)
Si: P-DOPED Si (AS DEPOSITED; AMORPHOUS)	34
(ANNEALED at 650°C ; POLY-CRYSTAL)	7.6
(ANNEALED at 800°C ; POLY-CRYSTAL)	6.6
SINGLE CRYSTAL	0
SiO ₂ : THERMAL OXIDE	52
VITRIOUS QUARTZ	45
CRYSTALLINE QUARTZ	36

* DOSE = STORAGE RING CURRENT (A) x ETCHING TIME (min)

very strong dependence on the crystallinity. These results suggest that the etching reaction strongly depends on the electrical conductivity.

This suggestion becomes more clear by investigating the dopant concentration dependence. The etching rates of sample group B as a function of sheet resistance are shown in Fig.2. The etching rates are presented as desorbed Si atom number per dose under the equivalent condition (total pressure 0.08 Torr,

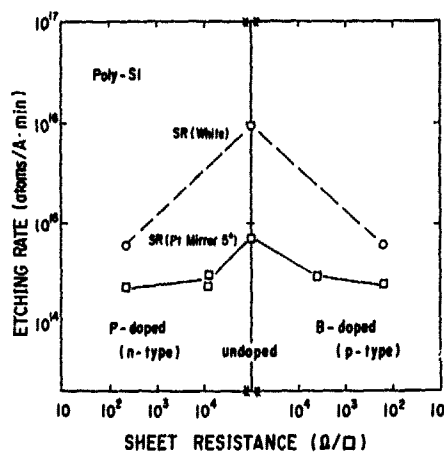


Fig.2. Etching rate of poly-Si as a function of sheet resistance on the condition of SF₆ total pressure 0.08 Torr and substrate temperature 300K.

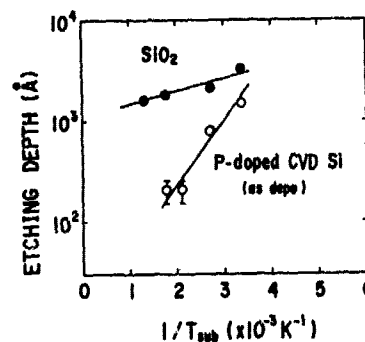


Fig.3. Dependence of SR-stimulated etching rate on substrate temperature on the condition of SF₆ total pressure 0.13 Torr and dose 22 A min.

substrate temperature 300K). The etching rate was increased with decreasing dopant concentration, regardless of the type conductivity. The broken line is for white SR and the solid line is for a mirror angle of 5° . Because crystallinity of this sample group is equivalent (polycrystal), the decrease in etching rate is due to electric conductivity increase. This is quite different from what happens during plasma- and laser-excited etching, particularly for n-type crystals.

The substrate temperature dependence of the SR-stimulated etching rate is shown in Fig.3. The filled circles are for SiO_2 (thermal oxide) and the opened circles are for P-doped CVD silicon films (group A) as deposited (amorphous). It appears that the effective activation energies for these reactions are negative, in contrast to the situation for plasma etching [4]. This result suggests that the etching reaction is induced by photo-excitation of the substrate surface, and not by the thermal effect. It is supposed that the reason the substrate temperature dependence for the amorphous Si is much steeper is because it includes the temperature dependence of conductivity.

In order to clarify the surface excitation process, we investigated the wavelength dependence of the etching rate. In this experiment, the spectrum of the irradiated SR beam was changed by varying the Pt mirror angle in the middle of the beam line (See Fig. 1). The spectra of the SR beam we used in this experiment at each mirror angle is shown in Fig.4. Without a mirror in the figure means a white SR beam. The spectra are expressed as the number of photons irradiating on the sample surface, which were calculated from the theoretical SR spectrum

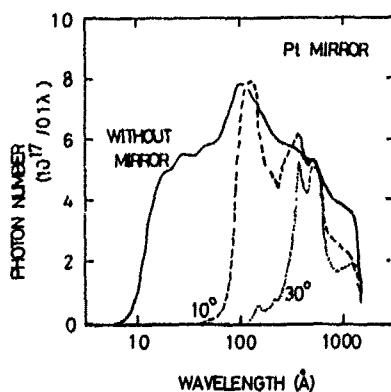


Fig.4. SR spectra irradiated on the sample surface for various mirror angles.

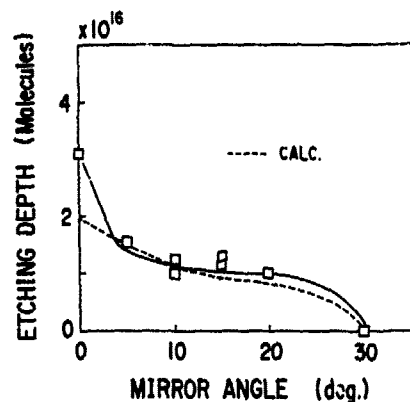


Fig.5. Wavelength dependence of SR-stimulated etching of SiO_2 on the condition of SF_6 total pressure 0.05 Torr and substrate temperature 300K. The etching amounts were attained by corresponding SR doses shown in Fig.4. Broken line indicates calculated value according to the reaction model.

of this beamline, reflectivity of the Pt mirrors at these angles, and the photo-absorption cross section of SF_6 . It must be noted that the irradiation dose was changed for each mirror angle so that a moderate amount of etching could be observed in each case.

Figure 5 shows mirror angle dependence of SiO_2 etching amount under the SR dose indicated in Fig.4. In Fig.5, a 0° mirror angle means SR white beam irradiation without Pt mirror reflection. The etching proceeds well at low mirror angles, which corresponds to a wavelength between about 20 and several hundred Å. In general, high energy photons have a large influence on the etching. The broken line in the figure indicates the calculated etching amount according to the reaction model which is mentioned in the discussion section. The total etching amount is assumed to be proportional to

$$\int V(\text{SiO}_2^*) \times V(\text{SF}_6^*)^4 dt \quad (1)$$

where $V(\text{SiO}_2^*)$ and $V(\text{SF}_6^*)$ are excitation rates of SiO_2 and SF_6 , respectively. The integration is carried out during the etching time. In this calculation, it is assumed that the excitation of core electrons (Si_{2p} , O_{2s}) of SiO_2 has as much an influence as that of binding electrons. However, the discrepancy between the experimental and calculated results in low grazing incident angles, especially in the case of white beam irradiation, suggests that the assumption is not valid and that the excitation of the core level contributes to the etching reaction much more than that of the binding energy excitation.

DISCUSSION

Dopant concentration dependence is quite different from that of other dry etching processes [5,6]. In plasma or excimer laser etching using fluorinated gas, n-type silicon etching rate is greater than that of undoped or p-type silicon. Furthermore, the n-type silicon etching rate is increased with increasing dopant concentration. In these works these phenomena are explained as a free electron transfer [5] or a valence electron transfer [6,7] mechanism through the surface fluorinated layer.

In our SR-stimulated etching case, the material selectivity and substrate temperature dependence strongly suggest that photo-excitation of the substrate surface is important and the etching rate depends on material conductivity.

It is well known that "self trapped excitons", which are a kind of crystal defect, are formed by the electronic excitation of insulating crystals such as halogenated metal and quartz, and that photo-induced defects are generated in amorphous Si. It is quite probable that these kinds of defects are centers for photochemical reactions in the solid or on the surface. The present data on the material selectivity of etching strongly suggest that these kinds of excitations contribute to the etching reaction. In addition, it is known that fluorine atoms or ions adsorbed on the surface diffuse into the substrate during etching using fluorinated gas, resulting in the formation of a surface insulating layer of fluorinated Si [5,7]. With these considerations in mind, the reaction model for present SR-stimulated etching is proposed as follows:

- (1) SF_6 is decomposed by the SR excitation in the gas phase or on

the surface, and a fluorinated layer is formed on the surface.

(2) Reaction centers are produced by the excitation of Si or fluorinated Si.

(3) The reaction centers react with the surrounding F atoms to produce volatile SiF_n molecules. From the pressure dependence of the etching rate, n is assumed to be 4 [2].

It is speculated that the reaction centers are less stable in materials with a higher conductivity. The effect of doping, that is, etching reaction rate reduction with increasing conductivity, can be interpreted as a quenching of the reaction centers by majority carriers.

For the purpose of constructing a precise reaction model, it is necessary to have more detailed information concerning the surface state or desorbed species.

CONCLUSION

Material selectivity in SR-stimulated etching of Si and SiO_2 was investigated. The etching rate depends on the electrical conductivity. This result can be well explained by the reaction model, which is based on quenching of excited reaction centers by majority carriers. On the basis of the experimental results concerning the wavelength dependence, it is assumed that the reaction centers are produced by both core and binding electronic excitation of Si or fluorinated Si in the surface layer.

ACKNOWLEDGMENTS

The authors would like to thank Tetsushi Sakai for his continuous guidance and encouragement. They are grateful to Takahiro Makino and Yutaka Sakakibara for their sample preparation, and also grateful to Izumi Kawashima for his SIMS measurement. Our constant appreciation is given to the staff of the Photon Factory KEK for their collaboration in these experiments.

REFERENCES

- 1) T.Urisu and H.Kyuragi, J.Vac.Sci.&Technol. B5, 1436 (1987).
- 2) J.Takahashi, Y.Utsumi, and T.Urisu, in Extended Abstracts of the 20th Conference on Solid State Devices and Materials, (Business Center for Academic Societies, Tokyo, 1988), p.73.
- 3) T.Urisu, H.Kyuragi, Y.Utsumi, J.Takahashi, and M.Kitamura, Rev. Sci. Instrum. 60, 2157 (1989).
- 4) D.L.Flamm, V.M.Donnelly, and J.A.Mucha, J.Appl.Phys. 52, 3633 (1981).
- 5) H.F.winters and D.Haarer, Phys.Rev.B 36, 6613 (1987)
- 6) M.Hirose and T.Ogura, in Photon, Beam, Plasma Stimulated Chemical Processes at Surfaces, edited by V.M.Donnelly, I.P.Herman, and M.Hirose (Mater. Res. Soc. Proc. 75, Pittsburg, PA 1986) p.357.
- 7) T.Ogura, T.Hayashi, S.Miyazaki, and M.Hirose, Jpn.J.Appl.Phys. 27, L2256 (1988).

PART II

Laser Deposition I

LASER-BASED AREA-SELECTIVE PROCESSING TECHNIQUES FOR HIGH-DENSITY INTERCONNECTS

Y.S. LIU and H. S. COLE

GE Research and Development Center; P.O. Box 8, Schenectady, NY, 12345

ABSTRACT

This paper reviews several laser-based area-selective processing techniques developed for high-density multichip interconnection applications. Key material and process requirements for the development of a viable laser-direct-write interconnect technique on polyimide are addressed.

1. INTRODUCTION

The rapid advances in VLSI processing technology have outpaced the development of the electronic packaging and interconnect technology. Shrinking feature sizes, increasing gate density and clock rates have made electronic devices faster, and more complex. As a result of the increasing number of pin-counts and power dissipation, the VLSI packaging and interconnect become a very complex task. The chip-to-chip delay is becoming a limiting factor of the system performance. To reduce the chip-to-chip interconnect length and improve circuit performance, multichip module packaging and high density interconnect are the key technologies.

Laser processing has been shown to be a viable technology for depositing and/or etching a variety of metals and dielectric materials and has been the subject of many research activities. [1-3]. Laser metal patterning on polymers, either direct-write or projection patterning, is particularly relevant to high-density interconnect. For HDI applications, the relatively long focal depth achievable with a Gaussian laser beam is a very important property which is unique to laser processing. [4] This property is particularly critical when the substrate surface is not completely planar, as is frequently encountered in polyimide structures. For HDI applications, key laser process steps include fabrication of micro-vias and metal interconnects. In the following sections, several laser-based processing techniques that have been developed for HDI applications are discussed.

2. HIGH-DENSITY INTERCONNECT TECHNOLOGY (HDI)

Various HDI approaches have been developed. The topic has been discussed in a review paper by Neugebauer et al [5] and the results are summarized in Table 1. The Table also illustrates the requirements of various HDI technologies in terms of substrate, metal, dielectric materials, method of patterning, chip attachment and interconnect technology. As the Table shows copper or aluminum is the most commonly used metal for high-density multichip interconnect, while polyimide is the most commonly used dielectric material due to the fact that the polymeric material is compatible with the standard IC processing technology, has good thermal stability, and more importantly, has a low dielectric constant. Therefore, it reduces capacitive coupling

between metallization stripes and results in higher device speeds when it is used as the dielectric material.

Among those HDI approaches described in Table 1, only GE [6] and Livermore [7] utilize lasers as the processing tool for fabrication of interconnect structures. Although the two processes differ significantly in interconnect fabrication, use of the adaptive and maskless laser processing technique makes these processes suitable for quick turn-around prototyping design. In addition, higher degree of precision and interconnect resolution are also better achieved with laser techniques.

In the GE HDI process using an overlay structure, bare chips are mounted into recesses in the substrate. A polyimide sheet is laminated over the chips, vias are drilled to the chip pads, and interconnect lines are formed on the polyimide surface. This is followed by applying the new dielectric, fabrication of the vias, and interconnects paths for the upper signal layer with the line direction generally orthogonal to those in the lower layer. The entire process for via formation and metal patterning steps were carried out using an adaptive laser lithography system, summarized briefly as follows: [6]

**HIGH PERFORMANCE INTERCONNECT TECHNOLOGIES -
MULTI-CHIP HYBRID MODULE**

USER	SUBSTRATE	CONDUCTOR				INSULATOR	CHIP ATTACH	MODULE I/O
		MATERIAL	WIDTH	THICKNESS	PITCH			
				(μm)				
MOSAIC	SI	Al	11	2	22	SiO ₂	WIRE-BOND	WIRE-BOND
IBM	Al ₂ O ₃	Cu	8	6	25	POLYIMIDE	SOLDER-BUMP	PIN-GRID-ARRAY
HONEYWELL	SI	Cu	50	5	125	POLYIMIDE	WIRE-BOND TAP-BOND	WIRE-BOND
ATT	SI	Cu	25	5	50	POLYIMIDE	SOLDER-BOND	PIN-GRID-ARRAY
RAYCHEM	SI	Al	40	5	100	POLYIMIDE	WIRE-BOND	WIRE-BOND
GE	Al ₂ O ₃	Cu	25	5	75	POLYIMIDE	OVERLAY THIN FILM	WIRE-BOND
LIVERMORE	SI	Au	15	3	25	SiO ₂	BEVELED EDGE THIN FILM	WIRE-BOND

Table 1 - High Performance Multichip Module Interconnect Technology. (Ref.1)

A laser is used to cut recesses in an alumina substrate with a thickness chosen to be slightly less than that of the thinnest chip. Power/ground lines and I/O pads are formed on the substrate by aluminum deposition and patterning. Tested bare chips are then bonded into the recesses in the substrate. An image scan locates the chips and their pad positions. A polymer adhesive layer is sprayed over the frame and chips and a sheet of Kapton is laminated to the frame and chips using heat and pressure. Vias are then drilled by a laser over the chip pad positions. Polymer debris and residues are removed by plasma etching. The via formation step is followed by interconnect metallization. The signal metallization is patterned by exposing a negative resist using a laser. A subtractive process is used to define the interconnect path. Chip misalignment is accommodated by computer-adaptive writing. The ideal chip pad locations and interconnect network are stored in software. Comparison of the actual positions of two chip pads in a slightly misaligned chip serves to define the real position of all pads in a particular chip. The final interconnect configuration is then achieved by introducing slight modification in order to adapt to the actual chip pad positions. The next signal layer is built up following a process sequence similar to that of the first layer. The polyimide dielectric layer is spun over the first metal layer. Via holes are opened with the laser, and metal deposition and patterning are carried out as before. Power and ground lines can be incorporated into the signal layers, or, for better impedance control, separate power and ground planes can be formed between, on top, or beneath the signal layers. A thermoplastic adhesive layer is used to bond polyimide to the chips and substrates. This allows removal of the overlay and rework without damage to the chips. Since the chips are mounted in the substrate with a thermoplastic adhesive, they also can be individually replaced during the rework procedure. Additional advantages of this approach for multichip packaging include rapid prototyping, quick design changes, and high-density interconnect of 50 micron pitch.

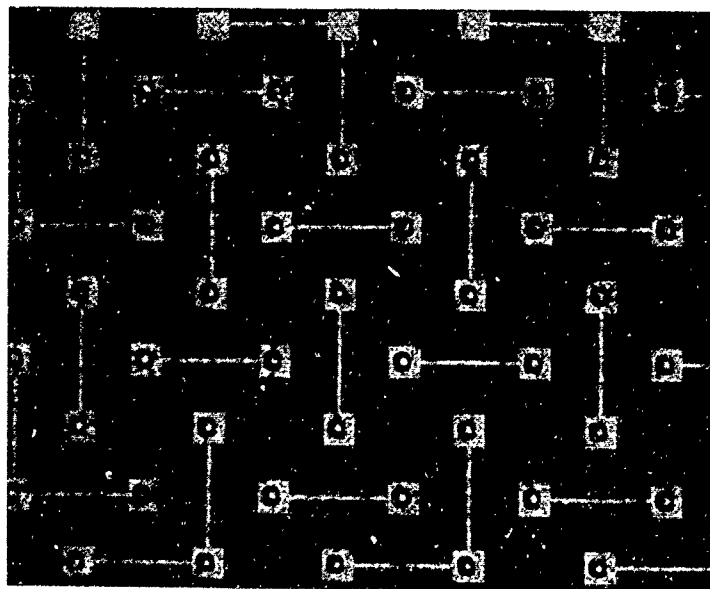


Fig. 1 - Optical Micrograph showing micro-vias fabricated in polyimide film of 25 micron thick using a frequency quadrupled UV YAG laser. The pad size is 100 microns.

3. LASER-BASED PROCESSING TECHNOLOGY FOR HDI

3.1 Laser Fabrication of Micro-Vias

Fabrication of micro-vias in polyimide has been successfully demonstrated using various lasers as the source. [8]. The mechanism of laser via drilling has been attributed to a combination of photo- and thermal- processes, depending on the wavelength and the type of laser used. The use of excimer lasers for via drilling in polyimide has attracted particular attention and has been the most extensively studied micro-vias drilling technique [9]. Etch rates are typically on the order of a fraction of a micron per pulse at a fluence level of several hundred millijoules per square centimeter. The fabrication of blind micro-via holes using KrF excimer lasers for IC printed circuit board with high process through-put has been recently reported. [10] Although excimer lasers produce high quality micro-via holes, the drilling speed and thus the process through-put are limited by the pulse repetition rate in the process requiring serial drilling. We have overcome this problem by employing a high repetition rate Q-switched YAG laser frequency-quadrupled to UV at 266 nm. We were able to achieve high speed drilling of micro-vias at a drilling speed up to several milliseconds per via hole which significantly improved the process throughput. Fig. 1 is an optical micrograph showing micro-vias fabricated using a frequency-quadrupled UV YAG laser in polyimide film of about 25 μm thick. Specific physical properties of the polymer, such as absorption coefficients and thermal stability, and match to the appropriate laser wavelength must be taken into account. [11]

3.2 Laser Area Selective Metallization

Several laser area selective metallization techniques for high density interconnect applications are discussed in the following sections. Techniques include laser patterning of photoresist used in conjunction with thin film metallization processes, laser surface modification for selective metallization, and selective electrolytic metal deposition.

Laser Patterning Photoresist -

Use of laser to pattern photoresist followed by conventional thin film metallization processes is being used in the current HDI process for fabrication of interconnect paths using either additive or a subtractive metallization process. [12,13] In the additive approach, a thin adhesive metal such as chromium or titanium is sputtered followed by deposition of thin copper. A photoresist layer of about 25 μm is coated over the sputtered metals, laser exposed, and developed to form the desired interconnect patterns. Thicker copper is then electroplated to a thickness of 3 to 6 μm . After the resist is removed, the sputtered metal is back etched to yield the final interconnect metal pattern. In a subtractive process, the electroplating and photoresist steps are reversed. Use of laser to pattern photoresist is a useful technique as long as the substrate surface is reasonably planar. In HDI processing using polymer overlays, the substrate surface is not completely planar and therefore the resist uniformity becomes a problem. The variation of resist thickness could lead to nonuniform exposure and development, and thus limit the interconnect resolution. Special resists with lower values of absorbance at the exposure laser wavelength have to be developed to accommodate the topography non-uniformity.

Laser Surface Modification -

An alternate approach to resist patterning is to utilize laser selective metal deposition, either direct-writing or projection patterning to form the interconnect. A key requirement for the development of a direct-write process compatible with multichip interconnect is the writing speed. For interconnect runs of total length of several meters, a writing speed must be greater than several cm/s in order to achieve an acceptable process throughput [12]. A review of various gas phase photolytic and pyrolytic laser direct-write processes has shown that thermally induced processes have usually higher deposition rates over photochemical ones [13]. Although many interesting photochemical deposition processes have been reported [5], none of the reported processes are able to provide a writing speed fast enough to be useful for direct-write in HDI applications. Further research effort in this area is certainly warranted. Our approach to improve writing speeds is to utilize a two-step process, namely, laser irradiation is first used to area selectively modify the polymer surface, then followed by a batch thin film process to yield interconnect patterns of desired dimension and thickness. Several processes using this approach have been developed using the two-step process using either electroless or electrolytic metal deposition, and are described in the following section.

Selective Electroless Metal Deposition -

Electroless deposition has been commonly used for deposition of copper on non-conducting substrates such as polymers. The electroless metal deposition is also useful for providing thin copper film on polymer substrates for further electrolytic deposition to form a thicker metal layer. Among several selective metallization techniques we have developed, two processes are described as follows: (1) Positive metal patterning technique: Use of an Argon laser to selectively deposit a trace amount of palladium on polyimide surfaces. The surface area exposed to the laser thus becomes catalyzed and is selectively metallized when the sample is placed in an electroless copper solution. (2) Negative metal patterning technique: an excimer laser is used to desensitize a polyimide surface, and thus inhibit the exposed area from metallization when the sample is placed in an electroless plating bath. These two interconnect metallization techniques have been previously discussed [14] and are briefly summarized below.

Fig. 2 schematically illustrates the positive metal patterning technique in which an Argon laser is used to selectively catalyze a polyimide surface. A Pd-containing organometallic compound such as palladium acetate (PdAc) was dissolved in chloroform and spun on the polyimide surface. [14, 15] A 351-nm argon laser was used to direct write the surface to thermally decompose the organometallic compound. The Pd-surface concentration was controlled by varying the initial amounts of PdAc dissolved in the solvent. After irradiation, the sample was immersed in an electroless copper plating solution and copper was selectively deposited onto the surface areas exposed to laser writing. Fast writing speeds of several cm's/sec were achieved. Only a few monolayers of palladium are required to catalyze electroless copper deposition. Because of the strong absorption of polyimide at 351 nm, local heating induced by laser irradiation on the polyimide surfaces thermally decomposes PdAc at a laser power of a few milliwatts. Fig. 3 shows optical micrographs of copper lines

Fig. 2 - Schematically illustrates the positive metal patterning technique in which an Argon laser is used to selectively catalyzed a polyimide surface. A Pd-containing organometallic compound such as palladium acetate (PdAc) was dissolved in chloroform and spun on the polyimide surface. [14,15]

LASER-ACTIVATED COPPER DEPOSITION — THIN FILM APPROACH

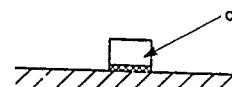
- 1 DISSOLVE ORGANOMETALLIC IN SOLUTION AND SPIN ON, THEN LASER ACTIVATE



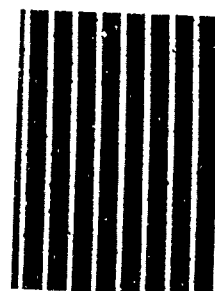
2. RINSE



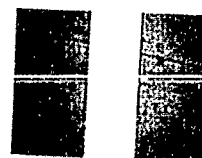
- 3 ELECTROLESS Cu DEPOSITION



Laser-Activated Cu Deposition on Polyimide (Argon Laser at 351 nm, 20 mW, 2 mm/s)



100 μm



20 μm

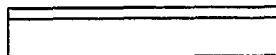
Fig. 3 - Optical micrographs of copper lines fabricated on polyimide using two-step laser surface modification technique described in the text.

fabricated using this technique. Depending on power and scan speed, copper line widths of about 7 to 50 μm with a thickness of 1.5 μm have been fabricated. Recently, this technique has been further developed and demonstrated using excimer lasers [16], incoherent VUV source, [17] and synchrotron source. [18]

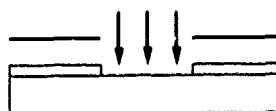
The negative patterning process is illustrated in Fig. 4 in which an excimer laser is used to desensitize the polyimide surface which has been spin-coated with a thin layer of Pd-containing compound. After the sample surface is exposed to the excimer laser using a contact mask or projection method. The laser radiation desensitizes the surface once the irradiating fluence is above a certain threshold level, a value depending on the wavelength of the excimer laser used. After the irradiation, the sample is immersed in an electroless copper plating solution to form a copper pattern shown in Figure 4. Due to the strong absorption of polyimide at both 193 and 248 nm, the threshold fluence was observed to be as low as 20 mJ/cm². Once the exposed laser fluence exceeds the threshold level, the copper patterns formed were found to be almost identical independent of the number of irradiating pulses.

EXCIMER LASER SELECTIVE METALLIZATION

A. Surface Sensitization



B. Excimer Laser Patterning



C. Selective Metallization

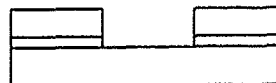


Fig. 4 - Schematic of negative laser metal patterning technique - An excimer laser is used to desensitize the polyimide surface which has been spin-coated with a thin layer of Pd-containing compound. The sample surface is exposed to the excimer laser using a contact mask or projection method, and the desensitized surface thus inhibits the electroless copper deposition.

Selective Electrolytic Deposition -

Electrolytic deposition is a common process used for metallization in electronic packaging and printed circuit board fabrication. The deposition rate is fast, and metal patterns of several microns thick can be readily fabricated using the electrolytic deposition method. Patterning a spun-on photoresist is commonly used for fabrication of metal interconnect patterns, followed by either an additive or subtractive electrolytic deposition process for form the final interconnect paths.

In the course of our studies of surface modification techniques, we have discovered that electrolytic copper deposition takes place selectively on certain metal surfaces such as copper and gold, but not on certain other types of metal such as titanium. The presence of thin but highly resistive surface titanium oxide layer is attributed to the selectivity observed in the electrolytic deposition process. This kind of subtle difference in surface property has led to the development of Selective Electrolytic Deposition (SED) process which is illustrated schematically in Fig. 5. The initial structure is a Cu surface deposited with a thin Ti film about 40 nm thick. The thin Ti layer is patterned and serves as a mask. The copper lines are selectively deposited onto the Cu surface when this kind of structure is placed in an electrolytic copper plating solution. A test structure of copper lines fabricated using the SED process on polyimide is shown in Fig. 6. The process is highly selective if an appropriate combination of metals are used, and 6 μm copper lines have been fabricated with a thickness of 3 μm . Work is in progress to further understand the fundamental mechanism of the SED process and to apply this technique to HDI structures.

4. DISCUSSION

The laser surface modification reactions described here provide a sensitive technique for area selective metallization. Both direct-write and projection patterning techniques can be used to produce interconnect structures. However, several technically challenging problems remain to be solved in order to make laser processing an important processing tool for the high density interconnect technology. First, any direct-write interconnect process must be capable of achieving low-resistance contacts to contact pads as well as having good adhesion to polyimide. Secondly, techniques have to be developed to accommodate large differences in thermal conductivity and optical reflectivity between the polyimide surface and the region in the vicinity of the metal contact pads underneath the via holes. Thirdly, a laser direct-write interconnect process must be compatible with the metal adhesion layers used. Lastly, adhesion of metal interconnects using laser direct-write processes is also affected by oxide formation on the primer layers used. This oxide layer must be removed prior to deposition of the catalytic surface. Use of inert environments during laser deposition or selective catalytic desensitization is required.

SELECTIVE ELECTROLYTIC DEPOSITION (SED)

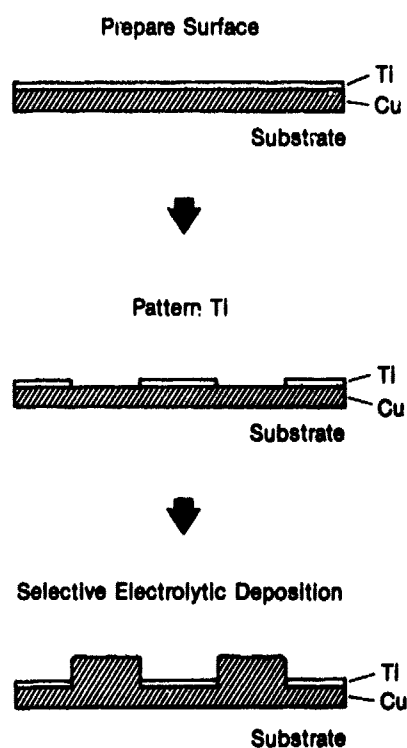


Fig. 5. -The initial structure is a Cu surface deposited with a thin Ti film of about 40 nm thick. The thin Ti layer is patterned while the remaining thin Ti layer serves as a mask. The copper lines are selectively deposited onto the Cu surface when this kind of structure is placed in an electrolytic copper plating solution.

SELECTIVE ELECTROLYTIC DEPOSITION OF COPPER

Process

- Sputter Thin Ti (1000 Å) on Cu (1000 Å)
- Pattern Ti
- Selective Electrolytic Deposition of Cu ($3\mu\text{m}$)



Fig. 6 - Copper lines fabricated using the Selective Electrolytic Deposition process described in the text.

In summary, surface modification using lasers provides a sensitive technique for interconnect metallization. A positive selective metallization process in which an organometallic palladium compound is laser decomposed to form palladium catalyst for selective electroless copper deposition has been described, and a negative metal patterning process in which a polymer surface is desensitized using laser-ablated catalyst has also been shown. In addition, we have also discussed a selective electrolytic deposition process which is particularly useful for Cu/polyimide structures for HDI applications.

ACKNOWLEDGEMENT

We thank R. Guida and J. Rose for their excellent technical assistance and J.E. Norton for the SEM work. Helpful discussions with C.A. Neugebauer, R.A. Fillion, C.W. Eichelberger and R.J. Wojnarowski are also acknowledged. This work has been partially supported by ONR/SDIO under contract number N00014-85C-0890.

REFERENCES

1. D.J. Ehrlich and J.Y. Tsao, Ed. "Laser Microfabrication: Thin Film Processing and Lithography," Academic Press, (1989).
2. Y.S. Liu, in "Tungsten and Other Refractory Metals Deposition for VLSI Applications," edited by R.I. Blewer, Materials Research Society, p. 43 (1985).
3. Y.S. Liu and H.S. Cole, in "Electronic Packaging Materials Science IV," ed. by R. Jaccodine, K.A. Jackson, D. Lillie and R.C. Sundahl, Mat. Res. Soc. Proc. Vol. 154, (1989)
4. Y.S. Liu, "Sources, Optics and Laser Microfabrication Systems for direct Writing and Projection Lithography," in "Laser Microfabrication and Thin Film Processes and Lithography," Ed. by D.J. Ehrlich and J.Y. Tsao, Academy Press, p.3, (1989)
5. C.A. Neugebauer, R.O. Carlson, R.A. Fillion, and T.R. Haller, Solid State Tech. p. 93 (June 1988), and the related references cited in the paper.
6. C.W. Eichelberger, R.J. Wojnarowski, R.O. Carlson, and L.M. Levinson, SPIE Symposium on Innovative Science and Tech. Paper 877-15 (January 1988).
7. D.W. Tuckerman, IEEE Elec. Dev. Lett. EDL-8, 11, pp. 540-543 (1987)
8. H.S. Cole, Y.S. Liu, J.W. Rose, and R. Guida, Appl. Phys. Lett. 53, 2111 (1988).
9. H.S. Cole, Y.S. Liu, R. Guida, and J. Rose, SPIE 877, p. 92 (1988).
10. F. Bachmann, Chemtronics, Vol.4, No.3, (1989)
11. Y.S. Liu, H.S. Cole, H.R. Philipp and R. Guida, Proc. of SPIE, "Lasers in Microlithography," Vol. 774, (1987)
12. H.S. Cole, Y.S. Liu, J.W. Rose, R. Guida, L.M. Levinson, and H.R. Philipp, Conf. Proc. For Microelectronic Applications, Honolulu, Hawaii (1987).

13. H.S. Cole, Y.S. Liu, H.R. Phillip, and R. Guida, Mat. Res. Soc. Symp. Proc. 72, p. 241 (1986).
14. Y.S. Liu and H.S. Cole, Chemtronics, Vol.4, No.3, 209, (1989)
15. M.E. Gross, Chemtronics, Vol.4, No.3, 197, (1989)
16. H. Esrom and G. Wahl, Chemitronics, Vol.4, No.3, 216 (1989)
17. H. Esrom, J. Demny and U. Kogelschatz, Chemtronics, Chemtronics, Vol.4, No.3, 202, (1989)
18. Y. Zhang and M. Stuke, Chemtronics, Vol.4, No.3, 212, (1989)
19. Y.S. Liu, W.T. Grubb, and H.S. Cole, in Tech Digest of Conf. on Lasers and Electro-Optics, WX-5, p. 286 (1988).

TIME-RESOLVED STUDIES OF SURFACE MELTING DURING LASER-INDUCED CHEMICAL VAPOR DEPOSITION WITH LASER INTENSITY MODULATION

PAUL B. COMITA*, PETER E. PRICE, JR., **, and TOIVO T. KODAS***

*IBM Research Division, Almaden Research Center, 650 Harry Road, San Jose, CA 95120

**Dept. of Chemical Engineering and Materials Science, University of Minnesota, Mpls., MN 55455

***Chemical and Nuclear Engineering Dept., University of New Mexico, Albuquerque, NM 87131

ABSTRACT

Thermal laser-induced chemical vapor deposition of gold deposits has been studied using a modulated Ar⁺ laser. Deposition of gold from dimethylgold hexafluoroacetylacetonate is accompanied by surface melting of the deposit when the laser source is modulated. Time-resolved reflectance measurements have been used to study the surface reflectance during growth with modulated and unmodulated laser source. The reflectance measurements indicated that surface melting does not occur under unmodulated cw irradiation at equivalent laser intensities. Variation in the modulation duty cycle indicates that there is a minimum laser-off cycle time length required for surface melting to be observed. Evidence is presented which suggests that surface melting is due to the heat released by the exothermic decomposition of reactant adsorbed during the time that the laser intensity is off.

INTRODUCTION

Laser-induced chemical vapor deposition (LCVD) of metallic gold has been studied under a range of experimental conditions.(1) The shape and morphology of the polycrystalline gold deposits produced have been shown to exhibit a strong dependence on laser power, and the nature and partial pressure of buffer gas.(2) The ability to control deposit shape and morphology by influencing the growth kinetics can allow the control of important material properties such as adhesion and resistivity of the deposited metal. In order to introduce non-linear temperature effects that can influence the growth dynamics and microstructure of deposits, we have investigated the use of a modulated laser as a heat source for thermal laser-induced surface reactions. This paper concerns our observations of previously unreported surface melting that accompanies deposition when a modulated laser source is used. The surface melting of gold during deposition with a fixed, modulated laser beam results in structures whose shape and morphology are markedly different than deposits grown with an unmodulated beam.

EXPERIMENTAL SYSTEM

The light reflected at normal incidence to the surface has been measured as a function of laser fluence, wavelength in a two color experiment, length of duty cycle, and frequency of modulation with the experimental apparatus shown schematically in Figure 1. A 514 or 488 nm argon ion laser beam is either mechanically chopped or electro-optically modulated with a high power 25 MHz ADP Pockels cell coupled to a polarizing beam splitter. The output of the modulator is focussed with a microscope objective onto a polished alumina substrate, resulting in an approximately 10 micron focal spot at the surface. The substrate was supported in a vacuum cell to which Me₂Au(hlac) and argon gas could be admitted. The light emitted or reflected normal to the surface was collected and dispersed in a 0.24 m monochromator. The detector consisted of a photomultiplier tube, with amplification, digitizing, and waveform averaging accomplished with a Tektronix 7854 signal averaging oscilloscope.

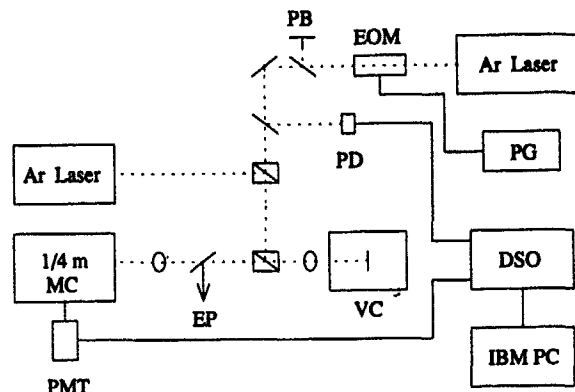


Figure 1. Schematic of Reflectance Apparatus. PB is a polarizing beamsplitter; EOM is an electrooptic modulator; PD is a photodiode; PG is a pulse generator; MC is a monochromator; VC is a vacuum cell; DSO is a digital storage oscilloscope; and PMT is a photomultiplier tube.

RESULTS AND DISCUSSION

Several general observations can be made about the surface melting phenomenon. First, the surface melting is observed only when a modulated laser source is used. Identical experiments using a continuous laser source, either at twice the continuous power of the modulated source (same fluence as the on-cycle) or at equivalent continuous power (one-half the fluence of the on-cycle), results in no surface melting of gold deposits over the fluence range that we have studied. The phase change is observed when the continuous wave laser light is modulated over a very large range of frequencies, between approximately 0.5 Hz and 100 KHz. In addition, the surface melting occurs with a substantial increase in emitted light at normal incidence to the laser-irradiated surface. This is due to a change in the reflected laser light normal to the surface of the metal deposit because of decreased surface roughness (see below).

In order to probe the dynamics of the surface phase change, the increase in light emission due to melting has been examined during the stationary growth of a gold deposit using time-resolved measurements. The reflectance intensity versus time for a typical deposition with an unmodulated source is shown in Figure 2(b). In this case, the laser power was 1.0 W, and the precursor pressure was 0.35 Torr. The intensity increased sharply at the beginning of the deposition (at 2.0 seconds), corresponding to the increased reflectivity of the gold deposit relative to the alumina substrate. As the deposit grew larger, the emission intensity decayed, reaching a nominal value after approximately two seconds of deposition. A plot of emission intensity versus time for a typical modulated beam deposition is shown in Figure 2(a). In this case, the modulation frequency was 1000 Hz, and the laser power was 1.0 W. The emission intensity reached values almost six times as large as the peak values of the unmodulated case. Larger values in the emission intensity were observed up to eight seconds after the start of deposition. At longer times, the intensity again decayed to a nominal value. Visual observation of this deposit revealed that the deposited structure melted twice, at approximately 1.7 and 2.8 seconds, corresponding to the two largest peaks in the emission intensity profiles.

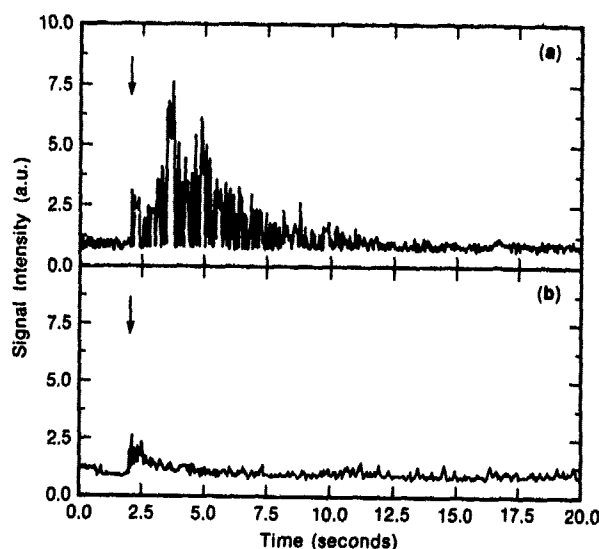


Figure 2. Normal reflectance intensity as a function of time with (a) a modulated argon ion source and (b) an unmodulated, continuous argon ion source at equivalent laser intensities. The arrow indicates the initiation of deposition.

In order to verify that the observed signal was due to reflected light, the visible emission normal to the substrate was detected throughout the visible wavelength range by dispersing the light in a monochromator. For a 514 nm pump beam, the intensity of the emitted light after subtracting the scattered, diffusely reflected background radiation from the 514 nm pump beam was found to have an intensity maximum at 514 nm. In addition, the intensity of the light emitted at normal incidence (after subtracting the intensity of the diffusely reflected light) was found to be directly proportional to the pump beam. Two color experiments were also performed using a 488 nm driving beam and a 514 nm low intensity probe. The peak in emission intensity was detected with a monochromator at the probe wavelength (as well as at the pump wavelength). The results were qualitatively the same as those in Figures 2 indicating that the emission was reflected light and not specific to the driving wavelength. Similar results were also obtained when the driving and probe beam colors were reversed.

The time evolution of the reflectance during a single pulse has been examined in order to obtain information about the dynamics of the surface melting. The characteristic reflectance intensity during deposition peaks immediately after the leading edge of the light-on period of the waveform, followed by an exponential decay. The exponential decay of the reflectance was characteristic of all measurements performed with comparable laser-on and laser-off times. This rate of decay of the reflectance signal was found to be a strong function of the spot size. In the early stages of deposition, the reflectance was found to decay rapidly within the laser-on cycle to a nominal value almost twenty times smaller than the peak reflectance just after the laser turns on. A series of time-resolved reflectance measurements were made as the modulation duty cycle was varied. Starting from an initial modulation frequency of 1000 Hz with a 50% duty cycle and holding the laser-on time constant, the laser-off time was decreased in stages

down to approximately 2% at 1950 Hz. As the laser-off time was decreased the peak reflectance also decreased until at the 2% off-time there was no discernable peak or decay. This data suggests that a minimal laser-off time during growth is needed to sustain the surface melting.

The morphology of a deposit grown with a modulated source is clearly different than in the unmodulated case. With a modulated beam, the melting of the deposited gold occurs with a collapse of the deposit shape. The overall structure after growth beyond the melting stage is volcano-like with smaller grain sizes and layered growth indicative of melting and spreading, with similar deposit structures being obtained at laser powers less than 1.0 W under 0.35 Torr of $\text{Me}_2\text{Au}(\text{hfac})$ for a wide range of modulation frequencies. Emission measurements, SEM micrographs, and visual observations during deposition all suggest that the deposited structures undergo growth periods interspersed with transient surface melting when the beam is modulated. During this time the rough surface of a deposit becomes smooth and the incident light is specularly reflected primarily normal to the surface. When the surface of the deposit is a rough polycrystalline solid, the incident beam is diffusely reflected, and the normal reflected light is thereby reduced in intensity (4). The spots grown with a modulated beam also tend to be more volcano-like throughout all stages of the deposition. When the laser source is not modulated, depositions performed even at much higher incident powers grow continuously without observable melting. Visual observation through the microscope during deposition revealed continuous, uninterrupted growth of the gold crystals. Therefore, some process occurs during the laser-off part of the modulation cycle that results in surface melting when the laser light is turned on.

Several possible explanations for the explosive melting phenomena and the reflectance decay behavior exist. One possibility is that the laser modulation resulted in modulation of the temperature of the deposit which resulted in stresses because of the differences in the thermal expansion coefficients of the gold and the substrate. However, experiments with modulated laser light on a deposit with no reactant present resulted in no melting. Another explanation is that the surface melting is the result of rapid exothermic decomposition of adsorbed layers of $\text{Me}_2\text{Au}(\text{hfac})$ that develops during the laser-off part of the modulation cycle. Differential scanning calorimetry results indicate that $\text{Me}_2\text{Au}(\text{hfac})$ decomposes exothermically with an overall heat of reaction of approximately -40 kcal/mol (5). Based on this exothermicity and experimentally determined surface coverages on Au films (6), the energy released in a 10 micron reaction zone (approximately 10^{-9} cal.) is sufficient to cause the observed changes in reflectance intensity.

Heating of a structure from a rapid, highly exothermic reaction of multilayers of adsorbate on the surface should give rise to a temperature increase that is significantly larger at the start of a laser-on cycle. The temperature necessary to melt gold is substantial (m.p. = 1064 C), and the increase in temperature should be readily detectable experimentally. We have used photothermal deflection spectroscopy (7) to accomplish this, and indeed have measured excess heating at the beginning of a light pulse in time-resolved experiments during deposition.(8)

SUMMARY AND CONCLUSIONS

In summary, we have reported a new surface melting phenomena that occurs during the laser-induced chemical vapor deposition of gold crystals from $\text{Me}_2\text{Au}(\text{hfac})$ using a modulated Ar^+ laser beam. When a modulated source is used surface melting is observed by reflectivity measurements. Deposits formed with a modulated source are generally volcano-like and have smaller grain sizes than structures grown with an unmodulated source. An intensive analysis of the melting phenomena involving metal-producing reactions which are both exothermic and endothermic, time-resolved photothermal deflection studies, detailed scanning electron microscope studies of deposit morphology, as well as theoretical calculations are currently underway.

REFERENCES

1. T. T. Kudas, T. H. Baum, and P. B. Comita, *J. Appl. Phys.*, **62**, 281 (1987).
2. T. T. Kudas, T. H. Baum, and P. B. Comita, *J. Cryst. Growth*, **87**, 378 (1988).
3. P. B. Comita and T. T. Kudas, *Appl. Phys. Lett.*, **51**, 2059 (1987);
4. P. Beckmann and A. Spizzichino, *The Scattering of Electromagnetic Waves from Rough Surfaces*, Artech House, Norwood, 1987.
5. T. H. Baum, unpublished results.
6. A. D. Dubner and A. Wagner, *J. Appl. Phys.*, **66**, 870 (1989).
7. A. Skumanich, H. Dersch, M. Fathallah, and N. M. Amer, *Appl. Phys. A*, **43**, 297 (1987).
8. P. E. Price, T. T. Kudas, and P. B. Comita, unpublished results.

VISIBLE-WAVELENGTH LASER PHOTODEPOSITION OF COBALT INTERCONNECTS

M. ROTHSCILD, J. H. C. SEDLACEK, D. C. SHAVER, and
D. J. EHRLICH
Lincoln Laboratory, Massachusetts Institute of Technology,
Lexington, Massachusetts 02173-9108
S. N. BITTENSON, D. EDWARDS, Jr., and N. P. ECONOMOU
Micrion Corporation, Peabody, Massachusetts 01960

ABSTRACT

Cobalt interconnects were deposited with a cw visible-wavelength laser from gaseous $\text{Co}_2(\text{CO})_8$. The deposited material was high-purity Co, and its electrical resistivity was as low as $13 \mu\Omega\text{-cm}$ (twice that of bulk resistivity). The deposition is initiated by photochemical decomposition of $\text{Co}_2(\text{CO})_8$, and therefore process parameters (pressure, power, writing speed) are insensitive to the optical and thermal properties of the substrate.

Introduction

Laser induced deposition of metals, semiconductors, or insulators has been the subject of numerous studies [1,2]. Laser direct write deposition of material from a gaseous precursor generally occurs by one of two mechanisms. One mechanism relies on photolytically induced decomposition of the precursor, which typically requires ultraviolet light since few materials are photochemically active in the visible. However, at wavelengths longer than $\sim 350 \text{ nm}$ there are few convenient cw sources. The other mechanism involves pyrolytically induced deposition using visible light, where durable cw lasers do exist, but where most precursors are transparent. Pyrolytic processes are strongly dependent on the optical absorption and thermal conductivity of the substrate, and may require large thermal excursions which can damage nearby structures or the substrate itself. We report here on a Co deposition process which is notable in that it provides visible-wavelength photodeposition of a high-conductivity metal. The only previous visible-wavelength photodeposition process is for insulating chromium oxides [3]. Specifically, we describe the deposition of high-purity, low-resistivity cobalt from its carbonyl $\text{Co}_2(\text{CO})_8$, using an Ar^+ laser at power levels of only a few mW. This process is being incorporated in various applications, including circuit repair on flat-panel displays, which have optically transparent substrates.

Results and Discussion

$\text{Co}_2(\text{CO})_8$ is a crystalline compound at room temperature, with a vapor pressure of 0.3 to 0.7 Torr. The exact value of the vapor pressure is difficult to measure since the carbonyl vapor slowly decomposes, resulting in the evolution of CO. Nevertheless, even the lower figure, 0.3 Torr, is sufficient for laser photodeposition at significant rates. The transmission spectrum of $\text{Co}_2(\text{CO})_8$ vapor in the range 200 to 800 nm is shown in Fig. 1. Intense absorption bands are observed below 400 nm, with a long-wavelength tail extending to ~600 nm. The 488.0- and 514.5-nm lines of an argon ion laser are also shown in Fig. 1. It is apparent that radiation from an Ar^+ laser is partially absorbed by gaseous $\text{Co}_2(\text{CO})_8$, and this raises the prospect of low-power visible-laser photochemical reactions. Mass-spectrometric studies confirm that 488- and 515-nm radiation causes photodecomposition of gas-phase $\text{Co}_2(\text{CO})_8$. In these experiments a continuous flow of $\text{Co}_2(\text{CO})_8$ is introduced through a thin nozzle into a vacuum chamber, ~10 cm in front of the ionizer of a quadrupole mass

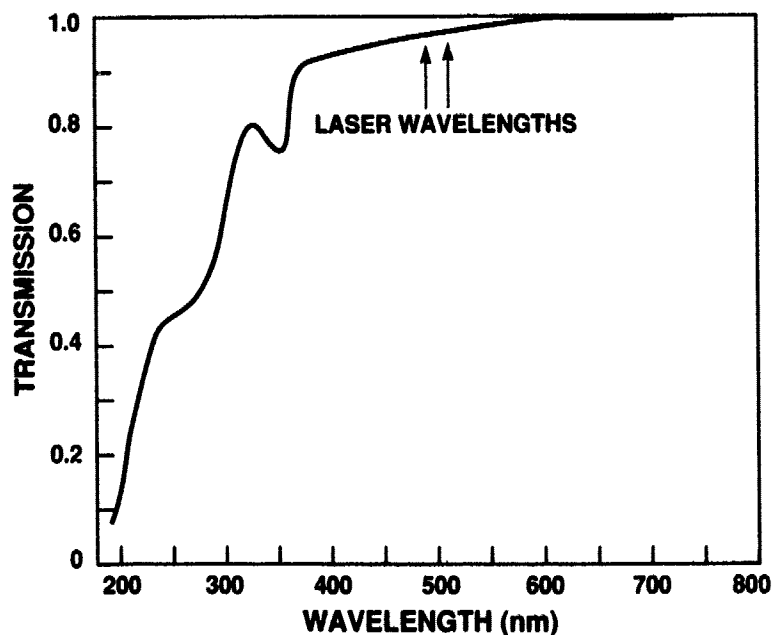


Figure 1 The transmission spectrum of gaseous $\text{Co}_2(\text{CO})_8$ in the range 200 to 800 nm. The pressure was 0.13 Torr and the pathlength was 10 cm. The arrows indicate the location of the 488.0- and 514.5-nm lines of an Ar^+ laser, and show that the laser lines lie on the long-wavelength absorption tail of $\text{Co}_2(\text{CO})_8$.

spectrometer (QMS). The $\text{Co}_2(\text{CO})_8$ is cryopumped through the ionizer and the mass filter of the QMS. A cw Ar^+ laser is weakly focused next to the nozzle, at the point where the $\text{Co}_2(\text{CO})_8$ density is highest, ~ 1 mTorr. The mass spectrum with the laser off is a series of peaks corresponding to the cracking pattern of $\text{Co}_2(\text{CO})_8$ in the ionizer. When the laser is turned on, the amplitude of all the heavy-mass peaks is reduced. As shown in Fig. 2 for the $\text{Co}_2(\text{CO})_8^+$ and $\text{Co}_2(\text{CO})_5^+$ signals, the change is linear in intensity up to at least 0.4 kW/cm^2 , and it can exceed 50 percent of the initial magnitude. The very existence of a laser-induced reduction in the mass-spectrometric signal of $\text{Co}_2(\text{CO})_8$, as well as its linear dependence on laser intensity, indicates that photofragmentation of gas-phase $\text{Co}_2(\text{CO})_8$ takes place at 488 nm. The details of this process are still under study.

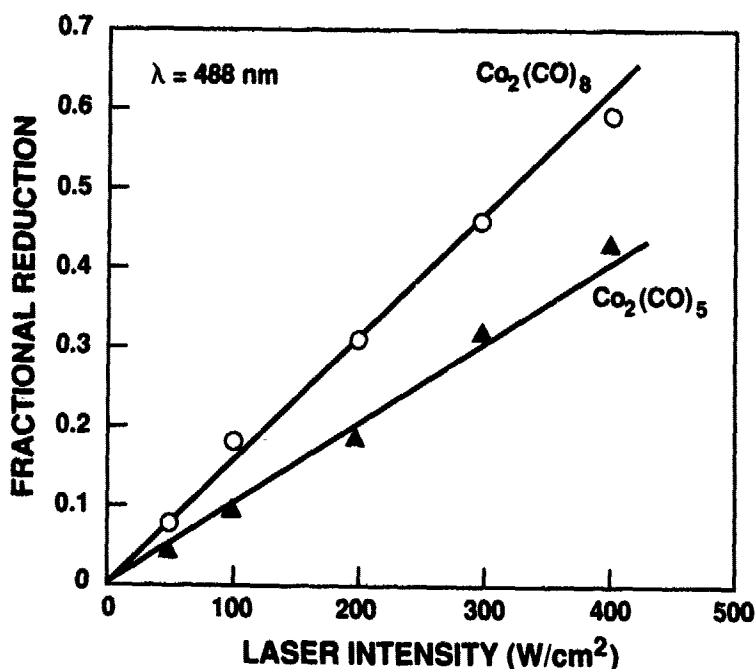


Figure 2 The fractional reduction in the QMS signal of the parent molecule $\text{Co}_2(\text{CO})_8$ and of one of its ionization fragments, $\text{Co}_2(\text{CO})_5$, as a function of laser intensity. The laser wavelength was 488 nm, the irradiated zone was ~ 10 cm from the QMS ionizer, and the pressure in the irradiated volume was estimated to be $\sim 10^{-3}$ Torr. The existence of a laser effect and its linearity with intensity are interpreted as evidence of 488-nm-induced photodecomposition of $\text{Co}_2(\text{CO})_8$ molecules.

The visible-laser photodissociation of $\text{Co}_2(\text{CO})_8$ has been applied to the localized photodeposition of metallic Co on various substrates in a direct write configuration. Because of the photochemical nature of the initial decomposition step, the deposition process at low laser power is largely independent of the substrate: Co is laser-deposited on transparent glass, and on chromium which absorbs a considerable fraction of the incident light. Figure 3 shows two scanning electron micrographs of Co lines "drawn" with a 515-nm laser across sections of glass and Cr films. No "necking" of the Co lines is observed upon transition from Cr to glass, as is typically the case with processes having a significant thermal component. In fact, preliminary results using a Ti-Co junction as a thermocouple indicate that laser induced deposition of Co from $\text{Co}_2(\text{CO})_8$ takes place even at power levels causing a local temperature rise of less than 5°C . At such low temperatures no significant thermal decomposition of $\text{Co}_2(\text{CO})_8$ is expected. Indeed, rapid thermal decomposition of $\text{Co}_2(\text{CO})_8$ is known to occur at temperatures above $\sim 52^\circ\text{C}$ [4], probably into the black, nonvolatile $\text{Co}_4(\text{CO})_{12}$, which in turn will thermally decompose to metallic cobalt.

The laser-deposited material is predominantly metallic cobalt. Auger electron spectroscopy indicates elemental composition of 100 percent Co (within the ~ 2 percent instrumental detection limit of impurities). Electrical measurements show resistivities as low as $13 \mu\Omega\text{-cm}$, twice the bulk value of Co. The difference between bulk and the laser-deposited film may be attributed to crystalline defects in the latter. The amount of material deposited at a given ambient temperature and $\text{Co}_2(\text{CO})_8$ pressure depends mainly on the laser power and dwell-time. Figure 4 shows the interplay between power and writing speed for a $1\text{-}\mu\text{m}$ -diameter laser focus. For instance, in order to achieve significant deposition at $75 \mu\text{m/s}$, the laser power must be relatively high, $\sim 140 \text{ mW}$. On the other hand, at writing speeds below $\sim 10 \mu\text{m/s}$ the required power can be reduced to $\sim 40 \text{ mW}$. It is noted that at these power levels there may still be a thermal component to the deposition process.

Conclusions

In summary, a laser-induced process has been developed to deposit low-resistivity ($13 \mu\Omega\text{-cm}$) metallic cobalt. This process requires a conventional low-power laser operating at visible wavelengths, and is applicable to a wide range of substrates, including transparent or heat-sensitive materials. It is thus a convenient process, with numerous potential applications. An example of such an application is the repair of active matrix flat-panel displays. The laser-deposition process of Co is initiated by the photo-induced dissociation of $\text{Co}_2(\text{CO})_8$ molecules near the surface, or molecules adsorbed

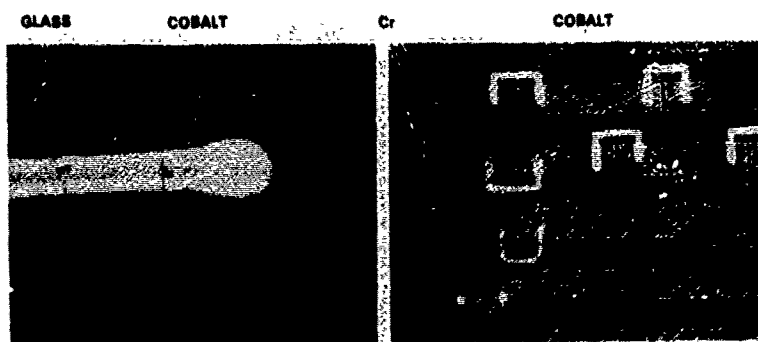


Figure 3 Scanning electron micrographs of Co lines written on Cr and on glass, in the presence of gaseous $\text{Co}_2(\text{CO})_8$. The Cr and glass lines are 25- μm -wide each, and the Co lines are 3- to 10- μm -wide depending on laser power and scan speed. The Co resistivity is as low as 13 $\mu\Omega\text{-cm}$. In the right half of the Figure, both cuts in the chromium lines (made by a frequency-doubled Q-switched Nd:YLF laser) and Ar^+ laser-deposited cobalt links (U-shaped) are shown.

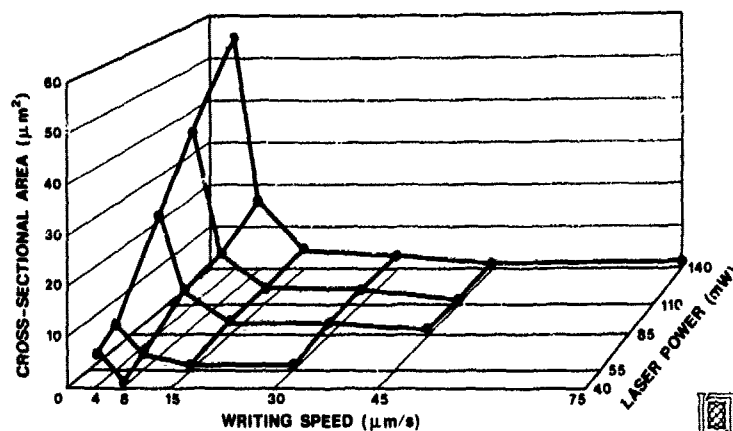


Figure 4 Dependence of the amount of deposited Co, given by the cross-sectional area of the laser-written line, as a function of laser power and writing speed. The laser wavelength was 514.5 nm, the focal spot was $\sim 1 \mu\text{m}$ in diameter, and the $\text{Co}_2(\text{CO})_8$ was kept at room temperature.

on it. The details of the photochemistry, as well as those of the subsequent steps of nucleation and growth, are the subject of further studies.

Acknowledgment

The Lincoln Laboratory part of this work was sponsored by the Defense Advanced Research Projects Agency and by the Department of the Air Force, in part under a specific program supported by the Air Force Office of Scientific Research.

References

1. R. L. Jackson, T. H. Baum, T. T. Kodas, D. J. Ehrlich, and P. B. Comita, in *Laser Microfabrication*, edited by D. J. Ehrlich and J. Y. Tsao (Academic, Boston, 1989).
2. J. P. Herman, *Chem. Rev.* **89**, 1323 (1989).
3. C. Arnone, M. Rothschild, J. G. Black, and D. J. Ehrlich, *Appl. Phys. Lett.* **48**, 1018 (1986).
4. *CRC Handbook of Chemistry and Physics*, edited by R. C. Weast, M. J. Astle, and W. H. Beyer (CRC Press, Boca Raton, Florida, 1984).

LASER CHEMICAL VAPOR DEPOSITION OF W ON Si AND SiO₂/Si

Jian-Yang Lin, Susan D. Allen*

Chung Cheng Institute of Technology, Department of Electrical Engineering
Ta-Shi, Taiwan 33509, R. O. C.*The University of Iowa, Center for Laser Science and Engineering
Iowa City, IA 52242, U. S. A.

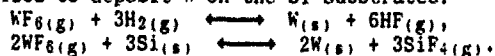
ABSTRACT

Direct write of W on bare Si and native SiO₂/Si substrates has been investigated in an laser chemical vapor deposition (LCVD) system. W deposits on bare Si surface via the Si and/or H₂ reduction of WF₆ were self-limited in thickness to 200 - 600 Å in both cases. Auger electron spectroscopic analysis showed that Si-H bonds could be poisoning the further growth of W. W deposits on native SiO₂/Si were only obtainable via the H₂ reduction of WF₆ in our laser direct-write system. Our experimental kinetic study indicated that HF desorption from the surface is the rate-controlling step for W deposition via the H₂ reduction of WF₆. The as-deposited W line deposits were 2 - 10 μm wide, 0.2 - 6 μm thick with resistivities in the range of 11 - 56 μΩ-cm. Growth rates as high as 2.2 nm/s have been achieved.

INTRODUCTION

The demand for new processing technology useful for application specific VLSI fabrication and circuit modification has significantly increased the interest in maskless and adaptive thin film deposition techniques such as laser-induced processing. Laser chemical vapor deposition (LCVD) is a pyrolytic process similar to conventional CVD using a highly focused laser beam as the heat source. The earliest studies made use of CO₂-laser to deposit materials on SiO₂ [1,2]. Recently, visible-laser irradiation has been used for achieving smaller deposited linewidths and for coupling radiation into semiconductor substrates more efficiently [3,4]. Further reductions in size can be made if nonlinearities associated with deposition or further processing steps are properly exploited.

Tungsten possesses several properties that are well suited to VLSI applications [5]. In this work, the following reduction reactions were utilized to deposit W on the Si substrates:



Although many kinetic studies have been done on conventional CVD systems, the results may not be applicable to analogous LCVD systems, as the growth regimes are quite different. The main requirement for LCVD is fast localized processing. This implies that a much higher temperature-pressure regime is usually necessary for achieving high growth rates. The goal of this work was two-fold: a) to study the reaction kinetics in an LCVD system so as to optimize the growth conditions for the direct-write tungsten deposits; b) to study the regimes for selective and non-selective LCVD of tungsten on Si and SiO₂/Si via the reduction of WF₆ in terms of surface conditions and gas composition.

EXPERIMENTALS

The substrates were Boron-doped p-type (resistivity ≈ 10 Ω-cm) (100)

Si wafers. In this work, two kinds of Si wafers with different surface conditions were used: one with native SiO_2 ($< 40 \text{ \AA}$) and the other the bare Si with native SiO_2 etched away by buffered HF solution.

For the LCVD of W, the light source was chosen to be the 514.5 nm cw Ar ion laser wavelength which is transparent to the reactant gases H_2 and WF_6 , and is strongly absorbed by the Si substrate. The laser beam was focused down to $3 \text{ }\mu\text{m}$ in diameter ($D_{1/e}$) with an 8X objective and the laser power levels used ranged from 0.2 to 0.6 watts to develop a temperature rise of 200 to 1400 $^\circ\text{K}$ on the Si surface. The total pressure of H_2 and WF_6 was kept at 600 torr and the partial pressure ratio of $\text{H}_2:\text{WF}_6$ (β) was varied from 1 to 40. The scan speed of the laser beam was varied from 20 to 5120 $\mu\text{m/s}$ for W line direct writing.

Scanning electron microscope (SEM) and high resolution Auger electron spectroscopy (AES) were used to characterize the W features.

RESULTS AND DISCUSSION

A. Effects of the Si surface preparation

As mentioned above, Si substrates with two different surface preparations were used in this work. The LCVD W deposits were found to be very sensitive to the presence of the native oxide, as shown schematically in Fig. 1.

On the etched Si surface, the W deposits were always self-limited to 200 - 600 \AA in thickness, no matter whether only WF_6 or both WF_6 and H_2 were loaded into the reaction cell. This means that between the two competing reactions, the Si reduction and the H_2 reduction, the former is initially faster than the latter, but the resulting surface inhibits the H_2 reduction of WF_6 . The deposit geometry of a W layer inside a Si trench can be explained if both the stoichiometric ratio of the Si + WF_6 reaction and the atomic densities of W and Si are considered. The widths of the as-deposited W lines were in the range of 1.5 - 3 μm under the growth conditions used.

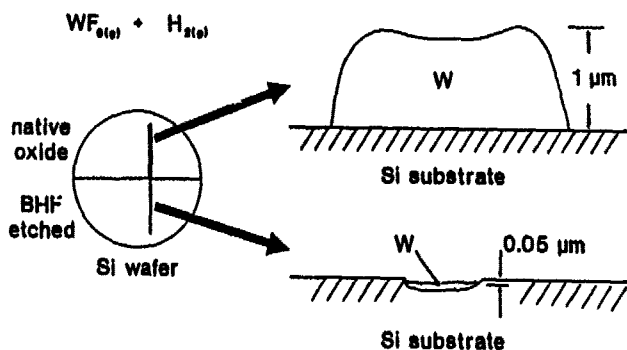


Fig. 1. A schematic diagram for the surface effects on the LCVD of W.

On the native SiO_2/Si area, no W deposits could be obtained within the growth conditions used if only WF_6 but no H_2 was loaded into the reaction cell. This shows that a native SiO_2 layer acts as a barrier to the Si + WF_6 reaction [6]. However, if both H_2 and WF_6 reactants were used to deposit W on the SiO_2/Si surface, the resulting W deposits were not self-limited in thickness. Much thicker W deposits of 0.2 - 6 μm thickness were obtained under such condition. This discrepancy between the growth

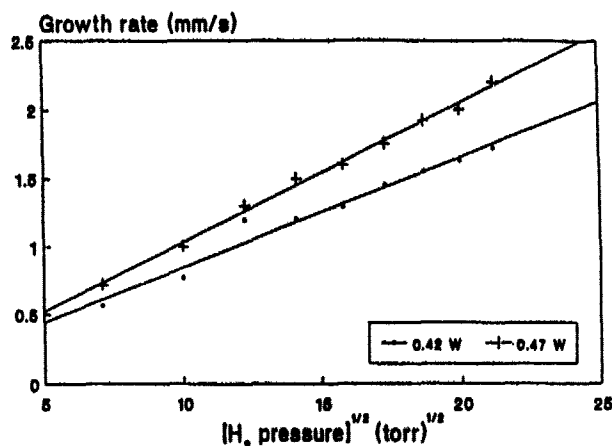


Fig. 2. Growth rate of W line on SiO_2/Si versus H_2 partial pressure (total pressure = 600 torr, $[\text{WF}_6] = 150$ torr, buffer gas: Ar).

on bare Si and SiO_2/Si indicates that the nucleation of the W deposits from the H_2 reduction of WF_6 on SiO_2/Si is heterogeneous.

B. Reaction kinetics of W from $\text{H}_2 + \text{WF}_6$ on SiO_2/Si

Fig. 2 shows that the growth rate of the W deposits has 1/2 order dependence on the H_2 partial pressure. The reaction order of WF_6 was found to be 1/6, as shown in Fig. 3. Following the reaction scheme for the H_2 reduction of WF_6 proposed by McConica et al. [7], we have identified HF desorption from the surface is the rate-controlling mechanism. The growth rates showed a maximum value at $\beta = 3$ which is the stoichiometric ratio for the hydrogen reduction of WF_6 , and decreased drastically if β deviates from 3. With a given laser scan speed, the width of the W deposit increases with increased laser power level, as shown in Fig. 4, where the scan speed was 5120 $\mu\text{m/s}$.

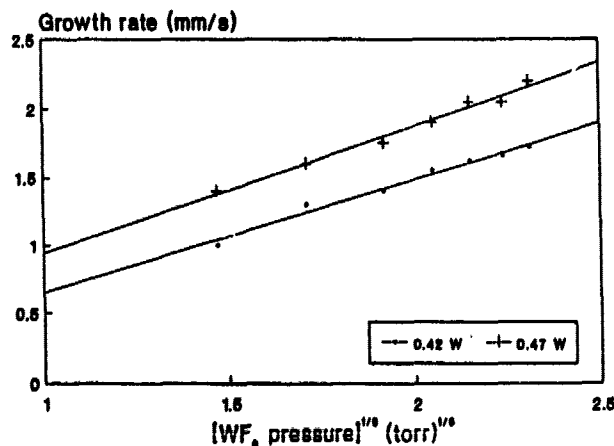


Fig. 3. Growth rate of W line on SiO_2/Si versus WF_6 partial pressure (total pressure = 600 torr, $[\text{H}_2] = 450$ torr, buffer gas: Ar).

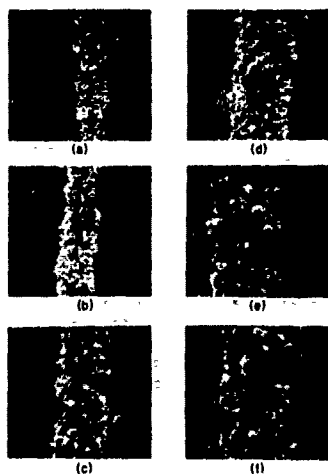


Fig. 4. SEM photographs of W line deposits on SiO_2/Si grown at various laser power levels: (a) 0.33 watts; (b) 0.38 watts; (c) 0.42 watts; (d) 0.47 watts; (e) 0.52 watts; (f) 0.56 watts. Scan speed = $5120 \mu\text{m/s}$.

C. SEM and AES results

The deposited lines on the native SiO_2/Si were identified as W using EDX and WDX spectroscopies. Auger electron spectroscopic (AES) analysis of the W line in Fig. 5 also showed that there was primarily W inside the thick deposits. No fluorine, carbon, nitrogen or oxygen were found in the W deposits or at the W/Si interface.

Surface-composition AES analysis of the W deposits on the bare Si surface showed that besides tungsten there was silicon on the as-deposited W surface. As seen from the depth-composition profile of the W deposit (Fig. 6), the surface composition is about 70 atomic percent W and 10 atomic percent Si with the remaining 20 atomic percent consisting of C, O and N surface impurities. The atomic concentration of Si increases monotonically to more than 86% while the atomic concentration of W

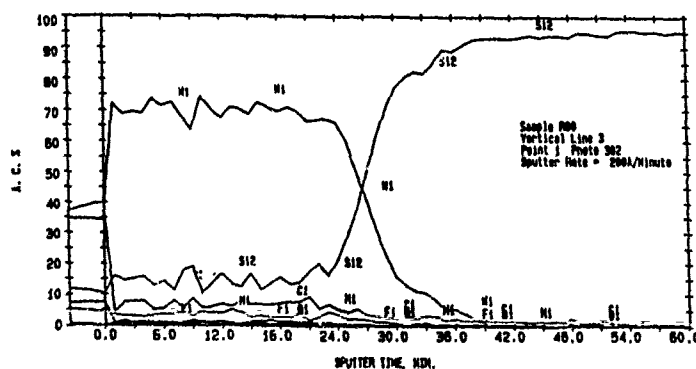


Fig. 5. AES depth-composition profile of W deposits on SiO_2/Si .

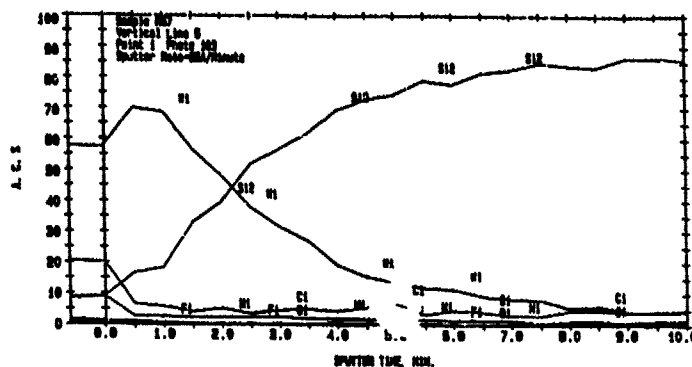


Fig. 6. AES depth-composition profile of W deposits on bare Si.

decreases monotonically to an un-detectable level at a depth of 225 Å. It is possible that H atoms are dissociatively adsorbed on the W surface and then captured by the exposed Si atoms, forming strong Si-H bonds on the surface. The Si-H bonds can poison the Si + WF_6 reaction [8] thus substantially reducing the amount of W atoms available on the surface which are necessary for the further growth of W via the H_2 reduction of WF_6 .

D. Electrical properties

The as-deposited W lines on native SiO_2/Si had resistivities of 11 to 56 $\mu\Omega\text{-cm}$ depending on the growth conditions. The resistivity decreases with increasing scan speed and/or decreasing laser power level. Higher scan speeds and lower laser power levels result in smaller grain sizes in the deposited W. As a consequence, the resistivity of the as-deposited W line decreases with decreasing grain size, for smaller grain sizes occur in conjunction with higher packing densities [9].

CONCLUSIONS

For W deposition on Si substrates via the Si or H_2 reduction of WF_6 , the surface condition is critical to the growth of W deposits. Si-H bonds appear to poison the further growth of W deposits on etched Si surfaces. Via the kinetic studies, we have identified HF desorption from the surface as the rate-controlling mechanism for the H_2 reduction of WF_6 on SiO_2/Si . W growth rates as high as 2.2 nm/s have been achieved in our LCVD system. The high growth rates achievable with LCVD systems show promising potential in applications to micro-fabrication and micro-modification of VLSI circuits, such as mask repair, application specific IC's and packaging.

ACKNOWLEDGMENT

This work was supported in part by the Semiconductor Research Corporation.

REFERENCES

1. V. Barananskas, C. I. Z. Mammana, R. E. Klinger, and J. E. Greene, Appl. Phys. Lett. **36**, 930 (1980).
2. S. D. Allen, J. Appl. Phys. **52**, 6501 (1981).
3. G. Leyendecker, D. Bauerle, P. Geittner, and H. Lydtin, Appl. Phys. Lett. **9**, 921 (1981).

4. D. J. Ehrlich, R. M. Osgood, Jr., and T. F. Deutsch, Appl. Phys. Lett. 39, 57 (1981).
5. B. W. Shen, and G. C. Smith, J. Vac. Sci. Tech. B4, 1369 (1986).
6. H. H. Busta and C. H. Tang, J. Electrochem. Soc. 133, 1195 (1986).
7. C. M. McConica and K. Krishnamani, J. Electrochem. Soc. 133, 2542 (1986).
8. F. R. McFeeley (private communication).
9. P. H. Su and S. D. Allen (to be published).

LASER INDUCED CHEMICAL VAPOR DEPOSITION OF GaN

A. KOBAYASHI, T. ASAI, S. KAWAI AND P.J. CHONG*

The Institute of Scientific and Industrial Research, Osaka University,
Ibaraki, Osaka 567, Japan*Korean Research Institute of Chemical Technology, Daduck Science Town,
Seoul, Korea

ABSTRACT

Thin films of GaN were grown on the Al_2O_3 (0001) substrate by the laser-induced chemical vapor deposition technique. Morphology were different for the films grown with and without laser irradiation. Moreover, the density of nucleus and the growth rate in the case of the growth with the parallel irradiation were greater than those without irradiation. Differences were attributed to presence of photo-dissociated species in the case of the laser irradiation. Additional irradiation normal to the substrate decreased the rate, probably because of the accelerated desorption of the reactive adsorbed species.

INTRODUCTION

Gallium nitride, one of semiconducting materials, has a direct energy gap ($E_g = 3.504$ eV at room temperature [1]) and good light emitting efficiency [2]. It is presently a very promising compound for light emitting diodes in the visible to ultraviolet region. It is also expected to find applications both to a passive dielectric film on GaAs [3] and to an active semiconductor for high temperature devices.

In spite of these attractive potential applications, the synthetic technique for an epitaxial film with little defects has not been established. The main reason for this is the very high decomposition pressure of GaN, leading to high background carrier concentrations (10^{17} - 10^{20} cm^{-3} [4,5]) due to nitrogen vacancies. GaN thin films grown to date by techniques, such as metallorganic vapor deposition (MOCVD) with NH_3 and trimethylgallium (TMG) as precursors, have all been of the n-type.

Recently some attempts have been made to overcome this difficulty by using rf-excited plasmas [6], dc-biased reactive sputtering [7], or electron cyclotron resonance (ECR) plasma [3]. The common idea to these technique is that lower growth temperatures should be employed to reduce the concentration of nitrogen vacancies. However, the precursor gases are highly excited both electronically and kinetically. Since substrates are exposed to this plasma during deposition, GaN films obtained by these techniques have been polycrystalline, except for that by the ECR plasma one.

On the other hand, the laser can excite selectively a certain energy level and is well-suited to promote a specified chemical reaction. Indeed the laser-induced chemical vapor deposition of refractory metals using metallo-organics or the photo-stimulated catalytic reaction on the solid surface are prominent examples in its application.

In this paper, we will describe experiments of the GaN deposition with the aid of the ArF excimer laser and demonstrate its characteristics.

EXPERIMENT

A schematic diagram of the reaction chamber is shown in Fig. 1. GaN films were grown on the sapphire (0001) substrate. It was etched with a 1:1 solution of H_2SO_4 and H_3PO_4 , loaded on a Ta heater, and heat-treated at

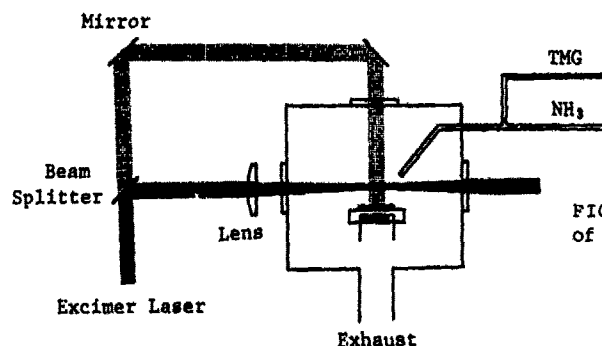


FIG. 1 Schematic diagram of the reaction chamber

1000°C for 30 min just before the deposition. After evacuation of the chamber down to its background pressure of 2×10^{-6} Torr, ammonia gas flew at the rate of 300 ml/min through a tube from 25 mm distant from and at the angle of 45° with the substrate. After the substrate temperature was stabilized at 900°C, TMG gas was added from a cylinder maintained at 0°C without any carrier gas. The precursor gases were mixed and preheated at about 400°C before introduction to the chamber. Total pressure of the chamber during the deposition was kept typically at 0.1 Torr. Effects of disuse of any carrier gas upon the film deposition will be discussed later.

An irradiation source was an ArF excimer laser (193 nm) operated with the pulse duration of 17 ns and at 150 Hz repetition rate. In the case of the parallel irradiation, the laser beam of 25.9 mJ per pulse was focused with a cylindrical lens and introduced parallel to and at about 10 mm above the substrate. In the case of additional substrate irradiation, the laser beam of 4.1 mJ per pulse was simultaneously irradiated perpendicular to the substrate without focusing.

The crystal structure and surface morphology of the deposited GaN films were examined by means of reflection electron diffraction (RED) and scanning electron microscope (SEM), respectively.

RESULTS AND DISCUSSIONS

Figure 2 shows the SEM observation of the deposited films at different lapse of deposition time. In these experiments films were not smooth over the substrate, but composed of granular particles. Three characteristic features were observed:

- (1) Number density of particles is greater in the deposition with the laser irradiation than without the irradiation.
- (2) Growth rate of the particles is larger in the case of only the parallel irradiation than in the case of the simultaneous irradiation of parallel and perpendicular beams.
- (3) In the early stage of the deposition with the laser irradiation, thin and roughly hexagonal plates were observed, which is more evident in Fig. 3. In the later stage, however, particles took an irregular form.

In the nucleation stage, difference of the depositions with and without irradiation is evident in their number density. In the case of thermal decomposition, the TMG molecule loses its methyl radical one by one. When TMG gas is irradiated with the laser beam of 193 nm, it decomposes into the neutral gallium metal [11]. Similarly the ammonia gas decomposes into the amidogen radical NH_2 and hydrogen atom in the primary step [12]. Because the focal

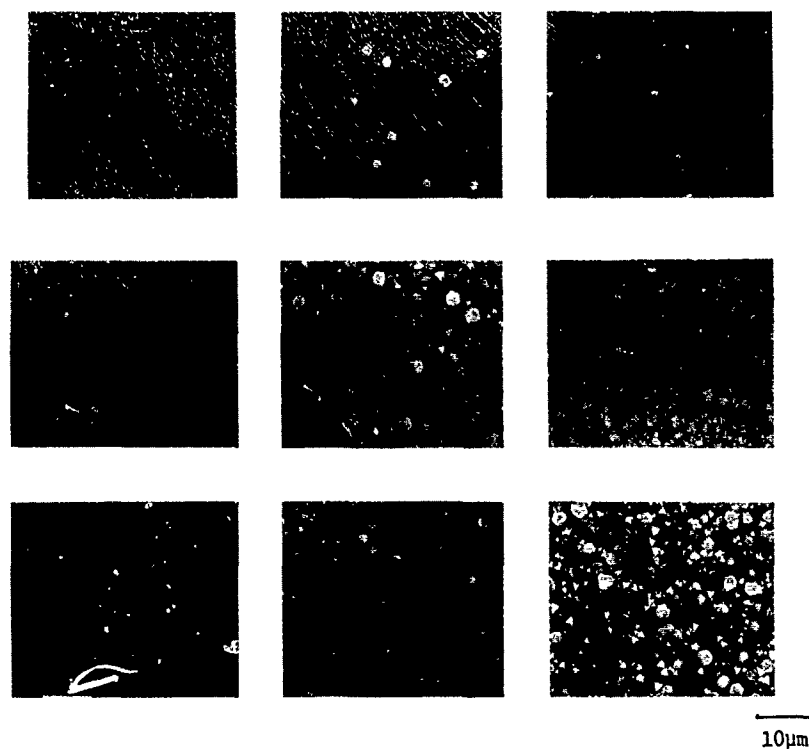


FIG. 2 SEM observation of the deposited GaN films (top view). Top row: thermal CVD, central row: laser CVD only with the parallel irradiation, bottom row: laser CVD with both parallel and perpendicular irradiations. In each row, the deposition time increases from left to right, 20, 30 and 40 min. Reaction conditions are: $[TMG]=5$ sccm, $[NH_3]=300$ sccm, total pressure= 0.17 Torr, and substrate temperature= $900^\circ C$.

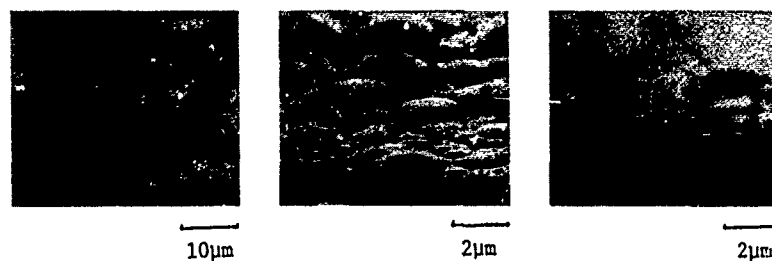


FIG. 3 SEM observation of the deposited GaN films (sideview). Left: thermal CVD (90 min), middle: laser CVD only with the parallel irradiation (30 min), right: laser CVD with both parallel and perpendicular irradiations (40 min). Other reaction conditions are the same as in FIG. 2.

position of the parallel-incident beam was 10 mm above the substrate, these radicals might react each other to form other types of radical or clusters before they reach the substrate. Formation of these photo-produced radicals seems to affect positively the nucleation, for example, by their high reactivity or sticking properties.

In the case of the deposition with the laser irradiation, the nucleation density and the habits of the particles were the same for both depositions with and without the substrate irradiation as seen in Fig. 2. On the other hand, the growth rate was higher for the deposition without the substrate irradiation as seen from the particle size. It is supposed from these that the additional substrate irradiation had no effect on the photo-decomposed species but that it accelerate desorption of the absorbed reacting species, thus reducing the growth rate.

Concerning the habit of the deposited particles in the case of the laser irradiation, it had the hexagonal shape and belonged to the hexagonal system in the early stage (see next paragraph). After 20 min of deposition, it still showed the hexagonal shape for most particles from the top view (Fig. 2). From the side view, however, it consisted from the pyramidal plane, rather than the prism plane expected for the hexagonal plate (Fig. 3). As mentioned later, the particles belonged to the cubic system in this stage and the planes would be {111}. On the basal {111} plane, there was a heap which did not form a distinct plane. This might trigger the irregular growth in the prolonged deposition. In the case of the deposition without the laser irradiation, no hexagonal plates were observed at any stage in the present experiments.

In Fig. 4, RED patterns of the deposited film were shown. The same trend was observed irrespective of the irradiation conditions. Though the films were composed of particles, the RED pattern was that from a single crystal, indicating that all particles have the same crystallographic orientation. For the deposition of 20 min, the RED pattern could be indexed as the wurtzite-type structure with the (0001) plane parallel to the substrate surface. This is the stable structure of GaN in the usual condition. In the later stage, however, it could be indexed as the twinned zinc blende-type structure with the {111} plane parallel to the substrate. Dendritic GaN [9] and the very thin GaN film of a few hundred Å grown on the GaAs {111} substrate [10] were claimed to have this structure. The observed twinned structure can be formed by inserting a stacking fault of a wurtzite-type layer along the [111] direction of the zinc blende-type structure.

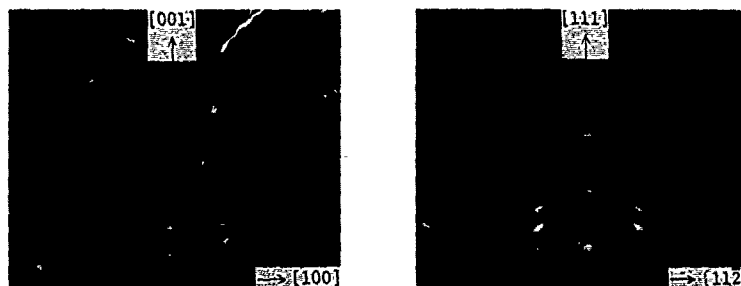


FIG. 4 RED patterns from the deposited GaN film only with the parallel irradiation.

Left: 20 min deposition, belongs to the hexagonal system.

Right: 30 min deposition, belongs to the cubic system.

The wurtzite-type structure observed at the beginning stage seems to be influenced by the substrate structure. The hexagonal structure is possible to change smoothly to the cubic one only by an accidental change of the stacking on the growing surface and subsequent growth of the second structure. As mentioned above, the similar stacking fault is concerned with the twin structure, but once the cubic structure was formed, it did not bring formation of the hexagonal structure again and only introduced the twinning. The growth of the cubic structure, which should be unstable from the viewpoint of energy, may thus be kinetically preferred owing to a high degree of supersaturation in the present experiment. The condition of supersaturation must be due to the disuse of any carrier gas.

CONCLUSION

In the present laser-induced chemical vapor deposition of GaN, the nucleation density increased more than that in the thermal CVD. Hexagonal plates appeared in the early stage of deposition. These characteristics were attributed to the formation of the photo-decomposed radicals and/or atomic Ga. The additional substrate irradiation had no effect on the nucleation density nor the morphology of the particles. It decreased the growth rate, probably due to the photo-desorption of the absorbed reacting species.

REFERENCES

- [1] T. Ogino and M. Aoki, *Jan. J. Appl. Phys.* **19**, 2395(1980).
- [2] J.I. Pankove, *J. Lumin.* **7**, 114(1973).
- [3] H. Haniu, T. Usuda, H. Adachi and Y. Shibata, *Appl. Phys. Lett.* **23**, 252(1978).
- [4] H.M. Manasevit, F.M. Erdmann and W.I. Simpson, *J. Electrochem. Soc.* **118**, 1864(1971).
- [5] M. Ilegems, *J. Cryst. Growth* **13/14**, 360(1972).
- [6] J.C. Knights and R.A. Lujan, *J. Appl. Phys.* **49**, 1291(1978).
- [7] S. Zembutsu and M. Kobayashi, *Thin Solid Films* **129**, 289(1985).
- [8] S. Zembutsu and T. Sasaki, *J. Cryst. Growth* **77**, 250(1986).
- [9] W. Seifert and A. Tempel, *Phys. Status Solidi (a)* **23**, K39(1974).
- [10] M. Mizuta, S. Fujieda, Y. Matsumoto and T. Kawamura, *Jap. J. Appl. Phys.* **25**, 1945(1986).
- [11] S.A. Mitchell, P.A. Hackett, D.M. Rayner and M.R. Humphries, *J. Chem. Phys.* **83**, 5028(1985).
- [12] M. Suto and L.C. Lee, *J. Chem. Phys.* **78**, 4545(1983).

LASER DIRECT WRITING OF OPTICAL INTERCONNECTS IN POLYIMIDES AND $\text{SiO}_2/\text{TiO}_2$ COATINGS

D.W. HEWAK AND H. JEROMINEK

National Optics Institute, 369, rue Franquet, P.O. Box 9970, Sainte-Foy, Quebec, Canada, G1V 4C5

ABSTRACT

Commercially available polyimides and $\text{SiO}_2/\text{TiO}_2$ coatings are experimentally studied for their potential application in optical guided-wave interconnect networks. Optical properties are measured, including transmission spectra, refractive index and loss, with the aim of determining the materials most suited for this application. On the most promising candidates, direct writing of strip waveguides with Ar-ion laser at 514.5 and 457.9 nm was performed. Localized thermal curing by writing with speeds up to 250 microns per second allows the achievement of multimode guiding structures. Light propagation loss measurements reveal that attenuation in strip waveguides is of the same order as in slab structures of the same material, typically 5-10 dB/cm at 633 nm.

INTRODUCTION

Polyimides have been suggested [1-3] as promising materials for wafer-scale optical guided-wave interconnects. This is a result of their well established compatibility with both Si and GaAs fabrication technology, good dielectric properties, temperature resistance over 300°C and relatively good chemical and mechanical stability.

The standard process developed for waveguide fabrication in polyimides uses spin-deposition, and film solidification by thermal curing, followed by reactive ion etching or focused ion beam etching. These have been reviewed in a recent publication [1]. We concentrate here on laser writing by thermal curing, followed by the removal of uncured polyimide which has not been exposed to the laser beam.

Thin films prepared from colloidal silica and titania solutions are used as optical coatings, filters, protective layers and optical waveguides [4]. As a material for waveguide fabrication, they offer several advantages, namely, relatively simple deposition process, low optical loss and variable refractive index governed by the mixture composition. We expect that the fabrication procedure for channel waveguide structures in such solutions will be similar to that of polyimides, and have thus explored their application in parallel with the application of polyimides.

To summarize, the aim of the present study is twofold:

- to select, among commercially available polyimides, those having optimal properties for fabrication of wafer scale optical interconnects in the form of strip waveguides,
- to investigate application of a laser direct writing technique for optical waveguide fabrication in selected polyimides and $\text{SiO}_2/\text{TiO}_2$ coatings.

This laser direct writing technique should permit maskless patterning of thin films and thus allow a fast turnover in fabrication of customized or prototype optical interconnects. To the best of our knowledge, this study represents the first attempt to perform laser writing in polyimides by their localized thermal curing with a scanned optical beam.

EXPERIMENTAL PROCEDURE AND RESULTS

Slab Optical Waveguides: Fabrication and Evaluation

Slab optical waveguides from commercially available polyimides (see Table I) and $\text{SiO}_2/\text{TiO}_2$ coatings were fabricated by spin coating on Corning 7059 glass, oxidized silicon or GaAs substrates, which had been previously treated with commercial adhesion promoters. This was followed by the soft and hard bake procedures recommended by the manufacturer.

Preliminary evaluation of the materials began with UV-VIS-NIR transmission spectra of the films deposited on the glass substrates. Transmission over the wavelength range of 200 to 2000 nm were recorded using a Varian Cary 2400 double beam spectrophotometer with an uncoated substrate as a reference. In addition to giving an indication of the loss which can be expected of these materials, the transmission spectrum reveals the wavelength at which absorption begins in the polyimide. This information is crucial for understanding the thermal curing mechanism by which the strip waveguides are achieved. Typical results are presented in Figure 1.

The refractive index and thickness of the films were determined by the prism coupler method [5] using a computerized measurement system with a He-Ne laser light source. An example of a measured mode spectrum of a polyimide slab waveguide is shown in Fig. 2. In multimode waveguides, the refractive index and thickness were derived from the solution of the mode equation for an asymmetric slab guiding structure using the measured coupling angles of the modes observed. The values of the thickness obtained were also verified with a Sloan Dektak IIA surface profiler.

Light propagation loss in the waveguides was evaluated from images of the light scattered out of the waveguide [8]. Losses ranged from 5 to 10 dB/cm for the fully cured polyimides.

Laser Writing Apparatus

The laser writing experiments described in this paper were performed using a Coherent Innova 100-15 Ar-ion laser, an optical microscope and a Melles Griot Nanomover X-Y translation system. Two wavelengths, 514.5 and 457.9 nm were used. A second more sophisticated system for laser writing is currently being tested. It is built around a computer controlled Micro-Control FAB-200C air bearing, X-Y translation stages. The system is equipped with autofocus, an automatic substrate delivery mechanism and a He-Cd laser operating at 442 nm. Another light source, for example, the Ar-ion laser, can also be retrofitted into this system. A double path interferometer built into the system allows X-Y resolution to 0.04 microns. The He-Cd laser is equipped with an acousto-optic modulator for computer controlled power adjustment during the laser writing process.

Table I. Refractive index at 633 nm and thickness of selected commercially available polyimides.

No.	Tradename	Manufacturer	Thickness (microns)	Refractive Index
1.	Probimide 293	Ciba-Geigy	5 - 10	1.64
2.	Probimide 412	Ciba-Geigy	1 - 15	1.62
3.	Pyrallin 2566	Dupont	1 - 4	1.59
4.	SPI - 135	G.E.	10 - 60	1.65
5.	Thermid 5010	National Starch	5 - 40	1.64
6.	Thermid 5510	National Starch	5 - 30	1.60
7.	T-Polyimide	Brewer Science	1 - 15	1.60

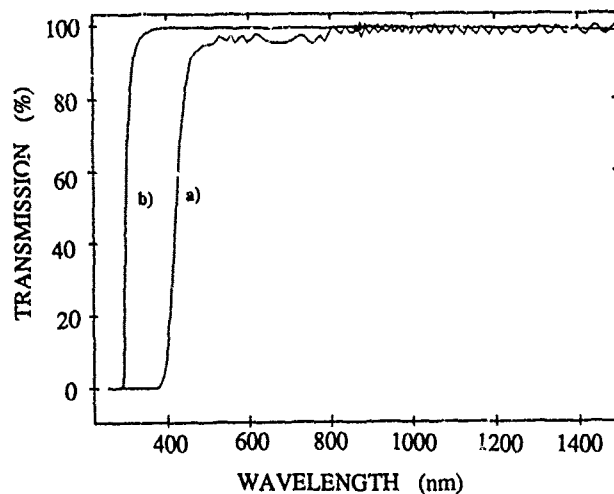


Fig. 1. Transmission spectra of a) polyimide Probimide 293 and b) Liquicoat Si:Ti thin films deposited onto glass substrates. Film thickness is $9.5 \mu\text{m}$ and $0.25 \mu\text{m}$ respectively.

Laser Writing Results

Proof of concept laser writing experiments were performed first in the Probimide 293 polyimide. Directly after spin coating onto Si wafers with 2 micron SiO_2 buffer layer, the polyimide film was prebaked (softbake) to set the film and initiate solvent evaporation. Next laser writing was performed at one of two wavelengths, 514.5 or 457.9 nm, from the Ar^+ laser. Scanning with the focused laser beam served to locally heat and cure the thin film in a series of strips. After laser writing, the unilluminated parts of the films were removed with a wet etching procedure, leaving a series of straight strip optical waveguides.

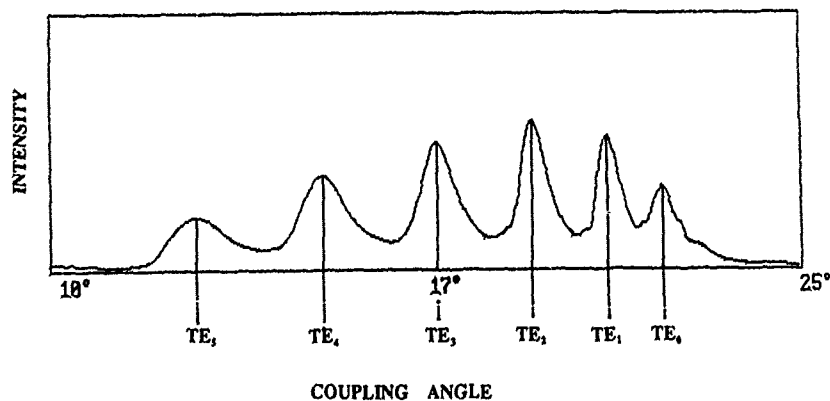
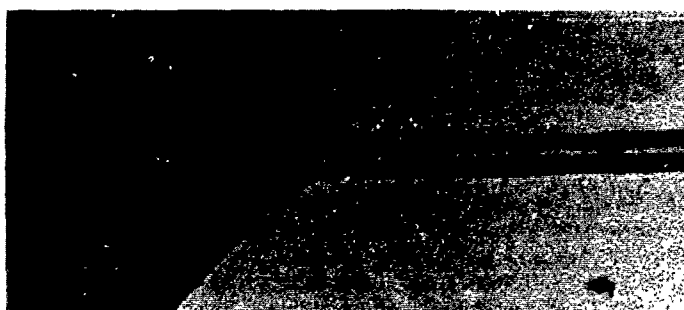


Fig. 2. Mode spectrum of a slab optical waveguide in $3.6 \mu\text{m}$ thick film of Probimide 293 polyimide

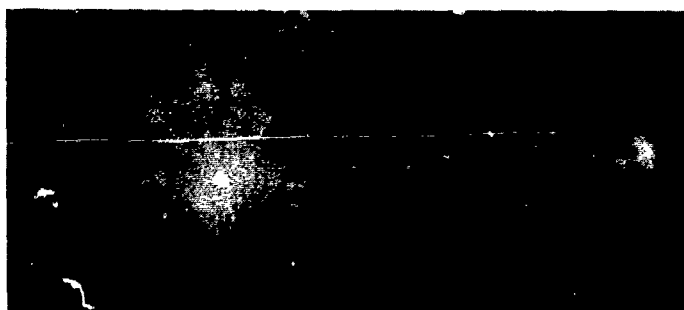
At 514.5 nm, light is weakly absorbed in the polyimide, thus the mechanism for polyimide curing may be attributed to heat generation in the semiconductor substrate, which strongly absorbs light at this wavelength. Indeed, high laser output power, of the order of 500 mW, was required to generate patterns in the polyimide. Writing at a speed up to 250 microns per second was achieved with this laser power. On the other hand, at a wavelength of 457.9 nm at which the polyimide begins to absorb, writing with laser output powers below 200 mW was possible. At this wavelength, we believe that heat generation in both the polyimide film and the semiconductor substrate is responsible for localized heating of the polyimide.

In general, the light propagation loss measurements revealed that attenuation in strip waveguides fabricated by laser writing in the Probimide 293 polyimide was of the same order as in slab waveguides made of the same material, typically 5 - 10 dB/cm at 633 nm. Light coupling from an optical fibre into a polyimide strip waveguide is illustrated in Figure 3.

With a similar procedure, Liquicoat Si:Ti was spun onto oxidized Si wafers and followed by a softbake and then Ar⁺ laser writing at 457.9 nm. After laser writing and wet etching, the structures were hard baked for typically 1 hour at 300°C. The best results, i.e. structures of uniform shape and resistant to the developer, were obtained with a laser output power of 0.2 W and scanning speeds between 50 and 150 microns per second.



a)



b)

Fig. 3. Light coupling from an optical fibre into a polyimide strip waveguide.
a) Structure b) Light scattered out of the structure

CONCLUSIONS

Seven commercially available polyimides were selected as potential materials for fabrication of wafer scale optical interconnects in the form of strip waveguides. Proof of concept experiments showed that laser direct writing of polyimide strip guiding structures with loss levels equal to those of slab structures of the same material, is feasible. Localized laser thermal curing is due to light absorption in the semiconductor substrate or due to absorption in both the substrate and polyimide film. Fabrication of optical waveguiding structures in $\text{SiO}_2/\text{TiO}_2$ coatings by laser direct writing is also achievable.

REFERENCES

1. B.L. Booth, J. Lightwave Technol., 7, 1445 (1989).
2. R. Selvaraj, H.T. Lin and J.F. McDonald, J. Lightwave Technol., 6, 1034 (1988).
3. C.T. Sullivan, in Optoelectronics Materials, Devices, Packaging and Interconnects II, SPIE, 994, 92 (1988).
4. D.W. Hewak and J.W.Y. Lit, Can. J. Phys., 66, 861 (1988).
5. H. Nishibara, M. Haruna and T. Suhara, Optical Integrated Circuits, (McGraw-Hill, New York, 1987).

SELECTIVE AREA DEPOSITION OF CONDUCTING PALLADIUM FILMS ON POLYIMIDE RESINS

YOON-GI KIM*, S. BIALY*, R.W. MILLER*, J.T. SPENCER*, P.A. DOWBEN* AND SASWATI DATTA**

*Center for Molecular Electronics, Departments of Physics and Chemistry, Syracuse University, Syracuse, NY 13244-1130

**International Business Machines, 1701 North Street, Endicott, NY 13760

ABSTRACT

We have demonstrated that the selective area deposition of palladium on polyimide substrates is possible through the U.V. photolysis of $(\pi\text{-allyl})(\pi\text{-cyclopentadienyl})$ palladium. This photolytic deposition process did not result in any apparent damage to either the Ultem 1000 (polyetherimide) or Kapton substrates (polyimide substrates). The resistivity of the palladium films ($< 0.1\text{ }\mu\text{m}$) suggests that the films are porous.

INTRODUCTION

Recently, attempts to deposit palladium on polyimide films have used organometallic complexes such as palladium acetate [1,2] with the goal of selectively depositing conducting films through the photolytic decomposition of the complex. Several studies of organometallic source compounds, including $(\pi\text{-allyl})(\pi\text{-cyclopentadienyl})$ palladium, suggest that these complexes can be used to deposit relatively pure palladium films [3,4]. These studies have shown that the U.V. photolysis of $[(\eta^3\text{-C}_3\text{H}_5)(\eta^5\text{-C}_5\text{H}_5)\text{Pd}]$ can be used to selectively deposit palladium with submicron spatial resolution [5]. In this paper, we describe the U.V. photolysis of $[(\eta^3\text{-C}_3\text{H}_5)(\eta^5\text{-C}_5\text{H}_5)\text{Pd}]$ on polyimide substrates.

EXPERIMENTAL

The $(\pi\text{-allyl})(\pi\text{-cyclopentadienyl})$ palladium was synthesized and purified using the procedure described previously by Shriver [6]. The photolytic deposition was carried out in a glass vacuum system as described previously [7]. The ultraviolet light was a commercially available nitrogen laser (Molelectron, model UV 24) with a wavelength of 337 nm. The maximum energy per pulse delivered by this laser was 15 mJ, with a flux density of no greater than 1 J/cm^2 . The film thicknesses were estimated from the palladium XES (EDAX), WDS signals and a film thickness monitor (a Taylor-Hobson Talysurf 4). The film thicknesses determined from XES and WDS

followed from good correlations between the data to model scattering calculations. The film morphology was characterized by scanning electron microscope (SEM). The purity of the films were determined using a wavelength dispersion spectroscopic (WDS) analysis and Auger electron spectroscopy (AES). Sheet resistance measurements were also undertaken.

The polyimide substrates were exposed to a vapor of $[(\eta^3\text{-C}_3\text{H}_5)(\eta^5\text{-C}_5\text{H}_5)\text{Pd}]$ for between 17 and 19 hours while irradiating the substrate with the laser beam.

RESULTS

We have shown that palladium can be deposited on polyimide and the resulting conductive strips are shown in figure 1.



Figure 1 - Palladium films on different polyimide substrates Pd on Kapton (left), Pd on Ultem 1000 (rough side) (middle), and Pd on Ultem 1000 (smooth side) (right).

Scratches through the films on Kapton and Ultem 1000 did not reveal the presence of any obvious damage to the polyimide films and, in general, the palladium films were found to adhere well to the substrates.

The conducting strips were deposited so that the film thickness was varied along the strip (approximately 500 Å thick at one end but with a decreasing thickness along the length of the strip). We deposited these wedge shaped strips across previously deposited copper lines spaced equally approximately 980 μm apart on Kapton. Using this procedure we were able to determine the approximate volume resistance of palladium films for a variety of thicknesses, as shown in figure 2.

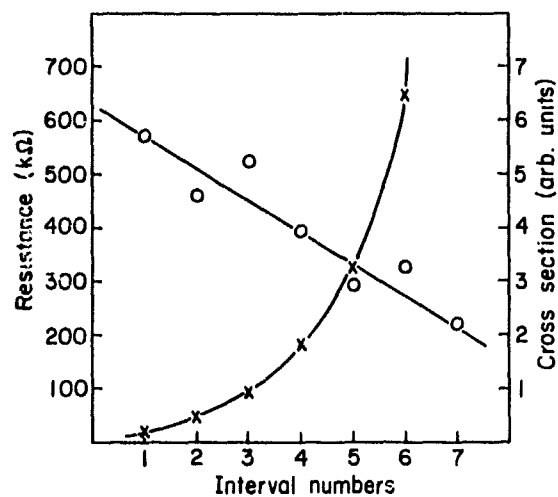


Figure 2 - Resistance (o) and cross-sectional area (x) as a function of interval numbers.

By replotting the data against the palladium strip cross sectional area, it is apparent that the volume resistivity and the conductance of the palladium film is dependent on the film thickness. This is shown in figure 3.

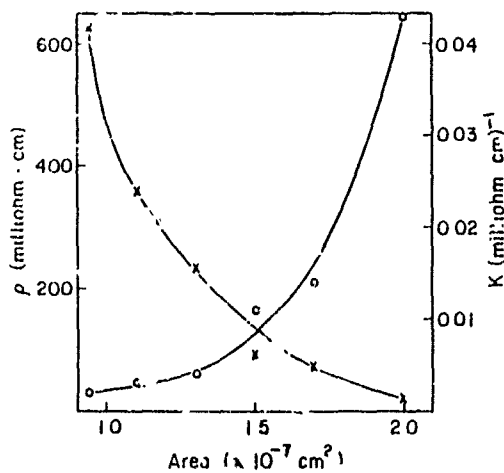


Figure 3 - Volume resistivity (x) and Conductivity (o) as a function of area.

While substantial errors in the estimates of the film thickness are possible, the relative thicknesses cannot in error by more than 15%. It can thus be surmised that the resistivity is strongly dependent upon film thickness. With a thickness of approximately 500 Å, the wire on the Kapton has a resistivity between 2.3×10^{-2} ohm-cm and 62.3×10^{-2} ohm-cm. This is significantly greater than the resistivity of pure palladium (1.08×10^{-5} ohm-cm). From figure 3, it is apparent that the volume resistance increases monotonically as the palladium cross-section decreases. It can be inferred from this result that for films of thickness less than 500 Å, the films are very porous. For uniform films, one expects no variation in the volume resistivity. With a film thickness of 150 Å, the resistivity of the palladium film on the Ultem 1000 is 7.8×10^{-2} ohm-cm. Palladium films on the Ultem 1000 are therefore also very porous, but less so, than for the films on Kapton.

Porous films have also been observed in platinum films deposited by the U.V. photolytic decomposition of $[(\eta^3\text{-C}_3\text{H}_5)(\eta^5\text{-C}_5\text{H}_5)\text{Pd}]$ [8]. These films were observed, however, to contain substantial amounts of carbon. Porous films can result from rapid deposition at catalytically active sites. The rapid growth of films at catalytically active nucleation sites has been observed previously and can accompany the photolysis of organometallic species [9-12]. We propose that for the deposited palladium on polyimide substrates from $(\pi\text{-allyl})(\pi\text{-cyclopentadienyl})$ palladium, a nucleation mechanism must be involved, i.e., palladium islands are more catalytically active for photolytic decomposition of $[(\eta^3\text{-C}_3\text{H}_5)(\eta^5\text{-C}_5\text{H}_5)\text{Pd}]$ as the source material.

For thicker palladium films, $(\pi\text{-allyl})(\pi\text{-cyclopentadienyl})$ palladium $[(\eta^3\text{-C}_3\text{H}_5)(\eta^5\text{-C}_5\text{H}_5)\text{Pd}]$, may be a suitable alternative to palladium acetate, since $[(\eta^3\text{-C}_3\text{H}_5)(\eta^5\text{-C}_5\text{H}_5)\text{Pd}]$ is significantly more volatile than palladium acetate. For selective area deposition, deposition from the gas phase may have applications where spin coating does not.

CONCLUSION

From analysis of our films on polyimide substrates and other [1,2] studies on silicon substrates, we know that the process is photolytic and the films are very pure by more than 99% by wt%.

Adhesion of the palladium films to polyimide substrates is very good. The volume resistivity of the very thin palladium films ($< 0.1 \mu\text{m}$) on the Kapton and polyimide substrates is significantly greater than for pure palladium. It is proposed that these results show that CVD palladium films can be applied to the fabrication of thin film resistors and interconnects.

ACKNOWLEDGEMENTS

This work was funded by I.B.M. (research agreement number 8074), by A.F.O.S.R. (contract number F30602-88-D-0027 administered by RADC as task A91913), and by the National Science Foundation (CHEM-8900471). The authors would like to thank H. Cole for his generosity in providing substrate materials.

REFERENCES

- [1] H. Esrom, G. Wahl and M. Stuke, Mat. Res. Soc. Proc. 131, 581 (1989).
- [2] Y.S. Liu and H. Cole, Mat. Res. Soc. Proc., 129, 579 (1989).
- [3] G.T. Stauf, P.A. Dowben, K. Emrich, S. Barfuss, W. Hirschwald and N.M. Boag, J. Phy. Chem., 93, 749 (1989).
- [4] K.-H. Emrich, G.T. Stauf, W. Hirschwald, S. Barfuss, P.A. Dowben, R.R. Birge and N.M. Boag, Mat. Res. Soc. Proc. 131, 401 (1989).
- [5] G.T. Stauf and P.A. Dowben, Thin Solid Films, 156, L31 (1988).
- [6] D.F. Shriver ed., Inorganic Synthesis, John Wiley and Sons, vol. 19, p. 221, 1979.
- [7] G.T. Stauf, P.A. Dowben, N.M. Boag, L. Morales de la Garza and S.L. Dowben, Thin Solid Films, 156, 327 (1987).
- [8] D. Rooney, D. Negrotti, T. Byassee, D. Macero, J. Chaiken and B. Vastag, Use of Laser Directed Chemical Vapor Deposition to Fabricated Durable-Optically Transport, Platinum Thin Film Electrodes, J. Electrochemical Soc. (unpublished).
- [9] M. Paunovic and C.H. Ting, in Electroless Deposition of Metals and Alloys, edited by M. Paunovic and I. Ohno (Proceeding of the Electrochemical Society, Vol. 88-12, Pennington, NJ 1988).
- [10] W. Krauter, D. Bauerle and F. Fimberger, Appl. Phys. A 31, 13 (1983).
- [11] C. Arnone, M. Rothschild, J.G. Black and D.J. Ehrlich, Appl. Phys. Lett., 48(15), 1018 (1986).
- [12] H. Yokoyama, F. Uesuqi, S. Kishida and K. Washio, Appl. Phys. A 37, 25 (1985).

UV EXCIMER LASER-INDUCED DEPOSITION OF PALLADIUM FROM PALLADIUM ACETATE FILMS

Hilmar Esrom and Georg Wahl
Asea Brown Boveri, Corporate Research, D-6900 Heidelberg, FRG

ABSTRACT

UV excimer laser-induced deposition of palladium from spin coated palladium acetate films in air is described. We have investigated mainly the deposition of palladium on aluminum oxide and quartz substrates and its dependence on the fluence and the number of excimer laser pulses. The decomposition mechanism was studied by measuring in situ the transmitted pulse energy during the exposure process. We have found that the excimer laser-induced decomposition of palladium acetate films is mainly pyrolytic and a simple model can be used to describe the decomposition process.

INTRODUCTION

For many applications in electronic and hybrid technology a new two-step deposition method is very interesting [1,2]. The first step deals with the photo-induced deposition and patterning of a thin activator on a substrate surface followed by the second step, the selective electroless metal deposition on the activated surface. The activation of substrate surfaces can be achieved by laser-induced decomposition of thin metalorganic or inorganic films on non-active surfaces [3-9]. The decomposition of the films can be performed in air, and no specialized vacuum equipment is needed. R.C. Sausa et al. [1] reported the pyrolytic Ar⁺ laser-induced decomposition of platinum metal-organic films and H.G. Cole et al. [2] reported the Ar⁺ laser-induced decomposition of palladium acetate films which are used as activators for electroless copper plating. Recently, we have shown that UV excimer laser-induced pre nucleation of various surfaces with palladium is very suited for electroless metallization [10]. In this paper, we report the results of our investigations concerning the deposition of palladium by means of excimer laser-induced decomposition of thin palladium acetate films on rough ceramic surfaces and the results of in situ measurements of the transmitted pulse energy during the decomposition process.

EXPERIMENT

Without special cleaning or pretreatment the palladium acetate films were spin-coated onto quartz or rough Al₂O₃ substrates. The spin-on films were prepared from palladium(II)acetate (MERCK) dissolved in chloroform using a concentration of about 0.15 mole/l. The spin-on films were irradiated by the excimer laser (Lambda Physik, Model EMG 103). The intensity distribution across the rectangular beam profile (20x6mm²) is inhomogeneous and therefore a homogeneous part was defined by a circular beam stop (diameter 4 mm) to minimize the spatial intensity inhomogeneity. The laser pulse energy was measured with a joulemeter (Gen Tec

PRJ-D, ED 200/500). After laser exposure, the undecomposed palladium acetate was removed by rinsing with chloroform. The optical transmittance of the palladium acetate film on a quartz substrate was measured with a Perkin Elmer UV Spectrophotometer 550. Film thickness was determined by scanning electron microscopy JEOL JXA-733 ELECTRON MICRO PROBE (EMP). The thickness of the palladium layers was determined by energy dispersive x-ray analysis by measuring the intensity of the palladium line. For the calibration we used films of various thicknesses, sputtered on glass substrates. The thickness of the films was measured with an interference microscope (Carl Zeiss). To achieve an effective thickness of the discontinuous palladium layers which are typical for the excimer laser deposition process [11] a scanning area of $40\text{ }\mu\text{m} \times 30\text{ }\mu\text{m}$ for the electron beam was chosen.

RESULTS AND DISCUSSION

Excimer Laser-induced Deposition of Palladium

Fig. 1 shows the palladium thickness on Al_2O_3 substrates (after washing process) achieved at $\lambda=193\text{ nm}$ with one excimer laser pulse from a $\sim 1000\text{ }\text{\AA}$ thick palladium acetate film as a function of the fluence. In the fluence region between $10\text{ mJ}/\text{cm}^2$ and $50\text{ mJ}/\text{cm}^2$ a linear dependence of the thickness on the fluence is determined and the slope was estimated to be $\sim 0.63\text{ }\text{\AA}/\text{mJcm}^{-2}$. It is evident from Fig. 1 that a threshold fluence E_{th} of $\sim 10\text{ mJ}/\text{cm}^2$ for palladium deposition exists. High fluences $> 4\text{ J}/\text{cm}^2$ lead to complete ablation of the palladium acetate films so that copper

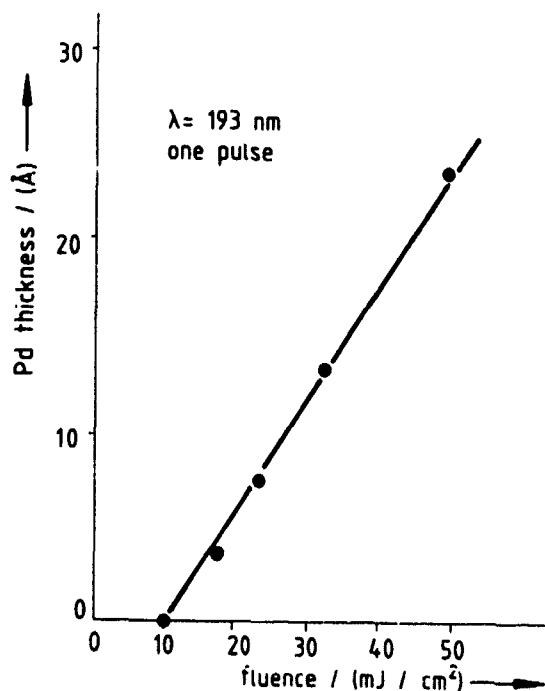


Fig. 1 Palladium thickness as a function of the fluence at $\lambda=193\text{ nm}$ (one pulse)

plating is impossible. Fig. 2 shows the dependence of the thickness of the deposited palladium (after washing process) on the number of laser pulses. At a fluence of $\sim 50 \text{ mJ/cm}^2$ ($\lambda=193 \text{ nm}$) 5 pulses are needed to achieve a constant Pd thickness of $\sim 60 \text{ \AA}$ from the palladium acetate film (thickness $\sim 1000 \text{ \AA}$). From the slope of the linear part of this curve we estimated a deposition rate of $\sim 10 \text{ \AA/pulse}$. At fluences lower than 50 mJ/cm^2 , smaller final palladium thicknesses are achieved. During the irradiation a discoloration of the spin-on palladium acetate film occurs from yellow to grey. Below the threshold no discoloration and no deposition of palladium was possible, even by irradiation of the samples for a long period. For example, at 6 mJ/cm^2 and 200 Hz repetition rate no deposition of palladium was achieved after 5 min. Using KrF* excimer laser light we found nearly the same curves as in Fig. 2 for ArF* light, however with a slightly higher deposition rate of about 15 \AA/pulse at $\sim 50 \text{ mJ/cm}^2$ and a slightly higher threshold energy of $\sim 15 \text{ mJ/cm}^2$. For the wavelengths $\lambda=308 \text{ nm}$ and $\lambda=351 \text{ nm}$ threshold fluences of $E_{th} \sim 80 \text{ mJ/cm}^2$ and $E_{th} \sim 200 \text{ mJ/cm}^2$ were determined.

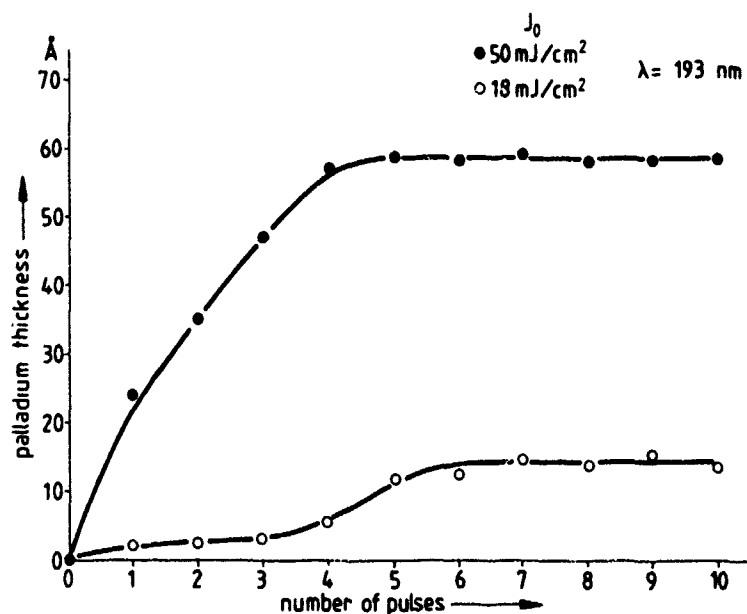


Fig. 2 Thickness of palladium on Al_2O_3 in dependence on the number of pulses at 50 mJ/cm^2 and 18 mJ/cm^2 ($\lambda=193 \text{ nm}$); initial palladium acetate film thickness $\sim 1000 \text{ \AA}$

Transmittance Change During Laser-induced Decomposition

To study the mechanism of the excimer laser-induced decomposition process we performed in situ pulse energy measurements. The measurement was performed by using a circular beam (diameter 4 mm). The transmitted fluence during the pulse-to-pulse experiments was measured with a joulemeter behind quartz substrate which was spin-coated with palladium acetate. At a fluence of ~ 50 mJ/cm^2 ($\lambda=193$ nm) the transmittance increases with the number of pulses to a saturation value of about 60 % after 5 pulses (Fig. 3). This is in agreement with Fig. 2, where the same number of pulses was necessary to reach saturation. Further

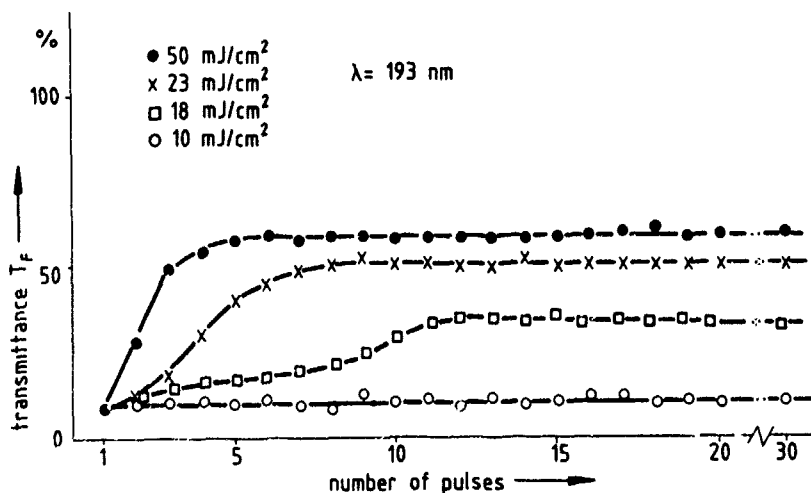


Fig. 3 Transmitted pulse energy during the decomposition process in dependence on the number of the laser pulses at 50 mJ/cm^2 , 23 mJ/cm^2 , 18 mJ/cm^2 and 10 mJ/cm^2 ($\lambda=193$ nm); initial palladium acetate thickness $\sim 1000\text{\AA}$

pulses have no influence on the transmission. The increase of the transmission is due to the decrease of undecomposed palladium acetate in the film. The layers produced in the saturation range at 50 mJ/cm^2 showed a constant transmission which was measured with the UV spectrometer in the UV region between the wavelengths $\lambda=200$ nm and $\lambda=400$ nm. This is in contrast to the UV spectrum of palladium acetate (see Fig. 4). XPS measurements have shown that these layers contain mainly palladium with a carbon impurity of about 30 at %. An oxygen impurity of < 1 at % was measured in films on silicon. We conclude from these measurements that in the saturation range at a fluence of 50 mJ/cm^2 films are produced with almost no palladium acetate content. At lower fluences more pulses are necessary to achieve a constant transmittance T with values $T < 60$ %. Obviously incompletely decomposed parts of palladium acetate lead to the lower transmittance in accordance with Fig. 2, where it is shown, that lower fluences lead

to thinner deposited palladium films on Al_2O_3 substrates. At fluences $< 10 \text{ mJ/cm}^2$, no decomposition is observed and we can verify the threshold fluence to be about 10 mJ/cm^2 . In case of the KrF* excimer radiation ($\lambda=248 \text{ nm}$) we determined nearly the same curves as shown in Fig. 4, with a threshold fluence $E_{th} \sim 15 \text{ mJ/cm}^2$.

Discussion of the Excimer Laser-induced Deposition Process

The threshold nature and observed dependence of the deposition rate on fluence would appear to favor thermal decomposition rather than direct bond breaking as a possible mechanism responsible for significant material deposition. If bond breaking is dominant in the deposition process, then decomposition should be possible in the case of a cumulative light dose applied to the film at sub-threshold. Our multishot irradiation experiments indicate that it is clearly not the case. Table 1 shows the threshold fluences E_{th} and the absorption coefficients α determined from the transmittance measurements (Fig.4). The correlation which is evident between

EXCIMER	ArF*	KrF*	XeCl*	XeF*
Wavelength[nm]	193	248	308	351
Absorption Coefficient[10^5cm^{-1}]	7.2	2.3	.55	.21
Threshold Fluence[mJ/cm ²]	10	15	80	200

table 1 Absorption coefficients α of the palladium acetate film and the threshold fluences E_{th} at different excimer laser wavelengths λ

the threshold fluence E_{th} and the absorption coefficient α can be explained by a simple model, which is based on the thermal decomposition of the palladium acetate. It is assumed that a certain minimum absorbed energy density per unit volume ϵ_{th} is necessary for the decomposition process. This energy density ϵ_{th} is given by:

$$(I) \quad \epsilon_{th} = (1-R) \cdot E_{th} \cdot \alpha$$

where R is the reflectivity of the film. This energy density ϵ_{th} can be related to the minimum decomposition temperature T_d by:

$$(II) \quad \epsilon_{th} = (\chi + \rho \cdot C \cdot T_d)$$

with the energy for phase transformations χ , the density ρ and specific heat capacity C of palladium acetate. The minimum thermal decomposition temperature T_d is

measured to be $T_d \sim 500$ K [12]. Equation (I) shows that E_{th} should depend linearly on $1/\alpha$:

$$(III) \quad E_{th} = \beta \cdot \alpha^{-1} \quad \beta = \epsilon_{th} / (1 - R)$$

if ϵ_{th} and R are constant. Fig. 5 confirms this linear dependence, where E_{th} is plotted versus the photon penetration depth $\tau = 1/\alpha$. From the calculated slope of $\beta = 4.2 \cdot 10^3 \text{ Jcm}^{-3}$ the decomposition temperature of $T_d = 1100$ K was calculated using equations (I-III). For our calculations the following material properties were taken: $C = 0.3 \text{ cal/gK}$ (the value for sodium acetate [13]), $\rho = 3 \text{ g/cm}^3$ [12]. χ and R were assumed to be zero. This simplification for χ and R could be the reason for the larger value of T_d compared with the experimental value. Additional visual evidence supported the thermal nature of the decomposition process. At fluences $> 400 \text{ mJ/cm}^2$ ($\lambda = 193 \text{ nm}$) one pulse with a cross section of 4 mm leads to a deposited palladium area of $\phi \approx 8 \text{ mm}$. Most probably, the excimer laser-induced decomposition is highly exothermic in air and the self-heating (thermal runaway) increases the decomposition region. In thermoanalytical studies of palladium acetate the exothermic nature of the decomposition was estimated when the palladium acetate was heated in air or oxygen [12]. Characteristic of the

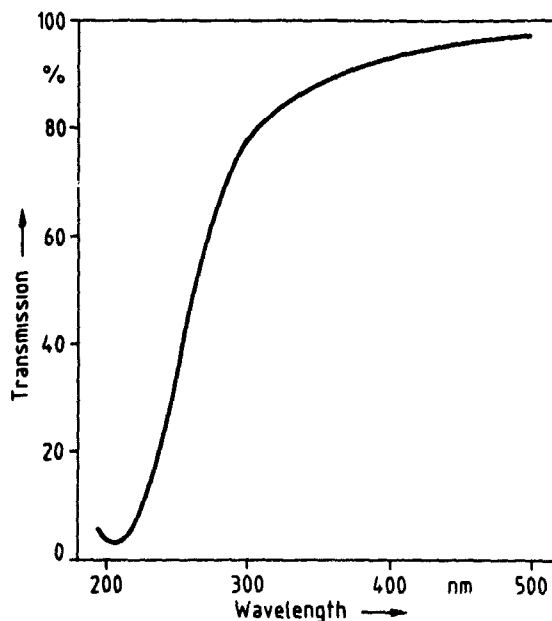


Fig. 4 Transmission spectrum of a 450 Å thick palladium acetate film in the UV region

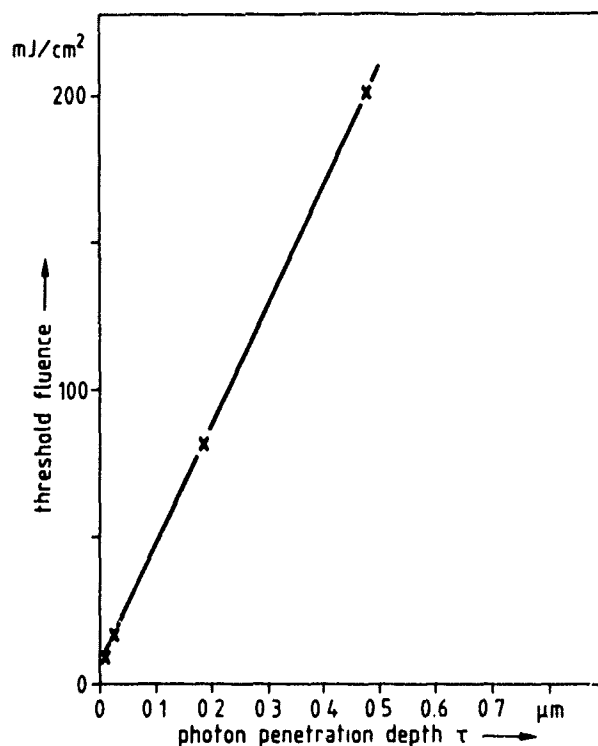


Fig. 5 Plot of the threshold fluence E_{th} versus the photon penetration depth τ

excimer laser-induced deposition process are the low final palladium thicknesses. In the case of a 1000 Å palladium acetate film and complete decomposition (e.g. at $\lambda=193$ nm, 50 mJ/cm², 10 pulses) we measured only 5 % of the initial palladium acetate film for the palladium film thickness. With the stoichiometric value of palladium content of palladium acetate, about 50 % of the precursor film thickness is expected for the final palladium thickness [12]. Probably the competition between evaporation and decomposition of palladium acetate explains the low efficiency of the deposition process [12]. The decreasing value of the palladium thickness in the saturation range (Fig. 2) with decreasing fluence is not completely understood. Perhaps the increasing transmission (Fig. 3) involves a smaller energy absorption, so that the decomposition process is stopped before a complete decomposition occurs.

CONCLUSIONS

Palladium deposition has been performed by exposing UV excimer laser light onto substrates spin-coated with palladium acetate. The investigated deposition process depends on the laser fluence. At about 50 mJ/cm² five excimer laser pulses are required to yield a complete decomposition of the palladium acetate films (thickness: ~ 0.1 µm) which leads to thin Pd layers (~ 60 Å) on an Al₂O₃ substrate surface. The results of threshold fluence measurements have shown that excimer laser light at 193 nm and 248 nm are more suited for large area deposition than excimer radiation of other wavelengths. We have found that the decomposition process is photothermal in nature and a simple model can be used to describe the decomposition mechanism.

ACKNOWLEDGEMENT

The authors would like to thank Dr.J.Demny and U. Feller for EMP and XPS investigations and Dr.M.Stuke, Max-Planck-Institut Göttingen, for stimulating discussions. This work was partly financed by the Bundesministerium für Forschung und Technologie[Nr.13 N 5397/6]

REFERENCES

1. R.C.Sausa, A.Gupta, and J.R.White, J.Electrochem.Soc.,Vol.134,No.11,2707(1987)
2. H.S.Cole, Y.S.Liu, J.W.Rose, R.Guida, L.M.Levinson, and H.R. Philipp, in LASER PROCESSES FOR MICROELECTRONIC APPLICATIONS,Vol.88-10 of the Proceedings of the Electrochemical Society, edited by J.J.Ritsko, D.J.Ehrlich, and M.Kashiwagi Pennington,NJ,1988); also article in this journal
3. G.J.Fisanick, M.E.Gross, J.B.Hopkins, M.D.Fennell, K.J.Schnoes, and A.Katzir, J.Appl.Phys.57(4),1139(1985)
4. G.J.Fisanick, J.B.Hopkins, M.E.Gross, M.D.Fennell, and K.J.Schnoes, Appl.Phys.Lett.46(12),1184(1985)
5. M.E.Gross, G.J.Fisanick, P.K.Gallagher, K.J.Schnoes, and M.D.Fennell, Appl.Phys.Lett.47(9),923(1985)
6. A.Auerbach, Appl.Phys.Lett.47(7),669(1985)
7. M.E.Gross, A.Appelbaum, and K.J.Schnoes, J.Appl.Phys.60(2), 529(1986)
8. M.E.Gross, A.Appelbaum, and P.K.Gallagher, J.Appl.Phys.61(4), 1628(1987)
9. A Gupta and R.Jagannathan, Appl Phys.Lett.51(26),2254(1987)

10. H.Esrom,G.Wahl, and M.Stuke,
Mat.Res.Soc.Symp.Proc.,Vol.131,581(1989)
11. H.Esrom and U.Kogelschatz, in these proceedings
12. P.K.Gallagher and M.E.Gross, J.Thermal Anal.31,1231,(1986)
13. W.Koglin, KURZES HANDBUCH DER CHEMIE, Göttingen, FRG,
Vandenhoeck & Ruprecht,1954

PART III

Laser Deposition II

IN SITU CHARACTERIZATION OF
METALLORGANIC CHEMICAL VAPOR DEPOSITION

R. SCARMOZZINO, T. CACOURIS, AND R.M. OSGOOD JR.
Columbia University, New York, N.Y. 10027

ABSTRACT

In situ measurement of resistance has been used for the real-time monitoring of metallorganic chemical vapor deposition (CVD) growth characteristics. In particular, a novel technique for measuring metallorganic CVD activation energies is presented. The micron scale geometry of the experiment makes it relevant to work in localized laser CVD. The technique has been used to measure the CVD activation energy of dimethylaluminum hydride (DMA1H). In addition, a variant of the technique has been used to study the growth stage of a resistless two-step metallization process (nucleation / selective CVD) employing DMA1H as the source gas in both steps.

INTRODUCTION

Chemical vapor deposition is an important process in the semiconductor industry, and a knowledge of the activation energy for CVD of various materials is extremely useful for process modeling. In the conventional method of measuring this quantity,¹ the scale of the geometry is such that there exist mass transport limitations^{2,3} which can complicate the measurement and/or put restrictions on the maximum deposition rate, and hence the temperature range that can be studied. For example, it would be difficult to pinpoint a deviation from the Arrhenius law at high temperature as being the result of mass transport limitations, or the result of a different reaction pathway at the higher temperature. If on the other hand a small reaction geometry is used, mass transport limitations are significantly reduced,^{2,3} simplifying the measurement considerably. In addition, experiments in a small microreaction geometry are of interest in the laser direct writing of semiconductors via pyrolysis.

Measurements of CVD activation energies in a microreaction geometry can be performed using focused laser beams. In this case, the measurements are done by pyrolytically depositing spots or lines at different laser powers, subsequently measuring the size of the deposit, calculating the laser induced temperature rise, and forming an Arrhenius plot of the results.⁴ In the method presented here, which is applicable to CVD of conducting materials, a thin line is deposited between two large test pads via laser photolysis, laser pyrolysis, or even conventional photolithography. A fixed voltage is placed between the pads, inducing a current in the line which resistively heats it, causing pyrolysis to occur and the line to grow. The subsequent decrease in resistivity increases the current and the power dissipation and causes the line to grow faster. By simply monitoring the current in the line as a function of time on a chart recorder, one simultaneously obtains information on the growth rate of the line versus the power dissipation in the line. After a calculation of the induced temperature rise, an Arrhenius plot can be made, from which the activation energy can be extracted. We note that the enhanced growth of laser deposited lines via passing current has

been recently reported for the case of a pulsed current.⁵ This new technique may have several applications. For example, it can be used for the selective growth of lines in the repair of integrated circuits.

EXPERIMENT AND RESULTS

In this experiment, thin ($< 1000 \text{ \AA}$) aluminum lines were deposited photolytically from the metallorganic gas DMAIH, using a focused cw UV laser beam as in [6]. The lines were deposited on a substrate consisting of 3000 \AA of SiO_2 on Si. The length and width of the lines were measured *in situ* from the video image, and were typically 1200 \mu m and 7 \mu m respectively. The lines were deposited between large ($300 \text{ \mu m} \times 300 \text{ \mu m}$) gold test pads, which were connected via a vacuum feedthrough to the external circuit of Fig. 1. This allowed *in situ* measurement of the resistance, which was typically $500\text{--}1000 \text{ \Omega}$ initially. In a 1 Torr ambient of DMAIH, application of approximately 30 V yielded sufficient current to heat the lines and cause pyrolysis.

A typical current versus time trace is shown in Fig. 2. The Arrhenius curve is obtained from this curve as follows. Given the fixed voltage V_0 , the current is given by $I = V_0 R^{-1}$, where R is the total resistance of the line, which consists of the initial resistance R_0 in parallel with the resistance of the growing deposit R_D , i.e. $R^{-1} = R_0^{-1} + R_D^{-1}$. The resistance of the deposit is given by $R_D = \rho L/wh$, where ρ is the resistivity of the deposit, and L , w , and h are the length, width, and thickness of the deposit. Therefore the current is given by:

$$I(t) = \frac{V_0}{R_0} + \frac{V_0 w}{\rho L} h(t) .$$

Differentiating shows that dh/dt , the growth rate at time t , is proportional to dI/dt , which we can easily obtain from Fig. 2. We have assumed for simplicity that w is constant (which is true for small enough times: the principal growth of a thin, wide line being in the thickness). This restriction can be removed to some extent.

The power dissipated in the line at time t is simply given by $P(t) = V_0 I(t)$. The average surface temperature is calculated from the power $P(t)$ by:

$$T(t) = T_0 + \frac{d}{K_G} \frac{P(t)}{Lw} u \left[\frac{w d K_G}{L w K_S} \right] .$$

Here d is the thickness of the SiO_2 layer, and K_G and K_S are the thermal conductivities for SiO_2 and Si respectively. This is obtained assuming the deposit is a good thermal conductor (which is true for aluminum), so that the power flows uniformly into the substrate surface over the area $L \times w$. Standard Fourier analysis on a semi-infinite domain can be used to obtain the above equation with u defined by:

$$u = \left[\frac{2}{\pi} \right]^2 \int_0^\infty \int_0^{\pi/2} \frac{1}{d\theta} \left[\frac{\sin(r \cdot \cos \theta)}{(r \cdot \cos \theta)} \frac{\sin(r \cdot \sin \theta)}{(r \cdot \sin \theta)} \right]^2 \frac{[1 - \alpha \cdot \exp(-2rD)]}{[1 + \alpha \cdot \exp(-2rD)]} d\theta dr$$

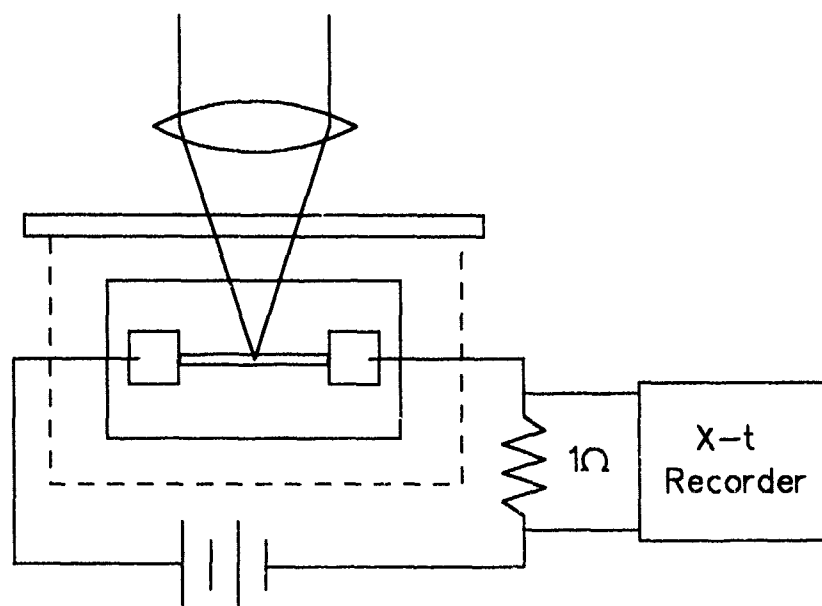


Figure 1. Diagram of experimental setup showing laser written aluminum line deposited between gold test pads, and external circuit for measuring current versus time.

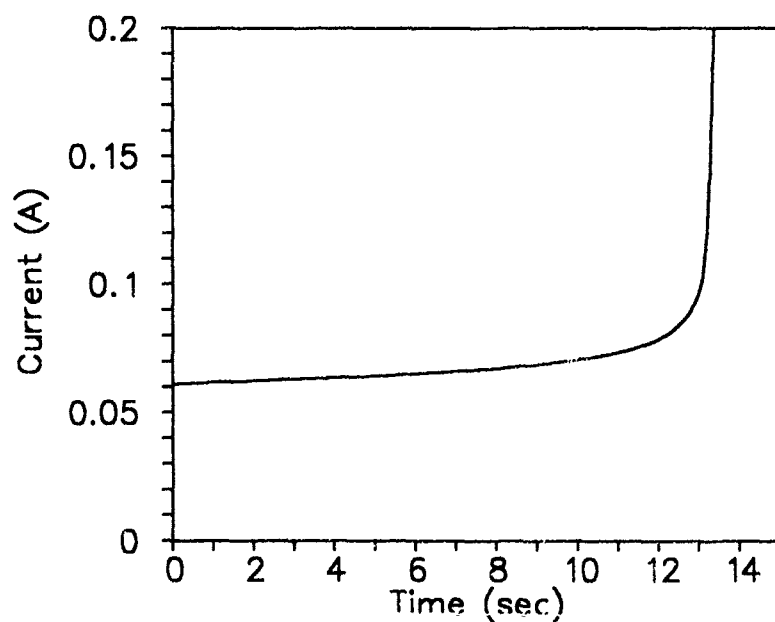


Figure 2. Typical current versus time curve obtained as in Fig. 1, after applying a voltage to a laser written line in an ambient of 1 Torr of DMA1H.

$$\text{where } D \equiv 2 \frac{d}{w} \left[\cos^2 \theta + \frac{w^2}{L^2} \sin^2 \theta \right]^{\frac{1}{2}}, \text{ and } \alpha \equiv \frac{1 - K_G/K_S}{1 + K_G/K_S}.$$

Note that in the limit $d \ll w$, $d \ll L$, $K_G \ll K_S$, u approaches 1. We have numerically evaluated u for our parameters ($w = 6\text{--}12 \mu\text{m}$, $L = 1200 \mu\text{m}$, $d = 0.3 \mu\text{m}$, $K_G/K_S = 0.01$), and its dependence on w is approximately $u(w) = 1.05 + 0.057 w$. Note also that for the temperature range of these experiments, the thermal conductivity is approximately constant.

This procedure applied to $I(t)$ data for several trials results in the Arrhenius curves shown in Fig. 3. The data follows the Arrhenius behavior well, as indicated by the linearity of $\ln(dI/dt)$ with $1/T$ over a wide range of growth rates. Most of the scatter of the data around the straight line is probably due to the manual digitization of the $I(t)$ curve, and the resulting error in numerical differentiation. The resultant activation energy is $E_a = 34 \pm 3 \text{ kcal/mole}$. While there is no accurate measurement of the activation energy for DMA1H in the literature, our number is reasonable considering other activation energies for aluminum compounds. For example, it is known^{7,8} that DMA1H vapor exists as an H-bridged dimer at low temperatures (the dimer-trimer equilibrium is 83–95 °C). If the rate limiting step in DMA1H CVD is the dissociation of these hydrides, then the CVD activation energy will be of the order of their heat of association, which is 15–20 kcal/mole per H-bridge.

This technique has several advantages. It can be performed entirely *in situ*. It is extremely simple and quick to apply, requiring only a single measurement of $I(t)$, which takes well under a minute to obtain. As is usually the case, the main source of error is probably in the calculation of the induced temperature rise, due to inaccuracies in the knowledge of geometric or material parameters. For example, when the deposition occurs via laser pyrolysis as in [4], the power absorbed by the deposit, and hence the temperature rise, depends on the reflectivity of the deposit which may differ considerably from that of the pure material. However, in this method the power dissipated is directly measured, which allows less reliance on questionable material parameters, and leads to improved accuracy. Also, if higher accuracy is desired, the experiment can be performed in the controlled geometry of a photolithographically deposited line.

We have employed a variation of this technique to study a two-step resistless process for forming aluminum metallization motivated by the work in [9]. The process consists of photolytic deposition of a nucleating deposit for the patterning stage, and selective CVD thermal growth for the bulk deposition stage, both using DMA1H as the source gas. The experimental setup is similar to that shown in Fig. 1, except that in this case the sample is heated uniformly by passing a current through a thin layer of chromium (50 Å) deposited on its underside. A cw laser (273–308 nm) is used to photolytically deposit a thin aluminum line (500 Å) between the two pads as in the previous experiment. This line provides a nucleation region for subsequent selective thermal growth. The external circuit applies a small fixed voltage to the line, and monitors the current in the line on a chart recorder. The current is proportional to the line thickness, and this allows an instantaneous measure of how rapidly the line is growing. This allows one to obtain much more information than simply recording the final line thickness after a fixed deposition time. Note that

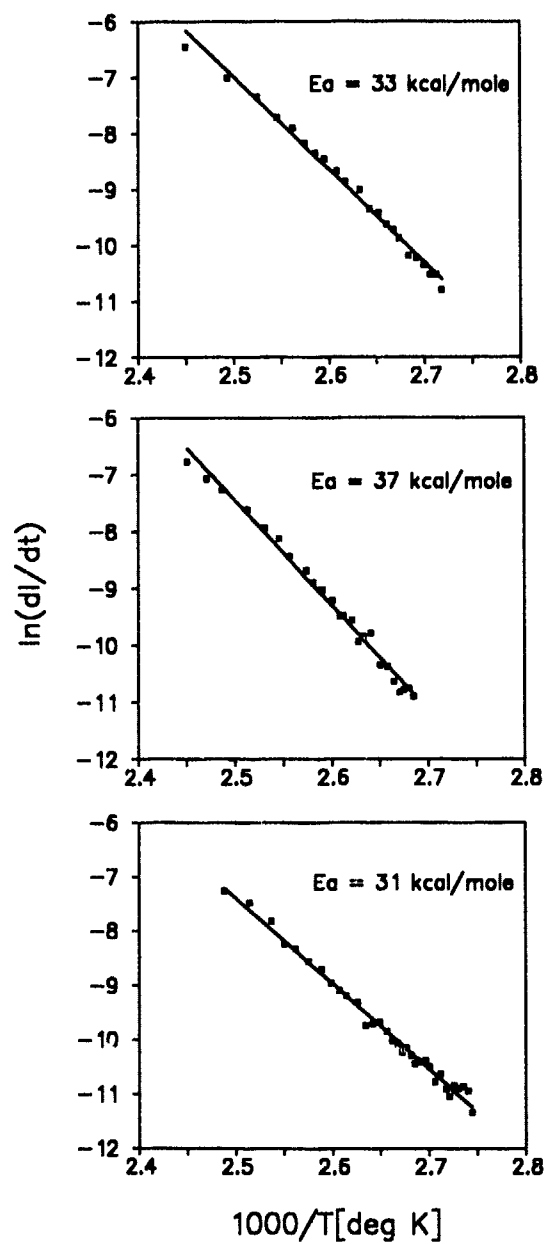


Figure 3. Arrhenius plots of $\ln(dI/dt)$ versus $1/T$ for several trials. The activation energy obtained from these plots is $E_a = 34 \pm 3$ kcal/mole.

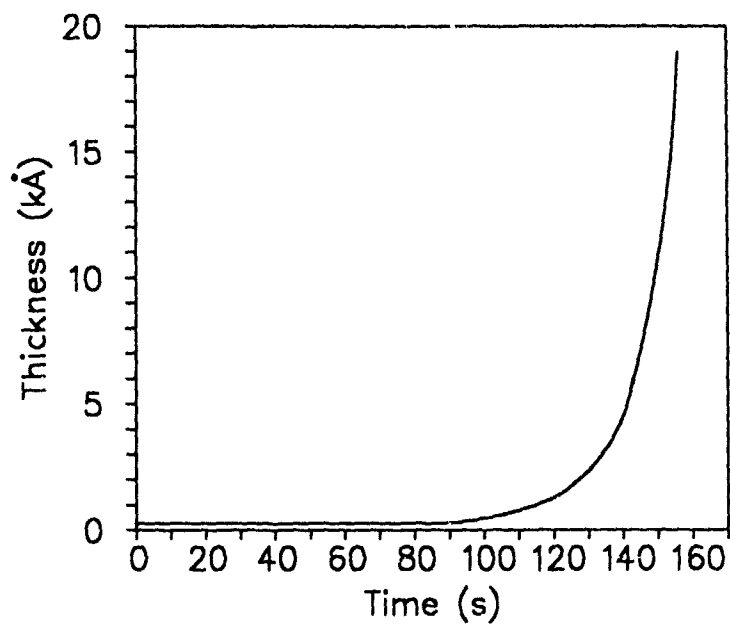


Figure 4. Typical growth curve obtained from measurement shown in Fig. 1, after uniform heating is applied to the sample. The growth temperature was 187 °C, and the vertical axis (current) has been rescaled to the final line thickness.

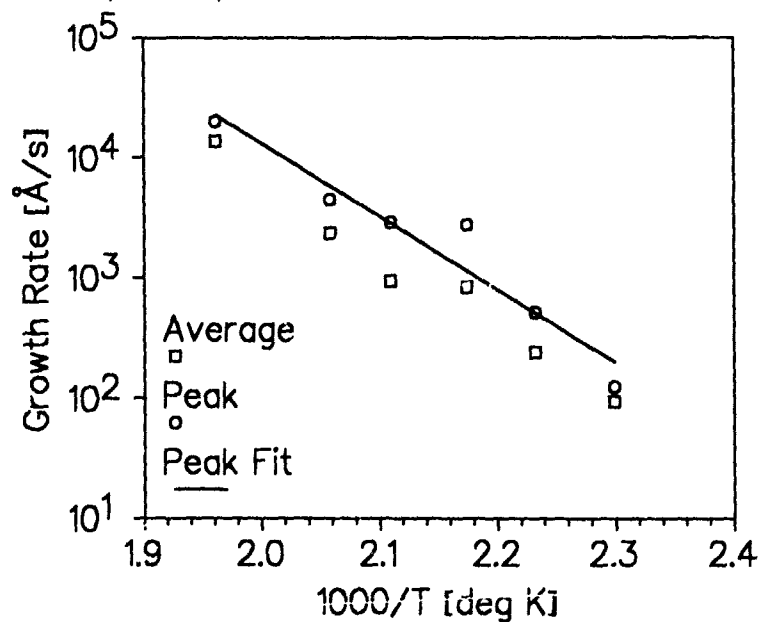


Figure 5. Arrhenius plot of log of growth rate versus $1/T$ obtained from growth curves as in Fig. 4. The measured activation energy is $E_a = 28$ kcal/mole.

here the current in the line is insufficient to cause heating.

In a typical measurement, the chart recorder is switched on at the same time that the uniform heating is applied. The temperature reaches steady state very rapidly compared with the line growth. A typical curve of current versus time is shown in Fig. 4 for a growth temperature of 187 °C. The curve exhibits a long latent phase, where growth is very slow, and then a more or less constant rapid growth phase. The cause of the latent phase is unclear at this time, however we have observed that a longer lag time between the nucleation phase and the thermal growth phase appears to yield a longer latent period. We are studying this effect further.

The above procedure was applied to obtain growth curves at several temperatures. We measured the final thickness of each line (via stylus profilometry) and used that to scale the current axis to thickness. The slope of the re-normalized curve during the constant growth phase was used as a measure of the CVD growth rate. An Arrhenius plot of the growth rate vs temperature data was made and is shown in Fig. 5. The slope of the data indicates an activation energy of $E_a = 28$ kcal/mole. This is similar to the result of the previous experiment. We also took the same growth curve data, and estimated a growth rate as the final thickness over the total time. The resulting Arrhenius plot is also shown in Fig. 5 for comparison with the more elaborate measurement. As can be seen from the figure, these two measurements can yield growth rates which differ by a factor of two to three, demonstrating the utility of monitoring the instantaneous growth.

In summary, *in situ* measurement of resistance has been used for the real-time monitoring of metallorganic CVD. We have described a new technique for measuring CVD activation energy in a microreaction scale geometry. In addition, a variant of the technique has been used to study a two-step resistless process for forming aluminum metallization.

This work was supported by the Semiconductor Research Corporation.

REFERENCES

1. H.E. Carlton and J.H. Oxley, *AIChE J.* **12**, 86 (1967).
2. D.J. Ehrlich and J.Y. Tsao, *J. Vac. Sci. Technol. B* **1**, 969 (1983).
3. D. Bauerle, "Chemical Processing with Lasers," (Springer, 1986), p. 92.
4. F. Petzoldt, K. Piglmayer, W. Krauter, and D. Bauerle, *Appl. Phys. A* **35**, 155 (1984).
5. O. Gottsleben and M. Stuke, *Appl. Phys. Lett.* **52**(26), 2230 (1988).
6. T. Cacouris, G. Scelsi, P. Shaw, R. Scarmozzino, and R.M. Osgood, *Appl. Phys. Lett.* **52**(22), 1865 (1988).
7. T. Wartick and H.I. Schlesinger, *J. Am. Chem. Soc.* **75**, 835 (1953).
8. G.A. Anderson, A. Almenningen, F.R. Forgaard and A. Haaland, *Chem. Commun.*, 480 (1971).
9. G.S. Higashi and C.G. Fleming, *Appl. Phys. Lett.* **48**, 1051 (1986).

LASER WRITING OF HIGH PURITY GOLD LINES

M. JUBBER, J.I.B. WILSON, J.L. DAVIDSON*, P. JOHN* AND P.G. ROBERTS*

Departments of Physics and Chemistry*

Heriot-Watt University, Riccarton, Edinburgh EH14 4AS, Scotland

ABSTRACT

Gold tracks have been deposited on thermally oxidised and single crystal silicon, gold and nichrome coated silicon wafers by pyrolytic decomposition of gaseous alkyl (triethyl phosphine) gold(I) complexes using focussed 514 nm radiation from an argon ion laser. The precursors, $\text{RAu(I)Et}_3\text{P}$, $\text{R} = \text{CH}_3, \text{C}_2\text{H}_5$ are low melting point crystalline solids with relatively high vapour pressures (~ 5 mtorr). They are representative of a class of compounds being evaluated for laser deposition of gold. Differential scanning calorimetry, DSC, shows that the thermal decomposition of $\text{MeAu(I)Et}_3\text{P}$ in the solid state is a two-stage process. The decomposition temperature is $63 \pm 1^\circ\text{C}$. Tracks were deposited at laser scan speeds up to $35 \mu\text{m s}^{-1}$ with a beam diameter ($1/e^2$) at the focus of $\sim 12 \mu\text{m}$. SIMS, EDX and laser ionisation microprobe analysis, LIMA, were used to determine the chemical composition of the tracks. The purity of $>98\%$ is consistent with the measured resistivities ($4.2 \mu\Omega \text{ cm}$) at room temperature compared to bulk gold ($\sim 2 \mu\Omega \text{ cm}$). These resistivities were achieved without post deposition annealing. Stylus profilometry and SEM data showed the lines produced from $\text{MeAu(I)Et}_3\text{P}$ have a virtually rectangular cross-section. Together with the absence of the ubiquitous λ -ripples, this feature suggests that deposition is more rapid on the gold surface than on the SiO_2 substrate. Laser power thresholds are lower for silicon substrates coated with thin ($5 - 10^\circ\text{A}$) films of gold or nichrome.

INTRODUCTION

Until recently [1] organogold precursors employed for the laser deposition of elemental gold have invariably been Au(III) complexes [2]. Low oxidation state, Au(I) , complexes are less stable towards atmospheric oxidation [3]. However, other features including thermal decomposition rates, uv spectra and volatility are advantageous. Low resistivity gold tracks ($\sim 4 \mu\Omega \text{ cm}$) have been deposited from trialkyl phosphine complexes, $\text{MeAu(I)Et}_3\text{P}$, using 514 nm Ar^+ laser photothermal 'direct writing' at scanning speeds up to $35 \mu\text{m s}^{-1}$ [1]. Improvement to the deposition rates are dependent on understanding the mechanism of the thermal decomposition. In this paper, we report some recent results obtained from differential scanning calorimetry, DSC, studies of the decomposition of $\text{MeAu(I)Et}_3\text{P}$. Further data is presented on 514 nm

photothermal deposition of gold on a variety of substrates including a prenucleated Au coated silicon substrate.

EXPERIMENTAL

The output from an Ar⁺ laser (Coherent Innova 100 - 10) at 514 nm was focussed by a quartz meniscus lens to a diameter ($1/e^2$) of 12 μm . Substrates were thermally grown SiO₂ (100 nm) on (100) crystalline silicon wafers, (100) crystalline silicon after HF removal of the 'native' oxide and Au and nichrome coated (5 - 10 $^\circ\text{A}$) crystalline silicon. The substrates were mounted in a stainless steel reaction cell fitted with a quartz window. The cell was translated under the laser beam by a 0.1 μm step size x-y translation stage. Prior to deposition, the cell is evacuated to better than 10⁻⁵ mbar with a turbomolecular/rotary oil pump combination. The precursors were synthesised by the reaction of chlorotriethylphosphine gold with either methyl lithium (MeAuEt₃P) or ethylmagnesium chloride (EtAuEt₃P) according to reported procedures [4].

The morphology of the deposits were examined by laser scanning optical microscopy and SEM. Laser ionisation microprobe analysis, LIMA, and SIMS were used to determine the chemical composition of the material. Tracks were profiled using a Dektak 3030 instrument.

Thermal analysis by differential scanning calorimetry, DSC, was performed using a Perkin Elmer DSC II instrument. Samples of MeAuEt₃P were encapsulated, under Ar, in metal pans within a dry box (H₂O <2 ppm, O₂ <0.1 ppm). DSC experiments were performed at temperature ramp rates, θ , of 10 K⁻¹ min⁻¹ or 20 K min⁻¹ with sample weights of 0.4 - 1.2 mg.

RESULTS

Samples of MeAuEt₃P were heated from 30 $^\circ\text{C}$ to 80 $^\circ\text{C}$ at $\theta = 20$ K min⁻¹. A sharp endotherm was observed at $63 \pm 1^\circ\text{C}$. After the sample was cooled to 20 $^\circ\text{C}$, subsequent scans at the same scan rate, showed no peak. The decomposition temperature, T_d , was independent of θ for $\theta = 10$ and 20 K min⁻¹ and identical results were obtained for samples sealed in a Au coated pan. Inspection of the contents after a single scan showed the endothermic peak was due to thermal degradation of the crystals. In a second series of experiments, five samples of MeAuEt₃P were heated at $\theta = 20$ K min⁻¹ until $T_d = 63^\circ\text{C}$ was attained. The temperature was kept constant for times, δt , ranging from 0 to 30 minutes. Subsequently the temperature was reduced rapidly to 25 $^\circ\text{C}$ and DSC scans were recorded up to 120 $^\circ\text{C}$ at $\theta = 20$ K min⁻¹. In all the experiments, no weight loss occurred during the decomposition ensuring the integrity of the pans during temperature cycling. Figure 1 shows a composite plot of the rate of heat change dq/dt for $\delta t = 0, 5, 30, 62$ and 130 min versus temperature. For

$\delta t = 0$, a single decomposition peak at $T_d = 63^\circ\text{C}$ is evident, whilst under isothermal decomposition conditions, two endotherms are apparent at $T_d = 63^\circ\text{C}$ and 55°C . The relative area under the peak at 55°C increased relatively to the peak at 63°C as δt increased. At the highest value of δt only the peak at 55°C was present. Thus at $\delta t = 130$ min the concentration of the starting material was reduced to the extent that the endotherm at $T_d = 63^\circ\text{C}$ was absent.

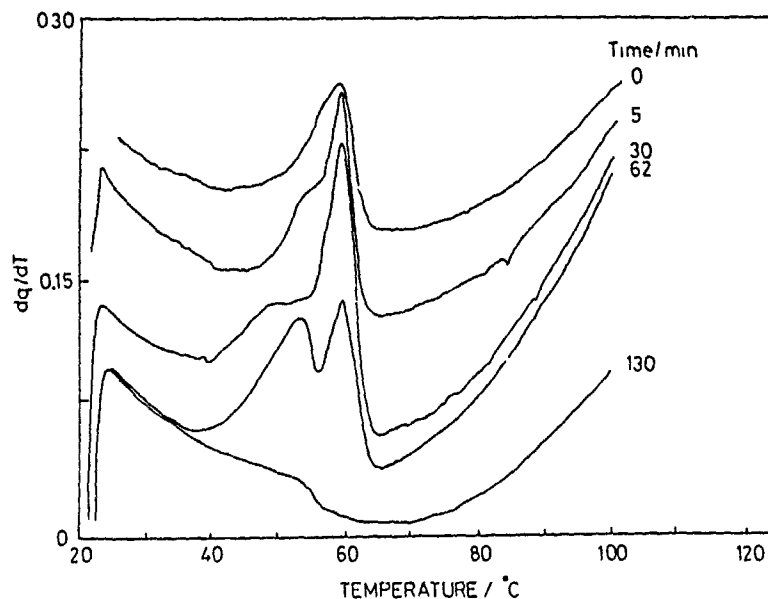


Fig. 1. DSC data for the solid state thermal decomposition of $\text{MeAu(I)Et}_3\text{P}$ under Ar

For a translation speed of $35 \mu\text{m s}^{-1}$, the threshold power for deposition is $1.0 - 1.2 \text{ MW cm}^{-2}$ for both MeAuEt_3P and $\text{EtAu Et}_3\text{P}$. Deposits near threshold appear as a discontinuous line of gold spheres ranging over a width of approximately $2 \mu\text{m}$. Beyond threshold, the tracks are continuous, with the high nucleation density producing a fine grained deposit. Unlike other material deposited by laser photothermal processes [4] the morphology of the tracks lacked the distinctive λ -ripple features. Tracks arising from both precursors range in width from $\sim 4 \mu\text{m}$ at 1.0 MW cm^{-2} to $\sim 20 \mu\text{m}$ at 2.0 MW cm^{-2} . At higher powers the centre of the track ablates to produce an irregular cross sectional profile.



Fig. 2. Gold tracks deposited over a silicon/nichrome junction

Gold tracks were deposited on evaporated gold and nichrome (5 - 10°A) thin films on silicon substrates. As shown in Figure 2, continuous tracks over a silicon/film interface was possible. A lower power threshold for deposition on the gold coating was observed.

CONCLUSIONS

Micron scale tracks of high purity gold with excellent electrical conductivities can be produced by Ar^+ laser direct writing from low oxidation-state Au(I) organometallic precursors. A high nucleation density produces a fine grained deposit. Conductivities within a factor of 2-3 times bulk values are achieved without further annealing. The nature of the alkyl ligands in the complex does not significantly affect the threshold powers. The solid state decomposition of MeAuEt_3P proceeds via a two-stage process in which the molecular decomposition occurs at $63 \pm 1^\circ\text{C}$. Laser power thresholds for deposition are reduced by prenucleation of the silicon surface by a thin gold film.

ACKNOWLEDGEMENTS

The authors thank Hughes Microelectronics (UK) Ltd., the Ministry of Defence (UK) and SERC for financial support. We are grateful to Miss P. Fernie for contributing to the synthetic work. We also thank Johnson-Matthey Ltd. for the provision of sodium tetrachloroaurate.

REFERENCES

1. M. Jubber, J.I.B. Wilson, J.L. Davidson, P.A. Fernie and P. John, Appl. Phys. Lett. 55, 1477 (1989).
2. F. Houle, T.H. Baum and C.R. Moylan, in Laser Chemical Processing for Microelectronics, edited by K.G. Ibbs and R.M. Osgood (Cambridge University Press, Cambridge, 1989), p 25.
3. R.J. Puddephatt, The Chemistry of Gold, (Elsevier Science Publishers, New York, 1978).
4. H. Schmidbauer and A. Shiotani, Chem. Ber. 104, 2821 (1971).

WAVELENGTH-DEPENDENT AREA SELECTIVITY IN PHOTOCHEMICAL VAPOR DEPOSITION OF ALUMINUM FILMS

MITSUGU HANABUSA AND MASASHI IKEDA

Toyohashi University of Technology, Dept. of Electrical and Electronic Engineering, Tenpaku, Toyohashi 441, Japan

ABSTRACT

Thickness profile of aluminum thin films deposited from dimethylaluminum hydride on silicon substrate changed with wavelengths of light chosen from the wide emission spectra of a deuterium lamp. Under illumination of the VUV around 160 nm deposits were formed preferentially in illuminated regions, while such area selectivity was lost and uniformly thick films were deposited all over the substrate when the UV around 240 nm was used. The observed area selectivity can be interpreted as arising from a wavelength-dependent nucleation mechanism; namely, surface photochemical reactions leading to nucleation are induced only by the VUV, while the UV photons are capable of producing photofragments in gas phase responsible for nucleation.

INTRODUCTION

Recently we succeeded in depositing highly conductive aluminum thin films via photochemical surface reactions of dimethylaluminum hydride (DMA1H) on silicon substrate at substrate temperatures lower than required by thermal reactions alone [1]. As the light source we used either a deuterium lamp or an ArF laser. The lamp emits light in a wide spectrum with two distinguished peaks, one around 160 nm and another around 240 nm. The vapor pressure in a reaction cell was kept low (typically at 6.7×10^{-3} Pa) to emphasize the surface reactions based on photolysis of the adlayer.

During the course of investigations we found that deposition did not start when the VUV below 180 nm was eliminated from illumination of the lamp, while normal growth was observed even without the VUV when the substrate was exposed initially to its full spectrum. Clearly, nucleation in photochemical surface reactions occurs via a wavelength-dependent mechanism.

In the present work we raised vapor pressure to levels where gas phase photolysis was not ignored. Under such conditions thickness profile of deposited films varied as the spectra of the focused light from the deuterium lamp were changed by various filters. This resulted from a shift in the relative importance of surface and gas phase reactions. Normally such a control on area selectivity is achieved by adjusting vapor pressures or substrate temperature. The present work has demonstrated an additional possibility via the selection of wavelengths in illumination.

EXPERIMENT

Figure 1 shows a schematic diagram for the experimental setup used in the present work. The reaction cell is similar to what was used in the previous work [1]. However, since the vapor pressure was higher than before, the CaF_2 lens that served also as an optical window to introduce light into the cell was protected from unwanted deposition on its inner surface by blowing argon gas. Also a booster pump was used instead of a turbomolecular pump.

The emission spectrum from the deuterium lamp (Hamamatsu L1835, 150 W) after passing through the CaF_2 lens is shown in Fig. 2 (a). To study area selectivity we needed to focus light on silicon substrate. The CaF_2 lens used for this purpose had a focal length of 50 mm. The spot size of the

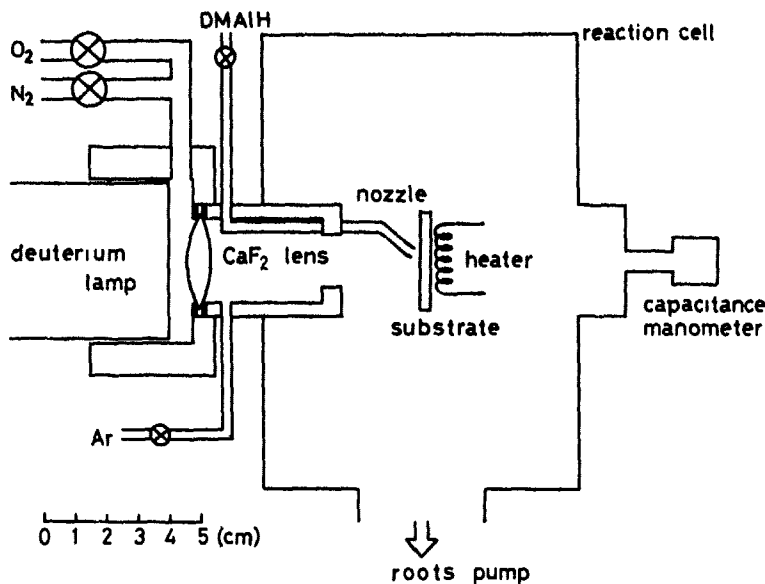


Fig. 1 Schematic diagram of experimental arrangement.

beam on substrate was approximately 5 mm in diameter. Because of the presence of this lens the VUV peak near 120 nm was lost. The remaining peaks appear near 160 nm and 240 nm. The VUV around 160 nm could be chosen by a narrow-band pass filter (Acton Research 160-N), as shown in Fig. 2 (b). In this case, the VUV intensity was also reduced appreciably (to one-fifth). The choice of the UV was easier to achieve; we either replaced nitrogen flowing in the space between the lens and the pump by oxygen to obtain a spectrum as shown in Fig. 2 (c), or inserted a low-pass filter (Hoya UV-22) in the region where nitrogen was flowing (Fig. 2 (d)).

The substrate was n-doped (100) silicon wafer. It was etched in a buffered HF solution for 2 min, cleaned ultrasonically in methanol for 10 min, and then blown dry with N₂ just prior to loading into the cell.

RESULTS

Figure 3 shows thickness profile of aluminum thin films deposited on the substrate heated to 200 °C at a low vapor pressure of 0.013 Pa. The pattern was obtained under illumination of the full spectrum shown in Fig. 2 (a). Deposition occurred only in the illuminated region. With the spectrum excluding the VUV (Fig. 2 (c) and (d)) no deposition was observed anywhere under otherwise identical conditions. This confirmed our previous result [1].

Next, vapor pressure was raised to 0.16 Pa and the results were shown in Fig. 4. In this case deposition occurred even with the UV only, but thickness profile of the deposits varied according to wavelengths. With either the full spectrum (Fig. 2 (a)) or only the VUV around 160 nm (Fig. 2 (b)) deposition occurred preferentially in the illuminated regions, just as in the case of the low vapor pressure. However, deposits were formed even outside the illuminated regions at the high vapor pressure. This is shown in Fig. 4 (a). This was observed again at a substrate temperature of 200 °C.

On the other hand the deposited films became uniform in thickness under illumination of the UV shown in Fig. 2 (c) and (d). The result is shown in

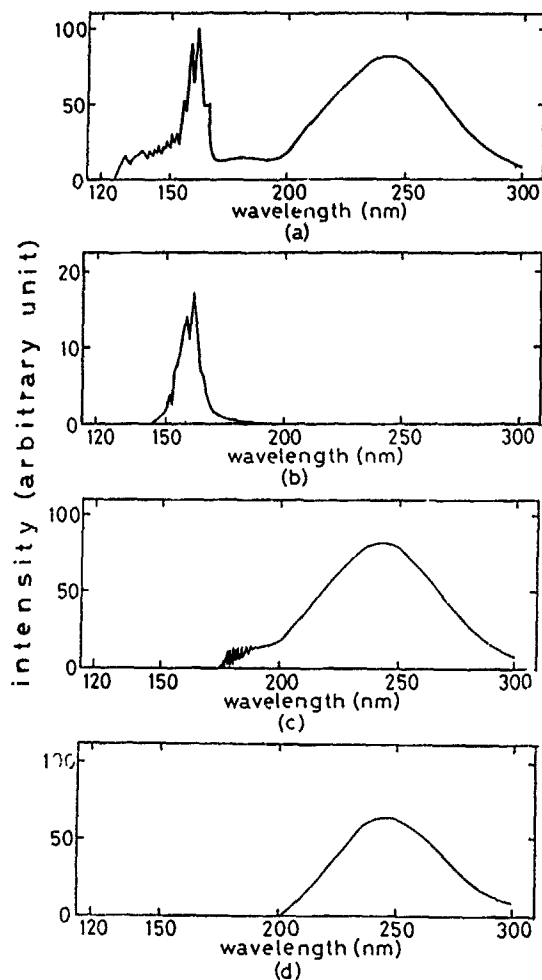


Fig. 2 Emission spectra from deuterium lamp after passing through (a) CaF₂ lens, (b) 160-nm bandpass filter, (c) oxygen gas, and (d) UV-22 filter.

Fig. 4 (b) for the case of the UV illumination of Fig. 2 (a). Film thickness was uniform throughout the substrate over a distance of 12 mm. A slope was observed in thickness distribution, but we believe that this was caused by spatial variation of vapor pressure or substrate temperature or both. Note that a similar tendency was observed in Fig. 4 (a). Therefore, the presence of the slope should not affect main features to be emphasized in the present experiment.

DISCUSSIONS

From our previous study it is known that at low vapor pressures below 1×10^{-2} Pa deposition occurs via photochemical surface reaction for DMAIH [1]. The evidence to support this conclusion was provided by area selectivity and the time needed to renew the adlayer on the surface for pulsed laser irradiation. Also the observed dependence of deposition rates on substrate temperature, vapor pressure, light intensity and others could be explained by a rate equation set for the adlayer, which was to be photolyzed and

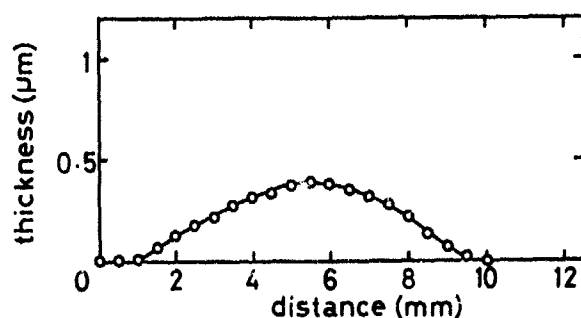


Fig. 3 Thickness profile of aluminum film deposited at vapor pressure of 0.013 Pa under illumination of the full spectrum shown in Fig. 2 (a).

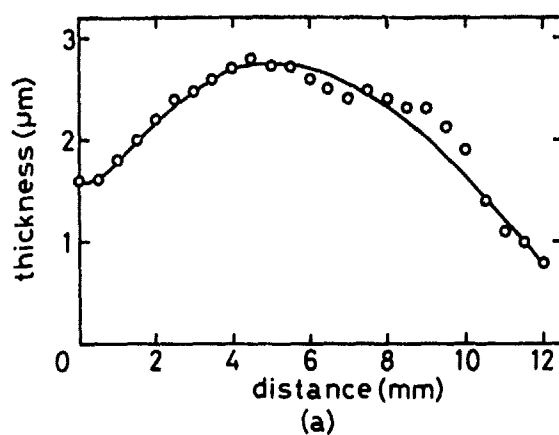
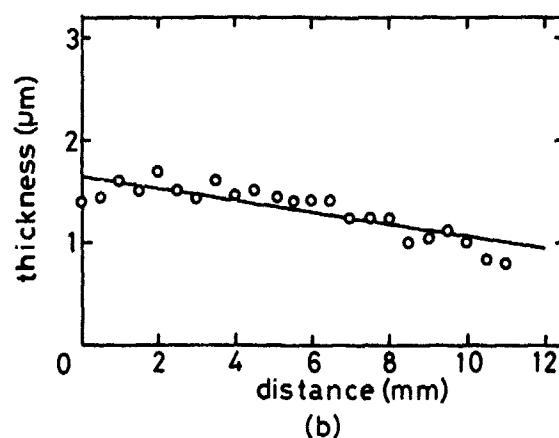


Fig. 4 Thickness profile obtained at 0.16 Pa under illumination of (a) the full spectrum (Fig. 2 (a)) and (b) the UV only (Fig. 2 (c)).



desorbed under illumination. In view of this we could interpret the wavelength dependence of deposition at low vapor pressures easily. Namely, nucleation induced by photochemical surface reactions can be initiated only by the VUV around 160 nm, and the UV is not effective for the formation of nuclei, even though it can induce the growth of films once nuclei are formed by other means.

At higher vapor pressures gas phase photochemical reactions take place in addition to surface reactions, as evidenced by formation of deposits outside the illuminated regions on substrate surface. In this case radicals

formed as photofragments in gas phase diffuse over a great distance, and therefore the nucleation and following growth take place over a wide area on substrate. When only the UV is present, nucleation must be induced by photofragments produced in gas phase, and as a result deposits are formed with uniform thickness all over substrate. On the other hand when the VUV is present, additional surface reactions are induced in the illuminated regions, and as a result deposits become thicker there. The VUV is also capable of inducing the gas phase reactions, because with the VUV alone (Fig. 2 (b)) thickness profile looked similar to Fig. 4 (a).

From the proceeding argument it is concluded that the change in thickness profile observed at high vapor pressures reflects a shift in the relative importance of surface and gas phase reactions with wavelengths. Previously a wavelength-dependent result was obtained for photodeposition of Fe-Ni alloy thin films [2]; in that case, the composition changed with wavelengths of laser beams because the absorption coefficient for source gases, ferrocene and nickelocene, showed a different wavelength dependence. On the other hand, the presently observed effect is related with photochemically induced nucleation.

As for the mechanism leading to the observed wavelength-dependent nucleation phenomena, we can not offer any definite explanation at this stage. It can be speculated, for instance, that precursors effective for the production of nuclei in the adlayer are formed by VUV photons only. Alternatively, the observed effect may be simply a result of surface cleaning induced by high-energy VUV photons. Recently, an X-ray photoelectron spectroscopy (XPS) study was carried out to study the initial stage of aluminum deposition under ArF laser illumination on silicon surface covered with oxides [3]. Similar studies performed at shorter wavelengths are expected to be useful to clarify the observed wavelength-dependent nucleation mechanism.

CONCLUSION

When aluminum thin films were photodeposited on silicon substrate under illumination of the deuterium lamp, the thickness profile changed with wavelengths. With the VUV present, films grew preferentially in illuminated regions. This effect was most remarkable at low vapor pressures, because then deposition occurred only within illuminated regions, while at higher vapor pressures thicker films were formed in those regions. With the UV only films were deposited uniformly over substrate at high vapor pressures, while deposition did not occur at low pressures. The observed effects should reflect a change in relative importance of surface and gas phase reactions with wavelengths. Nucleation based on photochemical surface reactions is induced only by the VUV, while photofragments generated in gas phase and responsible for nucleation can be produced by either the VUV or the UV. The mechanism responsible for such wavelength-dependent nucleation is not understood yet.

ACKNOWLEDGEMENT

We thank Tosoh Akuzo Corporation for supplying DMAIH. This work was supported by Grant-in-Aid for Scientific Research on Priority Areas from the Ministry of Education.

REFERENCES

1. M. Hanabusa, A. Oikawa, and Peng Ying Cai, J. Appl. Phys. 66, 3268 (1989).

2. J.V. Armstrong, A.A. Burk, Jr., J.M. Coey, and K. Hoorjani, Appl. Phys. Lett. 50, 1231 (1987).
3. D.A. Mantell, Appl. Phys. Lett. 53, 1387 (1988).

KrF EXCIMER LASER DEPOSITION OF TITANIUM FROM TiCl_4

R. IZQUIERDO, C. LAVOIE and M. MEUNIER, Ecole Polytechnique de Montréal, Groupe des Couches Minces et Département de Génie Physique, Montréal, Canada.

ABSTRACT

We have investigated the deposition of titanium lines from TiCl_4 induced by KrF excimer laser (248 nm). Substrates are primarily LiNbO_3 , for the possible formation of Ti:LiNbO_3 optical waveguides, as well as silicon and glass. Titanium lines contain $[\text{Cl}] < 2$ at% and are typically 200 to 1000 Angstroms thick with a width ranging from 3 to 20 μm . Results suggest that the process is controlled by photochemistry of TiCl_4 but it is difficult at this point to assert which of the gas or adsorbed layer is the primary source of thin film growth.

INTRODUCTION

There is a technological interest in development of processing technique of titanium (Ti) thin film for optoelectronic applications (Ti:LiNbO_3 optical waveguides[1]) as well as for microelectronic applications (contacts for silicon devices [2]). Compared to the standard evaporation technique, the laser direct writing method eliminates the time consuming and critical photolithography steps and also allows the deposition of a titanium thin film with a variable thickness permitting the production of Ti:LiNbO_3 optical waveguides with novel properties. Tsao et al. [3] were the first to report the formation of titanium thin film by laser direct writing using a frequency doubled Ar^+ laser. In this paper, we report a preliminary study of KrF excimer laser deposition of Ti lines from TiCl_4 , with a special emphasis on the description and characterization of the process.

DEPOSITION SYSTEM

Figure 1 describes schematically the experimental set up consisting of a KrF excimer laser ($\lambda=248\text{nm}$) with a maximum pulse energy of 100 mJ and a repetition rate of 5 Hz. After the laser beam passes through two filters (F1 and F2) which decrease the intensity to avoid damaging the substrate, the beam is focalized with a reflection objective (X15; NA 0.28) which offers the advantages of long work distance and low aberrations needed for our system. The microscope is also used to observe

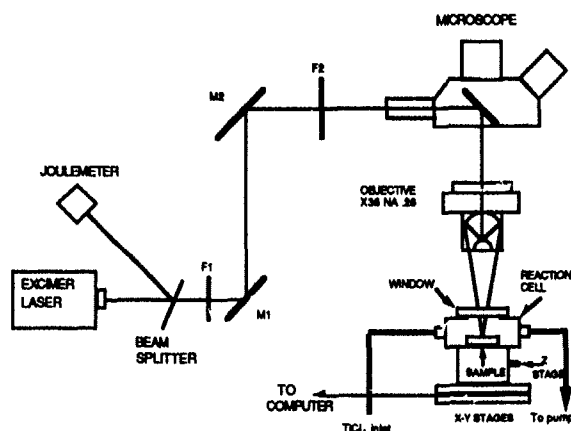


Figure 1: Deposition system




the sample before and after the process. Pattern formation is achieved by moving the substrate under the static beam using two computer-controlled translation stages mounted in a x-y configuration. A manually controlled z axis is used to set the focal point. The programmable stages have a resolution of $0.1\text{ }\mu\text{m}$ and the maximum speed is $100\text{ }\mu\text{m/s}$. The Ti lines are processed at scan speeds ranging from $0.2\text{ }\mu\text{m/s}$ to $5\text{ }\mu\text{m/s}$. The window of the reaction chamber is made of fused silica (suprasil 2). After we reach the basic vacuum of 10^{-3} Torr, the cell is purged with argon before the deposition process. The reactive gas is TiCl_4 (99.999% Alpha products) which is a liquid at room temperature with a vapor pressure of around 10 Torr. To prevent powder formation, TiCl_4 pressure has to be kept below 500 mTorr. After the process the TiCl_4 is condensed in a cryogenic trap to avoid any damage to the pump. Every month, we neutralize the used TiCl_4 with a basic solution of NaOH.

The substrates used are LiNbO_3 , glass, crystalline silicon (c-Si). We have also investigated the use of LiNbO_3 covered by a thin layer of titanium ($100\text{ }\text{\AA}$) to check if the nucleation of initial layer influences the thickness. Before deposition, all substrates are washed in organic solvents, rinsed in deionized water and heated at $120\text{ }^\circ\text{C}$ in a vacuum oven for an hour to eliminate any trace of water which could react with TiCl_4 .

Compared to the cw frequency doubled Ar^+ laser, excimer laser is a possible alternative UV source which presents many possible UV wavelengths at a reasonable price. However, the fact that excimer lasers are pulsed might bring two different causes of thickness variation along the lines. In addition to the energy pulse variation, depositing step by step will cause a regular oscillation with thickness which will increase as the pulses become more distant from each other. Assuming a Gaussian beam of $10\text{ }\mu\text{m}$ diameter, Table I gives numerical simulation results of the thickness variation along the line as a function of beam displacement when there is no pulse energy variation as well as when this variation is $\pm 6\%$

which represents our conditions. To obtain a uniform film thickness of a few percent variation, a beam displacement smaller than the spot radius is necessary. In order to have thicknesses ranging from 200 to 1000 Å, a beam displacement of 0.1 μm has been chosen which assures us a thickness variation of $\pm 0.6\%$.

TABLE I
THICKNESS VARIATION WITH ENERGY
VARIATION AND DISPLACEMENT

displacement \ E variation	0 %	± 6 %
 10 μm	± 17 %	± 19 %
 5 μm	± 0.1 %	± 2.5 %
 0.1 μm	$<10^{-5}$ %	± 0.6 %

CHARACTERIZATION OF THE DEPOSITION PROCESS

All the substrates used are opaque at $\lambda=248$ nm. Because of their low reflectivities, glass and LiNbO_3 are highly absorbant. The short laser pulse of 9 ns, might give a local temperature rise which can cause severe damage to the sample. We optically observed thermal damages on LiNbO_3 at energy pulse as low as 100 nJ which corresponds to a power density of several MW/cm^2 . The glass is less sensitive with a damage threshold of 140 nJ. When we cover LiNbO_3 with a 100 Å layer of Ti we observe damages at around 250 nJ/pulse. For c-Si the threshold is much higher due to its high reflectivity and higher thermal diffusivity.

Figure 2 shows a typical titanium line on LiNbO_3 covered with a 100 Å titanium thin film. The choice of the substrates is justified by the fact that it enables us to take a scanning electron microscope picture without any charging effect. The scan speed is 0.5 $\mu\text{m}/\text{s}$, the TiCl_4 pressure is 0.2 Torr and the laser repetition rate is 5 Hz.

Line composition made at different energies and pressures and on all type of substrates was measured by micro Auger electron spectroscopy with a spatial resolution of 0.1 μm . Results show that all Ti films are oxydized due to air exposition and they all contain a very low Cl concentration ([Cl] < 2 at%).

Fig. 2: Morphology of a Ti line written on LiNbO_3 covered by 100 Å Ti thin film.

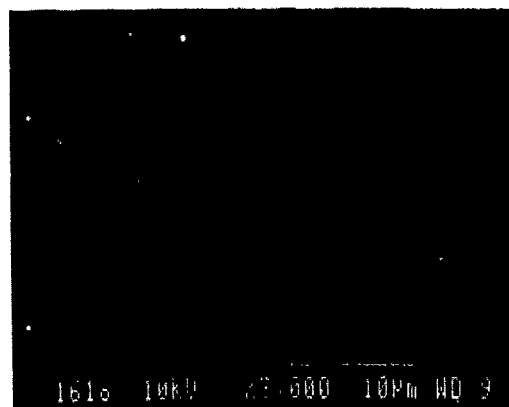


Fig. 3: Variation of linewidth as a function of pulse energy and TiCl_4 pressure.

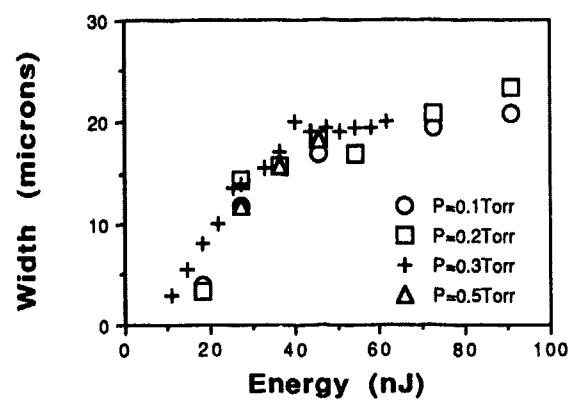


Fig. 4: Ti line written on silicon showing irregular deposition.

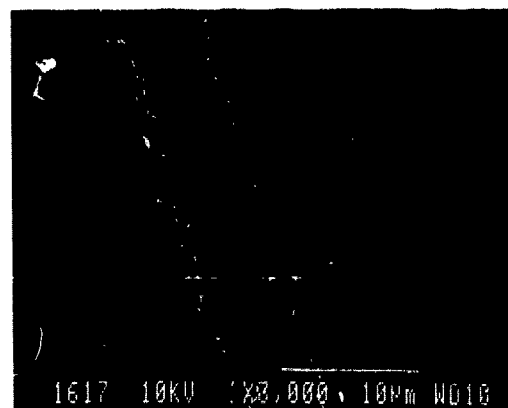


Fig. 5: Deposited thickness of Ti on LiNbO_3 as a function of energy pulse and pressure.

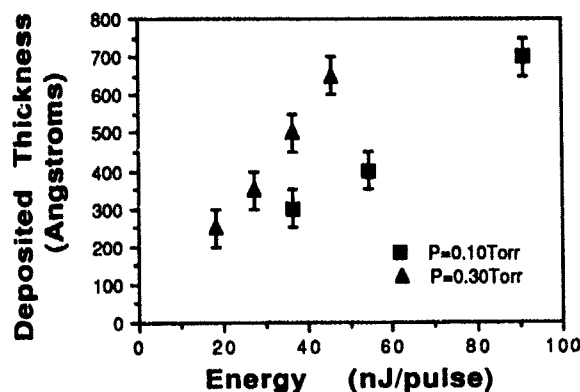


Figure 3 shows the linewidth W as a function of pulse laser energy E for films made on LiNbO_3 at different pressures and at a speed of $0.2 \mu\text{m/s}$ with a repetition rate of 2 Hz (to improve pulse stability). We notice that W is independent of TiCl_4 pressure and increases monotonically with E . Assuming a threshold energy to get a deposit, an increase in energy will increase W and this variation will depend on the beam shape.

Figure 4 shows a Ti line on silicon made at a TiCl_4 pressure of 0.3 Torr, laser energy of 36 nJ and at a speed of $0.2 \mu\text{m/s}$. Notice the sudden thickness decrease near the middle of the line. This is probably due to either a TiCl_4 desorption due to substrate heating at high laser energy[4] or to an ablation of the film deposited. It is not clear which one is more important and more experiments are necessary to clarify this phenomenon.

Figure 5 shows the Ti line thickness as measured by a profilometer (Dektak, Sloan) as a function of laser energy at two different TiCl_4 pressure conditions. Typical thicknesses vary from 200 to 700 Å for Ti lines deposited on LiNbO_3 at a speed of $0.2 \mu\text{m/s}$. As the pressure increases, more molecules in the gas, as well as on the adsorbed layer, can react leading to a thicker film. As the energy increases, more photons arrive in the reaction zone leading again to a thicker film.

MODELING THE DEPOSITION PROCESS

In principle the process is either thermal or photolytic or possibly both. However, it is not a thermal process because of the high temperature (600°C) necessary to thermally dissociate the TiCl_4 [5]. If this was due to the short pulse (10 ns), severe thermal damage would certainly occur because LiNbO_3 is well known to be extremely fragile. Tsao et al [3] did check that Ar^+ laser focalised on LiNbO_3 in presence of TiCl_4 lead to severe damage but no deposition. Due to the low gas absorptivity [6] thermal

reaction is not expected to occur in the gas. This process is certainly not controlled by thermal reaction.

The process is rather based on photochemical reaction. Photon energy of 4.98 eV at $\lambda=248$ nm is certainly enough to break a Ti-Cl bond of 4.47 eV bonding energy [7]. However, it is difficult at this point to say which of the gas or adsorbed layer is the primary source of thin film growth. The presence of powder at pressure higher than 0.5 Torr suggests that gas phase reaction occurs, but at lower pressures, the absence of powder as well as the pressure independence of linewidth (Figure 3) suggest the opposite, i.e. that the adsorbed layer is probably the primary source of thin film growth. More experiments are necessary to distinguish between the two processes.

CONCLUSION

We have deposited Ti lines by KrF excimer laser direct writing primarily on LiNbO_3 and also on silicon and glass. Titanium lines contain $[\text{Cl}] < 2$ at% and have linewidths between 3 to 20 μm with film thickness of 200 to 1000 Å. Work is under progress to model this process.

ACKNOWLEDGEMENTS

The authors would like to thank M. Moreau and J.P. Lévesque for their technical assistance and S. Boivin, J. R. Simard and I. Najafi for valuable discussions on Ti: LiNbO_3 optical waveguide technology. We also acknowledge the National and Engineering Research Council of Canada (NSERC) for their financial assistance.

REFERENCES

1. M.N. Armenise, IEEE Proceedings **135**, 85 (1988).
2. D.B. Fraser, in VLSI Technology, edited by S.M.Sze (Mc Graw-Hill Book Company, New York, 1983), P. 347.
3. J.Y. Tsao, R.A. Becker, D.J. Ehrlich and F.J. Leoneberger, Appl. Phys. Lett. **42**, 559 (1983).
4. D. Braichotte and H van den Bergh, Appl. Phys. **A45**, 337 (1988).
5. A. Chretien and W. Freundlich, in Nouveau Traité de Chimie Minérale, edited by Masson et Cie, Paris 1963), p. 1.
6. M. Rothschild, in Laser Microfabrication Thin Film Process and Lithography, edited by D.J. Ehrlich and J.Y. Tsao (Academic Press, San Diego, 1989), p. 163.
7. R.T. Sanderson, Chemical Bonds and Bonds Energy, 2nd ed. (Academic Press, New York, 1976), p.52.

SELECTIVE RAPID THERMAL CVD OF GERMANIUM

D.T. Grider*, M.C. Öztürk*, J.J. Wortman*, M.A. Littlejohn*, Y. Zhong*, D. Batchelor**, P. Russell**

*North Carolina State University
Department of Electrical and Computer Engineering
Box 7911, Raleigh, NC 27695-7911

**North Carolina State University
Department of Materials Science and Engineering
Box 7907, Raleigh, NC 27695-7907

ABSTRACT

Selective depositions of germanium thin films have been investigated in a cold-wall, lamp heated rapid thermal processor. Films were deposited at low pressures (1 Torr-8 Torr) using the thermal decomposition of germane. Selectivity was maintained throughout the temperature range investigated, 350°C-600°C. Growth rates as high as 800 Å/min were obtained at 425°C where deposition is controlled by the surface reactions, making germanium compatible with the throughput requirements of single wafer manufacturing. Three dimensional growth was seen at temperatures above 450°C resulting in a rough surface morphology. Smooth films were deposited below 450°C with the films characterized by two dimensional growth. In this work, germanium is considered as a potential material to fabricate MOS transistors with raised source and drain junctions (UPMOS). Kelvin structures were fabricated to study the effect of the intermediate germanium layer between aluminum and silicon on contact resistance. It is shown that contact resistivity is improved by approximately 17% using an Al/p-Ge/p⁺-Si structure. In this work, it is also shown that titanium germanide formation can be used as a means of reducing the resistivity of the Ge buffer layer.

INTRODUCTION

As device dimensions are continually scaled into the submicron regime, new materials and processing techniques must be explored to alleviate shortcomings in conventional processing. The current trend towards reduced thermal budgets and in-situ, single wafer processing has led to the development of Rapid Thermal Processing (RTP) as an alternative processing technique. The effective use of rapid thermal processors for dopant activation, oxidation, and silicidation has been demonstrated [1]. Rapid Thermal Chemical Vapor Deposition (RTCVD) is now being investigated as a means of depositing a wide variety of films used in the semiconductor industry [2-7]. RTCVD systems usually are cold-walled chambers which can allow multiple steps to be performed in-situ while maintaining a vacuum environment. In-situ processing is expected to reduce particulate problems which can occur during wafer transport between conventional CVD steps. There is also the potential of reducing the number of cleaning steps.

Germanium received much attention after the invention of the transistor in 1947. With the rapid advancement of silicon processing technology in the 1960's, germanium was abandoned for silicon in the fabrication of semiconductor devices. There has been a renewed interest recently in germanium and silicon-germanium alloys for superlattice, quantum well, and heterojunction transistor structures [8,9]. There are, however, other applications where germanium may be beneficial in solving problems with existing devices. It is known that current silicided contacts to ultra-shallow source/drain junctions are limited by the ability to controllably deposit thin metal

layers to minimize silicon consumption above the junction. This silicon consumption during the silicidation anneal can lead to large leakage currents and eventual device failure [10]. In order to alleviate this and related problems, UPMOS (raised source & drain junctions) using selective silicon epitaxy has been suggested [11]. We have reported before, selective LPCVD of germanium in a rapid thermal processor as a low temperature/high throughput process for UPMOS [7]. Here we report the fabrication and testing of Kelvin structures to investigate the contact resistivities utilizing a germanium layer over source and drain.

EXPERIMENTAL

Germanium depositions were performed in a LEISKTM rapid thermal processor. The deposition chamber has water cooled stainless steel walls with two quartz windows through which the wafer is heated via tungsten-halogen lamps. A detailed description of the system used in this study can be found in an earlier publication [4].

Depositions of germanium were performed on <100> p-type silicon wafers with resistivities of 16-24 Ω -cm. The wafers underwent an RCA clean followed by a 10 second buffered HF dip. A thermal oxide was then grown and patterned using a standard photolithography sequence. The photoresist was stripped in a $\text{H}_2\text{SO}_4:(\text{NH}_4)_2\text{S}_2\text{O}_8$ solution. The wafers then underwent a final RCA clean and buffered HF dip before germanium deposition. In this study 7% GeH_4 diluted in a hydrogen carrier gas was used. Process pressure was varied from 1 Torr to 7 Torr by controlling the germane flow and the pumping speed. Deposition rates were obtained by measuring film thicknesses using a profilometer.

LPCVD OF GERMANIUM

Germanium was deposited using the thermal decomposition of GeH_4 . The temperature dependence of the germanium deposition rate is shown in Figure 1a. Two distinct regions of growth, typical of most CVD reactions, were obtained. At temperatures below 425°C the depositions were surface reaction limited with an activation energy of 41.7 kcal/mol. Above 425°C the depositions became mass transport limited with an activation energy of 5.1 kcal/mol. The pressure dependence of the germanium deposition rate is shown in Figure 1b. The linear dependence of the deposition rate at high temperatures is indicative of a mass transport limited growth, while at low temperatures the deposition rate saturates with increasing pressure indicating a surface reaction limited growth. Similar results have been previously reported for LPCVD germanium in a hot-wall furnace [15]. In order to minimize the effects of the gas flows on film uniformity one can operate in the surface reaction limited regime. In a single wafer processing environment, such as with RTP, it is also important to maintain a growth rate that will allow sufficient throughput. This is indeed possible with germanium, where growth rates as high as 800 Å/min are possible at the transition from surface reaction to mass transport limited growth which occurs at a relatively low temperature of 425°C.

Growth of germanium on silicon results in a pseudomorphic growth, which affects the surface morphology of the deposited films. In addition to the critical thickness where misfit dislocations develop in lattice mismatched systems, there is a critical temperature above which three dimensional growth occurs [8]. Above this critical temperature islanding is energetically favorable and growth proceeds by the formation of discrete islands with the eventual coalescence into a continuous film. This can lead to rough surface morphologies as evidenced in Figure 2 by the scanning tunneling micrograph of a 380 Å thick Ge film deposited at 500°C and at a pressure of 3 Torr. In our work, rough surface morphologies resulted at depositions performed above 450°C. Below 450°C, a layer by layer growth occurred producing smooth films [12]. An SEM micrograph

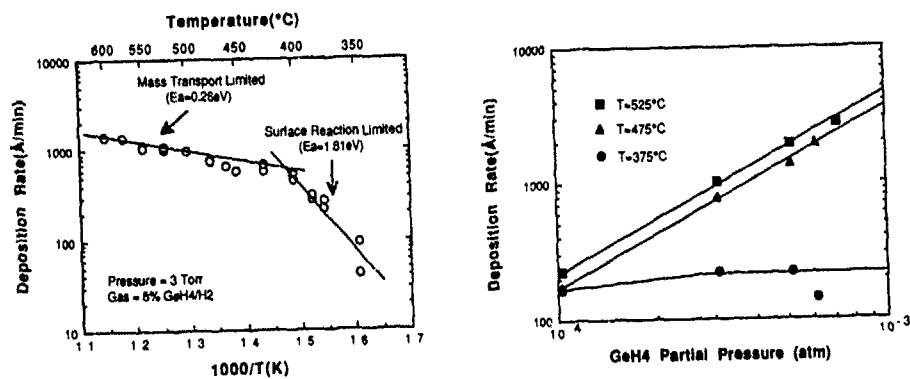


Figure 1: a) temperature and b) pressure dependence of the germanium deposition rate

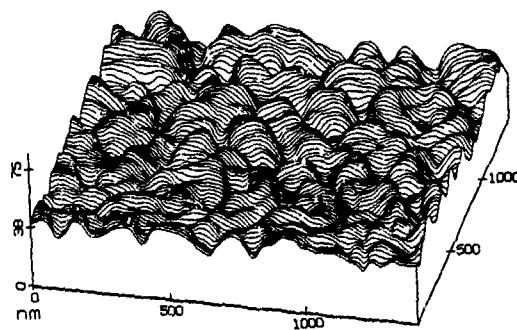


Figure 2: STM image of rough surface morphology produced at 500°C

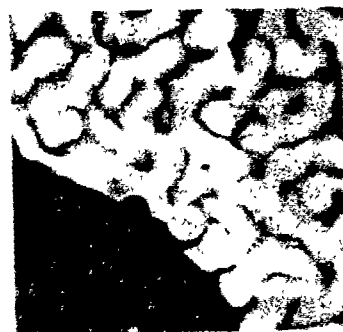


Figure 3: Scanning electron micrograph of germanium deposited at 635°C

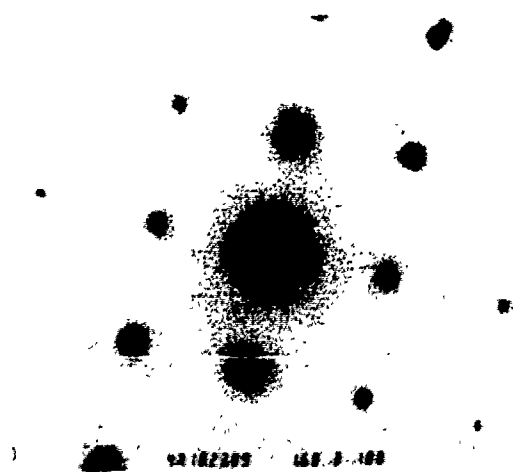


Figure 4: Electron diffraction pattern of germanium deposited on silicon

a 400 Å thick Ge film deposited at 635°C and 3 Torr is shown in Figure 3. The islanding seen is typical at temperatures above 450°C. Increasing temperatures increase the island size along with a corresponding increase in spacing between the islands. This same behavior has been reported by other researchers in both CVD and MBE systems [13,14].

Germanium depositions in this work were naturally selective up to temperatures as high as 600°C. This is well above the 425°C limit previously reported by other researchers [15]. We feel this is likely due to the cold-wall chamber used in our study which minimizes any possibility of furnace contamination. The selective nature of germanium has been attributed to several factors. The low number of adsorption sites on SiO₂ inhibits the nucleation and growth of germanium [15]. Germanium atoms from the thermal decomposition of GeH₄ react with SiO₂ through a series of reactions yielding the highly volatile GeO which is then easily desorbed [16]. Therefore, etching and deposition may occur at the same time leading to a selective deposition process. It is also interesting to note that germanium films were crystalline as evidenced by the diffraction pattern shown in Figure 4 obtained from a 400 Å thick film deposited at 525°C. This may indicate a reduction of the native oxide during the initial stages of germanium growth.

APPLICATION OF SELECTIVE LPCVD GERMANIUM

Low resistivity contacts to source/drain regions of MOSFET's are commonly formed using silicided contacts. There are inherent problems with this technique that must be addressed in submicron devices. During the silicidation anneal, a consumption of silicon in the source/drain region occurs due to the reaction between silicon and the reactive metal. This may ultimately lead to excessive leakage currents when the silicidation front is in the vicinity of the depletion region. Therefore, in ultra-shallow junctions, very thin refractory metal layers must be deposited to minimize this silicon consumption during silicide formation. One potential solution to this problem is the implementation of a buffer layer between the reactive metal and underlying junction [11]. Since germanium can be deposited selectively at low temperatures where any dopant diffusion is negligible, germanium has the potential of being the buffer layer when junctions are formed prior to silicidation [7,12].

To study the effect of the intermediate germanium layer on contact resistances, four terminal Kelvin structures, as shown in Figure 5, were fabricated. A field oxide was first grown and patterned using photolithography to open active areas for the devices. Boron was implanted in the silicon at 10keV/1e16cm⁻² and annealed for 15 s in an argon ambient in a rapid thermal processor. A low temperature oxide was then deposited at 450°C and patterned to open contact holes to the implanted regions. Germanium was deposited selectively in the contact holes on half of the wafers, implanted with boron at 10keV/3e15cm⁻² and annealed at 700°C for 15 s in argon. Complete activation of boron in germanium has been observed at temperatures as low as 500°C [7]. Aluminum was then evaporated on the wafers and annealed at 375°C for 30 minutes in H₂. By forcing a current between terminals 1 and 3 and measuring the resultant voltage drop across terminals 2 and 4 in Figure 5, the resistance of the contact can be determined [19].

Histograms showing the contact resistivity with and without Ge are given in Figure 6. As shown, the measured contact resistivities were, on the average, 17% lower on the germanium samples than those obtained from the monitor wafers without a selective germanium deposition.

For heavily doped semiconductors, contact resistances of metal semiconductor contacts are exponentially dependant on the barrier height between the metal and semiconductor as given by [20]:

$$R_c \propto \exp \left[\frac{2\sqrt{em}}{\hbar} \left(\frac{\Phi_b}{\sqrt{N_D}} \right) \right]$$

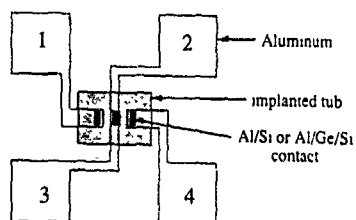


Figure 5: Structure used to measure contact resistance

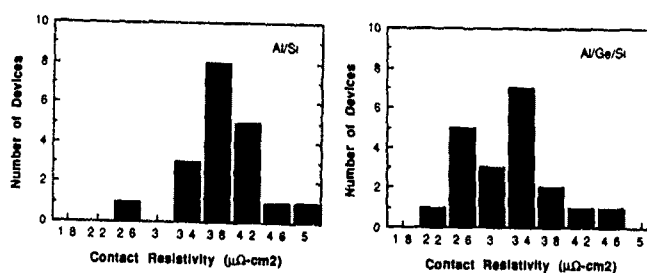


Figure 6: Contact resistivity histograms of test devices

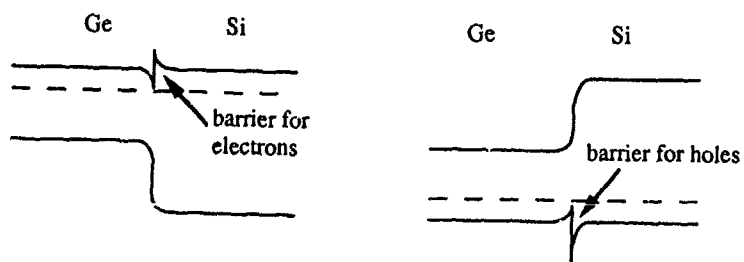


Figure 7: Band diagrams of n and p-isotype heterojunctions

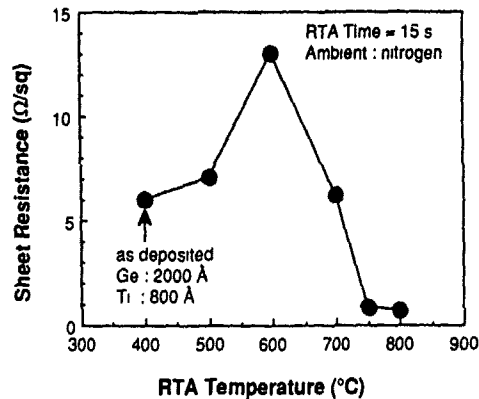


Figure 8: Sheet resistance of Ti/Ge annealed structures

The barrier height is determined by the pinning of the fermi level from surface states and is approximately $E_g/3$ for p-type semiconductors. We would therefore expect to obtain a lower contact resistivity from the Al/Ge system than the Al/Si system.

Another contributing factor to the contact resistance is the barrier due to the band discontinuities between germanium and silicon. The band diagrams of p-Ge/p-Si and n-Ge/n-Si systems are shown in Figure 7. In Ge/Si heterostructures it is known that the conduction band and valence band discontinuities are ~ 0.1 eV and ~ 0.3 eV respectively. Therefore, as demonstrated in Figure 7, the barrier will be greater in p-Ge/p⁺-Si structures than in n-Ge/n⁺-Si structures. For this reason, in this study we chose to investigate the worst case condition, and p-Ge/p⁺-Si devices were studied.

Self-aligned silicided contacts using titanium require a two step anneal accompanied by an etch step between the anneals to remove unreacted titanium over the SiO₂ [17]. This two step sequence can be avoided by using a selective deposition of reactive metal. It has been previously demonstrated that tungsten can be selectively deposited on silicon [18] and germanium [12] using WF₆.

In this work, we have considered titanium as a potential material to form germanide/silicide structures over source/drain junctions. We have reported before the complete elimination of silicon consumption during titanium silicidation utilizing a germanium buffer layer [7]. In this study, titanium and germanium were annealed in a rapid thermal processor in an argon ambient to study the resistivity of the resultant germanide/silicide structure. Resistivities of the annealed germanides are shown in Figure 8. An initial increase in the resistivity, likely due to the incorporation of oxygen in the films from the oxidation of titanium, was observed at temperatures below 600°C. Above 600°C the resistivity dropped rapidly to a final value of 30 $\mu\Omega$ -cm. This behavior is very similar to the behavior of titanium silicide formation [21]. These resistivities were calculated using the profiles of the annealed species obtained by secondary ion-mass spectroscopy.

CONCLUSIONS

We have demonstrated the ability to deposit germanium selectively on silicon using the thermal decomposition of germane at temperatures as high as 600°C. Smooth depositions may be accomplished at temperatures below 450°C where two dimensional growth occurs. Rough surface morphologies from three dimensional growth occur at temperatures above 450°C. Contact resistivity improvement using germanium layers deposited selectively on silicon has been observed, with measured resistivities 17% lower than those obtained using conventional Al/Si contacts. This is largely attributed to the lower bandgap of germanium, resulting in a lower barrier height Al and Si. We have shown that germanium buffer layers may be used to eliminate silicon consumption during silicidation anneals in the formation of low resistivity, silicided contacts to source/drain regions of MOS transistors.

ACKNOWLEDGMENTS

This work has been partially supported through the Center for Advanced Materials Processing (Grant CDR-8721505) and SRC Microstructures Sciences Program (Grant 88-SJ-081). The authors would like to acknowledge the efforts of J. Corial, E. Wrasmann, and D. Abercrombie of Harris Incorporated for their help in tungsten depositions. We are also indebted to J. O'Sullivan for helpful technical discussions and processing assistance, and H. Taylor for his efforts in maintaining and upgrading the LEISKTM rapid thermal processor.

REFERENCES

- [1] R. Singh. *Journal of Applied Physics*, **63** (8), R59-R114 (1988).
- [2] C.M. Gronet, C.A. King, J.F. Gibbons. *MRS Symposia Proceedings*, **141**, 107-112 (1986).
- [3] G.P. Burns, J.G. Wilkes. *Semiconductor Science Technology*, **3**, 442-447 (1988).
- [4] M.C. Öztürk, J.J. Wortman, Y. Zhong, X. Ren, R. Miller, F.S. Johnson, D.T. Grider, D.A. Abercrombie. *MRS Symposia Proceedings*, **146**, 109-114 (1989).
- [5] F.S. Johnson, R.M. Miller, M.C. Öztürk, J.J. Wortman. *MRS Symposia Proceedings*, **146**, 345-350 (1989).
- [6] R.M. Miller, M.C. Öztürk, J.J. Wortman, F.S. Johnson, D.T. Grider. Accepted for publication in *Materials Letters*.
- [7] M.C. Öztürk, D.T. Grider, J.J. Wortman, M.A. Littlejohn, Y. Zhong, D. Batchelor, P. Russell, "New Applications of Germanium in ULSI Technologies". To be published.
- [8] J.C. Bean, L.C. Feldman, A.T. Fiory, S. Nakahara, I.K. Robinson. *Journal of Vacuum Science Technology*, **A2** (2), 436-440 (1984).
- [9] S.S. Iyer, G.L. Patton, J.M.C. Stork, B.S. Meyerson, D.L. Hareme. *IEEE Transactions on Electron Devices*, **36** (10), 2043-2064 (1989).
- [10] L. VanDen Hove, R. Wolters, K. Maex, R.F. DeKeersmaecker, G.J. DeClerck. *IEEE Transactions on Electron Devices*, **34** (3), 554-561 (1987).
- [11] H. Shibata, Y. Suizu, S. Samata, T. Matsuno, K. Hashimoto. *International Electron Device Meeting*, 590-593 (1987).
- [12] M.C. Öztürk, J.J. Wortman, D.T. Grider, Y. Zhong, S. Johnson. Presented at Electronic Materials Conference, Cambridge, MA, June 21-23, 1989.

- [13] B.Y. Tsaur, M.N. Geis, J.C.C. Fan, R.P. Gale. *Applied Physics Letters*, **38** (10), 779-781 (1981).
- [14] T.F.Kuech, M. Mäenpää, S.S. Lau. *Applied Physics Letters*, **39** (3), 245-247 (1981).
- [15] H. Ishii, Y. Takahashi, J. Murota. *Applied Physics Letters*, **47** (8), 863-865 (1985).
- [16] G.R. Srinivasan. *Journal of Crystal Growth*, **70**, 201-217 (1984).
- [17] N. deLanerolle, D. Hoffman, D. Ma. *Journal of Vacuum Science Technology*, **B5** (6), 1689-1695 (1987).
- [18] E.K. Broadbent, C.L. Ramiller. *Journal of Electrochemical Society: Solid State Science and Technology*, **131** (6) 1427-1433 (1984).
- [19] S.S. Cohen, G. Gildenblat, M. Ghezzi, D.M. Brown. *Journal of the Electrochemical Society: Solid-State Science and Technology*, **126** (6), 1335-1338 (1982).
- [20] S.M. Sze. *Physics of Semiconductor Devices*, (John Wiley and Sons publishers, New York, New York 1981), p. 99, Eq. (99).
- [21] L. Van Den Hove. Ph-D Thesis, Katholieke Universteit Leuven, Belgium, (1988)

LASER-INDUCED LOCAL DECOMPOSITION OF ADSORBED TUNGSTEN FLUORINE MOLECULES FOR METAL DEPOSITION ON SILICON.

Geoffroy AUVERT, Yves PAULEAU, Didier TONNEAU
C.N.E.T, B.P.98, 38243 Meylan, France.

ABSTRACT

Decomposition of tungsten hexafluoride on silicon substrates under CW argon laser irradiation in the visible domain has been extensively studied in presence of various buffer or reactive gases. The decomposition rate is found to be limited either by a mass transport phenomena or by a thermally activated process. It has been found that no photolytic decomposition can be invoked as the limiting step in the decomposition rate. Depending on the partial pressure of added hydrogen, irradiation results in a local deposition of tungsten, having good electrical properties. In the high pressure domain, deposition kinetics are consistent with mechanisms invoked in conventional chemical vapor deposition reactors. A different mechanism appearing in a lower hydrogen pressure domain will be tentatively interpreted in correlation with the laser-induced temperature.

INTRODUCTION.

Over the last few years, laser-assisted chemical vapor deposition (LCVD) of various metals using different kinds of lasers has been investigated. The gaseous precursors were those commonly used in conventional furnace CVD studies. For example, the feasibility of LCVD of nickel or aluminium has been clearly demonstrated by using the laser-induced decomposition of $\text{Ni}(\text{CO})_4$ or $\text{Al}(\text{CH}_3)_3$ respectively (1,2).

Recently, the use of tungsten-CVD in IC fabrication has been considerably developed for applications such as contact and diffusion barriers between silicon and aluminium (3). Consequently a considerable interest has to be devoted to tungsten LCVD.

The purpose of the present work is to study the growth kinetics of tungsten dots promoted by laser-irradiation of silicon in presence of $\text{WF}_6\text{-H}_2$ mixtures. The influence of laser-induced temperature, reactant gas pressures and concentrations is investigated and a growth mechanism of metallic tungsten is proposed. The purity of the deposits is evaluated by Auger spectroscopy, X-ray and electrical test measurements.

EXPERIMENTAL SET-UP.

The experimental set-up has already been described in detail in previous papers (5,6). After placing a substrate in a chemical chamber and pumping down to a primary vacuum, the chamber is filled with a $\text{WF}_6\text{-H}_2$ mixture at a constant pressure value. The partial gas pressures are adjusted with a capacitance gauge and can be varied in the range of 1 to 760 Torr. A CW Ar^+ laser beam is focused onto the substrate with a 50 cm focal length lens providing a 200 μm diameter spot on the substrate. The laser is tuned in the visible range of 480 to 514 nm and operates in the gaussian mode TEM_{00} . The beam is maintained in a fixed position during a given time determined by

switching on and off the laser beam with a mechanical shutter. The substrates used are 1 mm thick quartz plates having both sides coated with a 1 μm thick polycrystalline silicon layer deposited by conventional CVD. The laser light is totally absorbed into the silicon thin film and the substrate is locally heated up. The gaseous molecules impinging on the hot zone are dissociated and gaussian dot-shaped deposits start to grow. After switching off the beam, the laser spot is displaced using two deflecting mirrors and another tungsten dot can be grown under other experimental conditions.

The spot diameter is wide enough to carry out profilometer measurements of the tungsten dots and small enough to remain within the localized CVD limits. By scanning the laser during the chemical reaction tungsten lines can be deposited and then electrically characterized by a two point test method. Tungsten films up to 1 cm^2 can be achieved and characterized by X-ray diffraction, Auger spectroscopy and nuclear reaction analyses.

RESULTS AND DISCUSSION.

The tungsten resistivity has been measured on strips by a two point test method. It was found to be independent of the temperature and gas pressures investigated. The average value of 10 $\mu\Omega\cdot\text{cm}$ is in good agreement with the bulk resistivity confirming that the tungsten deposits are of high quality.

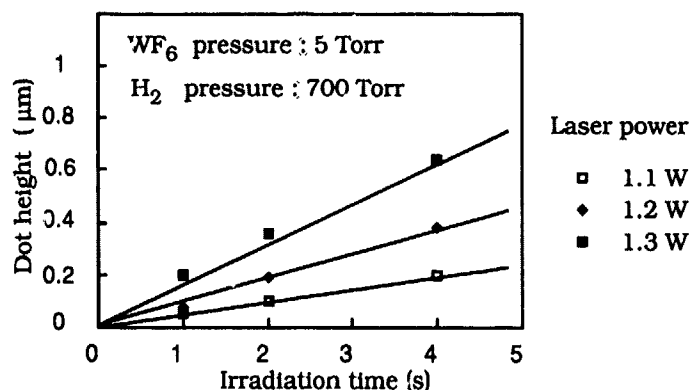


Figure 1: Height of Gaussian tungsten dots versus irradiation time for laser powers of 1.1, 1.2 and 1.3 W and 700 Torr of hydrogen.

The influence of irradiation time on dot height is presented in Fig.1. The WF_6 and H_2 pressures were 5 and 700 Torr respectively. Under given experimental conditions, the dot height is proportional to the irradiation time, and the chemical reaction is considered to occur at a constant temperature even for an irradiation time as short as 1 sec. The deposition rate of tungsten is equal to the slope of these curves. The corresponding temperature is evaluated by using a previously described manner (7,8).

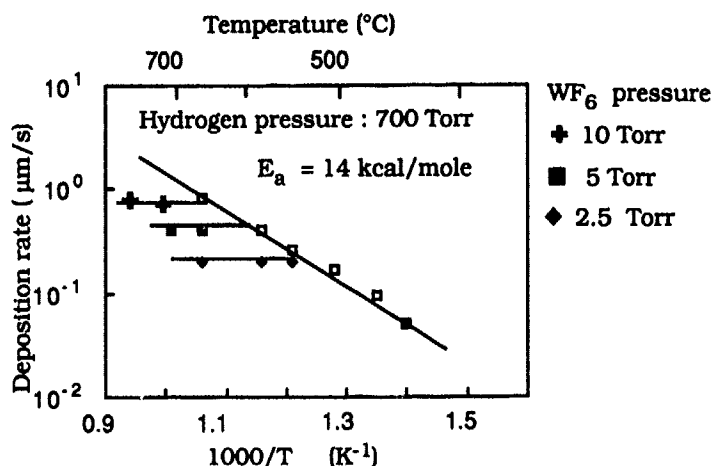


Figure 2: Dependence of the tungsten deposition rate on the reciprocal temperature at a hydrogen pressure of 700 Torr. In the high temperature domain, the \times , \square , \diamond correspond to a WF_6 partial pressure of 2.5, 5 and 10 Torr respectively. In the low temperature domain, the observed deposition rate is independent of the WF_6 partial pressure.

The dependence of the tungsten deposition rate on laser-induced temperature is shown in Fig.2 for 2.5, 5 and 10 Torr of WF_6 . The hydrogen pressure was maintained at a constant value of 700 Torr. A significant WF_6 reduction reaction by H_2 occurs at temperatures higher than 400°C . Under low temperature conditions, the chemical reaction is thermally activated with an activation energy of about 14 kcal/mole. The reaction rate was found to be independent of the tungsten hexafluoride pressure. In this temperature range

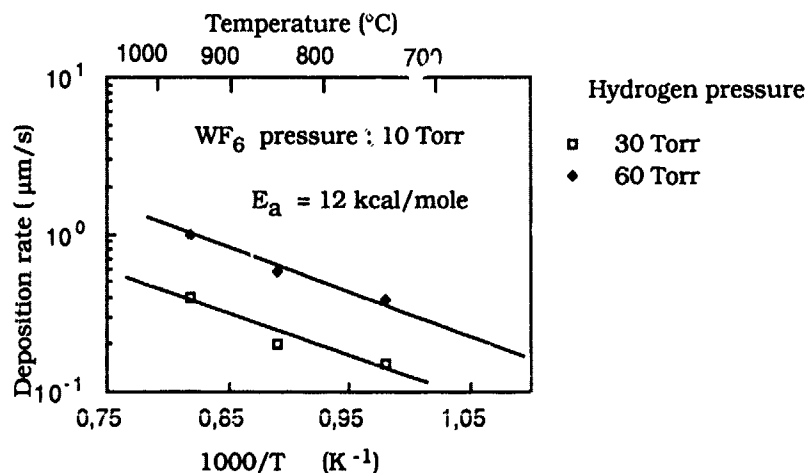


Figure 3: Dependence of tungsten deposition rate on the reciprocal temperature at hydrogen pressures of 30 and 60 Torr.

the W dots are gaussian-shaped. Above a temperature threshold which increases with WF_6 pressure, the deposition rate becomes independent of the surface temperature and proportional to the WF_6 partial pressure. Under these experimental conditions, the tungsten dots are flat-topped.

The dependence of the tungsten deposition rate on the laser-induced temperature for a low hydrogen pressure is shown in Fig.3. For a hydrogen pressure of 30 Torr, the deposition rate is lower than at 60 Torr but the activation energy is the same, within the experimental accuracy, as at 700 Torr. The deposition rate is smaller for a lower hydrogen pressure and a significant deposition thickness is achieved at temperatures above 700 °C.

Fig.4 shows the influence of the hydrogen pressure on the tungsten deposition rate. When gaussian dots are obtained, under hydrogen pressures higher than 80 Torr, the growth rate increases linearly with the square root of the hydrogen pressure. Similar behavior can be found in a conventional CVD reactor (9). When the hydrogen pressure is lower than 80 Torr, the deposition rate of gaussian dots was found to be proportional to the hydrogen pressure (Fig.5). As far as we know, a similar behaviour has not been found in conventional CVD and is an originality for the laser-induced chemical process. In both cases, i.e. hydrogen pressure below or above 80 Torr, the deposition rate of gaussian tungsten dots is controlled by a thermally activated process.

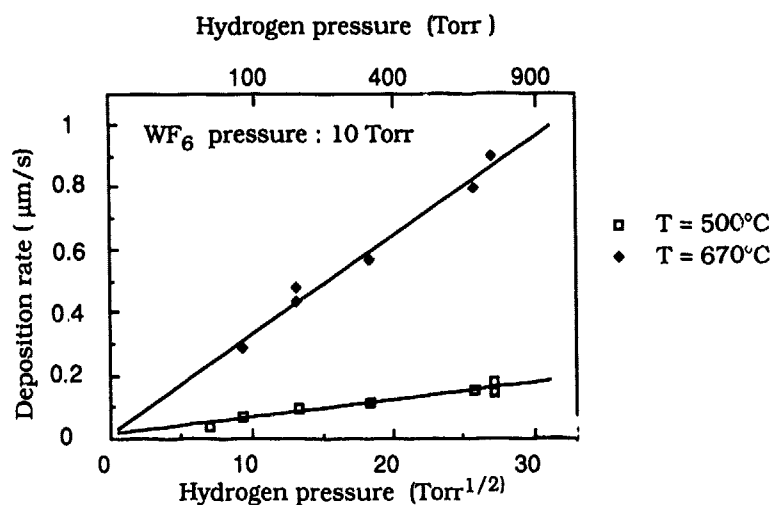


Figure 4: Dependence of tungsten deposition rate on hydrogen pressure for a hydrogen pressure above 80 Torr.

$\text{WF}_x + (1/2) \text{H}_2 = \text{WF}_{x-1} + \text{HF}$	Square root / Hydrogen pressure
$\text{WF}_x + \text{H}_2 = \text{WF}_{x-2} + 2 \text{HF}$	linear / Hydrogen pressure

Table1: Correspondence between a chemical reaction and the variation of rate with the gas pressure.

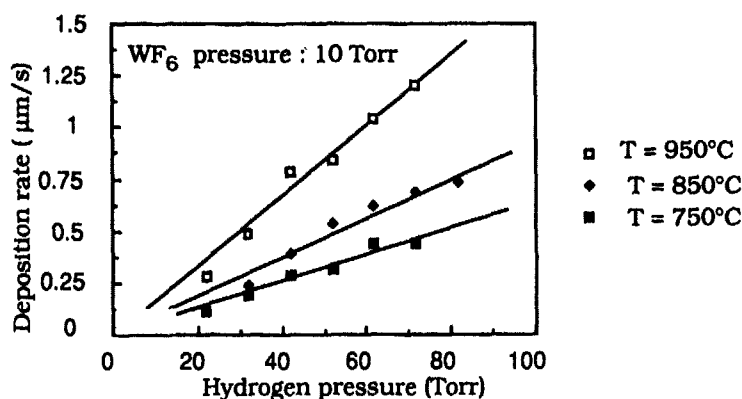


Figure 5: Dependence of tungsten deposition rate on hydrogen pressure for hydrogen pressure below 80 Torr.

Table 1 shows the pressure dependence of the chemical reaction classically invoked for tungsten deposition from hydrogen reduction of tungsten hexafluoride.

At a hydrogen pressure above 80 Torr and a tungsten fluorine pressure above 2 Torr, all the available sites for WF_x radicals are occupied and the number of physically adsorbed hydrogen molecules are in equilibrium with the gas pressure. These hydrogen molecules dissociate in a thermally activated manner and an equilibrium is reached between the atomic and molecular hydrogen. The hydrogen atoms react with the WF_x radicals and the tungsten deposit is formed. This reaction is described by the first one in table 1 and corresponds to the Langmuir-Inchelwood model.

At a pressure below 80 Torr, the equilibrium between hydrogen atoms and hydrogen molecules is no longer reached and all the atoms formed react almost instantaneously and the deposition rate is in this case dependent on the number of hydrogen molecules adsorbed on the surface. This reaction is described by the second one in table 1 and corresponds to the Rideal model (11).

The deposition kinetics of flat-topped tungsten dots is characteristic of a gas diffusion limited chemical reaction (1). In fact, the deposition rate is independent of the surface temperature and proportional to the WF_6 pressure.

In this high rate regime, the deposition rate is proportional to the surface collision frequency Φ of the WF_6 molecules. Φ is given by:

$$\Phi = \frac{D p}{r k T}$$

where D is the diffusion coefficient of WF_6 molecules through hydrogen, p the WF_6 partial pressure, T the temperature of the gas phase and r the radius of the deposit (about 100 μm).

Since the laser-heated area is very small, the gas phase can be assumed to be at room temperature. Consequently the calculated deposition rate is independent of the surface temperature and proportional to the WF_6 partial pressure.

By comparing Φ and the observed deposition rate in the flat topped regime, the sticking coefficient of tungsten fluorine molecules on a tungsten surface can be estimated at around 50% of the molecules impinging on the laser-spot area. These adsorbed molecules are then decomposed and participate in the growth of the flat topped tungsten dot.

CONCLUSION.

The CW Ar^+ laser-induced CVD of tungsten dots obtained from the WF_6 reduction reaction by hydrogen occurs at temperatures higher than 400°C via a thermal process. Pure tungsten films have been obtained and the resistivity of the deposits is only twice as high as the bulk resistivity. The deposition rate has been investigated as a function of irradiation time, reactive gas partial pressures and laser-induced temperature. The reaction is either surface or gas diffusion controlled depending on the hydrogen pressure-temperature combinations. At high hydrogen pressures, the surface is saturated in hydrogen and the reaction is controlled by the formation of hydrogen atoms in the adsorbed phase. At low hydrogen pressure, the rate limiting step is the adsorption of hydrogen molecules and the orders of the reaction regarding hydrogen and tungsten hexafluoride are 1 and 0 respectively.

REFERENCES.

1. D.Tonneau, G.Auvert, Y. Pauleau, J. Appl. Phys. 64 (1988) 5189.
2. J.Flicstein, J.E. Bourée, Applied Surf. Science 36 (1989) 443.
3. Ph. Lami, Y. Pauleau, J. Electrochem. Soc. 135 - 4 (1988) 980.
4. O. Gottsleben, M. Stuke, Appl. Phys. Lett., 52 (1988) 2230.
5. D.Tonneau, G.Auvert, Y. Pauleau, Europ. Mat. Res. Soc. Proc., 15 (1985) 125.
6. D.Tonneau, G.Auvert, Y. Pauleau, Thin Solid Films, 155 (1987) 75.
7. D.Tonneau, G. Auvert, Mat. Res. Soc. Symp. Proc. 101 (1987) 131.
8. F.Ferrieu, G.Auvert, Appl. Phys. 54 (1985) 2646.
9. Y.Pauleau, Ph. Lami, J. Electrochem. Soc. 132 - 11 (1985) 2779.
10. W.A.Bryant, J. Electrochem. Soc. 125-9 (1978) 1534.
11. K.J.Laidler, "Chemical Kinetics" Mc Graw-Hill Book Co. (1965).

EXCIMER LASER INDUCED DEPOSITION OF TUNGSTEN FROM W(CO)₆ AND WF₆

BERND OLD RAGER AND FRIEDRICH BACHMANN

Siemens AG, Corp. Production and Logistics Department.
Otto-Hahn-Ring 6, D-8000 Munich 83, Fed. Rep. Germany

Abstract

ArF laser induced deposition of W from W(CO)₆ and WF₆ on Si/SiO₂ surfaces was investigated. With an in-situ reflectivity measurement the growth of the layer could be monitored during the deposition process. We find that the initial stage of layer growth as well as the reflectivity as a function of deposition time depends on the laser fluence and on other deposition parameters. Model calculations, using the optical constants of deposited films, determined by ellipsometry, have been performed to compare the measured reflectivity curves with the calculated curves. The deposited layers have been analyzed by XPS, AES, X-ray Diffraction and Raman Spectroscopy. Additionally, experiments of direct pattern transfer deposition (via contact mask) with W(CO)₆ show the presence of an involved surface process, which by Fresnel diffraction caused structures smaller than 0.5 μm.

Introduction

The trend in microelectronics towards smaller geometries and higher packaging requires new production processes and materials. Laser induced chemical vapor deposition processes, and tungsten as a material for metallization have gained considerable interest because of their favourable qualities. Metallization processes as well as other deposition processes with excimer lasers have further the advantages like low processing temperature and the possibility for direct resistless pattern transfer.

Therefore many investigations of excimer laser induced deposition processes of different materials have been performed with the aim to achieve application in production for VLSI [1-3]. But the application of such processes requires an understanding of the chemical processes involved. For this purpose we have built up an experiment to investigate excimer laser induced metal deposition processes.

Experimental

At first a brief description of the experimental arrangement will be given. The samples are mounted in the process chamber on a manipulator. The base pressure is $<10^{-6}$ mbar before the process starts. The process gases were pumped away by a two stage rotary vane pump and then introduced into a scrubber. All experiments were carried out under gas flow conditions. The gases are separately controlled by mass flow controllers and the total pressure by a capacitive pressure gauge and a throttle valve. W(CO)₆ is introduced by flowing carrier gases of Ar or H₂ through the reservoir of W(CO)₆.

The laser entrance window is gas purged (Ar) and equipped with a special protection tube to prevent depositions on the window.

The laser pulses from a Lambda EMG 1003i excimer laser could be varied in the range of 0-130mJ by a dielectric laser beam attenuator. In most cases the laser beam was shaped by a rectangular aperture and focused by a cylindrical lens, in order to enhance the fluence range on the substrate surface. In nearly all deposition experiments the laser (repetition rate 20 Hz) irradiated the sample perpendicularly.

The reflectivity measurement system consists of an unpolarized HeNe laser and two photo diodes (for measurement signal and reference signal), both shielded by an optical filter. We observed at an incidence angle of 40° the reflectivity changes due to the growing layers in-situ. In order to eliminate intensity fluctuations of the HeNe laser, the measurement signal is corrected by dividing the measurement signal by the reference signal electronically.

Results and Discussions

In the first part the deposition experiments with $W(CO)_6$ will be presented, and then some of the preliminary results of the WF_6 experiments will be given.

Most of the layers were deposited on pieces of n-doped Si(100) wafers (with native oxide) at room temperature. Due to the ArF laser beam, shaped as mentioned above, the layers cover an area of about $4 \times 6 \text{ mm}^2$. Fig.1 shows measured reflectivity curves as a function of deposition time, at 3 different total pressures.

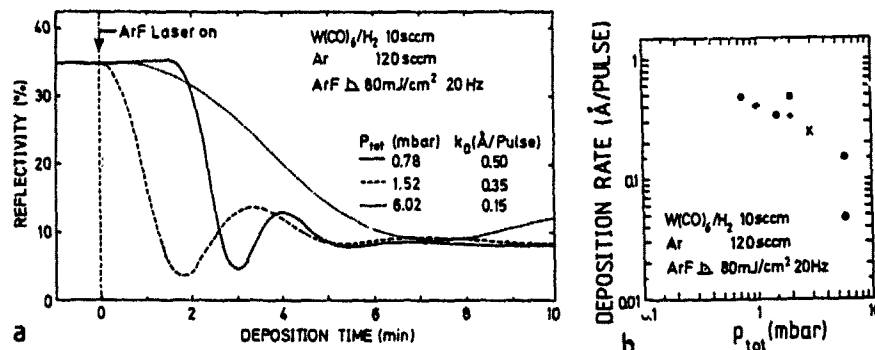


Fig.1: Reflectivity of layers deposited from $W(CO)_6$ in H_2 and Ar at 3 different total pressures and by ArF laser (a). Dependence of deposition rate on total pressure (b).

The reflectivity curves exhibit two typical features, which were characteristic for the depositions of W from $W(CO)_6$ carried out under these and comparable conditions. First, the oscillations in the reflectivity and second, a lower reflectivity value at the end of the deposition process than at the beginning. At the beginning the reflectivity is determined by the optical constants of Si and should be about 35% in the given arrangement. The reflectivity value of the deposited layer is far away from that expected for a metallic W layer. An estimation with the optical constants of W bulk material (even at a small thickness) should yield $R \approx 50\%$ (see Fig.3). The measured reflectivity

tivity curves show clearly that the deposited film is different from W bulk material.

The dependence of the (averaged) deposition rate on the total pressure is given by the diagram of Fig.1b. The behavior of decreasing deposition rate with increasing total pressure can be explained by the stronger absorption of the laser light in the gasphase and by reaction- and diffusion-rates of the photoreaction products changed due to the increasing number of collisions. This is consistent with the results of ref.[4,5].

In Fig.2 further reflectivity curves show the influence of the laser fluence; all other parameters were kept constant.

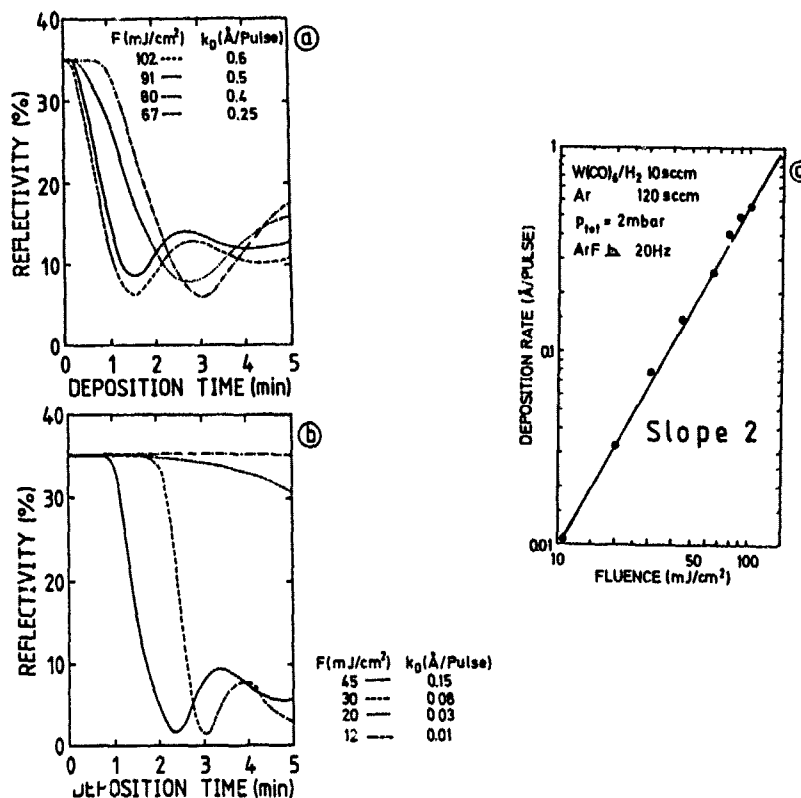


Fig.2: Reflectivity of layers deposited from $W(CO)_6$ in H_2 and Ar at different ArF laser fluences (a,b). Dependence of the deposition rate on fluence (c).

The curves in Fig.2a,b exhibit the mentioned two typical features, but it is also noticeable that in the fluence range considered, the moment at which the reflectivity is decreasing faster (but always with nearly the same slope) shifts towards later times. This means that at lower fluences the deposition starts after a certain "incubation" time.

Fig.2c shows the dependence of the deposition rate on the laser fluence. In the semi-logarithmic plot the slope of ≈ 2 shows that a two-photon process must be responsible for the dissociation of $W(CO)_6$ and the deposition. Such kind of processes have been discussed for the depositions of W from $W(CO)_6$.

with excimer lasers and also for the Group 6 Hexacarbonyls [6,7].

The chemical composition of the deposited films were investigated by XPS and AES. It should be mentioned that the samples to be analyzed were exposed to the air. AES depth profiles of W films produced from $W(CO)_6$ exhibit distributions of $\approx 65\%$ W, $\approx 30\%$ O and $\approx 5\%$ C. These distributions seem to be typical for deposition processes performed under comparable conditions. The results agree with the distributions of deposition experiments from $W(CO)_6$ and UV laser excitation carried out by other groups [8,9].

In order to clarify the chemical nature of the elements involved in the deposited films, a XPS analysis of the W_{4f} peaks yields the following results: In the surface region of the layer the peaks were shifted towards higher binding energies, in comparison to W bulk material, and can be identified to WO_3 . After sputtering, the W_{4f} peaks were shifted towards the binding energies characteristic for W bulk [10].

The crystallographic structures of the laser induced films have been measured by X-ray Diffraction (XRD) and Raman Spectroscopy (RS). The XRD measurement of a $\approx 300\text{nm}$ thick layer shows no crystalline W structure, but it seems that with increasing thickness the amorphous phase becomes more crystalline. In another film diffraction peaks of WO_3 and WC could be found but they were laying on a broad background of amorphous W.

In contrast to XRD, with RS it was possible to detect crystalline parts of WO_3 together with amorphous parts, by comparing our Raman spectra with those measured in ref.[11], where amorphous and crystalline structures of evaporated WO_3 films have been investigated. Evaporated films annealed at 350°C (crystallisation temperature of $\alpha\text{-}WO_3$), show peaks in RS at $\approx 720\text{cm}^{-1}$ and 807cm^{-1} , which are characteristic for $\alpha\text{-}WO_3$, but they are still laying on a broad background from parts of $\alpha\text{-}WO_3$. It is interesting to note, that these samples, consisting of a mixture of $\alpha\text{-}$ and $\beta\text{-}WO_3$ phases, have revealed no peaks in XRD.

We used a simple model, based on the assumption of a constant deposition rate during the entire film formation, the layer growth can be simulated for arbitrary optical constants. The reflectivity has been calculated by applying generalized equations given in ref.[12] for the optical system of an absorbing layer on top of an absorbing substrate, interacting with monochromatic light. Because of the simplification of the model, it can not be expected to reproduce the measured curves exactly, but the trends will be given in the correct way. In Fig.3 some calculated reflectivity curves were presented. The upper curve shows the reflectivity, calculated by the optical constants of W bulk material. Due to the high absorption coefficient k , a W layer of about 60nm has already a thickness avoiding any interference of the light wave with the substrate. The contrary case is given by the 4 lower curves in Fig.3. In this calculation the optical constants (measured by ellipsometry) and the measured (averaged) deposition rates of the films given in Fig.1 have been applied. The trend in the behavior of the shapes of the measured curves is reproduced, and by choosing certain values for the parameters (the optical constants n, k , and the deposition rate k_0) the agreement becomes satisfactory.

The arithmetical reproduction of the reflectivity curves given in Fig.2a,b is difficult and unsatisfactory, probably due to the more complicated situation under the conditions of a varying laser fluence, which can not be described by the model.

Direct pattern transfer deposition experiments have been carried out in its simplest form, by applying a contact mask. The mask of a 25 μ m thick tantalum foil, structured with stripes as shown in Fig.4, was laying on a Si/SiO₂ substrate and irradiated perpendicular with the excimer laser (both ArF and KrF). The following deposition parameters have been applied: W(CO)₆/Ar=10sccm, Ar=120sccm, p_{tot}=2-3mbar, fluence=30-200mJ/cm² and deposition time 5-10 min.

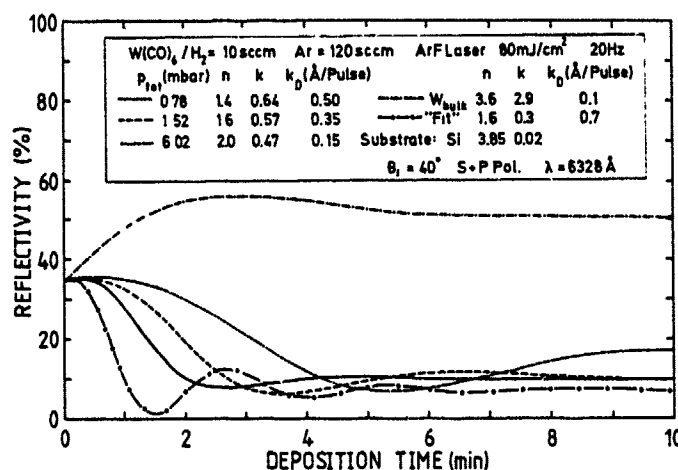


Fig.3: Calculated reflectivity curves as a function of deposition time for different n, k and k_0 values.

At the borders of the deposited stripes we can observe both by light- and scanning-electron-microscope structures with dimensions smaller than 0.5 μ m, as is shown in the photo of Fig.4.

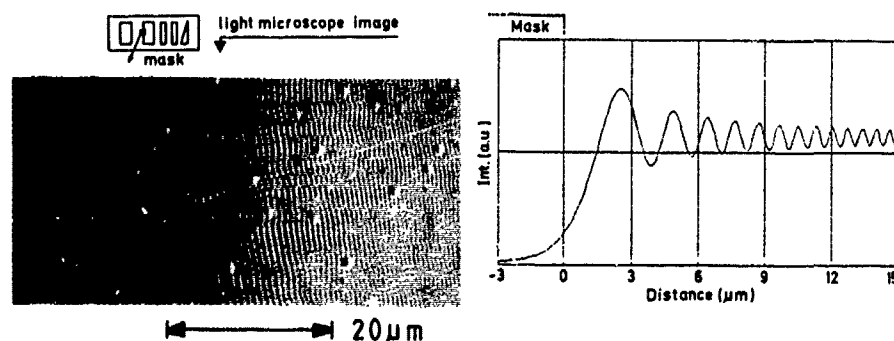


Fig.4: Structures caused by Fresnel diffraction in a deposition from W(CO)₆ by ArF laser. Spatial light intensity calculated by Fresnel diffraction theory.

These structures are caused by diffraction of the laser light at the mask. The light intensity on the substrate surface was calculated for the given arrangement via Fresnel diffraction theory as illustrated in Fig.4 too. The agreement is rather good and the assumption of surface processes besides these in the gasphase involved in the deposition from $W(CO)_6$ is supported.

Therefore we suppose that the deposition from $W(CO)_6$ can be a possible model process to test the resolution capability in direct resistless pattern transfer processes by optical imaging, despite the conclusion given in ref.[5]. Jackson et al. reported here about a direct pattern transfer deposition experiment with $W(CO)_6$. Applying an optical imaging system, which should yield a certain resolution, they could not achieve this resolution in their deposition experiments with $W(CO)_6$.

The results achieved by depositions from $W(CO)_6$ indicate the unfavourable qualities of $W(CO)_6$ as precursor molecule and require to test other W containing compounds. Therefore we have carried out deposition experiments with WF_6 diluted in H_2 and Ar using ArF laser excitation. The laser was irradiated perpendicular onto the Si/SiO₂ substrate at room temperature. Fig.5 exhibits the reflectivity of film formation carried out under these conditions.

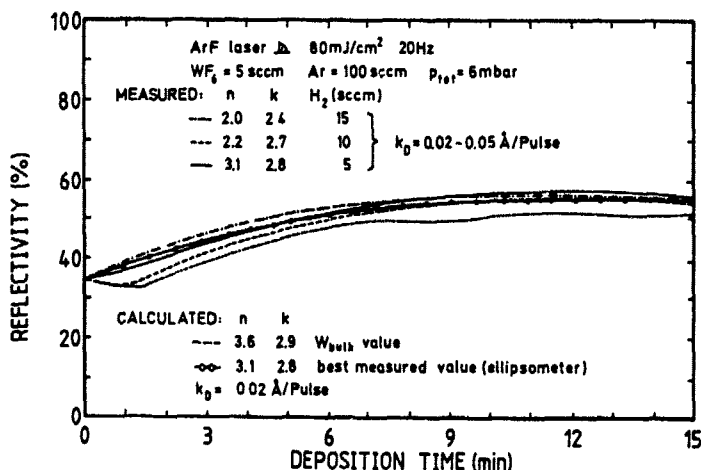


Fig.5: Reflectivity curves of depositions from WF_6 ; measured (—, ---,) and calculated (---, ---, ---).

The agreement with theory is very satisfactory, and only at the beginning of the depositions were small differences. The curve (---) has been calculated by employing optical constants of deposited W films measured by ellipsometry. The layers deposited from WF_6 show a totally different behavior than the layers deposited from $W(CO)_6$. They looked metallic and the optical constants were very similar to the bulk values of W. Although there were problems of the adhesions of the deposited films from WF_6 at room temperature, the first results were very promising, and the experiments will be continued.

Conclusions

The deposition experiments from $W(CO)_6$ showed results indicating the unfavourable qualities of this molecule as a precursor for laser induced deposition of tungsten metallic layers. Despite of this it seems interesting to perform direct pattern transfer depositions from $W(CO)_6$ by optical imaging. The first results of film formation from $W(CO)_6$ were very promising and it should be possible to produce laser deposited W films with good metallic qualities [2]. The reflectivity measurement system has proved to be a good applicable instrument to observe the growing layers in-situ. It is possible to control film quality during the deposition process.

References

1. M.Hirose, Annual Research Report, 11 (1989), Department of Electrical Engineering, Hiroshima University
2. A.Matsushashi, S.Nishikawa and S.Ohno, Jap.J.Appl.Phys., 27 L2116 (1988)
3. G.E. Blonder, G.S.Higashi and C.G.Flemming, Appl.Phys. Lett., 50, 766 (1987)
4. M.S.Chin, Y.G.Tseng and Y.K.Ku, Optics letters, 10, 113 (1985)
5. R.L.Jackson, G.W.Tyndall and S.D.Sathers, Appl.Surf.Sci., 36, 119 (1989)
6. D.K.Flynn and J.I.Steinfeld, J.Appl.Phys., 59, 3914 (1986)
7. W.Radloff, H.Hohmann, H.-H. Ritze and R.Paul, Appl.Phys. B 49, 301 (1989)
8. R.L.Jackson and G.W.Tyndall, J.Appl.Phys., 64, 2092 (1988)
9. N.S.Gluck, G.J.Wolga, C.E.Bartosch, W.Ho and Z.Ying, J.Appl.Phys., 61, 918 (1987)
10. C.D.Wagner, W.M.Riggs, L.E.Davis, J.F.Moulden, G.E.Muilenberg (Ed.), Handbook of X-Ray-Photoelectron Spectroscopy, Perkin Elmer Corp. 1979
11. Y.Shigesato, A.Murayama, T.Kamimoni and K.Matsuhiro, Appl. Surf. Sci., 33/34, 804 (1988)
12. M.Born and E.Wolf, Principles of Optics, Pergamon Press 1970 (4th Ed.)

DIRECT WRITING OF COPPER LINES FROM COPPER FORMATE PRECURSORS USING A ND:YAG-LASER

HEINRICH G. MÜLLER AND SIEGFRIED SCHULER
TU Berlin, Forschungsschwerpunkt Mikroperipherik,
Sekt. TIP 3.1, Gustav-Meyer-Allee 25,
D-1000 Berlin 65

ABSTRACT

An effective method is described for laser induced additive formation of copper conductor lines on alumina substrates. The direct writing process allows for depositions with speeds of up to 50 mm/s and a resolution of about 10 microns with reliable adhesion of the deposited patterns.

INTRODUCTION

For interconnection techniques, a laser directed deposition process is very promising, because of its flexibility in small production series, and due to its value as a general method for easy deposition of conductor lines on thin film hybrids.

Differing from on chip applications, the most important goals to be reached are high writing speeds, easy processing, and good adhesion and conductivity of the deposited layers, rather than the best spatial resolution. To reach high pin count without deterioration of the dc conductivity or deviations from the wave resistance of 50Ω, conductor thicknesses of several microns are indispensable. However, such thicknesses are difficult to achieve with high writing speeds.

To overcome this problem, very thin seeds of a noble metal may be laser deposited instead of the complete conductor line. The thickness of the conductor line can subsequently be enhanced to the desired value by currentless deposition of copper.

Several authors [1,2] have pointed out that depositions from solid precursors can be performed much faster than by gas phase processes, because the writing speed in the former is not limited by gas diffusion processes. So, decomposition of palladium acetate or gold inks has been used quite successfully, however, the deposition speed was still quite low and the deposited materials were expensive.

More recently, Gupta and Jagannathan [3,4] have been able to decompose copper formate films with an Ar⁺ laser in a pyrolytic process, with speeds of up to 10 mm/s. This gives good conducting copper lines by use of an easy process.

Here we describe a different method that uses a Nd:YAG laser and can offer writing speeds of up to 50 mm/s.

EXPERIMENTAL

Thin film alumina substrates from Hoechst (Rubalit 710, 99.6% Al_2O_3) were immersed in a room temperature saturated solution of copper formate in deionized water. The solution was evaporated at 60°C to produce flat films of copper formate. On drying in air, these films form mixtures of the weakly blue dihydrated copper formate with crystals of the royal blue anhydride [5]. The grain boundaries between these two different crystal modifications do not seem to disturb the subsequent copper deposition process. Film thicknesses of one to fifteen μm were determined by profilometer (Sloan Dektak 3030) scans.

For the deposition process, a laser trimmer (ESI, model 80), providing very high mechanical speeds, was used. The built in Nd:YAG laser was used in the cw mode, at a TEM₀₀ power of up to 2W. The beam was focused to give a reaction zone of 10 microns in diameter. Scanning speeds between 1mm/s and 200 mm/s were employed and the results were evaluated. The lowest speed resulted in conglomerates of copper grains, many microns in size, without any mechanical adhesion to the substrate. The highest speeds gave very few and small seeds, which could not be used for a later chemical copper deposition with reliable results. As an optimum procedure, the deposition region was scanned at a speed of 50 mm/s with a line overlap of 5 μm . This way, the whole scanning area was double illuminated, except for the outermost left and right 5 μm regions of the scanned area.

To remove the precursor film after illumination, the substrate was immersed into a 10% solution of formic acid in water. Ultrasonic treatment during this step can remove loosely bound copper particles from the substrate surface. This helps in preventing these particles from getting lost later in the solution for chemical copper deposition, which may be seriously degraded by such pollution effects.

The final step was a chemical copper deposition process. The commercially available solution (Schering Printoganth ML) was maintained at 60°C and copper conductor lines grew at a rate of about 3 $\mu\text{m}/\text{h}$. Tape tests were performed for proof of good adhesion of the deposited lines.

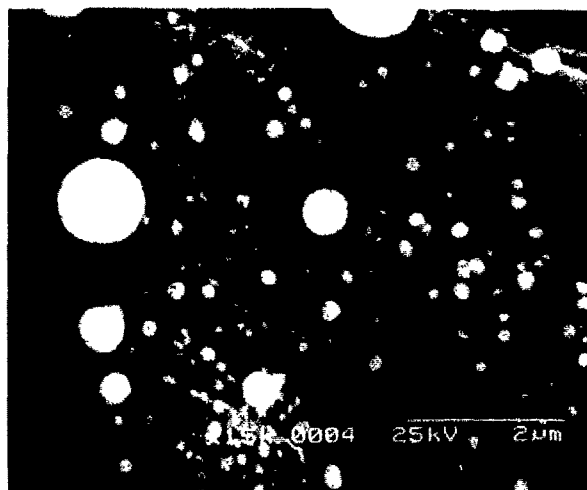
RESULTS

SEM photographs of the laser deposited seeds are shown in fig 1 (a) and (b). Fig 1 (a) gives a close view of the metallic spheres 0.1 to 1 μm in diameter. Fig. 1 (b) shows an overview on a fivefold scanned line. Strong changes of the substrate surface can be seen. The metal density is found to be maximum at the borderline of each scanning line and the following one. The outermost left line, written last, gives hardly any copper deposits. This suggests that the writing of the preceding line provides some seeds for the subsequent one. This effect cannot be achieved by simply writing the same lines repeatedly with the laser spot, because in this case, the second illumination does not encounter any more regions of unexposed precursor.

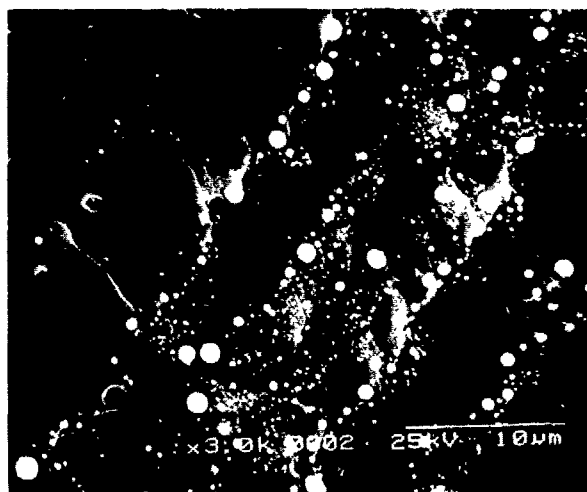
Figure 2 shows a laser written feature before (a) and after (b) currentless deposition of 3.5 μm copper. Each

Fig.1 :
laser depo-
sited copper
seeds

(a)
close view



(b)
survey on
fivefold
scanned area



conductor line was written by six subsequent scans of the laser. A resolution of better than 10 microns was achieved.

A measurement of the electrical conductivity of the direct written laser deposits was impossible, because no contiguous film is formed during this process. After the line thickness has been enhanced by the currentless copper deposition, the conductivity is about 70% that of bulk copper. Fig.3 shows a

100 x 100 μm^2 pad, deposited to provide these measurements. It also demonstrates the electronic relevance of the deposition technique.

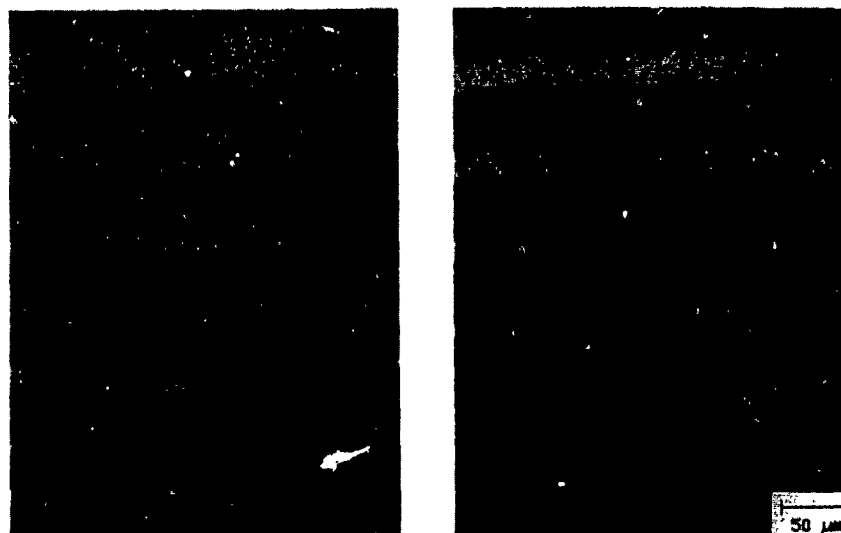


Fig.2 (a) Laser written seeding (b) features after subsequent chemical copper deposition

The tape tests of the final deposits revealed a good adhesion.

The dependence of the laser deposits on copper formate precursor film thickness was carefully investigated. This parameter could be governed by the amount of copper formate solution evaporated during the precursor film formation. At thicknesses of less than 3 μm , no seeding was observed. Between 10 and 15 μm , the laser deposition resulted in relatively big grains, which decrease the spatial resolution and cause an inhomogeneous thickness of the final copper layers. Best results were obtained with about 5 μm precursor thickness. The maximum reliable writing speed did not depend on this parameter. This suggests, that mainly the heat generated on the substrate surface itself governs the reaction mechanism.

To characterize the deposits chemically, an XPS-analysis of the laser written deposits was performed (Fig.4a). Copper was found to be in oxidation state I (Cu_2O) and 0 (metallic Cu). According to the incomplete surface coverage by the laser deposits, a huge amount of oxygen and aluminum were to be expected from the substrate background. This was found, but unexpectedly, detailed peak analysis also revealed metallic aluminum (Fig.4b, peak at 73.5 eV), which must stem from substrate interactions with the deposition reaction. Surface contamination with carbon and traces of sulphur and nitrogen were also found. Apparently, these impurities do not have any important influence on the chemical copper deposition.

*Fig.3 Copper pad after
chemical copper
deposition,
100x100 μm^2*



The unexpected observation of some reduction of the Al_2O_3 to metallic Al complements the changes observed by SEM on the substrate surface. These results may be attributed to the very high power density ($2.5 \times 10^6 \text{ W/cm}^2$) of the laser.

CONCLUSIONS

A reliable laser direct writing method for copper on alumina substrates could be established. Cw Nd:YAG laser scanning on precursor films at speeds of 50 mm/s with subsequent chemical copper deposition produce electronic grade interconnection conductors. SEM- and XPS-Analysis suggest a strong interaction of the substrate material with the deposits.

The Authors wish to thank Dr. U. Roll for performing the XPS-Analysis.

REFERENCES

- 1) M.E.Gross, A. Appelbaum, and P.K.Gallagher, J. Appl. Phys. 61, 1628 (1987).
- 2) G. Arjavalingam, M.M. Oprysko, and J.E.Hurst, Jr, in Laser and Particle-Beam Chemical Processing for Microelectronics, ed. by D.J.Ehrlich, G.S.Higashi, and M.M.Oprysko (Mater. Res. Soc. Proc. 101, Pittsburgh, PA 1988) pp. 81-87.

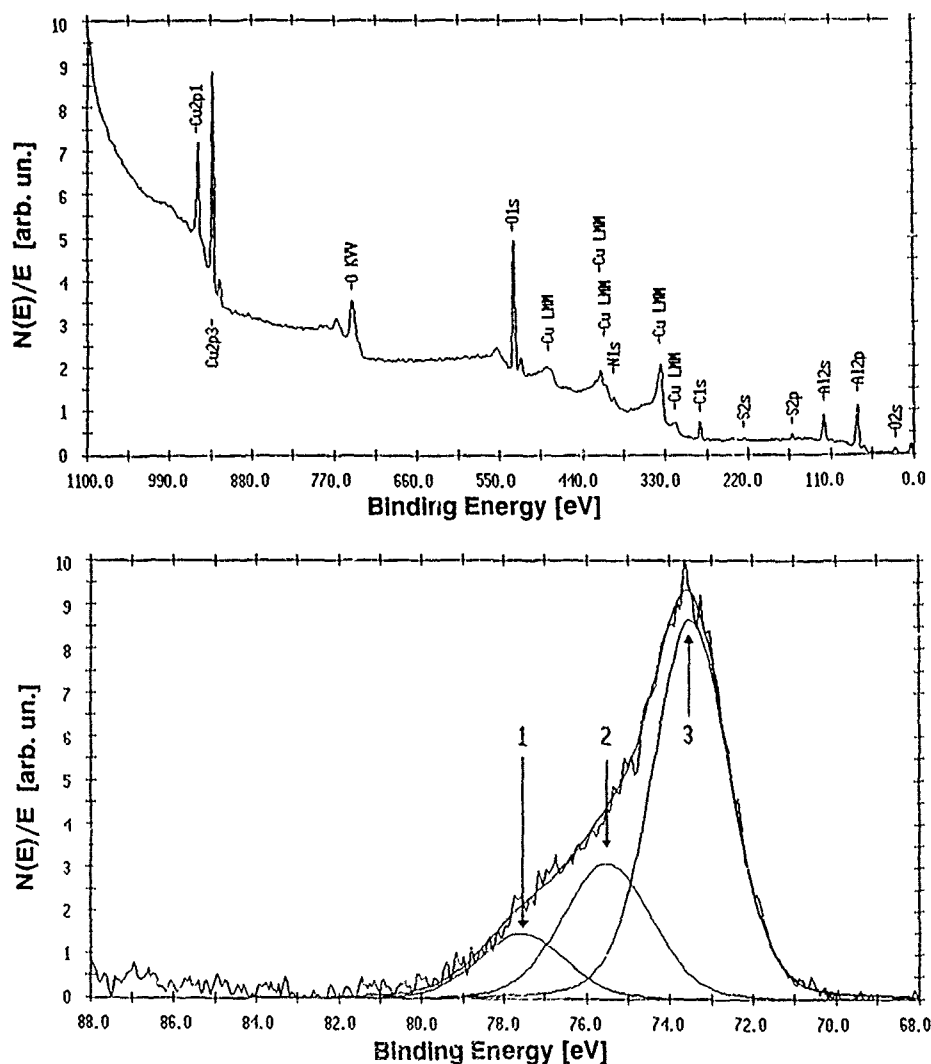


Fig.4 XPS-spectrum of laser deposit
 above (a): survey
 below (b): Al peak analysis. (1) 77.6 eV - Cu3p;
 (2) 75.5 eV - Al2p, oxidized; (3) 73.5 eV - Al2p, metal

3) A. Gupta, R. Jagannathan, in *Laser and Particle-Beam Chemical Processing for Microelectronics*, ed. by D.J.Ehrlich, G.S.Higashi, and M.M.Oprysko (Mater. Res. Soc. Proc. 101, Pittsburgh, PA 1988) pp. 94-100.

4) A. Gupta, R. Jagannathan, *Appl. Phys. Lett.* 52, 2254 (1987).

5) R.L.Martin, H. Waterman, *J. Chem. Soc.* 1959, 1359.

ROLES OF GAS PHASE AND SURFACE PHOTOLYSIS IN LASER CHEMICAL VAPOR DEPOSITION FROM $\text{Fe}(\text{CO})_5$

XIN XU* AND J.I. STEINFELD*

*Department of Chemistry, Massachusetts Institute of Technology, Cambridge, Massachusetts 02139, U.S.A.

ABSTRACT

The chemical state of the carbon and oxygen incorporated in iron films formed by laser photolysis of $\text{Fe}(\text{CO})_5$ has been examined by profiling XPS analysis. A significant portion of the codeposited CO is photodissociated at the growing surface.

INTRODUCTION

Deposition of metallic films by laser photolysis of volatile metal carbonyls has been the subject of numerous investigations [1-8]. In particular, deposition of iron from $\text{Fe}(\text{CO})_5$ has been brought about by u.v.-laser excitation [1,7,9], synchrotron radiation [9], laser-driven thermal decomposition [2], and broad-band u.v. photolysis [10,11]. Considerable contamination of the deposited films by carbon and oxygen is a common feature in these investigations [4-6,12]. A study of the deposition mechanism is essential for understanding the origin of this contamination, and may also shed light on CO dissociation processes taking place on transition-metal catalysts in the Fischer-Tropsch reaction.

With 193 and 248-nm excimer lasers, the major products from one-photon photolysis of $\text{Fe}(\text{CO})_5$ in the gas phase are $\text{Fe}(\text{CO})_x$, $x=2$ or 3 [13-16]. At higher fluences, sequential photon absorption leads to loss of the remaining CO ligands. Both $\text{Fe}(\text{CO})_x$ and bare Fe atoms are deposited at the surface; this is a significant source of the C and O content in the deposited films. Studies on decomposition of $\text{Fe}(\text{CO})_5$ adsorbed on silver [17], silicon [18], or platinum [19] single crystals indicate that the principal process which occurs on these surfaces is Fe-C bond breakage and subsequent desorption of molecular CO. We are thus led to the set of interrelated questions: what is the fate of the "codeposited" CO? Is it simply desorbed, or both desorbed and dissociated on the surface, and in either case, is the driving force primarily thermal or photochemical?

EXPERIMENTAL

We have addressed these questions by carrying out a series of photodepositions from $\text{Fe}(\text{CO})_5$ over a wide range of experimental conditions, and analyzing the C and O content and chemical states in the deposited Fe films using profiling AES and XPS. Although XPS analysis of the chemical state of the incorporated C and O is a very incisive probe, few such analyses have hitherto been reported. The deposition apparatus used in our earlier work [5] was extensively improved to reduce background pressure to $<5 \times 10^{-7}$ Torr in the deposition region; this results in less than 3% contamination of the film from background gas adsorption, under our deposition conditions. Entrance window fouling was also eliminated by incorporating several concentric baffles between the deposition region and the window. The pentacarbonyl iron (Alpha, 99.5+%) was further purified by several freeze-pump-thaw cycles and introduced by a dosing tube located ~1 cm above the substrate. 100 mTorr of flowing argon (Matheson 99.9995% purity) was used as both purge and buffer gas. Photolysis was carried out using a Lumonics TE-861 pulsed excimer laser at the ArF^* (193 nm or 6.4 eV, $0.3 - 28 \text{ mJ/cm}^2$) and KrF^* (249 nm or 5.0 eV, $20 - 90 \text{ mJ/cm}^2$) wavelengths.

Characterization of the resulting films was conducted *ex situ* on an SSX-100 XPS spectrometer and a PHI 660 Scanning Auger Multiprobe located at the Harvard-M.I.T. "Cambridge Surface Facility". The film samples were

stored in small double desiccators filled with high purity Ar gas, and the necessary transfers were done in glove bags under flowing N_2 . While this method unavoidably led to surface contamination of the sample, such contamination was limited to the top $\sim 100\text{\AA}$ of the material, since the oxidized overlayer protects the integrity of the underlying material [9]. As shown in Fig. 1, the C and O content of the material below the topmost layer can be as low as $\leq 3\%$ (near the detection limit for carbon). In profiling XPS, therefore, after the top layer is sputtered off, subsequent XPS scans are representative of as-deposited material (Fig. 2a). The XPS spectrometer was calibrated using gold and copper reference standards for peak positions [20], and Fe_2O_3 for sensitivity factors.

RESULTS AND DISCUSSION

Depositions were carried out with the wavelengths and fluences noted above, on both Si(100) and silica substrates. We found that the C/Fe and O/Fe ratios increase with decreasing fluence at both 193 and 248 nm; analysis of the C and O XPS spectra showed that, at all fluences, the major portion of these elements was present in the carbide or oxide forms [19,21], rather than as undissociated CO. An example of such an analysis, at low laser fluence (0.3 mJ/cm^2 at 193 nm), is shown in Fig. 2b. At this fluence, the temperature rise in the film due to the laser pulse, estimated using Eq. (10) of ref. 22 or Eq. (5) of ref. 23, is less than 1 or 2°K . Since the thermal dissociation of CO adsorbed on Fe takes place only at temperatures above 375°K [21,24], this result provides clear evidence for photochemically induced dissociation of CO in the growing Fe film. This is supported by the following observations: (1) At higher laser fluences, or when using substrates having lower thermal conductivity (such as silica), the temperature increase is correspondingly larger. Under these conditions, the C and O content of the film is decreased, since laser-thermal desorption of CO molecules dominates thermal dissociation. (2) Based on the data in Ref. [21], thermal dissociation of $\alpha_3\text{-CO}$ on Fe (100) results in only about 0.05 monolayers of C and O being incorporated at the surface. This is in accordance with the observation [9,11(a)] that Fe films pyrolytically deposited from $Fe(CO)_5$ in UHV usually contain less than 5% C and O.

The ability of 193 nm (6.4 eV) or 249 nm (5.0 eV) photons to bring about disruption of CO adsorbed on transition-metal surfaces can be understood in terms of the considerable weakening of the CO bond from its gas-phase value [25]. A substantial decrease in the C-O stretching frequency has been noted for CO adsorbed on Fe [24,26,27], Mo [28,29], and Cr [30]. Using the empirical relationship between stretching frequency and bond dissociation energy proposed by Zavitsas [31], we may estimate the bond energy for $\alpha_3\text{-CO}$ to be in the range 4.3 - 6.7 eV, easily accessible by excimer laser photon energies. Nonthermal photolysis of adsorbed molecules has also recently been reported for O_2 on Pd(111) [32] and NO on Si(111) 7×7 [33], which suggests that this may be a quite general phenomenon [34].

A complete model for the photodeposition process, incorporating gas-phase and surface-phase reactions, which accounts successfully for the dependence of film growth rate and carbon/oxygen incorporation on laser fluence and wavelength, and substrate temperature and composition, has been developed. This model, and comparison with experimental measurements, will be described in detail in a forthcoming publication [35].

ACKNOWLEDGMENTS

This research was supported in part by the Air Force Office of Scientific Research (Contract F49620-86-C-0003) and the Digital Equipment Corporation. We thank S. Bellon for assistance with the initial experiments, and Dr. M. Kanal and J. Shorter for helpful discussions. We are grateful to J. Martin, E. Shaw, and Y. Lu, of the Cambridge Surface Facility for assistance with the analyses.

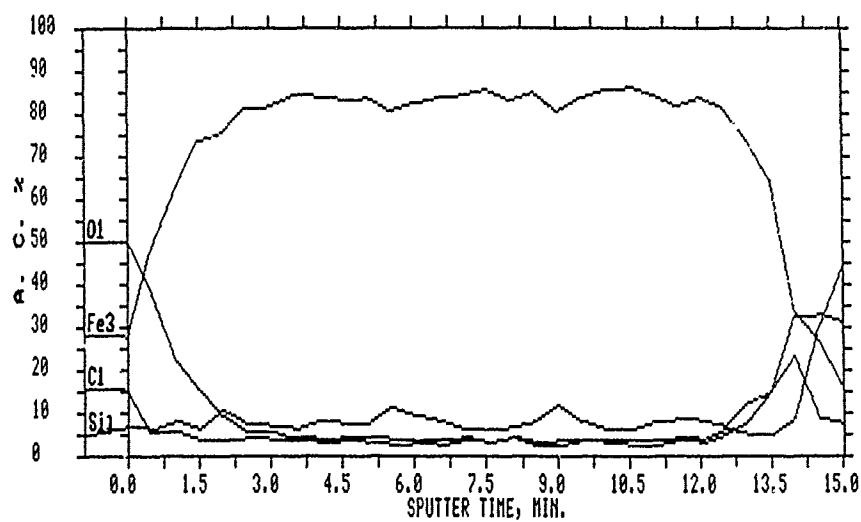


Figure 1. Profiling AES (PHI-660) scan of film deposited on silica by photolysis of $\text{Fe}(\text{CO})_5$ by KrF excimer laser (10 Hz, 300 sec exposure at $24 \text{ mJ}/\text{cm}^2$ per pulse). The C and O content in the bulk of the film are (2.0-2.5%) and (2.5-3.0)%, respectively.

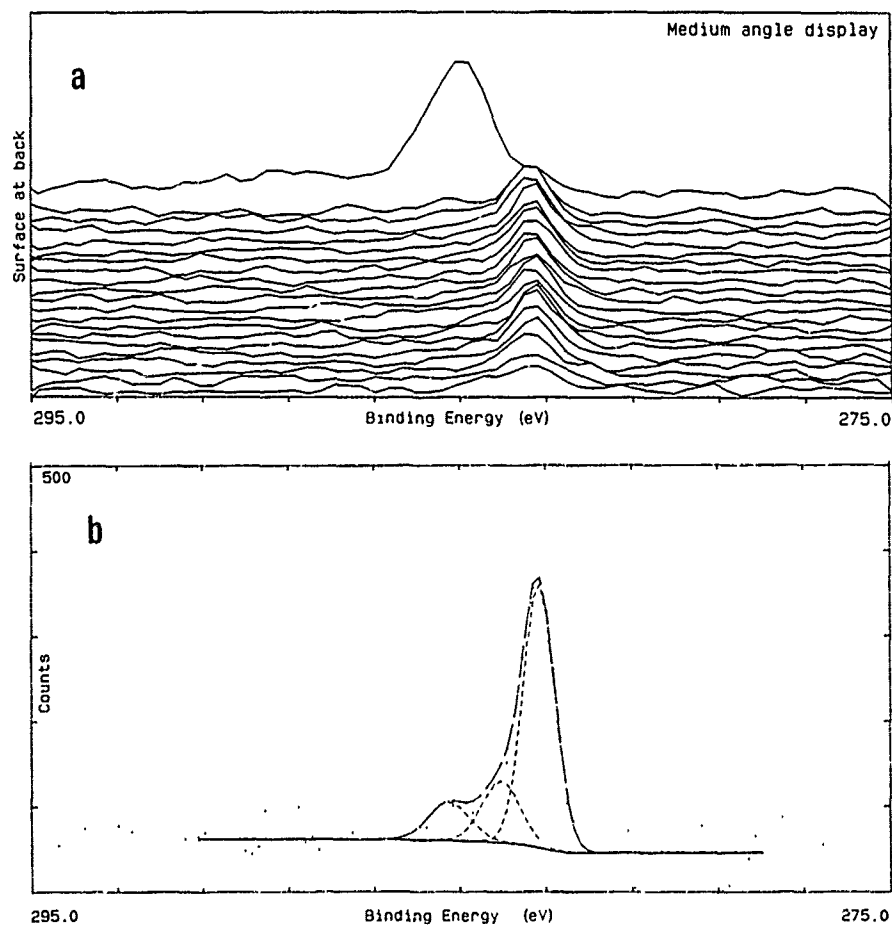


Figure 2. Profiling XPS (SSX-100) scan of carbon (1s) peak in film deposited from photolysis of $\text{Fe}(\text{CO})_5$ by ArF excimer laser (20 Hz, 500 sec exposure at 0.3 mJ/cm^2 per pulse). The C/Fe and O/Fe ratios in this film are each approximately 0.46. (a) C(1s) peak during sputter profile sequence. The top trace represents adventitious C introduced during sample transfer; the next 20 scans are taken after successive 98-sec sputtering intervals. The total film thickness is estimated as 2000 Å from the total sputtering time required to reach the Si(100) substrate. (b) Analyzed C(1s) spectrum at the 15th scan in (a). The major peak at 283.15 eV, constituting $\approx 70\%$ C, is assigned to carbidic C in iron; the remaining C(1s) intensity at higher binding energies is assigned to undissociated CO, either embedded in or at the surface of the iron film.

REFERENCES AND NOTES

1. D.J. Ehrlich, R.M. Osgood, Jr., and T.F. Deutsch, *J. Electrochem. Soc* **128**, 2039 (1981).
2. S.D. Allen and A.B. Tringubo, *J. Appl. Phys.* **54**, 1641 (1981).
3. R. Solanki, P.K. Boyer, and G.J. Collins, *Appl. Phys. Letts.* **41**, 1048 (1982).
4. J.R. Creighton, *J. Appl. Phys.* **59**, 410 (1986).
5. D.K. Flynn, J.I. Steinfeld, and D.S. Sethi, *J. Appl. Phys.* **59**, 3914 (1986).
6. N.S. Gluck, G.J. Wolga, C.E. Bartosch, W. Ho, and Z. Ying, *J. Appl. Phys.* **61**, 998 (1987).
7. N.S. Gluck, Z. Ying, C.E. Bartosch, and W. Ho, *J. Chem. Phys.* **86**, 4957 (1987).
8. R.L. Jackson and G.W. Tyndall, *J. Appl. Phys.* **64**, 2092 (1988).
9. P.J. Love, R.T. Loda, R.A. Rosenberg, A.K. Green, and V. Rehn, In Laser Assisted Deposition, Etching, and Doping, SPIE Proc. **459**, 25 (1984).
10. P.M. George and J.L. Beauchamp, *Thin Solid Films* **67**, L25 (1980).
- 11(a) J.S. Foord and R.B. Jackman, *Chem. Phys. Letts.* **112** 190 (1984);
(b) R.B. Jackman and J.S. Foord, *Surf. Science*, **209**, 151 (1989).
12. K.A. Singmaste F.A. Houle, and R.J. Wilson, *Appl. Phys. Letts.* **53**, 1048 (1988).
- 13(a) G. Nathanson, B. Gitlin, A.M. Rosan, and J.T. Yardley, *J. Chem. Phys.* **74**, 361 (1981);
(b) J.T. Yardley, R. Gitlin, G. Nathanson, and A.M. Rosan, *ibid*, 370.
14. I.M. Waller, H.F. Davis, and J.W. Hepburn, *J. Phys. Chem.* **91**, 506 (1987).
15. U. Ray, S.L. Brandow, G. Bandukwalla, B.K. Venkataraman, Z. Zhang, and M. Vernon, *J. Chem. Phys.* **89**, 4052 (1988).
16. B.K. Venkataraman, G. Bandukwalla, Z. Zhang, and M. Vernon, *J. Chem. Phys.* **90**, 5510 (1989).
17. F.G. Celii, P.P.M. Whitmore, and K.C. Janda, *Chem. Phys. Letts.* **138**, 257 (1987).
18. J.R. Swanson, C.M. Friend, and Y.J. Chabal, *J. Chem. Phys.* **87**, 5028 (1987).
19. F. Zaera, *J. Vac. Sci. Tech.* **A7**, 642 (1989).
20. M.T. Anthony, in Practical Surface Analysis. D. Briggs and M. Seah, Eds. (J. Wiley and Sons, New York, 1983, p. 431).
21. D.W. Moon, D.J. Dwyer, and S.L. Bernasek, *Surf. Science*, **163**, 215 (1985).

22. D. Burgess, Jr., P.C. Stair, and E. Weitz, J. Vac. Sci. Tech. A1, 1362 (1986).
23. P. Baeri and S.U. Camisano, in Laser Annealing of Semiconductors, J.M. Poate and J.W. Mayer, eds., (Academic Press, New York, 1982, p. 78).
24. J.-P. Lu, M.R. Albert, and S.L. Bernasek, Surf. Science 217, 55 (1989).
25. L.J. Whitman, B.A. Gurney, L.F. Richter, J.S. Villarubia, and W. Ho, J. Vac. Sci. Tech. A5, 538 (1987).
26. C. Benndorf, B. Krüger, and F. Thieme, Surf. Sci. 163, L675 (1985).
27. D.W. Moon, S.L. Bernasek, D.J. Dwyer, and J.L. Gland, J. Am. Chem. Soc. 107, 4364 (1985).
28. F. Zaera, E. Kellin, and J.L. Gland, Chem. Phys. Letts. 121, 464 (1985).
29. J.P. Fulmer, F. Zaera, and W.J. Tysoe, J. Chem. Phys. 87, 7265 (1987).
30. N.D. Shinn and T.E. Madey, Phys. Rev. Letts. 53, 2481 (1985).
31. A.A. Zavitsas, J. Phys. Chem. 91 5573 (1987).
32. X. Guo, L. Hanley, and J.T. Yates, Jr., J. Chem. Phys. 90 5200 (1989).
33. Z.C. Ying and W. Ho, J. Chem. Phys. 91, 2689 (1989).
34. In a recent XPS study of Cr films photodeposited from $\text{Cr}(\text{CO})_6$ at 248 nm, Nowak et al. [Applied Surf Sci., in press] have also found significant amounts of C and O in the carbide and oxide forms.
35. Xin Xu and J. I. Steinfeld, in preparation.

PHOTO-OXIDATION OF HYDROGENATED
AMORPHOUS SILICON-CARBON ALLOYS

P. John*, I.M. Odeh*, A. Qayyum and J.I.B. Wilson, Departments of
Physics and Chemistry*, Heriot-Watt University, Riccarton,
Edinburgh EH14 4AS, Scotland

ABSTRACT

Hydrogenated amorphous silicon-carbon alloys, a-Si:C:H, have been deposited as thin films ($d=0.1-0.5$ micron) on crystalline silicon substrates from a capacitively coupled rf discharge in silane-propane mixtures. Variations in the stoichiometry of the films were achieved by altering the ratio of SiH_4 to C_3H_8 flow rates at a substrate temperature in the range $240-260^\circ\text{C}$ and total pressure between 30-70 mtorr. The silicon to carbon ratios were established by X-ray photoelectron spectroscopy, XPS, and the hydrogen content and distribution by infra-red spectroscopy.

For films with a carbon fraction 0.15-0.30, the surfaces oxidise on illumination with the collimated output of a 150W xenon arc lamp. At the maximum light irradiance of 30mW cm^{-2} the measured surface temperature did not exceed 50°C . Photo-oxidation also occurred using the frequency doubled output (257nm) of an argon ion laser.

Films deposited on 7059 glass were photo-oxidised for increasing illumination periods until the absorption curves were unchanged. The increase in the band-gap was measured by conventional Tauc plots. The slopes, and thus Tauc B-values, were identical in the as-prepared and oxidised films.

Infra-red absorption measurements, using attenuated total reflectance, ATR, have been performed on the oxidised a-Si:C:H films. Inductive effects on the nearly degenerate symmetric and asymmetric Si-H stretching modes were correlated with the degree of oxidation. Additional vibrational modes at wavenumbers greater than 2100cm^{-1} have been assigned to SiH_x , $x=1$ or 2, groupings with contiguously bound oxygen. In contrast, the band envelope of the C-H stretching mode remains virtually unchanged when the films oxidise. Oxygen contents were determined by SIMS and laser ionisation microprobe analysis.

Films prepared with a lower carbon content undergo less rapid or negligible photo-oxidation. Hydrogenated amorphous silicon, a-Si:H, does not oxidise when illuminated with uv radiation at powers of the order of 50mW cm^{-2} .

INTRODUCTION

Hydrogenated amorphous silicon and the corresponding silicon-carbon alloys, a-Si:C:H, are technologically important materials. The latter has received increasing attention following its use as wide band-gap p-doped window layers in pin a-Si:H photovoltaic cells. Carbon incorporated into a-Si:C:H prepared by rf discharges is not randomly distributed throughout the network. Electron diffraction and EELS studies [1] indicate the preference for carbon to coordinate to four silicon atoms in dilute alloys. Current models for the structure of a-Si:C:H invoke a degree of ordering of carbon in the framework. The first comprises stoichiometric, but not necessarily crystalline, domains of SiC embedded in amorphous silicon. An alternative description involves a tetrahedral framework where each carbon atom is coordinated to silicon.

The surface structure and chemistry is equally complex. An examination of the surface layers of a-Si:C:H by XPS [2] shows that atmospheric oxidation is facile but that the oxide thickness is self limiting. Differences in the film morphology could influence the surface reactivity as in a-Si:H itself. In particular, the conditions of film growth changes the reactivity of the surface layers to atmospheric oxidation. Certainly films prepared by SiH_4/CH_4 discharges in a H_2 diluent are less reactive towards oxygen [3]. Concomitant structural differences in the bulk material occur especially the hydrogen content and its distribution within CH_x groupings, as a consequence of the presence of H_2 in the plasma.

Amorphous silicon-carbon alloys prepared from $\text{SiH}_4/\text{C}_3\text{H}_8$ mixtures undergo photo-oxidation [4] on uv illumination at low powers. At the irradiances used the surface temperatures do not exceed ca. 50°C . Evidence from the spatial resolution of the process, low surface temperatures and the dependence of the oxidation rate on carbon content demonstrates that the phenomena is not thermal in character. The irreversible photo-structural change has been studied by ATR infr-red spectroscopy, XPS, SIMS, laser ionisation microprobe analysis and silicon edge EXAFS [5].

The conversion of a-Si:C:H into an insulator has been utilised by photochemically fabricating the gate electrodes in a-Si:H field effect transistors [6]. Further applications in

electronics and optoelectronics are envisaged. The present study reports the changes in the optical absorption of thin a-Si:C:H films subject to uv illumination.

EXPERIMENTAL

Thin films (approx. 150 Å) of a-Si:C:H were deposited on optically polished (100) crystalline silicon, silicon trapezoids or Corning 7059 glass substrates in a capacitively coupled rf (13.56MHz) discharge reactor. The substrates were attached to the upper grounded electrode and independently heated. Electronic grade gases, SiH₄ and C₃H₈, were admitted to a stainless steel chamber via mass flow controllers. The total pressure in the plasma chamber was measured with a Baratron capacitance manometer. During deposition the pressure in the reactor remained constant and the gases were vented via a mechanical rotary pump. Prior to deposition the chamber was purged with argon and evacuated to less than 10⁻⁶ torr in several consecutive cycles with a Fomblin filled diffusion pump. Residual gas analysis was performed with a quadrupole mass spectrometer (Hiden Analytical) independently pumped to less than 10⁻⁹ torr with a turbomolecular pump. Gases from the plasma chamber were sampled through a needle valve.

Films were illuminated orthogonally by the collimated output of a 150W Xe-arc lamp. Irradiation was carried out either directly or through a polycarbonate or glass filters to remove wavelengths below ca. 300nm. Thermocouples attached to the front face of the wafer indicated temperatures below 50°C even at the highest illumination powers. Unfiltered light intensities from the lamp (Wotan) were measured to be 30mW cm⁻² at the film surface. Film thicknesses of 100-150 Å were deposited on 7059 glass substrates. Absorption measurements were made on a Shimadzu spectrophotometer. The band-gap of a-Si:C:H alloys, prepared from SiH₄/C₃H₈ mixtures, are empirically related [7] to the carbon content via $E_g = E_g^0 + ax_c$ where x_c is the carbon content below 0.6. Standard Tauc plots were linear for values of the absorption coefficient greater than 10⁴. Temperature profiles in continuously irradiated films can be estimated from the heat flow equations described by Lax. The maximum temperature rise at the surface, T_m , of an infinite solid is given by equation(1). This equation is valid for the case where the beam radius, w , is

greater than the absorption length, α^{-1} , and that T_m is sufficiently small that the temperature dependence of α and the thermal

$$T_m = P_o (2\pi^{1/2} Kw)^{-1} \quad (1)$$

conductivity, K , can be ignored. For an incident power, P_o , of 50mW and $w=2\text{mm}$ then T_m is approx. 0.05K for crystalline silicon ($K=145\text{W m}^{-1}\text{K}^{-1}$). The thermal conductivity of a-Si:H and its alloys depend on the composition of the sample but lies in the range $0.7\text{--}30\text{W m}^{-1}\text{K}^{-1}$. The lower limit is a factor of 2-3 smaller than that of a-SiO₂ or a-C:H. Adopting $K=0.7\text{W m}^{-1}\text{K}^{-1}$ then T_m is less than 10K for $P_o=50\text{mW}$ at 257nm. According to the Einstein-Smoluchowski equation, the rms diffusion length is smaller by x2-3 orders of magnitude than the observed oxide thickness produced on illumination. Evidently, a thermal mechanism can be excluded from consideration.

The a-Si:C:H films for ATR infra-red measurements were deposited directly onto one side of a silicon trapezoid. A single pass configuration was employed with a 45° angle of incidence. With this configuration, the effective sample thickness is approx. 50d where d is the film thickness. Infra-red measurements were made with a ratio-recording spectrometer (Perkin-Elmer 580) equipped with a microcomputer for data acquisition.

RESULTS

Absorption Measurements

Figure 1 shows the dependence of the absorption coefficient prior to and after illumination with the collimated output of a 200W Xe-arc lamp. The corresponding Tauc plots are shown in Figure 2. The shift in E_g is approx. 0.5eV when the films are completely oxidised. At this point the value of E_g corresponds closely to that in a-SiO₂. It is evident from the data in Figure 2 that the Tauc B-values are similar for the original and photo-oxidised material.

Infra-red Studies

Figure 3 illustrates a typical infra-red ATR(45°) spectrum

of an a-Si:C:H film with $d=0.1$ micron deposited on a silicon trapezoid. Radiation introduced through the entrance aperture of the trapezoid propagated via a single pass to the exit aperture

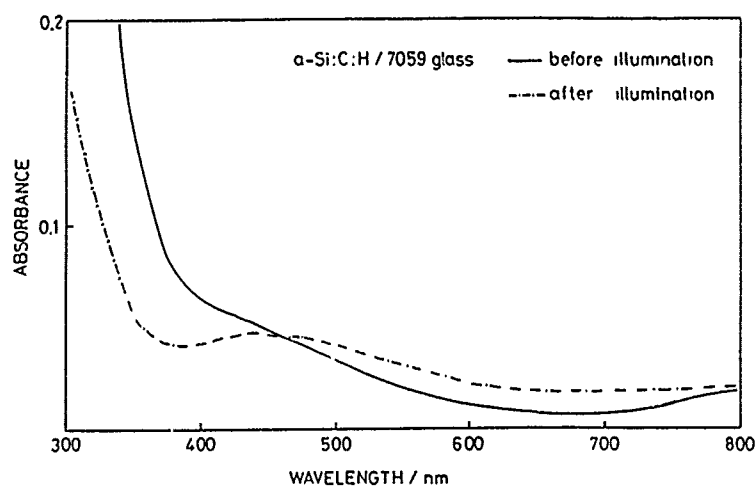


Fig.1. Absorption spectrum of thin a-Si:C:H film ($d \sim 200\text{\AA}$) before and after illumination for a period of 120 min.

Due to absorption in the silicon, the wavenumber range was limited to $4000\text{--}1400\text{cm}^{-1}$. The stretching mode of isolated SiH occurs near 2000cm^{-1} . Absorption bands in the $2100\text{--}2000\text{cm}^{-1}$ region are assigned to the virtually degenerate symmetric and asymmetric SiH stretching modes in SiH_2 groupings. As shown in Figure 4, an intense band was observed in the SiH stretching

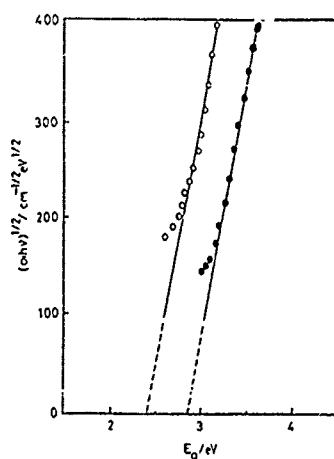


Fig.2. Tauc plot
O, before illumination;
●, after illumination.

region due to SiH_x groups attached both to silicon and carbon

atoms. The structured band in the $3000\text{--}2800\text{cm}^{-1}$ region, as illustrated in Figure 4, is due to the fundamental stretching modes of CH_x , $x=1\text{--}3$, groupings. A comparison of the spectral data with

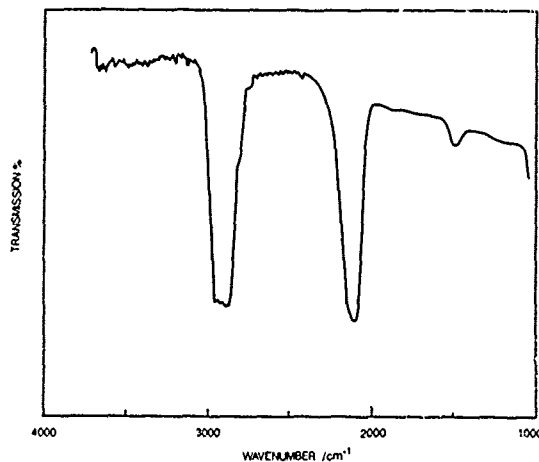


Fig.3. ATR infrared spectrum of an a-Si:C:H film.

the contour produced by the superposition of the five stretching modes associated with the $\text{sp}^3 \text{CH}_x$ groupings show that each group is present in the films. As shown in Figure 4 spectral changes were evident after the a-Si:C:H films were illuminated in air at room temperature. The Si-H stretching band exhibited a shoulder at higher wavenumbers following irradiation. Prolonged illumination produced a broad absorption which extended to almost

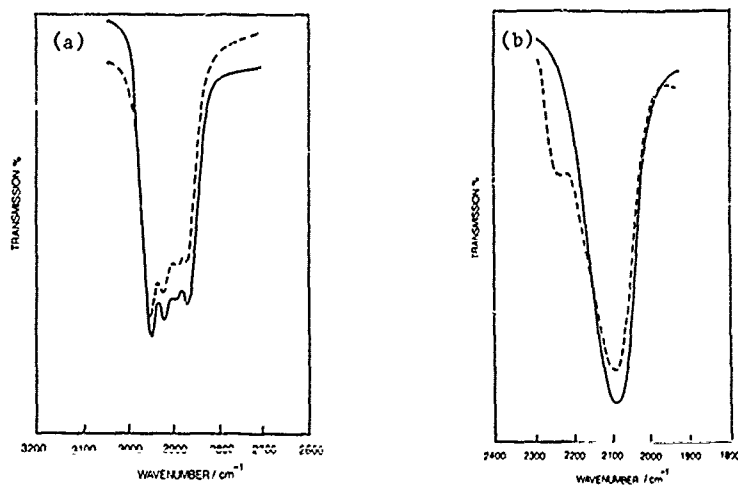


Fig.4(a) Carbon-hydrogen and (b) silicon-hydrogen stretching modes, — before illumination; ---- after illumination. 2300cm^{-1} . The unstructured band is assigned to the inductive

infra-red shifts caused by selective oxidation of SiH or SiH₂ groups which engenders additional modes extending to ca. 2300cm⁻¹. The band envelope of the C-H stretching modes remained virtually unchanged upon oxidation.

CONCLUSIONS

The photo-oxidation of thin films of a-Si:C:H may be monitored by absorption spectroscopy. An increase in the band-gap of ca. 0.5eV was observed when a thin film on 7059 glass was fully oxidised. The negligible effect on the Tauc-B values suggest that there is little added disorder caused by the oxidation.

ACKNOWLEDGMENTS

The authors wish to thank the Government of Pakistan for the award of a studentship to AQ and The British Council for financial support to IMO.

REFERENCES

1. Y. Tawada, H. Ikamoto and Y. Hamakawa, Appl. Phys. Lett. 39, 237(1981).
2. J. Tafto and F.J. Kampas, Appl. Phys. Lett. 46, 949(1985).
3. Y. Katayama, K. Usami and T. Shimada, Phil. Mag. B 43, 283(1981)
4. S.E. Hicks, A.G. Fitzgerald, S.H. Baker and T.J. Dines, Phil. Mag. B submitted for publication.
5. P. John, A. Qayyum and J.I.B. Wilson, Elect. Lett. 25, 930(1989)
6. P. John, I.M. Odeh, A. Qayyum and J.I.B. Wilson, in preparation.
7. J.I.B. Wilson, A. Qayyum, S. Al-Sabbagh, M. Jubber and P. John Proc. Int. Conf. Amorph. and Liquid Semiconductors, N. Carolina 1989.
8. A. Qayyum, Ph.D. thesis, Heriot-Watt University, Edinburgh 1989.

METAL DEPOSITION WITH INCOHERENT EXCIMER RADIATION

Hilmar Esrom and Ulrich Kogelschatz*

Asea Brown Boveri AG

Corporate Research Heidelberg, D-6900 Heidelberg, FRG

*Corporate Research Baden, CH-5405 Baden, Switzerland

ABSTRACT

VUV light-induced decomposition of palladium acetate films was performed by using a new incoherent excimer source. With pure xenon this excimer source emits radiation peaking at a wavelength of 172 nm. We investigated mainly the palladium deposition from spin-on palladium acetate films on aluminum oxide substrates. By using EMP we determined the palladium thickness as a function of UV intensity and exposure time. A remarkable temperature effect of the photolytic deposition process was observed also in a temperature range in which no thermal decomposition is possible. The exposure of spin-on palladium acetate films on ceramic substrates was also accomplished through metal contact masks. Patterned palladium films were reinforced by electroless copper and nickel plating processes [1]. The obtained structures had the same high edge quality as those produced by using excimer lasers [2].

INTRODUCTION

In the past several years photo-induced deposition techniques have emerged as a new important area of thin film technology. In particular, photochemical vapor deposition (photo-CVD) techniques have been studied extensively [3]. This method has potential applications in semiconductor processing and device fabrication. Utilizing photo-CVD high quality thin films of metals, dielectrics, and semiconductors have been produced with highly resolved structures $< 1 \mu\text{m}$. However, it is very difficult to metallize large substrate surface areas ($\sim \text{mm}^2$ up to some m^2) with film thicknesses $\gg 1 \mu\text{m}$ using light-induced deposition methods only. Many applications in the fields of hybrid circuit technology, sensors, and EMI shielding require large area processing. For these purposes, the combination of light-induced deposition techniques with conventional deposition methods is very well suited [1,2,4-7]. The hybrid deposition process is a two-step method. The first step is the photo-induced deposition and patterning of thin catalysts on arbitrary substrate surfaces. The second step is the amplification of the prenucleated areas in conventional electroless metallizing baths. For the first step, the use of thin solid films as source for deposition of the catalysts has many advantages compared with deposition from the gas phase [8-13]. The decomposition of the spin-on metalorganic films can be performed in air or inert gases. No specialized reactors and gas transport or distribution systems are needed. In most cases the pyrolytic decomposition of the spin-on films was performed by using CO_2 lasers and Ar^+ lasers. The application of deposition methods to plastics (polyimide, polyamide, etc.) or other thermally fragile substrates requires low temperature processing e.g. the photolytic activation or

passivation of substrate surfaces followed by electroless metal deposition processes. D.J. Sharp et al. [15-19] reported on the UV light-induced inhibition of electroless copper plating using a low pressure Hg lamp. This low temperature technique is a three step method : latent image formation by photo-oxidation of a sensitizer, activation in a solution and electroless metallization. Recently, we investigated a two-step deposition method by using an excimer laser in the first step for the photo-induced decomposition of thin spin-on palladium acetate films [1,2]. The deposited thin palladium films were successfully used as a catalyst for electroless copper and nickel plating. With one laser pulse it is possible to deposit large areas and features with high resolution simultaneously. Especially remarkable is the sharpness of the edges of the structures (Fig.1) without particles in the surrounding area which are often present at lines written with an Ar⁺ laser [13]. The investigated two-step deposition method using an excimer laser with metal contact masks leads to structured copper coatings on Al₂O₃ substrates with excellent adhesion > 30 N/mm². The main aim of this work was to study the new two-step deposition technique by using a new incoherent excimer source for the decomposition of palladium acetate films instead of an expensive excimer laser.

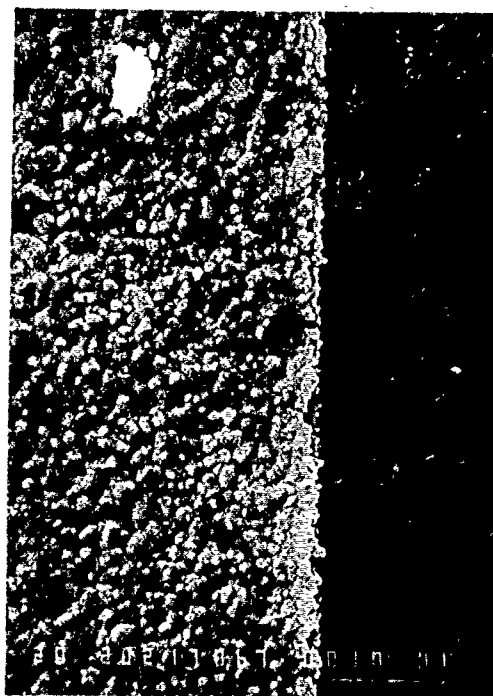


Fig. 1 Typical edge quality of structures achieved by the two step deposition method by using UV excimer sources; scale: 10 μ m

EXPERIMENT

Incoherent Excimer Source

For the photo deposition experiments we used incoherent excimer radiation from a dielectric-barrier discharge (silent discharge) operating in pure xenon. The discharge was initiated in an annular gap between coaxial quartz tubes which was filled with xenon at a pressure of 600 mbar. In the performed experiments the outer quartz tube had a diameter of 4 cm and an active length of 15 cm. The radial width of the annular discharge gap was about 0.8 cm. Inside the inner quartz tube an aluminum foil served as one electrode while the other electrode was formed by a wire mesh around the outer quartz tube. More details about this special UV source can be found in references [20-23]. The discharge was operated with a power supply delivering a sinusoidal voltage of about 20 kV peak value at about 15 kHz. Up to 500 W electrical power was fed into the discharge which corresponded to an electrical power density of $\sim 2.5 \text{ W/cm}^2$ of electrode area. With an assumed UV efficiency of 5% we estimate the UV output to reach 125 mW/cm^2 . In such silent discharge configurations [20-23] the current flows in a large number of statistically distributed microdischarges. Inside the microdischarge filaments xenon atoms can be excited by electrons and, under certain conditions, can form Xe_2^* dimers. The unstable Xe_2^* dimers decay within nanoseconds and give off their binding energy in the form of vacuum UV radiation centered at 172 nm and having a half width of about 12 nm. There is practically no other radiation coming from this discharge in the wavelength region between 100 nm and 800 nm. The energetic UV radiation (7.2 eV) is very effective for the described deposition process. Some special properties of this UV source may be of importance for the photo deposition process. Like every silent discharge the xenon UV source has two "active" phases during each cycle of the feeding voltage in which bursts of UV pulses are emitted [22]. Since the individual light pulses are very short (10 ns) their peak intensity is by orders of magnitude higher than the quoted average intensity. The 172 nm radiation is completely absorbed in oxygen over a short distance leading to ozone formation if the UV source is operated in open air. For our deposition experiments the UV source was operated in a reactor (Fig. 2) that could be evacuated and flooded with nitrogen or argon. The distance between sample and UV source was about 1 cm and typical exposure times reached several minutes. Without a special cleaning and pretreatment, palladium acetate films were spin-coated onto rough Al_2O_3 substrates (Hoechst Ceram Tec AG) usually used in hybrid circuit techniques. The palladium acetate layers were irradiated with VUV light. The thickness and the morphology of the films were determined by the electron microprobe (EMP) (JEOL JXA-733 ELECTRON PROBE). For the thickness measurement we calibrated the EMP with an interference microscope (Carl Zeiss). For this purpose we used various film thicknesses on glass substrates. The purity of the palladium films was investigated with ESCA.

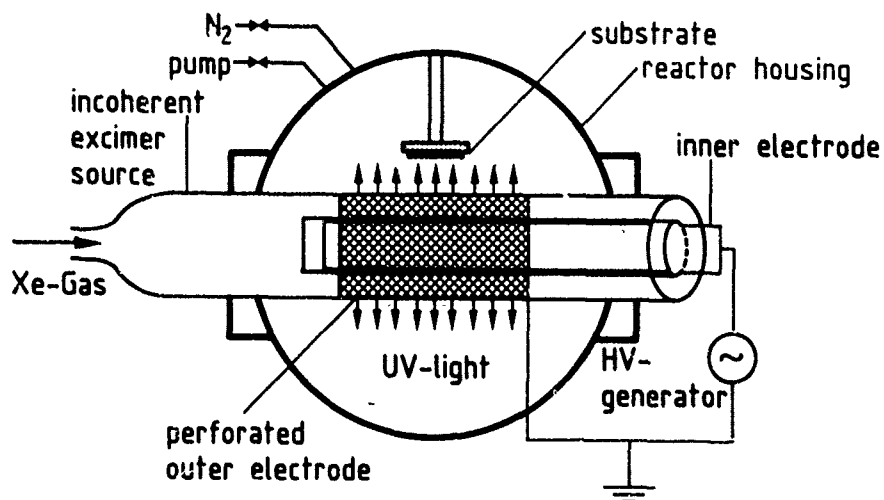


Fig. 2 Experimental set-up of the UV exposure reactor

RESULTS

Deposition Experiments

The absorption properties of the palladium acetate films were obtained with a quartz (suprasil) plate dip-coated in a solution of 1 g palladium acetate in 180 ml chloroform. The transmission curve in Fig. 3 was measured with a vacuum

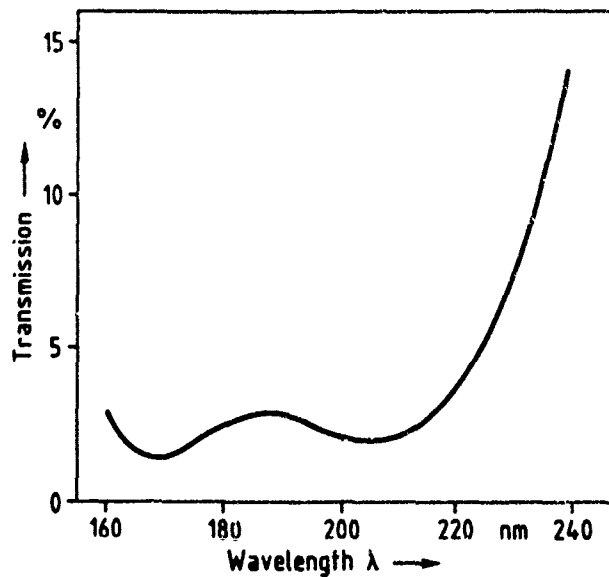


Fig. 3 Transmission of a dip-coated palladium acetate film

monochromator and a deuterium lamp. It is normalized by the transmission of an uncoated quartz plate. Strong absorption is observed at wavelengths below 230 nm. The wavelength of the xenon excimer source (172 nm) coincides with the minimum of the transmission curve. In the performed deposition experiments we investigated mainly the decomposition of a 800 Å thick spin-on palladium acetate film on rough Al_2O_3 . The spin-on films were prepared from palladium(II)acetate dissolved in chloroform using a concentration of about 0.15 mole/l. After UV light exposure, the unexposed parts of the palladium acetate film were removed by washing them away using chloroform. With EMP we measured the film thickness in the grain boundaries and on the Al_2O_3 grains. In these cases the electron beam diameter was about 2 μm . To achieve a mean film thickness we used a scanning area of about $\sim 10^{-3} \text{ mm}^2$. We found most of the palladium acetate in the grain boundaries. Typically for a mean thickness of about 800 Å we estimated in the grain boundaries a thickness of about 1400 Å, however on the grains only ~ 40 Å. In first experiments we investigated the influence of the UV light intensity on the deposition rate. Fig. 4 shows the mean palladium thickness as a function of the electrical power P_{el} at an exposure time of 10 min. The increase of the power from 70 W to 450 W leads to an essentially tenfold increase in the palladium thickness. One also observes that in the low power region up to about 250 W the thickness depends linearly on the electrical power of the UV source. Fig. 5 shows the mean palladium thickness as a function of the exposure time at $P_{\text{el}} = 400 \text{ W}$. At short exposure times of ~ 3 min the palladium thickness is estimated to be ~ 5 Å. At exposure times < 12 min the deposition rate amounts to ~ 4 Å/min. The complete decomposition of the palladium acetate film is apparently reached at ~ 15 min leading to the final mean palladium thickness of ~ 55 Å. In this case we estimated in the grain boundaries ~ 85 Å and on the

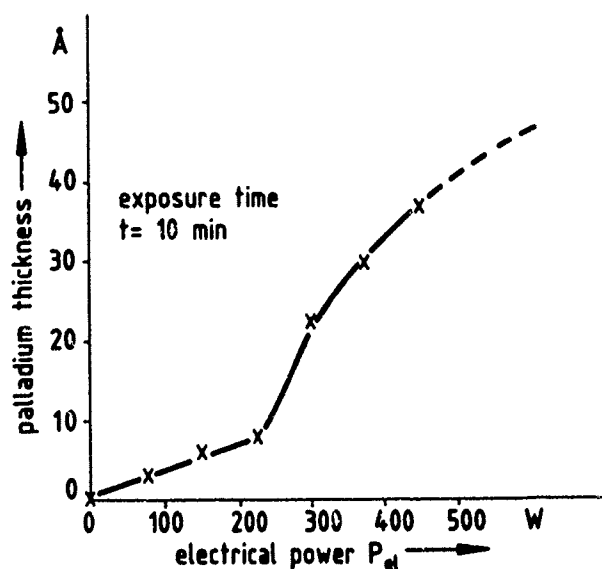


Fig. 4 Palladium thickness as a function of the electrical power P_{el} ; initial palladium acetate thickness ~ 800 Å

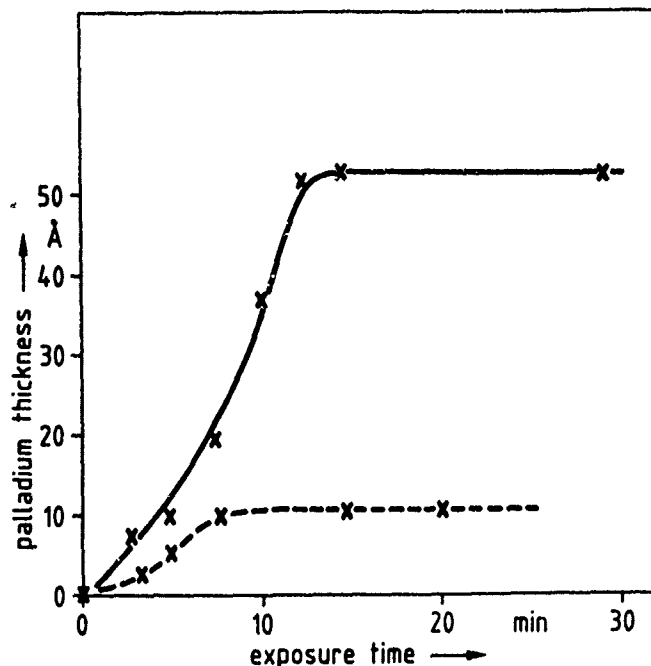


Fig. 5 Palladium thickness as a function of the exposure time: exposure of a 800 Å (—) and a 100 Å (---) thick palladium acetate in N_2 .

grains a thickness of about 12 Å. The curve with the broken line describes the deposition of palladium from a thinner palladium acetate film (~ 100 Å) at different exposure times. In this case the complete decomposition yields a ~ 10 Å thick palladium film.

The effect of the substrate temperature on the deposition rate was examined by heating the substrate holder. At $P_{el} = 300$ W we determined the decomposition times t at different substrate temperatures T . As can be seen in Fig. 6 the temperature has a remarkable influence on the deposition rate (dashed curve). Such strong temperature effects on the decomposition were also found by Ye and Hunsberger [24] in the case of the UV light-induced decomposition of ammonium tetrachloroaurate/nitrocellulose (s. Fig. 6).

Morphology and Purity of the Deposited Palladium Films

Interesting differences were found between palladium films deposited with the incoherent Xe_2^* excimer source at $\lambda = 172$ nm and with an ArF^* excimer laser at $\lambda = 193$ nm. In the first case as shown in Fig. 7 we obtained smooth palladium films following the roughness of the Al_2O_3 substrate (Hoechst Ceram Tec, Rubalit 710). Excimer laser-induced deposition, on the other hand resulted in discontinuous palladium layers with nuclei of about ~ 0.1 μm

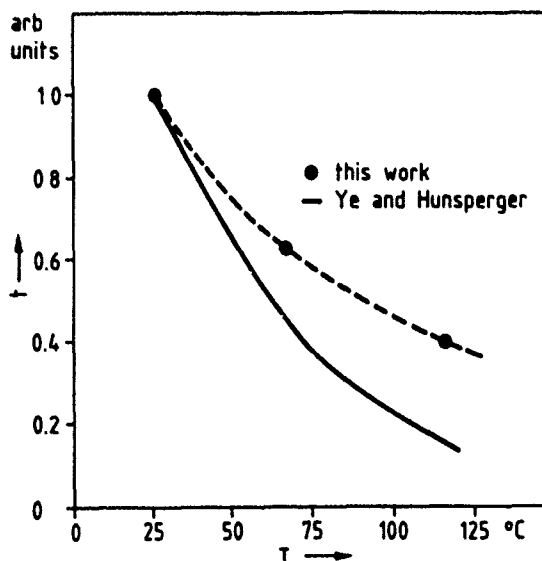


Fig. 6 Influence of the substrate temperature $T(^{\circ}\text{C})$ on the decomposition time t

average diameter (Fig. 8). Similar results were obtained with smooth surfaces of quartz and silicon. Deposition with the incoherent excimer source resulted in smooth films of almost specular reflection. The SEM picture in Fig. 9 shows only the fine structure of the quartz surface in the deposited films. Again, excimer laser-induced deposition resulted in discontinuous palladium layers (Fig. 10), which are characteristic for decomposition of the palladium acetate film with UV laser pulses independent of the wavelength and the initial palladium acetate film thickness [25]. Using excimer laser pulses, the fast energy coupling into the palladium acetate film leads to a thermal component so that discontinuous palladium films are produced independent of the special excimer laser parameters [25]. As far as the purity of the palladium layers is concerned we determined with ESCA measurements about 30 atomic % carbon in the excimer laser induced-films and only 15 atomic % carbon in the palladium films deposited with the incoherent VUV source. In both cases, no oxygen could be detected in the palladium layers.

SUMMARY

We have demonstrated, that the new incoherent source of Xe_2^* excimer radiation is well suited for the new low temperature, two-step deposition method. At room temperature, the VUV light exposure at 172 nm leads to decomposition of spin-on palladium acetate films on various substrate surfaces. The deposited palladium layers are effective catalysts for electroless copper and nickel plating processes. Structuring of the palladium films can be achieved with metal contact masks or quartz masks near the surface. With one UV light exposure through masks metallization on large areas and features with high resolution can be performed simultaneously [1]. Compared with the

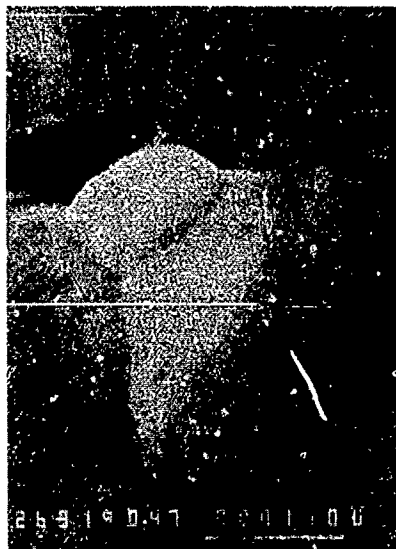


Fig. 7 Smooth palladium film on a rough Al_2O_3 substrate deposited with the incoherent excimer source ($\lambda = 172$ nm; exposure time 15 min); scale: 1 μm

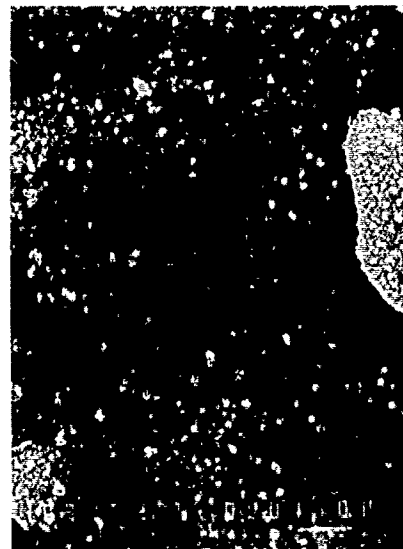


Fig. 8 Discontinuous palladium layer on a rough Al_2O_3 substrate deposited with an excimer laser ($\lambda = 193$ nm; fluence = 50 mJ/cm^2 ; 5 pulses); scale: 1 μm

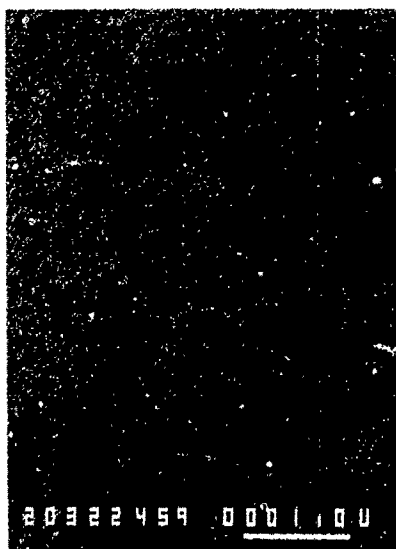


Fig. 9 Smooth palladium film on a quartz substrate deposited with the incoherent excimer source ($\lambda = 172$ nm; exposure time 15 min); scale: 1 μm

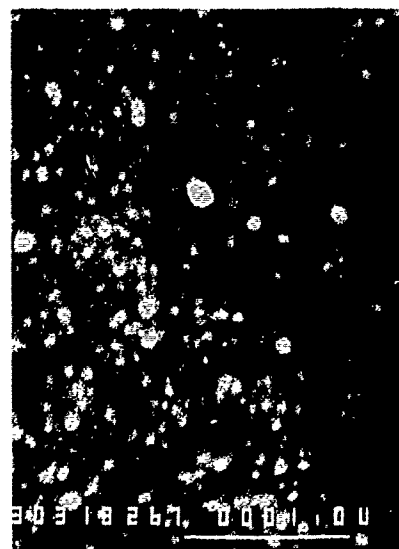


Fig. 10 Discontinuous palladium layer on a quartz substrate deposited with an excimer laser ($\lambda = 193$ nm; fluence = 50 mJ/cm^2 ; 5 pulses); scale: 1 μm

results achieved by an excimer laser we observed considerable differences in the mechanism of the decomposition process of palladium acetate films and in the morphology of the deposited palladium films. We found that the decomposition of palladium acetate films is even possible at low UV intensities of the Xe_2^* excimer source. From all achieved results we conclude that the decomposition process is mainly photolytical. Apparently, the decomposition of palladium acetate films with the incoherent excimer source results in very smooth palladium films independent of the initial palladium acetate film thickness. The incoherent Xe_2^* excimer source used in this work can be used for photo-induced CVD experiments as well. First experiments with this VUV source in a stagnation flow reactor [26] show that SiO_2 from SiH_4 and O_2 can be deposited at low substrate temperature $\sim 200^\circ\text{C}$, at which no thermal CVD is possible. The simple, efficient and reliable incoherent source of VUV radiation utilizing excimer formation in silent discharges compares favourably with excimer lasers in several applications. Especially in cases where molecules show strong absorption only in the deep UV potent VUV sources are required to initiate photodissociation. Because of the variable geometry of this source [21] large area processing with a high throughput is possible.

ACKNOWLEDGMENT

The authors are indebted to G. Wahl for the initiation and continuous support of this work. They also would like to thank U. Feller, B. Heiliger and J. Demny for EMP and ESCA investigations and R. Löbe for his assistance in performing the experiments.

REFERENCES

1. H. Esrom, G. Wahl, and U. Kogelschatz, *Journal De Physique, Colloque C5*, 719 (1989)
2. H. Esrom, G. Wahl, and M. Stuke, *Mat. Res. Soc. Symp. Proc.* Vol. 131, 581 (1989)
3. I. W. Boyd, *J. Phys. D: Appl. Phys.* 21, S23 (1988)
4. R. C. Sausa, A. Gupta, and J. R. White, *J. Electrochem. Soc.*, Vol. 134, No. 11, 2707 (1987)
5. H. S. Cole, Y. S. Liu, J. W. Rose, R. Guida, L. M. Levinson and H. R. Philipp, in Laser Processes For Microelectronic Applications, Vol. 88-10, of the Proceedings of the Electrochemical Society, edited by J. J. Ritsko, D. J. Ehrlich, and M. Kashiwagi (Pennington, NJ, 1988)
6. O. Gottsleben and M. Stuke, *Appl. Phys. Lett.* 52(26), 2230 (1988)
7. R. R. Thomas and J. M. Park, *J. Electrochem. Soc.*, Vol. 136, No. 6, 1661 (1989)
8. G. J. Fisanick, M. E. Gross, J. B. Hopkins, M. D. Fennell, K. J. Schnoes, and A. Katzir, *J. Appl. Phys.* 57(4), 1139 (1985)

9. G.J.Fisanick, J.B.Hopkins, M.E.Gross, M.D.Fennell, and K.J.Schnoes, Appl.Phys.Lett.46(12),1184(1985)
10. M.E.Gross, G.J.Fisanick, P.K.Gallagher, K.J.Schnoes, and M.D.Fennell, Appl.Phys.Lett.47(9),923(1985)
11. A.Auerbach, Appl.Phys.Lett.47(7),669(1985)
12. M.E.Gross, A.Appelbaum, and K.J.Schnoes, J.Appl.Phys.60(2),529(1986)
13. M.E.Gross, A.Appelbaum, and P.K.Gallagher, J.Appl.Phys.61(4),1628(1987)
14. A.Gupta and R.Jagannathan, Appl.Phys.Lett.51(26), 2254(1987)
15. D.J.Sharp, Abs. 262, p. 651, Electrochem.Soc.Extended Abstracts, Spring Meeting, New York, May 4-9, 1969
16. D.J.Sharp, J.F.Henrickson, J.F.D'Amico, and J.T.Kenney, Abs. 136, p. 367, Electrochem.Soc. Fall Meeting, Detroit, Mich., Oct. 5-9, 1969
17. D.J.Sharp, J.F.Henrickson, J.F.D'Amico, and J.T.Kenney, 23rd Annual Conference, Photographic Science and Engineering, New York, N.Y., May 1970
18. D.J.Sharp, Plating, 58, 786(1971)
19. J.F.D'Amico, M.A.De Angelo, J.F.Henrickson, J.T.Kenney, and D.J.Sharp, J.Electrochem.Soc., Vol. 118, No. 10, 1695(1971)
20. B.Eliasson, U.Kogelschatz, and H.J.Stein, Europ. Photochem.Ass. Newsletter, No. 32, 29(1988)
21. B.Eliasson and U.Kogelschatz, Appl.Phys.B.46, 299(1988)
22. B.Eliasson and U.Kogelschatz, Proc. IX Int. Conf. on Gas Discharges and their Applications, Venice 1988, pp.709
23. B.Eliasson and U.Kogelschatz, Proc. Wasser Berlin 1989, Ozone + UV in the treatment of water and other liquids, Berlin 1989, W.J.Masschelein, ed., pp.IV-6-1 to IV-6-11
24. Y.Ye and R.G.Hunsperger, Appl.Phys.Lett., Vol. 51, No. 25, 2136(1987)
25. H.Esrom, G.Wahl, and M.Stuke, to be published in Chemtronics (1989)4
26. G.Wahl and R.Weber, private communication (1989)

PART IV

E-beam and Ion Beam Processing

ELECTRONIC EXCITATION-INDUCED SURFACE CHEMISTRY AND ELECTRON-BEAM-ASSISTED CHEMICAL VAPOR DEPOSITION

F. BOZSO and Ph. AVOURIS

IBM Research Division, T. J. Watson Research Center
P. O. Box 218, Yorktown Heights, N.Y. 10598

ABSTRACT

Selective area deposition of thin films and surface structures with precise control over their composition is possible in UHV by using low energy electron beams to induce electronic excitations in adsorbed molecular layers. Upon electron impact, adsorbed/co-adsorbed molecules decompose into reactive species, resulting in film growth. The composition of the film reflects that of the adsorbed molecular layer, which at cryogenic temperatures can sensitively be controlled by the partial pressure of the reactant gases. We present results of detailed studies of adsorption, thermal and electron-beam-induced dissociation of disilane and ammonia on silicon. We show that by proper choice of temperature, gas phase composition and electron beam, amorphous silicon, silicon nitride, oxide, silicon oxinitride films can be grown with nearly monolayer thickness resolution.

INTRODUCTION

There has been an increasing interest in selective area chemical vapor deposition (CVD) for direct patterning with precise control over spatial growth and material composition. Direct patterning offers an advantage in mask repair, custom wiring, fabrication of nanometer scale material structures for faster and novel electronic devices as well as for fundamental research purposes [1,2]. The small dimensions of such device structures, and their abruptly and unconventionally changing material compositions, require a high level of spatial and kinetic control over the surface chemical reactions, which are involved in the materials' growth and modification.

These requirements exclude high temperature processes based on thermally activated chemical reactions. Inducing surface reactions by directed energetic beams (electrons, ions, photons), however, can provide for both spatial and kinetic control in microfabrication processes.

Energetic electrons, ions, photons are known to cause fragmentation and the desorption of adsorbed molecules or fragments of them, by inducing electronic transitions to dissociative states [3]. The surface fragment species after such excitations are mostly of highly reactive radical character. This radicals readily react with the substrate and with other radical or molecular species in the adsorbed layer. The formation of such reactive surface species provides a basis for controlled non-thermal selective area chemical vapor deposition.

The spatial control referred to, implies the capability of turning on and off the

above reactions, i.e. the capability to induce desired electronic transitions at selected areas of the substrate surface, as required by some predetermined pattern.

The kinetic control implies the capability of adjusting reaction rates in a usually multi-component surface layer either by selective electronic excitation to activate particular reaction paths, or by controlling the concentration of precursor molecules in the adsorbate layer. Spatial and kinetic control together enable the growth of material structures with desired geometry, composition, material distribution and thickness.

In this paper we summarise the results of detailed studies, which show that by forming adsorbed molecular layers at cryogenic temperatures ($\approx 100\text{K}$) and by using low-energy electron-beam excitation to induce surface reactions, both spatial and kinetic control are obtained for selected area growth of thin films and surface structures in ultra high vacuum systems.

RESULTS AND DISCUSSION

1. The reactivity of Si(100)-2x1 and Si(111)-7x7 surfaces

In chemical vapor deposition process, precursor molecules react at the substrate surface, followed by formation of new bonds with the substrate and other surface species. The critical step is usually the former, i.e. dissociation, which in gas phase may require considerable activation energy. At silicon surfaces, dissociation of molecules has been observed at rather low temperatures, indicating the need of very low activation energy [4,5,6,7,8]. The microscopic mechanism of the dissociation of molecules on semiconductor surfaces is not in general understood. In broad terms dissociation is possible as a result of charge transfer processes, in which bonding levels get depopulated and/or antibonding levels get populated. The latter is possible by direct charge transfer from highest lying substrate levels, or via excitations from deeper lying adsorbate bonding levels or substrate levels. Concerted surface reactions involve simultaneous bond-formation and bond-dissociation processes and are characterised by low activation energies. Semiconductor surfaces with low binding-energy dangling bond states, therefore, have the potential of high reactivity.

Adsorption and dissociation of disilane (Si_2H_6) and ammonia (NH_3) on Si(100)-2x1 and Si(111)-7x7 surfaces provide prototype systems to illustrate the reactivity of semiconductor surfaces.

On Si(100)-2x1 and Si(111)-7x7 surfaces disilane and ammonia partially dissociate at as low temperature as 150-200 K [4,6,7]. Fig. 1 shows ultraviolet photoemission (UPS) spectra of clean and disilane-exposed Si(100, 2x1 and Si(111)-7x7 surfaces. From the spectral changes upon annealing, and from recent vibrational spectroscopic studies [9,10] it can be inferred that on both surfaces the disilane dissociates by Si-Si bond cleavage at low temperatures ($T < 200\text{ K}$). The dissociation products tie up the dangling bonds, which is shown by the disappearance of the S_D and S_2 dangling-bond states in spectra (c) and (d). On the Si(111)-7x7 surface the S_2 state is quenched preferentially, implying that disilane dissociates selectively at rest-atom sites of the 7x7 surface [11].

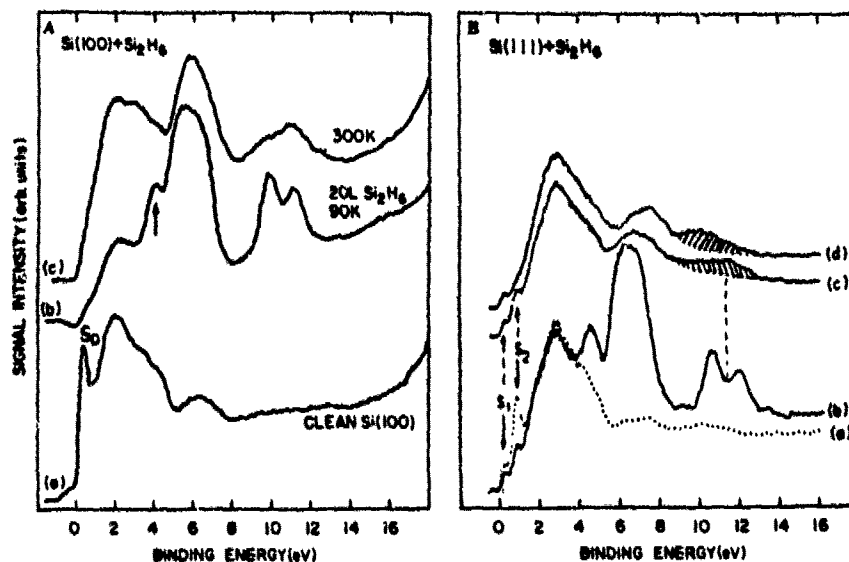


FIG. 1A. He II UPS spectra of clean and disilane exposed Si(100)-2x1. Curve a: Clean Si(100)-2x1. Curve b: After 20 L Si₂H₆ exposure at 90K. Curve c: After annealing to 300 K.

FIG. 1B. He II UPS spectra of clean and disilane exposed Si(111)-7x7. Curve a: Clean Si(111)-7x7. Curve b: After 1.2 L Si₂H₆ exposure at 100 K. Curve c: After annealing to 300 K. Curve d: After annealing to 600 K.

High reactivity of the Si(100)-2x1 and Si(111)-7x7 surfaces to dissociate ammonia at low temperatures ($T < 300\text{K}$) has also been reported and is correlated with the presence of dangling-bonds [4,6,7]. Although the clean silicon surfaces exhibit high reactivity, the reactions stops at sub-monolayer level as the dangling-bonds get tied up by reaction products.

Passivation by reaction products and restoration of surface reactivity by thermal desorption is well demonstrated by the reaction of ammonia with Si(100)-2x1. Fig. 2a shows that hydrogen desorbs from the reacted surface above 700 K. In Fig. 2b N(1s) X-ray photoemission spectroscopy (XPS) peak intensities are shown, taken after ammonia exposures at increasing temperatures. The constant peak intensity between 90K and 575 K, i.e. below the hydrogen desorption temperature, shows that after the initial sub-monolayer adsorption and dissociation the surface is passivated. Above the hydrogen desorption temperature, however, a sudden increase in the N(1s) signal indicates ammonia decomposition and silicon nitride formation at a high rate. Similar temperature dependence of disilane decomposition and silicon film growth can be observed when disilane reacts with silicon surfaces. The thermal activation of the above reactions under the described conditions apparently means restoring surface reactivity by thermal desorption of hydrogen, which ties up dangling bonds at the reacted surfaces [7] For these reactions to proceed at lower temperatures, removal of the reaction blocking products by non-thermal means is necessary.

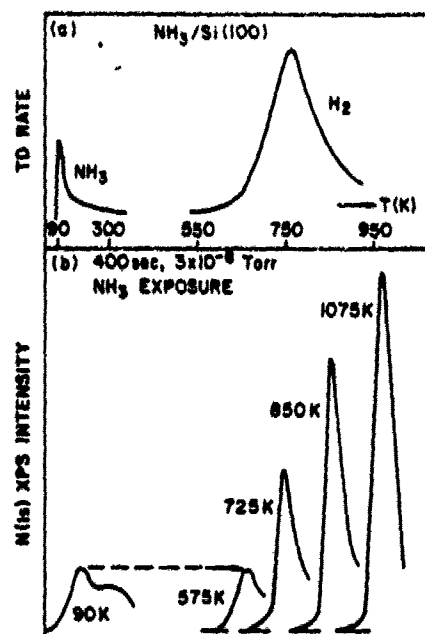


FIG. 2.

(a) Thermal desorption spectra of NH_3 and H_2 from $\text{Si}(100)\text{-}2\times 1$ surface after 10 L NH_3 exposure at 90 K.
 (b) $\text{N}(1s)$ XPS peak intensities after sequential exposure of 400 sec $\times 10^{-8}$ torr NH_3 at the indicated temperatures.

2. Desorption and fragmentation on surfaces induced by electronic excitations

Desorption (and molecular fragmentation) induced by electronic transitions at surfaces has long been studied and gained increasing interest [12,13,14]. A general model to describe the mechanism of electron-stimulated desorption (ESD) was introduced by Menzel, Gomer [15] and Redhead [16]. The Menzel-Gomer-Redhead model is schematically illustrated in Fig.3a.

After an initial electronic excitation (Franck-Condon transition) the adsorbed species is in a repulsive excited state and moves on the potential energy surface (in Fig. 3a, $S\text{-}A^*$ curve), converting potential energy into kinetic energy. Quenching after a certain lifetime in the excited state brings back the adsorbate to the ground state with an acquired kinetic energy. If the kinetic energy is larger than the potential barrier along the $S\text{-}A$ ground state potential energy curve, the A species desorbs, otherwise it is recaptured by the surface. The electronic excitation which result in desorption/fragmentation in the model involve valence excitations i.e. bonding \rightarrow anti-bonding transitions and valence ionizations [3].

An other electronic process which also can result in desorption and fragmentation in adsorbed layers is the dissociative electron attachment. The physics of dissociative electron attachment is schematically illustrated in Fig.3b. When a low energy electron collides with a molecule, it can be captured into an autodetaching state of molecular negative ion. In case of an AB^- molecular negative ion, where one of the component atoms, say A, has high electron affinity, the molecule can break up into an atom B and an atomic negative ion A^- [17]. The cross section for dissociative electron attachment peaks at rather low energy ($E < 10$ eV), therefore it may be a significant channel in electronic excitation induced surface

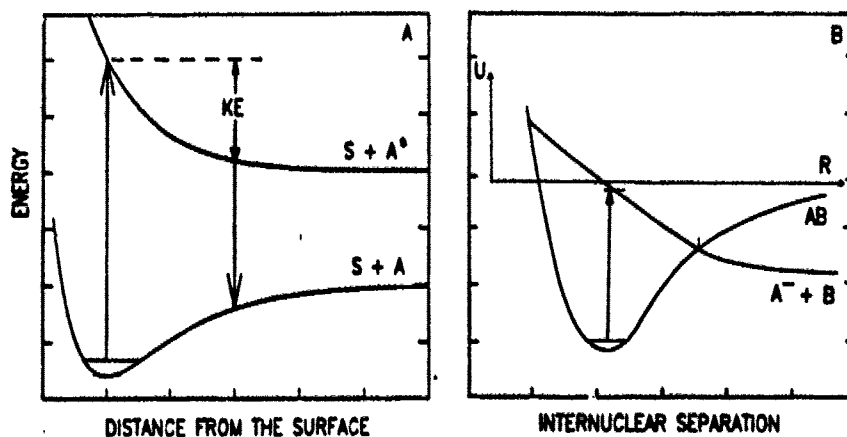


FIG. 3A. Ground state ($S + A$) and repulsive excited state ($S + A^*$) potential energy curves for schematic illustration of the Menzel-Gomer-Redhead model for electron stimulated desorption.

FIG. 3B. Potential energy curves of an AB molecule in ground state and in autodetaching molecular negative ion state for schematic illustration of dissociative electron attachment.

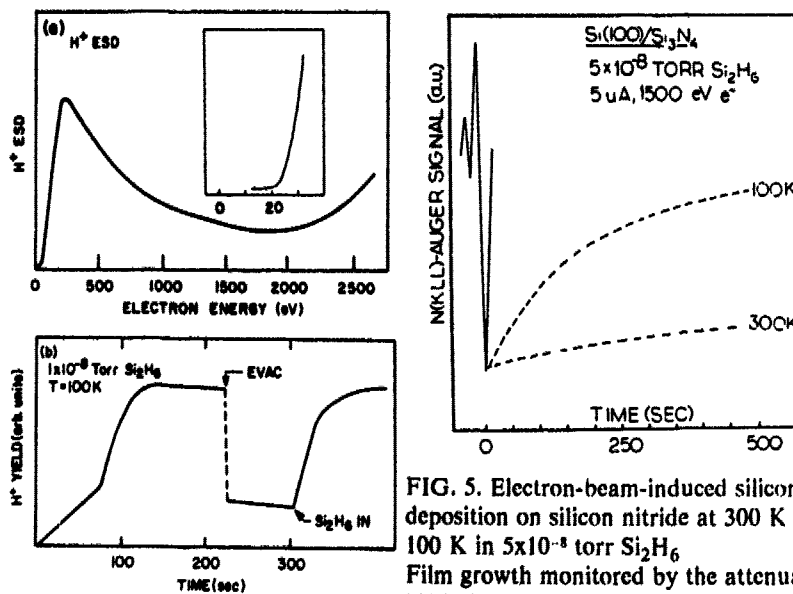


FIG. 5. Electron-beam-induced silicon film deposition on silicon nitride at 300 K and 100 K in 5×10^{-8} torr Si_2H_6 . Film growth monitored by the attenuation of N(KLL) Auger signal at its negative extreme.

FIG. 4a. Electron energy dependence of H^+ ESD yield from a monohydride species on $Si(100)$ surface.

FIG. 4b. H^+ ESD yield from a $Si(100)-2 \times 1$ surface at 100 K in a 1×10^{-8} torr Si_2H_6 ambient and after evacuation of the disilane. Electron beam: 200 nA, 200 eV.

chemistry where secondary electrons, photoexcited or photoemitted electrons are generated.

An example of desorption induced by electronic transitions is shown in Fig. 4a, where the electron energy dependence of H^+ electron stimulated desorption yield from monohydride species on a Si(100) surface is reproduced. The desorption cross section peaks at ≈ 200 eV and the inset shows that the threshold energy for H^+ desorption is ≈ 22 eV. The threshold energy is much higher than the 13 eV valence band width of the H/Si system, which indicates a multi-electron excitation mechanism.

Fig. 4b shows H^+ yield from disilane-adsorbed Si(111)-7x7 surface, as a function of disilane exposure at 100 K. In the first 70 seconds a monolayer of chemisorbed disilane is filling up and the H^+ yield linearly increases with the disilane coverage. The cross section of the 200 eV electrons to remove hydrogen ($H + H^+$) from this chemisorbed layer is $\approx 10^{-16} \text{ cm}^2$. After 70 seconds a second layer of physisorbed molecular disilane starts building up on top of the chemisorbed layer, and this results in a much higher desorption yield. Upon evacuation of disilane the H^+ yield rapidly drops to the value characteristic of the electron exposed chemisorbed disilane layer. The ultraviolet photoemission spectrum of such a surface resembles that of a monohydride silicon surface, indicating a complete dissociation of disilane by the electron beam [5].

3. Electron-beam-induced deposition of silicon films

The electron-induced disilane dissociation and hydrogen desorption, described above, provides a method for low temperature silicon deposition. The realization of this possibility is demonstrated in Fig. 5. A thermally nitrified Si(100) surface was exposed to disilane and an electron beam at 300 K and 90 K to grow silicon films. The progress of silicon film growth is shown by the attenuation of the nitrogen Auger peak from the underlying silicon nitride layer. At 300 K the silicon deposition rate is rather slow. Upon cooling the silicon substrate to 100 K, however, the silicon deposition rate strongly increases. The increase in film growth rate at 100 K is related to the facts that the sticking probability of disilane is higher at 100 K, and that adsorbed disilane molecules have long lifetime on the surface to undergo electron induced reactions, while adsorbed disilane almost instantaneously desorbs at 300 K. As a result, cryogenic temperatures enable high adsorption rate and surface coverage of precursor molecules, thus growth rates sufficient for practical applications (1 ML/sec) can be achieved with gas partial pressures in the high vacuum (10^{-6} torr) range.

4. Electron-beam-induced deposition of multi-component insulator films

In the following we show the capability of the above method to grow silicon nitride, silicon dioxide and silicon oxynitride multi-component insulator films. In the electron-induced deposition of the insulator films, co-adsorbed disilane-ammonia, disilane-oxygen and disilane-nitrous oxide molecular layers were formed at 100 K and exposed to electron beam. In these experiments the film growth was followed by monitoring the Si(LVV) Auger peak intensity at 88 eV [18]. It is shown in Fig. 6a that the Si(LVV) Auger peak in silicon nitride,

oxinitride and dioxide is at 8 eV, 12 eV and 16 eV lower energy than in clean silicon. Fig 6b shows how the the 88 eV signal changes as silicon oxinitride film is deposited on silicon or silicon is deposited on silicon oxinitride. The signal decreases and approaches zero as the thickness of oxinitride film grows and exceeds the escape depth of the 88 eV electrons (≈ 0.6 nm). The initial growth of silicon film on nitride, dioxide or oxinitride films is in turn monitored by the increase of the 88 eV signal.

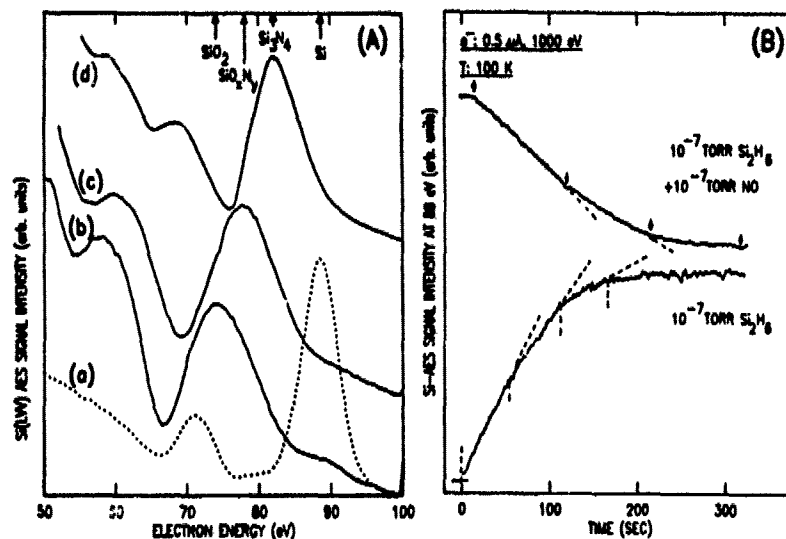


FIG. 6A. Si(LVV) Auger spectra of clean silicon (a), silicon dioxide (b), silicon oxinitride (c) and silicon nitride (d).

FIG. 6B. Si(LVV) Auger signal intensity at 88 eV during electron-beam-induced deposition at 100 K. Curve 1: Silicon oxinitride deposition on silicon in 10^{-7} torr Si_2H_6 and 3×10^{-7} torr NO. Curve 2: Silicon deposition on silicon oxinitride in 1×10^{-7} torr Si_2H_6 . Electron beam: 0.5 uA, 1000 eV.

In Fig. 7 curves (1) show the progress of silicon nitride, silicon dioxide and silicon oxinitride film growth as a function of time. Curves (2) show silicon film growth on top of the previously deposited insulator films. On the right hand side, corresponding silicon Auger peaks are shown after 300 sec reaction. The data show that the thickness of the insulator films exceeds ≈ 0.6 nm after ≈ 200 sec reaction, and that of the silicon after ≈ 150 sec. The position of silicon Auger peaks indicate the deposition of silicon nitride, dioxide and oxinitride film. The deposited films are hydrogenated, which is indicated by release of hydrogen upon annealing.

The rate and efficiency of the electron-induced deposition can be estimated from the fact that ≈ 0.6 nm thick film grows in 150-200 sec. A more precise determination can be made by help of the silicon and silicon oxinitride deposition curves shown in Fig. 6b, which exhibit breaking points at ≈ 70 sec and ≈ 100 sec regular intervals. The breaking points indicate that one monolayer silicon or silicon

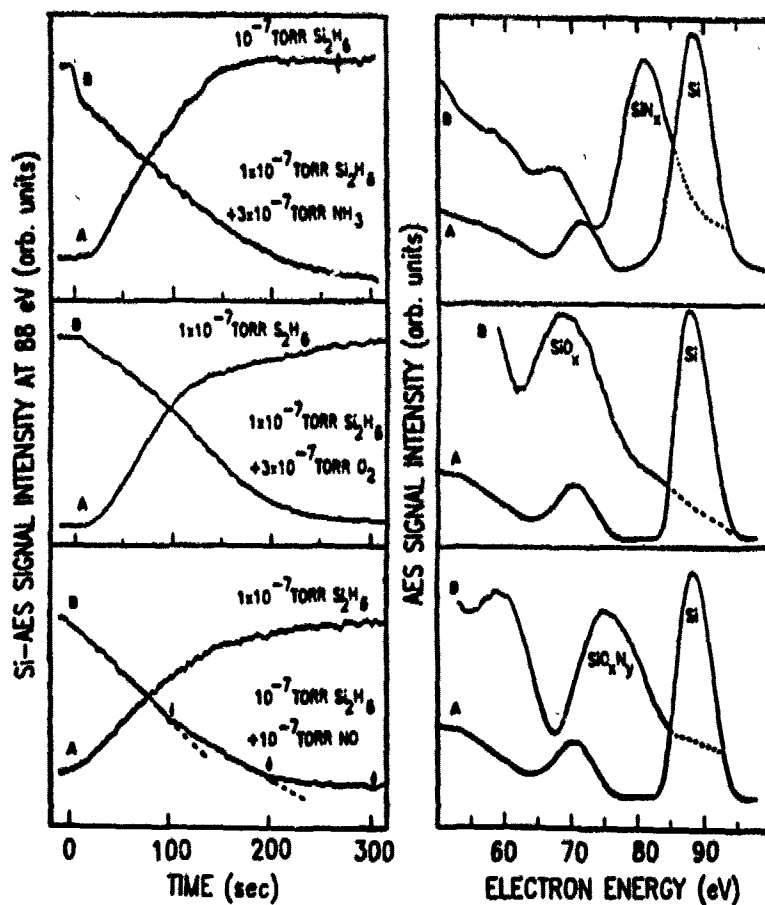


FIG. 7. Left panel: Si(LVV) Auger signal intensity at 88 eV during electron-beam-induced deposition of silicon nitride, silicon dioxide, silicon oxinitride and silicon films at 100 K. Right panel: Silicon Auger spectra after 300 sec deposition. Gas pressures: 10^{-7} torr Si_2H_6 and 10^{-7} torr $\text{Si}_2\text{H}_6 + 3 \times 10^{-7}$ torr NH_3 , O_2 and NO , respectively. Electron beam: 0.5 uA, 1000 eV.

oxinitride film grows in ≈ 70 sec or ≈ 100 sec, respectively [19]. This corroborates the 0.6 nm/150-200 sec estimated above. From the data presented, it can also be estimated that nearly thirty electrons are needed to add an atom to the growing film. The well resolved growth of the first few monolayers shows that ultra-thin films can be deposited with monolayer resolution by the above method.

The composition of the films is determined by that of the adsorbed layer. Since the latter can be precisely controlled by the partial pressure of the reactant gases, the composition of the deposited films can virtually be adjusted monolayer by monolayer.

The spatial control of the film growth is provided by the capability of focusing and directing electron beams. Recent direct electron-beam deposition of 30-50 nm gold lines and three-dimensional structures, using organometallic complexes, demonstrates both the capabilities and potential applications of electron-beam-induced surface reactions for selective area chemical vapor deposition [20].

REFERENCES

1. D. J. Ehrlich, G. S. Highashi and M. M. Oprisco, eds., *Laser and Particle Beam Chemical Processing for Microelectronics*, Mater. Res. Soc. Symp. Proc. **101**, Pittsburgh, PA 1988.
2. Y. Yamamura, T. Fujisawa and S. Namba, eds., *Nanometer Structure electronics*, OHM-North Holland, Tokyo 1985.
3. Ph. Avouris and R. E. Walkup, *Ann. Rev. Phys. Chem.*, **40**, 173 (1989).
4. F. Bozso and Ph. Avouris, *Phys. Rev. B* **38**, 3937, (1988).
5. F. Bozso and Ph. Avouris, *Phys. Rev. B* **38**, 3943, (1988).
6. M. J. Dresser, P. A. Taylor, R. M. Wallace, W. J. Choyke and J. T. Yates, *Surface Sci.* **218**, 75 (1989).
7. B. G. Koehler, P. A. Coon and S. M. George, *J. Vac. Sci. Technol B* **7**, 1303 (1989).
8. B. G. Koehler, C. H. Mak and S. M. George, *Surface Sci.* **221**, 565 (1989).
9. R. Imbuhl, J. E. Demuth, S. M. Gates and B. A. Scott, *Phys. Rev. B* **39**, 5222 (1989).
10. K. Uram and U. Jansson, *Surface Sci.*, submitted.
11. Ph. Avouris and F. Bozso, *J. Chem. Phys.*, submitted.
12. M. M. Traum, N. N. Talk, J. C. Tulli and T. Madey, eds., *Desorption Induced by Electronic Transitions-DIET I*, Springer Verlag, Berlin 1983.
13. W. Brenig and D. Menzel, eds., *Desorption Induced by Electronic Transitions-DIET II*, Springer Verlag, Berlin 1985.
14. R. H. Stuhlen and M. L. Knotek, eds., *Desorption Induced by Electronic Transitions-DIET III*, Springer Verlag, Berlin 1988.
15. D. Menzel and R. Gomer, *J. Chem. Phys.* **41**, 3311 (1964).
16. P. A. Redhead, *Can. J. Phys.* **42**, 886 (1964).
17. B. M. Smirnov, *Negative Ions*, McGraw-Hill, New York 1982.
18. F. Bozso and Ph. Avouris, *Appl. Phys. Lett.* **53**, 1095 (1988).
19. C. Argile and G. E. Rhead, *Surface Sci. Rep.* **10**, 277 (1989).
20. K. L. Lee and M. Hatzakis, *J. Vac. Sci. Technol. B* **7**, 1941 (1989).

PATTERNING OF GaAs/AlGaAs WAFERS BY FOCUSED ELECTRON-BEAM INDUCED CHLORINE ETCHING AND SUBSEQUENT MBE GROWTH

M.TANEYA, Y.SUGIMOTO, H.HIDAKA, AND K.AKITA

Optoelectronics Technology Research Laboratory, 5-5 Tohkodai, Tsukuba,
Ibaraki 300-26, Japan

ABSTRACT

In-situ patterning of $\text{Al}_x\text{Ga}_{1-x}\text{As}$ ($0 \leq x \leq 0.7$) using a electron-beam (EB) and chlorine gas (Cl_2) and the application to "In-Situ EB Lithography" are investigated. In this patterning method, an ultra-thin GaAs oxide is utilized as a resist film. The oxide resist prevents Cl_2 gas etching of the underlying material and can be also patterned by an EB irradiation under a Cl_2 pressure, which brings about selective etching of GaAs/AlGaAs layers. Etch rates of $\text{Al}_x\text{Ga}_{1-x}\text{As}$ ($0 < x \leq 0.7$) are 20-30 nm/min, which is almost equal to that of GaAs (20 nm/min). Using this technique of EB-induced patterning, a novel concept "In-Situ EB Lithography" is proposed, where the whole processes for EB lithography are successively conducted in a ultra-high vacuum multi-chamber system. An overgrown layer on a GaAs surface patterned by this "In-Situ EB Lithography" shows a good morphology.

INTRODUCTION

It has been recognized that the in-situ wafer processing in an ultra-high vacuum (UHV) environment is necessary for patterning of III-V semiconductors.[1] The in-situ patterning makes it possible to repeat crystal growth and fine pattern formation without unintentional contaminations of the wafer surface. To date, a lot of researches have been done on this field and almost all of them are concentrated on direct patterning using a focused ion beam or a laser beam.[2,3] However, we believe that electron-beam (EB)-induced patterning is more hopeful, because it introduces much less damage to a processed wafer as compared with ion beam-induced patterning,[4] and also because one can easily obtain a rather narrow beam diameter (< 10 nm) with commercial scanning EB instruments.

Recently, we have reported an EB-induced patterning of GaAs in a Cl_2 gas ambient.[5,6] The results indicated that a GaAs oxide formed by air exposure of the wafer surface fulfills the role of a resist film, which can be removed (or corroded) by an EB exposure under a Cl_2 pressure. This EB-induced patterning of the oxide resist brought about chemical reactions of GaAs and Cl_2 , resulting in local etching of GaAs. In practical use of a patterning process for fabrication of optoelectronic devices such as laser diodes, etching of layers containing Al is often required. In this paper, we describe etching of AlGaAs by this EB-induced patterning. Moreover, we demonstrate "In-Situ EB Lithography", where the whole processes required for a lithographic sequence are conducted in a UHV multi-chamber system, without air exposure of the wafer surface. Overgrowth on a GaAs surface patterned by the in-situ EB lithography is performed with a molecular beam epitaxy (MBE) system. The overgrown layer shows a good morphology, which confirms that this technique is hopeful for patterning of GaAs/AlGaAs material.

EB-INDUCED PATTERNING OF AlGaAs

The experimental method of the in-situ patterning of an GaAs/AlGaAs wafer is illustrated in Fig. 1. The sample was a AlGaAs/GaAs wafer prepared by MBE, which consisted of 2 μm -thick $n\text{-Al}_x\text{Ga}_{1-x}\text{As}$ layer and a 50 nm-thick $n\text{-GaAs}$ surface protective layer on a (001) $n\text{-GaAs}$ substrate. Both layers were Si-doped with a concentration of $5 \times 10^{17} \text{ cm}^{-3}$. Next, this wafer was exposed to air in a room light for about 70 min to form an GaAs oxide at the surface. (We did not carry out an in-situ oxidation in this case, since this was a preliminary experiment

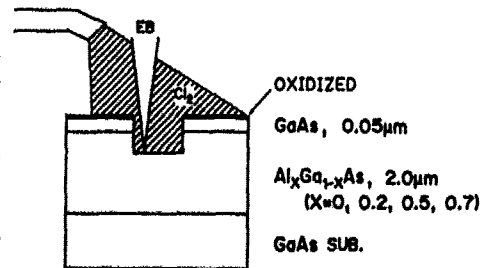


Fig. 1. Etching method of the EB-induced patterning of a GaAs/AlGaAs wafer. There is an ultra-thin GaAs oxide at the surface as a resist film.

for etching of AlGaAs.) Then, the sample was loaded into the same UHV etching system as reported earlier[5], whose base pressure was 2×10^{-8} Torr. Electron beam current of about 10 nA at 10 keV was irradiated to the sample surface with the oxide resist under a Cl_2 pressure. The substrate temperature was 70 °C. Etching region was defined by the EB-scanning area, as described above, which was $60 \times 50 \mu\text{m}^2$ in this case. The averaged EB flux ϕ_{EB} and the Cl_2 flux ϕ_{Cl_2} at the sample surface were 2×10^{15} electrons/($\text{cm}^2 \cdot \text{s}$) and 7×10^{16} molecules/($\text{cm}^2 \cdot \text{s}$), respectively.

We prepared 4 samples in which the AlAs mole fractions of their AlGaAs layers were varied as $x=0, 0.3, 0.5$, and 0.7 . After etching, to evaluate etch rate of AlGaAs, we measured etch depth with a contact type surface profilometer (Tencol Alpha-Step). In the depth measurement, the wafer surface outside the EB-scanning area is used as a reference, because the GaAs oxide resist prevented etching in that area.

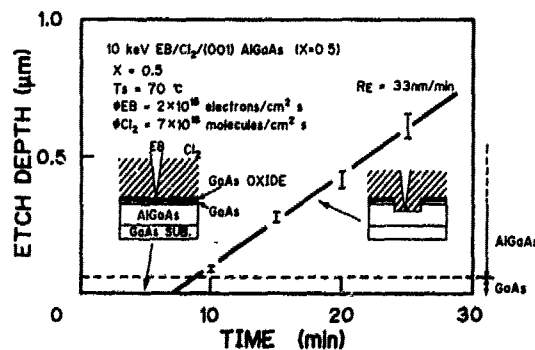


Fig. 2. Etch depth vs. etch time characteristics of a GaAs/ $\text{Al}_{0.5}\text{Ga}_{0.5}\text{As}$ wafer. Etch depth linearly increases with increasing etch time, after a delay time of about 6 min. The etch rate is determined to be 33 nm/min from the gradient.

To evaluate the etch rate of AlGaAs, we measured the etch time vs. etch depth characteristics. For example, a result of the sample for $x=0.5$ is shown in Fig. 2. The broken line indicates the position of interface between the $\text{Al}_{0.5}\text{Ga}_{0.5}\text{As}$ layer and the GaAs protection layer. Considering the fact that the etch rate of GaAs is 25-30 nm/min under this condition[6], it is found that there is a delay time of about 6 min before etching begins. This delay time is considered to be a time required for removal of the surface oxide resist by the EB-irradiation under the Cl_2 pressure. After the oxide resist patterning and also the GaAs protection layer etching, etch depth of $\text{Al}_{0.5}\text{Ga}_{0.5}\text{As}$ increases

linearly with the increase of etch time. The gradient of this graph gives the etch rate of 33 nm/min. This result confirms that not only GaAs, but also $\text{Al}_{0.5}\text{Ga}_{0.5}\text{As}$, can be etched by using this EB-induced patterning method.

Such evaluation of etch rate was done for each sample. The results are summarized in Fig. 3 as a function of the AlAs mole fraction. It is seen that etching of AlGaAs by this patterning method is possible in the range of AlAs mole fraction from 0 to 0.7. An approximately uniform etch rate of 30 nm/min is obtained in this AlAs mole fraction range, including GaAs. This feature is important to obtain a smooth wall in etching through some AlGaAs/GaAs heterostructures.

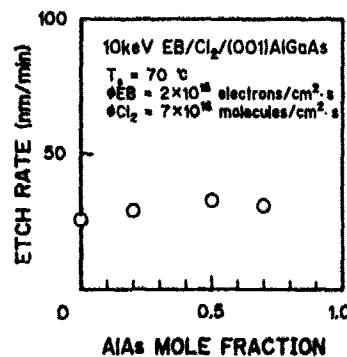


Fig.3. Etch rate of AlGaAs plotted as a function of AlAs mole fraction. In the fraction range from 0 to 0.7, an approximately uniform etch rate of 30 nm/min is obtained.

IN-SITU EB LITHOGRAPHY AND OVERGROWTH

Here, we propose a novel "In-Situ EB Lithography", in which the whole processes for EB lithography are successively carried out in a UHV multi-chamber system. In the in-situ EB lithography, the GaAs oxide resist is formed with pure O_2 gas by a photo-oxidation technique.[7] A processed wafer is never exposed to air throughout the whole processes, including pre-growth and overgrowth by MBE.

The sequence of the in-situ EB lithography and the UHV multi-chamber system used in this experiment are shown in Figs. 4 and 5, respectively. First, a (001) n-GaAs substrate was loaded into the UHV system and was heated for surface cleaning in the preparation chamber. Then, a 1 μm -thick n-GaAs layer with a carrier concentration of $5 \times 10^{17} \text{ cm}^{-3}$ was grown using the MBE chamber. This crystal growth process prepares a clean GaAs surface. Next, the GaAs surface was oxidized in pure oxygen with a simultaneous illumination using a halogen lamp in the oxidation chamber, for the purpose of resist film formation. The oxygen pressure and the illumination intensity were 1 atm. and 35 mW/cm², respectively. The thickness of the GaAs oxide formed by this photo-oxidation process is evaluated to be less than 1 nm.[8] Next, in the etching chamber, the EB-induced direct

patterning of the oxide resist was carried out under the same Cl_2 pressure as the previous experiment for AlGaAs etching ($\phi\text{Cl}_2=7 \times 10^{16}$ molecules/($\text{cm}^2 \cdot \text{s}$)) at 70°C. The current and the diameter of EB were 100 pA and 1 μm , respectively. After the EB irradiation with a dose more than $5 \times 10^{16} \text{ cm}^{-2}$, which is the minimum value required for direct patterning of the oxide resist under this condition[9], pattern transfer to the underlying GaAs was carried out by Cl_2 gas etching without EB. The Cl_2 flux and substrate temperature were fixed at the same values as those in the EB-induced direct patterning process for the oxide resist. Next, the sample was transferred back to the MBE chamber and heated to about 630°C in an arsenic ambient for the oxide resist removal and surface cleaning.[10,11] Finally, layers of AlGaAs and GaAs were overgrown on the patterned GaAs surface.

As an example of patterning by the in-situ EB lithography, a Nomarski microphotograph of the sample, to which the characters of "OTL" was drawn by the in-situ lithography, is shown in Fig. 6. (In this case, the last two processes of the sequence were not carried out because of observation of the etched pattern itself.) The time of the Cl_2 gas etching for pattern transfer was 20 min, from which the etch depth is expected to be about 50 nm. The pattern width is 2 μm . This result of pattern formation confirms that this technique is actually considered as an in-situ lithography using a GaAs oxide as a resist film.

Here, we show a result of overgrowth on a surface patterned by the in-situ EB lithography. Figures 7 (a) and (b) indicate a Nomarski microphotograph of the overgrown layer surface on a

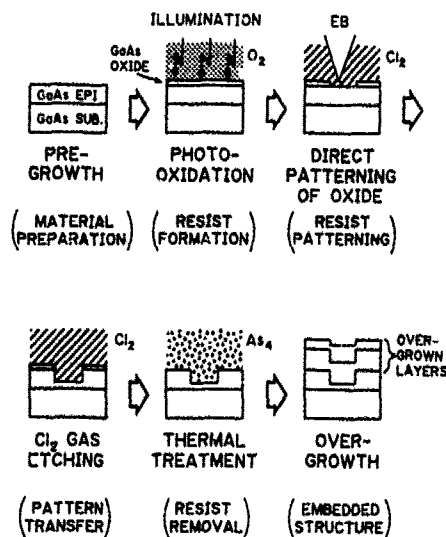


Fig.4. Process sequence for "In-Situ EB Lithography" and overgrowth. The wafer is never exposed to air throughout the sequence.

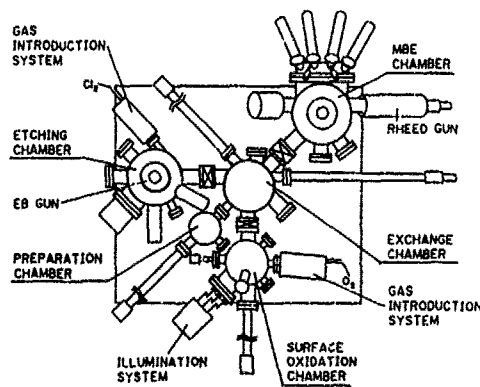
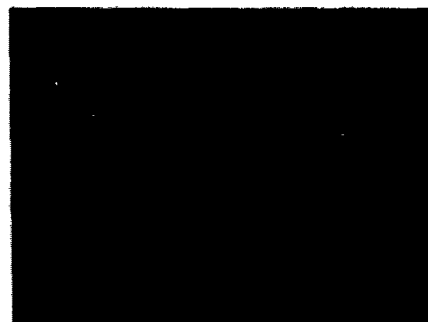


Fig.5. UHV multi-chamber system used for the "In-Situ EB Lithography". The processes shown in Fig.4. are successively carried out in this UHV system.

patterned GaAs surface and a illustration of the cross sectional structure, respectively. The etched area is a rectangle of $15 \times 600 \mu\text{m}^2$ and the etch depth is 50 nm. The surface GaAs overgrown layer shows an excellent morphology outside the etched area, which is the same as that of a layer grown on a flat substrate. On the other hand, it is seen that the surface morphology in the etched area is slightly rough. However, this roughness is caused by the etched surface morphology itself, not by abnormal crystal growth due to damage or contamination at the surface processed by the in-situ EB lithography. The ability of in-situ overgrowth suggests that an embedded microstructure such as AlGaAs/GaAs quantum wires and quantum dots can be fabricated by this lithographic method.



10 μm

Fig.6. Nomarski microphotograph of a patterned sample by "In-Situ EB Lithography". The minimum width of the pattern is about 2 μm .

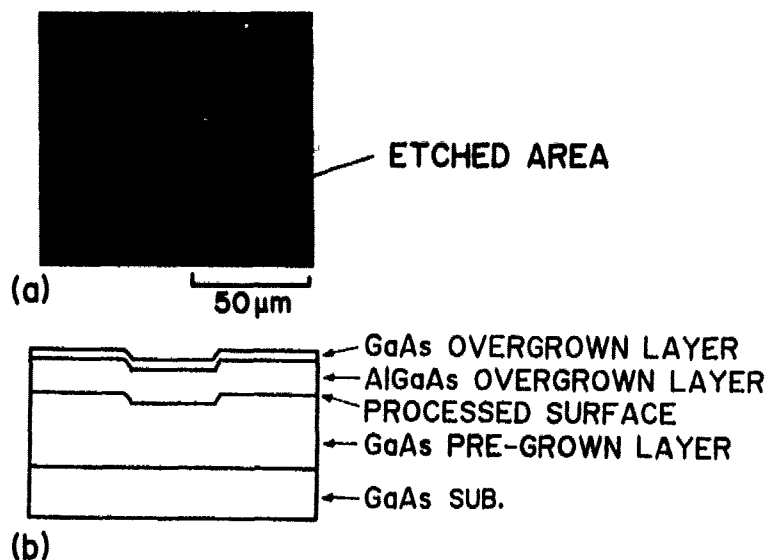


Fig.7. Nomarski microphotograph of an overgrown layer on a patterned surface by the "In-Situ EB Lithography" (a), and a schematic illustration of the sample structure (b). The etched area is a rectangle of $15 \mu\text{m} \times 600 \mu\text{m}$ with the etch depth of about 50 nm. A 0.5 nm-thick $\text{Al}_{0.5}\text{Ga}_{0.5}\text{As}$ layer and a 0.1 nm-thick GaAs layer are successively grown on the GaAs patterned surface, after the thermal treatment.

SUMMARY

We have demonstrated an in-situ EB-induced patterning of AlGaAs with a GaAs protection layer and an ultra-thin surface GaAs oxide which acts as a resist film. In the AlAs mole fraction range of $0 \leq x \leq 0.7$, an approximately uniform etch rate of 30 nm/min was obtained when the substrate temperature and the Cl_2 flux were 70 °C and 7×10^{16} molecules/(cm²·s), respectively. This uniform etch rate of AlGaAs is useful to apply this patterning method to fabrication of some devices with GaAs/AlGaAs heterostructure.

Furthermore, we have proposed a novel "In-Situ EB Lithography" concept and have actually performed the whole processes for the lithographic sequence, from pre-growth through in-situ patterning to overgrowth. The wafer was never exposed to air throughout the whole processes. An overgrown layer on a patterned GaAs surface showed a good morphology.

REFERENCES

1. D.J. Ehrlich, J.G. Black, M. Rothschild, and S.W. Pang, J. Vac. Sci. Technol. **B6**, 895 (1989).
2. For example, Y. Ochiai, K. Gamo, and S. Namba, J. Vac. Sci. Technol. **B1**, 1047 (1983).
3. For example, A.E. Willner, M.N. Ruberto, D.J. Blumenthal, D.V. Podlesnic, and R.M. Osgood, Jr., Appl. Phys. Lett. **54**, 1839 (1989).
4. M. Taneya, Y. Sugimoto, and K. Akita, J. Appl. Phys. **66**, 1375 (1989).
5. M. Taneya, Y. Sugimoto, H. Hidaka, and K. Akita, Jpn. J. Appl. Phys. **28**, L515 (1989).
6. K. Akita, M. Taneya, Y. Sugimoto, H. Hidaka, and Y. Katayama, J. Vac. Sci. Technol. **B7**(6), (to be published).
7. M. Taneya, K. Akita, H. Hidaka, and Y. Sugimoto, Appl. Phys. Lett. **56**(1), (to be published).
8. F. Bartels and W. Monch, Surface Sci. **143**, 315 (1984).
9. M. Taneya, Y. Sugimoto, H. Hidaka, and K. Akita, (unpublished).
10. J.P. Contour, J. Massies, and A. Saletes, Appl. Phys. A, **38**, 45 (1985).
11. A.J. Spring Thorpe, S.J. Ingrey, B. Emmerstorfer, and P. Mandeville, Appl. Phys. Lett. **50**, 77 (1987).

DEEP STRUCTURES PRODUCED IN III-V MATERIALS BY COMBINED FOCUSED ION BEAM IRRADIATION AND DRY ETCHING

L.R. Harriott, Y.L. Wang, B.H. Chin, and H. Temkin
AT&T Bell Laboratories, 600 Mountain Ave., Murray Hill, New Jersey 07974

ABSTRACT

We have developed a direct patterning process for InP based materials which uses ion exposure followed by dry etching to produce surface topography. The substrate is first implanted with a 20 keV Ga⁺ beam focused to 0.2 micron diameter. The surface pattern is then developed in the substrate by etching with or without a low energy (25 -100 eV) flood Ar⁺ ion beam in a Cl₂ (5x10⁻⁴ Torr) atmosphere at 180 to 200° C. This process has been integrated in a common vacuum chamber with a gas source molecular beam epitaxy (GSMBE) system. *In-situ* patterning and high quality overgrowth has been demonstrated for low Ar⁺ ion energies during etching. In this paper, we will describe a model for the patterning mechanism and suggest how it may be exploited to achieve a complete vacuum lithography process compatible with epitaxial regrowth.

INTRODUCTION

The goal of our work has been to develop a high spatial resolution lithographic patterning process which is compatible with the vacuum and surface contamination requirements of molecular beam epitaxy (MBE) crystal growth. In this way, optoelectronic and quantum confinement devices with lateral dimensional control approaching the vertical layer thickness control and uniformity offered by epitaxy are possible. In addition, epitaxial regrowth on patterned substrates offers many possibilities in buried device structures not possible without such a vacuum lithography technique¹⁻⁵. The patterning process is required to produce a surface which is free of damage and process related contaminants. In addition, the patterning must take place entirely within the vacuum to avoid atmospheric contamination by hydrocarbons, water vapor, or oxide formation to allow for subsequent high quality regrowth. Such contaminants degrade the regrowth quality and attempts at surface cleaning generally reduce or even remove fine pattern features formed by conventional methods.

Direct resistless patterning using finely focused ion beams has included a broad range of techniques due to the unique ability of ions to deliver momentum as well as energy to a target, allowing some very different approaches to substrate patterning than those available with electron or photon beams. The simplest and most direct is physical sputtering. This method has been applied to III-V materials and is potentially useful for in-situ processing.⁶ The limitations of such micromachining as a lithographic technique are throughput (ion doses on the order of 10¹⁸/cm²) and lattice damage in the substrate. The throughput can be increased by about a factor of ten by using a reactive gas such as Cl₂ during the ion bombardment⁷ but the question of substrate damage still remains. Low energy finely focused beams used with a reactive gas at least partially address the damage issue⁸. It is not clear, however, that a sufficiently small beam spot can be maintained at the very low (<50 eV) ion energies necessary to avoid damage to the extent that high quality epitaxial regrowth is possible.

We have demonstrated a vacuum lithography process using focused Ga⁺ ion beam exposure and dry etching to pattern InP wafers in a common vacuum chamber with gas source molecular beam epitaxy (GSMBE).² A schematic diagram of the apparatus is shown in Fig. 1. The wafer is first patterned with the 20 keV Ga⁺ ion beam and then transferred to the etching chamber. The wafer is heated to 200° C, then exposed to a Cl₂ partial pressure of about 5x10⁻⁴ Torr. A nominally 50 eV broad-area Ar⁺ ion beam is sometimes used during the etching to achieve anisotropic etching as will be described later. The etching rate for the Ga⁺ ion irradiated areas is larger than that for the unexposed InP thereby transferring the pattern in positive tone. The Ga⁺ ion damaged regions are thus removed by the etching leaving a patterned surface with quality determined by the etching conditions and submicron spatial resolution, consistent with the Ga ion beam diameter³.

The degree of surface damage in etched samples has been evaluated by growing p-n junctions and measuring reverse-bias leakage current. We have been able to show that for Ar⁺ ion energies of less than 50 eV, damage-free etching can be obtained^{2,4}.

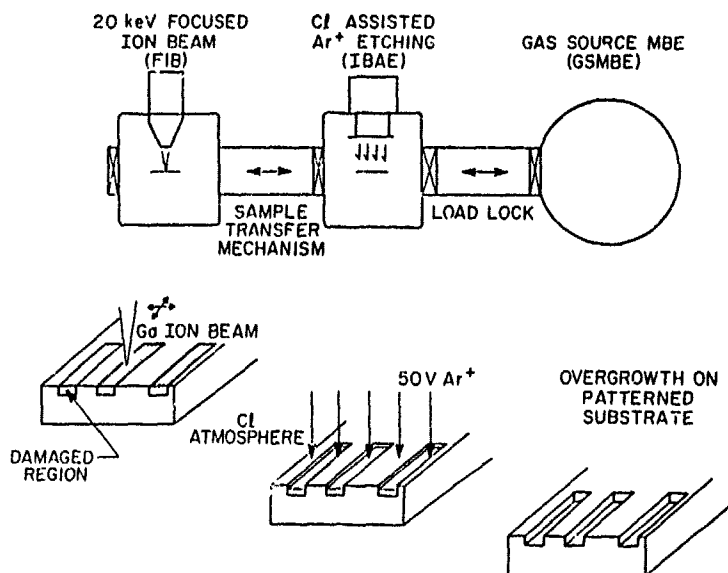


Fig 1. Schematic drawing of the experimental apparatus and the process sequences used in patterning and overgrowth experiments.

EXPERIMENTAL

Our initial observations of this patterning process typically involved the following sequence of steps: 1) the InP substrate was loaded into the vacuum system apparatus from atmosphere following a bromine-methanol polishing step. 2) A pattern of relatively large features (100 x 100 micron) was exposed with the Ga^+ beam at doses ranging from 10^{13} to 10^{15} ions/cm². 3) The substrate was transferred to the etching chamber, heated to 180 to 200°C, and exposed to a flood beam of 50 eV Ar^+ ions in an atmosphere of 5×10^{-4} Torr Cl_2 for 1 to 5 minutes. 4) The sample was then removed from the vacuum and the step heights of the features measured with a stylus profilometer. This procedure was used to evaluate the effects of various process parameters and study the differential etch rate mechanism.

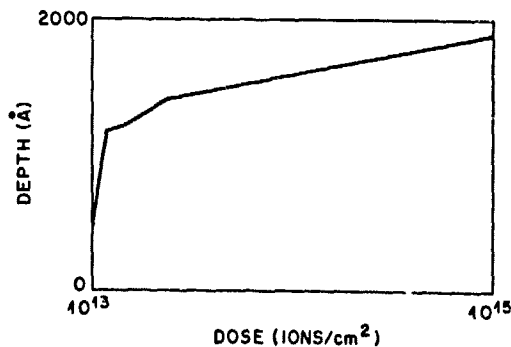


Fig 2. Step height of 100 x 100 micrometer squares in an In substrate as a function of 20 keV Ga^+ ion dose as measured with a stylus profilometer. The etching was for 2 min at 180°C and 5×10^{-4} Torr Cl_2 .

A typical plot of step height as a function of Ga^+ ion dose is shown in Fig. 2. The step height increases rapidly at low doses and saturates at a dose of about 2×10^{14} . This type of curve is universal for this process with the details of the shape and saturation depth dependent on the etching conditions used. In general, for the samples etched using the Ar^+ with the Cl_2 gas, the step heights reach the final values illustrated in Fig. 2 after a fairly short etching time. Significantly longer etching times do not result in increased step heights. The surface relief pattern simply is transferred deeper into the substrate. This suggests that some element of the patterning mechanism has been consumed and there is no longer any difference in the etching rates of the Ga ion exposed and unexposed regions.

A similar series of experiments was performed at fixed etching conditions at several Ga^+ ion beam energies from 20 keV to 150 keV. The results are shown in Fig. 3. As can be seen from the figure, the general shape of the dose dependence is the same at the different energies. The dose at which the step height saturates does not appear to change with beam energy but the ultimate step height does increase monotonically with energy. It is expected that the depth of any effect of the Ga ion beam scales with the mean range of the ions in the substrate. The data from Fig. 3 is replotted in Fig. 4 as step height vs calculated ion range (including straggle) for Ga ion doses of 5×10^{14} and $1 \times 10^{15} / \text{cm}^2$. It can be seen that the step height varies in a roughly linear fashion with ion range at the energies used in our experiment. However, the line drawn through the data points in Fig. 4 does not intersect the vertical axis at zero step height but at a quite large value, much larger in fact than any of the ion ranges involved. This suggests that two mechanisms are operating, one that depends on the kinetics of the ion-solid interaction, and one that does not.

Measurements were made at 20 keV Ga^+ energy where the ion dose rate was varied over three orders of magnitude by adjusting the beam scanning speed and by defocusing the beam. No dose rate effects were observed indicating only single-ion processes are involved.

Exposures were also performed at several angles of incidence of the Ga^+ ion beam up to 15° from the surface normal to assess the importance of ion channeling. After etching on a common sample plate, no measurable effect on the step height was observed. Although channeling must certainly be taking place, it is not an important part of the mechanism of our patterning process.

Measurements were also made at fixed Ga^+ ion exposure conditions (20 keV, 10^{13} to 10^{15} ions/ cm^2), fixed substrate temperature (190°C), and Cl_2 pressure (5×10^{-4} Torr) for several values of Ar^+ energies below 100 eV. It was found that the step height *increased* with decreasing Ar^+ energy. We separately determined, however, that the etch rate of the InP substrate increases monotonically with etching ion energy.

Finally, an experiment was performed to illustrate the importance of surface preparation. Figure 5 shows step height vs Ga ion dose for two surface preparations with all other conditions the same. Both samples were prepared with the usual bromine-methanol polishing. One of the samples was dipped in HF however prior to introduction to the vacuum system. It can be seen in the figure that, in general, the HF-dipped sample required *less* Ga ion dose to produce the same step height as the control sample. HF is known to remove surface oxide leaving only a very thin (tens of Angstroms) layer on surfaces prepared by this procedure⁹.

When no Argon beam is used at all during etching, free Cl_2 chemical etching is achieved for Ga ion doses above the 2×10^{14} ions/ cm^2 saturation dose. At 200°C , the etch rate reaches 1000 Å/min consistent with the thermodynamic prediction¹⁰. In the absence of the Argon beam, the etching in the Ga ion exposed areas continues virtually indefinitely with time and step heights as large as 3 microns have been produced in this way.

DISCUSSION

Initially the most striking aspect of our observations was the size of the step heights routinely achievable with our technique (see again Fig. 2). Step heights of 1500 to 2000 Å are produced using a 20 keV Ga ion beam even though the projected (calculated and measured) range of the Ga ions is only about 150 Å¹¹. It seems implausible that a purely kinetic damage (defect) or doping mechanism could be responsible for our observations. Indeed as pointed out above, the data of Fig. 4 indicated a small dependence on ion range with a large offset due to a second mechanism.

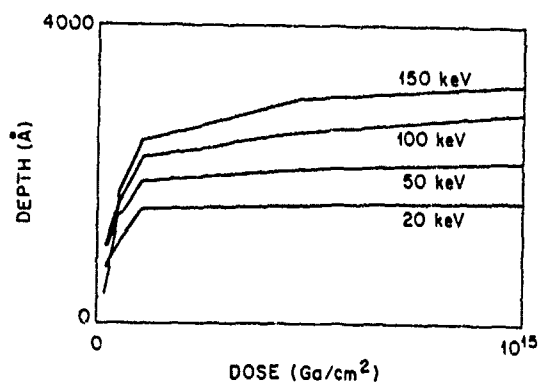


Fig 3. Step height as in Fig. 2 but for various ion energies.

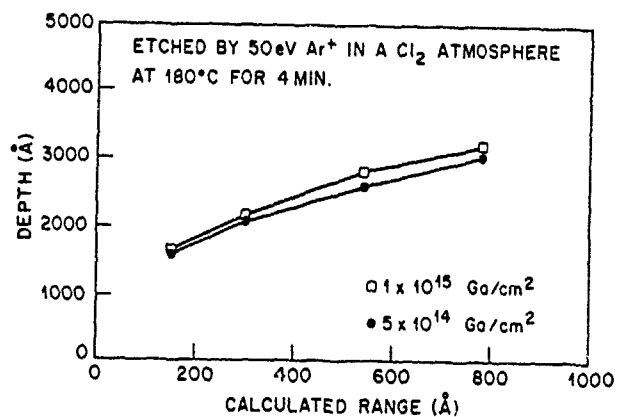


Fig 4. Step height plotted against calculated range plus straggle for ion doses of 2×10^{14} and 10^{15} ions/cm².

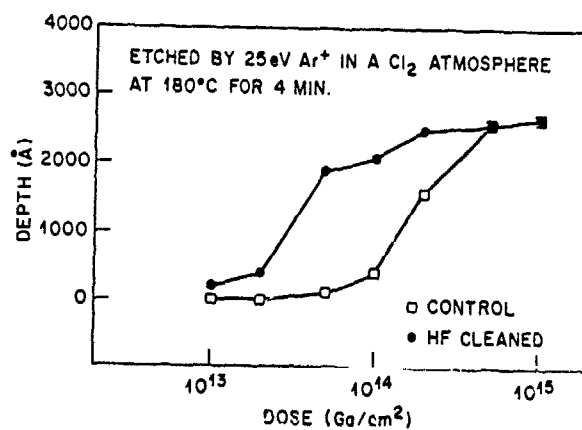


Fig 5. Step height versus ion dose for samples prepared with and without HF cleaning prior to 20 keV Ga⁺ implantation.

All of our observations are consistent with a mechanism which includes the role of a surface (native) oxide layer¹². The effect of the Ga ion beam is then to remove or modify the surface oxide layer in order to expose the underlying substrate to the Cl_2 etchant which will etch spontaneously even without the influence of the Ar bombardment. Such etching has been observed previously by DeMeo et al¹³. In the cases where the Ar bombardment is used during etching, the oxide mask is eroded by sputtering as the step heights are developing. Thus under those conditions, the ultimate step height is a reflection of the time required for the oxide mask to erode explaining the inverse relationship observed between step height and Ar^+ energy. In other words, the step formation continues as long as the oxide mask remains stable and intact.

Our model for the vacuum lithography process is then the following: The Ga ion beam modifies the sample surface by physical processes resulting in some sputter removal of the oxide and damage to the underlying substrate to a depth which is 1.5 to 2 times the ion range (the slope of Fig. 4). The etching is inhibited in the areas still covered by the intact oxide layer and proceeds in the Ga-irradiated areas. The damaged substrate material is removed by the etchant exposing clean undamaged substrate material. The steps thus produced will continue to develop as long as the surface oxide layer remains intact. Although the use of the Ar^+ bombardment during etching can result in increased anisotropy, the oxide mask is eroded, limiting the ultimate step height achievable.

We have verified this model in several ways. The first experiment was to remove the oxide layer after the sample had been introduced to the vacuum chamber and then perform the Ga exposure and etching steps. The oxide was removed either by thermal desorption (525°C under a P_2 beam) or by Ar^+ sputtering. We found that in the absence of the oxide masking layer the step heights of the features was very small, consistent with the ion range (200-300 Å for 20 keV Ga^+). Further we have found that if the samples are heated in air or oxygen to 350 to 400°C prior to Ga ion exposure, very deep (3 microns or more) can be produced with smooth morphology. The thermal pretreatment presumably creates a more uniform oxide layer coverage without much increase in thickness. Our TEM observations are consistent with this.

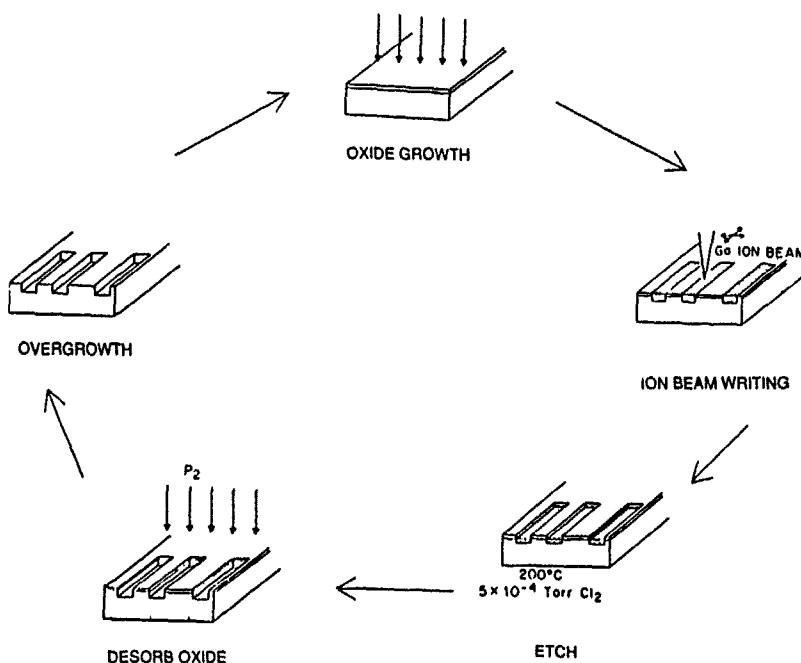


Fig 6. Vacuum lithography process including oxidation, pattern definition, etching, oxide desorption, and regrowth.

CONCLUSIONS

We have developed an all vacuum patterning process that makes use of a surface oxide as the imaging layer. It is possible or even preferable to use free Cl_2 for the pattern transfer resulting in a surface which is completely free of etching-related damage. Very high quality epitaxial overgrowth can be performed on these patterned substrates with a spatial resolution which seems to be limited only by the diameter of the focused ion beam. After patterning, the remaining oxide layer may be removed by thermal desorption prior to overgrowth (a normal step in the growth process anyway).

With the addition of an oxidation chamber to the vacuum processing apparatus, multiple applications of vacuum lithography are possible, as illustrated in Fig. 6. Here, the surface is oxidized, patterned by the focused ion beam, etched, the oxide is desorbed, and new epitaxial material is grown. If desired, the newly grown surface may be then oxidized and patterned and so on as many times as necessary without removing the substrate from the vacuum.

It is also possible to pattern the oxide layer with something other than a focused ion beam serial exposure system. Electron stimulated desorption of the oxide locally would produce the same end but perhaps without the underlying substrate damage¹⁴. This is likely to be a slow process however. Photon beam desorption is also possible but probably would not produce high resolution patterns. Ultimately, a broad-area projection ion beam lithography scheme would be preferable for the increased throughput of such a parallel process and the desorption/sputtering (momentum) efficiency of ions.

ACKNOWLEDGEMENT

We would like to thank W. Robinson, E. Young and the people at Microbeam Inc. for their time and cooperation in performing the high energy Ga^+ implants.

REFERENCES

1. A. Takamori, E. Miyauchi, H. Arimoto, Y. Bamba and H. Hashimoto, Jpn. J. Appl. Phys. 23, L599 (1984).
2. H. Temkin, L. R. Harriott, R. A. Hamm, J. Weiner, and M. B. Panish, Appl. Phys. Lett, 54, 1463 (1989)
3. L. R. Harriott, H. Temkin, R. A. Hamm, J. Weiner and M. B. Panish, J. Vac. Sci. Technol., November 1989, *to be published*
4. H. Temkin, L. R. Harriott, J. Weiner, R. A. Hamm, and M. B. Panish, MRS Proceeding, Spring 1989, *to be published*
5. H. Temkin, L. R. Harriott, and M. B. Panish, Appl. Phys. Lett, 52, 1478 (1988)
6. L.R. Harriott, R.E. Scotti, K.D. Cummings, and A.F. Ambrose, J. Vac. Sci. Technol. B5, 207, (1988).
7. N. Takado, K. Asakawa, T. Yuasa, S. Sugata, E. Miyauchi, H. Hashimoto, and M. Ishii, Appl. Phys. Lett. 50, 1891 (1987).
8. Y. Sugimoto, M. Taneya, H. Hidaka, K. Akita, H. Sawaragi, H. Kasahara, and R. Aihara, Proc. SPIE, 1039 (1989).
9. A. Guivarc'h, H. L'Haridon, G. Pelous, G. Hollinger and P. Pertosa, J. Appl. Phys. 55, 1139 (1984).
10. S. C. McNevin, J. Vac. Sci. Technol. B4, 1216 (1986)
11. "The stopping and range of ions in solids", J. F. Ziegler, J. P. Biersack, and U. Littmark, Pergamon Press, New York, 1985.
12. Y.L. Wang, L.R. Harriott, R.A. Hamm, and H. Temkin, Appl. Phys. Lett., *to be published*.
13. N. I. DeMeo, J. P. Donnelly, F. J. O'Connell, M. W. Geis and K. J. O'Connor, Nucl. Instrum. Methods Phys. Res. B7, 814 (1985).
14. K. Akita, M. Taneya, Y. Sugimoto, H. Hidaka, and Y. Katayama, J. Vac. Sci. Technol. B, November 1989, *to be published*.

MASKLESS FORMATION OF TUNGSTEN FILMS BY ION BEAM ASSISTED DEPOSITION TECHNIQUE

ZHENG XU, TOSHIHIKO KOSUGI, *KENJI GAMO AND *SUSUMU NAMBA

Faculty of Engineering Science, Osaka University, Toyonaka, Osaka 560, Japan
*Research Center for Extreme Materials and Faculty of Engineering Science, Osaka University, Toyonaka, Osaka 560, Japan

ABSTRACT

W films were deposited on n-GaAs by ion beam assisted deposition technique using low energy H_2^+ and Ar^+ , and film properties and residual damage in the substrate were investigated by measuring X-ray photoemission, current-voltage characteristics and deep level transient spectroscopy. Films with a resistivity of 10^{-3} ohm \cdot cm were formed. It was observed that damage can be reduced using the low energy beams and that Schottky contacts with n-factor of almost 1 and barrier height of 0.88 eV were formed.

INTRODUCTION

We have been investigating deposition of W using ion beam assisted deposition (IBAD) technique[1]. Ion beam assisted deposition using finely focused ion beam allows maskless deposition with submicrometer resolution, which is useful for various applications such as x-ray mask repair and integrated circuit restructuring. For mask repair and circuit restructuring, films with high purity is required to get high absorption coefficient and low resistivity, and low damage in the substrate is required to modify active parts of circuits such as contacts and interconnects between contacts.

Up to now, several experiments have been performed to deposit metal films using IBAD techniques. In the previous experiments, film purity was poor and resistivity was high except for Au films[2]. Contact characteristics of deposited films and damage in the substrate have not been investigated.

In the present work, ion beam assisted deposition of tungsten films was performed on (100) oriented, Si-doped GaAs crystal surface by irradiating 0.5 or 2keV, unfocused Ar^+ or H_2^+ beams in the WF_6 ambient, and usefulness of low energy beams to reduce the damage in the substrate has been investigated. The damage in the substrate and annealing properties were examined by Schottky barrier characteristics of deposited W contacts and deep level transient spectroscopy (DLTS). The composition and resistivity of deposited films were measured by x-ray photoelectron spectroscopy (XPS) and four point probe method, respectively.

ESTIMATION OF DAMAGE

Both damage and implanted ion in the substrate affect the contact characteristics of the deposited film. Therefore, it is important to estimate their concentration profiles. Figure 1 shows simulated distribution profiles of ion and damage for IBAD of W films by using 0.5 and 2keV Ar^+ and H_2^+ . The simulation was performed using TRIM code[3]. For the simulation, the observed deposition rate of 1.4 W atoms/ion was used. For H_2^+ , profiles were simulated for H^+ with half of the beam energy. For 2keV Ar ions, the surface may be amorphized up to the depth of about 20 Å and the density of implanted Ar decreases to less than 1% at the depth of about 80Å. Damage and implanted ion density is much less for H implantation, although they distribute deeper. For 0.5 keV ions, defect and implanted ion density is lower compared to the irradiation at 2keV. For Ar , the amorphous layer

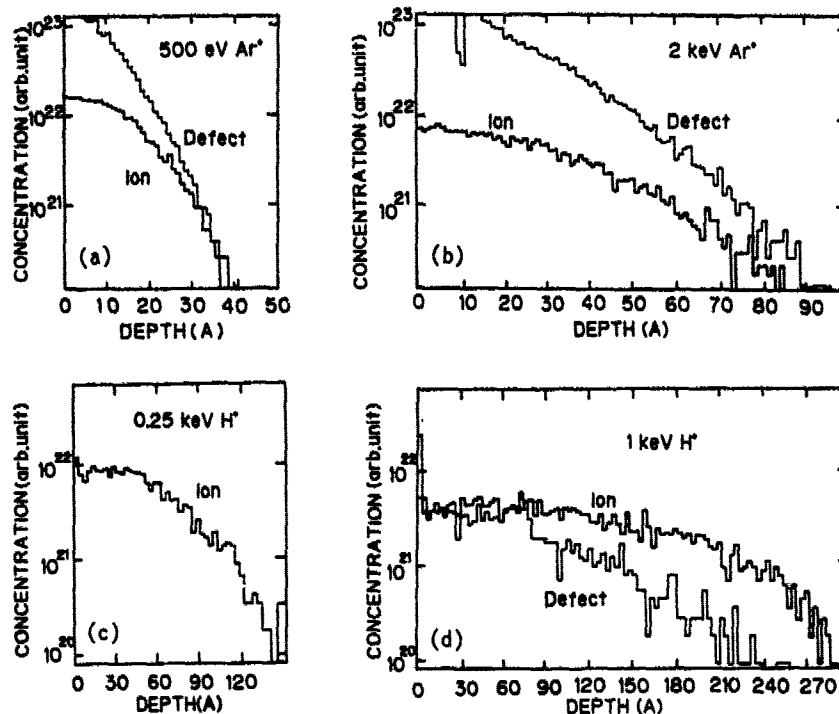


Fig.1 Calculated ion and damage profiles in GaAs substrate for IBAD of W. (a) 0.5keV and (b) 2keV Ar^+ , (c) 0.5keV (0.25keV) and (d) 2keV H_2^+ (1keV H^+)

thickness may be about 10 Å and density of implanted Ar decreases below 1 % beyond 30 Å.

For H, the maximum concentration of H is about 4×10^{21} and decrease less than $10^{20}/\text{cm}^2$ beyond 270Å. At 0.5 keV, no damage is produced by direct nuclear collision process because the maximum transferred energy is less than twice of displacement energy[4]. Therefore, we can expect very low damage.

EXPERIMENTAL PROCEDURES

The deposition was performed on (100) oriented, Si-doped, horizontal Bridgman (HB) grown GaAs single crystals with a carrier concentration of $2 \times 10^{16}/\text{cm}^3$. Figure 2 shows the experimental set-up. 0.5 or 2 keV Ar^+ or H_2^+ ions were irradiated at room temperature and a current density of about $10^{-7} \text{ A}/\text{cm}^2$ in WF_6 ambient. Before the introduction of the gas, the chamber was evacuated to a pressure lower than 1×10^{-6} Torr. The supply rate of the WF_6 was controlled by a needle valve and was such that the pressure measured by the ionization gauge was 8×10^{-5} Torr. This corresponds to the calculated flow rate of $1.5 \times 10^{-7} / \text{cm}^2/\text{s}$.

The chemical composition of deposited film was measured by soft x-ray photoemission spectroscopy(XPS). The XPS spectrometer was connected with the deposition chamber to measure XPS without exposing to the laboratory atmosphere. Conductivity of deposited films was measured by 4 point probe methods.

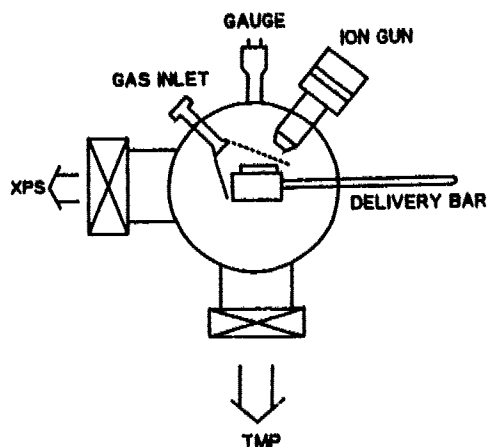


Fig. 2 Experimental set-up for IBAD.

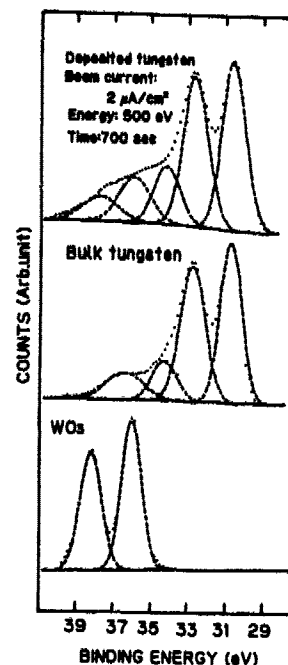


Fig. 3 XPS spectra of W deposited by IBAD, bulk tungsten and WO₃

Evaluation of damage in the substrate was done by measuring the Schottky properties of deposited contacts and trap concentration profiles by deep level transient spectroscopy (DLTS). For these measurements, the tungsten deposition was performed with a metal mask with 0.8 mm diameter holes put in close proximity to the surface of GaAs to deposit circular W dots. Au-Ge metal was deposited on the backside of the wafer and alloyed at 450°C for 5 min to form Ohmic contacts. Annealing characteristics were investigated for furnace annealing in a flowing pure hydrogen atmosphere at 350°C for 10 min.

RESULTS AND DISCUSSION

Film properties

Figure 3 shows XPS spectra of W(4f) for tungsten deposited by IBAD, bulk tungsten and WO₃. It is clear that there is no significant difference between deposited tungsten and bulk tungsten except the tail region. This suggests that metallic tungsten can be formed by the decomposition of WF₆ using ion beam irradiation. The tail region is the signal of oxidized tungsten. From the weak signal intensity, we see that the deposited tungsten includes only a small amount of W-O bond.

Deposition rate and properties of the deposited films are summarized in Table 1. The composition of as-deposited tungsten film was W: 93%, F: 5% and O: 2%, which was measured by XPS. The resistivity was found to be $1.5 \times 10^{-5} \text{ ohm}\cdot\text{cm}$. This value is only about 3 times larger than the bulk value.

The film purity is much higher and the resistivity is lower compared to the previous experiments[1]. This may be mainly because the deposition was performed in low residual oxygen pressure in the present experiment.

Table 1 n-factor and barrier height of W contacts formed on n-GaAs by IBAD

Ion	0.5 keV		2 keV	
	H ₂ ⁺	Ar ⁺	H ₂ ⁺	Ar ⁺
n-factor				
As-deposited*	1.61	1.65	Ohmic	Ohmic
Annealed*	1.14	1.01	1.28	1.21
Barrier Height(eV)				
As-deposited*	0.67	0.57		
Annealed*	0.88	0.73	0.86	0.79

* 350°C for 10 min in hydrogen.

Contact characteristics

Current-voltage characteristics of contacts formed by deposited W were measured to reveal damage effects in the substrate and evaluate usefulness of IBAD technique as circuit restructuring. Figure 4 shows the forward I-V characteristics of W-GaAs contacts formed by H₂⁺ and Ar ion irradiation. Contacts formed by 0.5 keV H₂⁺ showed Schottky barrier characteristics even without annealing, while contacts formed by 2 keV H₂⁺ showed Ohmic characteristics. This may be attributed to the fact that the heavier damage or thicker damaged layer is formed for 2 keV H⁺ than for 0.5 keV H⁺ as estimated by the calculation which is shown in Fig. 1. For 0.5 keV H⁺, no damage is induced by direct atomic collision process. For films formed by 2 keV H₂⁺, large leak, Ohmic current flows through high density of damage levels induced at the W/GaAs interface and Schottky current is masked and because damaged layer is thick, the current is determined by the damaged, high resistive layers.

Contacts formed by Ar⁺ irradiation also show similar behavior to contacts formed by H⁺ irradiation, although the forward current is much larger. For 2 keV irradiation, contacts showed Ohmic characteristics and for 0.5 keV, the contacts shows Schottky characteristics. The larger forward current may be due to a lower barrier height which results from the heavier damage, and the thinner damaged layer as can be seen from the simulation shown in Fig. 1, which results in smaller series resistance due to the damaged layer.

It was observed that low temperature annealing at 350°C improves Schottky characteristics. For 0.5 keV H⁺ irradiation, for example, the ideality factor n was improved from 1.61 to 1.14 and the barrier height increased from 0.67 eV to 0.88 eV by the annealing for 10 min. This value is almost the theoretical value for W/GaAs barriers. The large leakage current observed for the as-deposited samples decreased dramatically after the annealing.

The reverse I-V characteristics of W/GaAs contacts formed by H₂⁺ and Ar ion irradiation are shown in Fig. 5. As-deposited films formed by 0.5 keV H₂⁺ and Ar⁺ irradiation exhibited a large leakage current and soft breakdown due to the conduction through damage induced levels. After annealing at 350°C for 10 min, however, the leakage current diminished significantly. For 0.5 keV H⁺, for example, the leakage current became 10⁻⁸ A at the reverse bias of 3 V.

From the measurement of contact characteristics, it can be said that IBAD by low energy beam is useful to reduce damage and is applicable to circuit restructuring.

The contact characteristics are summarized in Table 1. The barrier height was estimated from the I-V characteristics.

To investigate damage in the substrate, the depth distribution of traps

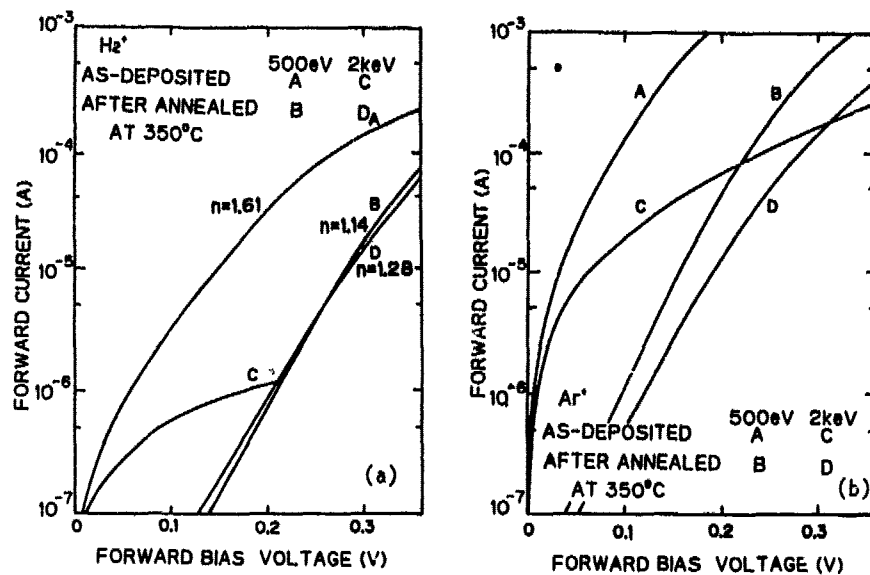


Fig. 4 Forward I-V characteristics of W contacts on GaAs formed by IBAD using (a) H_2^+ and (b) Ar^+ .

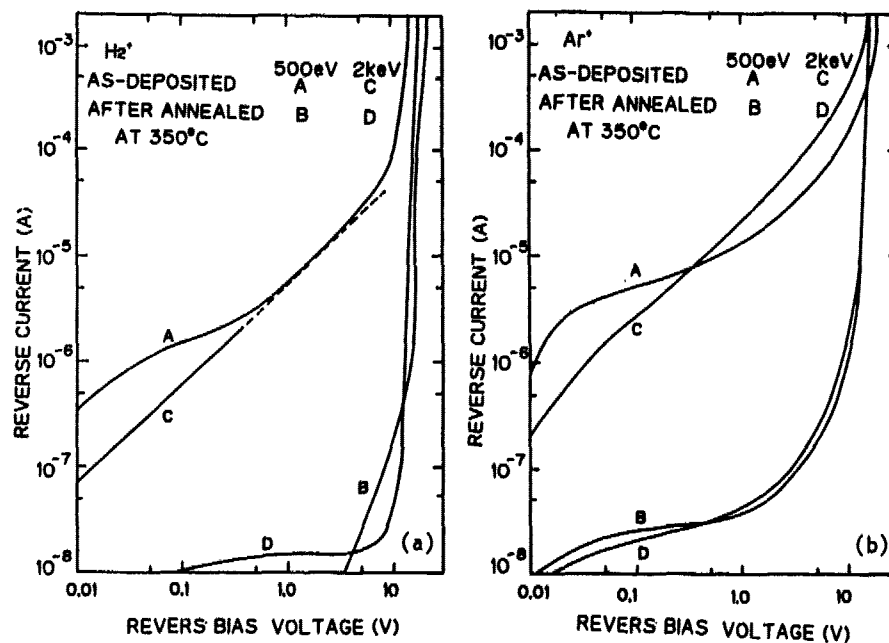


Fig. 5 Reverse I-V characteristics of W contacts on GaAs formed by IBAD using (a) H_2^+ and (b) Ar^+ .

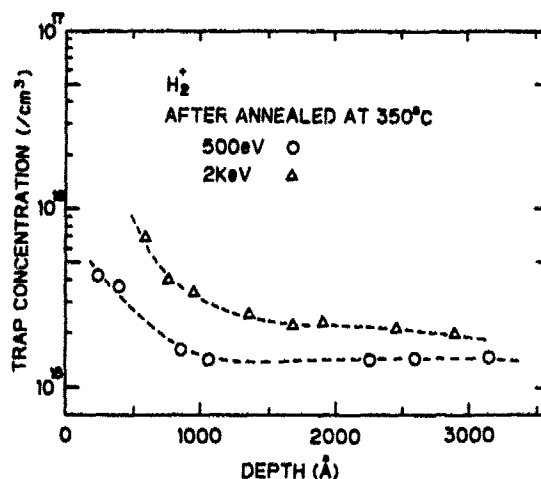


Fig. 6 Concentration profiles of trap center in GaAs formed during IBAD of W using 500 eV and 2 keV H_2^+ . Annealing was done for 10 min.

induced in the GaAs substrate was also measured by means of DLTS. Figure 6 shows the distribution profiles of trap centers in samples formed by 0.5 and 2 keV H_2^+ irradiation and annealed at 350°C for 10 min. The poor Schottky characteristics made it impossible to measure DLTS spectra of the as-deposited samples. It was observed that the trap concentration was only below $1 \times 10^{16}/\text{cm}^3$ and is comparable of grown-in defect with a concentration of $1 \times 10^{15}/\text{cm}^3$. The simulation of atomic collision process which is shown in Fig. 1 suggests that defect concentration should be less than $2 \times 10^{20}/\text{cm}^3$ at the depth of 200 Å for 2 keV H_2^+ . For 0.5 keV H^+ , no damage should be induced for 0.5 keV H^+ by nuclear collision process, but the observed trap concentration was smaller only by 1/2 than that induced by 2 keV H^+ . This indicates that damage is also induced by other process such as electronic excitation process.

SUMMARY

The present results suggest that ion beam assisted deposition using low energy beam is promising to form films without inducing severe damage and therefore, applicable to circuit repair and modification for active device parts. W films with purity of 93% and resistivity of $10^{-5} \text{ ohm}\cdot\text{cm}$ were formed by using 0.5 and 2 keV H_2^+ and Ar^+ . H_2^+ ions induce less damage than Ar^+ . Therefore, development of hydrogen focused ion beams are desirable for applications to ion beam assisted deposition process.

REFERENCES

- [1] K. Gamo, D. Takehara, Y. Hamamura, M. Tomita and S. Namba: Microelectronic Eng. 5 (1986) 163.
- [2] P.G. Blauner, Y. Butt, J.S. Ro, C.V. Thompson and J. Melngailis: J. Vac. Sci. Technol. (to be published).
- [3] J.F. Ziegler, J. P. Biersack and U. Littmark: The Stopping and Range of Ions in Solids (Pergamon, 1985)
- [4] G.H. Kinchin and R.S. Pease: Rep. Prog. Phys. 18 (1955) 1.

THE ROLE OF ADSORPTION AND VAPOR PRESSURE IN FOCUSED ION BEAM INDUCED DEPOSITION OF CARBON FILMS

S.J. KIRCH* AND D.E. SEEGER

IBM Research Division, T.J. Watson Research Center; Yorktown Heights, NY 10598

*Permanent Address: IBM East Fishkill; Z/E70; Route 52; Hopewell Jct, NY 12533

Abstract

Focused ion beam induced deposition of carbon from various organic molecules was studied for a range of temperatures and pressures. To study the effects of vapor pressure, deposition from styrene was compared to deposition from 2-chloro and 2-bromo styrene. To study the effects of the double bond on the vinyl substituent, deposition from ethyl benzene and 2-bromo ethyl benzene was compared to deposition from the 2-X-styrene materials. For each material, deposition yield is found to scale with vapor pressure as a function of temperature over the range studied (0 - 25 C). This behavior shows that physical adsorption plays the key role in determining deposition properties. The importance of the double bond observed in previous work is simply a manifestation of enhanced physical adsorption due to the presence of this double bond.

INTRODUCTION

Focused ion beam induced deposition (IBID) of carbon has recently become important in the repair of masks for photolithography. In this process, once the defect has been located, a gas of organic molecules is introduced into the vacuum system in the vicinity of the defect. Those molecules which adsorb to the mask surface can be decomposed by the impinging ions to build up an opaque layer of carbon. Vinyl benzene (styrene) is often used as the starting material and several studies¹⁻³ have been performed to understand the mechanism and the important parameters of this process.

This paper presents the results of a study into a series of starting materials similar to styrene in an effort to further elucidate this problem. To understand the effect of vapor pressure, depositions from styrene, 2-chloro styrene and 2-bromo styrene (denoted styrene, Cl-styrene, and Br-styrene, respectively) were compared. These materials have vapor pressures which vary by more than an order of magnitude while remaining chemically similar. To study the effect of the double bond of the vinyl substituent, deposition from these three materials was compared to that from ethyl benzene and 2-bromo ethyl benzene (denoted ethyl-benzene and Br-et-benzene). These materials differ in vapor pressure by less than a factor of two from their X-styrene analogs, but are chemically quite different from them.

It was found that deposition yield from all five materials scales directly with the vapor pressure of the starting material at the deposition temperature. This is a clear indication of the importance of physical adsorption in IBID of carbon. Deposition from materials with double bonds is possible at lower fractions of the vapor pressure, consistent with the observations of Vasile and Harriott², but this is simply a manifestation of the improved adsorption arising from the vinyl substituent. Above the region of deposition onset, yield increases with the series, H, Cl, Br. These trends may shed some light on the relative importance of the physical and chemical properties of starting materials for IBID of carbon. Finally, deposition onset pressures can be used to estimate sticking coefficients for incident molecules involved in these processes.

EXPERIMENTAL RESULTS AND DISCUSSION

The experimental arrangement used is typical for IBID experiments. The Ga^+ ion column, having a minimum spot size of $0.2 \mu\text{m}$, was operated at 20 keV. The Si wafer substrates sat on a thermoelectric cooler and the temperature was monitored with a thermocouple. The organic molecules were introduced by a small tube close to the deposition surface. The pressure was monitored by a capacitance manometer near the leak valve outside the chamber. The pressure at the sample was determined by moving a small aperture on a long tube into position under the opening of the gas jet. The pressure in the tube, as read by a convection gauge, was compared to the capacitance manometer over a range of pressures and a scale factor computed. Once this calibration was completed, the capacitance manometer reading was scaled to give the pressure at the sample during the deposition.

Deposits from the X-styrene materials with a finely focused spot have very irregular shapes making it difficult to measure the volume. To avoid these complications and consistently produce cylindrical pillars, the beam was defocused to form a spot with a diameter of approximately $8 \mu\text{m}$. The current density was typically 0.7 mA/cm^2 for the nominal beam current of 350 pA. To make each deposit, the beam was parked in the center of the deflection field for a set duration (typically 300 sec). Between depositions the beam was allowed to scan the entire 1mm deflection field while the stage moved to the next point and the temperature and pressure were set. The height of the pillar was measured with a stylus profilometer and the diameter measured in an SEM. Then the volume was computed and, assuming the film to be carbon at bulk density, the number of carbon atoms divided by the known ion dose gives a yield in atoms per ion. If sputtering occurred rather than deposition, no attempt was made to measure the depth of the crater and the yield was plotted as zero for those conditions. Only flat-topped pillars were used; if deposition occurred at the edge of the crater, this was still recorded as zero yield.

A typical run consisted of varying the pressure from high to low at a fixed temperature, then repeating the first pressure to verify the initial deposition measurement. The temperature was changed and the process repeated for each subsequent temperature. Finally, the initial temperature and pressure conditions were repeated to verify those values once again. The typical repeatability was better than 10%.

Figure 1a shows the deposition yield as a function of pressure at 10, 20 and 26 C using Cl-styrene as the starting material. In general, the yield increases with decreasing temperature (cf. e.g. 6 mTorr data) which is not surprising. The pressure values were divided by the vapor pressure⁴ of Cl-styrene at that temperature and the yield replotted versus this "normalized" pressure in Fig 1b. Notice that all the data fall along one curve when plotted in this fashion. According to the theory of Brunauer, Emmett, and Teller⁵, adsorption is expected to scale with vapor pressure, so the data suggest that physical adsorption plays a dominant role. This same feature is observed for all three styrene compounds. Similar behavior has also been observed for IBID of gold from $\text{Me}_2\text{Au}(\text{hfac})$ ⁶.

Figure 2a is a plot of the yield of styrene, Cl-styrene and Br-styrene versus normalized pressure⁴ for 10 C. Again for each compound, there is a single curve. Above about 0.2%, the Br-styrene points consistently lie above those of Cl-styrene. From similar data at 20 C (not shown) deposition yield from Cl-styrene lies above that from styrene, so yield increases in the series H-, Cl-, Br-styrene.

These differences in yield between deposition from different molecules may be due either to increased adsorption or increased efficiency of the ion-adsorbed molecule interaction. Without separate adsorption data, it is not possible to tell conclusively which is correct, but there are several possible explanations for the trend. One is that the vinyl bond is breaking since this is expected to be the weakest bond. If this were the case, the increase in yield should go as the reactivity ratios (another measure of vinyl bond strength). The reactivity ratios⁷, however, increase in the order H-, Br-, Cl-, so this does not explain the data. A second possibility is that the vinyl bond attaches to the surface as suggested by Vasile and Harriott². Then, the Ga^+ breaks apart the benzene ring and the next molecule attaches to the radical chain. This mechanism is attractive because of the large amount of excess energy in the ions over and above that necessary to break a single bond. One would expect the benzene ring opening process, however, to be nearly unaffected by the addition of Cl or Br to the ring. In addition, the contribution to chemisorption from the stabilization of the unpaired electron due to the presence of the halogen would be expected to go in the order of the electronegativity, which is again inconsistent with the data. Finally, it may be that the addition of the halogen changes the ion decomposition cross section. If the breaking of the halogen-carbon bond becomes the rate limiting step, this could explain the differences in yield, since the average strength of C-X bonds is 64, 77, 99 kcal/mole for X = Br, Cl, and H, respectively⁸. Obviously the process is quite complex and the correct

Figure 1 Deposition yield in carbon atoms per incident Ga^+ ion from 2-chloro styrene at 26 °C (○), 20 °C (Δ), 10 °C (+). Plotted versus (a) absolute pressure and (b) normalized pressure: ($\equiv P / P_v(T)$)

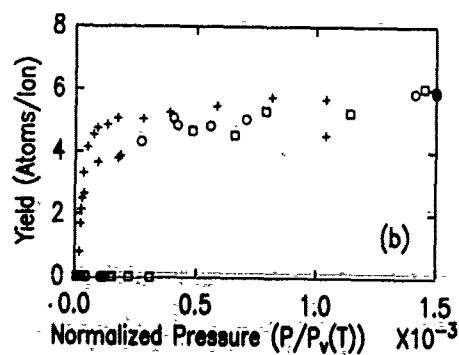
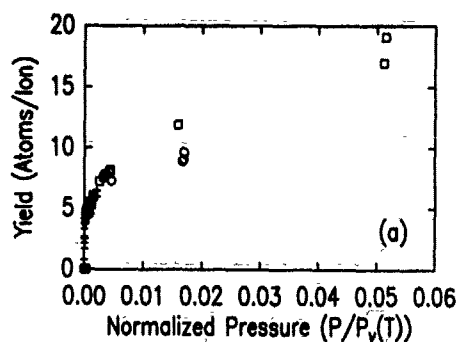
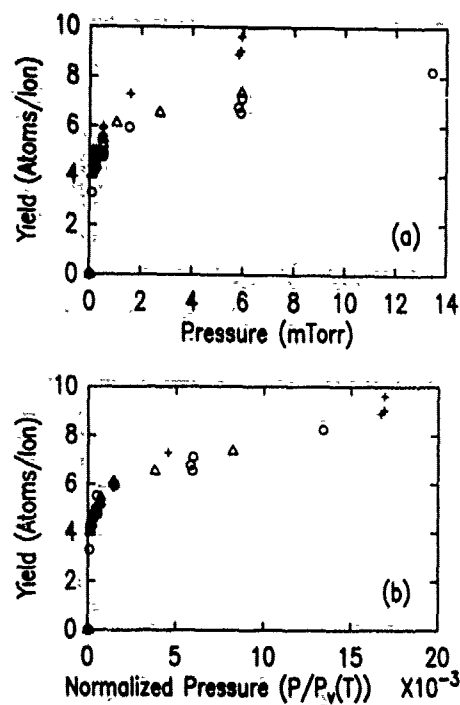


Figure 2 Deposition yield in carbon atoms per incident Ga^+ ion at 10 °C from styrene (+), 2-chloro styrene (○), and 2-bromo styrene (□) versus normalized pressure. (a) All data. (b) Low normalized pressure regime.

explanation is undoubtedly some combination of the above factors as well as others not mentioned here.

The lower normalized pressure region of the data of Fig 2a is shown in Fig 2b. The nearly step function onset may be due to the way zero yield is defined, but once deposition initiates, the yield for these lower pressures seems to be almost independent of which analog is used as a starting material. It is interesting to note that the onset pressure increases in the series styrene, Cl-styrene, Br-styrene. This trend is consistent throughout the temperature range studied. The fact that initiating deposition with Br-styrene is hardest, but that once deposition starts, the yield from it is highest, suggests that there is more than one factor contributing to the yield in these different pressure regimes. It also may indicate a difference between deposition on SiO_2 (deposition initiation) and on the carbon film formed (overall yield) by this process.

Figure 3a shows deposition yield versus pressure for ethyl-benzene at 10, 20 and 26 C. No deposition was observed for ethyl-benzene at room temperature for any pressure that could be tolerated by the vacuum system. This is similar to the result reported by Vasile and Harriott², however, we do observe deposition below room temperature. Note that when this data is plotted versus normalized pressure⁹ (Fig 3b), the data at 26 C are consistent with the data at other temperatures. Note also, that the onset of deposition occurs at a much higher pressure (both absolute and normalized) for ethyl-benzene than for the X-styrene compounds shown earlier. Thus, the reason deposition is not possible with ethyl-benzene at room temperature is because the adsorption is not sufficient. As the temperature is lowered, however, deposition becomes possible when a sufficient number of molecules adsorb.

Figure 4a shows a comparison of carbon yield from ethyl-benzene and Br-et-benzene at several temperatures plotted on the normalized pressure scale. Here we see that the yield from Br-et-benzene lies above that for ethyl-benzene for all temperatures and pressures studied. Thus the addition of the Br atom must either increase the adsorption or the decomposition cross section as previously discussed. The low pressure region of this plot is shown in Fig 4b. Again we see essentially one curve for each material, independent of temperature, and note the relative ease of deposition from Br-et-benzene as compared to ethyl-benzene. The onset pressure for deposition from Br-et-benzene is lower than that for ethyl-benzene by approximately a factor of four. It is also possible to compare the onset of deposition at 10 C from Br-et-benzene (0.2 mTorr, 0.1%) to that from Br-styrene (0.06 mTorr, 0.05%; cf. Fig 2b). This difference is probably due to increased physical adsorption brought about by the presence of the vinyl group.

The differences in adsorption can also be thought of as differences in sticking probability. Vasile and Harriott² claimed that a necessary (but not sufficient) condition for deposition is that the precursor molecular arrival rate exceed the ion arrival rate. In fact, these data indicate that the molecule must adsorb before it can contribute to deposition. Thus, the molecular arrival rate times the sticking probability, must exceed the ion arrival rate for deposition to occur from a stationary ion beam. For Br-styrene at 10 C, the onset of deposition occurs at about 0.06 mTorr, giving a molecular arrival rate of approximately $9 \times 10^{15}/\text{cm}^2\text{-sec}$. This gives a carbon atom arrival rate of $7 \times 10^{16}/\text{cm}^2\text{-sec}$ which is an order of magnitude larger than the ion arrival rate of $4 \times 10^{15}/\text{cm}^2\text{-sec}$. Thus the sticking probability of Br-styrene at 10 C can be estimated as about 0.05. This can be compared to an upper bound for the sticking coefficient of ethyl-benzene calculated from no apparent deposition at 29 mTorr at 26 C; this gives a carbon atom arrival rate of $5 \times 10^{19}/\text{cm}^2\text{-sec}$ or a sticking coefficient of less than 1×10^{-4} .

CONCLUSION

It has been shown that IBID of carbon is possible from styrene, Cl-styrene, Br-styrene, ethyl-benzene and Br-et-benzene. Further, for each of these materials, the deposition yield scales with the vapor pressure of the starting material at the sample temperature. This shows that physical adsorption plays a dominant role in IBID of carbon. Deposition efficiency (yield well above onset) increases in the series ethyl-benzene, Br-et-benzene, styrene, Cl-styrene, Br-styrene. These trends are related to an increase in adsorption and / or the ion-adsorbed molecule interaction. Deposition onset pressures at a given temperature increase in the series styrene, Cl-styrene, Br-styrene, followed by Br-et-benzene and finally ethyl-benzene. The importance of the double bond is that it increases adsorption and therefore yield. Rather than being essential, the vinyl substituent is helpful, but other materials with good adsorption would also be expected to work quite adequately as starting materials for IBID deposition of carbon. Finally, the sticking probabilities calculated from the deposition onset pressures, range from around 0.05 to 1×10^{-4} for the materials and temperatures studied here.

Figure 3 Deposition yield in carbon atoms per incident Ga^+ ion from ethyl benzene at 10 C (+), 20 C (X), and 26 C (O) versus (a) absolute pressure and (b) normalized pressure

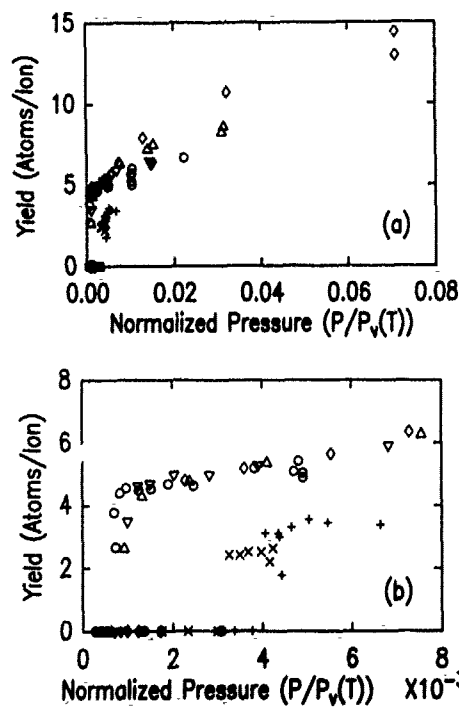
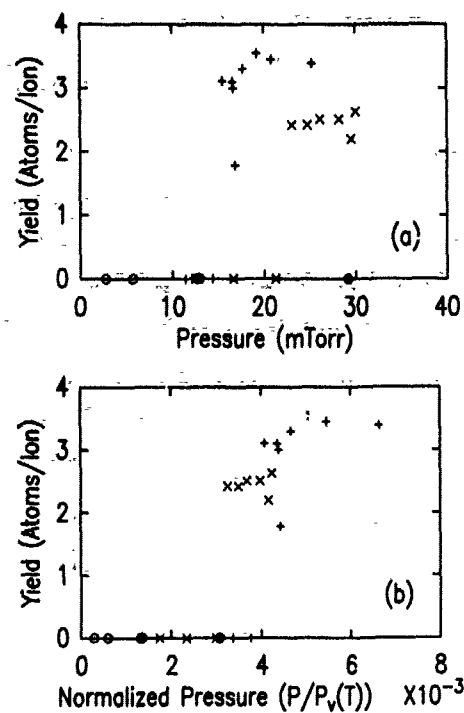


Figure 4 Deposition yield in carbon atoms per incident Ga^+ ion from ethyl benzene at 10 C (+), 20 C (X), and 26 C (O) and 2-bromo ethyl benzene at 0 C (◇), 10 C (△), 20 C (▽), and 26 C (○) versus normalized pressure. (a) All data. (b) Low normalized pressure regime.

ACKNOWLEDGEMENTS

The authors would like to thank Drs. A. Wagner, P. Blauner and C.R. Moylan as well as A. Dubner and J.P. Levin for their helpful discussions.

References

- ¹ L.R. Harriott and M.J. Vasile, J. Vac. Sci. Technol. B6, 1035 (1988).
- ² M.J. Vasile and L.R. Harriott, Journ Vac Sci Tech B7, (1989).
- ³ SJ Kirch and DE Seeger, to be published.
- ⁴ R.R. Dreisbach and R.A. Martin, Ind. and Eng. Chem. 41, 2875 (1949).
- ⁵ S. Brunauer, P.H. Emmett, and E. Teller, J. Amer. Chem. Soc. 60, 309 (1938).
- ⁶ A.D. Dubner and A. Wagner, J. Appl. Phys. 65, 3636 (1989).
- ⁷ T. Boublik, V. Fried, E. Hala, *Encyclopedia of Polymer Science and Technology*, (J Wiley and Sons, New York, 1966), Vol. 4, p. 215.
- ⁸ D.F. McMillen and D.M. Golden, Ann. Rev. Phys. Chem. 33, 493 (1982).
- ⁹ T. Boublik, V. Fried, and E. Hala, *The Vapour Pressures of Pure Substances*, (Elsevier, Netherlands, 1984).

SELECTIVE CHEMICAL VAPOR DEPOSITION OF TUNGSTEN FILMS ON TITANIUM-ION-IRRADIATED SILICON DIOXIDE

H. OKUHIRA, S. NISHIMATSU, AND K. NINOMIYA

Central Research Laboratory, Hitachi, Ltd., Kokubunji, Tokyo 185, JAPAN

ABSTRACT

Selective area deposition of adherent tungsten (W) film on titanium (Ti)-ion-irradiated silicon dioxide (SiO_2) is achieved. First, Ti-ion irradiation through a stencil mask is performed at 600 eV for 1.1×10^{16} atoms/ cm^2 in a reaction chamber. Next, ArF excimer laser ($\lambda = 193$ nm) chemical vapor deposition (CVD) with tungsten hexafluoride (WF_6) and hydrogen (H_2) is carried out for 40 seconds at 400 K. Finally, low-pressure (LP) CVD is carried out at 600 K and then W films are deposited selectively on the ion-irradiated SiO_2 . Without the laser CVD-step, the ion-irradiation pattern disappears during LPCVD and no W film deposition occurs. Therefore, laser CVD is essential in our experiments.

INTRODUCTION

The maskless metallization process using selective CVD is attracting much attention as a one-step interconnection technique for fabricating future Large Scale Integrated circuits (LSIs)[1]. The major effort in depositing metals by CVD has been in W deposition because of its excellent electromigration resistance and refractory nature. In this paper, we present selective area deposition of W films on a Ti-ion-irradiated SiO_2 surface via consecutive processes of ArF excimer laser CVD and LPCVD.

In conventional LPCVD with WF_6 and H_2 , W films are selectively deposited on Si but not on SiO_2 . Such selectivity originates in the reduction reaction of WF_6 by Si, not by SiO_2 [2]. To deposit W films on SiO_2 , laser CVD has been attempted, but good adhesion of as-deposited films has not been obtained[3]. In our experiment, in order to deposit W films on SiO_2 , Ti-ion irradiation is performed through a stencil metal mask. It is thought that Ti on SiO_2 reacts as a reducing agent of WF_6 , and ArF excimer laser radiation enhances the reduction reaction. Ti-ion-irradiation also improves adhesion between deposited W and SiO_2 . The improvement of adhesion can be interpreted by the reaction of thin Ti films with SiO_2 at room temperature[4, 5].

EXPERIMENTAL

The experimental apparatus consists of a reaction chamber, an ion beam system (COLUTRON Model G-2-D), and an ArF excimer laser (Lambda Physik EMG201 MSC). Si wafers, P-type, 3 - 6 $\Omega \cdot \text{cm}$, with $\langle 111 \rangle$ orientation, were thermally oxidized in steam at 1173 K. The SiO_2 -covered wafers were etched with a solution of 5 % hydrofluoric acid to remove surface contaminated layers before they were introduced into the reaction chamber.

The procedure of selective deposition of tungsten films was as follows. First, Ti-ion irradiation was performed through a stencil metal mask as shown in figure 1 (a). Typical ion energy was 600 eV, dose was 1.1×10^{16} atoms/ cm^2 , and background pressure during ion irradiations was 5×10^{-3} Pa. Pattern width of the stencil mask is 500 μm . Next, ArF excimer laser CVD with WF_6 (16 ccm) and H_2 (200 ccm) was carried out for 40 seconds at 400 K. Ar (200 ccm) was also fed near a laser introducing window to avoid undesired deposition of reaction

products on the inside of the window. Total pressure at the laser CVD step was 53 Pa. The excimer laser was operated at 100 mJ/pulse and 20 Hz. A laser beam was magnified about 6 times using a cylindrical concave lens and the wafer was irradiated perpendicular to the laser beam, as shown in figure 1 (b). Finally, LPCVD was carried out at 600 K. Total pressure at the LPCVD step was raised to 210 Pa by reducing the pumping speed of the reaction chamber.

RESULTS

Figure 2 shows the result of selective deposition of W film on Ti-ion-irradiated SiO_2 . An ion-irradiation pattern was not clear before ArF excimer laser CVD, as shown in figure 2 (a). After 40 seconds of laser CVD the pattern became clear, but metallic feature (gloss) had not yet appeared. At the beginning of subsequent LPCVD, the ion-irradiation pattern once faded but did not disappear completely. And then, a metallic pattern appeared preferentially on the ion-irradiated SiO_2 , as shown in figure 2 (b). Good adhesion of the deposited film was confirmed by a tape test.

Without the laser CVD step, the ion-irradiation pattern disappears during LPCVD and no W deposition occurs. Therefore, laser CVD is essential. However, longer laser CVD times cause selectivity loss during LPCVD, and deposition of weakly adherent W film on the entire SiO_2 surface. Therefore, adhesion of the deposited film is enhanced by Ti-ion irradiation. The improvement of adhesion can be explained by the reaction of thin Ti films with SiO_2 at room temperature [4, 5].

To examine the effect of laser CVD, the near surface of the Ti-ion-irradiated SiO_2 sample was analyzed before and after laser CVD by Auger electron spectroscopy, using argon ion sputtering. The sputtering rate was 2.5 nm/min. Samples were exposed to the air before they were introduced into the Auger-analysis chamber. On the Ti-ion-irradiated surface, no Si Auger peak was observed on the top surface, as shown in figure 3 (a). Therefore, the SiO_2 surface was entirely covered by Ti. The carbon (C) peak was decreased by sputtering, but the oxygen (O) peak was not changed. After laser CVD, the W and fluorine (F) peaks were newly observed on the top surface, as shown in figure 3 (b). These peaks were decreased by sputtering. A Ti peak was also observed on the top surface. Therefore, the SiO_2 surface was partly covered by $\text{W(F}_x\text{)}$ nuclei.

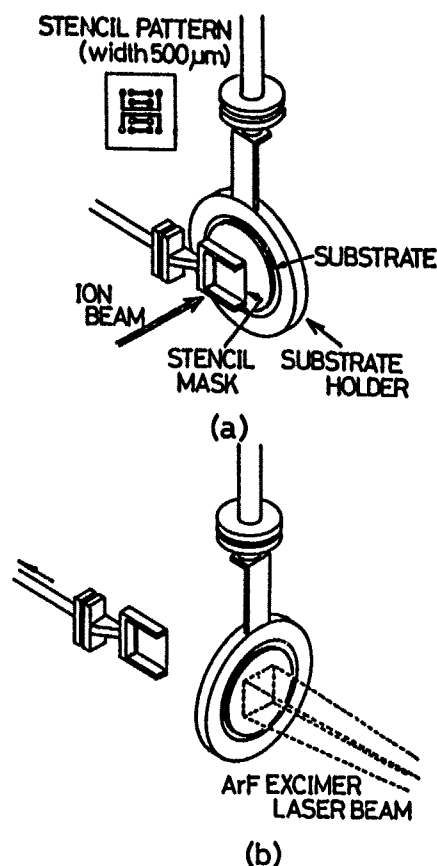


Figure 1. Experimental arrangement of substrate, stencil mask, Ti ion beam, and ArF excimer laser beam. (a): ion-irradiation step, (b): laser CVD step.

In figure 3, the behaviour of the O Auger peaks should be noted. In figure 3 (a), the shape of the O peak did not change with sputtering. This means that the peak energy of the O Auger spectra of $Ti(O_x)$ is not different from that of SiO_2 . On the other hand, in figure 3 (b), the shape of the O peak did change with sputtering. The peak energy of the O Auger spectra of $Ti(O_x)$ was different from that of SiO_2 after laser CVD. The shape and peak energy of the Auger spectrum is reflected by the chemical bond of the elements. The change in the O peak of $Ti(O_x)$ may be interpreted as a reduction of TiO_x during ArF excimer laser CVD.

DISCUSSION

A mechanism of W selective deposition on the Ti-ion-irradiated SiO_2 is explained as follows.

The material deposited by Ti-ion irradiation is fairly well oxidized titanium (TiO_2 ; chemical composition is not confirmed). The oxygen probably came from trace amounts of water and/or oxygen in the reaction chamber at the ion-irradiation step. In the early stage of laser CVD, a H_2 reduction of TiO_2

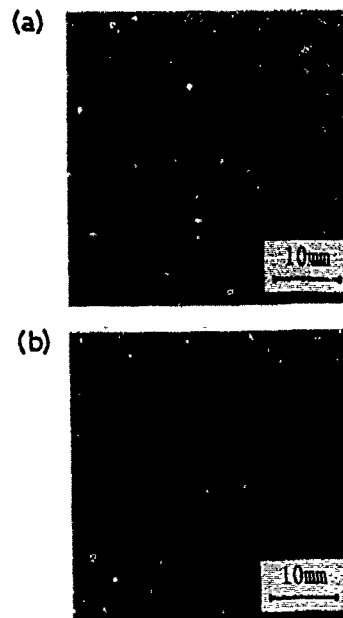


Figure 2. Selective deposition of W film on Ti-ion-irradiated SiO_2 . (a):after ion-irradiation, (b): after LPCVD.

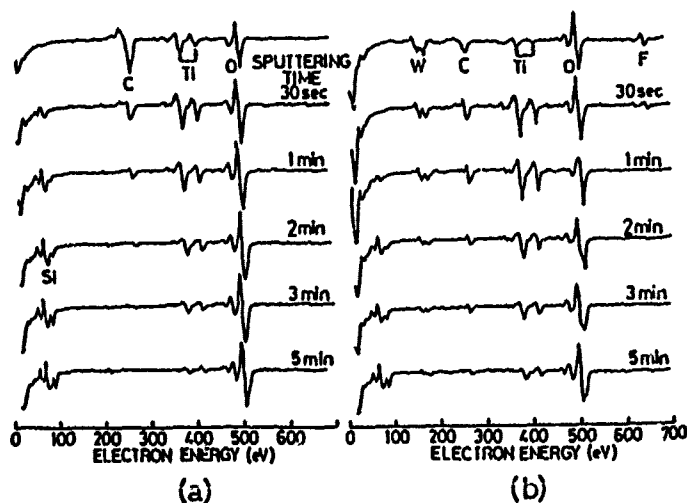


Figure 3. Auger spectra. (a):after Ti-ion irradiation, (b):after laser CVD. Ar-ion sputtering rate is 2.5 nm/min.



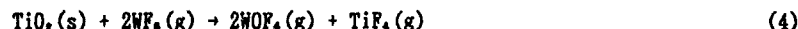
is induced by the photon absorption of TiO_2 . This speculation is based on the results of Auger electron spectroscopy. Next, a Ti reduction of WF_6



is induced under ArF excimer laser radiation. This reaction does not occur in pyrolysis, in which the reaction product is nonvolatile TiF_4 [6] which remains on the substrate. In our experiment, laser radiation can change the reaction path. W nuclei are formed on the SiO_2 surface by reaction (2) during laser CVD. Finally, at the LPCVD step, via a H_2 reduction of WF_6 on W nuclei



growth of nuclei occurs and continuous W films appear on the Ti-ion-irradiated SiO_2 . The TiO_2 which is not reduced in the laser CVD step is etched off at the LPCVD step by the reaction



in which the WOF_4 has a boiling point of 459 K. Therefore the ion-irradiation pattern once fades at the beginning of LPCVD. This is consistent with the experimental results.

SUMMARY

Adherent selective W film deposition on Ti-ion-irradiated SiO_2 is achieved via consecutive processes of ArF excimer laser CVD and LPCVD. Ti acts as a reducing agent of WF_6 and improves adhesion of the deposited W film with SiO_2 . No laser CVD results in no W deposition. Therefore, laser CVD is essential in our experiments.

ACKNOWLEDGEMENT

This study was performed through Special Coordination Funds of the Science and Technology Agency of the Japanese Government.

REFERENCES

- [1] W. A. Hennessy, M. Ghezzi, and R. H. Wilson, J. Electrochem. Soc. **135**, 1730 (1988).
- [2] E. K. Broadbent and C. L. Ramiller, J. Electrochem. Soc. **131**, 1427(1984).
- [3] H. Matsuhashi, S. Nishikawa, and S. Ohno, Extended Abstracts of the 20th (1988 International) Conference on Solid State Devices and Materials, Tokyo, 1988, p.89.
- [4] J. C. Barbour, A. E. M. J. Fischer, and J. F. van der Veen, J. Appl. Phys. **62**, 2582(1987).
- [5] M. Liehr, F. K. LeGoues, G. W. Rubloff, and P. S. Ho, J. Vac. Sci. Technol. **A3**, 983(1985).
- [6] E. K. Broadbent, A. E. Morgan, J. M. DeBlasi, P. van der Putte, B. J. Burrow, D. K. Sanada, and A. Reader, J. Electrochem. Soc. **133**, 1715(1986).

PART V

Laser Doping, Annealing
and Planarization

NANOSECOND THERMAL PROCESSING FOR ULTRA-HIGH-SPEED DEVICE TECHNOLOGY

Thomas W. Sigmon and Anthony M. McCarthy, Stanford University, Stanford, CA
Kurt H. Weiner, Lawrence Livermore National Laboratory, Livermore, CA
Paul G. Carey, Siemens, Munich, FRG

ABSTRACT

Progress in high-speed device technology is occurring by both scaling of conventional devices, such as MOSFETs and bipolars, and the development of new device structures which take advantage of multi-layer heterostructures. As scaling in lateral dimensions allows production of devices with dimensions approaching $0.1\mu\text{m}$, vertical scaling has become a topic of concern. In this paper we focus on nanosecond thermal processing (NTP), a new area of process technology which uses a pulsed uv -laser to perform selective doping and epitaxy on nanosecond time scales. The rapid thermal cycles and precise control of impurity profiles inherent to the new technique addresses many of the problems faced in vertical scaling for silicon MOS and bipolar structures and in the fabrication of selective heteroepitaxial layers. Following a brief historical overview and description of the process, successful applications in the fabrication of submicron MOSFETs and narrow base bipolar transistors in silicon will be presented. Structural and electrical results will be presented for heteroepitaxial layers fabricated in the $\text{Ge}_x\text{Si}_{1-x}$ and $\text{In}_x\text{Ga}_{1-x}\text{As}$ material systems by the technique.

INTRODUCTION

In this paper we introduce the concept of nanosecond thermal processing (NTP), a new regime of thermal processing in which the thermal cycles last from 100 to 1000 ns. The idea behind the new processing is best illustrated by reference to Fig 1. In this figure, we show a wafer being subjected to a high-energy pulse of uv energy. Using the laser the near surface region (10 to 500 nm) of the wafer is melted in a controlled fashion. Selective processing is accomplished by suitably masking the wafer in regions where laser energy is not desired. To date we have implemented several processes which incorporate this pulsed-laser technique. As is shown in Fig. 1, these processes include: a) dopant incorporation, by placing the wafer in a cell with appropriate gas ambient, b) selective epitaxial growth of homo-, and heteroepitaxial layers, both doped and undoped, and c) selective annealing and redistribution of previously deposited dopant layers. By substituting the laser for more traditional heating sources (e.g. flash lamps and furnaces), these processes are accomplished with *nanosecond* thermal cycles and *no significant* wafer heating. Furthermore, unlike other laser approaches which use small beams to individually write device structures, the NTP processes use a large area, homogeneous beam and conventional masking techniques to process wafers on a die by die fashion. Analogous to modern lithography steppers, this approach allows direct integration of the process into a modern semiconductor processing line with little or no change to the basic process sequence. Along with this ease of integration, NTP

PART V

Laser Doping, Annealing
and Planarization

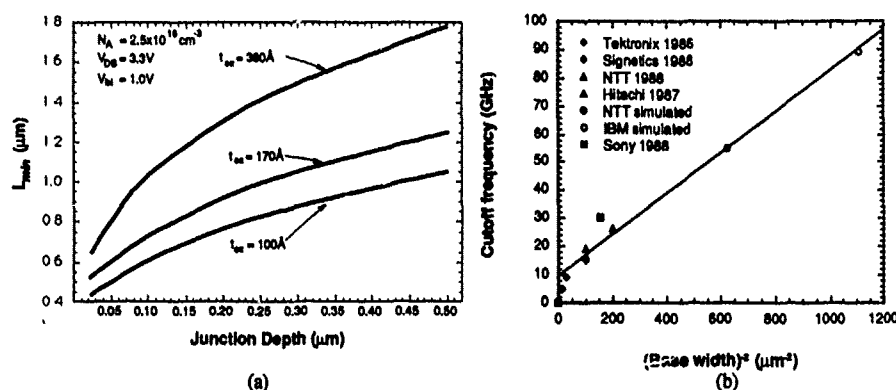


Figure 2. Effect of device scaling on a) vertical dimensions in MOS structures to eliminate short channel effects, b) to increase the performance in bipolar structures by decrease of the base width.

Work at Stanford began in 1984 [7], first using the alexandrite system discussed in Ref. [5] then evolving to a XeCl excimer laser. Devices were first demonstrated later in that year using the excimer laser source [8]. In the remainder of this paper, a complete review of the equipment, process, and device fabrication results obtained from this effort is discussed.

NANOSECOND THERMAL PROCESSING EQUIPMENT

The laser system, shown schematically in Fig. 3, is designed to allow determination of all parameters required for characterization of the melt/diffusion process *in-situ* and in *real time*. The equipment is designed around three process modules. The first consists of the excimer laser, beam splitters, beam-shaping optics, gas cell, and X-Y stages. The second module supplies the *in-situ* diagnostic capabilities and *real time* data acquisition. The third and final module supplies the excimer beam diagnostics which include spatial uniformity, beam size, and effective energy fluence.

The laser-melting equipment is built around a Questek 2860 excimer laser operating at the XeCl wavelength, 308 nm. The excimer beam is directed through a set of reflective beam splitters which allow course adjustment ($\Delta E \geq 10\%$) of the laser energy. Fine adjustments in the energy are made at the laser by varying the high voltage on the discharge capacitors. After the beam splitters, the beam passes through expanding optics and into an optical integrator which is used to reduce and homogenize the input laser beam. The refined beam can be focussed to a final spot size on the wafer which can be varied from a $3 \times 3 \text{ mm}^2$ up to $1 \times 1 \text{ cm}^2$ square. The wafer is contained in a portable vacuum cell filled with the dopant gas for *in-situ* doping or an inert gas for melt-recrystallization experiments only. The cell is mounted on a set of X-Y stages and the process is usually carried out on a die-by-die step and repeat mode under computer control.

Real-time process diagnostics are available which allow the measurement of: *i*) the duration for which the substrate surface remains molten, *ii*) the temporal profile of the excimer laser beam, *iii*) visual inspection of the processed areas, and *iv*) visual alignment of the wafers for die-by-die processing.

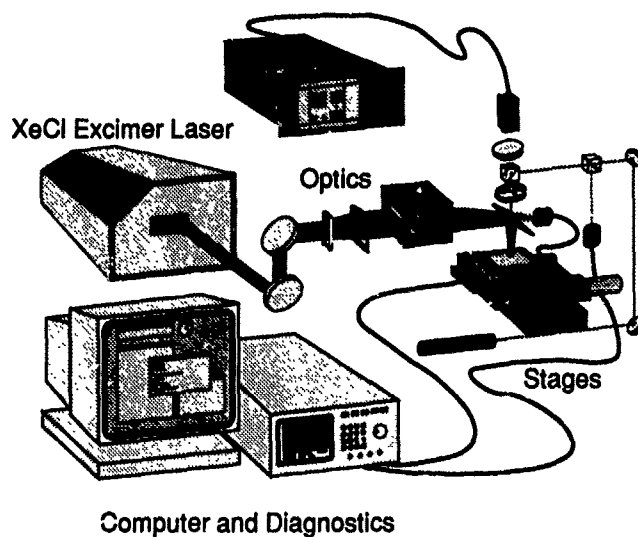


Figure 3. Schematic representation of the pulsed uv -laser nanosecond thermal processing system. The system is controlled by a computer work station and includes *in-situ*, digitized diagnostic capabilities for *real-time* process monitoring.

The surface melt duration is measured using a HeNe ($\lambda = 633$ nm) laser focussed on the silicon wafer and an avalanche photodiode (APD) to detect the reflected beam. Together, the laser and detector constitute a simple surface reflectivity probe. Since the HeNe beam is non-intrusive, the measurement can be made *in-situ*.

The temporal intensity profile of the excimer laser beam is acquired using a Si *pin* photodetector placed behind the final turning mirror shown in Fig. 3. The output of this detector and that of the APD are collected by a HP54111D digitizing oscilloscope. This output in turn is fed into the computer system controlling the X-Y stages and the laser. Typical examples of the temporal and

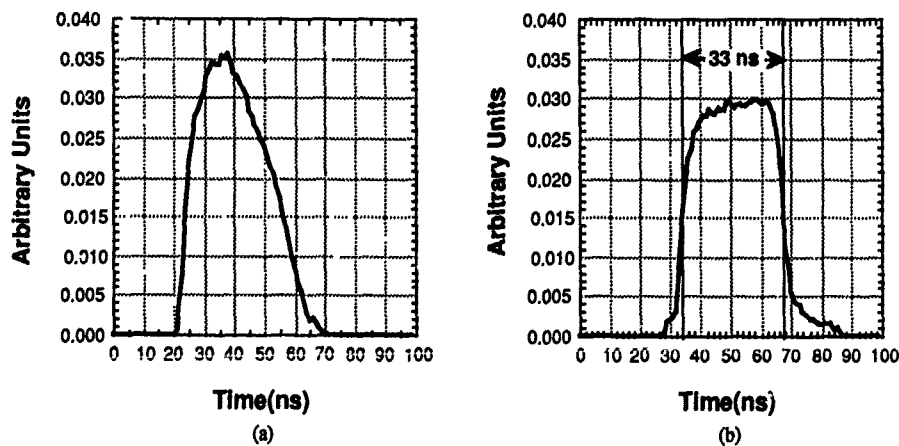


Figure 4. Typical examples of the a) temporal laser pulse profile and b) sample reflectivity obtained from the *in-situ* monitors.

reflectivity data acquired from the silicon surface are shown in Fig. 4.

The final module incorporated into the laser system allows spatial beam profiling and precise energy fluence determination. The ability to profile the beam and insure its homogeneity is perhaps the most critical requirement for accurate characterization of the process. Without detailed knowledge of the spatial uniformity, size, and energy of the beam, it is difficult to accurately determine the energy fluence. Furthermore, nonuniformities of the beam intensity, so called "hot spots" can cause erroneous results and create thermal gradients across the molten region which can lead to a breakup of the recrystallization front resulting in highly defected layers being grown. Examples of the spatial profiles acquired by the beam profiling system, consisting of a charge injection diode (CID) array, frame grabber, and control software, are shown in Fig. 5. In this figure, the uniformity of the laser beam at the output of the laser, Fig. 5(a) is compared to the beam at the output of the homogenization system, Fig. 5(b). The typical homogenized beam has absolute intensity variations of 7% across the central portion of the beam. Energy measurements are taken by replacing the CID camera with a Sciencetech calorimeter and are accurate to $\pm 3\%$.

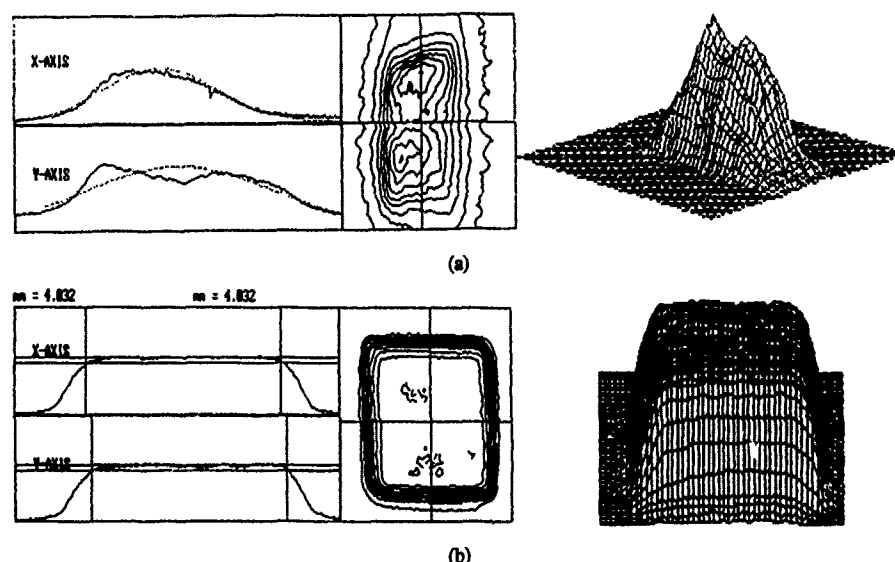


Figure 5. Spatial profiles of excimer laser beam obtained with the beam profiling system: a) excimer beam as produced by the laser, b) spatial profile after homogenizing optics.

PROCESS CHARACTERIZATION

We have used both materials and electrical measurements, combined with modeling to characterize the melt-doping process. The ability to model the process has allowed rapid determination of the important controlling variables. In Fig. 6 we show calculations of the melt-time vs melt-depth with laser energy density as a parameter for the XeCl excimer laser [9]. The idealized gaussian laser pulse used for the calculations is also displayed on the figure. Figure 7 shows experimentally determined melt-depths plotted versus melt-time. Also shown in this figure

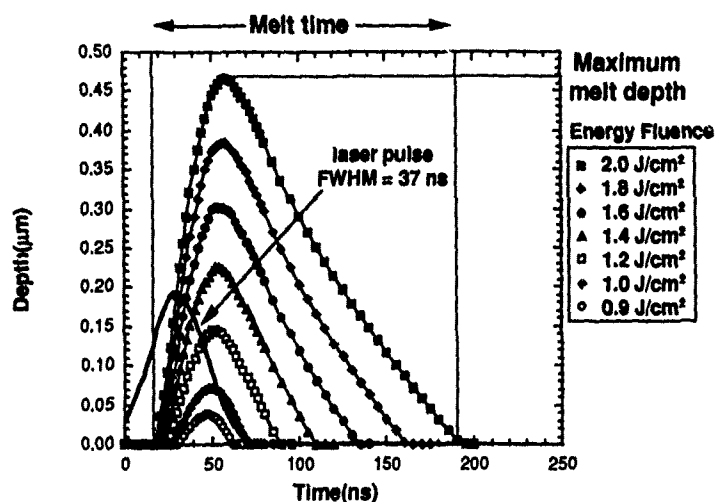


Figure 6. LASERMELT simulations of the silicon melt depth versus time for an idealized gaussian laser pulse.

are results calculated using the melt-depth simulator developed for this work, LASERMELT [10]. Using the melt simulator we can calculate the melt depth for a gaussian pulse similar to Fig. 6, as well as the actual laser pulse, digitized using the fast oscilloscope. As shown by the solid line in Fig. 7, simulations using the digitized profile provide excellent agreement with experiment. The disagreement between the two simulations underscores the importance of adequate *in-situ* diagnostics for determination of the laser pulse shape and sample melt-time.

Examples of dopant profiles that can be obtained using the process, along with simulated results

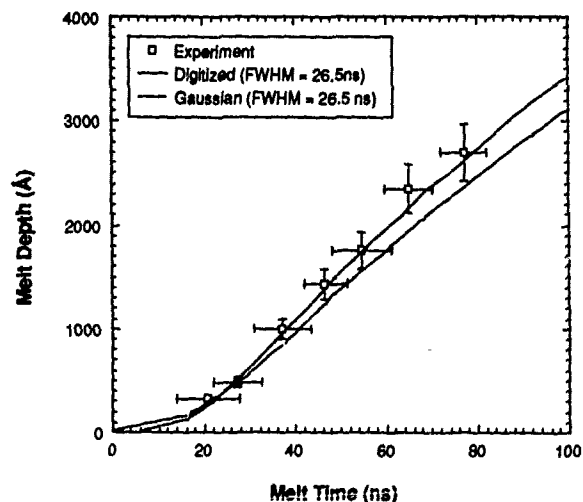


Figure 7. Single set of results for melt-depth versus melt-time experiments. Also shown are simulated results from LASERMELT using both a digitized temporal beam profile and a gaussian approximation. Agreement between experiment and simulation using the digitized pulse is very good, demonstrating the importance of *in-situ* monitors for the temporal profile of the excimer beam.

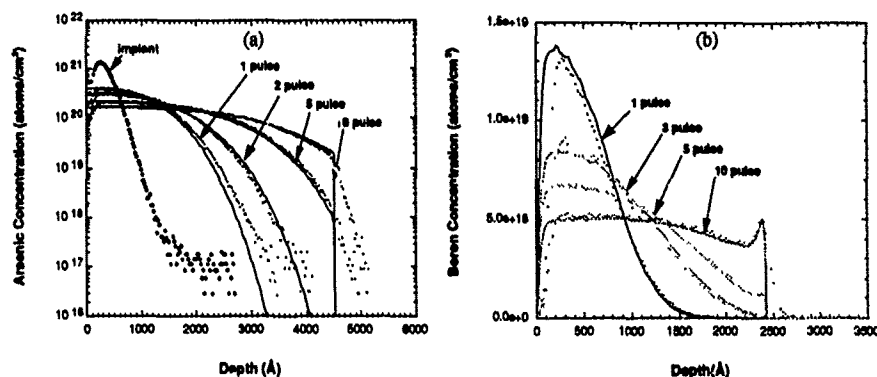


Figure 8. Examples of a) arsenic and b) boron profiles obtained by redistribution of an ion implanted profile using the NTP process using a fixed laser energy and varying the number of laser pulses. Also shown are simulated results from our LASERDOPE simulation program.

are shown in Fig. 8(a) and (b) for arsenic and boron dopants, respectively. For these experiments, the initial atom distribution is ion implanted in order to provide a known dopant concentration profile for the diffusion calculations. The profiles are then redistributed by varying the number of laser pulses while keeping the laser energy constant. The simulation is performed using a velocity dependent segregation coefficient [11,12] in order to obtain results which accurately reproduce the experimental data. In Fig. 9 we show SIMS results taken for gas immersion laser doping using 5% PH_3 in H_2 as the gas ambient. Details of the melt-times are shown on the figure. The ability to form true *box-like* profiles for junction depths as shallow as 30 nm is apparent from this figure.

One of the several advantages of the GILD process for junction formation is that the layers are electrically active following the process and thus require *no* post-doping anneal steps. We have investigated the electrical properties of these junctions and found that they can be made essentially free from defects, the devices being dominated by standard defects such as perimeter leakage.

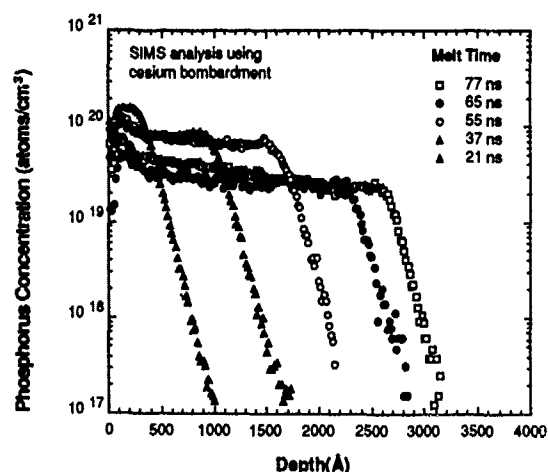


Figure 9. SIMS profiles obtained for GILD processing of silicon in a phosphorus dopant ambient. For these data the number of laser pulses is fixed at 20 and the melt depth is changed by changing the laser energy. This figure demonstrates the ability of the GILD process to produce true *box-like* profiles.

Although some thermal processing must be performed to transform a doped layer into a measurable device, the temperatures can usually be held below 600°C. Deep level transient spectroscopy measurements have been performed previously on GILD doped layers with no defects being found [13] for process conditions used for device fabrication. Although these results contradict others who have done similar experiments [14,15], we believe that our experimental conditions, *e.g.* laser parameters, device fabrication techniques, *etc.* play a major role in determining the quality of the final electrical results.

DEVICE FABRICATION RESULTS

MOS Transistors

We have fabricated *n*- and *p*-channel MOS transistors using the GILD process [16,17]. Standard polysilicon gate MOS processes are used, with the GILD process being inserted in place of the normal ion implantation steps. In Fig. 10 we show the wafer split between the GILD and ion implanted devices, the processes having been identical up to this point. The main advantage of using the GILD process, other than providing shallower, lower resistance source-drain regions, is in the reduction of dopant diffusion normally occurring during the implant activation step, by *elimination* of this step. This effect is dramatically illustrated in Fig. 11, where we show the change in device threshold voltage V_T versus polysilicon gate length, L_{POLY} . It is seen that GILD devices ($x_j \sim 125$ nm) can be fabricated with essentially no shift in threshold voltage down to $L_{POLY} \sim 0.6$ μ m, the stretched limits of our process. This is in contrast to the implanted devices ($x_j \sim 580$ nm) where loss of gate control, due to short channel effects, is observed at $L_{POLY} \sim 2.0$ μ m, the actual design length for the process.

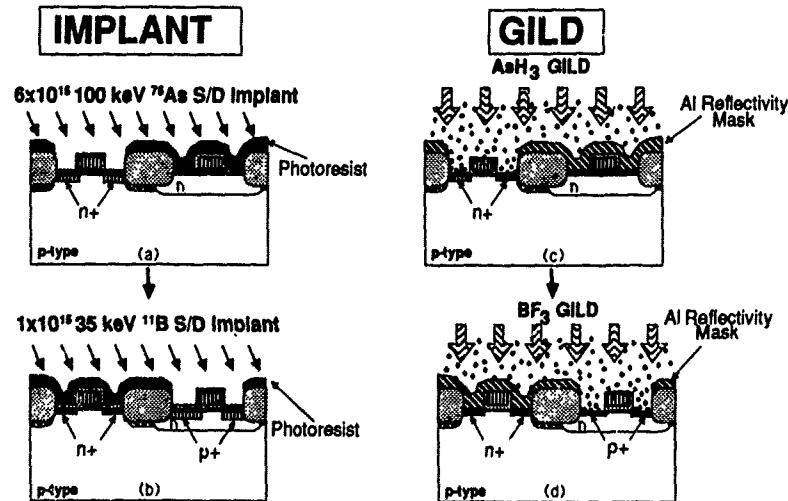


Figure 10. Wafer cross sections for NMOS and PMOS devices at the ion implant (a-b) - GILD (c-d) wafer split. The main differences between the GILD and implanted wafers are: i) an Al mask replaces the resist mask for the GILD wafers, ii) the source-drain oxides are removed for the GILD devices, and iii) the implanted wafers must be tilted during implant to minimize ion channeling effects.

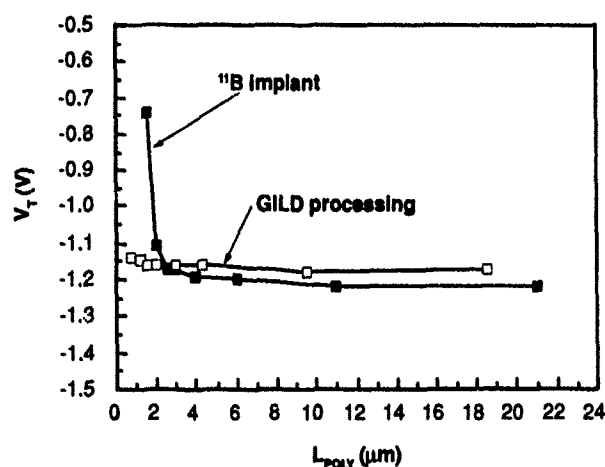


Figure 11. Threshold voltage shift, V_T vs polysilicon gate length, L_{POLY} for GILD processed and ion implanted PMOS transistors. These data show that essentially no threshold shift occurs for gate lengths down to $0.6 \mu m$ for the GILD devices while significant shift is observed for the ion implanted transistors.

In Fig. 12 we show a comparison of the high frequency CV, and quasi-static IV curves for thin ($t_{OX} = 20 \text{ nm}$) gate oxides beneath GILD melted polysilicon gates and unmelted controls. It is clear from these curves that the GILD process causes no deleterious effects on the gate oxide properties. Similar results are found for the density of interface states at the oxide/silicon interface. These results are crucial to the application of the GILD process in future VLSI process technology.

Bipolar Transistor Fabrication

The ability of the GILD process to fabricate shallow, box-like profiles lends itself particularly well to today's VLSI bipolar technology. For these technologies, reduction in base

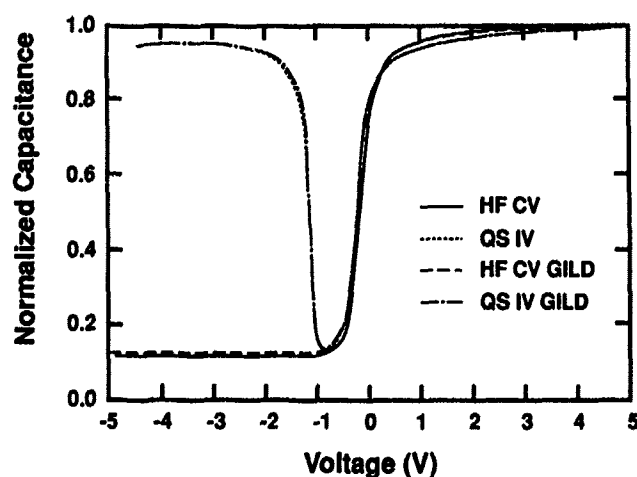


Figure 12. Comparison of high frequency CV and quasi-static IV characteristics of GILD processed and furnace annealed polysilicon on 20 nm gate oxide capacitors. There is no noticeable difference in the data between the GILD wafers and the furnace-annealed control wafers.

width is desired in order to optimize the performance of the bipolar transistor. Concurrently, the base dopant concentration must be increased to maintain a low base resistance in the thinner base region. In the future, as base widths shrink well below 100 nm, basic problems will limit the effectiveness of current doping technologies, such as ion implantation and diffusion from doped layers, in accomplishing these tasks. Two approaches exist, however, which allow NTP to offer a unique solution to the problems faced in bipolar transistor fabrication. One is to simply redistribute and simultaneously anneal, on a nanosecond time scale, previously implanted doped layers. The effect of this approach is shown in Fig. 13(a) and (b). In Fig. 13(a) we show SIMS analysis of an ion implanted *npn* structure. The gaussian distributions and long channeling tails associated with ion implantation are evident. Figure 13(b) illustrates how NTP processing can both redistribute the implanted profile to a more technologically useful one, while simultaneously annealing the implanted base and emitter layers. Using the technique of ion implantation with laser-induce activation and diffusion (I²LIAD) we have fabricated bipolar transistors with excellent forward and reverse bias electrical behavior which exhibit a maximum current gain approaching 200.

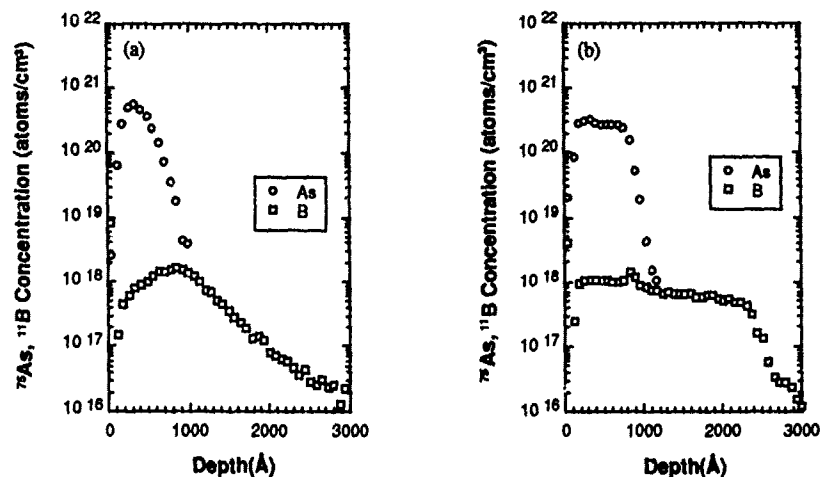


Figure 13. Comparison of ion implanted emitter-base profiles a) before and b) after laser redistribution and anneal.

In a recent publication [18] we have also demonstrated the fabrication of *npn* bipolar transistors *without* the use of ion implantation, using the GILD process to dope both base and emitter regions of the devices. The electrical characteristics of one of these devices are shown in Fig. 14(a) and (b). Figure 14(a) is the transfer characteristic of the device. Even though this device has a zero bias base width of less than 100 nm, it still exhibits a high punch-through and Early voltage, resulting from the relatively high base dose incorporated during the GILD process. In Fig. 14(b) we show the *dc* forward current gain h_{fe} of the device. Further improvement of h_{fe} can be easily accomplished by simply lowering the incorporated base dose. It should also be remembered that these devices have been fabricated *without* high temperature annealing steps, and as such can be easily incorporated into advanced ULSI BiCMOS circuits.

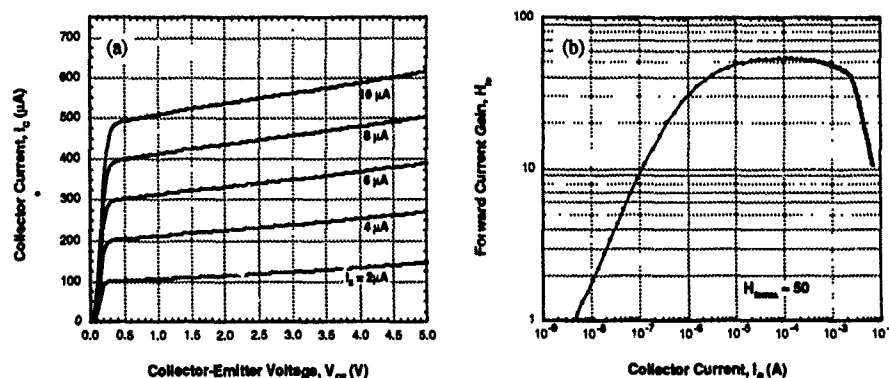


Figure 14. Electrical characteristics of an npn bipolar transistor fabricated using the GILD process without ion implantation: a) collector current versus collector-emitter voltage transfer characteristic, and b) common emitter current gain versus collector current.

Nanosecond Selective Epitaxial Processes

As increased demands are placed upon device performance, the use of epitaxial processes in the fabrication of high speed device structures will increase in importance. One difficulty in the use of epitaxial processes for fabrication of heterostructures is the non-selective nature of most common (e.g. MBE, CVD, RTCVD) epitaxial processes. In the following, we briefly describe an alternate to the above processes using NTP, which allows both selective epitaxial growth and *in-situ*, simultaneous doping. At this writing we have selectively grown both Si/Si and Ge_xSi_{1-x} /Si layers [19], and achieved large area growth of InGaAs/GaAs [20]. Figure 15 illustrates the procedures by which the laser induced, selective epitaxial process occurs. At this time we have fabricated and characterized p^+-n junctions fabricated in $Ge_{0.26}Si_{0.74}$ layers. The electrical characteristics of devices fabricated from these layers are shown in Fig. 16. In this figure we plot both the forward and reverse bias I-V characteristics for the diodes. It should be noted that using

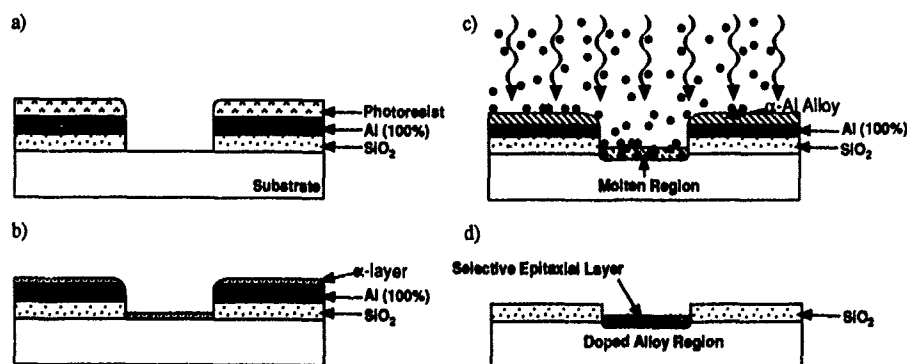


Figure 15. Schematic diagram of the selective LIE process: a) the wafer is patterned using standard photolithography, b) the photoresist and the amorphous material are deposited, c) the overlayer is alloyed with the underlying substrate, and d) the aluminum mask is removed leaving a selectively grown layer of heteroepitaxial material.

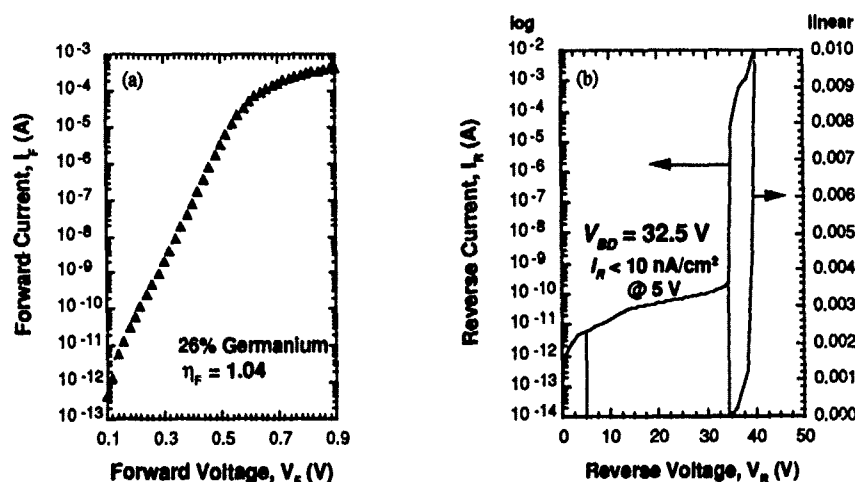


Figure 16. Forward and reverse IV characteristics for p - n $\text{Ge}_{0.2}\text{Si}_{0.8}/\text{Si}$ diodes fabricated using selective laser epitaxy: a) forward IV shows ideal diode behavior over many decades of current, b) reverse IV indicates the reverse leakage at 5V is less than 10 nA/cm^2 while reverse breakdown occurs abruptly between -32 and -33 volts. The depth of this junction is less than 20 nm.

RBS measurements we have determined that the alloy layer thickness for these films is less than 25 nm and that dislocation densities are $< 10^5 \text{ cm}^{-2}$.

CONCLUSIONS

Nanosecond thermal processing (NTP), a new process technology which allows fabrication of ultra-shallow, high concentration dopant layers suitable for ULSI technology has been described. The technology utilizes a broad beam, pulsed μv -excimer laser to melt, on a die-by-die basis, the near surface region of a suitably masked wafer on a nanosecond time scale. Dopant incorporation and activation of the region occurs within $\sim 100 \text{ ns}$, eliminating unwanted diffusions of other layers present on the wafer. Demonstration of the fabrication of submicron MOS and narrow base bipolar transistors fabricated using *in-situ* doping of the active layers has been carried out. Two unique extensions of NTP, annealing and redistribution of ion implanted layers and selective laser induced epitaxy, have also been described.

REFERENCES

1. P.M. Solomon, *Proceedings of the IEEE*, 70 (5), 489, 1986.
2. T.F. Deutch, D.J. Ehrlich, R.M. Osgood, Jr., and Z.L. Liao, *Appl. Phys. Lett.*, 36 (10), 847, 1980.
3. T.F. Deutch, J.C.C. Fan, G.W. Turner, R.L. Chapman, D.J. Ehrlich, and R.M. Osgood, Jr., *Appl. Phys. Lett.*, 38 (3), 144, 1981.
4. T.F. Deutch, D.J. Ehrlich, D.D. Rathman, D.J. Silversmith, and R.M. Osgood, Jr., *Appl. Phys. Lett.*, 39 (10), 825, 1981.
5. G.B. Turner, D. Tarrant, G. Pollock, R. Pressley, and R. Press, *Appl. Phys. Lett.*, 39 (12), 967, 1981.
6. K.G. Ibbs and M.L. Lloyd, *Optics and Laser Technology*, p 37, Feb., 1984.

7. T.W. Sigmon, P.G. Carey, R.L. Press, T.S. Fahlen, and R. J. Pressley, in *Energy Beam-Solid Interactions and Transient Thermal Processing*, edited by J.C.C. Fan and N.M. Johnson (North-Holland, New York, 1984) p.
8. P.G. Carey, T.W. Sigmon, R.L. Press, T.S. Fahlen, J.C. Huneke, and R. Crouch, *1984 IEDM Technical Digest*, p. C59, Dec. 1984.
9. M.O. Thompson, Ph.D. dissertation, Cornell University, Ithaca, New York, 1984.
10. E. Landi, P.G. Carey, and T.W. Sigmon, *IEEE Trans. Computer-Aided Design*, 7, (2) p. 205, 1988.
11. R.F. Wood, *Phys. Rev. B*, 25 (4), 2786, 1982.
12. M.J. Aziz, *J. Appl. Phys.* 53 (2), 1158, 1982.
13. P.G. Carey, Ph.D. dissertation, Stanford University, Stanford, CA, 1988.
14. R.T. Young, J. Narayan, W.H. Christie, G.A. Van Der Leaden, J.I. Levatter and L.J. Chen, *Solid State Technology*, 26, 183, 1983.
15. A. Slaoui, F. Foulon, M. Bianconi, L. Corra, R. Nipotti, R. Stuck, S. Unamuno, E. Fogarassy and S. Nicoletti, in *Materials Research Society Symp. Proc. Vol. 129*, edited by A.W. Johnson, G.L. Loper, T.W. Sigmon, to be published.
16. P.G. Carey, K. Bezjian, T.W. Sigmon, and P. Gildea, *IEEE Electron. Device Lett.*, EDL-7 (7), 440, 1986.
17. P.G. Carey, K.H. Weiner, and T.W. Sigmon, *IEEE Electron. Device Lett.*, EDL-9 (10), 542, 1988.
18. K.H. Weiner and T.W. Sigmon, *IEEE Electron. Device Lett.*, EDL-10 (6), 260, 1989.
19. J.R. Abelson, T.W. Sigmon, K.B. Kim, and K.H. Weiner, *Appl. Phys. Lett.*, 52 (3), 230, 1988.
20. Y. Chang and T.W. Sigmon, submitted to *Appl. Phys. Lett.*

IN SITU MEASUREMENT OF PULSED LASER INDUCED CARRIER GENERATION IN DOPED SILICON FILMS

T. SAMESHIMA, M. HARA and S. USUI
Sony Research Center, Yokohama 240, Japan

Abstract

Transient conductance measurements were used to study rapid carrier generation during the laser doping of a silicon film. The movement of the liquid-solid interface was measured and the point of initiation of carrier generation from dopant atoms diffused to the molten silicon was determined. It was established that the dopant atoms are activated at the moment the dopant diffused region solidified. Also, the laser doping technique was used to fabricate polycrystalline silicon thin film transistors (Poly-Si TFT's) at a processing temperature of 250°C.

§1. Introduction

Pulsed laser doping [1-3] is an attractive technique for fabricating source and drain regions with 0.1µm-deep junctions in metal-oxide semiconductor (MOS) transistors and in thin film transistors on a large-area insulating substrates. We have reported the laser-induced melting of predeposited impurity doping (LIMPID) technique [3,4]. This technique employs a radio-frequency glow discharge (rf-GD) to deposit a thin dopant film uniformly by decomposition of a dopant gas such as B_2H_6 or PH_3 , followed by irradiation with a pulsed XeCl-308nm excimer laser, leading to superficial melting of the silicon and diffusion of the dopant. Using this technique, heavy doping of silicon to dopant concentrations of $1 \times 10^{21} \text{ cm}^{-3}$ have been obtained.

In this paper, we analyzed carrier generation "in situ" using transient conductance measurements [5,6]. We first report our investigation of carrier generation in the doped region formed by laser doping of silicon-on-sapphire (SOS) films. Next we report our investigation of carrier generation in the doped region formed by laser-induced melting and regrowth, using doped amorphous silicon as the starting material. This paper then presents a new process for fabricating polycrystalline silicon thin film transistors (poly-Si TFT's) using the laser doping technique with doped amorphous silicon film for the dopant source.

§2. Transient conductance measurements

Figure 1 shows a schematic diagram of the apparatus used for transient conductance measurements of carrier generation in the region formed by laser doping. A 500nm-thick undoped SOS film with an orientation of (100) and resistivity of $100 \Omega \cdot \text{cm}$ was patterned into 1mm stripes and an Aluminum electrodes with a width and gap of 3mm were formed on the stripes. A 50nm-thick boron film was then deposited at 200°C on the silicon surface in the electrode gap by decomposition of 20SCCM B_2H_6 diluted to 1% with Ar ($B_2H_6(1\%)/\text{Ar}$) using rf-GD. The sample was then connected to a load resistance of 50Ω and a bias voltage was applied. Irradiation was provided by a pulsed 308nm-XeCl excimer laser ($\tau=30\text{ns}$ full-width at half maximum) in air at room temperature. The sample was irradiated with a laser beam whose spot size was focused from $3\text{mm} \times 6\text{mm}$ to $5\text{mm} \times 10\text{mm}$ through a lens. The transient current during and after irradiation was measured across the load resistance by a high-speed storage oscilloscope. The threshold melting laser energy and the duration of melt at the sample surface were determined by time-resolved optical reflectivity measurements [7] using an Ar-514.5nm laser beam as a probe light.

To measure carrier generation when a doped amorphous silicon film is annealed by laser irradiation, boron-doped and phosphorus-doped hydrogenated amorphous silicon (a-Si:H,B and a-Si:H,P) films were deposited on a glass substrate. 100nm-thick doped-films were deposited at 250°C by decomposition of 50SCCM $SiH_4(10\%)/\text{Ar}$ and 10SCCM $B_2H_6(1\%)/\text{Ar}$ and of 50SCCM $SiH_4(10\%)/\text{Ar}$ and 10SCCM $PH_3(1\%)/\text{Ar}$ using rf-GD. 1mm-wide silicon stripes were patterned.

Aluminum electrodes with a width and gap of 3mm were subsequently formed on the silicon stripes. The transient current during and after irradiation was measured.

§3-1. Carrier generation in the doped region formed by laser doping

Curve A in Fig.2 shows the conductance change during and after irradiation with a single pulse at an energy density of $1.04\text{J}/\text{cm}^2$ for an SOS film on which a 50nm-thick boron film has been deposited. Figure 2 also shows the conductance change during and after irradiation with a single pulse at an energy density of $1.33\text{J}/\text{cm}^2$ for SOS film on which a boron film was not deposited (curve B). The conductance associated with molten silicon appeared first stage and reached its maximum at 170ns. The maximum melt depth is estimated to be 420nm from the hypothesized conductivity of molten silicon ($12000\text{S}/\text{cm}$)[8] for both samples. The SOS film coated with the boron film was melted to a 420nm depth by irradiation at a lower energy density than the uncoated SOS film because deposition of the boron film reduced the optical reflectivity of the surface from 62% (bare silicon) to 50% by the antireflection effect. After 170ns, the molten region began to solidify at a velocity of $2\text{m}/\text{s}$, the value of which was obtained from the slope of the decreasing conductance. The initiation of carrier generation in the boron-doped region occurred rapidly at 260ns, because the conductance of the SOS film coated with boron decreased more slowly after 260ns than that of the uncoated SOS film. The residual conductance was measured at the termination of melt for the SOS film coated with the boron film, as can be seen Fig.2. This result shows that carriers were generated at the moment the boron-diffused region solidified, even while the superficial region was still melting. Most of the carriers are generated in the region shallower than 200nm because the top 200nm was melted when the initiation of carrier generation occurred at 260ns, as can be seen by curve A in Fig.2. Secondary Ion Mass Spectrometry (SIMS) measurements revealed that most of the boron atoms are concentrated in the region within 200nm of the surface, because the dose of boron atoms in the region below 200nm was $6 \times 10^{15}\text{cm}^{-2}$, which was only 3% of the total dose of $2 \times 10^{17}\text{cm}^{-2}$, as is shown in Fig.3. Figure 3 also shows the in-depth profile of boron concentration calculated using a simulation program which we previously reported [4]. The evolution of boron diffusion with time from the surface into the molten region was calculated using the change of the melt depth obtained experimentally, as shown by curve B in Fig.2. If the boron diffusion coefficient is assumed to be $2.7 \times 10^{-4}\text{cm}^2/\text{s}$, the calculated result agrees well with the experimental result, as can be seen in Fig.3. The p-n junction depth was 380nm, which was shallower than the maximum melt depth of 420nm, because the melt front moved too fast for boron atoms to diffuse throughout the molten region.

After termination of melt the conductance increased monotonously with time. The room temperature sheet conductance of $0.11\text{S}/\square$ is twice the value at the termination of melt. In order to determine whether the activation of boron atoms is complete at the termination of melt or whether it continues in the solid phase after resolidification, the following experiment was carried out. An SOS film was doped with boron by irradiation with a pulse at an energy density of $0.6\text{J}/\text{cm}^2$. The sample was successively irradiated with 10 pulses at an energy density of $0.45\text{J}/\text{cm}^2$, which is lower than the melting threshold energy of $0.5\text{J}/\text{cm}^2$. Figure 4 shows the transient conductance caused by irradiation with the first and 10th pulse at $0.45\text{J}/\text{cm}^2$. After each irradiation of the 10 pulses, the conductance changed in similar fashion -- it decreased rapidly with irradiation. Afterwards it increased gradually to the initial value of $0.021\text{S}/\square$. No further increase of room-temperature conductance was observed with laser treatment, meaning that no further activation of boron atoms was effected in the solid silicon by laser heating. The conductance change in Fig.4 can be interpreted to mean that carrier mobility first decreases by laser heating and then increased gradually with time as the silicon film is cooled through heat diffusion to the underlying region. In laser doping, therefore, the activation of boron atoms is completed at the termination of melt for the

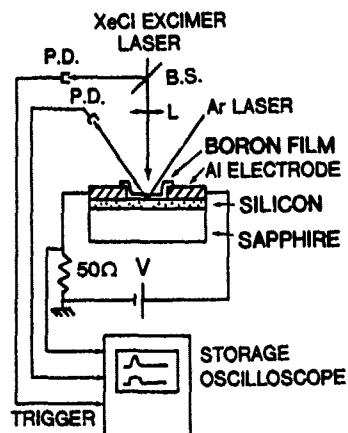


Fig.1 Schematic diagram of apparatus used for transient conductance and time-resolved optical reflectivity measurements.

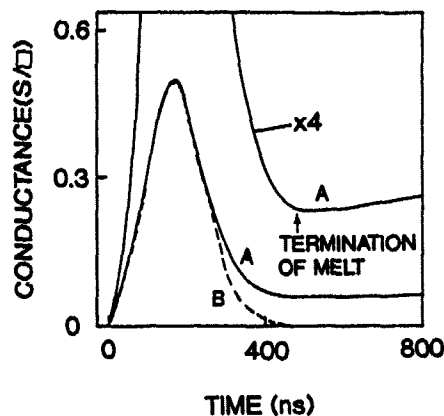


Fig.2 Conductance versus time with irradiation at $1.04\text{J}/\text{cm}^2$ for 500nm-thick SOS film coated with 50nm-thick boron film (curve A) and with irradiation at $1.33\text{J}/\text{cm}^2$ for uncoated SOS film (curve B). The arrow shows the termination of melt, which was determined by time-resolved optical reflectivity measurements.

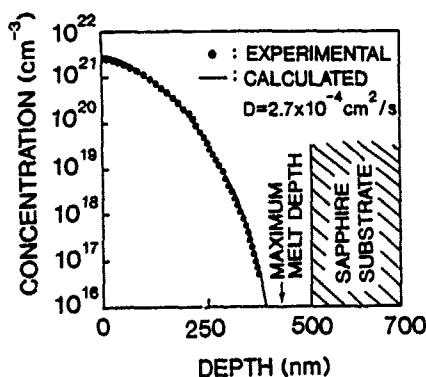


Fig.3 SIMS in-depth profile for boron concentration and calculated in-depth profile using melt front movement as shown by curve B in Fig.2 and hypothesized boron diffusion concentration of $2.7 \times 10^{-4} \text{cm}^2/\text{s}$.

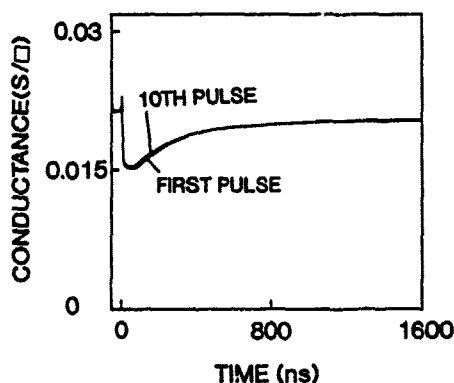


Fig.4 Conductance versus time for boron doped SOS film at first and 10th irradiation at $0.45\text{J}/\text{cm}^2$.

first pulse.

§3-2. Carrier generation during and after laser annealing of doped amorphous silicon

Carrier generation in the doped region was investigated when doped amorphous silicon films were irradiated by a laser pulse. The melting threshold energy was $130\text{mJ}/\text{cm}^2$ for the a-Si:H,B and a-Si:H,P films. Figure 5(a) and 5(b) shows the conductance change caused by irradiation with a single pulse with an energy density between 140 and $210\text{mJ}/\text{cm}^2$ for the a-Si:H,B and a-Si:H,P films, respectively. For both samples, the conductance associated with molten silicon occurred first, followed by conductance in the doped region, as can be seen by curve A in Fig.2. The maximum melt depth and conductance in the doped region increased with increasing energy density, as can be seen in Fig.5. Although the conductivity of as-deposited a-Si:H,B and a-Si:H,P films was 1×10^{-3} and $2 \times 10^{-3} \text{ S/cm}$, respectively, it was increased to 1.5×10^{-2} and $1.4 \times 10^{-2} \text{ S/cm}$, respectively, by irradiation with a single pulse at $210\text{mJ}/\text{cm}^2$. The increase of conductance was caused by the increase of the carrier mobility and the increase in the activation ratio of dopant brought about by the crystallization of a-Si:H through the laser induced melt-regrowth. The carrier concentration and mobility was obtained by Hall effect measurements. They were $3.1 \times 10^{21} \text{ cm}^{-3}$ and $8 \text{ cm}^2/\text{Vs}$ for boron-doped silicon and $1.0 \times 10^{21} \text{ cm}^{-3}$ and $9 \text{ cm}^2/\text{Vs}$ for phosphorus-doped silicon.

§4. Application of laser doping to the fabrication of Poly-Si TFT's

A doped region with low resistivity was obtained by laser irradiation of doped amorphous silicon at room temperature. This technique is useful for fabricating poly-Si TFT's[9]. Figure 6 shows the process of fabricating n-channel poly-Si TFT's using laser-induced crystallization of a-Si:H and laser doping with an a-Si:H,P film for the dopant source. A 20nm-thick a-Si:H layer was first deposited on a glass substrate at 250°C by decomposition of $50\text{SCCM SiH}_4(10\%)/\text{Ar}$ using rf-GD. Next, a photoresist layer was coated and patterned to protect the region not to be doped was defined. A 5nm-thick a-Si:H,P layer was subsequently deposited over the entire surface of the substrate at 100°C by decomposition of $50\text{SCCM SiH}_4(10\%)/\text{Ar}$ and $16\text{SCCM PH}_3/\text{Ar}$ using rf-GD. The a-Si:H,P layer on the photoresist was then removed by the lift-off technique. The sample was irradiated with a pulsed excimer laser beam with a $5\text{mm} \times 10\text{mm}$ spot size at room temperature. The multistep irradiation technique was used in order to prevent eruption of hydrogen which can break the film and cause surface roughness. In this technique, 10 pulses were irradiated with the energy density being increased from 140 to $210\text{mJ}/\text{cm}^2$, so hydrogen eruption did not occur with the surface of the film remaining very smooth. The a-Si:H region and a-Si:H region coated with a-Si:H,P film region were crystallized through laser-induced melting regrowth. Transmission electron micrograph measurements revealed that the grain size was between 10 and 60nm. Phosphorus atoms in the patterned a-Si:H,P layer were incorporated into the underlying silicon layer so that a region with a low sheet resistance of $600\Omega/\square$ was formed. After the irradiation, poly-Si islands were formed. An 100nm-thick SiO_2 layer was subsequently deposited at 250°C by decomposition of $2\text{SCCM SiH}_4(10\%)/\text{Ar}$ and $100\text{SCCM N}_2\text{O}$ for the gate insulator. Contact holes were opened for the source and drain regions, an Al layer was deposited and the gate, source and drain electrodes were defined. The sample was finally annealed in a hydrogen plasma at 150°C for 30 minutes at an rf power of 5W in order to terminate dangling bonds at the grain boundaries in the poly-Si film. The poly-Si TFT's were fabricated at a processing temperature of 250°C using laser-induced crystallization of a-Si:H and laser doping. Figure 7 shows the drain-current-vs-gate-voltage (I_D - V_G) characteristics of a poly-Si TFT with a gate width of $300\mu\text{m}$ and a gate length of $30\mu\text{m}$. On/off current ratio at a drain voltage of 5V between gate voltages of -5V and 20V is 1.5×10^4 . The effective carrier mobility in the linear region is $54\text{cm}^2/\text{Vs}$.

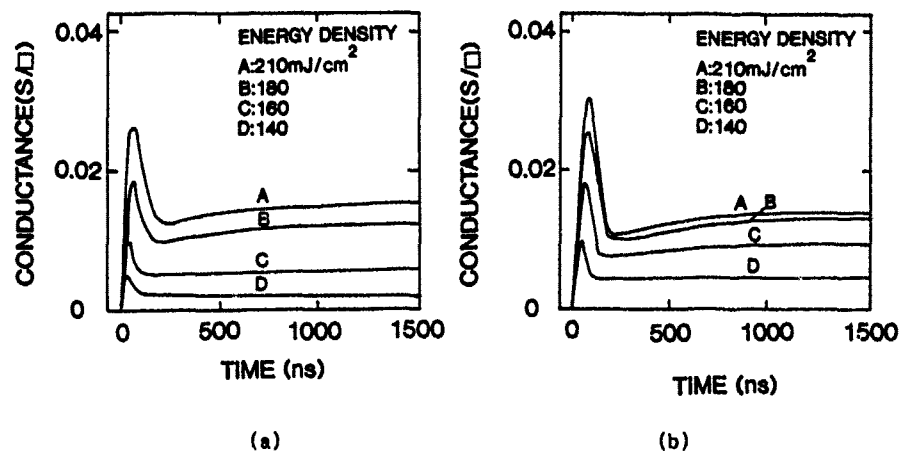


Fig.5 Conductance versus time caused by irradiation for energy density between 140 and 210 mJ/cm² for 100 nm-thick a-Si:H,B film (a) and 100 nm-thick a-Si:H,P film

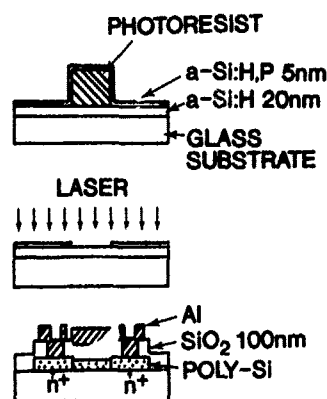


Fig.6 Schematic cross section of the poly-Si TFT's during fabrication.

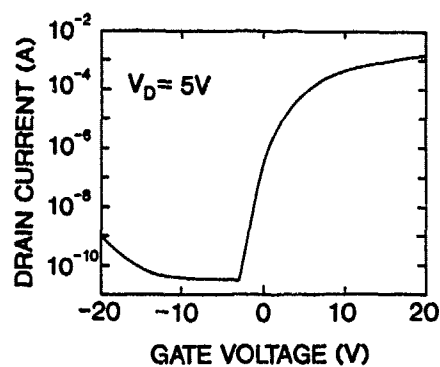


Fig.7 Drain current versus gate voltage characteristics for Poly-Si TFT. Gate width and length are 300 μm and 30 μm, respectively.

§5. Conclusions

Through transient conductance measurements, we obtained the carrier-generation characteristics of laser doping using a XeCl excimer laser. When SOS films coated with 50nm-thick boron film were irradiated with a single pulse at an energy density of $1.04\text{J}/\text{cm}^2$, the carrier generation in the boron-doped region was measured 260ns after the initiation of melt. A large conductance of $0.055\text{S}/\square$ for the doped region was obtained at the termination of melt at 470ns. This shows that the boron atoms were activated at the moment the boron-diffused region solidified. The conductance increased monotonously with time after the termination of melt because the carrier mobility increased as the silicon film cooled through heat diffusion to the underlying region. Boron atoms were concentrated within 200nm of the surface, while the silicon melted to a depth of 420nm because the melt front moved too fast for the boron atoms to diffuse throughout the molten region.

When the boron- and phosphorus- doped amorphous silicon films were irradiated by a laser pulse at an energy density over $140\text{mJ}/\text{cm}^2$, the silicon surface melted and carriers were generated in the doped region as the molten silicon solidified. A high conductivity of $1.5 \times 10^3 \text{S}/\text{cm}$ for B-doped poly-Si and $1.4 \times 10^3 \text{S}/\text{cm}$ for P-doped poly-Si was brought about by irradiation at an energy density of $210\text{mJ}/\text{cm}^2$.

Poly-Si TFT's with a maximum mobility of $54\text{cm}^2/\text{Vs}$ and a maximum on/off current ratio of 1.5×10^4 were fabricated at the low processing temperature of 250°C using excimer laser-induced crystallization and laser doping techniques. This process can be applied to large area devices on low cost substrate without high heat-resistivity, such as active matrices for a liquid crystal display panel.

Acknowledgement

The authors would like to thank M.Nakagoe and M.Kanada for their experimental support and Dr.Y.Kawana for the helpful discussions. They also wish to acknowledge the support of Dr.S.Watanabe.

References

1. T.F.Deutsch, J.C.C.Fan, G.W.Turner, R.L.Chapman, D.J.Ehrlich and R.M.Osgood, Jr, Appl. Phys. Lett., **38**, 144 (1981).
2. P.G.Carey, K.Bezian, T.W.Signon, P.Gildea and T.J.Magee, IEEE Electron Device Lett., EDL-7, 440 (1986).
3. T.Sameshima, S.Usui and M.Sekiya, J. Appl. Phys. **62**, 711(1987).
4. T.Sameshima and S.Usui, Jpn. J. Appl. Phys. Lett., **26**, 1208 (1987).
5. G.J.Galvin, M.O.Thompson, J.W.Mayer, R.B.Hammond, N.Paulter and P.S.Peercey, Phys. Rev. Lett., **48**, 33 (1982).
6. T.Sameshima, H.Tomita and S.Usui, Jpn. J. Appl. Phys. Lett. **27**, 1935 (1988).
7. D.H.Auston, J.A.Golovchenko, P.R.Smith, C.M.Surko and T.N.C.Venkatesan, Appl. Phys. Lett. **33**, 538 (1978).
8. V.M.Glazov, S.N.Chizhenskaya and N.N. Glagoleva, Liquid Semiconductors, (Plenum Press, New York, 1969) p.60.
9. T.Sameshima, M.Hara and S.Usui, Jpn. J. Appl. Phys., **28**, 1789 (1989).

LASER PROCESSED SILICIDES FOR GAAS HEMTS

W.T. ANDERSON, A. CHRISTOU, P.E. THOMPSON, J.L. DAVIS, C.R. GOSSETT,
AND J.M. ERIDON

Naval Research Laboratory, Washington, D.C., 20375

C. MICHELAKIS, G. KIRIAKIDIS, Z. HATZOPOULOS, T. ETHIMIOPOULOS,
AND M. KUDUMAS

Research Center of Crete, Heraklion, Crete, Greece

D.V. MORGAN, University of Wales, College of Cardiff, Cardiff, U.K.

ABSTRACT

Laser annealed refractory metal gates and Ohmic contacts have been developed for GaAs FETs and HEMTs fabricated on MBE layers grown on laser desorbed substrates. Amorphous refractory metal silicide films were sputter deposited by a method in which the RF power to separate refractory metal and silicon targets were set at predetermined deposition rates and the substrates were rotated with respect to the sputter targets receiving a 0.2 to 0.5 nm film on each pass. The gate resistance was reduced and Ohmic contacts formed by pulsed excimer laser annealing.

Introduction

Gallium arsenide field effect transistors (FET), high electron mobility transistors (HEMT), power FETs as well as high speed digital GaAs ICs and monolithic microwave integrated circuits (MMICs) require a stable metal contact technology, low parasitic resistance and a high degree of reliability and reproducibility. Self-aligned gate FETs in digital GaAs integrated circuits require gates which must withstand a high temperature anneal treatment. For long term high temperature applications, stable Ohmic contacts are also required since present AuGe contacts are stable only up to about 350°C. A promising approach for achieving high reliability is through the use of a refractory Ohmic and Schottky contact technology based on amorphous metallization.

Refractory Silicide Metallizations

An RF-magnetron sputtering technique was utilized for the deposition of amorphous (α -) refractory metal silicide films. The system consists of two targets with power splitting capability and substrate table rotation with variable speed. By adjusting the power delivered to the individual targets, Ta or TiW and Si, fine control of the composition of the amorphous metallization with atomic layer dimensions, as shown in Fig. 1, can be achieved. The sputtering pressure of Ar gas was 20 mtorr and the deposition rates were as low as 400-500 Å/hour. This method has the following advantages over sputter deposition from a single target: a) overall average composition can be better controlled by varying the power, and thus film thickness on each pass, to the separate targets; b) amorphous films, which are desirable as diffusion barriers, are always obtained because α -Si is deposited on each pass of the Si target, a glancing angle x-ray diffraction spectra is shown in Fig. 2, and c) because the substrate spends only a small time near the sputter target as it rotates, the surface temperature remains lower than if a single sputtering target were used and photoresist can be employed to lift 1.0 μ m long gates [1], as shown in Fig. 3.

Laser Annealing of Metallizations

Annealing of the layered films was carried out with a 308 nm excimer laser to reduce the resistance in these amorphous films and to form Ohmic contact. The uniformity of the laser beam was established by mounting a 1 mm diameter aperture in front of a power meter and measuring the intensity of the primary beam from the laser at 2 mm intervals across the 2.4 cm \times 3.4 cm beam in two

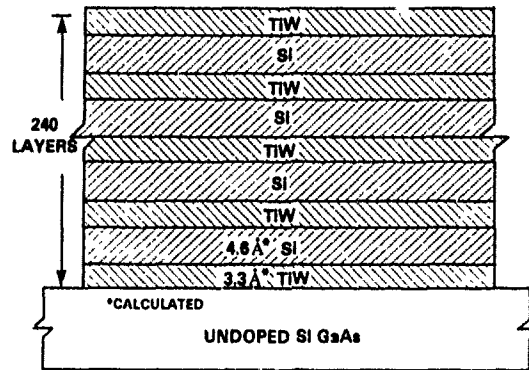
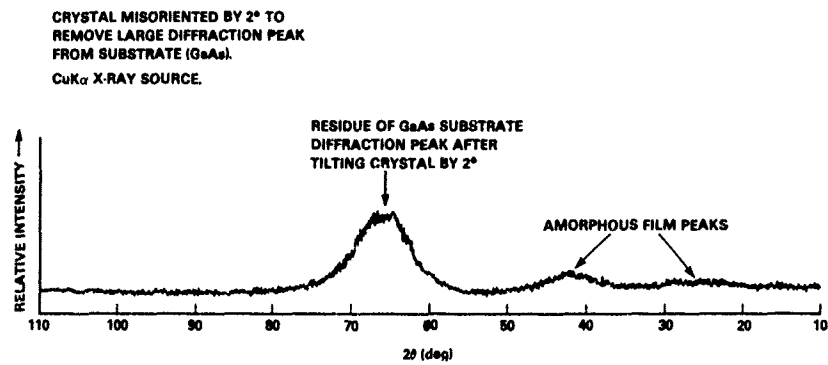
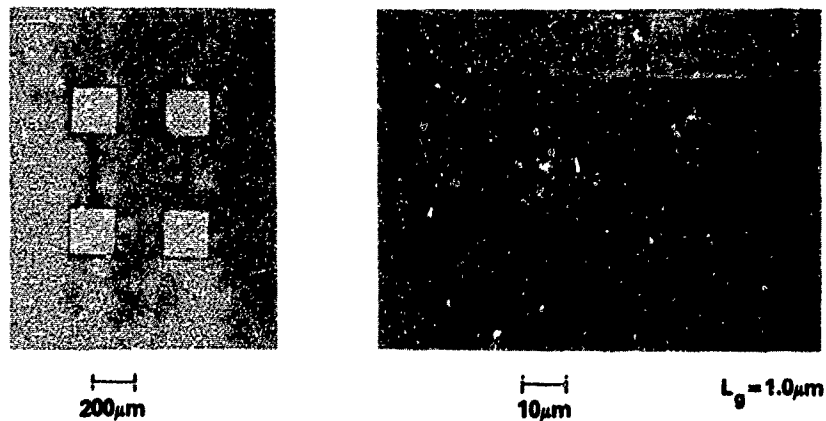


Figure 1. Schematic of the GaAs/TiWSi Amorphous Metallization.

Figure 2. X-Ray Diffraction Spectra of 3500 Å $\text{Ti}_{0.3}\text{W}_{1.3}\text{Si}_{1.84}$ Layered Film Sputter Deposited on GaAs.Figure 3. Micrographs of a α -TiWSi Gates

orthogonal directions. Only the outside 0.6 cm of beam had reduced intensity and only the center 1 cm \times 1 cm of the beam was used in the experiments by use of an aperture. Slight focussing of the beam was accomplished with a quartz lens to final position the beam on the refractory silicide films and to adjust the size of the beam. A He-Ne laser was utilized for alignment of the excimer to the desired spot. Power densities up to 500 mJ/cm² per pulse were obtained, but it has been found that values over 400 mJ/cm² are usually destructive. Best results were obtained when samples were maintained at 450°C during laser annealing. Laser annealing has the advantage over Rapid Thermal Annealing (RTA) or oven annealing in that it is not necessary to heat the entire wafer. Annealing is accomplished by adjusting the energy density to penetrate only part way into the films, ideally resulting in a phase change to polycrystalline material of lower resistivity at the top of the film leaving the bottom part of the film as a well behaved amorphous diffusion barrier.

The refractory α -metal silicides form Schottky barriers on n-type GaAs. It was found that laser annealing of these films results in significant increase (30% or more) in the conductivity for thicknesses ≤ 2000 Å. If the metallization is approximately 400 Å, Ohmic contact is formed because the heat pulse reaching the α -metal/substrate interface is sufficient to raise the temperature enough to cause interdiffusion.

Film resistivity was measured by the voltage drop between gate pads, see Fig. 3, for a given current through the width of the gate. The resistivity values in Figure 4 are based on the cross-section of the gate finger. As the film was laser annealed, it is likely that only the top of the film changed in composition or crystal structure. Only the average resistivity can be calculated at present since the depth of laser beam and heat pulse penetration have not yet been measured. Resistivity values above 500 $\mu\Omega$ -cm are too high for device applications, but it can be reduced by reducing the Si content and by laser annealing. As can be seen in Figure 4, the laser anneal threshold energy density for reduced resistivity is, for the α -Ti_{0.3}W_{0.12}Si_{0.85}, ~ 160 mJ/cm². As expected, raising the substrate temperature during laser annealing reduced the energy density required for a given resistivity. Because the energy density was limited to about 300 mJ/cm² due to film cracking, and in order to reduce the thermal shock to the surface and interfaces, the substrate temperature was raised to 450°C for other experiments. However, even at 300 mJ/cm² the unpassivated GaAs surface remained stoichiometric as measured by EDXA. All laser annealing was carried out in a vacuum of less than 5×10^{-5} Torr.

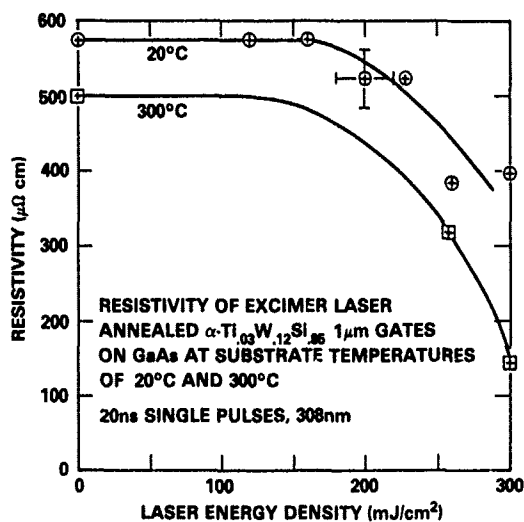


Figure 4. Average resistivity vs Laser Energy Density of Laser Annealed α -Ti_{0.3}W_{0.12}Si_{0.85} 1 μ m Gates

Rutherford Backscattering Spectroscopy (RBS) analysis of the laser annealed interfaces was carried out to determine the amount of interdiffusion as a function of laser anneal energy density and substrate temperature. Figure 5 shows the RBS spectra of a 180 nm thick layered TiW/Si/TiW/Si.../GaAs film on a commercially available undoped semi-insulating (SI) GaAs wafer "as deposited" and after two different laser anneals on different areas. The spectra revealed Ga and/or As outdiffusion into the $Ti_xW_ySi_z$ film and interdiffusion of Si, W and Ti into GaAs. Examination of the laser annealed surfaces with an optical microscope to $1000\times$ and by SEM to $20,000\times$ has shown smooth and continuous surfaces except at the beginning of laser ablation at sufficiently high energy density above which films are no longer useful. No defects such as ablated craters with raised rims that could result in similar RBS spectra were observed. Figure 6 shows a RBS spectra of a similar laser annealed film, deposited at the same time as the film of Figure 5, but on an In-doped substrate with reduced dislocation density. Note that compared to the spectra of Figure 5, very little interdiffusion occurred after a 180 mJ/cm^2 room temperature anneal while large interdiffusion occurred at 176 mJ/cm^2 on a typical undoped substrate. Also note that the interdiffusion is about the same in the two cases after 450°C substrate laser anneals but the energy density was 27 mJ/cm^2 higher in the case of the In-doped substrate. This result is in agreement with that reported previously [2] for RTA of $TaSi_x$ films and is explained by diffusion dominated by crystalline defects which are much reduced in In-doped substrates.

The indiffusion of Si, an n-type dopant, into GaAs revealed in Figures 5 and 6 suggests Ohmic contact might be formed under sufficiently high laser anneal conditions and this was indeed the case. Ohmic contacts were formed by laser annealing of layered $\alpha\text{-Ta}_{13}\text{Si}_{87}$ (175 nm), $\alpha\text{-Ti}_{07}\text{W}_{12}\text{Si}_{81}$ (150 nm) and $\alpha\text{-Ti}_{23}\text{W}_{33}\text{Si}_{24}$ (40 nm) on both unactivated and activated ion implanted n-type GaAs. The lowest specific contact resistance of the laser annealed $\alpha\text{-Ti}_{24}\text{W}_{33}\text{Si}_{23}$ Ohmic contact was $4 \times 10^{-4}\Omega\text{cm}^2$.

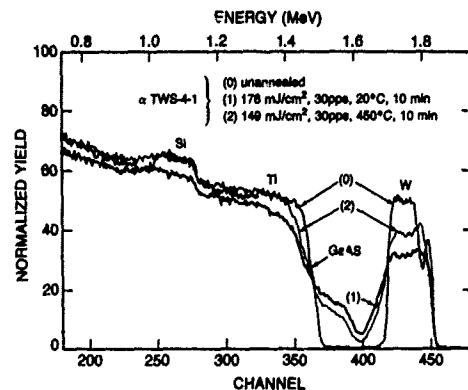
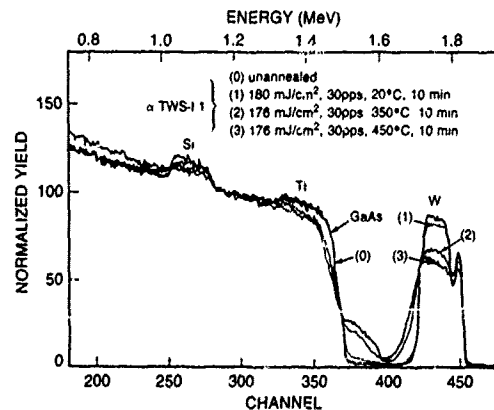


Figure 5. RBS Spectra of Pulsed Laser Annealed 1800 \AA thick $\alpha\text{-Ti}_{0.05}\text{W}_{1.1}\text{Si}_{8.4}$ Layered Film Sputter Deposited on a Commercially Available Undoped GaAs Substrate.

Figure 6. RBS Spectra of Pulsed Laser Annealed $\alpha\text{-Ti}_{0.05}\text{W}_{1.1}\text{Si}_{8.4}$ 180 nm Layered Film Sputter Deposited on an In-Doped GaAs Substrate.



In addition, it was found that shallow implanted layers could be activated under the proper laser anneal conditions. For example, for the $\alpha\text{-Ta}_{13}\text{Si}_{87}$ film on 120 keV, $3.5 \times 10^{12} \text{ cm}^{-2}$ Si implanted GaAs, the threshold for activation was 190 mJ/cm^2 for a 10 min. 30 pps anneal at a substrate temperature of 450°C . As the energy density was increased the Schottky barrier characteristics became softer and Ohmic contact was formed at 260 mJ/cm^2 .

All Refractory Metal FETs and HEMTs

All-refractory silicide GaAs FETs and HEMTs were fabricated with typically 2000 \AA thick laser annealed α -metal silicide gates and 400 \AA thick Ohmic contacts on MBE grown material. It was found that 140 mJ/cm^2 , 5 pulses at a substrate temperature of 450°C was sufficient to obtain the lowest contact resistance. After Au pads were deposited, the highest transconductance was 40 mS/mm for a $4 \mu\text{m}$ long gate FET and 72 mS/mm for a $2 \mu\text{m}$ gate device. I/V characteristics are shown for the $2 \mu\text{m}$ gate FET in Figure 7. The lower than expected transconductance values for the geometry and carrier concentration is attributed to high source resistance which is about 5Ω .

Table 1 compares the transconductance of all refractory metal FETs and HEMTs with devices of the same geometry but fabricated with conventional AuGe Ohmic contacts and Al or $\alpha\text{-TiWSi}$ gates. A higher transconductance was actually obtained with the all-refractory, laser annealed FET compared to the conventional FET with Al gate, but this may be attributed to a lower mobility and carrier concentration in FET 1197. The low transconductance of the all-refractory HEMT 314 is attributed to a high source resistance. HEMTs 336-B and 336-D with AuGe Ohmic contracts have much lower source resistance because during sintering or laser annealing of the Ohmic contract the AuGe melts and alloys [3,4,5] with the GaAs and AlGaAs. Thus spikes of conducting material can penetrate the 10 nm undoped AlGaAs spacer layer to form Ohmic contact with the two dimensional electron gas in the undoped GaAs. With the laser annealed refractory silicide Ohmic contacts no melting occurs and Ohmic contact is made only to the top N^+ -GaAs layer. Thus the source resistance is higher because electrons must tunnel through the 10 nm spacer layer. It should be possible to reduce this resistance by implanting an N^+ Si layer with a range in the center of the space layer, only at the source and drain contacts. Results of these experiments will be given at a later date.

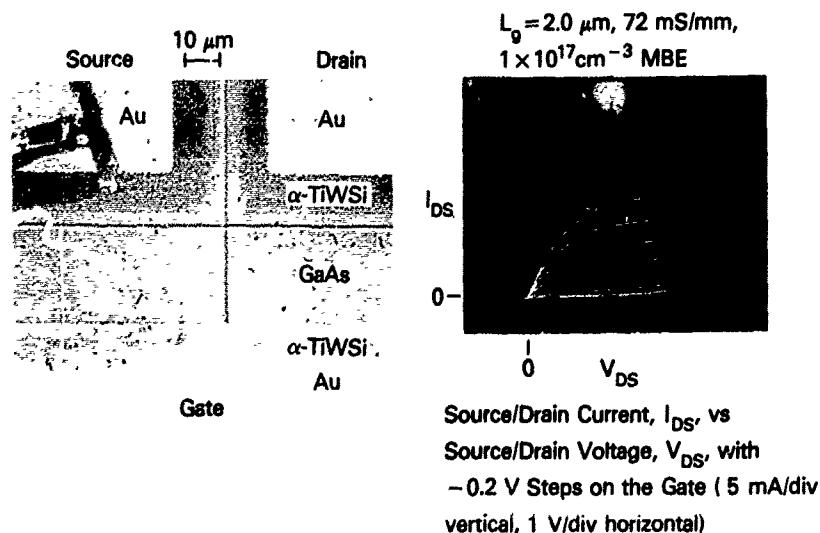


Figure 7. All-Refractory Silicide GaAs FET after Excimer Laser Anneal at 140 mJ/cm^2 , 5 Pulses at a Substrate Temperature of 450°C .

Table 1. Comparison of Transconductance Per Unit of Gate Width, g_m , of Sintered and Laser Annealed GaAs FETs and HEMTs

Device	g_m (mS/mm)	Source/ Drain	Gate
FET 310	72	40 nm TiWSi, LA**	200 nm TiWSi, LA
FET 1197	50	AuGe sintered,† N ⁺ InGaAs	Al
HEMT 336-B	57	AuGe sintered	1.0 nm TiW/200 nm TiWSi
HEMT 336-D	55	AuGe, LA	10 nm TiW/200 nm TiWSi, LA
HEMT 314	27	40 nm, TiWSi, LA	200 nm TiWSi, LA

*Gate length $L_g = 2.0 \mu\text{m}$

**LA-Laser Annealed at substrate temperature of 450°C

†Sintered 1 min at 450°C

Conclusions

Future metallization systems will be required to withstand short duration temperatures of 900°C (~10s) and long duration (~100 h) temperatures of up to 450°C. The present Schottky barrier and Ohmic contact metallizations, e.g. Al or TiPtAu gates and AuGe/Ni source/drain alloyed contacts, are sufficient only for the present technology, i.e. for dimensions above 0.5 μm and channel temperatures below 125°C. New metallizations will be required for VLSI and USLI chips of the future and for millimeter wave devices with source/drain separation less than 0.5 μm . The laser annealed Ohmic contacts discussed in this paper were developed for this purpose and also have high temperature and high reliability applications. All refractory metallized GaAs FETs and HEMTs were fabricated to demonstrate the feasibility of the methods discussed. In the case of the highest speed devices, no compromises should be made in the use of new metallizations, but new types of metallizations will be required to reach the desired performance. However, in the case of high temperature and high reliability applications, trade-offs may have to be made with performance.

Acknowledgments

Partial support by the Office of Naval Research, NATO and ESPRIT 1270 is gratefully acknowledged.

References

1. N.A. Papanicolaou, W.T. Anderson, Jr. and A. Christou, "Small signal MESFET with Sputtered Amorphous Metal Gate Defined by Lift-off," Gallium Arsenide and Related Compounds 1982, Institute of Physics Conf. Series No. 65, (Institute of Physics, Bristol), pp. 407-414 (1983).
2. D.V. Morgan, H. Thomas, W.T. Anderson, P. Thomson, A. Christou, and D.J. Diskett, Electron. Lett. (23) pp. 1154-1155 (1987).
3. A. Christou and K. Slegar, 6th Biennial Conf. on Active Microwave Semiconductor Devices and Circuits, Cornell (1977).
4. A.K. Sinha and J.M. Poate, Appl. Phys. Lett. 23, 666 (1973).
5. K. Chino and Y. Wada, Jpn. J. Appl. Phys. 16, 1823 (1977).

SUBSTRATE HEATING EFFECTS IN EXCIMER LASER PLANARIZATION OF ALUMINUM

Robert J. Baseman and Joseph C. Andreshak
IBM Research Division
IBM T.J. Watson Research Center
Yorktown Heights, NY 10598

Abstract

Substantial improvements in excimer laser planarization processes are observed with substrate heating. Cavities, associated with filling of high aspect ratio vias at low substrate temperature, can be eliminated by substrate heating. Damage associated with pulse overlap regions can be temperature sensitive, and is reduced as substrate temperatures are increased. While required fluences for planarization and sample damage both decrease as the sample temperature increases, the relative insensitivity of the damage threshold generally results in larger process windows at higher temperatures. We also report model calculations of the effect of substrate heating on sample temperature distributions and the durations of the laser driven melts.

Introduction

An especially simple and attractive technique for planarizing metal layers and efficiently filling interlevel vias was first reported by Tuckerman *et al.* [1]. Briefly, following the deposition of a metal layer by a standard technique, the metal layer is melted momentarily by irradiating the surface with a short laser pulse. While molten, the high surface tension of the liquid metal, given its relatively low viscosity, drives the metal to rapidly seek a planar surface. Mukai *et al.* [2] first reported auxiliary substrate heating during excimer laser planarization, and demonstrated substantial improvements in the process. In particular, auxiliary substrate heating was required to effectively fill high aspect ratio structures with typical excimer laser pulses. Here, we describe other improvements in excimer laser planarization processes due to substrate heating: reduction of defects in pulse overlap regions, and enlarged process windows. We also consider the extent to which substrate heating may affect temperature distributions produced by the laser.

Experimental

The 248 nm, 25 ns FWHM output of an excimer laser was used in these experiments. A laterally uniform (variations of 7% or less) portion of the beam was imaged onto the wafers at a magnification of 1/7 with a single lens. Maximum fluences of 10 J/cm² over .09 mm² were obtained at the wafer surface. Reduced fluences were obtained by inserting partial reflectors in the beam path. The wafers were clamped to a thermal coaxial cable heated copper block in a vacuum (10⁻⁵ torr) chamber which was mounted on a computer controlled xy table. Finite element model calculations [3] included temperature dependent thermal conductivities, heat capacities, densities, and reflectivity.

Results

Ideally, an entire semiconductor wafer, or at least an entire die would be processed with a single laser pulse. However, even with the use of absorption enhancing overlayers, (aluminum reflects more than 90% of the incident 248 nm light at room temperature) and a several J/pulse laser, single pulse processing of entire die approaching 1 cm² is unlikely. Stitching together of individually irradiated areas is required for practical processing.

Figure 1 shows the result of a single isolated planarizing laser pulse within an array in a multi(metal) level sample. The vias completely within the irradiated area are well planarized. The vias positioned at the edge of the irradiated zone are not planarized. In fact, it appears as if metal has receded out of the edge vias toward the bulk of the irradiated zone during the cooling process. Overlapping subsequent pulses over the edge vias is nominally expected to result in a completely planarized surface. Typical results obtained by overlapping pulses by roughly 10 μ m with the sample maintained at room temperature are shown in figure 2a. With the particular beam profile used in this work, the molten zone from a single laser pulse is very sharply defined and clearly visible in the final overlapped pattern. While most of the vias initially unfilled at edges are filled by the subsequent overlapping pulse, damage at several edge vias in the pulse overlap region is obvious. Figure 2b shows a typical region of an array irradiated identically, but at 200 °C. While

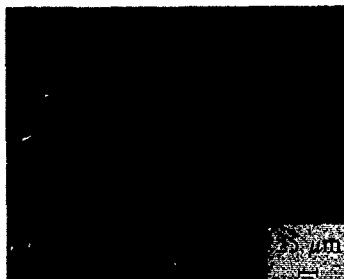


Figure 1. Nomarski view of single isolated planarizing pulse.



Figure 2. Nomarski views of stitching at a) 25 ° C b) 200 ° C.

the results of single isolated pulses appear very similar, adequate filling of edge vias in pulse overlap areas is much more likely at the elevated temperature. The number of vias left unfilled or damaged at 200 ° C is roughly a factor of 10 less than that left unfilled or damaged at room temperature.

Generally, manufacturing processes are easier to control if they are relatively insensitive to variations in processing conditions (large process windows). Demonstrating the viability of laser planarization for manufacturing requires demonstrating, among other things, that reasonable process windows exist under realistic manufacturing circumstances. Several recent experiments and model calculations have studied the process windows associated with excimer and dye laser planarization of square wave test structures [4-6]. These studies have shown that relative to dye laser induced melting, the process windows associated with excimer laser melting are rather small. Moreover, damage upon multiple pulse irradiation and evaporative recoil effects, leading to pattern amplification, were reported for excimer laser melting. The differences between the excimer and dye laser results have been attributed mainly to the difference in pulse duration. More recently, small process windows, on the order of 5 %, have been reported for the planarization of 0.5 μm thick Al 0.5 % Cu over 1. μm diameter vias [7].

In order to characterize the process windows associated with structures actually simulating the fabrication of an integrated circuit, one specific area of a multi-level test pattern, containing a variety (from 2. to 6. μm , as drawn) of via sizes in close proximity was irradiated with laser fluences (at the wafer's surface) from 0.9 to 3.9 J/cm^2 with the wafer held at 30 ° C and again with the wafer held at 400 ° C [8]. All the vias in the irradiated areas contacted first metal lines. The first metal lines had a variety of shapes and areas of between 200 and 400 μm^2 . The laser spot size was large enough to irradiate all the different sizes of vias in the pattern with a single pulse.

SEM views of the test structure before and after laser irradiation with several different fluences at 30 ° C are shown in figure 3. None of the features shown were effectively planarized by fluences below 2.5 J/cm^2 . With 2.6 J/cm^2 , figure 3b, all of the 2. μm vias are planarized. Some of the 2.5 μm vias have been planarized, but there is little planarization of any larger vias. As the fluence is increased to 2.9 J/cm^2 , figure

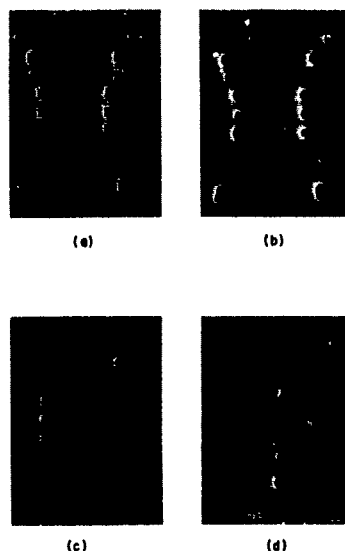


Figure 3. SEM views of the test structure a) as received and irradiated with b) 2.6 c) 2.9 and d) 3.2 J/cm² at 30 °C.

3c, the 2., 2.5, and 3. μm vias are all effectively planarized, and the 6. μm vias have nearly filled, but there is still little planarization of the 4. μm vias. Additionally, Nomarski views start to show the structures associated with complete melting of the Al layer and highly directional cooling through the vias to the underlying layers. With a fluence of 3.2 J/cm², figure 3d, the 6. μm vias have been completely planarized, but the filling of the 4. μm vias, while substantial, is not complete. Upon raising the fluence to 3.5 J/cm², the sample is damaged. The damage is most obvious over the group of 2. and 2.5 μm vias. Most of the aluminum originally deposited over this area has either receded beyond the perimeter of the group of 2. and 2.5 μm vias while molten, or been ablated, and while a thin layer of aluminum still covers the oxide between the vias, there is little aluminum in the individual vias themselves. Aluminum has also been removed from several of the larger vias.

While overall the fluences required for planarization are lower at 400 °C, the fluence required for planarization of a via still clearly increases as the via size increases. At 400 °C, the test structure is damaged with 3.2 J/cm². The damaged areas at 400 °C are centered over the largest, 6. μm vias, individually, rather than the group of smallest vias as they were for room temperature irradiation. The nature of the damage at 400 °C is also different than that at room temperature, consisting of near complete removal or ablation of the aluminum from areas roughly 40 μm in diameter, centered on the 6. μm vias.

Figure 4 shows the minimum laser fluence required to fill all the vias of a given size in the test structure as a function of size for 30 and 400 °C processing. (No data point is shown for planarization of the 4. μm vias at room temperature, as complete planarization was not observed, although a detailed study with fluences between 3.2 J/cm² and 3.5 J/cm² may have revealed complete planarization.)

From a purely scientific point of view, one might define the operating process window for planarization of a given size of via as the difference between the minimum fluence required for planarization and the minimum fluence causing damage to that size via. Given the experimental difficulty of identifying the damage threshold for each size via in this test structure, and possibly from a more practical point of view, here, we define the process window for planarization of a given size of via in terms of the minimum required for planarization of that size via and the minimum causing damage to any part of the test structure. These allowed fluence variations, or process windows, depend dramatically on both via size and temperature. At both temperatures, the absolute process window decreases as the via size increases. Given the concomitant increase in minimum fluence to planarize, the process window, as a fraction of the minimum fluence to planarize, decreases dramatically as the via size increases. Allowed variations (expressed as fractions of the minimum fluence to planarize) drop from near 50 % for 2. μm vias to less than 10 % for 6. μm vias at 400 °C, and overall are generally about a factor of two larger at 400 °C than at 30 °C. Compared to the minimum fluences required to planarize features, especially the smaller vias, the minimum fluence required to damage the sample is relatively insensitive to changes in the sample temperature. As the sample temperature

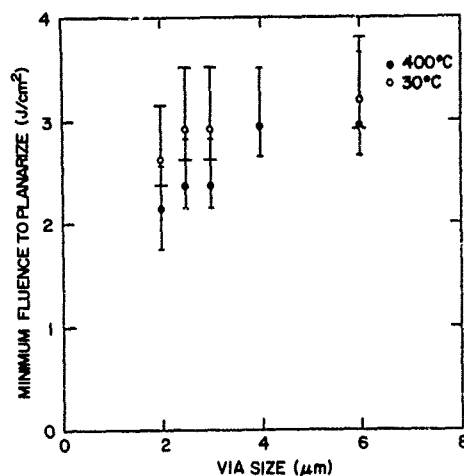


Figure 4. Minimum laser fluences required to planarize all vias of a given size in the test structure as a function of size at 30 and 400 ° C.

is increased, the process window for a given size of via, again as a fraction of the minimum fluence to planarize, increases dramatically for the smallest vias, though there is apparently little effect on the window for the largest vias.

The temporally short pulses used in the laser planarization process effectively confine significant heating to upper interconnect layers, insuring the survivability of underlying active devices, [2,9] and produce only brief temperature transients in those uppermost layers, minimizing possible interlayer reactions. However, due to diminished overall temperature gradients through the substrate, and the significant decrease in the thermal conductivity of silicon with temperature, auxiliary substrate heating will conceivably both increase peak temperatures experienced by individual layers and increase exposure times of a particular layer to any given elevated temperature.

The most thermally sensitive application of the planarization process may be planarizing Al used as the (Si) contact metallurgy. Finite element model calculations have been used to illustrate the magnitude of these effects in this case. The calculations shown below considered a structure of various thicknesses of Al directly on Si (blanket layers) as a possible worst case scenario. For each Al thickness, the heat necessary to melt the top 1.5 μm of Al was introduced in a 25 ns wide square pulse.

Figure 5a shows the calculated exposure times of the Si surface to temperatures over 400, 350, and 300 ° C with the substrate maintained at room temperature. The silicon surface is exposed to temperatures above 400 ° C for times only on the order of 100 ns, and is not exposed to any temperatures above 300 ° C for times longer than 1 μs in any case. As the aluminum thickness increases, and we consider melting only the top 1.5 μm, the length of time the silicon surface is exposed to any given temperature decreases, as expected.

Figure 5b shows the calculated exposure times of the Si surface to temperatures over 450 and 400 ° C with the substrate maintained at 350 ° C. These times are much longer than those with the substrate at room temperature due to reduced overall temperature gradients through the sample and the significant decreases in silicon's thermal conductivity with temperature. While the silicon surface's exposure to temperatures above 400 ° C is on the order of 100 times longer than that with the substrate at room temperature, the typical exposure is still only roughly 10 μs, in absolute terms, clearly an acceptably short exposure.

With the substrate held at 350 ° C, the exposure times are relatively insensitive to the total aluminum thickness, but show a small increase with thickness up to 3 μm and then decrease slowly. As a function of Al thickness, the length of time the Si surface is exposed to a given temperature reflects a competition between the additional energy required to melt the top 1.5 μm of Al as the thickness increases (tending to increase times the Si is exposed to a given temperature), and the insulation of the Si by thicker unmelted Al (tending to decrease exposure times). As the substrate temperature increases to 350 ° C, the thermal conductivity and diffusivity of silicon drop rapidly from values comparable to that of aluminum to roughly

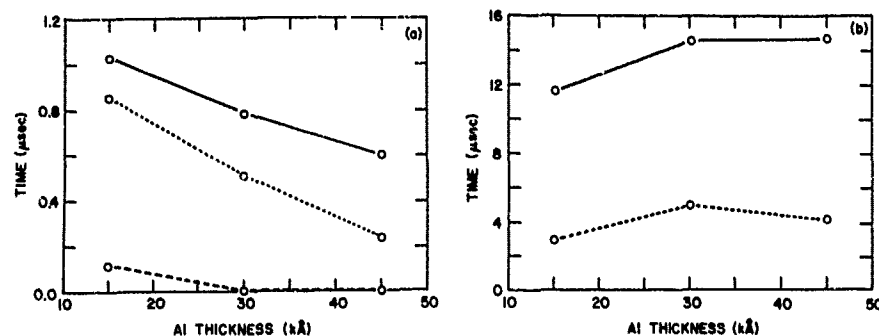


Figure 5. Calculated silicon surface exposures to temperatures above a) 300 (solid), 350 (dot), 400 (dash) ° C, substrate at room temperature, b) 400 (solid), 450 (dot) ° C, substrate at 350 ° C.

1/3 of the aluminum values. The large change in the thermal properties of the Si dramatically alter the net result of the competition. There is little insulation of the Si by the unmelted portion of relatively thin Al layers. Due to the low thermal conductivity of Si at 350 ° C, the extra heat necessary to melt the Al as the Al thickness increases accumulates at the Si interface, producing somewhat longer exposure times. Ultimately, the Al thickness becomes great enough to effectively insulate the Si, and exposure times decrease.

Acknowledgements

We would like to thank J. Havas and R.H. Schnitzel for providing the samples and encouraging this work, and A. Gupta for helpful discussions.

References

- 1) D.B. Tuckerman, R.L. Schmitt, Proc. 1985 V-MIC Conf., 24 (1985); D.B. Tuckerman, A.H. Weisberg, IEEE Electron Device Letters, **EDL-7**, 1 (1986); D.B. Tuckerman, A.H. Weisberg, Solid State Technology, **29**, 129 (1986).
- 2) R. Mukai, N. Sasaki, M. Nakano, IEEE Electron Device Letters, **EDL-8**, 76 (1987); R. Mukai, N. Sasaki, M. Nakano, in *Beam-Solid Interactions and Transient Processes*, edited by S.T. Picraux, M.O. Thompson, J.S. Williams (Mater. Res. Soc. Proc. **74**, Pittsburgh, PA 1987) pp.229-234; R. Mukai, K. Kobayashi, M. Nakano, Proc. 1988 V-MIC Conf., 101 (1988).
- 3) R.J. Baseman and J.C. Andreshak in *Fundamentals of Beam-Solid Interactions and Transient Thermal Processing*, edited by M.J. Aziz, L.E. Rehn, and B. Stritzker, Mater. Res. Soc. Proc. No. 100 (Materials Research Society, Pittsburgh, PA, 1988), pp. 627-633.
- 4) P.F. Marella, D.B. Tuckerman, and R.F. Pease, Appl. Phys. Lett., **54**, 1109 (1989).
- 5) P.F. Marella, D.B. Tuckerman, and R.F. Pease, in *Laser and Particle-Beam Modification of Chemical Processes on Surfaces*, edited by A.W. Johnson, G.L. Loper, and T.W. Sigmon, Mater. Res. Soc. Proc. No. 129 (Materials Research Society, Pittsburgh, PA, 1989) in press.
- 6) A.F. Bernhardt and R.J. Contolini, in *Laser and Particle-Beam Modification of Chemical Processes on Surfaces*, edited by A.W. Johnson, G.L. Loper, and T.W. Sigmon, Mater. Res. Soc. Proc. No. 129 (Materials Research Society, Pittsburgh, PA, 1989) in press.
- 7) R. Liu, K.P. Cheung, W.Y.-C. Lai, R. Heim, in *Proceedings of the 1989 VLSI Multilevel Interconnection Conference (V-MIC)* (IEEE, New York, New York, 1989), pp. 329-335.
- 8) R.J. Baseman, to be published in J. Vac. Sci. Technol. B, Jan./Feb. 1990.
- 9) R.J. Baseman, J.C. Andreshak, A. Gupta, C-Y. Ting, R.H. Schnitzel, and J. Havas, in *Selected Topics in Electronic Materials*, edited by B.R. Appleton, D.K. Biegelsen, W.L. Brown, and J.A. Knapp, MRS Extended Abstracts, Vol. EA-18 (Materials Research Society, Pittsburgh, PA, 1988) pp. 259-262.

LOW TEMPERATURE INTERLEVEL SiO_2 LAYERS BY PHOTOINDUCED PROCESSING

H. SIGMUND, A. KLUMPP AND G. SPRINGHOLZ

Fraunhofer Institute for Solid State Technology, Paul-Gerhardt-Allee 42,
D-8000 München 60, Federal Republic of Germany

ABSTRACT

Polysiloxane layers were deposited from the gas phase by photoinduced polymerization reaction of tetraethylorthosilicate (TEOS) and $\text{O}_2/\text{N}_2\text{O}$. The deposition kinetics can be described by a gas phase polymerization and the subsequent condensation of the siloxane molecules. As UV light sources an ArF excimer laser (193 nm) and a 185/253 nm low pressure Hg-discharge lamp were used, the polysiloxane deposition rates are 2000 Å/min or 1200 Å/min respectively. In a second thermal or combined thermal/photoinduced process step the as deposited siloxane layers are transformed by hydrolysis and condensation reactions to pure SiO_2 . The composition of the as deposited and transformed polysiloxane layers were investigated by FTIR spectroscopy. Typical examples of the step coverage and planarizing properties of the SiO_2 layers for the use as interlevel dielectrics are presented.

INTRODUCTION

Deposition of SiO_2 from tetraethylorthosilicate (TEOS) by LPCVD [1, 2] and recently also by PECVD [3] has become very convenient as interlevel dielectrics because of the better step coverage of the films than corresponding films deposited from silane. For low temperature planarization (< 400°C) SiO_2 layers multistep processing schemes such as deposit-etch-deposit by alternating plasma and thermal CVD are necessary to obtain the desired planarized profiles [4]. Process flows are then more complex and throughput is reduced.

In this paper we studied photoinduced polymerization reactions of TEOS in order to deposit polysiloxane layers with suitable viscosities and layer thicknesses. Dependent on the topological properties of the IC surface the viscosity and the film thickness can be controlled by the deposition parameters, so that different planarizing properties (step angle, step coverage) can be adjusted. In a second process step the polysiloxane layers are then transformed in a thermal or combined thermal/photolytical treatment to SiO_2 . This photoinduced deposition technique for polysiloxane layers shows distinct advantages compared to the known interlevel dielectric planarization techniques by the so-called spin-on-glasses [5] or other reflow techniques using boron/phosphorus doped silicate glasses.

EXPERIMENTAL

Photo-CVD of polysiloxanes

The experimental set-up is shown in fig. 1. It consists of an ArF excimer laser (Lambda, MSC 201) with an intelligent laser control unit for constant energy output. A dielectric energy attenuator (Laser Optic) was used in order to adjust the laser energy from nearly zero to 60% of the incident energy; the variation of the pulse energy by varying the discharge voltage would simultaneously alter the intensity profile. A typical integrated pulse energy output was 250 mJ at 1 Hz with a pulse duration of 17 ns.

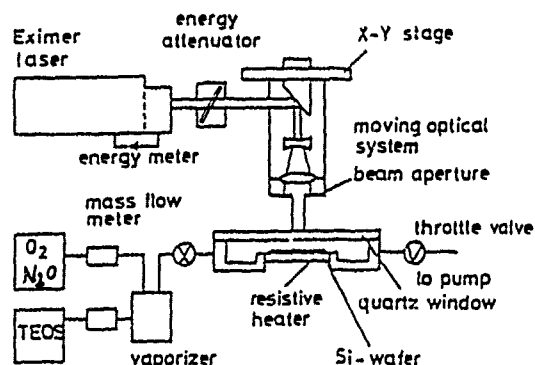


Fig. 1: Experimental set-up for polysiloxane deposition with ArF excimer laser radiation (193 nm).

The beam cross section was $10 \times 25 \text{ mm}^2$ at $1/e$ intensity, and we achieved constant intensity to an accuracy of $\pm 2.5\%$ over an area of $8 \times 21 \text{ mm}^2$, which was verified by intensity measurements. The laser beam was up-collimated ($T \approx 80\%$) and hits the substrate perpendicularly. The location of laser exposure within an $4 \times 4 \text{ inch}^2$ area can be selected via the xy stage consisting of two movable dielectric mirrors ($R_{\text{tot}} = 90\%$). The silicon wafer (max. 4 inch diameter) can be heated up to 400°C . In order to avoid condensation of TEOS inside the reaction chamber, the chamber itself was heated to roughly 100°C . The TEOS gas was brought into the reaction chamber by the $\text{O}_2/\text{N}_2\text{O}$ carrier gas. The overall pressure and the $\text{O}_2/\text{N}_2\text{O}$ flux was established by the usual methods. The laser energy was monitored above the quartz window with a pyroelectric detector (Gen Tec).

Experimental conditions of the photolytical deposition experiments of polysiloxanes are summarized in table 1. The oxygen flow and the pulse repetition rate were held constant at 100 sccm and 10 Hz, respectively. For the actual TEOS concentration in the reaction chamber we supposed that the carrier gas is saturated with the vapor pressure of pure TEOS at a temperature of 70°C .

Table 1: Experimental deposition parameters

$\text{N}_2\text{O}/\text{O}_2$ pressure	305 - 705 mbar
Gas flow	100 sccm
TEOS pressure	(70°C) 40 mbar
Substrate temperature	$50 - 100^\circ\text{C}$
Temperature of reaction gases	100°C
Laser energy density per pulse	$10 - 130 \text{ mJ}/\text{cm}^2$
Laser pulse rate	10 Hz

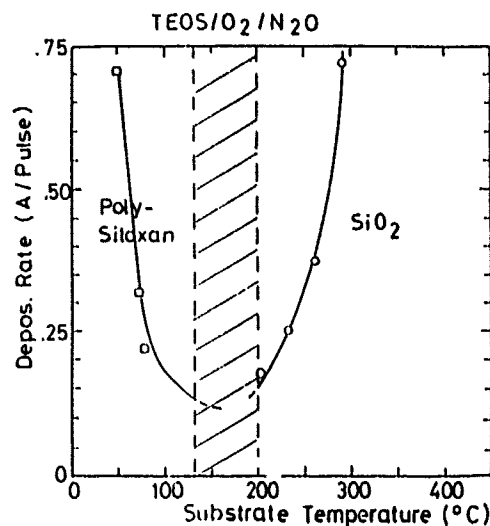
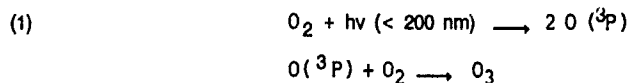


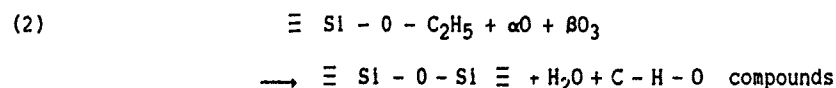
Fig. 2: Dependence of the deposition rate of polysiloxanes and SiO_2 on the Si substrate temperature, other parameters are given in table 1.

Dependent on the substrate temperature we found a characteristic behaviour in the deposition rates (see fig. 2). At lower temperatures polysiloxane layers can be deposited with high deposition rates, at substrate temperatures higher than $150 - 200^\circ\text{C}$ pure SiO_2 layers are formed. The details of the deposition conditions and physical and electrical properties of the laser deposited SiO_2 layers are given in a previous paper [6].

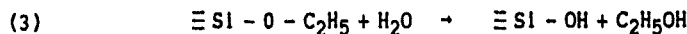
The deposition of polysiloxane layers can be described by a photopolymerization reaction of TEOS molecules in the gas phase and the subsequent condensation of polymerized siloxane at the substrate surface. For the system O_2/TEOS the following gas phase reactions occur.



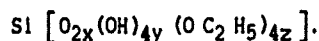
The photolytically produced atomic oxygen or ozone reacts with the ethyl group of the TEOS molecule forming a

$$\equiv \text{Si} - \text{O} - \text{Si} \equiv \text{bond}.$$


Furthermore, the produced H_2O from reaction (2) may form a silanol group in a hydrolysis reaction.



The deposition of polymerized layers is observed especially at low substrate temperatures in the range of 60–90°C (see Fig. 2). The as deposited layers were analysed by FTIR-spectroscopy (Perkin Elmer, Mod. 1700). Typical IR absorption spectra are shown in Fig. 3. The stretching mode of C-H bonds at 3000 cm⁻¹ and the absorption at 950 cm⁻¹ and 800 cm⁻¹ due to Si-O-C bonds were used to determine the chemical nature of the layers. The stretching modes of the O-H bonds and Si-OH at 3500 cm⁻¹ and 940 cm⁻¹ can also be used for the characterisation of the layer composition. The chemical composition of the polysiloxane layers can be described by the formula



The composition of the polysiloxane layers is strongly dependent on the deposition parameters. The investigated parameters are given in table 1. In our deposition experiments the siloxane layers could be characterized by $y = 0.5$ to 0.65 and $z = 0.1$ to 0.4 with $x + y + z = 1$.

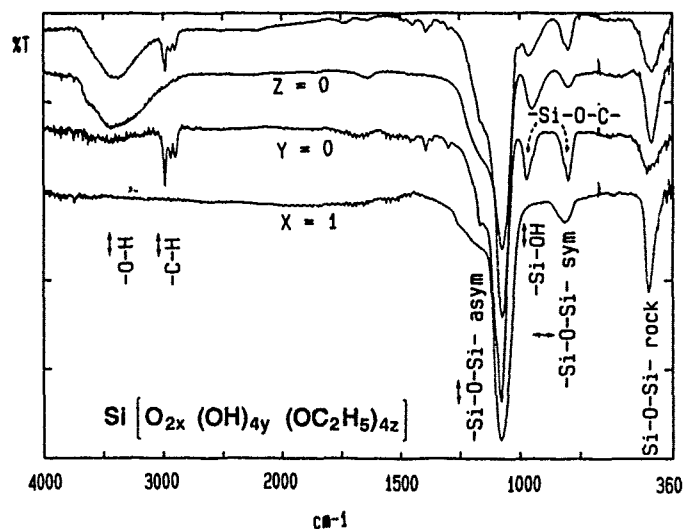
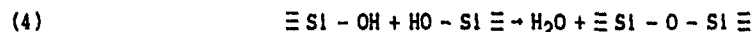


Fig. 3: Typical FTIR spectra of polysiloxane layers with different content of the functional groups: low CH ($z = 0$) and low OH ($y = 0$) in comparison with pure SiO₂ ($x = 1$).

Transformation of polysiloxane layers to SiO₂

The transformation of the polysiloxane layers to SiO₂ is achieved in a two step process sequence: hydrolysis and condensation-reaction. The hydrolysis is described already in equ. (3). In this reaction the H₂O molecule attacks the Si-O bond and an ethanol molecule is formed [7]. The residual OH group is attached to the Si atom. The condensation reaction occurs in the following manner:



Here two neighbouring OH groups in the SiO_2 network react by forming a H_2O molecule and a Si-O-Si bond. The hydrolysis (activation energy 6.0 kcal/mol) already proceeds in the temperature region of 20 to 400°C, whereas the condensation (activation energy 12 kcal/mol) typically occurs at appreciable higher temperatures from 350 up to 800°C, so that only a small overlap in the temperature regions for both reactions exists.

The hydrolysis reaction was also investigated by FTIR spectroscopy. A typical experimental run of isochronal curing is shown in fig. 4. We also studied the UV activated or UV supported curing of polysiloxane layers [8]. In these experiments a low pressure mercury grid lamp (Fa. BHK type 9660-02) was used; the integral intensity at 254 and 185 nm was roughly 20 mW/cm². The UV activated curing experiments were performed in-line in the deposition chamber after the deposition process.

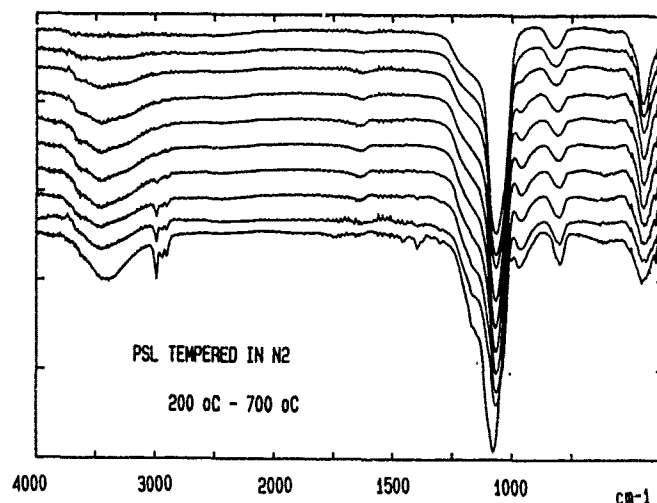


Fig. 4: FTIR spectra of isochronal curing of a polysiloxane layer (500 nm) in N_2 with $\Delta t = 20$ min and $\Delta T = 50^\circ\text{C}$.

RESULTS AND DISCUSSION

For an application of this fabrication technique of SiO_2 for planarization layers as interlevel dielectrics the flow properties of the as deposited polysiloxane layers are essential. In fig. 5 the film profile of an already tempered polysiloxane layer deposited on a structured poly-Si layer with vertical etch profiles, is depicted. It shows the good step coverage over sharp, rectangular edges and the flattening of the steep flanks.

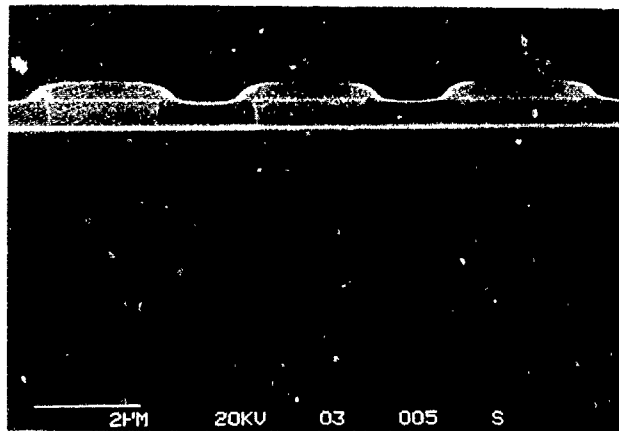
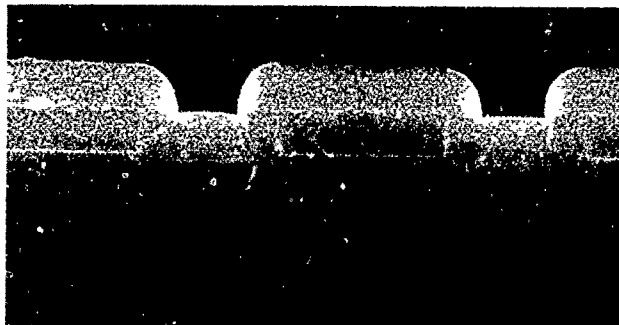
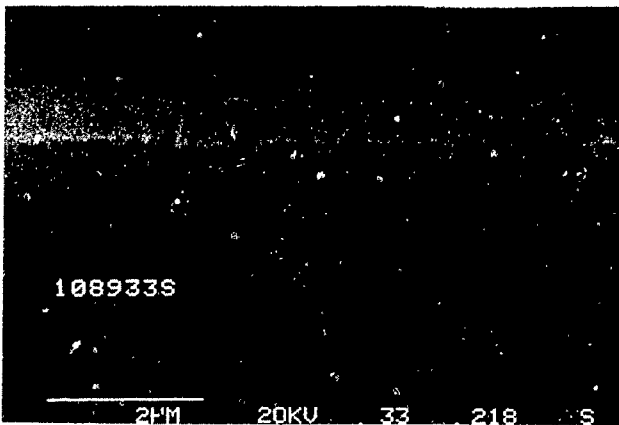


Fig. 5: Cured polysiloxane layer on a structured poly-Si layer of $0.5 \mu\text{m}$ thickness on top of an oxidized Si wafer.



a)



b)

Fig. 6: Local planarization of a $1.5 \mu\text{m}$ trench formed by a SiO_2 layer (a) and the planarized trench after photoinduced deposition of a thin ($0.1 \mu\text{m}$) polysiloxane layer and thermal curing to SiO_2 (b).

A further example for the excellent local planarization properties of a transformed polysiloxane layer is depicted in fig. 6a and b. In these samples a structured poly-Si surface was first covered with a 0.5 μm thick SiO_2 layer by PECVD (fig. 6a). Afterwards, a 0.1 μm thick polysiloxane layer was deposited by Photo-CVD. As can be seen in fig. 6b, a local planarization of 70% can be achieved.

Compared to other planarization techniques our new photoinduced planarization technique features two main advantages:

- 1) The photoinduced polysiloxane deposition is carried out at low substrate temperatures (below 100°C), compatible with multilevel Aluminium IC metallization and
- 2) the film properties (composition, viscosity, etc.) can be adjusted in a wide range by changing the deposition parameters, so that also the local and global planarization properties can be adjusted.

Work is in progress to adapt this photolytical process scheme in a improved deposition chamber attached to a modular multichamber processing system. Furthermore we believe that this new low temperature planarization technique will substitute the conventional high temperature reflow techniques of boron/phosphorous doped silicate glasses.

REFERENCES

- [1] H. Huppertz and W.L. Engl, IEEE Trans. Electron Devices ED-26 (1979), 658.
- [2] A.C. Adams and C.D. Capio, J. Electrochem. Soc. 126 (1979), 1042.
- [3] D.N.K. Wang, S. Somekh and D. Maydan, in: (Electrochem. Proc., 1987) VLSI Science and Technology, edited by S. Broydo and C.M. Osburn, p. 712.
- [4] O. Spindler and B. Neureuther, Thin Solid Films, (1989) 174
- [5] D.L.W. Yen and G.K. Rao, IEEE V-MIC Proc., (1988), 85.
- [6] A. Klumpp and H. Sigmund, Appl. Surf. Science 36, (1989), 141
- [7] E.G. Rochow, in Gmelin Nr. 15 (B) (New York - London, 1951), p. 12 - 15.
- [8] A. Klumpp and H. Sigmund, Photoinduced Transformation of Polysiloxane Layers to SiO_2 , Proc. of the E-MRS Conf. 1989, to be published

PHOSPHORUS DOPING INTO SILICON USING ArF EXCIMER LASER

ABDELILAH SLAoui, FRANCOIS FOULON, ERIC FOGARASSY and PAUL SIFFERT
 Centre de Recherches Nucléaires (IN2P3), Laboratoire PHASE (UPR du CNRS n°292),
 B.P. 20, F-67037 STRASBOURG CEDEX, France

ABSTRACT

Chemical doping of single-crystal silicon in a PF_5 atmosphere is performed by irradiation with an ArF excimer laser working at 193 nm. We have investigated the dependence of doping parameters such as the number of pulses and PF_5 gas pressure on the sheet resistance and the impurity concentration profiles. From these results, it is found that phosphorus atoms are produced by pyrolysis of PF_5 molecules adsorbed (chemisorbed at low pressure and physisorbed at pressure higher than 1 Torr) on the silicon surface. As for the incorporation mechanism, it is shown that the process is external rate limited for doping in PF_5 ambient whereas mainly diffusion limited for doping using only the chemisorbed layer.

INTRODUCTION

With the advent of very large scale integration, more restrictive requirements are placed on the heavily doped and shallow junctions used for source-drain contacts in metal-oxide-semiconductor devices. With conventional ion implantation techniques and thermal annealing, it is difficult to form such a shallow junction, particularly a p^+ shallow junction because of the inherent boron channeling tail. To overcome this problem, many alternative laser-doping techniques have been developed [1-6]. The more attractive of them is the Gas Immersion Laser Doping (GILD) process. This technique employs a pulsed laser to melt a controlled thickness of a silicon slice placed in a dopant vapour atmosphere and to photodissociate the dopant molecules. This photodecomposition gives rise to two sources for dopant atoms. The first one results from the dissociation by pyrolysis and photolysis of the adsorbed molecules on the sample surface. The second source is due to the dissociation by pyrolysis of the molecules impinging on the molten surface and by photolysis of the molecules in the gas phase. When the photon energy is not sufficient to induce the photolysis of the dopant molecule, the dissociation takes place only by pyrolysis. The dopant atoms resulting from the dissociation are partly incorporated into the molten layer where they are redistributed by a liquid phase diffusion before recrystallization. Since virgin silicon has a large absorption coefficient in the ultraviolet region, the use of excimer laser gives an advantage in forming very shallow junctions.

Many authors have reported the formation of shallow p^+ or n^+ junctions with excimer lasers by irradiating silicon immersed in various doping gas atmospheres containing boron or phosphorus, respectively [1,2,7-19]. However, few works have been done on the study of the mechanism of excimer laser doping. Recently, we investigated the incorporation of boron in silicon by irradiation with ArF or XeCl excimer lasers, using BCl_3 or BF_3 as doping gases [13, 14, 19]. Kato et al. [17] performed the doping using POCl_3 and an ArF excimer laser. Corra et al. [16] reported the fabrication of a phosphorus doped junction by irradiating silicon immersed in PCl_3 with a XeCl excimer laser. They showed that the process is flux limited and that the dopant source lies the large quantity of adsorbate formed on the silicon surface. However, the dependence of sheet resistances and the doping profiles on doping conditions was not investigated in detail.

In this work, we report the results of silicon doping by ArF excimer laser irradiation in PF_5 atmosphere. PF_5 has already been used as doping gas in the molecular implantation technique [20] but not yet, to our knowledge, in the laser doping process. The influence of the irradiation parameters (number of pulses and gas pressure) on the incorporation rate is studied.

EXPERIMENT

High resistivity p-type silicon samples <100> oriented were used. The samples were chemically cleaned with a HF-dip and a deionized H_2O rinse and immediately set at 6.4 cm from the quartz window in a stainless-steel chamber. The chamber was previously evacuated to 2×10^{-5} Torr, purged and evacuated again before filling with the dopant gas PF_5 . Pressures between 10^{-2} and 10^2 Torr were examined.

The samples were irradiated using a pulsed ArF excimer laser ($\lambda = 193$ nm) with a pulsed duration of 21 ns. The typical spatial beam uniformity was 3 %rms over the central area of the beam which was delimited by mean of apertures. The 6×20 mm² output laser was then focused to a beam size of 3×7 mm² on the sample surface. The laser energy density was fixed at 0.75 J/cm², value well above the melting threshold of crystalline silicon [21]. The laser was operated at 2 Hz throughout this work.

The absorption characteristics of PF₅ gas at 193 nm was estimated by measuring the transmission of the gas enclosed in a cylindrical quartz cell of 3 cm path length using the ArF laser as a light source. The transmitted intensity of UV light was measured by a pyroelectric joulemeter.

The sheet resistance of the doped layers was measured using the four-point probe method, the values being corrected for the finite size of the doped area [22]. The phosphorus concentration profiles were obtained by Secondary Ion Mass Spectroscopy (SIMS).

RESULTS AND DISCUSSION

At 193 nm, PF₅ has no measurable absorption even at a pressure of 100 Torr and laser fluences higher than 1 J/cm². Consequently, PF₅ is transparent at 193 nm and no photochemical effects occur in the gas phase. Thus, the phosphorus dopant atoms are mainly produced by pyrolytic decomposition of the PF₅ molecules at the gas-silicon interface.

Laser doping parameters

The dependence of the sheet resistance on the number of pulses and gas pressure is shown in Fig. 1. Curve (a) shows the doping results using an adsorbed layer, and curves (b), (c) and (d) correspond to doping in 1, 10 and 50 Torr PF₅ ambients, respectively. In the case of (a), prior to laser irradiation, the chamber was initially filled with 50 Torr PF₅ and pumped down to 10^{-2} Torr. Consequently, the dopant atoms are mainly supplied by molecules adsorbed strongly on the silicon surface. The curves in Fig. 1 are quite similar.

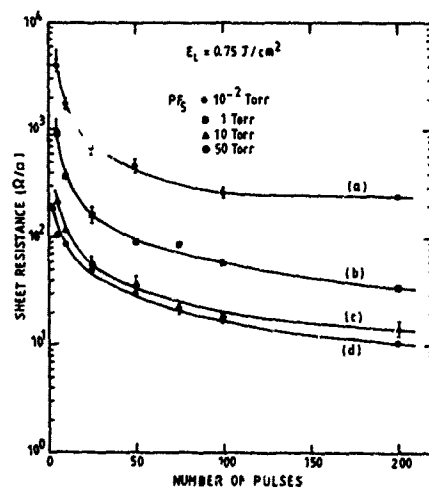


Fig. 1 : Sheet resistance as a function of the number of pulses after doping at 0.75 J/cm² in 1, 10 and 50 Torr PF₅ ambients and using an adsorbed layers.

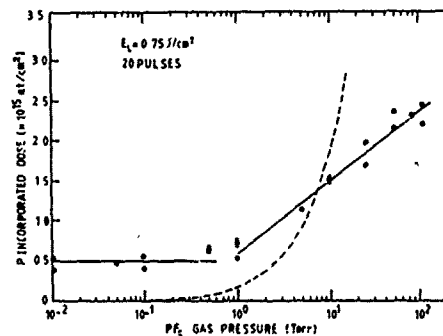


Fig. 2 : Total dose of incorporated phosphorus after 20 pulses at 0.75 J/cm² as a function of the PF₅ pressure. The number of molecules impinging on the silicon surface N_{imp} during the 20 laser pulses is also reported (dashed lines) versus the pressure.

After the first shot, the sheet resistance strongly decreases from the substrate value and continues to decrease with the number of pulses to reach values as low as 10 Ω/□ after 200 shots in 50 Torr PF₅. The decrease of the sheet resistance with repetitive laser irradiation is caused by the incorporation and subsequent activation of phosphorus atoms produced by the pyrolytic decomposition of PF₅ molecules at the surface during the melting. These dopant atoms can be supplied from two

sources : the impinging gas molecules and a large quantity of adsorbate. The first source relies on a continuous flux N_{imp} of gas molecules impinging upon the molten surface. This flux depends linearly on pressure. The second source relies on formation of a layer of adsorbate before melting. The pressure dependence of the sheet resistance shown in Fig. 1 can be attributed to the increase of the number of PF_5 -molecules striking the molten surface as well as to the fact that the thickness of the adsorbed layers grows rapidly with pressure in agreement with PF_5 adsorption isotherm.

In order to get more information about the dominant dopant supply in this process, the dependence of the incorporated dose I on the PF_5 pressure p was investigated by irradiating c-Si samples at a fixed fluence with 20 shots. A first set of samples was irradiated using the following procedure : the reaction chamber was pumped down to 2×10^{-5} Torr, and the required final pressure was then reached by introducing a controlled amount of PF_5 gas. In the second set, this procedure was reversed so that the pressures were decreasing towards 10^{-2} Torr. The results are displayed on Fig. 2. Both procedures give rise to the same relationship between I and p .

Two different pressure ranges can be distinguished. At pressures lower than about 0.5 Torr, the incorporation is constant. The quantity of molecules striking the silicon surface during the 20 laser pulses gives a negligible contribution to the incorporation mechanism in this pressure range. These results provide evidence that the dopant atoms are mainly supplied by a layer of strongly bounded chemisorbed molecules which does remain after the cell is evacuated. This layer has been evaluated to be at least of about 3×10^{14} PF_5 molecules/ cm^2 . The value is close than the calculated surface density for a monolayer of PF_5 ($\approx 3.9 \times 10^{14}$ mol/ cm^2).

In the high pressure range, the increase of I as a function of p seems to follow a logarithmic law. As a matter of fact, by changing the pressure by two orders of magnitude from 1 to 100 Torr, the incorporated dose after 20 shots varies from about 5×10^{14} to 2.5×10^{15} P/ cm^2 . The deviation of the experimental data from the dashed curve indicates that the pyrolysis of molecules crossing the hot surface gives a negligible dopant supply. These trends and the reversibility of the process, evidenced by the same behaviour of I versus p for the two sets of samples, suggest that pyrolysis of one or more weakly bounded physisorbed layers formed on the silicon surface is the dominant dopant supply process. This result was also found in previous studies of phosphorus [16] and boron [14] doping by a XeCl excimer laser using PCl_3 and BCl_3 , respectively.

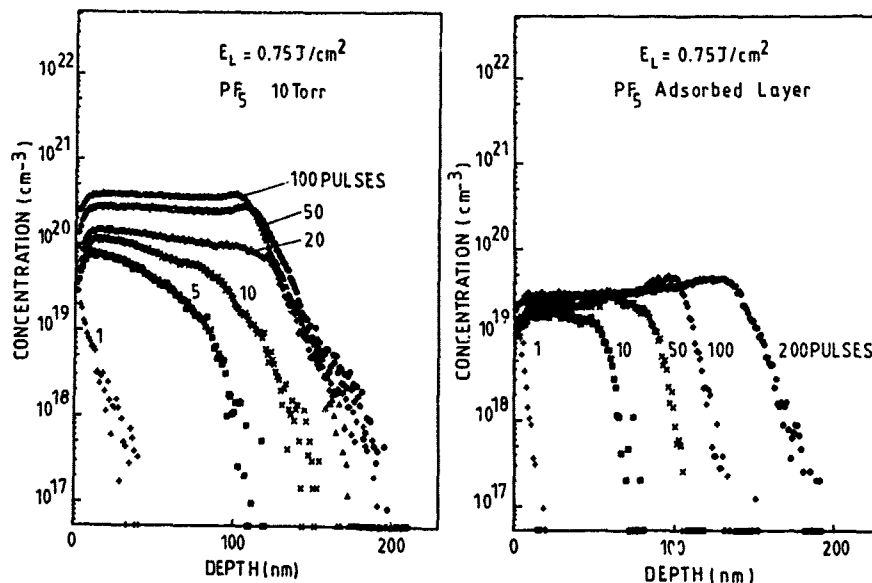


Fig. 3 : Phosphorus concentration profiles by SIMS measurements for samples doped (a) in 10 Torr PF_5 and (b) using an adsorbed PF_5 layer.

Figures 3(a) and 3(b) show profiles of incorporated phosphorus for samples doped in a 10 Torr PF_5 ambient and using the PF_5 adsorbed layer (10^{-2} Torr), respectively. The profiles were obtained at a fixed fluence (0.75 J/cm^2) with the number of laser pulses as a parameter. A comparison of profiles

determined at different positions of the $3 \times 7 \text{ mm}^2$ doped area has shown that the uniformity in the junction depth and the surface concentration is better than 10 %. The shape of the profiles can be explained by the very fast diffusion of the dopant atoms in molten silicon [19]. The diffusion coefficient D_d deduced from the profile of Fig. 3(a) for one pulsed approximated by the complementary error function is estimated to be in the range of $2.5 \times 10^{-4} \text{ cm}^2/\text{s}$. This value of D_d agrees well with earlier published data [23]. Due to this fast diffusion of the dopant into the molten layer, square shaped profiles are obtained within a few pulses (20 shots). Under our experimental conditions, the melt depth is estimated to be about 100 nm [24], in good agreement with the junction depth deduced from the profile for 20 pulses. Figure 3(a) shows that the junction depth did not vary with the number of pulses ($N > 20$ pulses). However, the surface concentration increases with N . This last feature was also found in a previous study of boron doping using BF_3 [17, 19] or BCl_3 [13, 14] as doping gas and ArF or XeCl lasers for the irradiation.

As for the PF_5 adsorbed layer doping case, it can be observed from Fig. 3(b) that the surface concentration is nearly constant with the number of pulses N . It varies from 10^{19} at/cm^3 after one shot to $3 \times 10^{19} \text{ at/cm}^3$ after 200 shots. The junction depth increases with N to reach the expected molten depth after 100 pulses. The incorporated dose for the sample exposed to 200 pulses is of about $5.6 \times 10^{14} \text{ p/cm}^2$, which is slightly higher than the calculated surface density for a monolayer of PF_5 . This result means that a new adsorbed layer is partially formed on the silicon surface between pulses. Another important feature is that the surface concentration saturates earlier in the case of adsorbed layer doping than in the ambient doping case.

The total doses of phosphorus, which are obtained by integrating the profiles as shown in Figs. 3(a) and 3(b) are reported in Fig. 4 as a function of the total melting time t_m . The relationship $t_m = N \cdot t_f$ is used, where t_f is the melting time per pulse. The silicon melt time t_f is deduced from the plot of computed melted depth versus melt time as given by heat flow calculation [24]. The curves show a t_m^α dependence, where α is 0.75 and 0.5 for doping in PF_5 ambient and using the adsorbed layer, respectively.

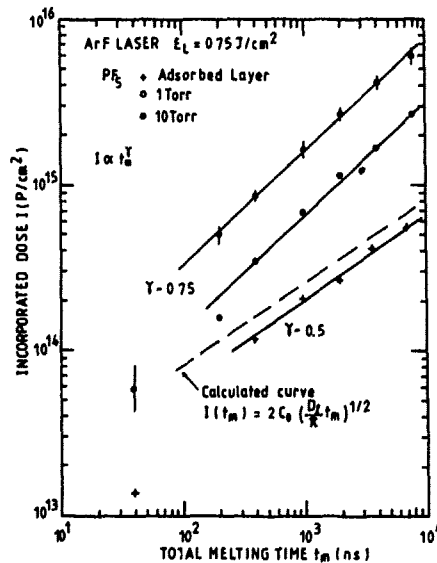


Fig. 4 : Total quantity of phosphorus as a function of the number of pulses for doping in PF_5 ambients (1, 10 Torr) and using an adsorbed layer.

Incorporation process

The process of incorporation and transport of the doping species in the molten silicon can be studied by solving the one-dimensional diffusion equation [25] :

$$\frac{\partial C}{\partial t} = D_e \frac{\partial^2 C}{\partial x^2} \quad (1)$$

where $C = C(x, t)$ is the dopant concentration and D_e is the diffusion coefficient. On the other hand, the total incorporation I can be expressed as a function of the total melting time and the flux F of molecules crossing the liquid surface as :

$$I = \int_0^{t_m} F \cdot dt = \int_0^{t_m} D_e \cdot \left. \frac{\partial C}{\partial x} \right|_{x=0} \cdot dt \quad (2)$$

The incorporation rate depends both on the diffusivity into the melt (D_e) and on the dopant supply at the silicon-ambient-interface $\left(\left. \frac{\partial C}{\partial x} \right|_{x=0} \right)$.

The SIMS profiles displayed in Fig. 3(b) for samples doped using the PF_5 adsorbed layer have shown that the surface concentration C_s is nearly constant with N , and hence with t_m . This behaviour suggests that the surface concentration in the silicon is in equilibrium with the partial pressure of dopant atoms at the gas-silicon interface. Then, there is no resistance to the transport of phosphorus atoms from the adsorbed layer to the surface. The doping is therefore performed under the "constant surface concentration" condition [25]. The diffusion equation must be solved using the boundary condition :

$$C(0, t) = C_s \quad (3)$$

The solution satisfying eq. (1) as well as the above condition is the complementary error function. The incorporated dose using eq. (2) is then given by :

$$I(t_m) = 2C_s (D_e t_m / \pi)^{1/2} \quad (4)$$

The curve displayed in Fig. 4 (dashed lines) has been computed using eq. (4) where $C_s = 1.5 \times 10^{19} \text{ at/cm}^3$ and $D_e = 2.5 \times 10^{-4} \text{ cm}^2/\text{s}$. A satisfactory agreement with the experimental data is observed. This result means that the diffusion model is suitable to describe the doping process from the PF_5 adsorbed layer. It also indicates that the incorporation is limited by the diffusion of the phosphorus atoms. In this case, the dopant source supplied by the pyrolytic dissociation of PF_5 molecules at the gas-silicon interface can be considered about infinite. This behaviour is markedly different than that obtained for doping using BF_3 adsorbed layer for which the process is rather limited by the quantity of dopant supplied by the pyrolysis of BF_3 molecules [19].

During doping in PF_5 ambient, we have found from Fig. 3(a) that the surface concentration increases with t_m . On the other hand, the incorporated dose depends on $t_m^{0.75}$. Thus, a deviation from the simple diffusion theory as described by eq. (4) is observed. We speculate that an external limitation to the rate of transport of the impurities influences the diffusion process. Indeed, it is known that in the initial step of predeposition in solid-state diffusion, surface concentration increases with diffusion time because the surface concentration cannot jump from zero to its final constant value instantaneously [25]. In this case, the rate limitation of the diffusion is the transport of dopant atoms from a diffusion source to silicon surface. Thus, we must now replace the boundary condition given by eq. (3), that of a constant surface concentration, with the condition [25] :

$$-D_e \left. \frac{\partial C}{\partial x} \right|_{0, t_m} = h [C_{\text{sol}} - C(0, t_m)] \quad (5)$$

where C_{sol} is the maximum solubility limit of phosphorus in the melt [26]. The $[C_{\text{sol}} - C(0, t_m)]$ term limits the dopant incorporation up to the solubility limit. h denotes the gas-phase mass transfer coefficient and controls both the dopant supply and the incorporation efficiency of the surface. In this case, using the equations (1), (2), and (5), the incorporated dose is expected to follow a t_m^α where α is in range 0.5 to 1 depending on the values of h , t_m and D_e . This result is consistent with our experimental data where $\alpha = 0.75$. We can suggest that the diffusion mechanism of dopant atoms is limited by the rate of transport of phosphorus atoms from the physisorbed layers to the silicon surface. Similar

results have been found for doping in BCl_3 gas with an ArF excimer laser [2,14].

CONCLUSION

We have shown that multipulse ArF excimer laser irradiation of silicon immersed in a PF_5 gas atmosphere allows to control both the sheet resistance and the concentration profile. The evolution of the incorporated phosphorus dose with PF_5 gas pressure shows that at pressure lower than 0.5 Torr the incorporation is caused by the presence of a strongly bounded chemisorbed layer, whereas at high pressure the supply may be due to the successive formation of weakly bounded physisorbed layers on the silicon surface.

As for the doping mechanism, the experimental data indicate that the process is external rate limited for doping in PF_5 ambient and mainly diffusion limited when using only the chemisorbed layer.

This work was funded by the Centre National d'Etudes des Télécommunications (CNET) and by the Agence Française pour la Maîtrise de l'Energie (AFME).

REFERENCES

1. T.F. Deutsch, D.J. Ehrlich, R.M. Osgood and Z.L. Liao, *Appl. Phys. Lett.* **36**, 847 (1980).
2. T.F. Deutsch, D.J. Ehrlich, D.D. Rathman, D.J. Silversmith, and R.M. Osgood, *Appl. Phys.* **39**, 825 (1981).
3. R.T. Young, R.F. Wood, and W.H. Christie, *J. Appl. Phys.* **53**, 1178 (1982).
4. E. Fogarassy, R. Stuck, J.J. Grob and P. Siffert, *J. Appl. Phys.* **52**, 1076 (1982).
5. R. Stuck, E. Fogarassy, J.C. Muller, M. Hodeau, A. Wattiaux and P. Siffert, *Appl. Phys. Lett.* **38**, 715 (1981).
6. T. Sameshima, S. Usui and M. Sekiya, *J. Appl. Phys.* **62**, 711 (1987).
7. P.G. Carey, T.W. Sigmon, R.L. Pres's and T.S. Fahlen, *IEEE Electron Device Lett.* **EDL-6**, 291 (1985).
8. K.G. Ibbas and M.L. Lloyd, in *Laser Diagnostics and Photochemical Processing for Semiconductor Devices*, edited by R.M. Osgood, S.R.J. Brueck, H.R. Schlossberg, (Mater. Res. Soc. Symp. **17**, North Holland, Amsterdam, 1983) p. 243.
9. T.W. Sigmon, in *Photon Beam and Plasma Stimulated Chemical Processes at Surfaces*, edited by V.M. Donnelly, I.P. Herman, M. Hirose (Mater. Res. Soc. Symp. Proc. **75**, Pittsburgh, PA 1987) p. 619.
10. S. Kato, T. Nagahori, and S. Matsumoto, *J. Appl. Phys.* **62**, 3656 (1987).
11. P.G. Carey, K.H. Weiner, and T.W. Sigmon, *IEEE Electron Device Lett.* **EDL-9**, 542 (1988).
12. E. Landi, P.G. Carey, and T.W. Sigmon, *IEEE Transactions on computer-aided design* **7**, 205 (1988).
13. F. Foulon, A. Slaoui, E. Fogarassy, R. Stuck, C. Fuchs and P. Siffert, *Appl. Surf. Sci.* **36**, 384 (1989).
14. A. Slaoui, F. Foulon, M. Bianconi, L. Corraera, R. Nipotti, R. Stuck, S. Unamuno, E. Fogarassy, and S. Nicoletti, in *Laser and Particle-Beam Modification of Chemical Processes on Surfaces*, edited by A.W. Johnson, G.L. Loper and T.W. Sigmon (Mater. Res. Soc. Symp. Proc. **129** 1989) in press.
15. G.G. Bentini, M. Bianconi and C. Summonte, *Appl. Phys.* **A45**, 317 (1988).
16. L. Corraera, G.G. Bentini, M. Bianconi, R. Nipotti, and D.A. Patti, *Appl. Surf. Sci.* **36**, 394 (1989).
17. S. Kato, H. Saeki, J. Wada and S. Matsumoto, *J. Electrochem. Soc., Sol. St. Sc. and Techn.* **135**, 1030 (1987).
18. T.M. Liu and W.G. Oldham, *IEEE Electron Device Lett.* **EDL-4**, 59 (1983).
19. F. Foulon, A. Slaoui, and P. Siffert, in *Beam Processing and Laser Chemistry* edited by I.W. Boyd and E. Rimini (Europ. Mater. Res. Soc. Symp. Proc., North Holland, Amsterdam, 1989) in press.
20. J.C. Muller, and P. Siffert, *Rad. Effects* **63**, 81 (1982).
21. F. Foulon, E. Fogarassy, A. Slaoui, C. Fuchs, S. Unamuno, and P. Siffert, *Appl. Phys.* **A45**, 361 (1988).
22. J.C.C. Tsai in *VLSI Technology*, edited by S.M. Sze (Mc Graw-Hill, New York, 1983) p. 185.
23. Y.M. Shashkov and V.M. Gurevich, *Russ. U. Phys. Chem.* **42**, 1082 (1967).
24. S. Unamuno and E. Fogarassy, *Appl. Surf. Sci.* **36**, 1 (1989).
25. A.S. Grove, in *Physics and Technology of Semiconductor Devices* (Wiley and Sons, New York, 1967) p. 65.
26. C.W. White, *J. Phys. Vol. 44*, n°10, **C5**, 145 (1983).

PART VI

Photo-Etching

THE INTERACTION OF LASER GENERATED METHYL RADICALS WITH Cd, Te, AND CdTe SURFACES

J.J. Zinck, G.L. Olson, P.D. Brewer, and J.E. Jensen
Hughes Research Laboratories, Malibu, CA

Abstract

The mechanism of the interaction of methyl radicals with Cd, Te, and CdTe surfaces has been studied in ultrahigh vacuum by Auger electron spectroscopy and thermal desorption mass spectrometry. Methyl radicals generated by the laser photodissociation of acetone at 193 nm efficiently etch both Te and Te-rich CdTe surfaces. However, there is no evidence for reaction of methyl radicals with Cd or stoichiometric CdTe. A temperature dependence in the rate of methyl radical etching of Te-rich CdTe is related to a competition between acetone scavenging of radicals on the surface and reaction of radicals to form volatile metalorganics. Acetone itself has a small but finite reaction probability with Te and Te-rich CdTe surfaces.

Introduction

Methods for dry etching of compound semiconductors are being actively investigated because they offer a degree of control not available with conventional wet etching techniques. In addition, dry etching is compatible with a closed system approach to growth, processing, and analysis of semiconductor materials and devices. The use of vapor phase etching techniques for II-VI semiconductors such as CdTe and HgCdTe is particularly desirable because of the sensitivity of these materials to the surface damage and compositional variation that can result from the wet etching process [1]. We have found that a detailed understanding of the reactions which occur during the interaction of the vapor phase reactants and the semiconductor surface is essential to the development and optimization of a dry etching procedure for these materials. In this paper we describe experimental studies of the reactions that occur between photo-generated methyl radicals and Cd, Te, CdTe, and Te-rich CdTe surfaces, and show how these reactions can be used to modify the surface composition and structure of CdTe and Te-rich CdTe layers.

The high volatility of dimethyl Hg, Cd, and Te compounds suggests that the interaction of methyl radicals with surfaces of CdTe and HgCdTe may lead to efficient etching of these materials. This hypothesis derives additional support from the well established activity of methyl radicals in the etching of metal films [2]. It was recently reported that HgCdTe could be etched in a flowing afterglow reactor where methyl radicals were purported to be the etchant species [3]. However, experiments performed in our laboratory in a low vacuum chamber using methyl radicals generated by 193 nm excimer laser irradiation of acetone have yielded results inconsistent with that work [4]. In those experiments an excimer laser operating at 193 nm, 10 mJ/cm², and 30 Hz, was directed parallel to a thin film of Cd, Te, or CdTe on a quartz substrate in the presence of 0.1 Torr of acetone. Acetone absorbs 193 nm radiation with 6% efficiency and is known to dissociate into two methyl radicals and a CO molecule with 96% probability upon absorption [5]. *In situ* reflectivity and *ex situ* profilometer measurements were used as probes of the reaction between laser generated methyl radicals and the surface. Te films and Te-rich CdTe were efficiently etched at 25°C; however, no significant etching of either Cd or CdTe was observed. In order to examine the mechanism of the etching process under controlled conditions, where issues of substrate cleanliness and surface poisoning could be probed, we simulated the etching reaction in an ultrahigh vacuum (UHV) environment. We describe experiments in which the interaction of laser generated methyl radicals with Cd, Te, and CdTe surfaces was investigated using Auger electron spectroscopy (AES) and thermal desorption mass spectrometry (TDMS).

Experimental

The essential features of the UHV chamber are depicted schematically in Fig. 1. The system was pumped by a 500 l/sec turbomolecular pump and had a base pressure of 5×10^{-9} Torr. The UHV chamber was connected to a load lock and sample transfer was effected via a bidirectional transfer device and a wobble stick. The sample was mounted on a Vacuum Generators high

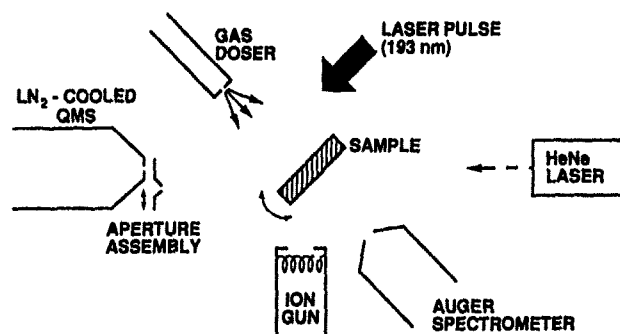


Figure 1. Schematic cross-sectional view of UHV reaction chamber and surface analysis system.

precision translator which could be heated, cooled, translated, and rotated. A low energy, broad area ion gun (Commonwealth Scientific) was available for sample cleaning. Acetone was admitted to the chamber via an effusive beam gas doser which was controlled by a servo driven leak valve (Granville Phillips 216) and a temperature controlled baratron (MKS 501A) operated in a feedback mode. A differentially pumped and cryoshrouded quadrupole mass spectrometer (EXTREL C50) was used for TDMS. An aperture assembly allowed the quadrupole to be alternatively isolated from the chamber during gas exposures or collimated to discriminate against background desorption from the manipulator during TDMS. A hemispherical analyzer and electron gun (VSW HA100 and EG5) were used for AES. The chamber was equipped with Suprasil windows to allow passage of the excimer laser beam into the system. A Lumonics 600 excimer laser operating at 193 nm was used for the photodissociation of acetone at an energy density of 50 mJ/cm² and a repetition rate of 250 Hz.

High purity, glass distilled acetone was obtained from Aldrich Chemical Co. The acetone was dried over molecular sieves for 12 hours and subjected to two freeze/thaw cycles prior to use. Purity of the acetone was confirmed by mass spectrometry in the UHV chamber. High resistivity CdTe (100) samples were obtained from II-VI Inc. and Cd foil (0.25 mm thick, 99.999%) was purchased from AESAR. Te films were obtained by thermal evaporation of Te metal onto quartz substrates. All samples were degreased and etched in 1.5% Br₂/methanol solution prior to installation in the load lock. Upon transfer to the vacuum chamber, the samples were ion sputtered at 100 eV and 3 μ A/cm² for 1 minute which was sufficient to remove any residual carbon and oxygen from the surface.

Two types of experiments were performed in the UHV chamber. In the first set of experiments CdTe substrates were made Te rich *in situ* by laser irradiation at 193 nm and 70 mJ/cm² [6]. The efficiency of methyl radical etching of the Te-rich CdTe surface was measured by monitoring the Cd/Te ratio as a function of temperature via AES. The second set of experiments were designed to trap the methyl radicals on the surface at low temperature and identify the product distributions of the etching reactions by TDMS.

Results

A: Temperature Dependence of Methyl Radical Etching of Te-Rich CdTe

The results of experiments in which Te-rich CdTe films were exposed to laser generated methyl radicals at various sample temperatures are shown in Fig. 2. Each data point represents a CdTe surface which was made Te-rich by laser irradiation prior to exposure to methyl radicals. AES depth profiling on CdTe samples which were made Te-rich by this treatment revealed that the depth of the stoichiometrically altered layer was 20 Å or less. The conditions of the exposure (10⁻⁶ Torr acetone for 5 minutes, 193 nm, 250 Hz, 50 mJ/cm²) corresponds to a total flux of methyl radicals to the surface during the exposure on the order of one monolayer (one monolayer $\sim 10^{15}$ molecules/cm²). The change in the Cd/Te ratio as measured by derivative AES is plotted as a function of the sample temperature. The data show a threshold temperature dependence to the etching reaction under the conditions used in our experiments. Below a substrate temperature of

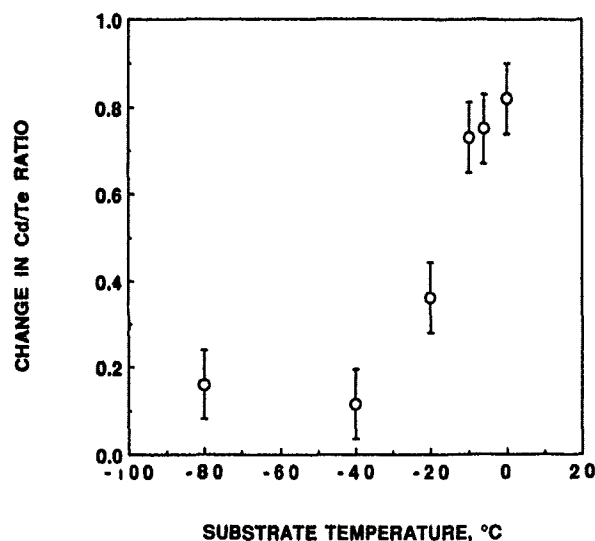


Figure 2. Change in Cd/Te ratio following exposure to laser generated methyl radicals as a function of substrate temperature. Cd/Te ratio determined by AES. Exposure conditions: 10^{-6} Torr acetone, 5 minutes, 193 nm, 250 Hz, 50 mJ/cm².

-40°C there is very little reaction; however, at temperatures greater than -40°C increasingly efficient etching is apparent from the magnitude of the change in the CdTe surface stoichiometry. Experiments performed at room temperature under these conditions reproducibly returned Te-rich CdTe films to a 1:1 surface stoichiometry.

Thermal desorption experiments were performed at each temperature following methyl radical exposure, but no metalorganic etch products were observed at any sample temperature between -80°C and 25°C. AES examination of a surface following methyl radical exposure at -60°C did not reveal the presence of carbon. These observations suggest that the rate of etching under these conditions is not limited by surface diffusion of methyl radicals or desorption of etch products, but that acetone itself is inhibiting the etching process by efficiently scavenging methyl radicals from the surface at low temperature.

B: Thermal Desorption from Te, Cd, Te-rich CdTe and CdTe Surfaces

Experiments probing the adsorption of acetone on Cd, Te, and CdTe surfaces have revealed that acetone is not trapped on these surfaces at temperatures greater than -130°C [7]. An adsorption temperature of -120°C was therefore selected as the lower limit for our methyl radical adsorption studies. In these experiments the exposure conditions (10^{-5} Torr, 15 minutes, 193 nm, 250 Hz, 50 mJ/cm²) corresponded to a total flux of methyl radicals to the surface of more than ten monolayers. In addition to each laser experiment, a background experiment in which the laser was turned off during exposure to acetone was also performed. An example of the TDMS results for Te films is shown in Fig. 3 in which peaks at the mass corresponding to dimethyltellurium ($\text{CH}_3\text{Te}^{130}\text{CH}_3$) are displayed. We also observed peaks at m/e 130 (Te^{130}), 260 (Te_2^{130}), and 290 ($\text{CH}_3\text{Te}^{130}\text{Te}^{130}\text{CH}_3$) at the same desorption temperature, and the masses 130:160:260:290 had relative intensities of 100:42:9:10. The cracking pattern of dimethyltelluride is not known, but from the reported cracking pattern of diethyltelluride [8] we suggest that the presence of masses 260 and 290 in our mass spectrometer are related to secondary wall reactions in the ionizer and not to primary desorption products.

Two points are evident from the data in Fig. 3. Acetone itself has a small but finite reaction with Te, and there is no enhancement of the desorption yield by exposure of the surface to laser generated methyl radicals. A rough calculation of the yield of all measured desorption products

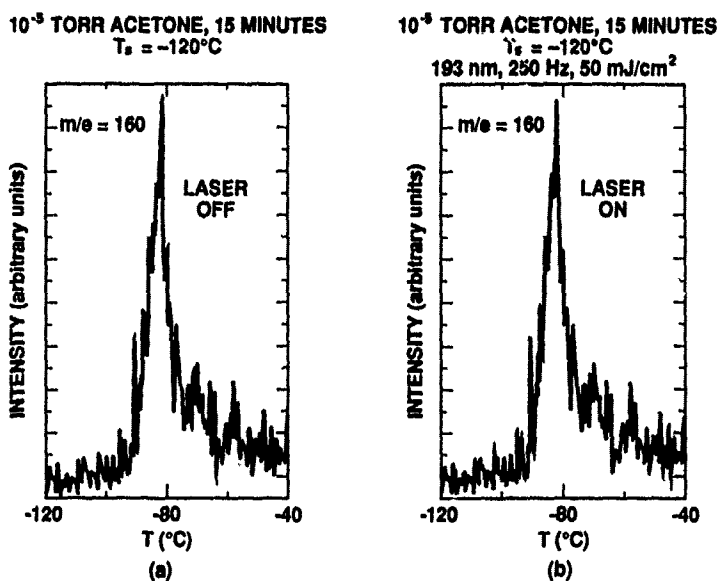


Figure 3. Dimethyltellurium TDMS signal from Te films exposed to a) acetone, b) acetone and laser generated methyl radicals.

resulting from acetone reaction with Te corresponds to less than 1% of a monolayer. We expect that the sticking coefficient of methyl radicals on the surface will be high on the basis of previous studies [8,9]. The absence of an enhancement in the desorption yield upon exposure to methyl radicals therefore supports the hypothesis that acetone scavenging reactions remove methyl radicals from the surface at low temperature.

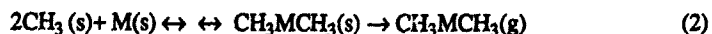
Identical experiments were performed on Te-rich CdTe, Cd, and stoichiometric CdTe surfaces. Te-rich CdTe surfaces behaved similarly to the Te surface. Again, there was a small but finite reaction with the surface to produce dimethyltellurium, but no enhancement of the desorption yield was observed when laser generated methyl radicals were exposed to the surface. In the case of Cd and stoichiometric CdTe surfaces however, there was no apparent reaction with either acetone or methyl radicals.

Discussion

Based on the above observations we propose the following mechanism. It is reasonable to assume that methyl radicals once formed in the gas phase will stick to the surface with high probability.



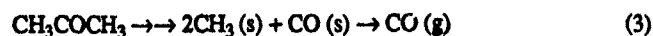
Once adsorbed these methyl radicals will combine with the surface atoms in a multistep process. Stinespring and coworkers have reported [11] that at room temperature dimethylcadmium and dimethyltellurium dissociatively adsorb on Si and GaAs surfaces, suggesting that each step of the reaction of methyl radicals with surface Cd or Te is reversible.



Any stable species that is successfully formed on the surface above its desorption temperature will desorb. In the case of CH_3TeCH_3 this temperature is $\sim -100^\circ\text{C}$. The difference in efficiency of the room temperature etching reaction between Cd and Te may relate to the strength of the monomethyl bond. The reported bond strength for monomethyl cadmium is on the order of 12.4

Kcal/mole with complete dissociation of dimethylcadmium requiring 72.4 Kcal/mole [12]. The bond strengths in dimethyltellurium are not known but it is estimated that the total energy required to dissociate the molecule is 115 Kcal/mole [13]. On this basis, the dissociation of the monomethylcadmium species may be rapid compared to the monomethyltellurium, and the formation of dimethylcadmium would be correspondingly more difficult.

Acetone itself has a small but finite reaction probability with Te and Te-rich CdTe surfaces. Dissociative adsorption proceeds by a one or two step mechanism to produce two methyl radicals and a CO molecule. Previous adsorption studies have shown that CO is not absorbed on the surfaces studied above -120°C [14,15].

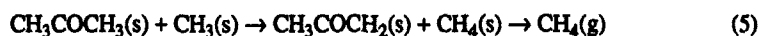


Acetone is not trapped in a physisorption state on the surface above -130°C; however, its residence time on the surface may be estimated from the reciprocal of the Arrhenius factor,

$$\tau \propto (\exp(-\Delta E_{\text{des}}/KT_{\text{des}}))^{-1} \quad (4)$$

where ΔE_{des} is the activation energy for desorption and T_{des} is the desorption temperature. We estimate from our data that ΔE for acetone for all the surfaces studied is on the order of 8 Kcal/mole and the desorption temperature is $\sim -140^\circ\text{C}$. The Arrhenius factor changes by over five orders of magnitude from -120°C to 25°C. Therefore a competition exists between the rate that acetone reacts with radicals on the surface and the rate at which the radicals themselves react with the surface leading to the observed temperature dependence in the rate of etching of Te-rich CdTe films.

The observation by AES that carbon does not accumulate on the surface following exposure to acetone and methyl radicals suggests that the acetone scavenging reactions produce predominantly stable species on the surface which subsequently desorb. Although evidence exists for direct radical desorption from semiconductor surfaces [16], this generally occurs at temperatures on the order of 300°C or higher, consistent with radical-surface bonds strengths of at least 25-30 Kcal/mole. Gas phase reactions between acetone and methyl radicals are varied and complex [17] and comparable reactions may occur on the surface. A suggested scheme for the scavenging of methyl radicals from the surface is given in (5) and (6).



Work is in progress to identify hydrocarbon species which may be generated by the acetone scavenging reactions.

Conclusions

We have found that methyl radicals generated by the photodissociation of acetone etch Te films efficiently (up to 300 Å/minute). Te-rich CdTe films are also etched by methyl radicals in a manner similar to Te. A temperature dependence in the rate of etching of Te-rich CdTe films is related to a competition between acetone scavenging reactions and reaction of methyl radicals with the surface to form volatile metalorganics. On the basis of both low vacuum and ultrahigh vacuum studies we see no evidence for etching of either Cd or CdTe by methyl radicals alone, suggesting that an additional source of energy is required to efficiently etch these materials. Work is underway in our laboratory to investigate this hypothesis.

References

1. A. A. Konova, A. Shopov, and I. Nedev, *Thin Solid Films* **140**, 189 (1986).
2. F. A. Paneth, and W. Hofeditz, *Ber.* **64B**, 2702 (1931)
3. J. E. Spencer, J. H. Dinan, P. R. Boyd, H. Wilson, and S. E. Buttrill, Jr., *J. Vac. Sci. Technol.* **A7**, 676 (1989).
4. P. D. Brewer, unpublished results.
5. E. L. Woodbridge, T. R. Fletcher, S. R. Leone, *J. Phys. Chem.* **2**, 5387 (1988).
6. P. D. Brewer, J. J. Zinck, and G.L. Olson, to be published.
7. J. J. Zinck, to be published.
8. K. J. Irgolic, *The Organic Chemistry of Tellurium*, (Gordon and Breach Science Publishers, NY, 1974), p. 364.
9. H. F. Winters, *J. Appl. Phys.* **49**, 5165 (1978).
10. S. Joyce, J. G. Langan, and J. I. Steinfeld, *J. Chem. Phys.* **88**, 2027 (1988).
11. C. D. Stinespring and A. Freedman, *Chem. Phys. Lett.* **143**, 584 (1988).
12. C. F. Yu, F. Youngs, K. Tsukiyama, R. Bersohn, and J. Preses, *J. Chem. Phys.* **85**, 1382 (1986).
13. J. B. Mullin and S. J. C. Irvine, *J. Vac. Sci. Technol.* **21**, 178 (1982).
14. H. S. Tan, A. Morawski, and W. E. Jones, *Surface Sci.* **195**, L193 (1988).
15. J. J. Zinck, unpublished results.
16. D. W. Squire, C. S. Dulcey, and M. C. Lin, *Chem. Phys. Lett.* **116**, 525 (1985).
17. E. W. R. Steacie, *Atomic and Free Radical Reactions*, Vol.1, (Reinhold Publishing Corp, NY, 1954), p. 331-340.

HOLOGRAPHIC PATTERN ETCHING OF SILICON-CARBIDE BY EXCIMER LASER

M. Murahara, M. Yonekawa* and K. Shirakawa*

Faculty of Engineering, Tokai Univ., 1117 Kitakaname,
Hiratsuka, Kanagawa, 259-12, JAPAN

* Graduate student of Faculty Eng., Tokai Univ.,

ABSTRACT

The diffraction grating on SiC mirror was performed by a laser holographic method. In the present method, KrF laser and ClF_3 was used for etchant gas. The ClF_3 gas has an absorption band in the range between 200 and 400 nm. Therefore, ClF_3 gas is effectively decomposed by the XeF, KrF and ArF excimer lasers' radiation. It is found that absorption of SiC is about 50% in the range of between 200 and 400 nm, and that the bonding energy of Si-C is lower than the photon energy of KrF laser beam. The above results indicate the direct decomposition of Si-C bond. On the other hand, the threshold fluence energy for etching was 800 mJ/cm^2 in 249 nm and in 193 nm as high as 7 J/cm^2 . In these results, the KrF laser is more effective than ArF laser. Then we applied KrF laser to crystalline SiC in an atmosphere of ClF_3 gas. The divided two polarized KrF laser beams were interfered on the substrate. And the beams were used to photodissociate ClF_3 gas in the proximity of substrate. Fluence of KrF laser beam was 1 J/cm^2 . The incidental angle of KrF laser beams was 20° and the grating gaps were 7170 Å, etching depth 1000 Å, and etching rate was 5 Å/pulse.

Introduction

It is being needed to develop diffraction grating for X-ray laser or synchrotron radiation which has high reflectivity and superior heat resistance in the range of soft X-ray. Under present conditions, the Au diffraction grating is applied for this purpose, but this material is damaged at synchrotron radiation of electron energy above 6 GeV. On the other hand, the melting point of SiC is as high as 2830°C and its reflectivity is as high as 60% in the range of soft X-ray. For these reasons, it is expected that SiC is effective optical material for soft X-ray. But etching of SiC is difficult and selective etching of minute patterns is almost impossible.

Recently, we have reported for selective area photo etching of SiC by using two-color excimer lasers and ClF_3 gas [1,2]. In this method, ClF_3 gas was used as etchant. This ClF_3 gas is very active and has high reactivity, and use of this gas has been reported for in relation to etching experiments on Si, Ta, Ta_2N , Ta_2O_5 , TaSi, SiO₂ and Si₃N₄ [3,4]. On the other hand, this ClF_3 gas has an absorption band in the range between 200 and 400 nm and this band range is a good agreement with the emission wavelength of the XeF, KrF and ArF excimer lasers. So I have experimented on resistless etching of SiC by using excimer lasers and ClF_3 gas. And we fabricated diffraction grating by laser holographic method [2]. These findings are reported below.

Photochemical reactions

In photochemical reactions, the material must absorb photons directly, and the photon energy must be larger than the bonding energy of constituent molecules[5]. In general, the chemical resistance of SiC is very strong and its chemical or mechanical etching is very difficult. However, the photon absorption of SiC is approximately 50% at proximity of 249 nm as shown in Fig.1, the bonding energy of Si-C bond is 104 Kcal/mol, and the photon energy of KrF laser beam is 114 Kcal. Therefore, the SiC bond can be cut directly by means of KrF laser beam. On the other hand, the ClF₃ gas has absorption in the band of 200 to 400 nm as shown in Fig.2, and the bonding

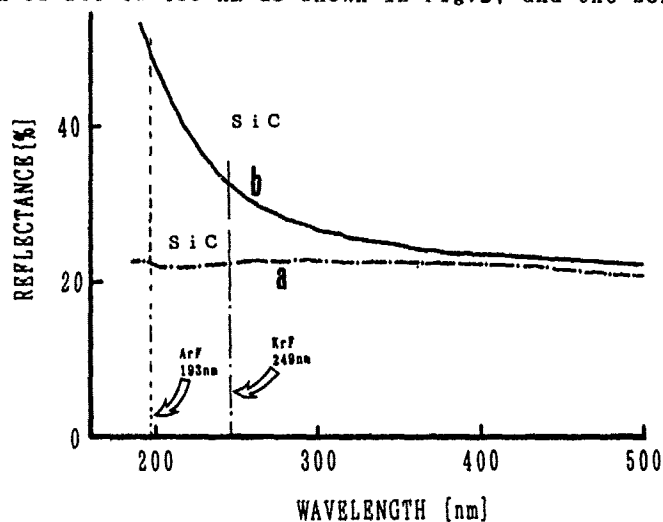


Fig.1 Reflectance for SiC as a function of wavelength.
a: amorphous SiC, b: crystalline SiC

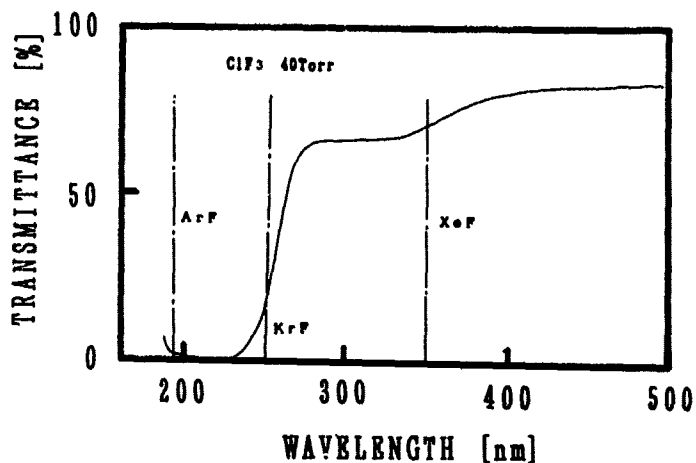


Fig.2 UV transmittance of gaseous ClF₃

energy between Cl-F is as low as 60 Kcal/mol. Therefore, this chemical bonding can be dissociated easily by XeF, KrF and ArF laser beams. In this results, halogen radicals are produced.

But this ClF_3 gas is very active, and when it is excited by the laser beam, it reacts quickly with the etched materials and produce the intermediate products. So we have made the UV and IR spectroscopy analysis in order to inspect the intermediate products which were created by this surface reactions as in Fig.3. Then the SiC substrate is put and ClF_3 gas is sealed in a cubic cell. And this gas is excited by XeF laser beam to

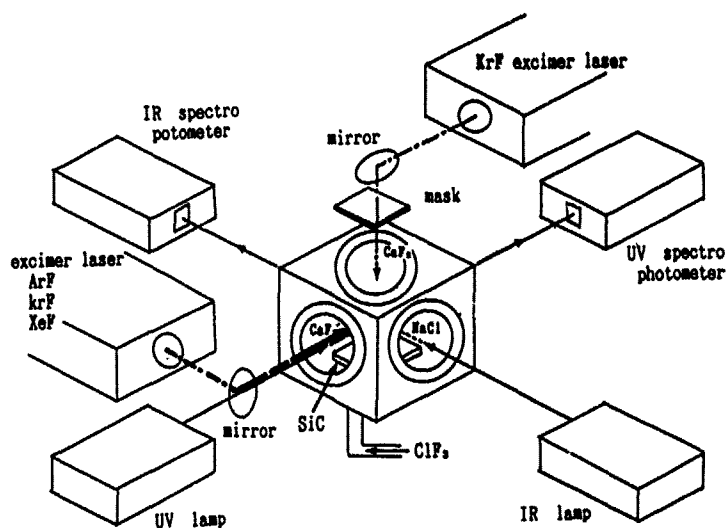


Fig.3 Measurement of the intermediate product on the etching gas by UV and IR spectroscopy.

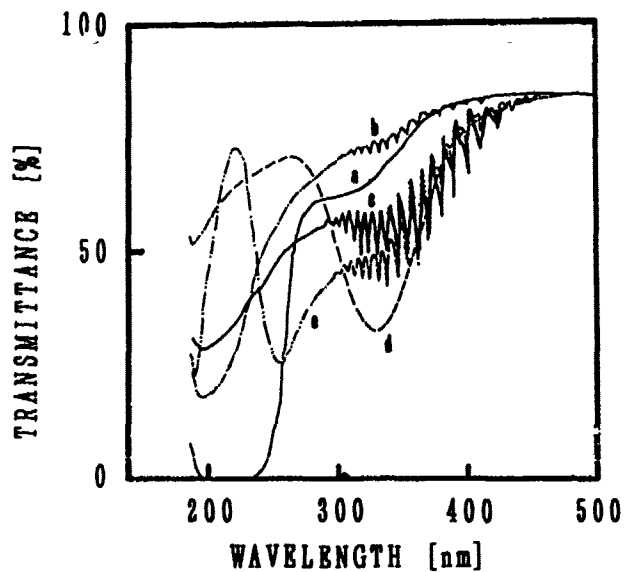


Fig.4 UV transmittance of gaseous ClF_3 and intermediate products
a: ClF_3 without laser irradiation
b, c: Intermediate products with XeF laser irradiation
d: Final products with XeF laser irradiation
e: intermediate products with ArF laser irradiation

produce halogen radicals, and at the same time, amorphous SiC surface in a chamber was excited by KrF laser beam. By the combined effect of these two laser beams, the CH radicals isolated from amorphous SiC surface reacts with halogen radicals, and exhibit particular absorption spectra of 300 to 430 nm as shown in Fig.4.b,c. When we kept on irradiating with the XeF laser, the intermediate products which have high absorption are decomposed as shown in Fig.4.d. When ClF_3 gas is excited by ArF laser beam, stable radicals of CF_2 is produced around 250 nm as in Fig.4.e, and these radicals absorb the KrF laser beam which is used to excite the SiC substrate. This phenomena also reduces the etching efficiency. As discussed above, the effect of the photo reactions must be consider the intermediate product. Therefore, when we make the etching gas to flow, XeF, KrF, and ArF lasers beam can be used for excitation of etching gas.

Experimental set up

When we fabricate SiC diffraction grating, the substrate surface must be polished like a mirror. Then, we polished amorphous SiC, which is deposited on a stainless steel substrate by plasma CVD method, and a crystalline SiC which is grown on a graphite substrate by thermal CVD, and measured their reflection coefficients. The results are given in Fig.1. According to this experiment, the reflection coefficient of amorphous SiC (Fig.1.a) was uniformly 40% in the range from 200 to 400 nm, while the value of crystalline SiC increased at shorter wavelength, and 50% with ArF laser of 193 nm.

Next the ClF_3 gas was kept flowing, and irradiated on the amorphous and crystalline SiC surfaces with KrF and ArF lasers, for all combinations. When the sample is amorphous SiC, the etching rate is the same for ArF and KrF laser, and the threshold fluence for etching was 200 mJ/cm^2 . When crystalline SiC was used, the threshold fluence was 7 J/cm^2 by ArF laser, but it was 800 mJ/cm^2 by KrF laser of 249 nm. This result was brought about by the fact that, as in Fig.1, the coefficient of SiC by 20% at 193 nm and 249 nm. Therefore, we can conclude that either ArF or KrF lasers can be used for etching of crystalline SiC.

On the other hand, any of XeF, KrF, or ArF laser can be used for photodecomposition of ClF_3 . As the incident laser beam is wasted for decomposition of the intermediate product when the gas is contained. We conducted experiments by keeping ClF_3 gas flowing. The experiments were conducted by using one KrF laser, because when two lasers, one for SiC substrate excitation and another for ClF_3 gas excitation, are used, it is difficult to control the excitation, timing, and it is more expensive, although two lasers would provide higher etching efficiency. Then we applied KrF laser beams to SiC substrate in an atmosphere of ClF_3 as in Fig. 5. The divided two polarized KrF laser beams were interfered on the substrate, it was used to locally excited the substrate[2] and the both of KrF laser beams were used to photodissociate ClF_3 gas in the proximity of substrate.

Results

The amorphous and single crystalline SiC substrate were

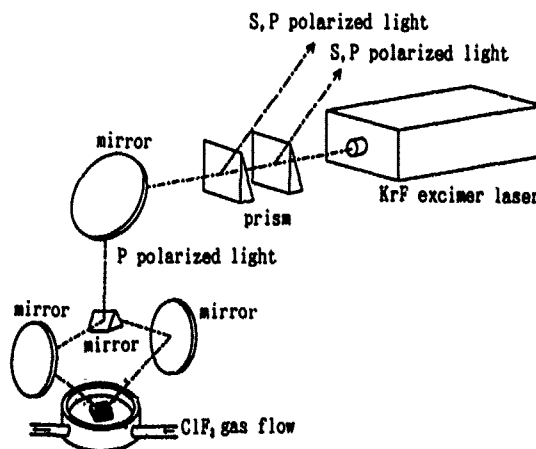


Fig.5 Schematic diagram of the exposure system for laser holography.

used as specimens. The amorphous SiC was deposited on stainless substrate by plasma chemical vapor deposition and film thickness was $4\mu\text{m}$. And the crystalline SiC was created on graphite substrate by thermal CVD, and film thickness was $100\mu\text{m}$. And KrF laser fluence which was irradiated on the amorphous SiC was 250 mJ/cm^2 . On the other hand, the fluence of the laser irradiation on the single crystalline SiC was 1 J/cm^2 at wavelength of 249 nm .

The photo etched pattern is shown in Fig.6. The line and space on amorphous SiC were 7170 \AA , etching depth 1000 \AA , and etching rate 5 \AA/pulse . And the line width of the crystalline SiC were $10\mu\text{m}$, etching depth 1000 \AA , and etching rate 1 \AA/pulse .

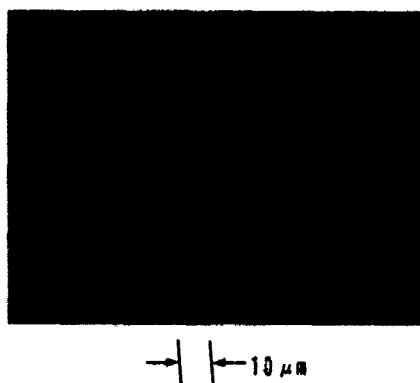


Fig.6. Photograph of the holographic grating taken by the optical microscope. Line and space period is 7170 \AA .

Discussion

The flow chart of the photo chemical reaction is given in Fig. 7. The Si and C atoms, released from SiC by photo dissociation of KrF laser, promptly react with F radicals which are released from ClF_3 gas by KrF laser beam. As F has higher electronegativity than Cl in general, the bond energy of C-F is 128 Kcal/mol, that of C-Cl 95, Si-F 129, and Si-Cl 107. For this reason, it can be assumed that Si-C is converted to SiF and CF_4 . The temperature at which the vapor pressure of SiF becomes 200 Torr is -107.2°C , while this value for ClF_3 is -143.6°C . Therefore, chemical compounds are evaporated without substrate heating, thereby making it possible to create etching patterns of high contrast.

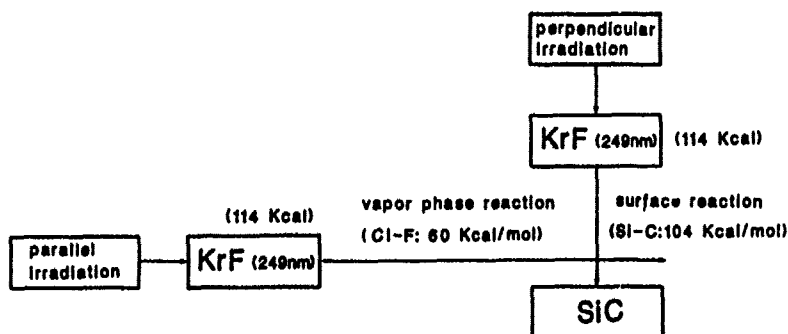


Fig.7. Flow chart of the photo etching process for SiC by vapor phase and surface reactions

Conclusion

To summarize the above discussion, this photochemical reaction is created by the cumulative effect of surface reaction and gas phase reaction caused by laser beams. And the effect of the photo chemical reaction must be considered the intermediate product. In this method, holographic resistless pattern etching of SiC was performed.

References

1. M.Murahara, T.Matsumura, H.Arai, M.R.S. 1988 Fall Meeting, B5-3, 56 (1988)
2. M.Murahara, C.L.E.O. '89, (Baltimore) Postdeadline papers PD-24, (1989)
3. D.E.Ibboston, J.A.Mucha, D.L.Flamm and J.M.Cook, J. Appl. Phys. 56(10) 2939 (1984)
4. D.E.Ibboston, J.A.Mucha, D.L.Flamm and J.M.Cook, Appl. Phys. Lett. 46(8), 794 (1985)
5. M.Murahara and K.Toyoda, Springer Series in Chemical Physics 39, 252 (1984)

CONTROL OF ETCHING IN LASER-CHEMICAL REACTION OF Mn-Zn FERRITE BY MeV ION IMPLANTATION

Y. F. LU, M. TAKAI, H. SANDA*, A. CHAYAHARA**, M. SATOU**, T. MINAMISONO***
AND S. NAMBA

Faculty of Engineering Science and Research Center for Extreme Materials,
Osaka University, Toyonaka, Osaka 560, Japan

*Sensor Device Laboratory, Central Research Institute, Glory Co. Ltd.,
Hyogo 670, Japan

**Government Industrial Research Institute Osaka, Ikeda, Osaka 563, Japan

***Faculty of Science, Osaka University, Toyonaka, Osaka 560, Japan

ABSTRACT

The change in the behavior of laser-induced etching of Mn-Zn ferrite by MeV ion implantation has been investigated. The etching induced by Ar⁺ laser irradiation in a H₃PO₄ solution was completely suppressed by implanting 3 MeV Au⁺ to a dose of 1×10^{16} cm⁻² when the laser induced local temperature rise was below the melting point of the ferrite. The etching suppression disappeared when the Au⁺ implanted sample was thermally annealed at 900 °C for 30 min. The suppression is found to be related to the crystallinity change induced by ion implantation.

INTRODUCTION

Single-crystalline ferrite is an important magnetic material which is widely used for magnetic head devices such as audio and video tape-recorders or floppy and hard disk drives. Increasing in recording capacity, requiring higher recording density of magnetic devices, could be simply satisfied by reducing the gap width of the magnetic head. Recently developed laser-induced processing provides an effective way to masklessly etch the ferrite with a high etching rate. In our previous studies, laser etching of Mn-Zn ferrite by focused Ar⁺-laser beam irradiation both in a CCl₄ gas atmosphere and in a H₃PO₄ solution was investigated [1-3]. High etching rate up to 340 μm/s has been achieved [2,3]. However, the width of the etched groove was limited by the focusing properties of the laser beam and it could not be easily reduced to a micron order or sub-micron like in the case of focused ion beam (FIB) processed grooves.

In this study, the etching properties of high-energy ion-implanted Mn-Zn ferrite by laser-induced chemical reaction have been investigated. The change in the etching property is expected to play an important role in the further research to obtain ultra-fine structures in a ferrite material when laser etching techniques are combined with FIB techniques. The purpose of using MeV ion implantation is to produce thicker and heavily disordered surface layer in order to obtain obvious change in the etching behavior.

EXPERIMENTAL

(100)-oriented single-crystalline Mn-Zn ferrite (MnO : ZnO : Fe₂O₃ = 31:17:52) samples were partly masked and implanted with 3 MeV Au⁺ ions, to a dose of 1×10^{16} cm⁻². The sample stage was water-cooled to avoid temperature rise during ion implantation.

The gold implanted samples were mounted on the bottom of an etching cell and, then, an etchant solution was added. The etching cell was fixed

on an electrically controlled X-Y-Z stage. A laser beam was scanned over the sample from unimplanted areas to implanted areas by moving the cell with a speed of $9 \mu\text{m/s}$. The 514.5 nm -line of an Ar^+ laser was focused by a convex lens, with a focal length of 40 mm , down to a spot diameter of about $13.2 \mu\text{m}$ (at $1/e$ intensity) on the sample surface. The distance from the sample surface to the etchant surface was adjusted to 2 mm . 85% phosphoric acid (H_3PO_4) solution was used as an etchant. Etched patterns were observed by scanning electron microscopy (SEM) and a stylus measurement (DEKTA) to obtain etched depth and width.

Distribution of the implanted ions was calculated by the TRIM (TRansport of Ions in Matter) code [4]. Total ion number and ion energy for simulation were 10^4 and 3 MeV , respectively. Surface lattice damage induced by ion implantation was also investigated by $2 \text{ MeV } ^4\text{He}^+$ RBS (Rutherford Backscattering) with ion channeling.

RESULTS AND DISCUSSION

Figure 1 shows the SEM top view of etched grooves across the unimplanted area on the left-hand side and the implanted area on the right-hand side with a laser power ranging from 66 mW to 266 mW and a scan speed of $9 \mu\text{m/s}$. When the laser power is equal to or below 86 mW , the implanted area remained unetched though the unimplanted area was etched and uniform grooves were fabricated. The laser-induced chemical etching was completely suppressed by high energy ion implantation. As the laser power increases, the depth and width of the etched grooves in the unimplanted surface increase. The implanted surface, however, still remains unetched until the laser power increases up to 133 mW . When the laser power exceeds a value of 133 mW , the etching on the implanted surface occurred. According to the relationship between the local temperature rise and incident laser power

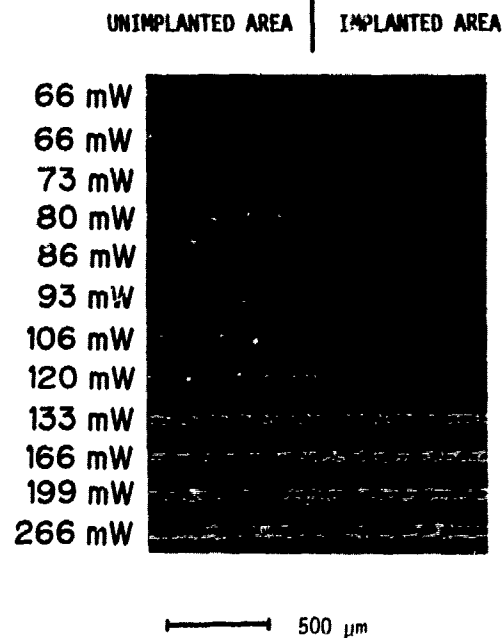


Fig.1. Etched grooves across unimplanted and implanted areas, with a laser power ranging from 66 mW to 266 mW , and a scan speed of $9 \mu\text{m/s}$

[1], the maximum local temperature rise due to a laser power of 133 mW is estimated to be 1600 °C, which is the melting point of the Mn-Zn ferrite. Ripple structures can be observed when the laser power is at and above 133 mW. It is known as the result of local melting [2]. The edges of the etched grooves near the boundary of implantation differ because of different scanning direction of laser beam.

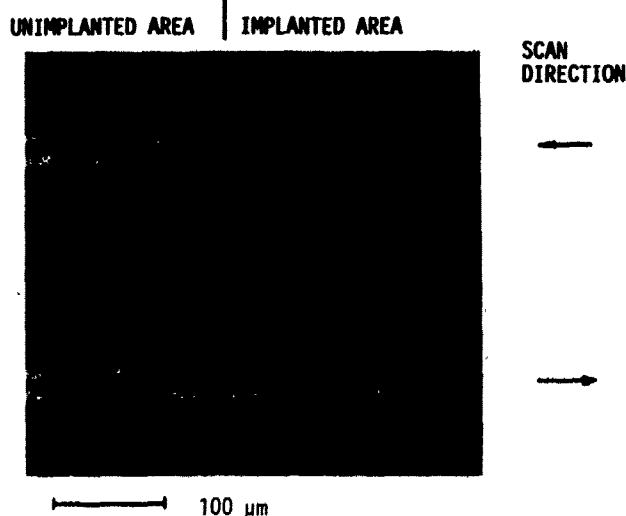


Fig.2. Etched grooves across the boundary of unimplanted and implanted areas with different scan directions under a condition: a laser power of 66 mW and a scan speed of 9 $\mu\text{m/s}$.

The etching behavior at the boundary of the unimplanted area and implanted area differs when the scan direction of the laser beam differs. Figure 2 shows the SEM top view of two etched grooves obtained by scanning laser beam from implanted to unimplanted area (upper line) and from unimplanted to implanted area (lower line), with a laser power of 66 mW and a scan speed of 9 $\mu\text{m/s}$. In the first case, the laser beam irradiation started at the implanted area. The etching reaction can not occur because of the modified surface layer by ion implantation. Etching only starts when the laser beam reached the unimplanted area on the left-hand side. In the second case, laser induced etching occurred in the unimplanted area, but the etching did not stopped immediately when the laser beam reached the implanted boundary, and it continued into the implanted area and stopped at a point with a distance more than 100 μm from the boundary. This phenomenon is considered to be the result of different exposure condition of the modified surface layer in the etching process. When the laser beam scans from the left to the right and reached the implantation boundary, the etching reaction still continues because the thickness of modified layer is very thin compared with the groove depth. The surface continues to be etched under laser irradiation in this case.

Figure 3 shows the etched depth and width in unimplanted areas as a function of laser power ranging from 40 mW to 160 mW. The etched depth increases linearly with laser power from 40 mW to 132 mW. This suggests that the etching reaction in this power region might be a photochemical process. In order to verify this point, laser etching with irradiation parallel to the sample surface was also performed in H_3PO_4 . An Etched groove with a depth of 1.2 μm was formed by a laser power of 10 mW within 30 min. Further increase in laser power above 133 mW gives rise to the dramatic increase in etching rate due to surface melting. Although photo-

chemical enhancement in decomposition reaction is not yet clear, the decomposition reaction under laser irradiation is considered as follows:
 $6\text{H}_3\text{PO}_4 + (\text{Fe}_2\text{O}_3 + 3\text{MnO} + 3\text{ZnO}) \rightarrow 2\text{FePO}_4 + \text{Mn}_3(\text{PO}_4)_2 + \text{Zn}_3(\text{PO}_4)_2 + 9\text{H}_2\text{O}$

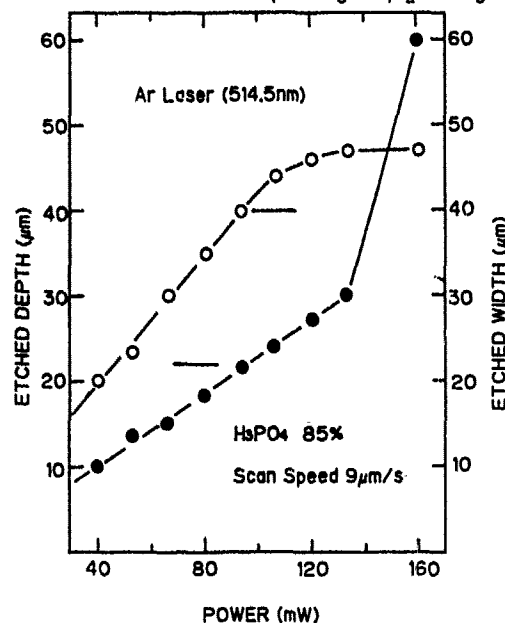


Fig.3. Etched depth (solid circle) and width (open circle) in unimplanted area as a function of incident laser power ranging from 40 mW to 160 mW.

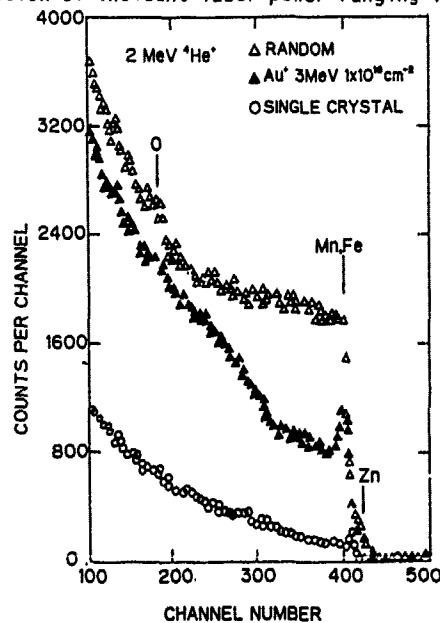


Fig.4. Aligned and random BBS spectra for a sample implanted with 3 MeV Au⁺ to a dose of 1x10¹⁶ cm⁻². An aligned spectrum for a virgin ferrite is also shown for comparison.

Thus, the etching reaction induced by laser can be totally suppressed by high energy implantation, which would provide ultra-fine structures with high aspect-ratio when the laser etching process is combined with focused ion implantation.

In order to study the mechanism of the etching-suppression by ion implantation, the change in surface reflectivity was measured before and after ion implantation. The reflectivity decreased to a value of 15.2% from its original value of 19.2%. Therefore, the etching suppression can not be explained by the surface reflectivity change due to ion implantation as in the case of laser-induced etching of amorphous Silicon [5].

The surface lattice damage induced by ion implantation was also investigated by 2 MeV $^4\text{He}^+$ RBS with ion channeling. The channel-to-depth conversion factor was 50.6 angstrom per channel [6]. Figure 4 shows the aligned (solid triangle) and random (open triangle) spectrum for the sample implanted with 3 MeV Au^+ to a dose of $1 \times 10^{16} \text{ cm}^{-2}$. The aligned spectrum for single-crystalline ferrite (open circle) is also shown for comparison. The dechanneling rate of the Au^+ implanted surface is much higher than that of the virgin surface. The lattice of the surface layer was heavily damaged by ion implantation. The minimum scattering yield obtained behind the surface peak is 44.3%, which is almost the same as the value of the mechanically polished surface (44.4%) [6]. Results of the TRIM calculation indicate that the projected range for 3 MeV Au^+ in ferrite is about $0.4 \mu\text{m}$ with a standard deviation near $0.09 \mu\text{m}$.

For investigating the relationship between the behavior of the laser-induced etching and the crystallinity of the implanted surface, the 3 MeV Au^+ implanted samples were thermally annealed at 900°C for 30 min before laser etching. Figure 5 shows the SEM top view of the grooves in the thermally annealed sample across the unimplanted and implanted regions with

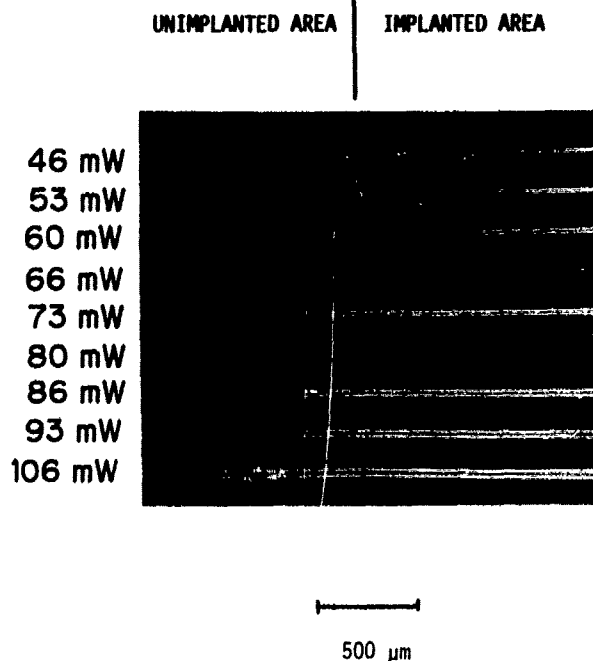


Fig.5. Etched grooves across unimplanted and implanted areas after thermal annealing at 900°C for 30 min, with a laser power ranging from 46 mW to 106 mW, and a scan speed of $9 \mu\text{m/s}$.

a laser power ranging from 46 mW to 106 mW and a scan speed of 9 $\mu\text{m/s}$. In this region of laser power, etching suppression in the implanted area disappeared after thermal annealing. Smooth grooves were fabricated with the same width and depth between two regions. From the results of our previous study [6], it is known that the lattice damages induced by both ion implantation and mechanical polishing can be completely recovered by thermal annealing at 900 °C for 30 min. From this fact, it is suggested that the laser etching-suppression after ion implantation is related to the lattice damages, which also suppress electrochemical reaction between the ferrite surface and etchant.

Further investigation of etching-suppression by focused heavy ion implantation at MeV range is now in progress.

CONCLUSIONS

The etching induced by Ar^+ laser irradiation in H_3PO_4 solution could be completely suppressed by implanting 3 MeV Au^+ to a dose of $1 \times 10^{16} \text{ cm}^{-2}$ when the laser induced local temperature rise was below the melting point of the ferrite. The etching suppression disappeared when the Au^+ implanted sample was thermally annealed at 900 °C for 30 min. The suppression was found to be related to the crystallinity change induced by ion implantation.

ACKNOWLEDGMENTS

The authors are indebted to M. Matsuzawa, M. Shimizu, F. Takeya, and H. Sandaiji of NGK Insulators Co. Ltd. for their supplying single-crystalline ferrite samples. The authors would also like to thank K. Mino, and K. Kawasaki for their technical assistance through this study.

REFERENCES

1. M.Takai, Y.F.Lu, T.Koizumi, S.Nagatomo, and S.Namba: Appl. Phys., **A46**, 197(1988)
2. Y.F.Lu, M.Takai, S.Nagatomo, and S.Namba: Appl. Phys., **A47**, 319(1988)
3. Y.F.Lu, M.Takai, S.Nagatomo, T.Minamisono, and S.Namba: Japan J. Appl. Phys. **28**, 2151(1989)
4. J.F.Ziegler, J.P.Biersack, and U.Littmark, The Stopping and Range of Ions in Solids, Vol. 1, (Pergamon, New York, 1985) p.202
5. E.F.Krimmel, A.G.K.Lutsch, R.Swanepoel, and J.Brink: Appl. Phys., **A38**, 109(1985)
6. M.Takai, H.Rysel, Y.F.Lu, T.Minamisono, and S.Namba: Nucl. Instrum. & methods, **B39**, 728(1989)

X-RAY PHOTOEMISSION INVESTIGATION OF EXCIMER LASER INDUCED ETCHING OF InP

R. MATZ*, J. MEILER* AND D. HAARER**

* Siemens AG, Corporate Research and Development, Otto-Hahn-Ring 6,
D-8000 München 83, FRG** Universität Bayreuth, Lehrstuhl für Experimentalphysik IV, Postfach 101251,
D-8580 Bayreuth, FRG

ABSTRACT

ArF excimer laser induced etching of InP in various etch gases (HBr, HCl, Cl_2) is discussed with regard to its spatial resolution capability. X-ray photoemission spectra and large-area etch rate measurements published before lead to fundamental understanding and interpretation of the characteristics of etched test structures. HBr and HCl require gas phase photodissociation. Cl_2 , in contrast, has the advantage to react spontaneously.

INTRODUCTION

Laser induced etching of semiconductors has attracted substantial and increasing interest over the past few years [1]. An especially promising and flexible application is pattern transfer etching by optical projection of a reticle onto an unpatterned wafer surface in a processing chamber filled with a suitable etch gas. An assumption frequently found in literature has been that optimum results are expected when the gas has minimum spontaneous reactivity or etch rate in the dark. Because of its high bond energy of 3.8 eV and efficient photodissociation by ArF excimer laser light, etching with HBr was considered ideal and has been extensively studied on GaAs [2]. We recently described the large-area etch rates, which can be induced by an ArF laser on InP in HBr and HCl [3]. New XPS results and etched test structures have stimulated now further-reaching concepts. We discuss them here under the aspect of the spatial resolution capability of the process and show finally that, in contrast to the frequent assumption, spontaneously reacting etch gases like Cl_2 may be more promising than the hydrogen halides.

EXPERIMENTAL

The bakeable ultrahigh vacuum system used and described before [3] comprises an etching chamber with sample introduction and XPS analysis chamber. The temperature of the resistively heated sample can be controlled during etching with a calibrated pyrometer. For simple gas exposure studies, given in units of 1 Langmuir = $1\text{L} = 10^{-6}$ Torr-s, the gases were introduced through leak valves. Patterned, laser induced etching of n-doped (100)InP wafers was achieved by optical projection of a stainless steel mask with an ArF excimer laser (193 nm, 6.4 eV, 150 mJ/pulse, 1-80 Hz rep. rate) through a suprasil lens doublet onto the wafer surface (image ratio 1:4). For this case, the gas inlet was recently changed to obtain better window protection. Mass flow controllers and a 200 μm inner diameter stainless steel nozzle directed under 30° at the sample surface and ending 3mm in front of it are now in use. A typical flow rate of 50-100 sccm yields an effective HBr pressure in front of the sample of 0.35-0.7 mbar while a turbopump keeps the background pressure in the 10^{-3} mbar range. The effective pressures in front of the sample were determined experimentally from the dependence of the etch rate on the background pressure (varied by the pumping speed). They agree with the theory for gas effusion from small apertures [4]. Etched profiles were analyzed with a stylus profilometer, light microscope and scanning electron microscope (SEM).

RESULTS AND DISCUSSION

We first describe etching by the hydrogen halide gases before we conclude the section with XPS results on the interaction of Cl_2 with InP . As long as HCl and HBr behave similar it will be sufficient to consider only HBr in order to demonstrate the main features and implications for photolithography.

First of all it is important to distinguish between normal and grazing incidence of the laser light since the P is removed from the top monolayer in a single pulse when a fluence above the melting threshold of 120 mJ/cm^2 is incident on the sample surface [3]. XPS spectra after exposure to 9000 pulses of 200 mJ/cm^2 (Fig.1(a)) clearly reveal the metallic indium accumulation. XPS spectra after only a few laser pulses show that the amount of metallic In formed per pulse just above the threshold is near the detection limit of about 1% of a monolayer and that it increases exponentially with laser fluence. When a stoichiometric or a P-depleted surface are exposed to HBr (e.g. 10^6 L in spectra (b) and (c), respectively) the only observable change is the growth of a bromine signal which we assign to adsorbed HBr . The absence of a spontaneous chemical reaction is in agreement with the expected stability of the HBr molecule [2] (high bond energy of 3.8 eV [5] and short bond length of 0.14 nm [6]). Only photodissociation of the gas, as realized for spectrum (d) by grazing incidence of additional 300 pulses (60 mJ/cm^2) in 0.2 mbar HBr , leads to a chemical reaction in which InBr_3 is formed. A bulk reference sample was used for peak assignment. Probably due to their higher vapor pressures, phosphorus compounds are not present.

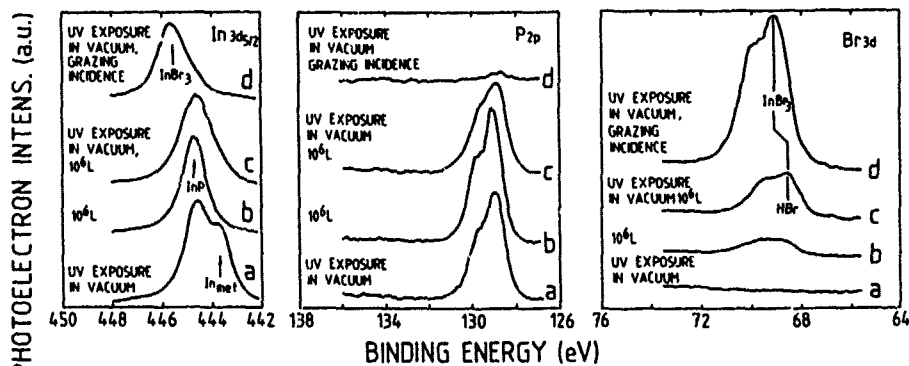


Fig.1. In, P and Br XPS spectra from (100)InP after laser irradiation, 9000 pulses, 200 mJ/cm^2 (a); exposure to HBr , 10^6 L (b); laser irradiation with subsequent exposure to HBr (c) and finally laser irradiation with subsequent exposure to photodissociated HBr (d) (from bottom to top).

For a continuous etch process, also the most stable product, the InBr_3 , must be removed from the surface. Its thermal stability was therefore studied by XPS. The initial InBr_3 spectrum shown in Fig.2 was obtained after grazing incidence of 1000 laser pulses (60 mJ/cm^2) at room temperature in 0.2 mbar HBr . Successive annealing for 1 min at the temperatures indicated causes evaporation so that finally at 140°C only little InBr_3 is left. The behavior is consistent with the vapor pressure curve of InBr_3 (10^{-2} mbar at 140°C [7]). Hence, the reaction products are either desorbed spontaneously at elevated substrate temperature or by the next laser heat pulse.

The large-area etch rate, as described previously [3], was found to be determined by: (i) Diffusive mass transport of photogenerated halogen atoms through the etch gas, (ii) the thermally activated reaction between adsorbed halogen and substrate and (iii) the presence of defect or reaction sites, which

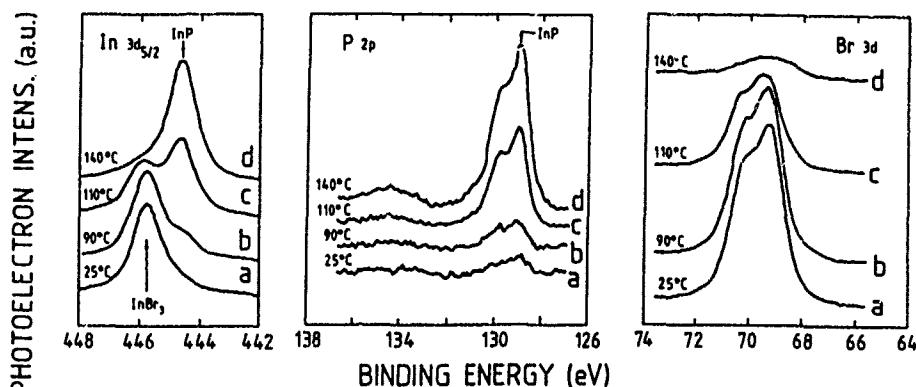


Fig.2. In, P and Br XPS spectra from (100)InP after growth of a thick InBr_3 layer (prepared according to text) and after annealing for 1min at 90°C, 110°C and 140°C (from bottom to top). Almost complete desorption of the layer and restoration of the substrate signals are evident from the 140°C-spectra.

are left on the surface after transient melting. Here we summarize these results in the phenomenological etch rate equation (etched depth per pulse)

$$R_{\text{kin}} = (0.1\text{nm}) \cdot \Theta(\Phi(x), p, f) \cdot k_0(\Phi(x)) \cdot \exp(-E/kT), \quad (1)$$

where Θ means the coverage of Br atoms in fractions of a monolayer ($6 \times 10^{14} \text{ cm}^{-2}$), which can be accumulated between two laser pulses, $\Phi(x)$ the patterned laser fluence, p the gas pressure, f the pulse repetition rate, k_0 a fluence-dependent pre-exponential factor describing the required presence of reaction sites on the surface, E the activation energy and T the substrate temperature. The normalization factor 0.1 nm is used in (1) because

$$R_{\text{diff}} = (0.1\text{nm}) \cdot \Theta(\Phi(x), p, f) \quad (2)$$

represents the maximum diffusion-limited etch rate to be expected at higher temperatures when the P has already been removed by the laser pulse and when every adsorbed Br reacts to InBr_3 . At temperatures below $E/k \cdot \ln(k_0)$, the term $k_0 \exp(-E/kT)$ can be interpreted as the reaction probability in the kinetically limited reaction according to (1). For higher temperatures, Equ. (2) is valid. The measured activation energy E is 0.26eV for HBr and 0.18eV for HCl. Since Θ can be calculated from gas phase diffusion theory and R_{kin} is experimentally determined [3], k_0 can be estimated from (1). For HBr we obtain $k_0 \approx 65$ on a surface exposed to a fluence of 160 mJ/cm^2 with the data of ref.[3] ($\Theta \approx 30$ with $f \approx 30 \text{ Hz}$ and a diffusion coefficient of 120 cm^2/s at 0.75 mbar, $R_{\text{kin}} = 6 \times 10^{-3} \text{ nm}$ at 300 K), i.e. the transition temperature between kinetic and diffusion limit is around 450°C. Since InP begins to decompose at these temperatures, only the kinetically limited reaction (1) is of practical interest here.

An illustrative demonstration for pattern transfer etching under conditions of Equ.(1) (sample heated, normal illumination) is given in Fig.3. Stationary conditions, i.e. no gas flow, were employed; the buffer gas H_2 served to reduce the mean free path. The lack of edge definition, the Gaussian-shaped trench profile and an etch depth decreasing with feature size are typical. The process is attractive for its high etch rate (0.5 $\mu\text{m/min}$, 0.23 nm/pulse) but is useful only for large-area applications or patterned surfaces. The behavior can be completely changed by reducing the substrate temperature. Fig 4 shows an example. The original mask is not only well reproduced but etched areas also

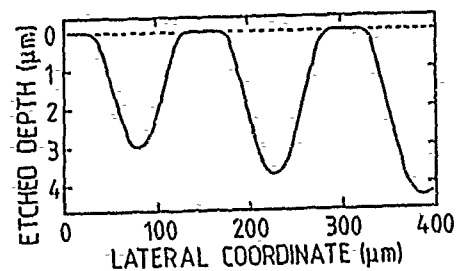
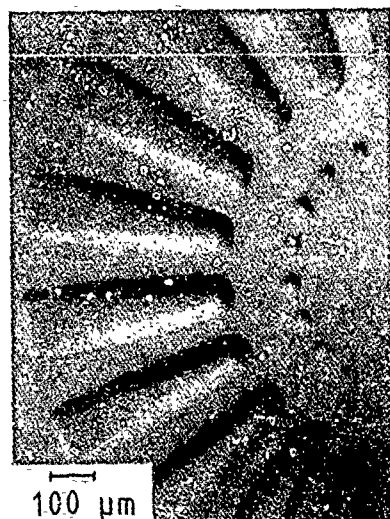


Fig. 3. Photograph and profile of test pattern etched into (100)InP at 200°C (diffusion-dependent); 0.25mbar HBr, 4.75mbar H_2 (buffer), 120mJ/cm² fluence, 36Hz repetition rate, 8min processing time.

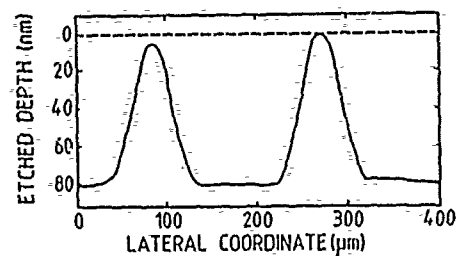
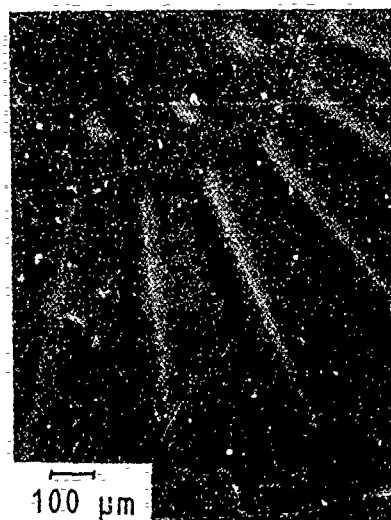


Fig. 4. Photograph and profile of test pattern etched into (100)InP at room temperature (surface-limited reaction); 30sccm HBr, 20sccm H_2 (window purge), 150sccm Ar (buffer), 1.2mbar background pressure, 120mJ/cm² fluence, 25Hz repetition rate, 2min processing time.

exhibit a smooth planar surface morphology. Edges are well defined down to a 10 μ m scale. However, the improved reticle reproduction is traded against a small etch rate (0.05 μ m/min, 0.03 nm/pulse).

Interpretation of these results is straightforward when the XPS spectra and Equ.(1) are considered. Above the desorption temperature of the indium halide, i.e. above approximately 150°C, etching is not hindered by a passivating film. This is also expressed by Equ.(1). Accordingly, the spatial information of Fig.3 can be contained only in the product $\Theta \cdot k_0$. But due to gas phase diffusion, the Br coverage $\Theta(x)$ is a smooth function. The diffusion coefficient of Br in 5 mbar H_2 , for example, is $D = 140 \text{ cm}^2/\text{s}$ [8] yielding a diffusion length $\sqrt{Dt} = 2 \text{ cm}$ for $t = 36 \text{ Hz}$. Therefore, gas phase photochemistry alone cannot explain the resolution of 100 μ m features in Fig.3. Contrarily, the second term $k_0(\Phi(x))$ is surface-specific because it describes the reaction probability of the halogen on a surface which was exposed to a laser fluence Φ . Therefore, the pattern in

Fig.3 probably reflects the spatial variation of the product $\Theta \cdot k_0$. When the lateral dimensions of an etched structure shrink below the diffusion length, increasingly more halogen is lost by lateral gas diffusion into unexposed regions so that the etch rate decreases with feature size. Unexposed portions of the surface, on the other hand, are much less reactive and etching is negligible there despite the presence of Br [3].

At room temperature, the indium halide is not volatile which explains the characteristics of Fig.4. Reactive sites on the surface become occupied and saturated when a sufficient amount of Br adsorbs. The reaction will be limited then by their coverage Θ^* . When they are identical with phosphorus vacancies, for example, removal of the associated In atom would yield a maximum etch rate

$$R_{\text{surf}} = (0.3\text{nm}) \cdot \Theta^* (\Phi(x)), \quad (3)$$

so that we have to distinguish now two temperature ranges

$$R = \begin{cases} \text{Min}\{R_{\text{kin}}, R_{\text{surf}}\} & \text{for } T < 150^\circ\text{C} \\ \text{Min}\{R_{\text{kin}}, R_{\text{diff}}\} & \text{for } T > 150^\circ\text{C} \end{cases} \quad (4)$$

where the function Min selects the smaller of the two arguments. The pattern of Fig.4 was etched with a laser fluence just above the threshold for P depletion so that Θ^* was small. According to (4), the etch rate is then limited by an expression like (3). Laser fluence Φ and etch rate are constant within the exposed areas. The edge definition is limited by the spherical lens aberration which was estimated with a ray tracing software. Hence, it turns out that two factors play an important role in the present hydrogen halide etch process: The distribution of gas phase reactants (determined by diffusion) and the distribution of surface reactants (representing a latent image of the reticle). The contribution of diffusion could be eliminated only by reducing temperature and etch rate.

We therefore suggest finally to choose a spontaneously reacting, nonabsorbing gas, so that the laser is required only for patterned removal of the corroded layer. This approach promises both high resolution and high etch rate. Fig.5, showing the growth of an InCl_3 corrosion layer on InP with increasing Cl_2 dose, identifies Cl_2 as a promising candidate in this respect. The steep

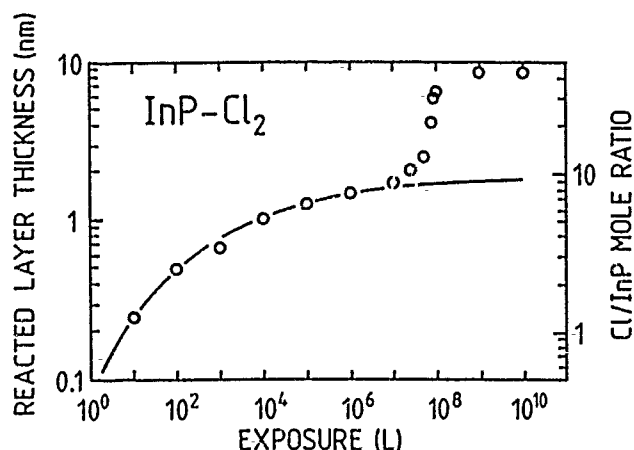


Fig.5. Spontaneous growth of InCl_3 on $(100)\text{InP}$ with increasing Cl_2 exposure. The layer thickness is derived from Cl and In (substrate and layer) XPS signals.

increase in Cl uptake at 10^4 L may be due to a structural change in the layer. Using the known density of the halide, the layer thickness can be converted into chlorine coverage which in turn yields the mole ratio, the number of chlorine atoms per surface InP molecule. According to thermodynamics [9], Cl reacts first with In to form InCl_3 (mole ratio 3 at 10^4 L) and then with P to form PCl_5 (mole ratio 3+5=8 at 10^4 L). Depending on whether the P has already been removed by the laser pulse or not, a dose of 10^{-3} Torr-s or 1Torr-s is necessary to etch the topmost atomic layer (0.3nm/pulse). We therefore expect an etch rate of 0.2 $\mu\text{m}/\text{min}$ at a repetition rate of 10Hz in a Cl atmosphere of 10^{-3} mbar, when the fluence is sufficiently above 120mJ/cm²; for lower fluences (30-120mJ/cm²) the P has to be removed chemically, so that a higher pressure of several mbar would be required to reproduce the conditions of Fig.5, i.e. formation of InCl_3 and PCl_5 which are then laser-evaporated. The achievable spatial resolution will be determined by the InP thermal conductivity (0.5-1 μm edge definition).

Similar values for etch rate and resolution have been mentioned for the Cl_2 process already in ref.[1], but in contrast to the present photothermal concept, the process there was understood in terms of gas phase photolysis. On the other hand, also photothermal etching with Cl_2 has been demonstrated in a direct-write experiment [10] with a cw laser, where spatial resolution is considerably reduced by thermal conductivity.

CONCLUSIONS

(i) For laser induced pattern transfer etching to InP, we found photoexcitation of hydrogen halide etch gases, although frequently studied, less desirable since either the spatial resolution is limited, when the process is efficient and diffusion-determined, or the etch rate is small, when the reaction is limited by the extent of the photoinduced surface modification.

(ii) Spontaneously reacting gases, as which Cl_2 was identified here on InP, promise a bundle of more desirable process features like (i) absence of lateral gas diffusion, (ii) high etch rate, (iii) low processing temperature, (iv) low laser fluence and (v) free selection of laser wavelength for meeting UV-optical requirements.

ACKNOWLEDGEMENT

This work was supported by the Federal Department of Research and Technology of the FRG. The authors alone are responsible for the contents. We wish to gratefully acknowledge fruitful discussions with H. Büttner and U. Wolff.

1. M. Rothschild and D. J. Ehrlich, J. Vac. Sci. Technol. **B6**, 1 (1988).
2. P. D. Brewer, D. McClure, and R. M. Osgood, Jr., Appl. Phys. Lett. **47**, 310 (1985).
3. J. Meiler, R. Matz, and D. Haarer, presented at the 1989 MRS Spring Meeting, Strasbourg, 1989 (to be published in Surface Science).
4. N. F. Ramsey, Molecular Beams (At The Clarendon Press, Oxford, 1956), p.11.
5. CRC Handbook of Chemistry and Physics, 61th ed. (CRC Press, Boca Raton, FL 1980), p.F-223.
6. H. R. Christen, Grundlagen der allgemeinen und anorganischen Chemie, 3rd ed. (Sauerländer, Aarau, 1968), p.91.
7. Gmelins Handbuch der anorganischen Chemie, Indium, 8th ed. (Verlag Chemie, Weinheim, 1936), p.88.
8. J. O. Hirschfelder, C. F. Curtiss, and R. B. Bird, Molecular Theory of Gases and Liquids (Wiley, New York, 1954), p.539.
9. S. C. McNevin, J. Vac. Sci. Technol. **B4**, 1216 (1986).
10. L. Ding, Q. Mingxin, and K. Zhong, J. Electronic Mat. **17**, 29 (1988).

SELECTIVE ETCHING AND PHOTO-BLEACHING IN THIN AMORPHOUS Ge-Sb-S FILMS

EVDOXIA B. SAVOVA AND B.I. PASHMAKOFF
Institute of solid state physics, 1784 Sofia,
72 Lenin blvd., Bulgaria

ABSTRACT

A mechanism is proposed for the selective etching effects in thin amorphous Ge-Sb-S films based on the combined action of photostructural changes and alkaline solvent with a surface active substance. Evidence is given in support of the assertion that the same photostructural changes (namely, the breaking of Ge-Sb bonds under the action of UV light) are responsible for the irreversible photo-bleaching of these layers.

Four different compositions in the system Ge-Sb-S have been studied under different preparation conditions (thermal evaporation and laser-beam sputtering). Photostructural changes were induced by UV light irradiation. Infrared spectra of the layers are presented in support of the proposed model.

INTRODUCTION

Ultraviolet light irradiation induces photostructural changes in most amorphous chalcogenide films which are manifested in a shift of the optical absorption edge [1] as well as in selective etching effects. These phenomena make it possible to use such films for optical memory media and photo-resist applications.

The goal of the present work is to give evidence in support of a common mechanism for the photostructural changes in thin amorphous Ge-Sb-S films which lead to the effects of irreversible photo-bleaching and selective etching. Within the proposed model, the effect of selective etching is explained as a result of the combined action of photo-structural changes and the presence of surface active substance (SAS) [2] in the solvent.

In this work we concentrate on the role of the photostructural changes, keeping both alkaline solution and SAS concentrations fixed in all selective etching experiments.

EXPERIMENTAL PROCEDURE

The films, 100 nm thick, were deposited by thermal vacuum evaporation or laser-beam sputtering onto glass substrates at room temperature. Bulk glasses of four different compositions in the system $\text{Ge}_x\text{Sb}_{40-x}\text{S}_{60}$ were used as source material. The glasses were prepared by melt-quenching the mixed high-purity elements, sealed in quartz ampoules and gradually heated up to 920°C in a rocking furnace [1]. The vacuum was $5 \cdot 10^{-5}$ torr and the deposition rate varied between 10-20 Å/s for the thermal evaporation procedure. A Nd-glass impulse laser was used for the laser-beam sputtering. Laser power was about 30 kW. Film thickness was measured in the course of evaporation with a quartz measuring device. The samples were exposed to UV light

from a HBO 500 mercury lamp for 5 min. CuSO_4 infrared filter was used to prevent the heating of the samples during exposure. Selective etching was measured by the time of dissolution of exposed (d') and unexposed (d) samples in alkaline solvent with or without the addition of surface active substance (SAS). Infrared transmission measurements were carried on 1400 nm thick layers, deposited on p-type Si substrates polished on both sides.

RESULTS AND DISCUSSION

Selective etching

The etching times of exposed and unexposed samples, immersed in alkaline solution of fixed concentration, with (curves 'a', 'b') or without (curves 'c', 'd') the addition of SAS, are plotted in Fig.1 versus the film composition. It can be seen that without the addition of SAS to the solvent, almost no selective etching effect is observed (the ratio of the etching times of unexposed/exposed samples is about 1). The addition of SAS to the solvent leads to a dramatic increase of the range of variation of the etching time ratio - from 1 to above 100. With the increase of the Ge content in the films, two distinct patterns of behaviour of the exposed and unexposed samples can be observed. The etching time of the exposed samples drops rapidly and for $x > 10$ it is below 10 min. The etching time of the unexposed samples has a ledge for $10 < x < 25$ and drops below 10 min for $x = 35$ or more. Thus, the region of the highest degree of selectivity is located (for the given solvent and SAS concentration) in the interval from $x = 15$ to $x = 25$. This can be clearly seen in Fig.2 where the etching time ratio of unexposed/exposed samples (d/d') is plotted versus the film composition - Fig.2 curve 'd'.

Optical transmission

As it was already mentioned, all $\text{Ge}_x\text{Sb}_{40-x}\text{S}_{60}$ layers showed irreversible photo-bleaching after exposure to UV light. The dependence of the optical transmission edge shift on the film composition is shown in Fig.2 curve 'e'. It is seen that the curve has similar behaviour and a maximum in the same range of compositions as curve 'd'. This fact suggests a common mechanism for both photo-induced phenomena. A structural interpretation of this mechanism based on infrared transmission measurements is given in the next section.

Infrared spectra

Infrared transmission spectra of films of five different compositions ($x = 5, 15, 20, 25, 35$) are shown in Fig.3a and b. There are two main features - around 370cm^{-1} and around 290cm^{-1} . The band at 370cm^{-1} is associated with a tetrahedral arrangement of four S atoms about a central Ge atom [3]. The band at 290cm^{-1} is associated with vibrations of pairs of atoms in Sb-S₃ pyra-

Fig.1 - Etching times of exposed (b,d) and unexposed (a,c) films, with (a,b) or without (c,d) SAS versus $\text{Ge}_{1-x}\text{Sb}_{40-x}\text{Se}_{60}$ film composition.

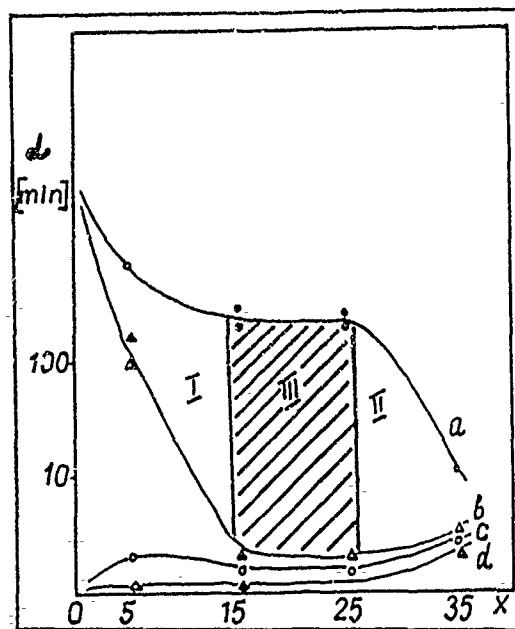
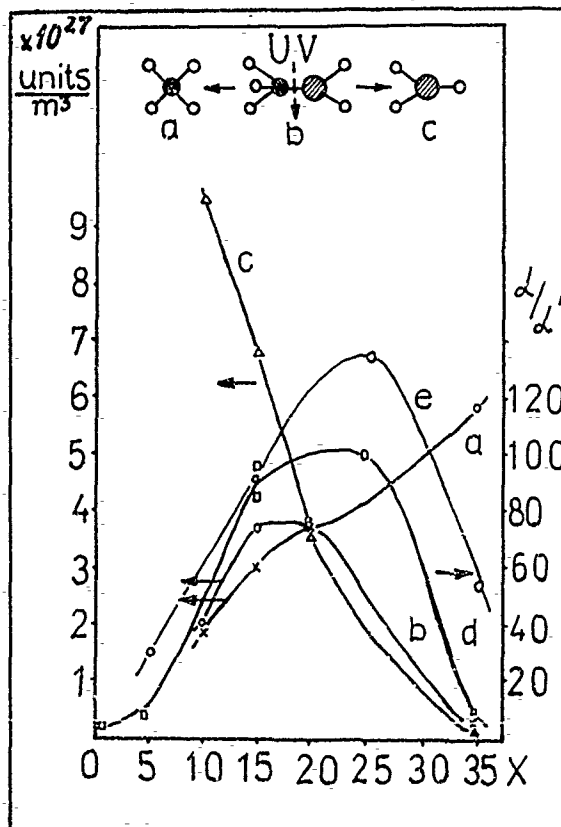


Fig.2 - Curves a,b,c - composition dependence of the concentration of respective units. Curve d - unexposed/exposed sample etching time ratio versus composition. Curve e - optical transmission edge shift versus composition (in a.u.)



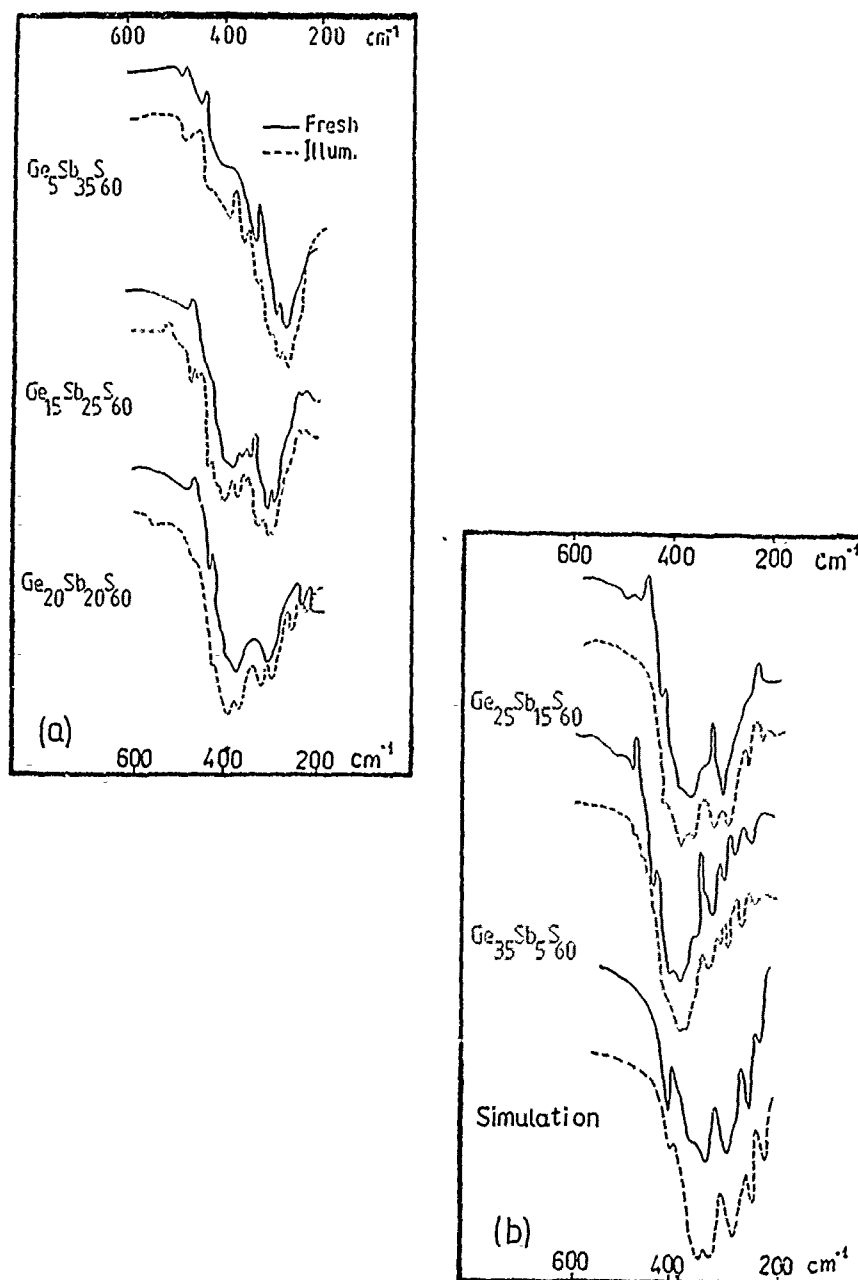


Fig.3 - Infrared transmission spectra of $\text{Ge}_x\text{Sb}_{10-x}\text{S}_{60}$ amorphous films. Spectra of exposed samples are given in dashed lines.

mids which form the basic and most stable structural unit of both crystalline and amorphous Sb_2S_3 thin films [4]. It is seen that both these bands scale well with the relative content of Ge and Sb in the ternary compositions.

The band at 250cm^{-1} is connected with Ge-centred tetrahedra with less than four S atoms [3], and the band at 220cm^{-1} is connected with Ge-S-Ge bonds [5,6].

The feature at 425cm^{-1} we connect with S atoms not-bonded to either Ge or Sb. The existence of such atoms can be explained by assuming the presence in the vacuum evaporated $\text{Ge}_x\text{Sb}_{10-x}\text{S}_{60}$ layers of Ge-Sb and Ge-Ge bonds. That is, if some of the S atoms in the Ge-S_4 tetrahedra are replaced by Ge (which gives the 250cm^{-1} band) or Sb (the minimum corresponding to the figure). Illumination with UV light breaks the weak Ge-Sb bonds and Ge-S bonds are formed which is evidenced by the weakening of the 425cm^{-1} band and the strengthening of the 370cm^{-1} and 220cm^{-1} bands.

A computer simulation of this process was attempted by a damped Lorentzian oscillator fit [7] to the spectra of GeS_2 and Sb_2S_3 thin films. Six oscillators were used to simulate the GeS_2 spectrum and three for the Sb_2S_3 thin film spectrum. Combining the spectra of the two compounds, we obtained the spectrum shown in the lower part of Fig.3b. The spectrum after exposition has been obtained by simulating the disappearance of the 425cm^{-1} minimum and increasing by a corresponding factor the strength of the 370cm^{-1} and 220cm^{-1} oscillators. It can be seen that the simulated spectra are in qualitative agreement with the spectra of unexposed and exposed $\text{Ge}_{20}\text{Sb}_{20}\text{S}_{60}$ films.

CONCLUSIONS

On the basis of the experimental results and model assumptions described in the previous section, we suggest a mechanism for the selective etching effect in Ge-Sb-S thin films based on the combined influence of photo-structural changes and the addition of SAS to the solvent.

We consider Ge-S_4 tetrahedra, Sb-S_3 pyramids and their combination through a Ge-Sb bond (Fig.2, upper part, units a, b, c) to be the predominant structural units in those layers [8]. Assuming complete randomness of bond distribution in the vacuum evaporated amorphous layers, the concentration of those units versus film composition is plotted in Fig.2 curves 'a', 'b' and 'c' for the respective units. Comparing curves 'b' and 'd' in Fig.2, it is seen that the region of maximum selectivity coincides with the maximum in the number of Ge-Sb bonds. At the same time, the number of GeS_4 tetrahedra scales in inverse proportion to the etching time of the unexposed samples (compare Fig.1 curve 'a' and Fig.2 curve 'a').

It is reasonable, therefore, to assume that GeS_4 tetrahedra are soluble in alkaline solution with or without the addition of SAS to it. That is why in the range of compositions with higher Ge content (region II in Fig.1), the etching process is not limited by diffusion. For this reason, in this composition range, the addition of SAS to the solvent has almost no effect on the etching rate both of the exposed and the unexposed samples.

The Sb-S_3 pyramids are soluble in alkaline solvent with-

out SAS, but become insoluble when SAS is added in suitable concentration. What SAS actually does is to impede the diffusion of the solvent molecules and to make the etching process diffusion limited.

In this way, the presence of both soluble and insoluble structural units in the amorphous Ge-Sb-S layers (in alkaline solution with SAS) makes it possible to change the etching rate at fixed solvent and SAS concentrations, by changing the relative content of those units. UV light induces such a change by breaking the Ge-Sb bonds and forming additional Ge-S₄ soluble structural units. The region of highest degree of selectivity (Fig.1 region III) is the region of compositions where the concentration of soluble structural units is low enough to make the etching process diffusion limited (for the given solution and SAS concentration) prior to exposure. In the same time, this is the region where the concentration of Ge-Sb bonds is high enough, so that UV light illumination creates sufficient number of additional soluble structural units to make the etching process not-limited by diffusion after exposure.

The proposed model for the photo-structural changes in amorphous Ge-Sb-S thin films explains on common grounds both the irreversible photo-bleaching and selective etching effects whose parallelism is proved by experiment. Getting a further insight into the kinetics of these processes will make it possible to develop a selective approach in determining the optimum film composition range, solvent and SAS concentration, in each practical situation.

REFERENCES

1. M. Frumar, H. Ticha, M. Vlcek, J. Klikorka, Czech. J. Phys. B 31, 441 (1981).
2. E. Vateva, M. Nickiphorova, E. Skordeva, Bulg. Patent No. 69799.
3. G. Lucovsky, F.L. Galeener, R.C. Keezer, R.H. Geils, H.A. Six, Phys. Rev. B 10, 5134 (1974).
4. Zacharov, Gerasimenko, Structura Amorfnich Poluprovodnikov, Kiev, 1976 (in Russian).
5. M.H. Brodsky, Amorphous Semiconductors, (New York, 1979), p. 288.
6. P. Tronc, M. Bensoussan, A. Brenac, Phys. Rev. B 8, 5947 (1973).
7. G. Lucovsky, J.P. deNeufville, F.L. Galeener, Phys. Rev. B 9, 1591 (1974).
8. L. Tichy, H. Ticha, M. Frumar, J. Klikorka, A. Triska, C. Barta, A. Nemeckova, Czech. J. Phys. B 32, 1363 (1982)

COPPER VAPOR LASER USED IN ETCHING AND DEPOSITION.

BELGACEM HABA, BRIAN W. HUSSEY, ARUNAVA GUPTA, AND ROBERT J. BASEMAN
IBM Thomas J. Watson Research Center Box 218, Yorktown Heights, New York 10598.

ABSTRACT

We have carried out experiments for etching manganese-zinc ferrite in aqueous KOH solution using a copper vapor laser. The high repetition rate (5-10 KHz), the high peak power (~ 250 KW), and the short pulse length (24-30 ns) result in rapid etching of grooves with high aspect ratios. The depth of the grooves increased with laser power and slower scan speeds while, the width was limited to the laser beam focus. The etching process is believed to be purely thermal in nature and limited only by the removal of the molten material out of the grooves.

The copper vapor laser was also used as a source for projection deposition of various metals on quartz substrate by a pyrolytic process. This system achieved patterns with fine feature sizes, good resolution, and metallic properties of the deposits. In this technique, both the spun-on organometallic films as well as LCVD were tried.

INTRODUCTION

In the last decade, laser processing of materials for device and packaging applications has been thoroughly explored, particularly the areas of deposition and etching. [1,2] There are primarily two modes of processing using the laser as a photochemical or photothermal source. In one approach the laser beam is focused down to a range of several microns which is then used for maskless deposition and etching of materials by direct writing. In the second approach, the laser beam is used in conjunction with a projection or contact mask for deposition and etching of patterned features. In both approaches, a number of processing steps related to conventional photolithographic processing are eliminated, thus simplifying the overall fabrication of devices and packages. In the first approach the writing speeds for deposition and etching are generally limited in the range of a few microns to a few hundred microns per second, making the processes too slow to be considered for any large area patterning applications. The second approach is, however, quite suitable to be scaled up for large area processing, as has been demonstrated, for example, in the case of via etching in polyimide by laser photoablation.

For projection deposition and etching, it is necessary to have a laser which can provide a uniform and high power density beam over a large area. For this reason, almost all the work which has been reported to date [3] using a projection source has been limited to using a pulsed laser with a relatively large beam size, like the excimer laser. While the excimer laser is ideally suited for etching of materials by rapid evaporation, or ablation, it is very difficult to use it for deposition or controlled chemical etching of materials. The reason for this is the difficulty in restricting the surface temperature rise to a range where deposition occurs but not ablation. To obtain a large area, uniform, high power density laser source for projection, the copper vapor laser is ideally suited.

We report the use of a copper vapor laser (CVL) for fast etching and for large area patterning of materials by projecting the beam through a mask. The copper vapor laser (wavelengths of 511 and 578 nm) provides a relatively large area beam (3-4 cm), with high average (30-40 W) and peak power (~ 250 kW), short pulse length (24-30 ns), and high repetition frequency (5-10 KHz). These characteristics make it well suited for patterned deposition and etching of materials using a projection mask. The temperature distribution produced on a substrate heated by a copper vapor laser oscillates between a high and low

temperature with each pulse, and the detailed modelling is described in another publication [4]. This is unlike a low repetition rate pulsed laser, such as the excimer laser, where the temperature on the substrate would drop back close to room temperature due to cooling in between pulses of low repetition rate.

EXPERIMENTAL

In the case of etching, the unstable resonator configuration of the CVL was used as the excitation source for the wet etching. The output was focused to a minimum spot size of 100 μm diameter using a combination doublet and meniscus lens. The sample (in this case Mn-Zn ferrite) was placed at the bottom of a sealed glass reservoir and kept flat to assure that the ferrite surface stayed in focus throughout the course of the scanning experiment. Aqueous KOH solution of variable concentration was circulated in the reservoir using a peristaltic pump. The procedure of introducing fresh influx of solution is used to dissolve the molten particles of ferrite as they leave the etched grooves which otherwise would saturate the solution and obstruct the laser beam path. The whole system (reservoir and ferrite sample) is mounted on a computer-driven X-Y stage.

In the case of projection patterning, the CVL optics were modified to use a stable resonator. The imaging was done by a combination of a 500 mm lens followed by a 25 mm air spaced triplet lens. In between the lenses we positioned the mask and a mechanical shutter. The projected image through the mask was reduced by a factor 10 to 30 depending only on the positions of both the mask and the 25 mm lens. Also, a gas cell was designed with optical port for use with various metallo-organic gases. This cell was mounted on a X-Y stage combined with a rotary stage to allow patterned deposition by a step and repeat process, and to allow for easy alignment. When spun-on films were used instead of the metallo-organic gases, toluene and chloroform were used to dissolve away the nonexposed regions leaving the developed features of the appropriate metal.

In the case of etching, the lens focal point was positioned with a telescope placed at 90 ° to the laser beam and on a level with the ferrite surface. In the case of pattern deposition, the same telescope was placed slightly off-axis to the laser beam, focused onto the image plane.

RESULTS AND DISCUSSIONS

As a first application of the CVL, etching was performed on many materials in different concentrations of aqueous solutions of KOH. We report the results on the Mn-Zn ferrite ($\text{MnO}:\text{ZnO}:\text{Fe}_2\text{O}_3 = 30:17:53$ mole per cent) etched in 8 molar solution. The ferrite was used here to compare with earlier work done with the argon ion laser. Figure 1 shows deeper grooves for lower scanning rates and for higher laser power. Within the experimental conditions, a maximum volume rate of removal of $10^{-5}\text{cm}^3/\text{sec}$ was achieved at a speed of 0.1 cm/sec. Contrary to the argon laser, where the grooves have a bell shape and depths increasing with widths, for the CVL, the width of the grooves is constant or only slightly increasing with higher laser power or lower scanning speed. In the case of the argon ion laser, the continuous laser source gives rise to an isotropic diffusion of heat in the sample, thus leaving a bell shaped groove [5]. However, in the case of the CVL a pulse with a high peak energy melts the ferrite and removes a layer of the material. When the pulse is off, the sample begins cooling off. When the second pulse arrives, it will strike the sample at a deeper level than that of the original surface of the ferrite, and more removal of material occurs and so on. As a result, the grooves etched by the CVL appear deeper and narrower with aspect ratios of ten or higher. A typical CVL etched groove is illustrated in Figure 2.

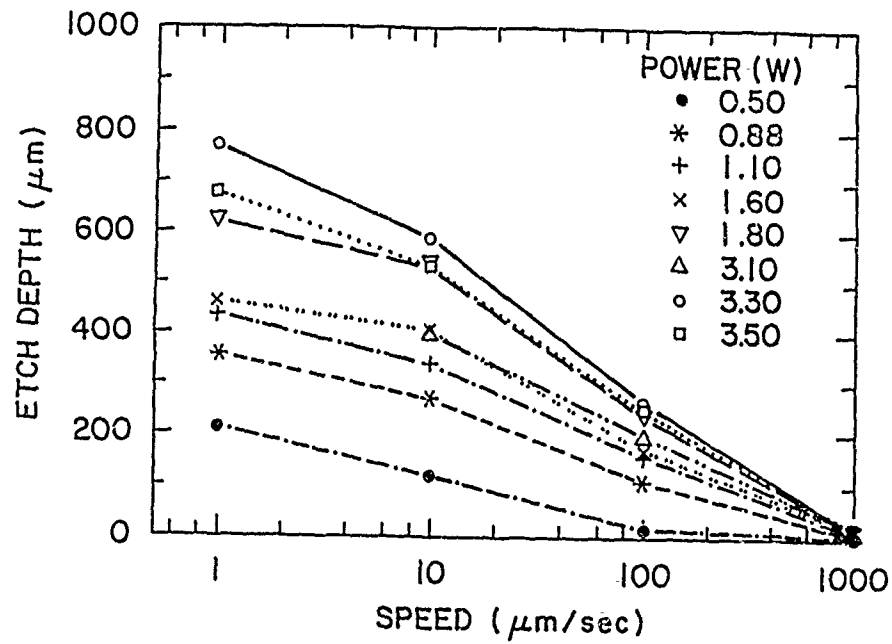


Fig. 1. Experimental data of the effect of laser power on groove depth-scan speed correlation.

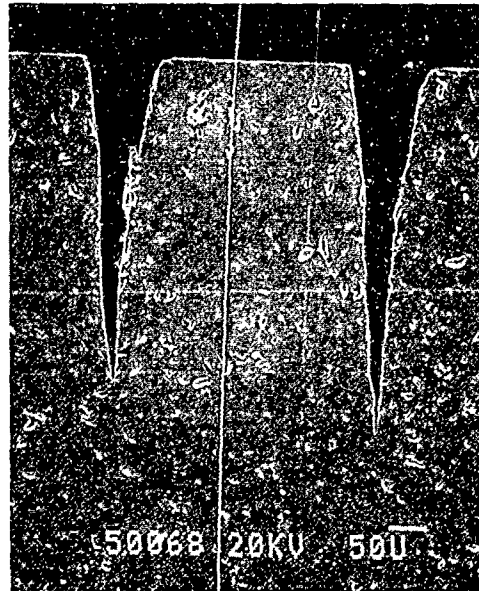


Fig. 2. SEM micrograph of an etched groove in Mn-Zn Ferrite material.

The laser-assisted deposition is believed to be purely pyrolytic and was tried both on spun-on films and from metallo-organic gas phase. Parameters (such as thickness, absorption, and heat diffusion of the spun-on films, laser fluence at the substrate, and the exposure time), were found to be extremely crucial for the deposition. In this report we give an overview of the feasibility of the CVL process, a more detailed and systematic work will follow.

Deposition from spun-on films was tried on quartz and sapphire substrates from precursors such as silver neodeconate, palladium acetate, and Engelhard Gold NW skin ink. One to five micron thick films were decomposed by laser after an exposure time of 100 to 500 milliseconds depending on the type of precursor. After the nonexposed regions were dissolved away, the projection of a desired mask gave feature sizes of 20 microns without distortion, see Figure 3. Surprisingly, shorter exposure times were required for larger holes in the mask. This phenomena can be explained by the temperature gradient between the center and the outer perimeter of the metal deposit. If the hole increases in size, the gradient decreases and thus built-up of heat in the center leading to higher temperatures (or shorter exposure time).

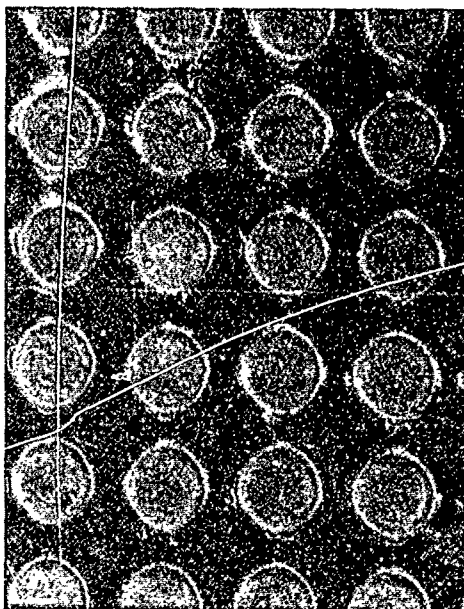


Fig. 3. Micrograph of palladium dots on quartz from spun-on palladium acetate precursor.

Deposition of gold from the gas phase (or LCVD) was tried on wide range of substrates such as quartz, silicon wafers, and polyimide. Using the dimethylgold hexafluoro acetylacetonate as precursor, Figure 4 shows deposition of 15 micron gold dots on silicon wafer. One to two seconds exposure time was required before the gold began to deposit on both the quartz and silicon substrates. This is so because of two competing mechanism in the two materials. Because of its transparency to laser, quartz behaves in a non-linear fashion, requiring a long exposure time before a threshold is reached. On the other hand, silicon has high absorption and heat conductivity. In the case of polyimide, the laser power was reduced to less than 1 watt which pushed the exposure time up to 60 seconds. The low power was required to avoid burning the polyimide which has a melting temperature somewhat higher than the decomposition of the gold precursor.

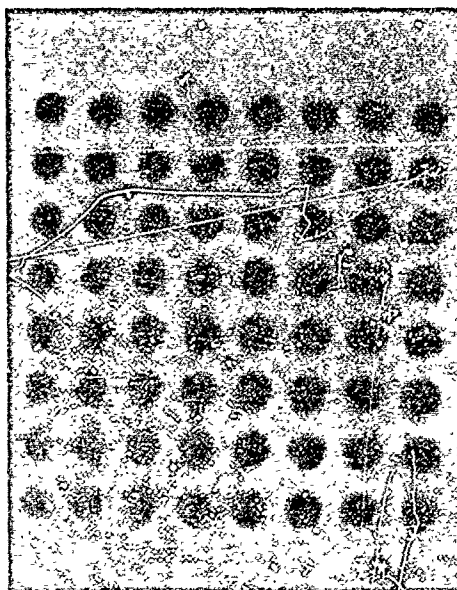


Fig. 4. Micrograph of gold dots on silicon wafer by LCVD.

CONCLUSION

The present work shows the feasibility of the copper vapor laser in both the etching and the deposition processes. The high aspect ratio etching and well defined deposition were achieved because of the localized heating achieved with the CVL. When more work is devoted to the CVL, this tool will prove itself as a powerful candidate for manufacturing.

ACKNOWLEDGEMENTS

We thank Doug Goodman for valuable advice on the imaging optics, Phil Bailey for SEM micrographs, and Sol Krongelb for supporting our efforts.

REFERENCES

1. D. Bäuerle, Chemical Processing with Lasers, edited by Hans_Joachim Queisser (Springer Series in Materials Science, Springer-Verlag Berlin Heidelberg, 1986) pp. 69-134,162-198.
2. W. W. Duley, Laser Processing and Analysis of Materials, (Plenum Press, New York, 1983).
3. D. Bäuerle, Chemical Processing with Lasers, edited by Hans_Joachim Queisser (Springer Series in Materials Science, Springer-Verlag Berlin Heidelberg, 1986) pp. 58-68
4. B. Haba, B. Hussey, and A. Gupta, Submitted to Appl. Phys. A, (1989).
5. E. Yung, B. Hussey, A. Gupta, and L. Romankiw, J. Electrochem. Soc. 136(3), 665-673 (March 1989).

EXCIMER LASER-ASSISTED ETCHING OF SILICON USING CHLOROPENTAFLUOROETHANE

S. D. RUSSELL AND D. A. SEXTON

Solid State Electronics Division, Naval Ocean Systems Center,
San Diego, CA 92152-5000

ABSTRACT

Laser-assisted photothermal chemical reactions have been observed with silicon in a chloropentafluoroethane ambient using a KrF⁺ laser at 248 nm. Etching occurs only if the incident fluence exceeds the melt threshold (~ 0.75 J/cm²), with the melt duration determined by observing the change in silicon reflectance at 633 nm. Above the ablation threshold (~ 2.2 J/cm²) increased surface roughness is observed. Etch rates ~ 7 Å/pulse have been measured using both stylus profilometer and SEM cross-sectional techniques. The etch rate dependence on incident fluence, ambient pressure, doping concentration, crystal orientation and substrate temperature have been examined suggesting an adsorption limited thermal process. This process allows single step patterning of silicon devices in a non-corrosive environment.

INTRODUCTION

Noncontact, maskless processing is of widespread interest in the microelectronics industry. Researchers have been pursuing a variety of laser-assisted processing techniques to modify materials used in this industry [1,2]. Laser-assisted etching of silicon has been examined under a variety of halogenated ambients: chlorine [3-5], fluorine [6], nitrogen trifluoride [7], xenon difluoride [8,9], and sulfur hexafluoride [10]. Typical etch rates ~ 1 Å/pulse have been reported for these ambients under a variety of conditions.

This study has examined the excimer laser-assisted reaction between crystalline silicon and chloropentafluoroethane. This ambient is used as a plasma etchant in the semiconductor industry, and both the chlorine and fluorine atoms may spontaneously react with silicon. Incident radiation at 248 nm, above the absorption band of this halocarbon [11], allows for examination of photo-thermal effects without initiating photolytic decomposition.

EXPERIMENTAL

Experiments were conducted using an excimer laser operating at 248 nm with a KrF⁺ gain medium. Pulse repetition rates up to 100 Hz were attainable with pulse energies up to 650 mJ. The laser intensity profile was homogenized, shaped and directed normal to the sample surface. Laser fluence was measured using a pyrolytic detector and monitored by observing the change in silicon reflectance at 633 nm. The FWHM temporal profile of the laser pulse was typically 23 ± 2 nsec, with melt durations observed between 30 to 80 nsec depending on fluence. Typical energy variations were ± 5 mJ corresponding to ± 0.125 J/cm² of surface fluence.

Samples were placed within a UHV processing chamber where etchant and purge gases were introduced with mass flow controllers. Pressure was measured with a capacitive manometer and electronically controlled via a downstream variable conductance connected to a turbomolecular pumping system. Stable pressures within $\pm 1\%$ of the setpoint were achieved with this setup. Temperature was monitored with a platinum-RTD attached to an OFHC (oxygen free high conductivity) copper sample platen whose temperature was controlled through a closed-cycle refrigerated recirculator. The platen temperature was maintained within ± 1 K.

Etch depths were measured using both stylus profilometer traces and SEM cross-sectional photomicrographs. Conversion to etch rates utilized the known laser repetition rate and processing time. The etching ambient used was commercially available chloropentafluoroethane, minimum purity of 98%, supplied as a liquified gas under its own vapor pressure.

RESULTS AND DISCUSSION

The etch rate as a function of pressure for silicon in a chloropentafluoroethane ambient is shown in Figure 1. Both the fluence and substrate (platen) temperature were kept at constant values, 1.8 J/cm^2 and 296 K , respectively. The sample was a single crystal silicon wafer fragment, oriented in the (100) orientation, boron doped p^+ with a resistivity between $0.006\text{--}0.02 \text{ } \Omega\text{-cm}$. At pressures below about 6 kPa (45 torr), no evidence of etching was observed. Increasing pressure to $\sim 27 \text{ kPa}$ resulted in a rapid increase in etch rate, with a more gradual increase with higher pressures.

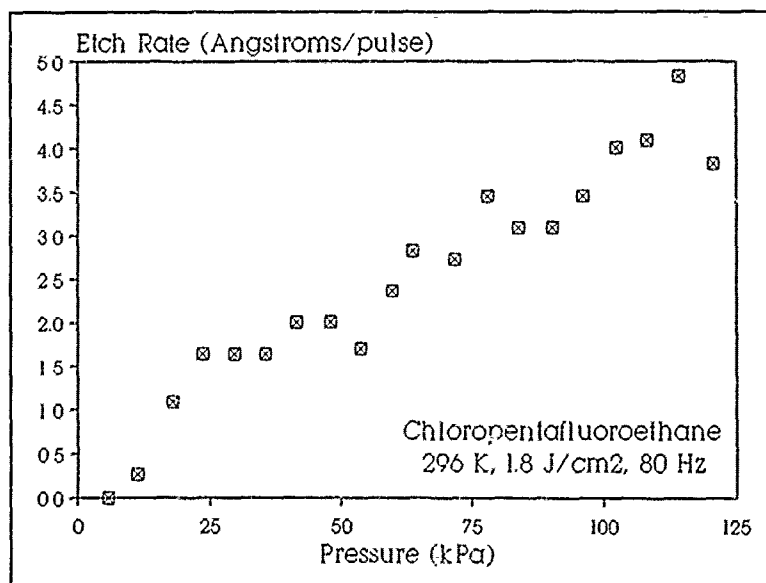


Figure 1. Etch Rate vs. Pressure

Figure 2 shows the etch rate versus laser fluence for a similar sample at 96.7 kPa (727 torr) of chloropentafluoroethane ambient and constant temperature (296 K). No etching was observed below the melt fluence, and a linear behavior was observed as the incident fluence was increased toward the ablation threshold ($\sim 2.2 \text{ J/cm}^2$). The square data points were taken with the laser at 80 Hz , the dotted line is a linear regression fit to these points exhibiting a correlation coefficient of 0.97 . This behavior can be explained by a 1D thermal model where the increase in temperature is linearly proportional to the absorbed surface fluence.

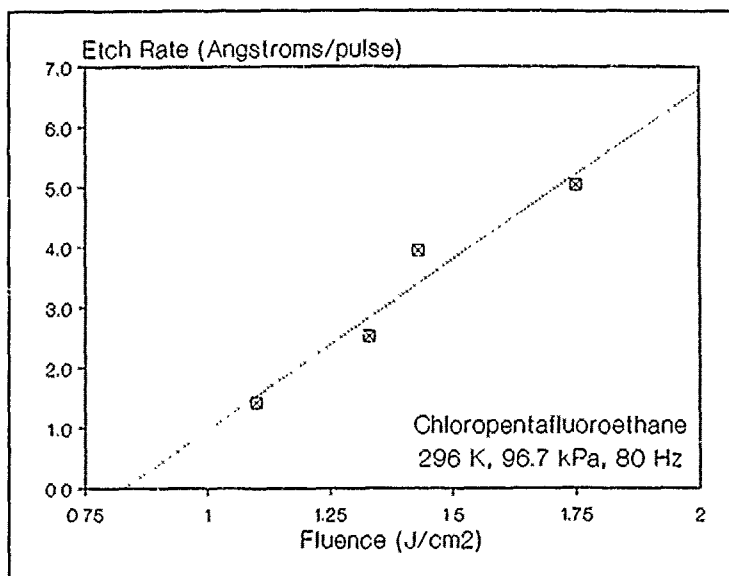


Figure 2. Etch Rate vs. Fluence

Comparison between the etch rate of similarly doped (100) and (111) silicon samples showed no significant difference under identical experimental conditions. This is attributed to the etching reaction occurring while the silicon is in the molten state. The anisotropy of the etch is therefore governed by both the incident intensity profile causing the melt and the thermal diffusivity.

Examination of etch rate as a function of doping type and concentration was performed using boron doped silicon with resistivity 0.006-0.020 $\Omega\text{-cm}$ (p^+) and 1.0-2.0 $\Omega\text{-cm}$ (p), and phosphorous doped with resistivity 1.1-1.8 $\Omega\text{-cm}$ (n) and 0.006-0.020 $\Omega\text{-cm}$ (n^+). Under the experimental conditions of 96.4 kPa, 285 K platen temperature, 0.3 J/cm² at 50 Hz, the p^+ Si sample exhibited a mean etch rate of 6.8 ± 0.3 Å/pulse. The p , n , and n^+ type Si samples showed a slightly higher etch rate of 7.3 ± 0.3 Å/pulse. This difference is not experimentally significant, and agrees with the results of Hurlike et al. who reported an etch rate independent of sheet resistance and type while etching silicon with fluorine atoms photodissociated from NF_3 [4]. This was attributed to the high Pauli electronegativity (4.00) of the fluorine atom allowing adsorbed fluorine species to take valence electrons from the silicon surface atoms independent of doping type. Note that these results suggest a mechanism different than the photo-oxidation/reduction reactions observed for the fluoro-silicon system which exhibit significant doping effects [1,12]. This implies that under the high fluence conditions used in this study, the most important effect on the silicon reaction is thermal activation rather than a field enhanced reaction.

Etch rate as a function of temperature is shown at 97.5 kPa (733 torr) and 1.05 J/cm² in Figure 3. This experiment was performed at a laser repetition rate of 20 Hz (0.84 W) to minimize the steady-state heating of the sample caused by the duty cycle of the laser pulses. At 276 K an etch rate of 15.3 ± 0.3 Å/pulse is observed, which decreases with increasing temperature. Such behavior is consistent with a B-E-T (Brunauer-Emmett-Teller) adsorption mechanism with higher sticking coefficients at lower temperatures.

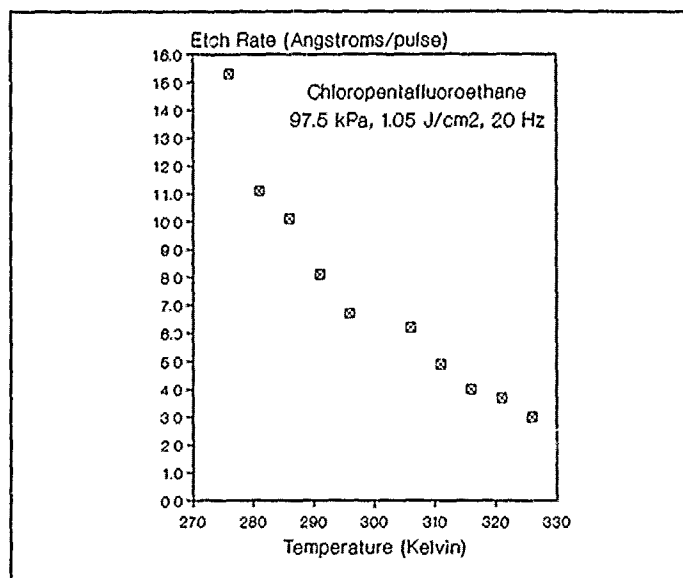


Figure 3. Etch Rate vs. Temperature

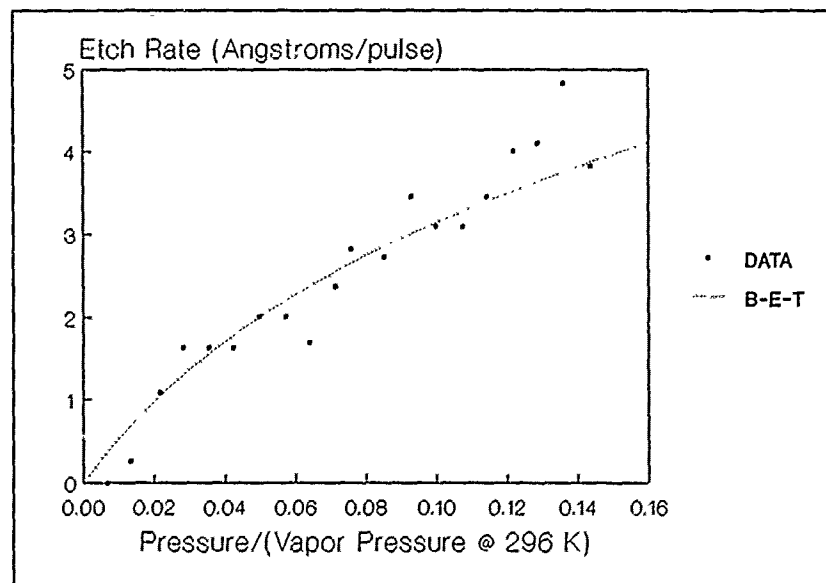
Figure 4. Etch Rate vs. P/P_0

Figure 4 shows the pressure dependence of the etch rate, with a dashed line showing a B-E-T isotherm. This was obtained with the assumption of a linear relationship between the etch rate and surface coverage. This suggests adsorption as the primary etch rate limiting mechanism. However, since physisorption bond energies are in the range 0.01 to 1 eV (van der Waals forces) and chemisorption processes exhibit covalent and ionic bonds whose energies are typically 1 to 8 eV, laser induced desorption via thermal heating can not be ruled out as a coexisting phenomenon [13].

Figure 5 shows the etch rate versus laser repetition rate at a constant sample (platen) temperature at 98 kPa (737 torr) and 0.80 J/cm². A dramatic decrease in etch rate with increasing laser repetition rate was discovered. This effect correlates with increased steady-state heating of the sample due to the increased duty cycle of the laser. At repetition rates ≥ 20 Hz, an uncooled sample exhibits significant temperature rise in an ambient of ~ 101 kPa (typical processing pressure). At 100 Hz (0.8 J/cm² fluence per pulse) a silicon sample rose to a steady-state temperature of 40 K above the ambient at atmospheric pressure. The decrease in etch rate between a sample processed at 100 Hz compared to 20 Hz under identical conditions was nearly identical to that of increasing the platen temperature 40 K (shown in Figure 3). This is consistent with the rate limiting mechanism discussed above.

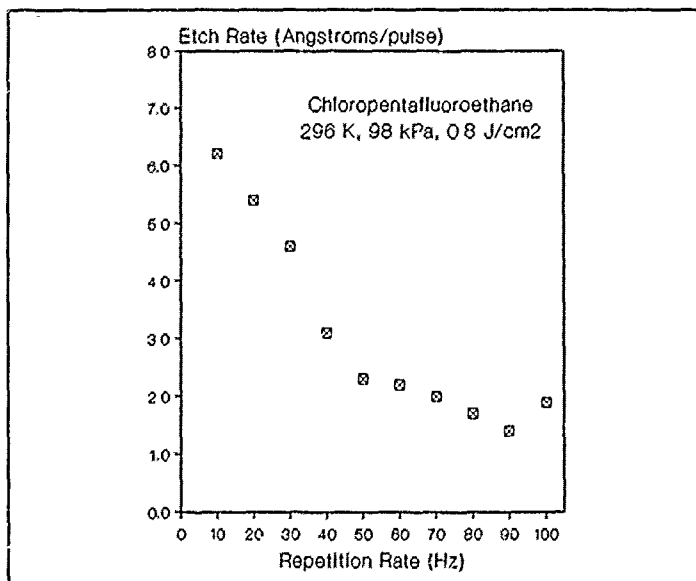


Figure 5. Etch Rate vs. Laser Rep. Rate

SUMMARY

Excimer laser-assisted etching of silicon has been observed in a chloropentafluoroethane ambient with incident fluences between the melt and ablation thresholds ($\sim 0.75 \text{ J/cm}^2 \leq \Phi \leq \sim 2.2 \text{ J/cm}^2$). Etch rate increased with increasing ambient pressure, while it decreased with increased sample temperature. These effects are consistent with an adsorption limiting mechanism and possibly coexisting laser induced desorption. This reaction was insensitive to crystal orientation and doping concentration and type, implying a purely photo-thermal

reaction. The linear dependence of etch rate with laser fluence is consistent with the proposed thermal reaction. Future experiments will examine the reactants to elucidate the reaction or reactions involved.

Converting to an etch rate in units of angstroms/sec we note that no significant advantage in processing time can be attained by increasing the repetition rate above ~50 Hz due to the rate limiting mechanism. However, the etch rates observed in this study are substantially greater than the ~1 Å/pulse reported previously for laser-assisted etching of silicon (below the ablation threshold), and therefore the rate limiting mechanism is not a detriment for practical processing. In addition, chloropentafluoroethane is a non-reactive gas with all microelectronic materials, and therefore allows the possibility of etching silicon in a partially manufactured device without masking.

REFERENCES

1. F. A. Houle, Appl. Phys. A, 41, 315 (1986).
2. D. Bauerle, Appl. Phys. B, 46, 261 (1988).
3. R. Kullmer, D. Bauerle, Appl. Phys. A, 47, 377 (1988) and references therein.
4. Y. Horiike, N. Hayasaka, M. Sekine, T. Arikado, M. Nakase, H. Okano, Appl. Phys. A, 44, 313 (1987).
5. W. Sesselmann, T. J. Chuang, J. Vac. Sci. Technol. B, 3, 1507 (1985).
6. S. Palmer, K. Orvek, Conference on Lasers and Electro-Optics Technical Digest Series 1988, Vol. 7, 284 (Optical Society of America, Washington D.C. 1988).
7. J. H. Brannon, Appl. Phys. A, 46, 39 (1988).
8. T. J. Chuang, J. Chem. Phys., 74, 1461 (1981).
9. F. A. Houle, J. Chem. Phys., 79, 4237 (1983); 80, 4851, (1984).
10. T. J. Chuang, J. Chem. Phys., 74, 1453 (1981).
11. D. E. Robbins, NASA-CR-154106, Int. Conf. Probl. Relat. Stratos., 255 (1976).
12. H. F. Winters, D. Haarer, Phys. Rev. B, 36, 6613 (1987).
13. R. Gauthier, C. Guittard, Phys. Stat. Sol. (A), 38, 477 (1976).

LOCAL LASER INDUCED ETCHING OF COPPER FILMS BY CHLORINE

HUA TANG and IRVING P. HERMAN

Department of Applied Physics and Microelectronics Sciences Laboratories,
Columbia University, New York, NY 10027

ABSTRACT

A focused argon ion laser was used to induce local thermal etching of copper films in the presence of chlorine gas. Raman scattering was used to follow the transformation of the copper film *in situ* to CuCl and CuCl₂. In some regimes the laser only induced transformation of copper to copper chloride, while in others the laser produced copper chloride and also desorbed it.

INTRODUCTION

Laser-assisted dry etching of copper films is of interest because of the difficulties encountered in other types of dry etching of this important electronics material, such as by plasma etching. Recently, excimer laser assisted etching of copper films [1,2] was examined, in which the laser was used only to desorb the copper chloride produced between laser pulses by the reaction of Cu and Cl₂ at the substrate temperature. In this paper, we report that cw argon ion laser radiation can be used to produce local copper chloride regions on copper films in the presence of chlorine, and sometimes to desorb this product. Based on *in situ* Raman scattering analysis, CuCl₂ is the dominant product remaining on the surface in this laser-induced process. As a result of the different temperature dependence of the rate of copper chloride formation and desorption, two very different etching regions are found to occur for some experimental conditions.

In an earlier study [3], we reported that at ambient temperature Cu films (with either no oxidized layer or a several-Å-thick oxide layer) react with Cl₂ gas to form a film of CuCl. In contrast, focused laser heating of a CuCl-on-Cu film (partially passivated) or Cu film (passivated by a thicker oxide layer) on glass in the presence of chlorine induces a different reaction [3]. Depending on experimental conditions, the result of this laser-scanned reaction is a deposition-like line, with cross-section resembling either a bump or a bump with a trench in the middle. After subsequent removal of chlorine, *in situ* Raman spectra were taken of these features at 298 K. The presence of CuCl₂ was determined by its strong, sharp Raman peak near 282 cm⁻¹ and its weaker peaks near 167 and 556 cm⁻¹, while a broad featureless peak below 250 cm⁻¹ signified the presence of CuCl. In many regimes, the CuCl₂ peak dominates. After *ex situ* removal of the copper chloride by

rinsing in hydrochloric acid, etched grooves remained in the copper with widths varying from 3 - 20 μm . For Cu samples with a thick overlaying oxide, there was no reaction between Cu and Cl_2 at room temperature. This reaction was induced only by laser heating. The relative importance of copper chloride formation and desorption during etching passivated Cu films is studied here by laser heating of Cu films in the presence of Cl_2 .

EXPERIMENTAL METHODS

Copper films ($\sim 1.5 \mu\text{m}$ thick) were deposited on glass substrates by evaporation and were then heated in air for 5 - 30 min at $T = 150^\circ\text{C}$ to form a thick passivation layer (passivated, $\sim 100 - 200 \text{ \AA}$ copper oxide (as Cu_2O [4])). Afterwards, these samples were mounted in a vacuum reaction chamber, which could be filled with Cl_2 gas. Once placed in the reaction chamber, the sample was viewed with a microscope through a window port in the chamber and was irradiated by a focused cw argon ion laser (4880 \AA , $\sim 2.2 \mu\text{m}$ full width at $1/e$ intensity, linearly polarized) for local laser heating and for Raman analysis. The unpolarized backscattered Raman radiation was then collected, dispersed by a triple spectrometer, and detected by an intensified diode array. The chamber was mounted on a translation stage to allow lateral scanning during laser heating. After processing, features were examined by profilometry.

RESULTS

Profilometry analysis was performed after laser etching, both before and after the samples were rinsed in 1.4 Molar hydrochloric acid. This procedure removed the copper chloride but left the underlying Cu film alone. At the site of laser heating and localized CuCl_2 formation, removal of some or all of the Cu film is observed. Raman spectroscopy was performed *in situ*, giving spectra such as that in Fig. 1, which shows CuCl_2 with some evidence of CuCl .

Figure 2 plots the depth of the etched copper feature after laser scanning and hydrochloric acid rinsing as a function of laser scan speed for laser powers of 200, 300 and 400 mW, with 10 Torr chlorine pressure. When the laser power is lower than about 200 mW, the etch depth decreases monotonically with increasing scan speed. Also, the copper chloride line formed by laser heating has a cross-section of a bump with no trench, which suggests there is no desorption of the copper chloride line during "etching". When the laser power is higher than 300 mW, similar behavior is observed for slow scan speeds. However, for faster scan speeds the etched line depth now increases with increasing laser scan rates. In this regime, there is a significant desorption trench running down the middle of the deposit-like copper chloride line. However, in no case is all the copper chloride

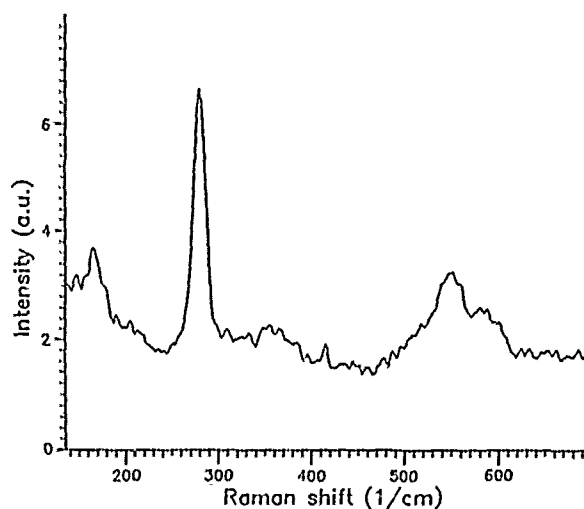


Figure 1. Raman spectrum (taken in vacuum using 20 mW 4880 Å) of a copper chloride deposition-like feature which was produced by using 70 mW of 4880 Å radiation to heat a 1.4 μm -thick copper film for 1 min in the presence of Cl_2 (1 Torr). The peaks at 167, 282, and 556 cm^{-1} belong to CuCl_2 , while the broad peak below 250 cm^{-1} shows evidence for CuCl .

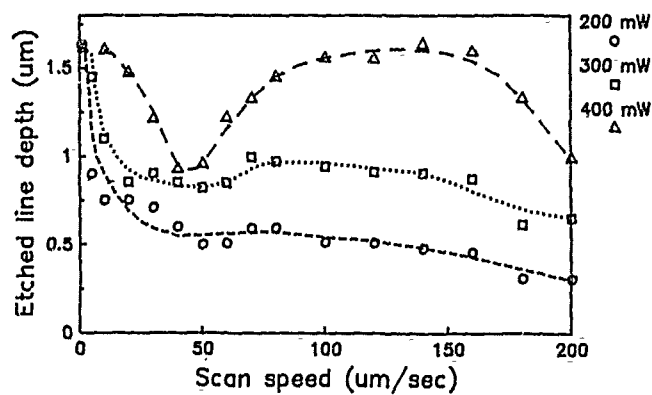


Figure 2. The depth of the etched copper features after copper chloride removal for 200 mW (circles), 300 mW (squares) and 400 mW (triangles) using 4880 Å radiation incident on a 1.6 μm -thick copper film-on glass sample (15 min oxidation at 150 °C) with 10 Torr chlorine pressure.

desorbed during laser heating. In particular, large deposits of copper chloride always remain on either side of the scanned line. At very high scan speeds the etched line depth again decreases.

In Figs. 3a and 3b, the depth of the copper etch is plotted as a function of scan speed with different chlorine pressures for laser powers of 300 and 400 mW, respectively. The change from a regime of decreasing etch depth and no copper chloride desorption at slow scan speeds to a regime with increasing etch depth with some desorption at faster scan rates is seen in many of these plots. As the pressure increases, this transition occurs at increasingly faster scan rates. The maximum etch depth decreases more slowly with increasing chlorine pressure at 400 mW than at 300 mW. Note that the initial copper film thickness is slightly different for the 300 and 400 mW experiments.

ANALYSIS

With chlorine present, copper converts to copper chloride even with a relatively small temperature rise (~ 30 K) due to laser heating. From these experiments, it is clear that the laser must heat the film to significantly higher temperatures for the second step of etching to occur, which is the desorption of the product. The expected rates for copper chloride formation as a function of temperature are plotted in Fig. 4 at different chlorine pressures using the model presented in [1] (which has been extrapolated to higher temperatures). The expected desorption rate of copper chloride is also plotted in this figure using the data in [6]. As seen in this figure, when the chlorine pressure is 10 Torr, the temperature must be > 630 K for the desorption rate to exceed the copper chloride formation rate ($7 \mu\text{m/sec}$). This cross-over temperature decreases with decreasing chlorine pressure (to 500 K for 1 Torr).

From Fig. 4 it is estimated that a temperature rise of $\sim 300 - 400$ K is required to obtain the needed desorption rate of copper chlorides for a complete, one-step laser etching process. The calculation of the steady-state surface temperature rise on an evaporated copper film ($1.5 \mu\text{m}$ thick) during laser heating [3] indicates that with a laser power of ~ 400 mW, the maximum temperature rise will be ~ 300 K. An incident laser power of 200 mW induces only a ~ 140 K rise on the copper film, which is too low for the rate of copper chloride desorption to be competitive with the rate of formation. However, even at higher laser powers where there is desorption in the center of the laser heating area, copper chloride remains at the sides because the temperature rise is lower there.

This explains many of the observations, such as why there is relatively more desorption for higher laser powers and lower chlorine pressures in steady state. It also

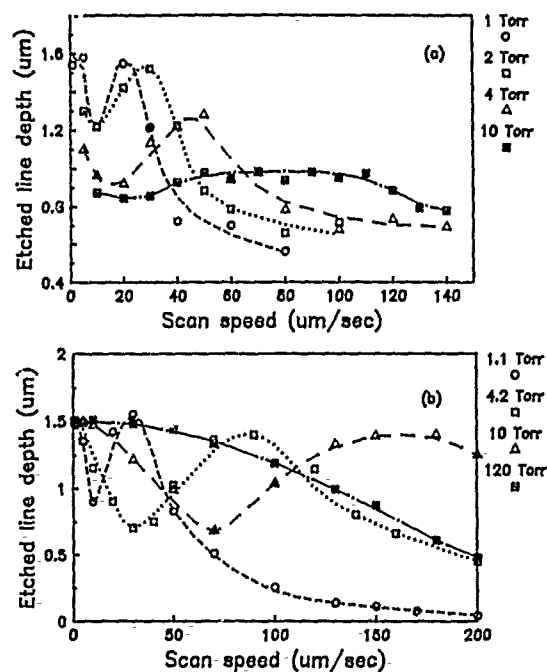


Figure 3. The depth of the etched copper features after copper chloride removal for (a) 300 mW of 4880 \AA radiation incident on a 1.6 μm -thick copper film and (b) 400 mW of 4880 \AA incident on a 1.5 μm -thick copper film (15 min oxidation at 150 $^{\circ}\text{C}$) for different chlorine pressures.

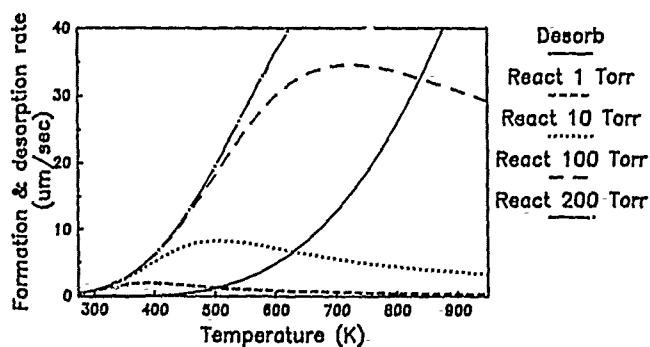


Figure 4. The formation rate (different broken lines for several different chlorine pressures) and desorption rate (solid line) of copper chloride as a function of temperature.

explains the observed dependence on scan rate. A given spot in the laser scan sees a temperature ramp from ambient temperature to the maximum laser-produced temperature and down again. The laser-induced temperature rise is in steady state for all scan rates used here. The duration of this ramp is approximately the width of the laser-produced temperature profile, which can be broader than the laser spot size [3], divided by the scan speed. For a 100 $\mu\text{m}/\text{sec}$ scan speed this duration is ~ 50 msec. During a scan with high laser power, the copper is at an intermediate temperature rise, where copper chloride forms but does not desorb, before reaching the maximum temperature, where both copper chloride formation and desorption can occur. For a slow scan, the dwell time at the intermediate temperature might be so long that the copper chloride formed may be too thick to be desorbed later. This does not occur for a fast scan.

Furthermore, once a copper chloride layer forms over the copper during the laser scan, the overall process changes. The temperature profile changes with a copper chloride layer on top, which may lower the surface temperature and slow desorption. The reaction rate may also change because the diffusion of Cu cations across the copper chloride layer depends on thickness and temperature [5,7]. In the experiments described in Figs. 2 and 3, the change from a regime with no copper chloride desorption at slow scan speeds to the regime with desorption at faster scan speeds is accompanied by an increase in the copper etch depth (though the dwell time is shorter). This can be explained by a decrease in the formation rate of copper chloride when there is a copper chloride layer on the Cu. This decrease may be due to a decrease in the laser-modified temperature profile attributable to the overlayer or by the increasingly long Cu cation migration time across the layer.

ACKNOWLEDGMENTS

The authors would like to acknowledge the financial support by the Office of Naval Research and IBM.

REFERENCES

- [1] J. J. Ritsko, F. Ho, and J. Hurst, Appl. Phys. Lett. **53**, 78 (1988), and J. Hurst, private communication.
- [2] W. Sesselmann, E. E. Marinero, and T. J. Chuang, Appl. Phys. A **41**, 209 (1986).
- [3] H. Tang and I. P. Herman, J. Vac. Sci. Technol. A **8**, (1990, in press).
- [4] R. J. Nika and P. M. Hall, IEEE Trans. CHMT-2, 412 (1979).
- [5] W. Sesselmann and T. J. Chuang, Surf. Sci. **173**, 32, 67 (1986).
- [6] H. F. Winters, J. Vac. Sci. Technol. B **3**, 9 (1985); A **3**, 786 (1985).
- [7] J. C. Poignet and M. J. Barbier, Electrochimica Acta, **26**, 1429 (1981).

PART VII

Epitaxy I

SELECTIVE SILICON EPITAXY FOR ADVANCED DRAM STRUCTURES

GARY B. BRONNER

IBM Research Division, TJ Watson Research Center
Yorktown Heights, NY 10598

ABSTRACT

In silicon microelectronics, memory cells and chips are used to develop the most advanced technology. In the future these chips will require three dimensional structures to achieve the needed density. This paper describes the use of selective silicon epitaxy to build truly three dimensional DRAM cells. The cell consists of a trench capacitor which is overgrown with single crystal silicon. A transistor and isolation are then built above the trench capacitor resulting in a cell that occupies the same area as the transistor alone. Fully functional memory cells have been built. The results show that selective silicon epitaxy is a realistic candidate for building three dimensional silicon devices.

INTRODUCTION

The trend in DRAM (dynamic random access memory) technology has shown an increasing use of three dimensional structures due to the need for both high capacitance and small cell size. Most 1Mb DRAMs have been fabricated with planar capacitors, but it is generally recognized that further decreases in cell size will require trench or stacked storage capacitors[1]. This is seen in the 4Mb and 16Mb cell arrays that have been published[2, 3]. In the future additional use of this third dimension will be needed to provide the necessary combination of stored charge and cell size. Here work is presented on the use of selective silicon epitaxy to grow single crystal silicon over trench storage capacitors, allowing the fabrication of buried trench DRAM cells[4, 5].

Buried Trench Cell Structure

Figure 1 shows the steps involved in the fabrication of a buried trench DRAM cell. Before patterning the deep storage trench a Si_3N_4 film is deposited over a thin pad oxide. This film is an etch stop for removing the polysilicon used to fill the deep trench. After the polysilicon is etched back, this same nitride film is used to provide a self aligned cap oxide on top of the trench. This structure is shown in Figure 1a. At this point the nitride and pad oxide are stripped off, leaving the trench with its cap oxide, surrounded by bare silicon. With the exposed silicon area surrounding the trench as a seed, a perfect silicon layer is overgrown on top of the capped trench. Since the lateral overgrowth rate in the [100] direction is the same as the vertical growth rate, a self-aligned opening window on top of the trench capacitor is achieved by controlling the vertical epitaxy growth rate and thickness (Figure 1b). Next the cap oxide is etched so that a connection can be formed to the buried trench. One way of doing this is shown in Figure 1c, where a second epitaxial growth is used to close off the self-aligned connection hole. A pyramid of polysilicon forms over the exposed trench polysilicon, but single crystal silicon still grows laterally and in time buries the trench below single crystal silicon. After this the isolation and transistor are formed leading to the final cell structure shown in Figure 1d.

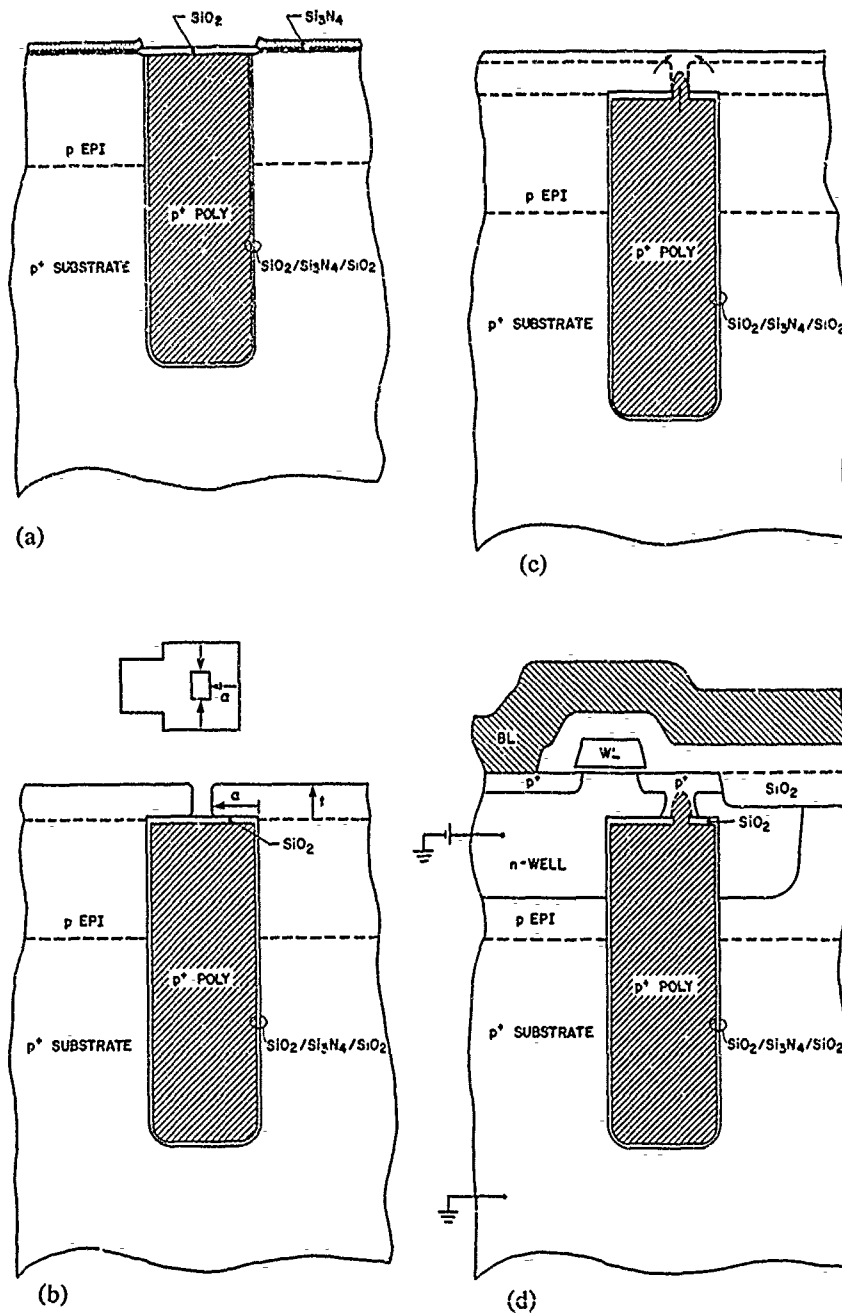


Figure 1 Cross section of storage trench after (a) self-aligned cap oxidation, (b) partial epitaxial overgrowth, (c) second epitaxy step, and (d) full DRAM cell processing.

SELECTIVE SILICON EPITAXY

Selective silicon epitaxy has been known for many years [6], but still has not received wide acceptance. In recent years the advent of reduced pressure epitaxial reactors has spurred a resurgence of interest[7], but questions related to material quality have persisted. The most troublesome aspect of the process is the tendency towards defect formation when patterns are aligned in any direction except the [100] direction[8].

The buried trench DRAM cell described here attempts to use selective epitaxy in an optimal manner. The two critical areas any such technology faces are selectivity and material quality, especially in regard to faceting. Our approach has no problems with selectivity because the ratio of silicon to insulator is high, with the only insulators being the cap oxides over the trenches. Faceting is also not a problem. The cap oxide over the trench is flush with the original silicon surface. Because of this the orientation of the trench capacitor does not constrain which planes grow laterally. Independent of the orientation of the trench we find that (100) planes converge from all sides of the trench to bury it.

Experimental Conditions

Selective epitaxial films were grown in a conventional barrel-type reduced pressure reactor. Unlike other work in the literature which uses $\text{SiH}_2\text{Cl}_2 + \text{HCl} + \text{H}_2$, with the HCl needed for selectivity[7], we use $\text{SiCl}_4 + \text{H}_2$. This chemistry offers several advantages[9]. HCl is a difficult gas to purify and can introduce metallic impurities into the system. When growing thin epitaxial layers the lower grow rates seen with SiCl_4 make it easier to control film thickness. Additionally we have found empirically that removal of HCl from the system improves uniformity of epitaxial growth from wafer to wafer and across a wafer.

Figure 2 shows growth rate data in an Arrhenius plot for the SiCl_4 process at 40 Torr and a flow rate of 1.88g/min of SiCl_4 . At temperatures less than 950°C the growth rate is strongly temperature dependent with an activation energy of 1.6 eV. Above that temperature the growth increases more slowly as the growth becomes mass transport limited. In the lower temperature regime growth is reaction-rate limited and relatively insensitive to changes in gas flow. For best uniformity we chose to operate in this reaction-rate limited regime, typically at 900°C.

Operating at this temperature guarantees that epitaxial growth is reaction-rate limited and thus uniformity is a function only of temperature control, not gas flow. Figure 3 shows a schematic cross section and SEMs of partially overgrown oxide patterns. The SEM is tilted at 70° so that one sees both the overgrown oxide patterns in cross section and the self aligned holes from the top. The size of these holes can be used as an indication of the uniformity of the epitaxy. Typically we see films thickness are controlled to better than 2% across a 5 inch silicon wafer.

Orientation Effects

The partial epitaxial overgrowth of the oxide patterns in Figure 3 also shows up an important orientation effect. It is apparent that the overgrowth does not mimic the shape of the oxide patterns; instead it is dominated by laterally growing (100) planes. Since the patterns were aligned in a [110] direction, the overgrowth initiates from the corners and grows in, resulting in a diamond shaped hole. The size of this hole can be related to the original shape and thickness of the epitaxial layer by geometrical calculations. The self-

aligned holes have their edges rotated 45° from the original trench shape. This effect is critical for achieving best material quality. Unlike other researchers who find that they must orient their patterns in a $[100]$ direction to achieve best material quality[8], our process allows (100) planes to grow independent of the original orientation of our patterns.

Figure 4 is a plane view TEM photomicrograph showing this effect. A rectangular oxide pattern has been partially overgrown. The darkest area is the region of the oxide pattern that has been overgrown while the bright region is that portion of the oxide pattern that is not overgrown. One can see that along the $[110]$ bounded oxide edge one has very little lateral overgrowth. The thickness fringes show that an

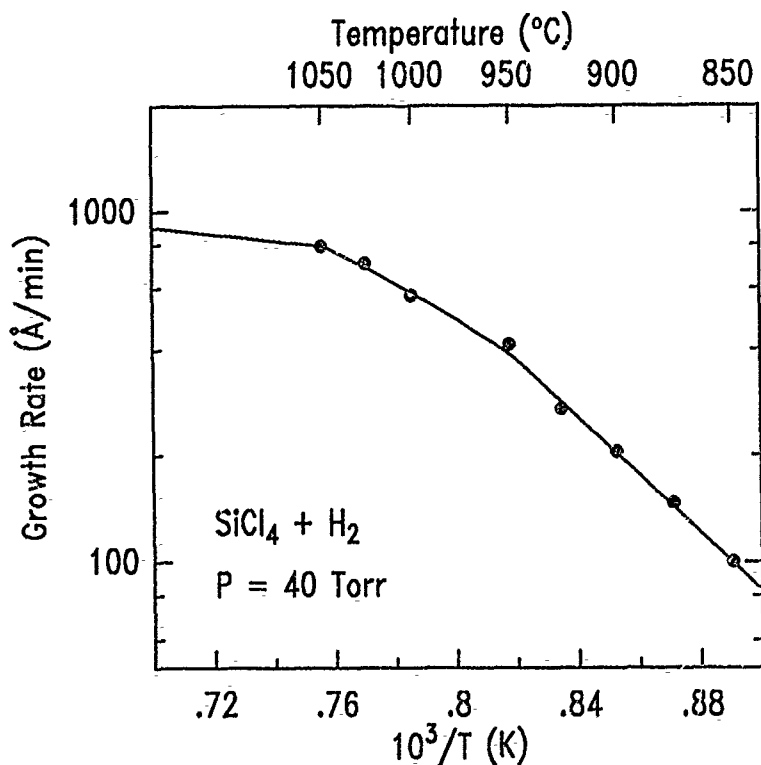


Figure 2 Growth rate of SiCl₄+H₂ process at 40 Torr as a function of temperature.

Uniformity of Films and Holes

- $T_{lat} = T_{epi} - T_{ox}$
- $H = \sqrt{2} W - 2 T_{lat}$
- Electron Microscope Cross Section
- Uniformity $\leq 2\%$ Across 5" Wafer

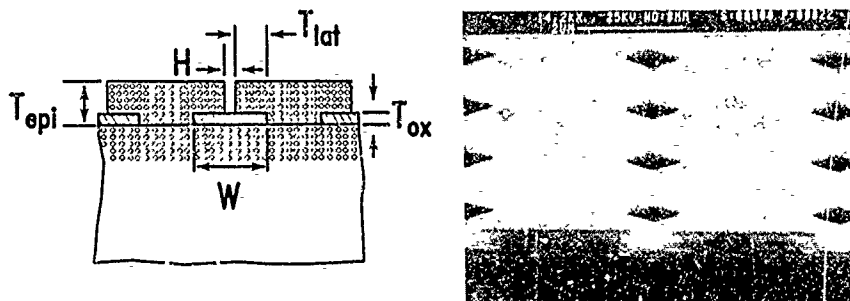


Figure 3 Schematic representation (left) and SEM cross section (right) of partially overgrown oxide patterns demonstrating the uniformity of the selective epitaxy process.

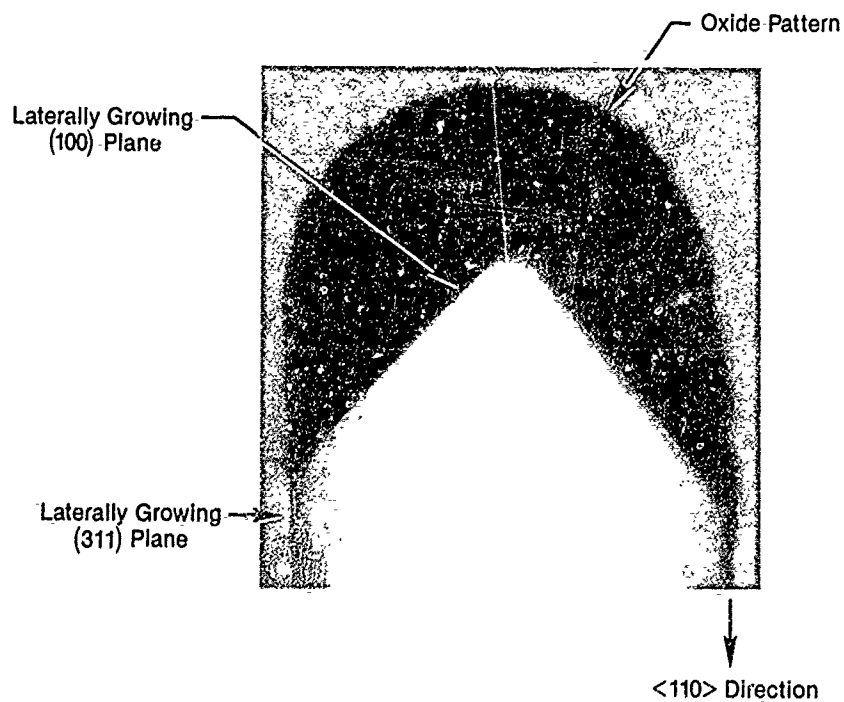


Figure 4 Plane-view TEM of partially overgrown oxide pattern showing the orientation dependence of epitaxial overgrowth.

inclined plane has formed and cross sectional SEMs show this to be a (311) plane. The epitaxial overgrowth occurs primarily in the [100] direction, which means that for a pattern oriented in the [110] direction, the overgrowth proceeds from the corners as seen here. This limits the ability to overgrow long rectangles, but in reality is no problem, since trench capacitors are typically small squares or rectangles.

Epitaxy Over Trenches

The growth of epitaxy over storage trench capacitors occurs in the same manner as the simple oxide patterns; independent of the original orientation of the trenches (100) planes converge from all sides to bury the capacitor. This is demonstrated in Figure 5, which is an SEM cross section of storage trenches completely buried below $1.2\mu\text{m}$ of epitaxial silicon and then SECCO etched for defect delineation[10]. The defect etch has removed most of the polysilicon inside the trenches and would similarly attack defects if they were present. As can be seen the trenches are buried with no voids and no defects associated with either the initial silicon surface or the point where planes from opposite sides of the trench converge to seal the trench. Cross sectional TEM analysis confirms that trenches are buried with defect free silicon. Another noteworthy feature is the planarity of the surface after the epitaxy. This is a direct result of the overgrowth being dominated by (100) planes. Other planes lead to faceting which can cause surface topography after epitaxial overgrowth.

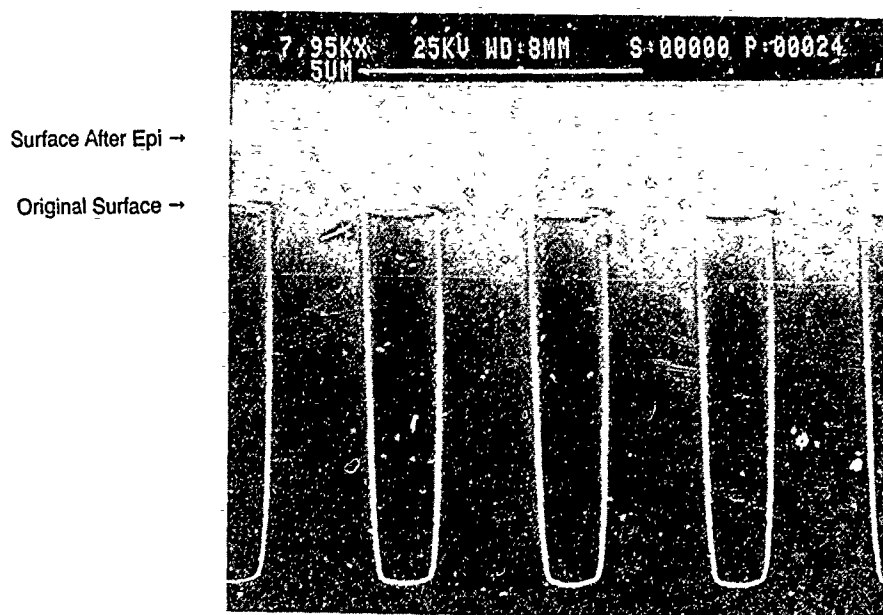


Figure 5 SEM cross section of trenches buried below $1.2\mu\text{m}$ of epitaxial silicon after SECCO etching to delineate defects. Note the planarity of the surface and the lack of defects associated with the overgrowth.

Table 1. Generation lifetime measurements in epitaxial silicon and epitaxial silicon grown laterally over oxide patterns. The data show that epitaxial silicon grown laterally on top of SiO_2 is as good as epitaxial silicon grown over bulk silicon.

DIE	Epitaxial Silicon	Epitaxy Over Oxide
5,8	134.7 μsec	52.4 μsec
8,4	90.2 μsec	47.5 μsec
8,8	80.9 μsec	130.8 μsec
7,8	72.9 μsec	116.6 μsec
7,7	70.7 μsec	122.7 μsec

ELECTRICAL CHARACTERIZATION

Electrical measurements also show good characteristics. Electrical testing provides a way of verifying the material quality of epitaxy grown laterally over a large number of trenches. With physical analysis such as cross sectional SEM or TEM one can look at a handful of trenches, while electrical measurements allow one to study thousands of trenches at a time.

MOS Lifetime

MOS capacitors were used to measure generation lifetime in material grown over an array of 5000 thin oxide layers patterned with the storage trench mask. The individual oxide patterns were $1.0\mu\text{m} \times 1.2\mu\text{m}$ while the MOS capacitor had an area of $230\mu\text{m}$ by $415\mu\text{m}$. Typical data are presented in Table 1. As can be seen, lifetime over the array of oxide patterns is the same as in the material grown over unpatterned silicon and is uniformly high. Results over actual storage trenches are comparable. The patterns in this experiment were overgrown with $1\mu\text{m}$ of silicon, so the capacitor could not deplete down to the buried oxide. Depletion layer depths were typically $0.5\mu\text{m}$. This is strong evidence that the material grown over the oxide patterns is of high quality, since any defects would create generation centers in the depletion layer and degrade the lifetime. For both the cases listed in Table 1, the measured lifetimes are greater than values typically seen in blanket epitaxial silicon grown at higher temperatures[11].

Diode Leakage

Large diodes have been built over an array of 5000 storage trenches. An n-well was implanted and p⁺ junctions were formed in the n-well directly above the trenches. Figure 6 shows leakage current measurements of diodes with and without buried storage capacitors. As can be seen the presence of the buried storage capacitors has no effect on the diode leakage, which in both cases is $0.21\text{fA}/\mu\text{m}^2$.

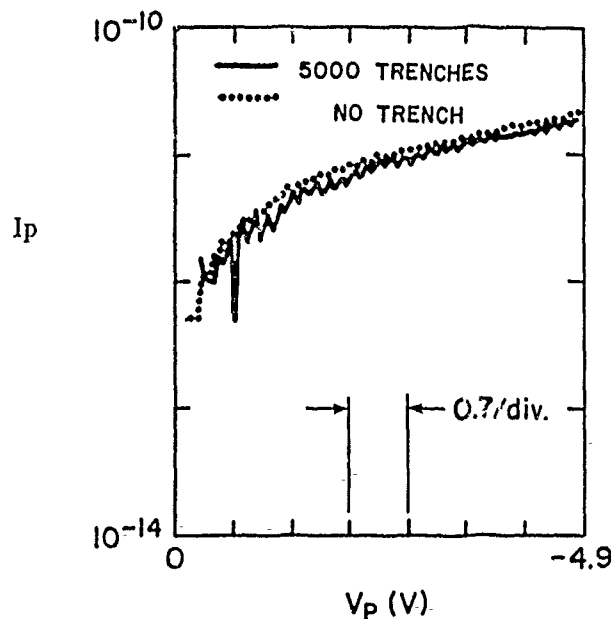


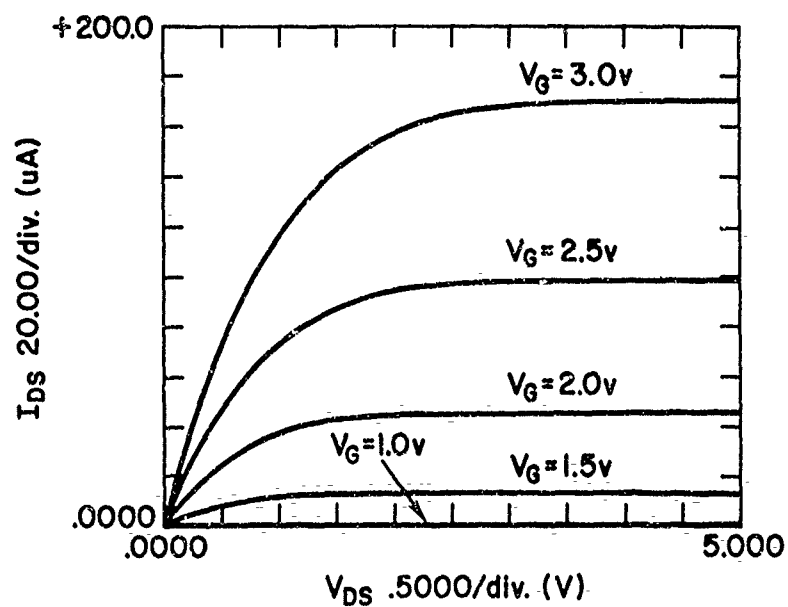
Figure 6 Leakage current of $415\mu\text{m} \times 230\mu\text{m}$ p⁺-n diode with and without 5000 buried trenches. Each trench was rectangular with dimensions $1.2\mu\text{m} \times 1.0\mu\text{m}$.

Transistor Characteristics

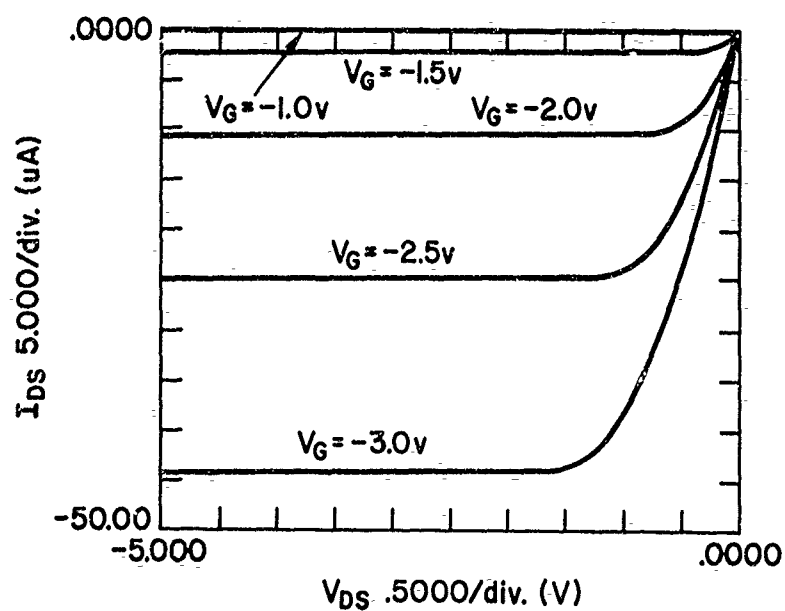
The measured characteristics of transistors made in the epitaxial films are shown in Figure 7 and are essentially identical to submicron MOSFETs fabricated in a conventional substrate. The transistors plotted are long channel devices, $L=20\mu\text{m}$. The apparent electron and hole mobilities, measured from long-channel devices, are about 405 and 120 cm^2/Vsec , respectively. Transconductances for NFETs and PFETs ranging around 103 mS/mm and 53 mS/mm , respectively, are measured for effective channel lengths of 1.0 μm with a drain bias of 3.5 V and a gate bias of 3.0 V above threshold.

BURIED TRENCH CELL FABRICATION

To prove the feasibility of the Buried Trench concept a special test site was designed allowing the integration of these cells into a submicron CMOS process. Storage trenches were fabricated in a conventional p⁺/p⁺ substrate and the process steps outlined in Figure 1 were performed. A cap oxide was formed over the trenches and they were then buried with the two step epitaxial process. From that point, isolation was formed using conventional local oxidation techniques, and NMOS and PMOS transistors were using 0.85 μm design rules. The completed cell is shown in Figure 8. The cells are fully functional with the smallest cell fabricated using less than 10.8 lithographic squares and having an area of 7.8 μm^2 . With improved lithography and processes such as a self-aligned bitline contact and/or smaller oxide isolation, the cell area can be further reduced toward use in 64Mb DRAMs or beyond.



(a) NMOS



(b) PMOS

Figure 7 Transistor characteristics of long channel (a) NMOS and (b) PMOS. Both have $W=L=20\mu m$, gate oxide thickness of 125\AA , and $0.2\mu m$ deep junctions.

Cell Cross Section



Figure 8 SEM cross section of Buried Trench DRAM Cell.

CONCLUSIONS

Selective silicon epitaxy offers the possibility of building truly three dimensional silicon structures. A novel DRAM structure, the Buried Trench DRAM cell, has been proposed and demonstrated. This structure uses selective silicon epitaxy in an optimal manner. The implementation offers intrinsically high selectivity due to the ratio of silicon to insulator during the growth and shows excellent material quality. The high material quality is a direct result of overgrowth by (100) silicon planes. The cell structure has been designed so that this occurs independent of the original orientation of the trench capacitors. High lifetime and low diode leakage have been measured in silicon grown laterally over oxide patterns and storage trenches, indicating that this technology is indeed suitable for DRAMs. Fully function DRAM Cells have been fabricated showing that selective silicon epitaxy does provide the high leverage needed to scale future generations of DRAMs.

ACKNOWLEDGEMENTS

The author would like to thank N.C.C. Lu, B. Ginsberg, S. Mader, T.V. Rajeevakumar, and B. Machesney for their contributions to this work. Support from the Yorktown Silicon Facility was also invaluable.

REFERENCES

- ¹ H. Sunami, IEDM Tech. Dig., 694 (1985).
- ² N.C.C. Lu, P.E. Cottrell, W.J. Craig, S. Dash, D.L. Critchlow, R.L. Mohler, B.J. Machesney, T.H. Ning, W.P. Noble, R.M. Parent, R.E. Scheuerlein, E.J. Sprogis, and L.M. Terman, IEEE J. Solid-State Circuits SC-21, 627 (1986).
- ³ D. Kenney, E. Adler, B. Davari, J. DeBrosse, W. Frey, T. Furukawa, P. Geiss, D. Harmon, D. Horak, M. Kerbaugh, C. Koburger, J. Lasky, J. Rembetski, W. Schwittek, and E. Sprogis, Symp. on VLSI Tech., Dig. of Tech. Papers, 25 (1988).
- ⁴ G.B. Bronner, N.C.C. Lu, T.V. Rajeevakumar, B. Ginsberg, and B. Machesney, Symp. on VLSI Tech., Dig. of Tech. Papers, 21 (1988).
- ⁵ N.C.C. Lu, T.V. Rajeevakumar, G.B. Bronner, B. Ginsberg, B.J. Machesney, and E.J. Sprogis, IEDM Tech. Dig, 694 (1988).
- ⁶ B.D. Joyce and J.P. Baldrey, Nature 195, 485 (1962).
- ⁷ K. Tanno, N. Endo, H. Kitajima, Y. Kurogi, and H. Tsuya, Jap. J. of Appl. Phys. 21, L564 (1982).
- ⁸ H. Kitajima, A. Ishitani, N. Endo, and K. Tanno, Jap. J. Appl. Phys. 22, L783 (1983).
- ⁹ B. Ginsberg, G. Bronner, and S. Mader, Extended Abst. Fall Meeting, Electrochem. Soc. 87-2, 991 (1987).
- ¹⁰ F. Secco d'Aragona, J. Electrochem. Soc. 119, 948 (1972).
- ¹¹ J. Borland and C. Drowley, Solid State Technology 28, 141 (1985).

SELECTIVE EPITAXY OF $\text{Al}_x\text{Ga}_{1-x}\text{As}$ AND $\text{Al}_x\text{Ga}_{1-x}\text{As}$ BASED STRUCTURES

M.S. Goorsky, T.F. Kuech, and R. Potemski
IBM T.J. Watson Research Center, P.O. Box 218 Yorktown Heights, NY 10598

ABSTRACT

Selective epitaxy of $\text{Al}_x\text{Ga}_{1-x}\text{As}$ by MOVPE was accomplished using diethyl gallium chloride and diethyl aluminum chloride as the metalorganic precursors. Selective epitaxy was achieved for Al containing compounds under certain growth conditions, but AlAs growth was not selective. Quantum wells were selectively grown on masked substrates and unpatterned GaAs wafers; QW luminescence was observed from all samples. Additionally, near gap luminescence was observed from $\text{Al}_x\text{Ga}_{1-x}\text{As}$ heterostructures over the entire 550 °C - 850 °C growth temperature range. The ternary alloy composition was found to be a strong function of the gas phase composition and growth temperature. A simple thermodynamic model explained the dependence of growth rate and composition on these parameters.

INTRODUCTION

The growth of epitaxial semiconductor layers on specific regions of a substrate is advantageous for several device applications. This technique, referred to as selective epitaxy (SE), has been advanced primarily for Si technology, where, for example, isolated pn arrays have been successfully fabricated.(1) Recently, truly selective area growth of GaAs has been demonstrated.(2) However, the selective area growth of ternary III-V semiconductors, especially $\text{Al}_x\text{Ga}_{1-x}\text{As}$, is difficult to achieve in conventional metal-organic vapor phase epitaxy (MOVPE) when using the usual $\text{Ga}(\text{CH}_3)_3$ and $\text{Al}(\text{CH}_3)_3$ growth precursors. While these precursors do produce excellent material, they promote conformal deposition of the $\text{Al}_x\text{Ga}_{1-x}\text{As}$. This result is due to the inherently high supersaturation of the precursors and the lack of a suitable etching or back reaction. The hot wall halide Vapor Phase Epitaxy technique (VPE) is suitable for the SE growth of at least GaAs(3). In this technique, the formation of GaCl is achieved by passing HCl over a Ga metal source upstream from the substrate. The halide is transported to the substrate and promotes the deposition of GaAs. This technique is also used to grow $\text{Al}_x\text{Ga}_{1-x}\text{As}$ via an Al-Ga metal source although VPE $\text{Al}_x\text{Ga}_{1-x}\text{As}$ is not necessarily selective. Drawbacks of the VPE method for the growth of $\text{Al}_x\text{Ga}_{1-x}\text{As}$ include: the inhomogeneous metal depletion of the source, the strong dependence of the epilayer composition on the source temperature and thickness, and the presence of excess HCl in the gas stream with which AlCl reacts to form AlCl_2 , a species that does not form AlAs at typical growth temperatures. An additional limitation involves the reaction between the hot quartz wall and the AlCl. This halide attacks the wall and Si from the quartz is transported through the gas phase and into the epilayer. Unintentional Si doping up to 10^{18} cm^{-3} attributable to this effect has been reported(4). Such a high background impurity level severely limits applications for $\text{Al}_x\text{Ga}_{1-x}\text{As}$ obtained from halide VPE.

Recently, the selective growth of high purity ($n < 10^{16}\text{ cm}^{-3}$) GaAs in a typical MOVPE reactor using Diethyl Gallium Chloride (DEGaCl , $(\text{C}_2\text{H}_5)_2\text{GaCl}$) has

Mat. Res. Soc. Symp. Proc. Vol. 158. ©1990 Materials Research Society

been successfully demonstrated.(2) In this presentation, the use of this novel chemistry has been extended to $\text{Al}_x\text{Ga}_{1-x}\text{As}$ growth, using DEGaCl and its counterpart, Diethyl Aluminum Chloride, (DEAlCl , $(\text{C}_2\text{H}_5)_2\text{AlCl}$). With this system, the benefits of MOVPE (controlled reactant introduction, cold wall system) and halogen VPE (selectivity, near equilibrium conditions) are combined. Single heterostructure layers and GaAs quantum wells (QW) were grown with this chemistry. The layers were characterized and a model was developed to show that growth is controlled by thermodynamic factors.

EXPERIMENTAL PROCEDURE

DEGaCl and DEAlCl were introduced into a cold wall chamber with AsH_3 and Pd-purified H_2 . The system was operated at 0.1 atm with estimated mole fractions of DEGaCl and DEAlCl ranging from 1.5×10^{-4} to 2.2×10^{-5} and a V/III ratio of 30 for growth of $\text{Al}_x\text{Ga}_{1-x}\text{As}$ heterostructures. The binary AlAs was also grown, with a DEAlCl mole fraction of about 2.7×10^{-4} . All layers were grown on bare GaAs wafers and SiO_2 and Si_3N_4 coated wafers which were patterned to introduce arrays of windows of various shapes to the GaAs substrate. The growth temperature ranged from 550 to 850 °C. The GaAs quantum wells (QW) were grown at 700 °C. The structures were characterized with Double Crystal X-ray Diffraction (XRD) and Photoluminescence (PL). The XRD apparatus used (400) reflections and $\text{Cu}_K\alpha$ x-rays with the reference GaAs crystal and the sample crystal in the (+,-) configuration. The PL was excited with an Ar+ laser and analyzed with a 2/3 m spectrometer and a photomultiplier detector. The spectra were recorded at $T = 2.8\text{K}$.

EXPERIMENTAL RESULTS

SELECTIVITY

AlAs could not be grown selectively even at 800 °C. However, $\text{Al}_x\text{Ga}_{1-x}\text{As}$ could be grown selectively over a suitable range of composition and growth temperatures. Increasing the relative DEGaCl mole fraction improved the selectivity as did increasing the growth temperature. Growth of the quantum well structures was also selective. The properties of the layers were analyzed with XRD and PL.

X-RAY DIFFRACTION

The $\text{Al}_x\text{Ga}_{1-x}\text{As}$ heterostructures exhibited rocking curves that matched those predicted by kinematical modeling(5). Comparison of rocking curves from samples grown at different temperatures (same conditions otherwise) showed that the Al fraction increased non-linearly with growth temperature. This behavior is illustrated in Fig.1 where rocking curves from samples grown at 600 and 700 °C are shown. In general, the area under the epilayer diffraction peak decreased with increasing growth

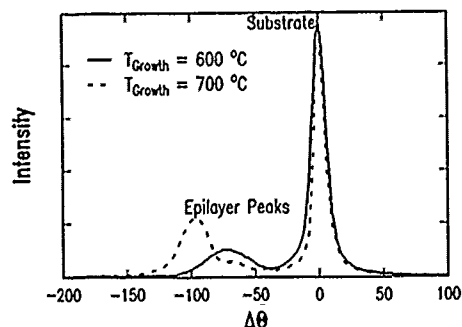


Figure 1: Rocking curves of $\text{Al}_x\text{Ga}_{1-x}\text{As}$ layers grown on GaAs at 600 °C and 700 °C.

temperature, showing that the epilayer thickness decreased. This behavior contrasts the situation for MOVPE with alkyl precursors where the Al mole fraction had been found to be relatively independent of growth temperature over the temperature range used here.

PHOTOLUMINESCENCE

The samples generally possessed strong near gap luminescence. Composition determination, using $E_{PL} = 1.512 + 1.455X_{Al}(6)$, where E_{PL} corresponds to the near gap luminescence emitted from the epilayer, was consistent with the composition found by XRD. Representative PL spectra are shown in Fig.2. In MOVPE material grown with alkyls, luminescence was generally observed to degrade as the growth temperature is reduced. This behavior has been attributed to the incorporation of oxygen or deep luminescence killers at low temperatures(7). With the present growth chemistry, however, near gap luminescence is observed even at the lowest growth temperature employed, 550 °C, as is shown in Fig.2. In contrast to MOVPE with alkyl precursors, the luminescence decreases as the temperature increases. This may be due to the reaction of the Cl-based precursors, most probably $AlCl_3$, with the masking SiO_2 which could lead to subsequent oxygen incorporation. Such an etching reaction would be accelerated as the growth temperature is increased.

Luminescence from QW structures, grown at 700 °C, is displayed in Fig.3. The luminescence from the $Al_xGa_{1-x}As$ layers was stronger on the patterned pieces than on the bare wafer with the highest energy peak corresponding to $Al_{0.30}Ga_{0.70}As$. The QW luminescence from the epilayer on the bare substrate was fairly sharp (27 meV) but the QW luminescence from the patterned wafer is much broader. This broadness partly results from non-uniform thickness of the GaAs well. Such conditions may arise if the growth of $Al_xGa_{1-x}As$ is not as strongly orientation dependent as GaAs.

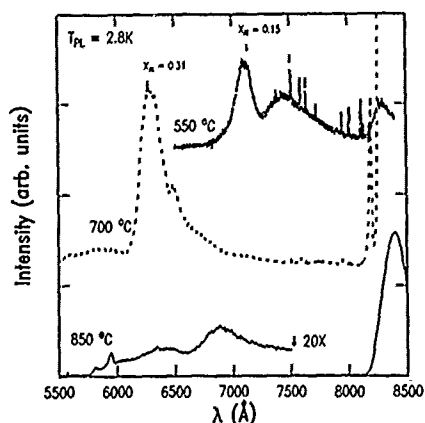


Figure 2: Photoluminescence spectra of samples grown at 550 °C, 700 °C and 850 °C.

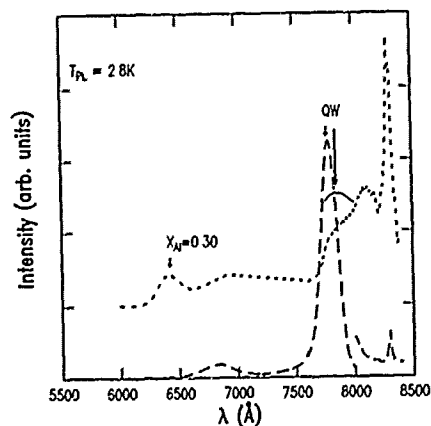
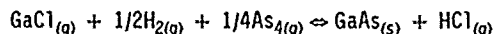


Figure 3: Luminescence from QW structure. The patterned piece exhibits broader QW luminescence and more pronounced $Al_xGa_{1-x}As$ luminescence.

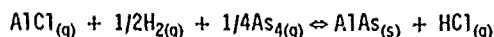
THERMODYNAMIC MODEL

Thermodynamic growth models had been used to explain growth trends observed in the halide process for both $\text{Al}_x\text{Ga}_{1-x}\text{As}$ (8) and $\text{In}_x\text{Ga}_{1-x}\text{As}$ (9). In those cases, however, the lack of knowledge concerning the source conditions limited the predictive powers of the models. In the present case, the initial gas phase constituent concentrations are known, thus improving the reliability of a model based on knowledge of the initial conditions. Although a supersaturated flowing gas system that promotes the precipitation of its gas phase constituents is not an equilibrium reaction, the general trends observed in both Si(10) and III-V (8,9) epitaxy involving Cl-containing species had been successfully accounted for using thermodynamic arguments. In this experiment, the ability to grow selectively suggests that the growth is near equilibrium, i.e., the supersaturation of the DEGaCl and DEAlCl is not so great so as to promote nucleation on the masking material.

In this spirit, a simple thermodynamic model is proposed to explain both the composition and growth rate changes with temperature. In this model, certain assumptions are made. The first, of course, is that the growth front is at equilibrium. This is equivalent to assuming that there is no transport limitation in the supply of nutrients to the growth front. Second, the growth of $\text{Al}_x\text{Ga}_{1-x}\text{As}$ is treated as the independent formation of AlAs and GaAs. The plausibility of this assumption is supported as the V/III ratio $\gg 1$, indicating that the metal-containing precursor limits the extent of the reaction, and because $\text{Al}_x\text{Ga}_{1-x}\text{As}$ behaves as an ideal solution under these growth conditions(11). Third, it is assumed that the DE(Ga,Al)Cl precursor cracks in the gas phase to inert hydrocarbons and $(\text{Ga,Al})\text{Cl}$ and that the arsine cracks to form As_4 . The overall reactions governing the growth of GaAs and AlAs are



and



The equilibriums established are

$$\frac{a_{\text{GaAs}}(P_{\text{HCl}}^0 + x)}{(P_{\text{GaCl}}^0 - x)(P_{\text{H}_2}^0 - 0.5x)^{0.5}(P_{\text{As}_4}^0 - 0.25x)^{0.25}} = K_{\text{GaAs}}$$

and

$$\frac{a_{\text{AlAs}}(P_{\text{HCl}}^0 + y)}{(P_{\text{AlCl}}^0 - y)(P_{\text{H}_2}^0 - 0.5y)^{0.5}(P_{\text{As}_4}^0 - 0.25y)^{0.25}} = K_{\text{AlAs}}$$

where $P_{(\text{gas species})}$ corresponds to the input gas species partial pressures, x and y are the amount of GaAs and AlAs deposited, respectively and K is the equilibrium constant for each reaction. The equilibrium constant for GaAs is derived from data by Kirwin(12) while that of AlAs was obtained from JANAF data(13). The activities of the solid phases are set to one and the amount of GaAs and AlAs produced (which equals the amounts of GaCl or AlCl reacted, x and y in the above equations) are determined as a function of temperature.

Fig.4 displays the thermodynamically predicted composition and experimental data. The upper line corresponds to a solution to the above equations using the input partial pressures of the reactants and the error bars correspond to a $\pm 5\%$ uncertainty in the enthalpy of the reactions. The difference

between the data and the model values can be due to several factors. For example, the vapor pressure of GaCl at room temperature is not well known. If this value is greater than that reported by the manufacturers, a shift in the model predictions will result. For example, the lower line corresponds to a higher P_{GaCl} (by about 40%) which gives almost identical compositions as found experimentally. Even without such manipulation, the good fit between the experimental data points and the model predictions reinforces the hypothesis that thermodynamic factors control the composition of the ternary using the DE(Ga,Al)Cl growth chemistry.

An alternate consideration of the dependence on temperature compares the growth rate of each species (which can be predicted by comparing the supersaturation of the species). For these experimental conditions, the AlCl is always in very high supersaturation over the entire temperature range and thus, the observed growth of the AIAs does not change with temperature. For GaAs, however, the reaction of GaCl to GaAs goes nearly to completion at low temperature (500 °C) but is negligible at higher temperatures (800 °C). Relative growth rates for these species are illustrated in Fig.5. Experimentally, the growth rate of the $\text{Al}_x\text{Ga}_{1-x}\text{As}$ was ≈ 0.017 , 0.014, and 0.011 $\mu\text{m}/\text{min}$, at 600, 700, and 800°C respectively. The ratio of these thicknesses compares favorably to the prediction displayed in Fig.5, indicating that the reduced growth of GaAs reduces the total film thickness and increases the Al mole fraction of the layer.

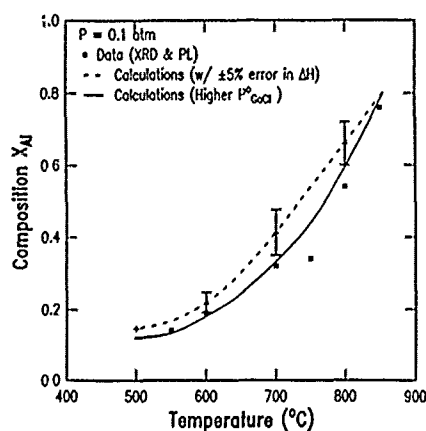


Figure 4: Changes in Al composition vs. temperature according to the equilibrium model. The experimental data tracks the predicted composition values.

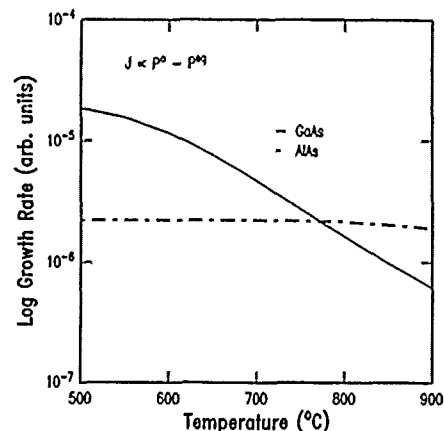


Figure 5: Growth rate of AIAs and GaAs determined by the equilibrium calculations described in the text.

The model indicates that the lack of AIAs selective growth, in the entire temperature range studied, results from the extremely high AlCl supersaturation. This high supersaturation promotes nucleation on the insulating field as well as in the GaAs window; similar behavior is observed for alkyl-based metalorganic precursors. It is conjectured, however, that AIAs growth here would exhibit selectivity at higher temperatures. Furthermore, based on the trends illustrated by the thermodynamic model, it is also expected that the growth of GaAs will not be selective at lower temperatures where the GaCl supersaturation is nearly 100%.

The model does not take into account the formation of other species such as AlCl_3 or the effect of the production of HCl on downstream deposition. This latter consideration impacts the overall growth uniformity. Future work will address these issues as well as the overall reaction involving the formation of a ternary semiconductor without the constraint of independent binary growth. For example, the production of HCl from the AlAs formation will reduce the growth rate of GaAs . Based on these thermodynamic considerations, the conditions for selective growth will also be explored.

CONCLUSION

The selective epitaxial growth of the $\text{Al}_x\text{Ga}_{1-x}\text{As}$ system has been demonstrated in a conventional MOVPE reactor using novel growth chemistry. Good luminescence and the physical integrity of these layers was observed; quantum wells grown selectively also show promise for future device applications involving this growth chemistry. A thermodynamic model was used to describe the growth parameter dependences of thickness and alloy composition. Reasonable agreement between the model and experimental results strongly suggest that thermodynamic factors control many aspects of the growth within the $\text{Al}_x\text{Ga}_{1-x}\text{As}$ system utilizing this growth chemistry.

REFERENCES

1. S.M. Blumenfeld, G.W. Ellis, R.W. Redington, and R.H. Wilson, IEEE Trans. Electron. Devices, **ED-18** 1036 (1971).
2. T.F. Kuech, M.A. Tischler, and R. Potemski, Appl. Phys. Lett. **54** 910 (1989).
3. F.W. Tausch, Jr. and A.G. Lapierre, III, J. Electrochem. Soc. **112** 706 (1965).
4. F. Hasegawa, et al., Jpn. J. Appl. Phys. **27**, L254 (1988).
5. V.S. Speriosu, J. Appl. Phys. **52**, 6094 (1981).
6. T.F. Kuech, et al., Appl. Phys. Lett. **51**, 505 (1987).
7. J. Hallais, J.P. Andrew, and A. Mircea-Roussel, J. Electron. Mater. **10**, 665 (1981).
8. S. Minegawa and H. Seki "4th International Conference on Chemical Vapor Deposition", G.F. Wakefield, ed., 51 (1973).
9. S. Minegawa, H. Seki, and H. Eguchi, Jpn. J. Appl. Phys. **11**, 855 (1972).
10. J. Bloem and L.J. Giling in "Current Topics in Materials Science" Vol.1, E.I. Caldis, ed. 303 (1983).
11. G.B. Stringfellow, J. Crystal Growth, **62**, 225 (1983).
12. D.J. Kirwan, J. Electrochem. Soc. **117**, 1572 (1970).
13. JANAF Thermochemical Tables (NBS, Washington, D.C., Supp 1974/1975) (1971).

SURFACE REACTION MECHANISMS IN SELECTED AREA EPITAXY OF II-VIs

STUART J.C. IRVINE, H. HILL, J.E. HAILS, A.D. PITT AND J.B. MULLIN
 Royal Signals and Radar Establishment, Malvern, Worcestershire. UK

ABSTRACT

Laser-induced selected area epitaxy of CdTe thin films on GaAs substrates has been investigated and the role of vapour phase and surface reactions considered. Photo-enhanced growth rates of CdTe have been measured as a function of UV laser intensity and as a function of Cd to Te alkyl ratios. The growth rates are not simply determined by vapour phase photo-dissociation but also by a photolytic reaction on the surface. The latter enables good pattern definition where the growth rate is enhanced by the incident uv radiation. The factors that determine the photo-enhancement are considered in the light of the Langmuir-Hinshelwood model.

INTRODUCTION

Photo-enhancement of epitaxial film growth rates using ultraviolet (uv) radiation has been attributed to the enhanced decomposition rate of the organometallic precursors [1]. This can arise from photon absorption in the vapour resulting in photolysis, or absorption in the substrate with sufficient energy to enhance pyrolysis [1,2]. Pyrolysis can be enhanced using a pulsed laser source or focussed cw source to bring about heating of the substrate. The objectives of the present work are to use low intensity cw radiation so that the heating effect is negligible and to investigate photolytic reactions that can lead to patterning of II-VI semiconductor thin films. Earlier work in our laboratory has shown the potential for patterning of CdTe epitaxial films in this way [3,5]. In-situ diagnostic techniques such as time resolved reflectivity (TRR) [4-6] have been developed to investigate the growth process. TRR has enabled the precise measurement of growth rate at a predetermined position on the substrate and at the centre of the Gaussian laser beam profile [5]. Photo-patterned growth of epitaxial films could be a key process for in-situ fabrication of devices in II-VI materials such as arrays of mercury cadmium telluride (MCT) infrared detectors. However, the usefulness of this process will be determined by the ability to control the photo-enhancement process and achieve sufficient pattern definition. This paper considers in greater detail these surface photolytic reactions and ways in which they may be enhanced.

EXPERIMENTAL

The growth experiments were carried out in a horizontal MOVPE reactor with a silica window and separate purge flow described previously [5]. The precursors were electronic grade dimethyl cadmium (Me_2Cd), with either diethyl telluride (Et_2Te) or dimethyl telluride (Me_2Te) and molecular sieve dried helium carrier gas. Substrates were GaAs (100) $2^\circ\text{--}110$ supplied by ICI Wafertech. The substrates were etched for five minutes in a 5:1:1 solution of H_2SO_4 : H_2O_2 : H_2O . Epitaxial growth was preceeded by a 10 minute heat clean in pure hydrogen at 350°C and the growth of a CdTe nucleation layer approximately 1000Å thick. Layers nucleated in this way were assessed using an x-ray texture camera and found to be epitaxial [4,5].

An intra cavity frequency doubled argon ion laser with cw output of 100 to 150 mW at 257nm was used for photo-excitation. A 2mW HeNe laser was used for in-situ monitoring of growth by the TRR method [5,6]. The experimental arrangement is shown in Fig 1 with the uv laser beam illuminating the substrate perpendicularly and the HeNe beam reflected from the surface. For photo-patterning experiments a silica lens and mask are inserted in the uv beam above the silica window.

RESULTS AND DISCUSSIONS

Growth rates for CdTe have been measured as a function of uv intensity using TRR. A comparison was made between the tellurium precursors Et_2Te and Me_2Te to help

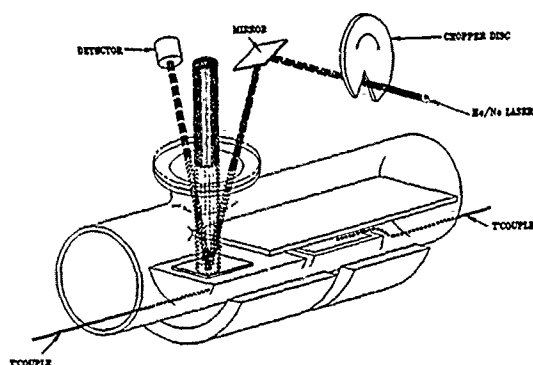


Fig 1. Reactor cell for laser-epitaxy of CdTe with TRR diagnostics

concentrations of Te and Cd have been calculated from which the diffusion limited growth rates have been estimated as a function of uv intensity. As the decomposition process is photolytic, the estimated growth rates only show a small variation between 250°C and 300°C. The calculated, diffusion limited, growth rate is shown as a broken line in Fig 2, and is proportional to uv intensity. The experimental growth rates differ in three respects, (a) the growth rates at 250°C and 300°C are significantly different, (b) the function of growth rate with uv intensity is different and (c) the growth rates are lower than the diffusion limited values over the range of intensities 5mW/cm² to 90mW/cm². These results indicate that growth rate is limited by surface kinetics.

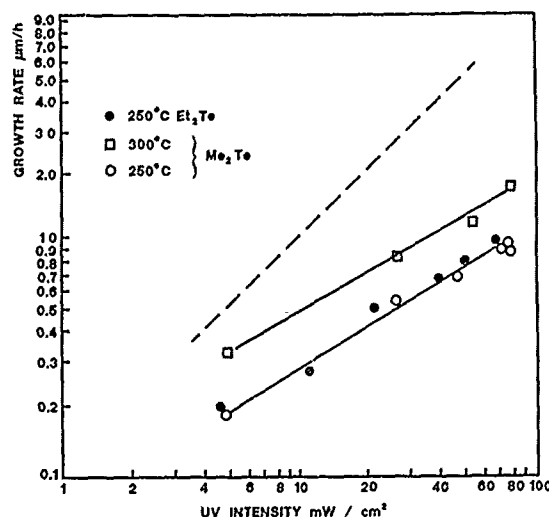


Fig 2. CdTe growth rates as a function of uv intensity (at 257nm), the predicted transport limited growth rate is shown as a broken line

illuminate photo-enhancement behaviour. The precursor partial pressures were 1.3 Torr Me₂Cd, 0.6 Torr Et₂Te and 0.7 Torr Me₂Te. The growth rates plotted in Fig 2 all show a sub-linear dependence on uv intensity ranging from I^{0.56} at 300°C to I^{0.75} at 250°C. Growth rates at 250°C do not show any significant difference between Et₂Te or Me₂Te. Measurements of absorption cross sections by Hails et al [7] for Et₂Te and Me₂Te at the laser wavelength of 257nm were 0.091Å and 0.118Å respectively. This, combined with the slightly higher inlet partial pressure for Me₂Te, would be expected to give a higher yield of Te in the vapour. The vapour phase

Fig 3 shows a comparison of growth rates at 250°C measured with (a) a continuous HeNe beam and (b) a chopped HeNe beam. The growth rates measured in the continuous beam are significantly higher. The 633nm wavelength beam is absorbed in the vapour and therefore could not contribute to the vapour photolysis yield. The estimated intensity on the surface was 70mW/cm² for the continuous beam, approximately 60% of which would be absorbed. The absorbed photons could help to enhance growth rate by charge transfer aided desorption of reaction products [8]. Enhancement of growth rate for photon energies greater than the band gap have also been observed by Fujita et al [9] for ZnSe growth. Micrographs of the CdTe surface after experiments with

chopped and continuous HeNe beams are shown in Fig 4. Fig 4(b) shows some roughening where the continuous HeNe beam was incident on the surface. This was seen every time a continuous beam was used but rarely occurred with the chopped beam.

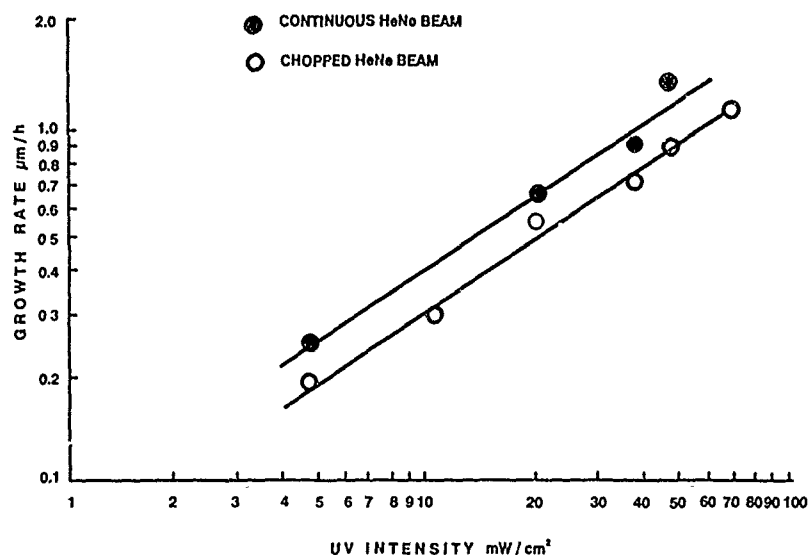


Fig 3. Comparison of growth rates, between chopped and continuous HeNe laser beam used for reflectivity experiment. The substrate temperature was 250°C and the precursors used were Me_2Cd and Et_2Te .

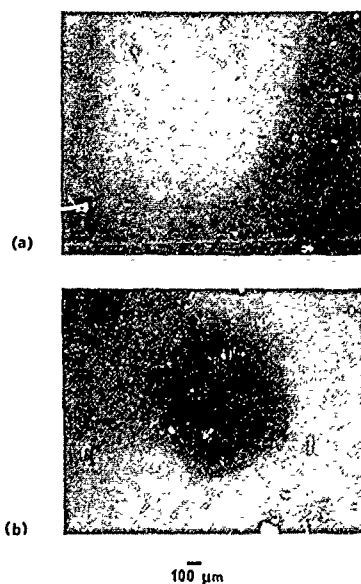


Fig 4. Micrographs of CdTe surface after growth with (a) chopped and (b) continuous HeNe beam

A requirement for selected area photo-epitaxy is that the photolytic growth rate is much greater than the pyrolytic which can be expressed as the photo-enhancement factor [3]. The data in Fig 2 are shown replotted, as photo-enhancement, in Fig 5. The main difference with the growth rate plot is the widely differing photo-enhancement factors at 250°C for Me_2Te and Et_2Te . The photo-enhancement factors for Me_2Te are higher because of the lower pyrolytic growth rates; consistent with its greater thermal stability.

Growth rates have also been determined as a function of Cd:Te alkyl ratio for photolytic and pyrolytic growth. The data shown in Fig 6 compares pyrolytic growth at 320°C using Et_2Te (0.66 Torr), photolytic growth at 300°C using Me_2Te (0.67 Torr), at a low uv intensity of 31mW/cm²; and at 320°C with a higher uv intensity of 110mW/cm². The pyrolytic growth and low uv intensity show a saturation in growth rate above an alkyl ratio of 2. The growth rate at the higher uv intensity continues to rise up to the highest ratio measured of 4.35.

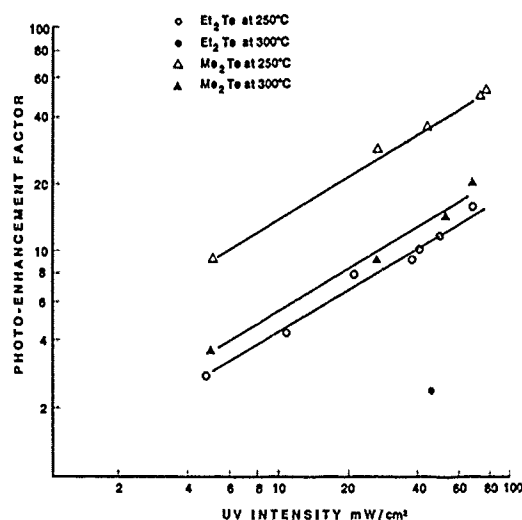


Fig 5. Comparison of photo-enhancement factors for CdTe from the precursors Me_2Cd with Me_2Te and Et_2Te at 250°C and 300°C

Modelling of surface kinetics

The functions of growth rate with uv intensity and Cd/Te alkyl ratio can be modelled assuming surface kinetically limited growth. The Langmuir-Hinshelwood model has been used by previous authors to describe the surface kinetic processes in MOVPE growth of II-VI's [10,11]. This model can be modified to include photo-decomposition of the precursors, site blocking from reaction products and laser assisted desorption of these products.

Firstly, allowing for photo-decomposition and assuming that the reactant species on the surface are Cd and Te, the elemental partial pressures can be equated to the alkyl partial pressures.

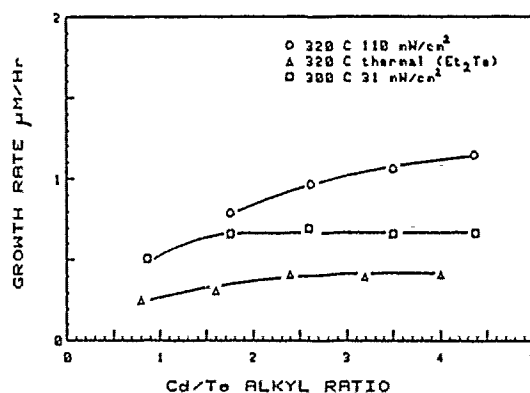


Fig 6. CdTe growth rate as a function of Cd/Te alkyl ratio for Te alkyl partial pressures given in text.

$$P_{\text{Cd}} = \frac{k_1}{V} I P_{\text{Me}_2\text{Cd}} \quad (1)$$

$$P_{Te} = \frac{k_2}{v} I p_{Me_2Te} \quad (2)$$

Where k_1 and k_2 are rate constants for photo-decomposition, I is the laser intensity and v the flow velocity. For independent adsorption on the group II and group VI sites, the Langmuir-Hinshelwood equation can be written as follows.

$$R = \frac{k \beta_{Cd} \beta_{Te} p_{Me_2Cd} p_{Me_2Te} I^2}{(1 + \gamma_1 I p_{Me_2Cd}) (1 + \gamma_2 I p_{Me_2Te})} \quad (3)$$

where R is the growth rate, k is a rate constant, β_{Cd} and β_{Te} are ratios of rate constants for adsorption and desorption for Cd and Te respectively. The factors γ_1 and γ_2 are defined as follows:

$$\gamma_1 = \frac{\beta_{Cd} k_1}{v} \quad (4)$$

and

$$\gamma_2 = \frac{\beta_{Te} k_2}{v} \quad (5)$$

It can be seen from equation (3) that at low intensities $R \propto I^2$ and at high intensities R saturates and becomes independent of I . It can be assumed that for the regime of intensity and alkyl vapour pressures for the data in Fig 2 that the sub-linear dependence on I is closer to the saturation limit.

However, the behaviour with Cd/Te alkyl ratio cannot be explained by the simple model given in equation (3). For a leveling off of growth rate with p_{Me_2Cd} , $\gamma_1 I p_{Me_2Cd} > 1$. This will occur at a lower p_{Me_2Cd} for higher values of I , the opposite behaviour to that observed in Fig 6. This behaviour can be explained if a third, site blocking, species is introduced on the surface. This could be free radicals such as CH_3^{\cdot} or $C_2H_5^{\cdot}$ released from photo-decomposition of the alkyls. For simplicity of calculation just radicals released from Me_2Cd will be introduced here, the qualitative results are the same as those derived from including all radicals. The partial pressure of the blocking species p_b , by analogy with equations (1) and (2), is

$$p_b = \frac{k_3}{v} I p_{Me_2Cd} \quad (6)$$

Assuming adsorption onto both Cd and Te sites, equation (3) can be modified as follows:

$$R = \frac{k \beta_{Cd} \beta_{Te} p_{Me_2Cd} p_{Me_2Te} I^2}{(1 + I p_{Me_2Cd} (\gamma_1 + \gamma_3)) (1 + I (\gamma_2 p_{Me_2Te} + \gamma_4 p_{Me_2Cd}))} \quad (7)$$

$$\text{where } \gamma_3 = \frac{\beta_{Me}^{(Cd)} k_3}{v} \quad (8)$$

$$\text{and } \gamma_4 = \frac{\beta_{Me}^{(Te)} k_3}{v} \quad (9)$$

$\beta_{Me}^{(Cd)}$ and $\beta_{Me}^{(Te)}$ are the ratios of adsorption to desorption of methyl radicals on Cd and Te sites respectively. If photon absorption on the surface assists desorption of the site blocking Me radicals then γ_3 becomes an inverse function of intensity. The criterion for levelling off of growth rate with increasing p_{Me_2Cd} is now $I p_{Me_2Cd} (\gamma_1 + \gamma_3) > 1$. If at low

intensities γ_3 is dominant over γ_1 (effective site blocking) and $\gamma_3 \propto I^{-n}$ where $n > 1$ then the criterion becomes $c p_{\text{Me}_2\text{Cd}}^{1-n} > 1$ where c is a constant. This can explain an increase in $p_{\text{Me}_2\text{Cd}}$ for higher intensities as observed in Fig 6.

These results have very important consequences for selected area photo-epitaxy because photo-assisted desorption of site blocking species will bring about a modulation of growth rate according to incident uv intensity. The photo-assisted desorption model can also explain the enhancement in growth rate when visible radiation is incident on the surface.

Selected area epitaxy of CdTe

A series of Nomarski contrast micrographs of CdTe patterns produced by projecting mask patterns onto the surface are shown in Fig 7. The growth conditions were $\text{Me}_2\text{Cd}/\text{Me}_2\text{Te}$ ratio of 1.75, substrate temperature 300°C and maximum uv intensity of $110\text{mW}/\text{cm}^2$. The bar pattern in Fig 7(a) has been profiled by Dektak scan and shown similar behaviour to a bar pattern reported previously and deposited from Me_2Cd and Et_2Te [5] where the actual peak-to-valley ratio is less than the photo enhancement factor. The reduced photo-enhancement on patterned structures is due to vapour spread of Cd and Te atoms. With a better understanding of the site blocking mechanism, growth rates could be reduced further in the "dark" areas by suitable choice of blocking species and concentrations.

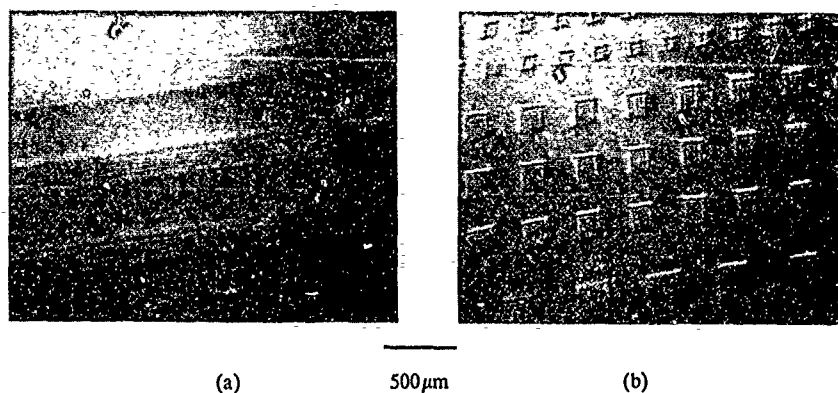


Fig 7. Nomarski contrast micrographs of CdTe selected area epitaxy at 300°C using Me_2Cd and Me_2Te precursors, showing (a) bar pattern and (b) mesa pattern

CONCLUSIONS

Detailed measurements of photo-enhanced growth rates for CdTe using TRR measurements have shown that the growth rate is not vapour transport limited but is limited by surface kinetics. The behaviour of growth rate as a function of uv intensity and as the ratio of Cd and Te alkyl partial pressures can be explained by the Langmuir-Hinshelwood model with a term for photo-assisted desorption of a site blocking species. Well defined bar and mesa patterns of CdTe have been grown by the projection of mask patterns with the uv laser beam. The ability to produce these patterns is further evidence for the photo-desorption mechanism. Further improvements in pattern definition are expected with improved understanding and control of this mechanism.

ACKNOWLEDGEMENTS

Mrs J Clements is warmly thanked for technical assistance with the epitaxial growth experiments and substrate preparations.

REFERENCES

1. S.J.C. Irvine, CRC Critical Reviews in Solid State and Materials Science, 13, 279 (1987).
2. V.M. Donnelly, J.A. McCaulley, V.R. McCrary, C.W. Tu and J.C. Beggy, Mat. Res. Soc. Symp. Proc. vol 129 (1989).
3. S.J.C. Irvine, H. Hill, O.D. Dosser, J.E. Hails, J.B. Mullin, D.V. Shenai-Khatkhate and D. Cole-Hamilton, Materials Lett. 7, 25 (1988).
4. S.J.C. Irvine, H. Hill, G.T. Brown, S.J. Barnett, J.E. Hails, O.D. Dosser and J.B. Mullin, J. Vac. Sci. Technol. (in press).
5. S.J.C. Irvine, H. Hill, J.E. Hails, J.B. Mullin, S.J. Barnett, G.W. Blackmore and O.D. Dosser, J. Vac. Sci. Technol. (in press).
6. J.J. Zinck, P.D. Brewer, J.E. Jensen, G.L. Olson and L.W. Tutt, Appl. Phys. Lett. 52, 1434 (1988).
7. J.E. Hails, S.J.C. Irvine, J.B. Mullin, D.V. Shenai-Khatkhate and D. Cole-Hamilton, Mat. Res. Soc. Symp. Proc. Vol 131, 75 (1989).
8. F.A. Houle, Mat. Res. Soc. Symp. Proc. 29, 203 (1984).
9. Sz. Fujita, A. Tanabe, T. Sakamoto, M. Isemura and Sg. Fujita, J. Crystal Growth 93, 750 (1988).
10. I. Bhat and S.K. Ghandhi, J. Electrochem. Soc.: Solid State Science and Technology, 131, 1923 (1984).
11. S. Haq, PhD. Thesis, University of Birmingham, 1988.

Novel Stacked CMOS Process by Local Overgrowth

René P. Zingg^o, B. Höfflinger^o and G. W. Neudeck*

^oInstitute for Microelectronics, Allmandring 30a, D-7000 Stuttgart 80, FRG;
Tel: 0049-711-685-5777, FAX: 0049-711-685-5930

*Purdue University, Dept. of El. Engineering, West Lafayette, IN 47907, USA

Abstract

A six mask process that yields stacked CMOS circuits is presented. Transistors that were built in reverse order (i. e. the gate first, the gate dielectric second, and only then the channel region) exhibit comparable parameters as conventional devices. A novel device has been built whose current drive is three times that of FETs built in substrate material. The vertical stacking of complementary MOS transistors made it possible to build an inverter with symmetric switching characteristic within the area of a single transistor.

I. Introduction

Three-dimensional integration is attracting growing interest due to the possibility of increasing circuit functionality and reducing interconnect wiring [1]. The silicon-on-insulator (SOI) films used for consecutive active layers have the potential to alleviate numerous parasitic effects of bulk circuits, effects such as latch-up, punch-through and hot carriers. Design studies reveal that up to 80% area reduction can be obtained with a second active layer [2]. Such circuits have been realized in recrystallized material [3], but lattice defects reduced their performance. In the following, a new process will be presented and characterized that yields transistors stacked on top of each other and novel devices with improved current drive.

II. Local Overgrowth Process

The processing for local overgrowth circuits starts with a standard NMOS in a (100)-oriented substrate with oxidized polysilicon gates. On top of the transistors, epitaxy is grown selectively and laterally over oxide on a device scale [4]. Crystalline seeding for local epitaxy is provided by rectangular openings in the gate oxide that also provide an electrical contact between the complementary devices (Fig. 1). These seeds in the drain regions of NMOS transistors are aligned with $\langle 100 \rangle$ directions to minimize stacking faults that occur on growth fronts with (110) orientation. No

lattice defects are caused by the drain implant in the seed area, apparently the growth conditions are sufficient to anneal implant damages. The epitaxy step is performed at reduced temperatures of 850-900°C to minimize the thermal budget on the substrate device and eliminate potential damage to oxide layers [5]. Growth rates for the selective epitaxy with trichlorosilane were 60-100nm/min in the temperature window considered here. This silicon source-gas allows selective growth without the addition of HCl, increasing the intrinsic resistivity of the material to 300Ω-cm. The quality of the overgrowth can be verified by the well-established crystalline facets on the local overgrowths (LOGs).

At the temperatures considered here, epitaxial growth is surface-reaction limited, which results in identical growth rates for (100)-planes, both laterally (on oxide) and vertically. Since channel and metallization contact have to be provided on the lateral part of the overgrowth, lateral extension and, therefore, the thickness of the overgrowth need to be about 10μm for a process with 3μm channel length. For further processing, the overgrowth is thinned by chemo-mechanical polishing [6] to about 0.5μm thickness. This polishing is made self-limiting by a uniformly applied plasma-oxide, which is removed readily on top and at the sides of the overgrowth, due to their small sizes. Once the bulk part of this oxide

is reached on the wafer surface, the selectivity of the chemo-mechanical polishing is about 20:1 for silicon compared to oxide, and further polishing virtually stops. Thickness and uniformity of the SOI film is controlled by the amount of applied plasma-oxide: 0.5 μ m and uniformity of 5% are readily maintained as shown in Fig. 2. Excellent planarity of the LOG and plasma-oxide surface is therefore reached, as schematically represented in Fig. 1 and demonstrated in Fig. 3.

After planarization, a standard PMOS process is implemented on the overgrowth. With the self-alignment for source and drain in substrate and SOI film, it is possible to produce 3 μ m CMOS devices with only 6 masking steps and very short processing time compared to bulk CMOS processes (Fig. 4). As CVD epitaxy and polishing can be considered standard manufacturing technology (although both steps are often performed at the wafer manufacturer), no new processes have to be introduced in device fabrication. Surface topography is smoother than in a bulk process, ena-

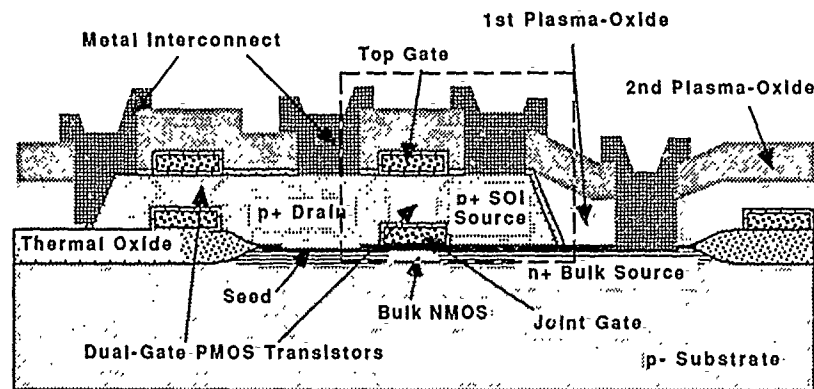


Figure 1: Schematic cross-section of stacked CMOS devices.

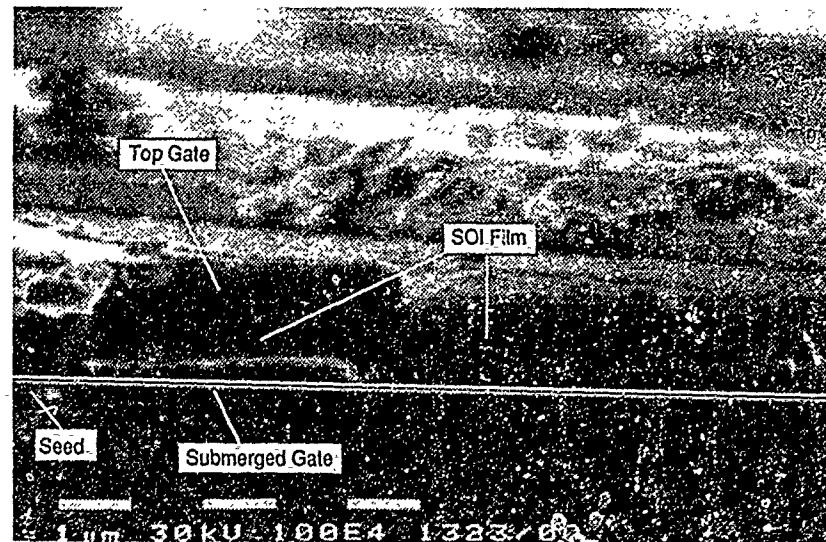


Figure 2: SEM view of cleaved overgrowth. Area enclosed with dashed line in Figure 1.

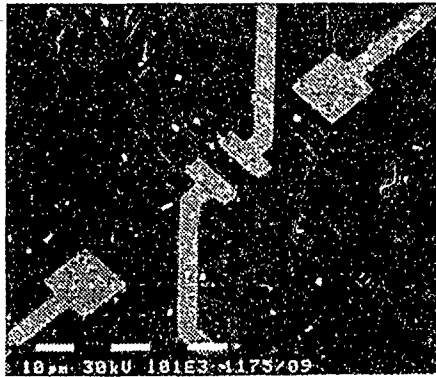


Figure 3: SEM view of inverter. Surface planarity is made more clear by tilting the sample 45°.

bling further stacking and simplified metalization lithography. Scaling gate and contact dimensions to a 1 μm process, both the overgrowth and planarization step will be simplified, since lateral overgrowth could be limited to about 4 μm . Similar scaling might be difficult for ZMR material, due to the finite size of the heat source and the occurrence of grain boundaries.

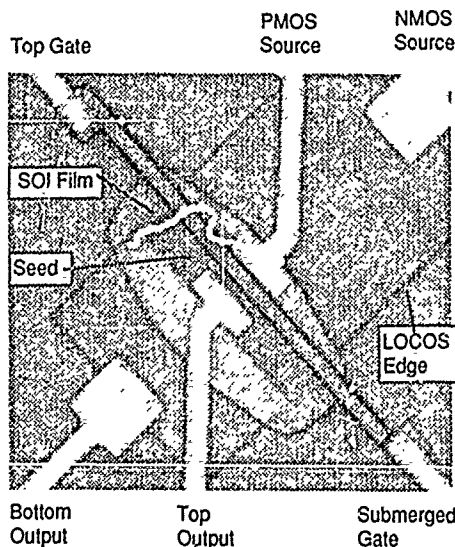


Figure 4: Optical micrograph of stacked inverter. Polysilicon gate width is 3 μm .

III. Devices and Circuits

The material was characterized by active devices built in the two semiconducting layers. The device properties are comparable to devices built in substrate silicon, and therefore indicate excellent quality of the fabricated films.

IIIa. Reverse-Built Transistor

Between the first polysilicon layer (field plate of the NMOS device in the bulk material) and the overgrowth a transistor is formed. It has been built in truly reverse order: the field plate first, the gate oxide second, and finally the channel region. This device has a number of potential problem areas, such as 1) leakage, 2) surface roughness, 3) non-uniform thickness of the gate oxide [7], 4) high interface-state density at the semiconductor-oxide interface [8] (caused by CVD formation rather than thermal oxidation), and 5) lattice defects in the channel region of the lateral overgrowth. None of these problems were observed [9], and excellent device properties were measured, as is shown in Fig. 5 and Table 1 as "Bottom PMOS". Hole mobilities of 200 cm^2/Vs for a surface channel show that the surface roughness due to the oxidized polysilicon grains have little effect. This is surprising, as the lower oxide is generated by thermal oxidation of polysilicon and subsequently is not as smooth as regular gate oxides. Additionally, the critical silicon/silicon-dioxide interface is generated by epitaxial lateral overgrowth. Interface-state densities comparable

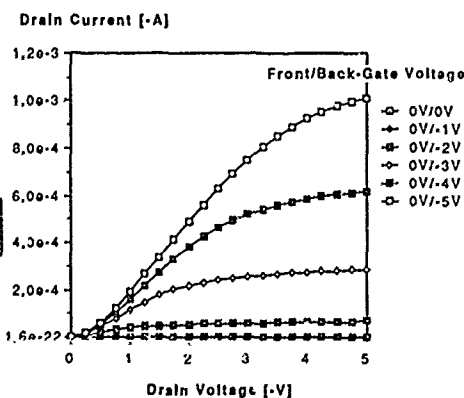


Figure 5: Output characteristic of reverse built PMOS transistor

to thermally-grown oxides were measured, probably due to the chlorine gas present during the overgrowth [10]. This is also illustrated by the good subthreshold slope for this oxide thickness of 120mV/dec. The devices show an exponential behavior in the low source-drain voltage regime, due to a degraded contact to the channel by the implant tails of the source/drain implant.

Devices built on top of the polished overgrowth were used for comparison with bulk devices for film quality calibration. The results, which are identical with bulk devices, are summarized in Table 1 under the "Top PMOS" heading. Low leakage currents were measured for junctions

built in the SOI film, and hence the lattice defect density must be low.

IIIb. Substrate Transistor

NMOS transistors realized in the bulk material were used to monitor the effects of the overgrowth cycle on impurity profiles. The separation of the two complementary transistor types in the two active layers eliminates any possibility of latch-up. Slight modifications were necessary on the implant parameters to maintain the characteristics and device parameters of conventionally processed transistors, as shown in Fig. 6 and Table 1. Electron mobilities were measured at

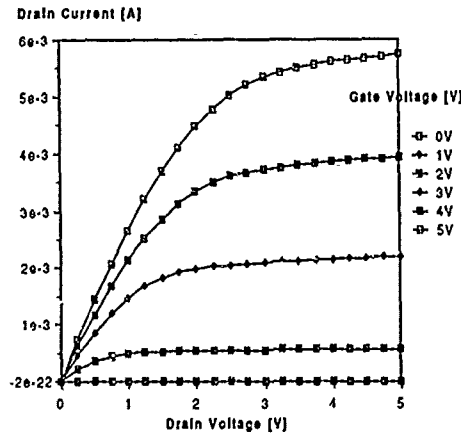


Figure 6: Output characteristics of bulk NMOS transistor. Device dimensions are $W=50\mu\text{m}$, $L=3\mu\text{m}$, $t_{\text{ox}}=40\text{nm}$.

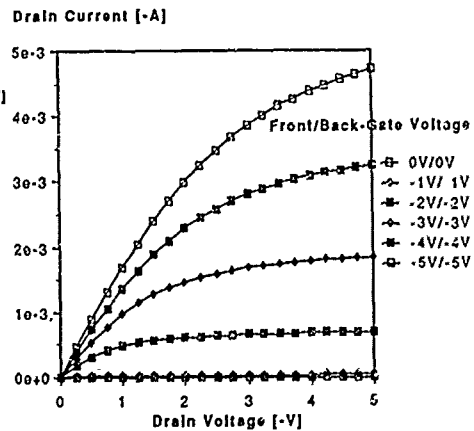


Figure 7: Output characteristics of dual-gate PMOS transistor in SOI film. Device dimensions are $W=60\mu\text{m}$, $L=3\mu\text{m}$, $t_{\text{si}}=0.5\mu\text{m}$, $t_{\text{ox}}=40/60\text{nm}$.

Table 1: Device parameters of the stacked transistors.

		Top PMOS	Bottom-PMOS	Dual-Gate PMOS	Bulk NMOS
Channel Width	W	$60\mu\text{m}$	$60\mu\text{m}$	$60\mu\text{m}$	$50\mu\text{m}$
Channel Length	L	$3\mu\text{m}$	$3\mu\text{m}$	$3\mu\text{m}$	$3\mu\text{m}$
Under-diffusion	L_d	$0.5\mu\text{m}$	$0.5\mu\text{m}$	$0.5\mu\text{m}$	$0.5\mu\text{m}$
Gate Oxide	t_{ox}	40nm	60nm	--	40nm
Threshold Voltage	V_t	-1.2V	-1.3V	-0.8V	0.9V
Surface Mobility	μ_0	$220\text{cm}^2/\text{Vs}$	$200\text{cm}^2/\text{Vs}$	--	$690\text{cm}^2/\text{Vs}$
Doping Level	N_b	$5 \cdot 10^{15}/\text{cm}^3$	$6 \cdot 10^{15}/\text{cm}^3$	$5.5 \cdot 10^{15}/\text{cm}^3$	$5 \cdot 10^{15}/\text{cm}^3$
Source/Drain Resist.	$R_{s,d}$	25Ω	50Ω	35Ω	25Ω
Junction Leakage	$J_{s,d}$	$50\text{nA}/\text{cm}^2$	$50\text{nA}/\text{cm}^2$	$50\text{nA}/\text{cm}^2$	$10\text{nA}/\text{cm}^2$
Subthreshold Slope	S	$109\text{mV}/\text{dec}$	$120\text{mV}/\text{dec}$	$60\text{mV}/\text{dec}$	$105\text{mV}/\text{dec}$

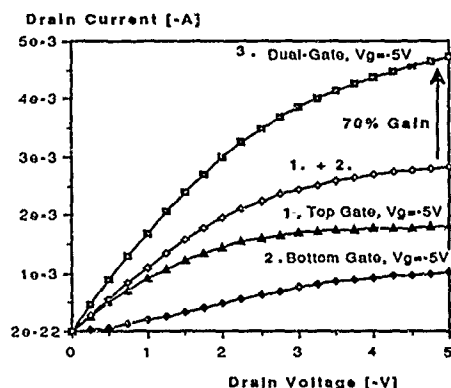


Figure 8: Comparison of the individual channels with the dual-gate operation of the device of Fig. 7.

690cm²/Vs and threshold voltage at 0.9V, in agreement with a doping level of $5 \cdot 10^{15}/\text{cm}^3$. Junction leakage was only slightly increased over standard devices at 20nA/cm², and the inverse subthreshold slope was 105mV/dec.

IIIc. Dual-Gate Transistor

The first PMOS devices with equivalent current drive as n-channel transistors of similar geometries were obtained by dual-gate operation (compare Fig. 6 and 7). This gain in transconductance was obtained by the superposition of the

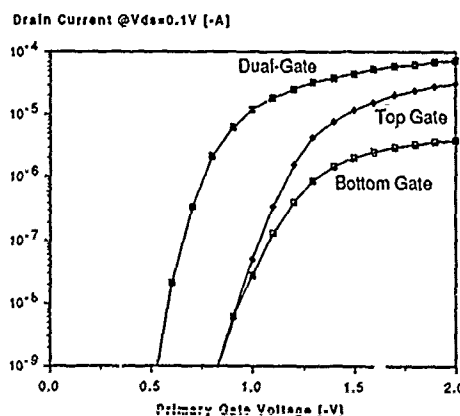


Figure 9: Subthreshold characteristics of SOI PMOS transistor of Fig. 7. Apparent are lowering of threshold voltage and steepening of subthreshold slope to 60mV/dec by dual-gate operation

two surface channel currents (shown in Fig. 8) plus an additional 70% increase by the coupling of the two channels [11,12]. Additionally, the threshold voltage was raised from -1.3V to -0.8V [13,14], which is preferable for CMOS applications. The inverse subthreshold slope is lowered to a near-ideal 60mV/dec by the full-depletion operation of the silicon film (Fig. 9). The device parameters of the fabricated transistors are summarized in Table 1. The excellent surface mobilities of both the PMOS channels (220cm²/Vs and

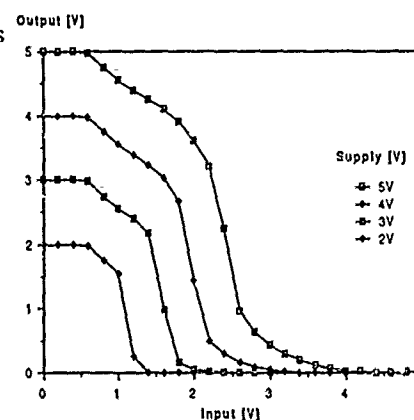


Figure 10: Transfer characteristics of symmetric stacked inverter built with devices of Fig. 6 and 7. Output voltage shows a 0.3V step at input voltages of 0.8V due to the connecting tunnel diode.

200cm²/Vs) demonstrate the quality of both the silicon film and the two interfaces. Further improvement of the device performance may be possible by volume-inversion [15], which requires silicon film thicknesses less than 0.4μm for doping levels below $1 \cdot 10^{15}/\text{cm}^3$.

IIId. Inverters

With the realization of complementary MOS transistors on top of each other (Fig. 1), an inverter can be built with the footprint of a single transistor. Two different approaches have been realized, a joint-gate and a dual-gate inverter. The former gate minimizes the capacitive load on the input node, as only the first polysilicon gate is driven; conversely, the output is limited by the

reduced driving capacity of the reverse-built PMOS transistor. The latter inverter utilizes the increased transconductance of the dual-gate device to yield the symmetric transfer characteristic of Fig. 10. At input voltages of 0.9V, the threshold voltage of the NMOS transistor, a step is visible in the characteristic. This step of 0.3V is produced by the forward voltage of the p+/n+ diode connecting the drains of the complementary devices. This diode could be strapped by a metal bridge, but should be of no concern for most applications.

IV. Conclusions

A new process has been presented here that yields stacked, complementary transistors with conventional technology and only six masking steps. Devices realized by this process are equal to, or even better than transistors built in a conventional manner. Inverters show the possibility of symmetric device-performance of N- and PMOS transistors. Significant area reduction and alleviation of parasitic circuit components gives this process advantages for the realization of high density circuits.

References

- [1] Y. Akasaka, "Three-Dimensional IC Trends", *Proc. of the IEEE* 74 (12), pp1703-1714, December 1986
- [2] B. Höfflinger, S. T. Liu and B. Vajdic, "A Three-Dimensional CMOS Design Methodology", *IEEE SC-19* (1), pp37-39, February 1984
- [3] J. F. Gibbons and K. F. Lee, "One-Gate-Wide CMOS Inverter on Laser-Recrystallized Polysilicon", *IEEE EDL-3* (8), pp117-118, June 1980
- [4] R. P. Zingg, G. W. Neudeck, B. Höfflinger and S. T. Liu, "Epitaxial Lateral Overgrowth of Silicon over Steps of Thick SiO₂", *J. of the El-chem. Soc.*, Vol 133 (6), pp1274-1275, June 1986
- [5] K. Hoffmann, G. W. Rubloff and R. A. McCorkie, "Detect formation in thermal SiO₂ by high-temperature annealing", *Appl. Phys. Lett.*, 49 (22), pp1525-1527, December 1986
- [6] R. P. Zingg, H. G. Graf, W. Appel, P. Vöhlinger and B. Höfflinger, "Thinning Techniques for 1 μ m ELO-SOI", *IEEE SOS/SOI Workshop Proc.* p. 52, October 1988
- [7] L. Faraone and G. Harbeck, "Surface Roughness and Electrical Conduction of Oxide/Polysilicon Interfaces", *J. of the El-chem. Soc.*, Vol 133 (7), pp1410-1413, July 1986
- [8] J. P. Colinge, E. Demoulin and M. Lobet, "Stacked Transistor CMOS (ST-CMOS), an NMOS Technology Modified to CMOS", *IEEE SC-17* (2), pp215-219, April 1982
- [9] R. P. Zingg, B. Höfflinger and G. W. Neudeck, "High Quality Dual-Gate PMOS Devices in Local Overgrowth (LOG)", *IEEE ED-25* (15), pp1009-1011, July 20, 1989
- [10] J. A. Friedrich and G. W. Neudeck, "Interface Characterization of Silicon Epitaxial Lateral Growth over Existing SiO₂ for Three-Dimensional CMOS Structures", *IEEE EDL-10* (4), pp144-146, April 1989
- [11] P. W. Barth, P. R. Apte and J. B. Angell, "The MISIM-FET in Thin Semiconductor Layers: Depletion-Approximation Model of I-V Characteristics", *IEEE ED-30* (12), pp1717-1726, December 1983
- [12] H. K. Lim and J. G. Fossum, "Current-Voltage Characteristics of Thin-Film SOI MOSFET's in Strong Inversion", *IEEE ED-31* (4), pp401-408, April 1984
- [13] H. K. Lim and J. G. Fossum, "Threshold Voltage of Thin-Film Silicon-on-Insulator (SOI) MOSFET's", *IEEE ED-30* (10), pp1244-1251, October 1983
- [14] T. Sekigawa and Y. Hayashi, "Calculated Threshold-Voltage Characteristics of an XMOS Transistor Having an Additional Bottom Gate", *Sol. State Electronics Vol. 27* (8/9) pp827-828, 1984
- [15] F. Balestra, S. Cristoloveanu, M. Benachir, J. Brini and T. Elawa, "Double-Gate Silicon-on-Insulator Transistor with Volume Inversion: A New Device with Greatly Enhanced Performance", *IEEE EDL-8* (9), pp410-412, September 1987
- [16] R. P. Zingg, B. Höfflinger and G. W. Neudeck, "Stacked CMOS Inverter with Symmetric Device Performance", *IEDM Meeting*, Washington, DC, December, 1989

OPTIMIZED MOLECULAR BEAM EPITAXY STRUCTURES FOR GaAs ON SILICON PHOTODETECTORS

A. Christou, N.A. Papanicolaou, and G.W. Anderson,
Naval Research Laboratory, Washington, D.C. 20375-5000

ABSTRACT

Two dimensional growth of GaAs on silicon has been achieved by modulation molecular beam epitaxy (where the arsenic beam is pulsed) with laser assistance at 308 nm (LAMBE). Photoconductive, low doping concentration layers were utilized for metal-semiconductor-metal photodetectors which were evaluated at 840 nm.

INTRODUCTION

Two dimensional growth of GaAs on silicon has been shown to be necessary for the reduction of threading dislocations, antiphase domain boundaries and stacking faults in the deposition of GaAs on silicon^{1,2}. On the other hand, three dimensional growth which results from surface roughness, defects and oxygen proceeds by island coalescence and a high dislocation density. The dislocations apparently are generated at island intersection points³. MBE layers for photodetectors require low doped n⁻ GaAs layers with typical impurity concentrations of less than $1 \times 10^{15} \text{ cm}^{-3}$. Such layers have been achieved by LAMBE techniques where the arsenic beam was pulsed at a period comparable to the growth of one monolayer, as determined from the RHEED oscillations.

The present investigation focuses on enhancing the substrate surface quality and the deposition conditions during the early stages of growth of GaAs on silicon. From thermodynamic stability requirements, due to the 4 percent mismatch of the two sublattices, a cross-grid of edge-type misfit dislocations at the interface must be generated. Most experimental evidence suggests that the interface dislocations for the GaAs/Si system form a random configuration⁴. A three-dimensional island-growth mechanism at the early stages of growth could be the mechanism for such a configuration. The different strains at coalescing islands might generate networks of boundary dislocations and as a result, multiple dislocations are introduced with number densities higher than those required for complete accommodation of the mismatch by misfit dislocations⁴. LAMBE's ultimate goal is to achieve conditions for two dimensional hetero-epitaxial growth free of threading dislocations.

In this paper we present results from GaAs n⁻ layers grown by LAMBE on silicon (100) whose surface was subjected to in-situ UV laser desorption prior to deposition and during the deposition of the 200Å nucleation layer. The photodetector layers were characterized both electrically and by cross-sectional transmission electron microscopy (TEM). The structural characterization of the GaAs on silicon suggests that the three-dimensional island growth has been suppressed resulting in a substantial reduction of linear defects.

EXPERIMENTAL - MATERIAL ASPECTS

The deposition of GaAs on silicon was carried out using high resistivity silicon substrates ($> 1000 \Omega \cdot \text{cm}^2$). In realizing a successful growth sequence by molecular beam epitaxy, it was necessary to initially optimize the GaAs nucleation layer deposited at 300°C which was followed by a strain accommodation layer, a GaAs spacer layer and two strained layer superlattices (SLS) grown at 700°C . The two SLS regions were separated by a second GaAs spacer layer. A 308 nm excimer laser at $120 \text{ mJ}/\text{cm}^2$ was used to assist the growth of the nucleation and accommodation layers. Substrate desorption was carried out at 850°C with the laser beam on and with an energy density as high as $150 \text{ mJ}/\text{cm}^2$. Mass spectroscopic analysis indicated the dissipation of C and O peaks occurring after 5 minute exposure at 1 pulse per second. A 300\AA GaAs nucleation layer was initially grown followed by a five period AlAs/GaAs multi-quantum well region each 100\AA thick. The SLS consisted of $\text{In}_{0.10}\text{Ga}_{0.90}\text{As}/\text{GaAs}$ each 120\AA thick as shown in Figure 1. Finally a $2\mu\text{m}$ undoped GaAs active layer was grown followed by a $0.2\mu\text{m}$ thick n layer and a $.05\mu\text{m}$ thick n^+ contacting layer in order to complete the structure.

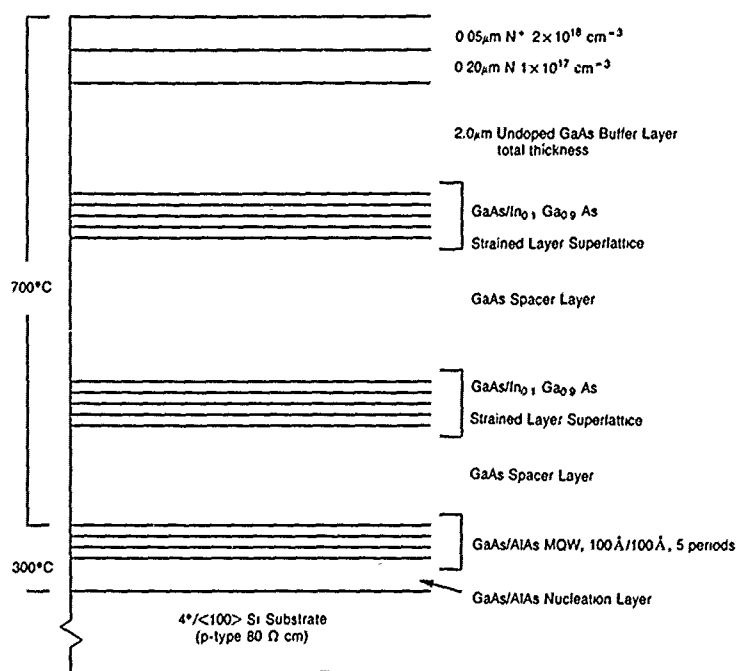


Fig. 1. Schematic cross-section of the GaAs/Si LAMBE photodetector structure.

Interfacial Investigations

For the transmission electron microscopy investigations, the materials were thinned by ion-beam techniques. The observation of the GaAs/Si interface was accomplished by initially thinning the material from the silicon substrate back side and then progressively from the GaAs top layer until the interface was reached. The cross-sectional TEM specimens were prepared according to the methods developed by Dupuy⁴.

Photodetector Fabrication

The photodetectors of GaAs on silicon were fabricated as follows: The wafers were initially cleaned in hot solvents (i.e. boiling TCE, boiling acetone, Isopropanol and de-ionized water). A standard photolithographic process was carried out to define the ohmic contacts for the devices. The ohmic contact metallization which consisted of AuGe/Ni/Au was deposited by e-beam evaporation and then lifted - off. Alloying of the contact was performed at 410°C in forming gas for one minute. The Schottky metal consisted of Ti/Pt/Au and was formed by a similar photolithographic and lift - off technique.

The types of photodetectors investigated included linear photoconductors and three types of interdigitated finger devices: metal - semiconductor - metal (MSM); Schottky diodes having one set of Schottky metal fingers and one set of ohmic fingers (S-O detectors); and photodetectors consisting of two sets of ohmic fingers (O-O detectors). The evaluation of the photodetectors was made using 840nm wavelength pulse light with a pulse width of 5 ns and rise (t_r) and fall (t_f) times of 200 ps.

EXPERIMENTAL RESULTS

Material Investigations

Electrical profiling of the undoped buffer layer into which the photodetectors were fabricated indicated a variation of $1 \times 10^{15} \text{ cm}^{-3}$ to $8 \times 10^{14} \text{ cm}^{-3}$ doping concentration over the 2 μm thickness. Therefore the grown structure successfully prevented the outdiffusion of silicon from the substrate during growth.

The TEM results concentrated on the differences in structural characteristics between the LAMBE grown films and those grown under conventional MBE conditions. Figure 2 shows a TEM micrograph which depicts the GaAs/Si interface for layers grown under standard conditions⁵. Displacement type moire fringes were formed because the e-beam diffraction originated from the superposition of the two lattices. Various defects and local strain variations result from the observed fringe irregularities. Non-uniformity of the fringe spacing from spot to spot indicates irregularities in the local misfit dislocation density. The most frequently observed defect structure of GaAs on silicon involves threading dislocations, stacking faults, microtwins and anti-phase domain boundaries. Such structures are also shown in Figure 2.

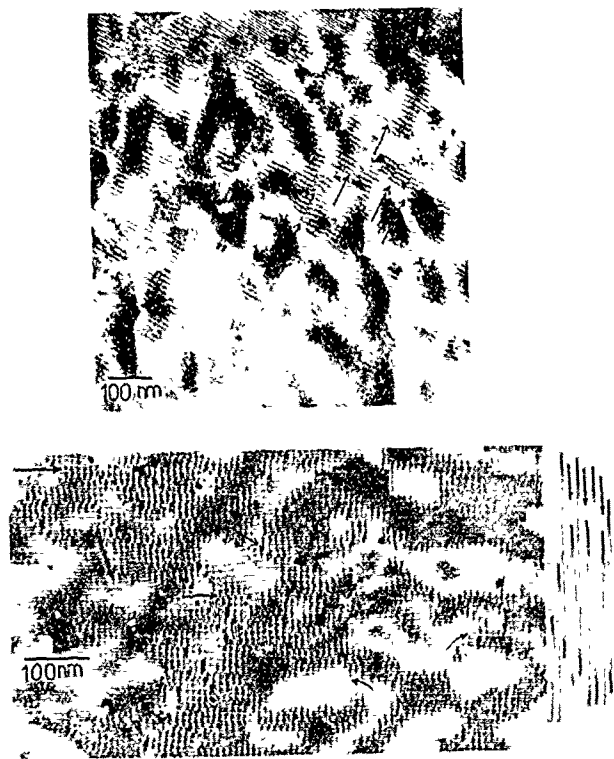


Fig. 2 TEM micrograph of the GaAs/Si interface grown under standard conditions

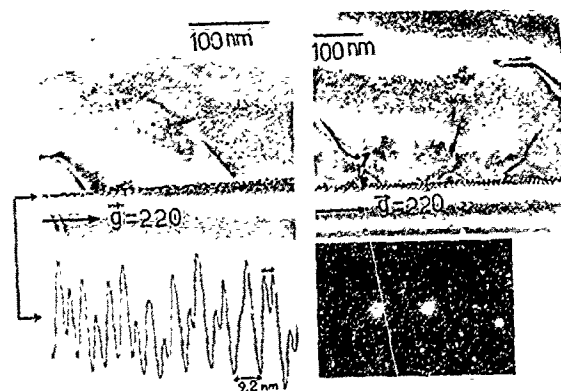


Fig 3. XTEM micrograph from the GaAs/Si interface of [110] which shows evidence of the 60° dislocations. The densitometer traces show the evenly spaced misfit dislocations along the $\langle 110 \rangle$ directions. The diffraction pattern shows the bright (220) operating reflections for GaAs and silicon.

The beneficial effects of excimer laser assisted growth of GaAs on silicon is shown in Figure 3. The dislocation density is relatively high near the interface but is reduced in the upper surface resulting in a dislocation density of 10^7 cm^{-2} in the active layer. The plane view of the GaAs/Si interface reveals moire fringes of translation type parallel to the $[110]$ and $[\bar{1}\bar{1}0]$ directions. The very regular moire pattern of Figure 4 shows the formation of a perfect alignment of the two lattices which are completely relaxed. In addition, the moire patterns are very sensitive to the existence of local strain and island nucleation. Other type of defects such as stacking faults and microtwins were not observed. Therefore the formation of a regular cross-grid of misfit dislocations indicates that conditions for two dimensional growth were achieved.

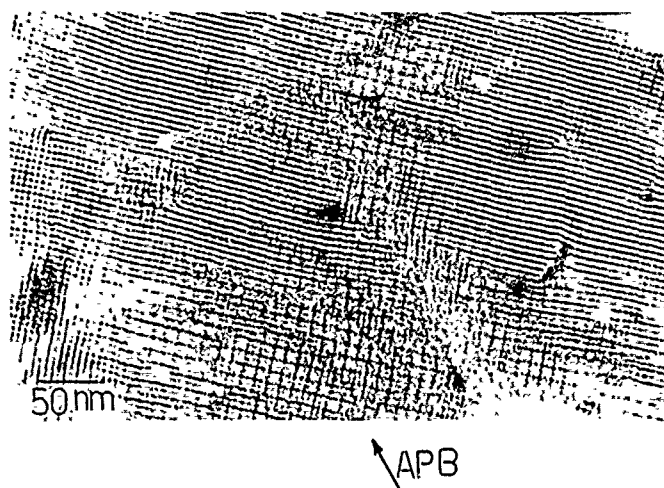


Fig 4. Plan view micrograph of the GaAs/Si interface showing well aligned moire figures

Photodetector Results

The evaluation of the photodetectors was made using 840 nm wavelength pulsed light with a pulse width of 5 ns and rise (t_r) and fall (t_f) times of 200 ps. The t_r and t_f of both the linear and interdigitated devices fabricated in the undoped GaAs layer were in the 1-2 ns and 3-4 ns ranges respectively. These results were comparable to those obtained for photoconductors fabricated directly in undoped GaAs/GaAs material. The responsivity and quantum efficiency values of the photoconductors were in the 0.6 - 0.9 A/W range.

CONCLUSIONS

GaAs on silicon epitaxial layers of high quality have been achieved by LAMBE techniques. TEM investigations showed that two dimensional nucleation has been achieved. Photodetectors fabricated in n-GaAs/Si layers indicated comparable behavior with GaAs/GaAs structures.

REFERENCES

1. M.H. Grabow and G.H. Gilmer, Mat. Res. Soc. Symp. Proc., 94, 15 (1987).
2. J.S. Ahearn and P. Uppal, Mat. Res. Soc. Symp. Proc., 91, 167 (1987).
3. D.K. Biegelsen, F.A. Ponce, B.S. Krusor, J.S. Tramontana, R.D. Yingling, R.D. Bringans and D.B. Fenner, Mat. Res. Soc. Symp. Proc., 116, 33 (1988).
4. M. Dupuy, J. Microsc. Spectrosc. Elect., 2, 163 (1984).
5. J.S. Harris, Jr, S.M. Koch and S.J. Rosner, Mat. Res. Soc. Symp. Proc., 91, 3 (1987).

LASER SELECTIVE AREA EPITAXY FOR THE POTENTIAL OF OPTOELECTRONIC INTEGRATION

H. Liu, J.C. Roberts, J. Ramdani and S.M. Bedair
Electrical and Computer Engineering Department, North Carolina State
University, Raleigh, North Carolina

ABSTRACT

We report for the first time the dopant behavior in laser assisted selective epitaxy of device quality GaAs films. DMZn and H_2Se were used as p-type and n-type dopants respectively. Uniform doping was achieved by introducing TMGa, AsH_3 and dopant gases simultaneously and was accompanied by a decrease in growth rate for both Zn and Se doping. For planar doping, several Se planes were embedded in a GaAs layer by simultaneously introducing AsH_3 and H_2Se during the LCVD process. A sheet carrier concentration in the $10^{12} - 10^{13} \text{ cm}^{-2}$ range was obtained for a single Se plane. Hall data of these films will be discussed. It was found planar doping results in better electrical properties and better growth rate control.

INTRODUCTION

Laser assisted chemical vapor deposition (LCVD) is a relatively new technique with potential for low temperature selective deposition of device quality films suitable for optoelectronic monolithic integration. Current difficulties in integrating optical and electronic devices on one chip mainly come from the differences of material and structural requirements between components. The necessary processing usually requires several growth steps as well as masking, etching and liftoff, which may result in low yield. Laser assisted selective area deposition can provide another approach to address these problems. In order to achieve selective area epitaxy using the LCVD approach, the substrate temperature should be in the range of $300^\circ\text{C} - 400^\circ\text{C}$. A higher substrate temperature will result in deposition on areas of the substrate not exposed to the laser light and the technique starts to lose its selective nature. On the other hand, if the substrate temperature is lower than this range, a higher laser power density is needed that may produce local heating and thermal stresses [1]. Also, p- and n-type dopants have to be selectively incorporated at this relatively low substrate temperature for several structures. We will report on the properties of dopants suitable for LCVD GaAs films. Dimethylzinc (DMZn, 50ppm in H_2) has been tried as a p-type dopant and Hydrogen Selenide (H_2Se , 20ppm in H_2) as an n-type dopant.

EXPERIMENTAL

The LCVD system consists of a vertical MOCVD reactor operated at atmospheric pressure, an Ar ion laser operated at multiple wavelength (488nm - 514nm) and a computer controlled X-Y laser scanner. Details of the set-up have been reported elsewhere [2,3]. Semi-insulated GaAs wafers 2° off (100) toward [110] attached to a graphite sus-

ceptor were RF heated to 300°C or 400°C. The Ar ion laser, focused to a spot size of approximately 500 μm , is multiply scanned (100-200 scans) for a distance of 1500 μm on a local area of the substrate. Trimethylgallium (TMGa, 10°C) and Arsine (AsH_3 , 10% in H_2) were used as source gases. The laser power density and gas flow rates were adjusted to give growth rates of 20 Å to 50 Å per scan. Hall measurements were done by using a photolithographic process to define Van Der Pauw patterns of 160 x 350 μm^2 on the deposited films. The Ar ion laser beam has a gaussian intensity distribution and as reported earlier [4], the deposited films also have a gaussian shaped cross-section. This results in about a 20% thickness variation across the Van Der Pauw pattern. We have used the maximum film thickness in our Hall measurement calculations which will result in an under estimating of about 10% in carrier concentration but with negligible error for mobility data.

Seven structures (A, B-1, B-2, C, D, E-1, E-2) were grown on five separate substrates, samples A, B, C, D and E. Samples A, B, and E were grown at 400°C, while samples C and D were grown at 300°C. Structures A and C were undoped and both have high resistivity. Structure B-1 was uniformly doped by introducing TMGa, AsH_3 and H_2Se into the growth chamber simultaneously. Structure B-2 was undoped and grown on the same substrate after structure B-1 was grown. Structure D was uniformly doped by introducing TMGa, AsH_3 and DMZn into the growth chamber simultaneously.

Hall data of these LCVF films are shown in Table 1. Structure B-1 has a carrier concentration of about $8 \times 10^{18} \text{ cm}^{-3}$ with relatively low mobility and a growth rate about 1/5 of the undoped structure B-2. These low mobilities and low growth rates may be due to the formation of GaSe_x which is favored at this low growth temperature. Similar results were obtained in Se doped GaAs grown by atomic layer epitaxy at 450°C [5]. Structure B-2 was undoped and grown immediately after structure B-1, but shows a carrier concentration as high as $6 \times 10^{17} \text{ cm}^{-3}$, which is possibly due to the H_2Se memory effect in the gas line and/or the pre-adsorption of H_2Se on the substrate surface. Structure D has a very high hole concentration and the growth rate is about 1/5 of the undoped line. The reason for this phenomenon is not yet clear but might be attributed to the formation of a Zn-As compound. Thus, uniform doping using H_2Se and DMZn seems to suffer from some difficulties due to low substrate temperature. These difficulties can be avoided by using planar doped (delta-doped) structures. This will avoid the possible reactions between the dopant molecules and TMGa or AsH_3 . Structures E-1 and E-2 were planar doped using H_2Se and were grown as follows: The growth started with 100 multiple scans (0.5 μm thickness) of a GaAs buffer layer (high resistivity). For structure E-1 (E-2) the growth was then interrupted by purging out

AsH_3 (TMGa) and H_2Se was introduced into the growth chamber and followed by a single laser scan. After 2 minutes of purging out H_2Se , 6 multiple scans (300 Å) of GaAs were grown before the next growth interruption to deposit a second delta-doped layer. This sequence was repeated 10 times to produce 10 planes of Se in the GaAs layer. Structure E-1 suffers from co-exposure of the GaAs surface to both H_2Se and TMGa and thus enhances the formation of GaSe_x . This resulted in a rough surface and low mobility. Structure E-2 has a higher mobility than E-1 indicating that avoiding H_2Se -TMGa reactions results in better electrical properties. Also the growth rate of structure E-2 does not deviate from that of undoped material, which is another advantage of using the planar doping technique in LCVF.

TABLE 1

Sample #	T _{sub} °C	Carrier type	Carrier Conc. cm ⁻³	Mobility(RT) cm ² /V-s	Growth rate Å/scan	Surface Morphology
A	400	--	High resistivity	---	50	smooth
B-1	400	n	8×10^{18}	277	11	smooth
B-2	400	n	6×10^{17}	1317	50	smooth
C	300	--	High resistivity	---	20	smooth
D	300	p	$\sim 10^{21}$	20	4	smooth
E-1	400	--	2×10^{18}	935	62	rough
E-2	400	n	8×10^{18}	1407	50	smooth

Selenium planar doping is found to be attractive to LCVD since better mobility and thickness control can be achieved. The nature of the n-type dopant is preserved in this low substrate temperature. Doping with Zn can probably be improved by using the planar doping technique. Also, doping with Si will be investigated in the future to discover its availability as a dopant in this low temperature range. Further investigation of doping level control and optimum growth conditions and device structures by LCVD are underway.

CONCLUSION

In conclusion, doping properties of LCVD films are studied using H₂Se and DMZn for n-type and p-type dopants respectively. Uniform doping showed a reduction in growth rates and relatively low mobilities, perhaps a result of reactions between dopant molecules and TMGa or AsH₃. Planar doping avoids these problems and a doping profile from C-V measurement was obtained [Fig. 1].

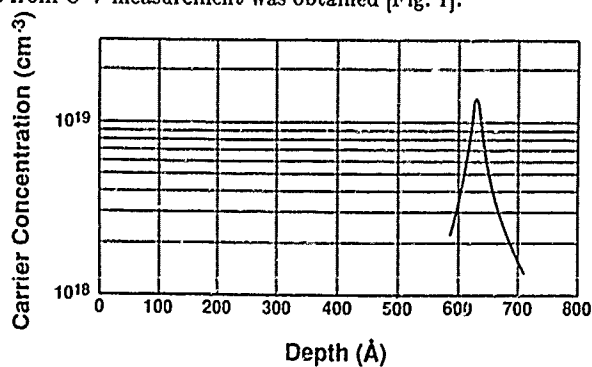


Figure 1. C-V Concentration Profile

ACKNOWLEDGEMENTS

This work is supported by National Science Foundation and Office of Naval Research [SDIO].

REFERENCES

1. N.H. Karam, H. Liu, I. Yoshida, B.L. Jiang and S.M. Bedair, J. Crystal Growth 93, 254 (1989).
2. S.M. Bedair, J.K. Whisnant, N.H. Karam, M.A. Tischler and T. Katsuyama, Appl. Phys. Lett. 48 (1986) 174.
3. S.M. Bedair, J.K. Whisnant, N.H. Karam, D. Griffis, N.A. El-Masry and H.H. Stadelmayer, J. Crystal Growth 77 (1986) 229.
4. N.H. Karam, H. Liu, I. Yoshida and S.M. Bedair, Appl. Phys. Lett. 53 (9), 29 August 1989.
5. A. Usui and Watanabe, 3rd International Conference on "Modulated Semiconductor Structures", Montpellier, France (1987).

LASER INDUCED SURFACE CHEMICAL EPITAXY OF II-VI MATERIALS

CHARTER D. STINESPRING AND ANDREW FREEDMAN

Center for Chemical and Environmental Physics, Aerodyne Research, Inc.,
Billerica, Massachusetts 01821

ABSTRACT

Studies of the thermal and photon-induced surface chemistry of dimethyl cadmium (DMCd) and dimethyl tellurium (DMTe) on GaAs(100) substrates under ultrahigh vacuum conditions have been performed for substrate temperatures in the range of 123 K to 473 K. Results indicate that extremely efficient conversion of admixtures of DMTe and DMCd to CdTe can be obtained using low power ($5 - 10 \text{ mJ cm}^{-2}$) 193 nm laser pulses at substrate temperatures of 123 K. Subsequent annealing at 473 K produces an epitaxial film.

INTRODUCTION

Thermal and photon-assisted deposition processes involving organometallic precursor species are currently being investigated for II-VI and III-V compound semiconductors.[1] These processes provide the potential for reduced growth temperatures and increased process flexibility. Illustrations include reduced pressure laser assisted chemical vapor deposition (LCVD) of CdTe[2] and ultra high vacuum (UHV) metalorganic molecular beam epitaxy (MOMBE) on GaAs.[3] These relatively new deposition processes raise important questions concerning chemical mechanisms which must be answered if the processes and materials they produce are to be optimized.

This paper describes ongoing experimental studies[4,5] of the thermal and photon-induced surface reactions of dimethyl cadmium (DMCd) and dimethyl tellurium (DMTe). The objectives of these studies are to provide an understanding of the underlying chemical and physical processes and to explore novel approaches to CdTe heteroepitaxy. The work focuses on CdTe heteroepitaxy because of the importance of this material in electro-optical systems.[6] DMCd and DMTe were the first precursor species selected for investigation because of their inherent scientific interest. The gas phase photochemistry of DMCd and DMTe has been extensively investigated; these molecules are known to undergo one photon dissociation to produce ground state metal atoms.[7-9] This behavior contrasts with that of trimethyl gallium and trimethyl arsenic which dissociate in the gas phase via a multiphoton excitation process.[10] The basic question is how can the photophysics of these molecules be used to obtain CdTe thin films.

EXPERIMENTAL

The experimental apparatus used in these studies is shown in Figure 1. It consists of a turbomolecular pumped, liquid nitrogen trapped UHV reaction cell interfaced to an ion/sublimation pumped UHV analysis chamber. The diagnostics used in these studies are X-ray photoelectron spectroscopy (XPS) and low energy electron diffraction (LEED). The sample is transferred between chambers using a linear motion feedthrough with sample heating (1200 K) and cooling (123 K) capabilities. Samples are exposed to

reactive gas species using an effusive molecular beam doser. For the sample-source geometry used here, the angular distribution of the effusive beam produced only a nominal 10% variation in exposure over the analyzed area of the surface. Photon-induced processes were studied by irradiating the surface with UV photons produced by an excimer laser. These were introduced through a Conflat mounted MgF_2 window (Harshaw). The wavelengths used in these experiments were 193 nm, 248 nm, and 351 nm. Laser fluence, controlled using a simple beam expander, ranged from 0.3 mJ cm^{-2} to 6.0 mJ cm^{-2} to minimize the effects of surface heating ($<3 \text{ K}$ to 60 K) [11].

The GaAs samples used in these studies were p-type electronic grade single crystal substrates provided by Litton. In situ sample cleaning involved Ar^+ ion etching at 1 kV until no trace of oxygen contamination could be observed. This was followed by annealing at 850 K [12] to restore surface order (as observed by LEED). The DMCd and DMTe (Alfa) were purified using a series of freeze-thaw cycles.

The XPS analyses were performed using a PHI 15 kV, $\text{Mg K}\alpha$ source and a PHI double pass cylindrical mirror electron energy analyzer operated at a pass energy of 25 eV. The analyzer was calibrated using the $\text{Au } 4f_{7/2}$ peak at 83.8 eV. All spectra were referenced to the $\text{Ga } 3d_{5/2}$ peak at 18.8 eV. No charging effects were observed except in the limit of very thick films. ($> 200 \text{ \AA}$).

RESULTS AND DISCUSSION

As discussed elsewhere [4], XPS analyses of the Cd and Te $3d_{5/2}$ peaks can indicate the nature of the chemical bonding of the metalorganic species on the GaAs surface. The interaction of the adspecies with the surface follows what one might expect from the chemical structure of the metal alkyl. DMTe , a closed shell molecule, has a lower sticking coefficient than DMCd at all temperatures. Furthermore, at 123 K where no thermal association takes place for either molecule, the characteristic Te peak does not shift as adspecies coverage increases from sub-monolayer to multilayer coverage. This would indicate that DMTe does not strongly interact with the GaAs surface. The Cd peak from DMCd , on the other hand,

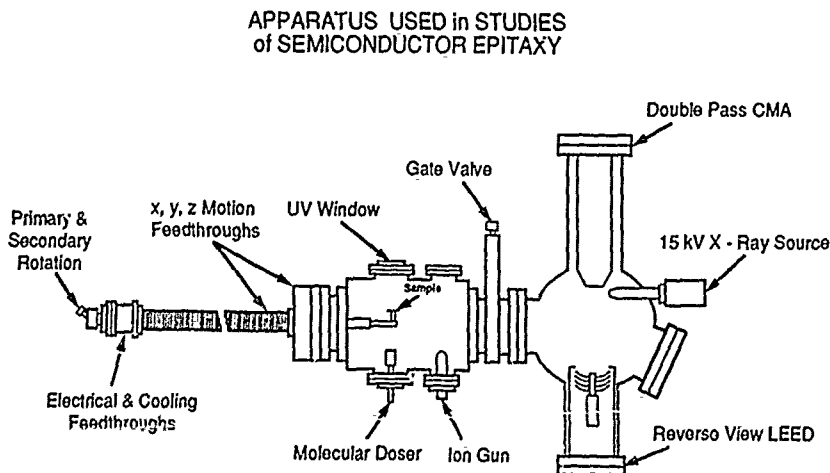


Figure 1. Cross sectional view of deposition and analysis system.

undergoes a several eV shift to higher bonding energies as coverage increases. The surface induced shift to low binding energies is consistent with electron flow from the GaAs to the vacant 3 p orbitals on the Cd atom.

A discussion of the photoinduced chemistry of submonolayer to monolayer coverages is beyond the scope of this paper but will be reported elsewhere[13]. In summary, the photochemistry is dominated by surface-mediated effects for GaAs even at 123 K, in contrast to the results obtained on quartz substrates[5]. It is difficult to cleanly photodissociate either DMTe or DMCd to metal atoms at 193 nm and 248 nm, even though the gas phase photochemistry produces cleavage of both metal-alkyl bonds. Irradiation produces a distribution of metal, dimethyl, and monomethyl species which varies with the total dose of laser photons.

Since our aim was to produce CdTe thin films at low temperatures, we began to use multilayer coverages (100-200 Å), which should have the effect of minimizing surface-induced effects. The result of irradiating thick (200 Å) admixtures of DMTe and DMCd with 193 nm photons is the production of CdTe thin films with stoichiometric ratios. Figure 2 shows the XPS signal from the Te $3d_{5/2}$ state as a function of laser dose. The rather broad spectrum of the unreacted film is immediately converted to a narrow peak at a binding energy indicative of metallic tellurium. Thermal annealing of the irradiated film produces cadmium telluride. Similar results are obtained when viewing the cadmium spectra. Figure 3 presents typical carbon 1s XPS spectra. The top spectrum shows two distinct peaks; based on single compound exposure, one is identifiable as carbon from DMTe (higher binding energy) and one as carbon from DMCd. Upon irradiation of 150 laser pulses at 193 nm (9×10^{17} photons total dose), all the carbon is converted to a new species (lower spectrum), whose binding energy is consistent with hydrocarbon production.

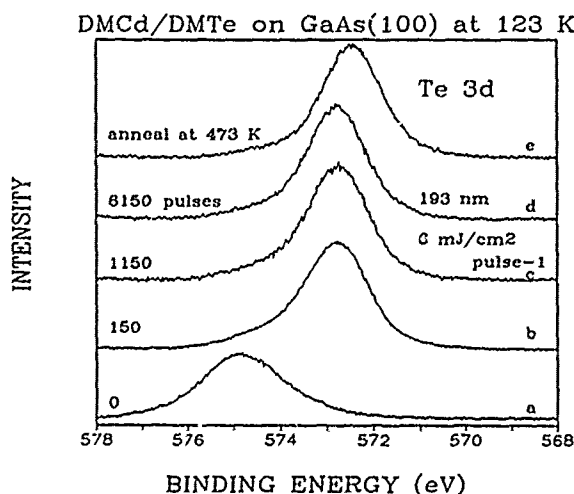


Figure 2. XPS spectra of the Te $3d_{5/2}$ peak of an $\sim 100\text{\AA}$ thick film of a DMTe/DMCd mixture on a GaAs(100) substrate at 123 K as a function of the number of 193 nm laser pulses at 6 MJ cm^{-1} . The top spectrum is the result of a subsequent thermal anneal at 473 K.

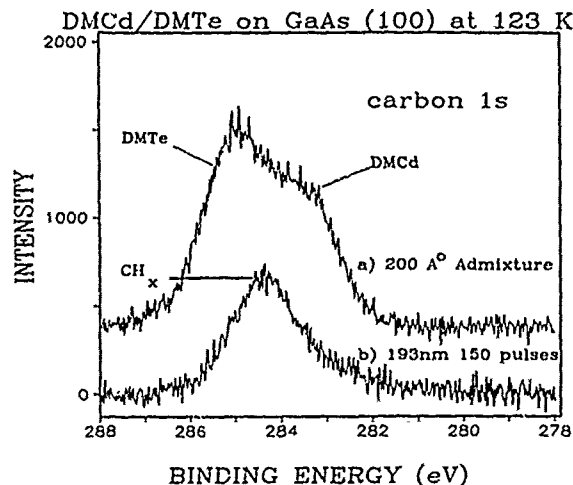


Figure 3. XPS spectra of the C 1s peak of a DMTe/DMCd admixture at a GaAs substrate temperature of 123 K before a) and after b) irradiation by 150 pulses at 6 mJ cm^{-2} of an ArF excimer laser operating at 193 nm.

Similar results are obtained no matter what the initial stoichiometry of the non-irradiated thin film. Cadmium to tellurium ratios of 0.5 to 2.0 always produced stoichiometric CdTe thin films with no excess of one species or the other. These results imply that the laser irradiation initiated a chemical reaction between the two metal alkyls, with any excess reactant being driven off the surface. The question arises as to whether this effect is due to the properties of the thin film or just to substrate heating effects. The films were therefore irradiated with 6 mJ cm^{-2} pulses from a XeF laser operating at 351 nm. At this wavelength, the thin film should be transparent. Figure 4 presents spectra of the Te $3d_{5/2}$ XPS peak for 351 vs. 193 nm. Clearly, the 351 nm laser pulses are not effective in inducing a chemical reaction. Thus the observed results are consistent with the energy being absorbed in the thin film; whether the reaction is catalyzed by photo-induced or electronically excited reactants or free radicals, increased precursor mobility, and/or thermal excitation cannot be deduced from the data.

We note that the CdTe films produced by 193 nm laser irradiation are heavily contaminated with carbon. Subsequent laser irradiation slowly reduces the level of carbon contamination but only annealing at 473 K for twenty minutes reduces carbon levels below detection limits ($\sim 0.5\%$). Upon annealing, we observe a 1×1 LEED pattern for the CdTe(100) surface indicating the presence of an epitaxial CdTe thin film. XPS indicates that the resultant film is on the order of 100\AA thick.

CONCLUSIONS

An epitaxial thin film ($\sim 100\text{\AA}$) of CdTe on GaAs(100) has been produced by 193 nm photon irradiation of beam deposited admixtures of dimethyl tellurium and cadmium at substrate temperatures of 123 K followed by a thermal anneal at 473 K. The resultant LEED pattern is 1×1 indicating an epitaxial (100) CdTe surface. The process is quite

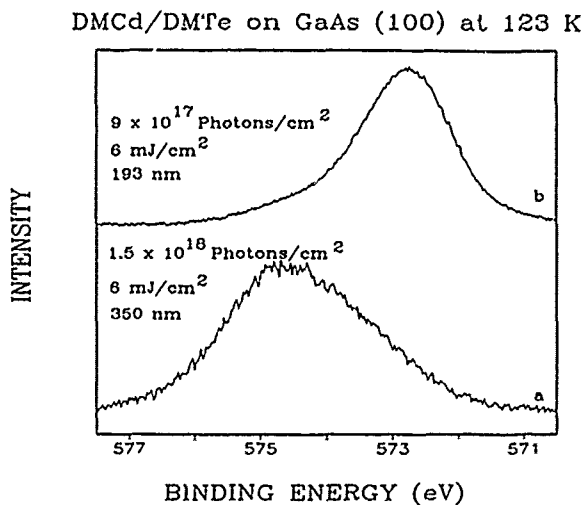


Figure 4. XPS spectra of the Te $3d_{5/2}$ peak upon irradiation at a) 351 nm and b) 193 nm for equal per pulse fluence and total energy dose. Film and substrate conditions are the same as in Figures 2 and 3.

efficient at laser fluences of $\sim 6 \text{ mJ cm}^{-2}$; lower fluences or much longer wavelengths (351 nm) are not effective. The process is linked to the absorption of photons in the thin film leading to a chemical reaction between the molecular species to produce CdTe and a hydrocarbon species.

The advantages of making II-VI compound semiconductors by this technique are apparent. By using a cold GaAs (123 K) substrate, we have increased sticking coefficients to .1 - .3, two to three orders of magnitude greater than that found at typical growth temperatures (500-600 K), thus saving on usage of metal alkyl precursors. Another potential advantage is the photo-induced "fixing" of the chemical reaction to produce CdTe, which opens the way to patterned deposition with reasonably fine resolution. A drawback at this point is the need to anneal the sample at 473 K to remove the carbon contamination and produce epitaxial ordering. But, if pulsed laser annealing could be utilized, this problem could be overcome. Future work is indicated in the area of ternary compounds, such as HgCdTe. Dimethyl mercury also absorbs strongly at 193 nm and thus is a candidate for laser surface chemical epitaxy.

ACKNOWLEDGEMENTS

This research was sponsored by the Air Force Office of Scientific Research under Small Business Innovative Research Program Contract No. F49620-86-C-0089.

REFERENCES

1. J.A. O'Neill, P. Shaw, E. Sanchez, Z. Wu and R.M. Osgood, Jr., "Surface Spectroscopic Studies of Organometallic Deposition," *Mat. Res. Soc. Symp.*, Vol. 129, (1983).
2. J.J. Zinck, P.D. Brewer, J.E. Jensen, G.L. Olsen and L.W. Tutt, *Appl. Phys. Lett.* **52**, 1434 (1988); J.B. Mullin and S.J.C. Irvine, *J. Vac. Sci. Technol.* **A4**, 700 (1986).
3. E. Tokumitsu, Y. Kurow, M. Kanogai and K. Takahashi, *J. Appl. Phys.* **55**, 3163 (1984).
4. C.D. Stinespring and A. Freedman, *Chem. Phys. Lett.* **143**, 584 (1988).
5. C.D. Stinespring and A. Freedman, *Appl. Phys. Lett.* **52**, 1959 (1988).
6. R.A. Wood and R.J. Huger, *J. Vac. Sci. Technol.* **A1**, 1608 (1983).
7. C. Jonah, P. Chandra, and R. Bersohn, *J. Chem. Phys.* **55**, 1903 (1971), C.F. Yu, F. Youngs, K. Tsukiyama, R. Bersohn, and J. Preses, *J. Chem. Phys.* **85**, 1382 (1986).
8. C.J. Chen and R.M. Osgood, *J. Chem. Phys.* **81**, 327 (1984).
9. P.D. Brewer, J.E. Jensen, G.L. Olsen, L.W. Tutt and J.J. Zinck, *Proc. Mat. Res. Soc. Symp.* **101**, 327 (1988); P.D. Brewer, *Chem. Phys. Lett.*, **141**, 301 (1987).
10. V.M. Donnelly, J.A. McCaulley, V.R. McCrary, C.W. Tu and J.C. Beggy, "Selective Area Growth of GaAs by Laser Induced Pyrolysis of Absorbed Gallium-Alkyls," *Proc. Mat. Res. Soc. Symp.*, Vol. 129 (1989).
11. D. Burgess, P.C. Stair, and E. Weitz, *J. Vac. Sci. Technol.* **A4**, 1362 (1986); P.C. Stair and E. Weitz, *J. Opt. Soc. Am.* **B4**, 255 (1987).
12. L.A. Kolodziejski, R.L. Gunshor, N. Otsuka, S. Datta, W.M. Becker and A.V. Nurmikko, *IEEE J. Quantum Electron.* **QE-22**, 1666 (1986).
13. Manuscript in preparation.

PART VIII

Etching II

XPS STUDIES OF CHLORINE ETCHING INTERACTIONS WITH GaAs(100)

ANDREW FREEDMAN AND C.D. STINESPRING

Center for Chemical and Environmental Physics, Aerodyne Research, Inc.,
45 Manning Road, Billerica, MA 01821

ABSTRACT

GaAs (100) substrates have been chlorinated with both atomic and molecular beams of chlorine under ultra high vacuum conditions. X-ray photoelectron spectra of the resulting samples indicate that at a substrate temperatures of 130 K, Cl atoms efficiently penetrate the GaAs lattice forming Ga and As chloride species. Exposure to Cl atoms at 173 K results in desorption of As, leaving GaCl_x species behind. Molecular chlorine reacts much less efficiently.

INTRODUCTION

The development of dry etching techniques for gallium arsenide has centered around the use of both atomic and molecular chlorine as a chemical etchant.¹⁻⁷ Recent experiments have shown that at low temperatures atomic chlorine is a much faster etchant of GaAs than molecular chlorine, and even faster still when combined with the effect of a low energy argon ion beam. Highly anisotropic etch features can be achieved by this technique. While the desorbing etch products of the chlorine reaction with GaAs have been detected mass spectrometrically,⁸⁻¹⁰ there has been no direct observation of the surface.

This paper describes studies of the interaction of beams of atomic and molecular chlorine with the GaAs(100) surface using x-ray photoelectron spectroscopy as a surface diagnostic. An ultrahigh vacuum compatible beam source utilizing microwave discharge induced chlorine dissociation has been used to irradiate GaAs samples that have been cooled to temperatures (130 K) sufficiently low to prevent the volatile etch products from desorbing.

EXPERIMENTAL

The experimental apparatus used in these studies comprises a turbomolecular pumped, liquid nitrogen trapped ultrahigh vacuum cell (ultimate vacuum - 3×10^{-10} torr) interfaced to an ion/sublimation pumped analysis chamber. The diagnostics available in the analysis chamber are x-ray photoelectron spectroscopy (XPS) and low energy electron diffraction (LEED). The sample is transferred between chambers using a linear motion feedthrough with sample heating (1200 K) and cooling (120 K) capabilities.

The GaAs samples used in these studies were p-type electronic grade single crystal substrates provided by Litton. In situ sample cleaning involved Ar^+ ion etching at one KeV until no trace of oxygen or carbon contamination could be observed. This was followed by annealing at 850 K¹¹ to restore surface order (as observed by LEED patterns as low as 33 eV).

The chlorine atom source is a slight modification of a fluorine atom source described elsewhere.¹² Briefly, it consists of a miniature fast flow tube whose output is sampled by an inverted skimmer with a small aperture

(40 μm). A 5% chlorine in argon gas mixture (2 torr) is flowed (500 sccm) through a quartz tube in which a microwave discharge has been induced by an Evenson type cavity. The tube walls downstream of the discharge are coated with fluorocarbon wax to minimize wall induced recombination. The flow tube exhaust is sent through a co-annular passage and pumped by a 16 cfm chemical plasma mechanical pump (Alcatel). Mass spectrometric analysis indicates that between 50 and 70% of the chlorine is dissociated to atoms.¹³

The XPS analyses were performed using a PHI 15 keV, Mg (K_{α}) and Al(K_{α}) x-ray source and a PHI double pass cylindrical mirror electron energy analyzer operated at a pass energy of 25 eV. The analyzer was calibrated using the Au $4f_{7/2}$ peak at 83.8 eV and is accurate to ± 0.2 eV. All spectra are referenced to the Ga peak at 18.8 eV.

RESULTS

Figures 1 and 2 show XPS spectra of the Ga and As $2P_{3/2}$ peak as a function of exposure to the chlorine atom source at a substrate temperature of 130 K. These peaks were chosen so as to be extremely surface sensitive. Electron escape depths for Ga and As at the electron kinetic energies associated with the binding energies (recorded using the Mg and Al x-ray sources respectively) are calculated to be on the order of 7 Å. Thus these spectra record the chemical reaction occurring in the first several layers (lattice parameter = 5.65 Å). Notice that the Ga peak immediately shows a large shift to higher binding energy as would be expected from a GaCl_x

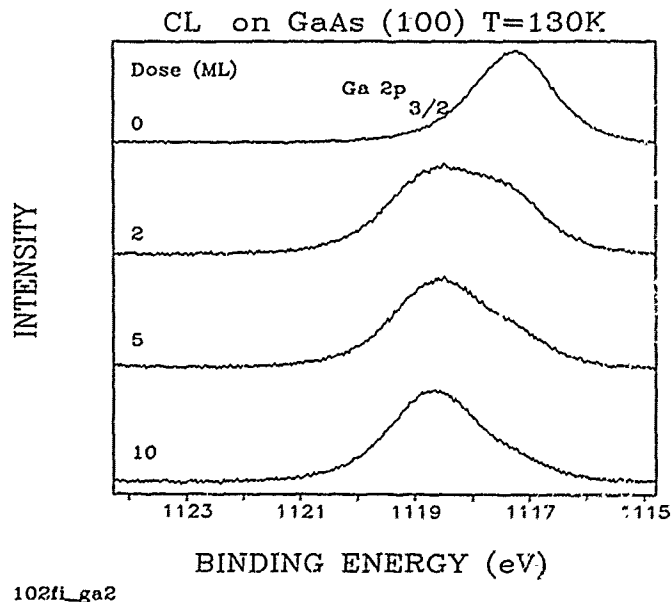


Figure 1. XPS Spectrum of the Ga $2P_{3/2}$ peaks as a function of exposure of GaAs(100) to Cl atoms at a substrate temperature of 130 K. (1ML = 6.3×10^{14} atoms cm^{-2})

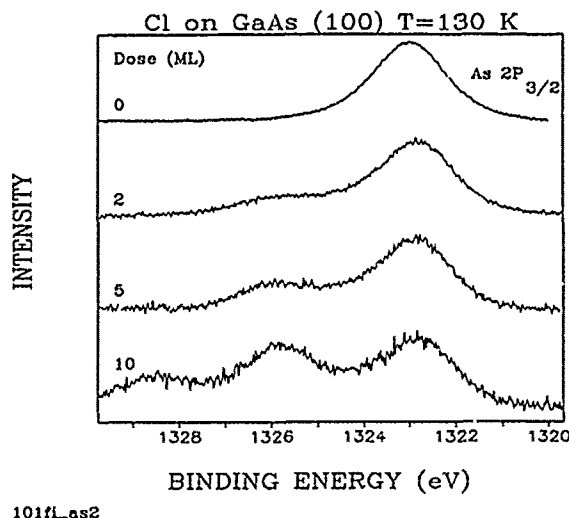


Figure 2. XPS spectrum of the As $2P_{3/2}$ peak as a function of exposure of GaAs(100) to Cl atoms at a substrate temperature of 130 K.

species. As the exposure is increased to only 10ML ($1 \text{ ML} = 6.3 \times 10^{14} \text{ atoms cm}^{-2}$), the bulk Ga signal is almost totally attenuated leaving behind a chlorinated peak at 1.1 eV higher binding energy. The arsenic peak shows similar behavior, with a chlorinated peak appearing at 3 eV higher binding energy. The assignment of a second peak which appears at 6 eV higher energy is unclear at this time.

Figures 3 and 4 show the same spectra for a sample exposed at a substrate temperature of 173 K. At this temperature, AsCl_3 has a vapor pressure of $\sim 10^{-4}$ torr while GaCl_3 is still not volatile. The gallium spectra show behavior similar to that recorded at 130 K although the complete shift to GaCl_x is not quite seen at 10ML exposure. The arsenic spectra on the other hand show no binding energy shifts but an extreme reduction in signal. This indicates that the As is being preferentially etched due to its high etch product volatility, leaving behind a GaCl_x matrix.

Preliminary results using molecular chlorine indicate the formation of both As and Ga chloride reaction products except at a much less efficient rate. The data are consistent with only a monolayer of chlorination. Much higher doses increase the level of chlorination, but the efficiency of the dissociative adsorption step is probably rate limiting.

DISCUSSION

It is clear from the data that even at substrate temperatures of 130 K, Cl atoms rapidly penetrate the GaAs lattice, chlorinating both gallium and arsenic. Furthermore, at higher substrate temperatures, the more volatile AsCl_3 desorbs leaving behind a GaCl_x matrix. This extremely efficient chlorination process is consistent with what is known about chlorine etching of GaAs.⁵ Etching with Cl_2 requires elevated temperatures to achieve similar etch rates.

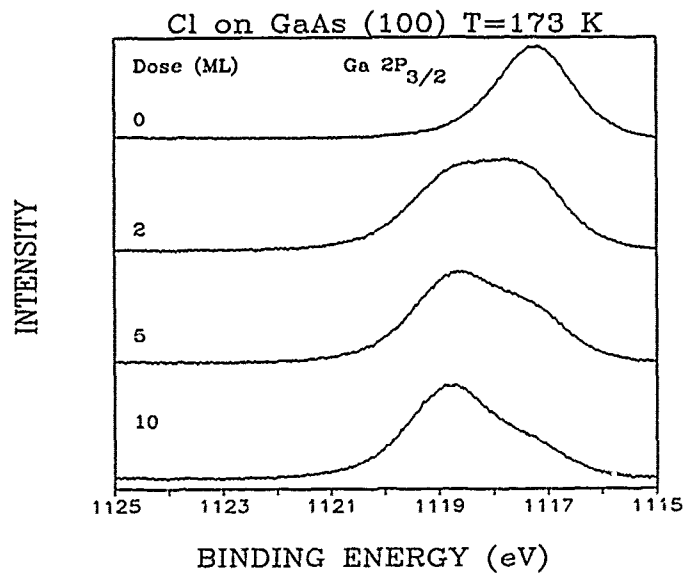


Figure 3. XPS spectrum of the Ga $2P_{2/3}$ peak as a function of exposure of GaAs(100) to Cl atoms at a substrate temperature of 173 K.

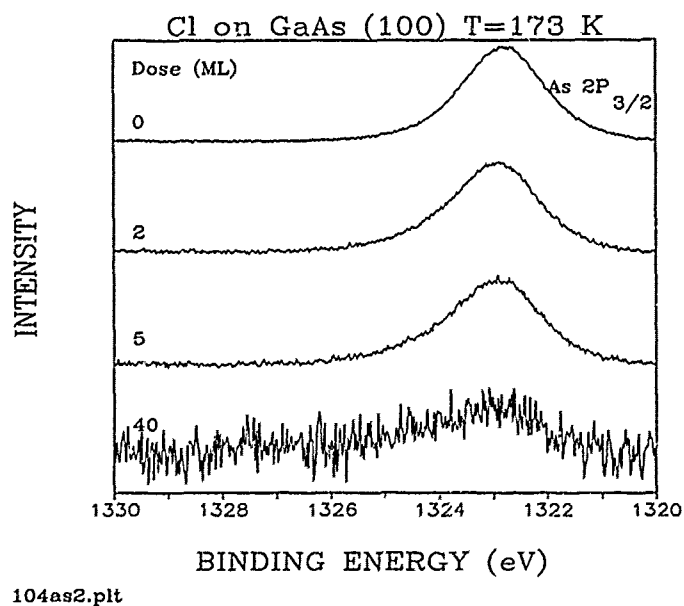


Figure 4. XPS spectrum of the As $2P_{2/3}$ peak as a function of exposure of GaAs(100) to Cl atoms at a substrate temperature of 173 K.

The etching behavior of chlorine atoms on GaAs is different from that found on silicon. Neither atomic nor molecular chlorine is a strong chemical etchant of silicon.¹⁴ This has been explained on the basis of an activation energy barrier to lattice penetration caused by repulsion between the lattice and chlorine electron clouds.¹⁵ Given the similar bulk structure (diamond lattice and similar atom densities) of silicon and gallium arsenide, it is somewhat surprising that chlorine atoms penetrate the gallium arsenide lattice (as fluorine atoms do the silicon lattice^{16,17}). Obviously, an explanation of this behavior awaits more experimental and theoretical evidence.

This work has been funded by the National Science Foundation under the Small Business Innovation Research program.

REFERENCES

1. M.W. Geis, G.A. Lincoln, N. Efremow and W.J. Piacentini, *J. Vac. Sci. Technol.* **19**, 1390 (1981).
2. S.W. Pang, M.W. Geis, N.N. Efremow and G.A. Lincoln, *J. Vac. Sci. Technol.* **B3**, 398 (1985).
3. H.F. Wong, D.L. Green, T.Y. Liu, D.G. Lishan, M. Bellis, E.L. Hu, P.M. Petroff, P.O. Holtz and J.L. Morz, *J. Vac. Sci. Technol.* **B6**, 1906 (1988).
4. S.W. Pang, W.D. Goodhue, T. Lyszczarz, D.J. Ehrlich, R.B. Goodman and G.D. Johnson, *J. Vac. Sci. Technol.* **B6**, 1916 (1988).
5. J.A. Skidmore, L.A. Coldron, E.L. Hu, J.L. Morz and K. Asakawa, *Appl. Phys. Lett.* **53**, 2308 (1988).
6. N. Furuhashi, H. Miyamoto, A. Akamoto and K. Ohata, *J. Appl. Phys.* **65**, 168 (1989).
7. M. Taneya, Y. Sugimoto, H. Hikada and K. Akita, *Jap. J. Appl. Phys.* **28**, L515 (1989).
8. S.C. Nevin and G.E. Becker, *J. Appl. Phys.* **58**, 4670 (1985).
9. W.L. O'Brien, C.M. Paulsen-Boaz, T. Rhodin and L.C. Rathbun, *J. Appl. Phys.* **64**, 6523 (1988).
10. H. Hou, Z. Zhang, S. Chen, C. Su, W. Yan and M. Vernon, *Appl. Phys. Lett.* **55**, 801 (1989).
11. L.A. Kolodziejewski, R.L. Gunshor, N. Otsuka, S. Datta, W.M. Becker and A.V. Nurmikko, *IEEE J. Quantum Electron.* **QE22**, 1666 (1986).
12. C.D. Stinespring and A. Freedman, *J. Vac. Sci. Technol.* **A4**, 1946 (1986).
13. C.D. Stinespring and A. Freedman, "Atomic Chlorine Source For Semiconductor Etching Studies," NSF Final Report. Aerodyne Research, Inc. Report No. ARI-RR-614 (1987).
14. J.W. Coburn and H.F. Winters, *J. Appl. Phys.* **50**, 3189 (1979).
15. J.Q. Broughton and P.S. Bagus, "Computer Modeling of Semiconductor Surface," P306 in the *Chemistry of the Semiconductor Industry*, S.J. Moss and A. Ledwith, eds., Chapman and Hall (New York) 1987.
16. J.F. Moran, F.R. McFeely, N.D. Shinn, G. Landgren, F.J. Himpsel, *Appl. Phys. Lett.* **45**, 174 (1984).
17. C.D. Stinespring and A. Freedman, *Appl. Phys. Lett.* **48**, 718 (1986).

A PROCESS MODEL FOR REACTIVE ION ETCHING AND STUDY OF THE EFFECTS OF MAGNETRON ENHANCEMENT

M. MEYYAPPAN AND R. C. BUGGELN
Scientific Research Associates, P. O. Box 1058, Glastonbury, CT 06033

ABSTRACT

Magnetron reactive ion etching has been receiving much attention since it offers low pressure, and low bias etching conditions with little damage. We have developed a process model for this process and present simulation results for boron trichloride etching of GaAs. The computed etch rates are uniform in the center with higher rates at the edges of the wafer. Flow rates and pressure can be optimized to improve uniformity. The etch rates with the aid of the magnetron are shown to be higher than the rates for conventional reactive ion etching.

INTRODUCTION

Reactive ion etching (RIE) has essentially replaced wet chemical etching as a preferable method for accomplishing fine-line patterning and selective etching. The ability of RIE to provide anisotropic etching with close control of the critical dimensions and selectivity has made this transition possible. As single wafer etchers are increasingly used, a high rate of etching is desirable. In addition, there is always the need to minimize the device damage introduced by high energy ion bombardment. To meet these demands, a variety of enhanced RIE processes have been introduced in recent years. Magnetron reactive ion etching (MIE) is a typical example wherein a magnetic field is used to provide a high degree of ionization, and low pressure, low bias etching [1]. In a commercial reactor by MRC [2], a magnet placed under the cathode confines the electrons in the discharge region due to the $\mathbf{E} \times \mathbf{B}$ field, which increases the ionization efficiency at low pressures. The magnetron discharge also has a much lower ion energy due to the lower sheath voltage and higher charged particle density than the conventional unmagnetized discharge. This results in a lower damage to the wafer than other dry etching processes. Bright et al [3], in a series of studies, reported application of MIE for the etching of Si and SiO₂. Contilini and D'Asaro [4] obtained high etch rates with very little under-etch by magnetron etching of GaAs using a freon plasma.

Process modeling needs

A particular disadvantage of all dry etching processes is the associated large parameter space and potential difficulties in scale-up. The parameters arise from the discharge, chemistry, plasma/surface interactions and geometric considerations of the etcher. This makes understanding of the effects of various parameters on the etch characteristics a complex task. A systematic model to address the issue then should include both the discharge physics and discharge chemistry. The discharge physics deals with creation and transport of charged particles such as ions and electrons. The key parameters here are power, nature of electrodes, electrode area, pressure, and excitation frequency. The discharge chemistry involves creation and transport of neutral species, active radicals, atoms etc. The controlling parameters are the etch gas, flow rate, pressure, and the glow discharge structure.

Fortunately, in situations of interest in dry etching, the etch gas is only weakly ionized. This means, the discharge physics and chemistry can be decoupled, which makes the analysis manageable. The physics of the discharge can be studied using numerical procedures which have long been used in device physics simulation [5]. The discharge chemistry is best studied using procedures that are routine in the fields of combustion and CVD. This involves solutions to the Navier-Stokes equation along

with energy and species conservation equations. The connecting links between the discharge physics and chemistry appear as source terms representing dissociation in the conservation equations. For a detailed discussion of modeling strategies, the reader is referred to a review article by Graves [6].

Details of the present model

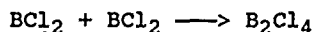
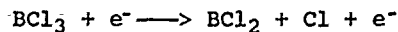
In the present work, we have developed a process model to describe the discharge chemistry. Reactive ion etching of GaAs using a boron trichloride discharge in a channel flow reactor, with and without the aid of a magnetic field, is considered. The continuum equations are assumed to be valid for the reactor conditions used in this study. The conservation equations for the neutral species in the discharge are as follows:

$$\frac{\partial C_i}{\partial t} + \mathbf{v} \cdot \nabla C_i = D_i \nabla^2 C_i + \sum_{j=1}^N \alpha_{ij} R_{ij}$$

Here C_i is the molar concentration of species i , D_i is the diffusivity of species i , \mathbf{v} is the velocity vector and α_{ij} are the stoichiometric coefficients relating to reaction j . R_{ij} is the rate of reaction for species i in reaction j .

In the present analysis, discharge physics modeling is not considered. The electron density distribution is assumed to be given by the ambipolar profile $n = n_0 \cos(\pi x/L)$. We also assume a fully developed flow in the channel flow reactor. For the low pressures and flow rates characteristic of the RIE reactors, the Reynolds number is small, and hence the entrance effects can be neglected [7]. Also, if the electrodes are well cooled, the temperature variation across the reactor is not significant. For these reasons, the Navier-Stokes equations and the energy equation need not be solved.

The following reactions are considered for the boron trichloride discharge [8].



The first reaction represents dissociation of boron trichloride due to electron bombardment. The second reaction describes recombination of BCl_2 . Cl atom recombination is considered to be negligible.

For boundary conditions, a mass balance is written for Cl at the wafer surface. A first order surface reaction is considered. The balance yields

$$D \nabla C_{\text{Cl}} = k_s C_{\text{Cl}}$$

where k_s is the surface reaction rate constant. The dimensionless number $k_s L/D$ compares the time scales for surface reaction and diffusion of Cl atom to the wafer. All surfaces other than the wafer are considered to be nonreacting; hence the normal gradient of the species is set to zero. At the inlet, the well-known Danckwert's boundary condition is used. The gradients in the flow direction are set to zero for outflow boundary conditions.

The governing equations were solved using a very efficient finite difference MINT code. This code was developed to solve the Navier-Stokes equations, energy and species conservation equations in three dimensions. The details of the algorithm can be found in ref. [9]. In the present problem, the conservation equations for Cl atom and BCl_2 radical were solved using 100 grid points in the flow direction and 50 grid points in the direction normal to the wafer (Figure 1).

Results

A channel flow reactor with a parallel plate electrode arrangement, as shown in Figure 1, is considered. The electrodes are 30 cm long and separated by 9 cm. The top electrode is grounded (anode) and the bottom electrode is powered (cathode). Reactive ion etching of a 3" GaAs wafer centrally placed on the cathode is simulated.

The rate of dissociation of boron trichloride is given by $k_1 n c$ where k_1 is the rate coefficient ($10^{-19} \text{ m}^3/\text{s}$) and c is the molar concentration of boron trichloride. A peak electron density (n_0) of 10^{10} cm^{-3} was assumed. The BCl_2 recombination is considerably more complex and the rate constant was taken to be $4 \times 10^5 \text{ m}^3/\text{s}$. The diffusivity of Cl atom is $950 \text{ cm}^2/\text{s}$ at 10 m Torr and has an inverse dependence on pressure.

Figure 2 shows the etch rate as a function of BCl_3 flow rate for two different pressures. Since the etch rate varies across the wafer, an average rate is computed. The etch rate for BCl_3 etching of GaAs is considerably smaller than the rates using Cl_2 , CCl_4 etc. Sonek and Ballyntyne [10] found that the small etch rate is due to inadequate generation of Cl atom from BCl_3 . The computed results at 10 mTorr and 20 sccm compare favorably with the etch rate of 170 Å/min at 11 m Torr and 20 sccm reported in ref. [12]. The etch rate is found to decrease with an increase in flow rate. The Damkohler number, Da , compares the time scale for Cl atom generation and the residence time determined by convection. The species generation rate is independent of axial location and feed flow rate. At low flow rates investigated here, an increase in flow rate means smaller Da . This denotes a reduction in residence time compared to the dissociation rate which causes smaller etching rates. The increase in etch rate with pressure is due to increased dissociation rates.

The variation of etch rate across the wafer is shown in Figure 3. At 10 m Torr, the etch rate is nearly uniform at the center with slightly higher rates at the edges. The etch rate is determined by a balance of Cl atom production, convection in the flow direction and diffusion of Cl atom. For a given pressure and dissociation conditions, the flow rate can be changed to obtain uniform etching. In fact, at 10 m Torr, the variation at the edges is smaller as the flow rate is increased from 20 sccm to 60 sccm. At 30 m Torr, the nonuniformity near the edges is more significant. The diffusivity at 30 Torr is lowered which results in strong variations in Cl atom concentration across the wafer. Figure 4 shows a contour plot of Cl atom mole fraction in the reactor at 10 m Torr and 20 sccm. The wafer acts as a sink for Cl atom. Hence, the Cl atom mole fraction in the vicinity of the wafer increases in a direction normal to the wafer. Preferably, the contours near the wafer should run parallel across the entire wafer to yield uniform etching. The prevailing local balance between diffusion, convection and generation of Cl atom determines the uniformity, as discussed before. In general, the flow rate and species generation can be optimized to obtain uniform etch rates.

Next we discuss the results for the magnetron enhanced etching. As mentioned before, when a magnetic field is imposed in a direction normal to the electric field, this enhances the local electron density near the wafer. Probe measurements [11] indicate an order of magnitude increase in electron density near the wafer. In the MIE computations, this was accounted by a modified electron density profile. At 10 m Torr and 20 sccm, the computed etch rate for MIE is 769 Å/min which is nearly 4.5 times higher than the corresponding rate for RIE. This follows an increase in Cl atom concentration near the cathode as displayed in Figure 5. The mole fraction of Cl in the reactor is about 0.02 indicating a higher generation rate compared to RIE. In order to obtain comparable etch rates by RIE, a substantial increase in pressure would be required; however this is undesirable since an increase in pressure often results in undercutting. A small amount of chlorine is normally added to BCl_3 to increase Cl atom production during RIE.

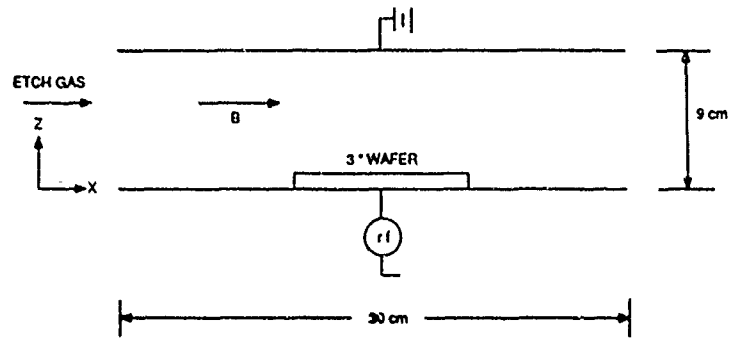


Figure 1. Schematic of the RIE reactor.
B field is for MIE.

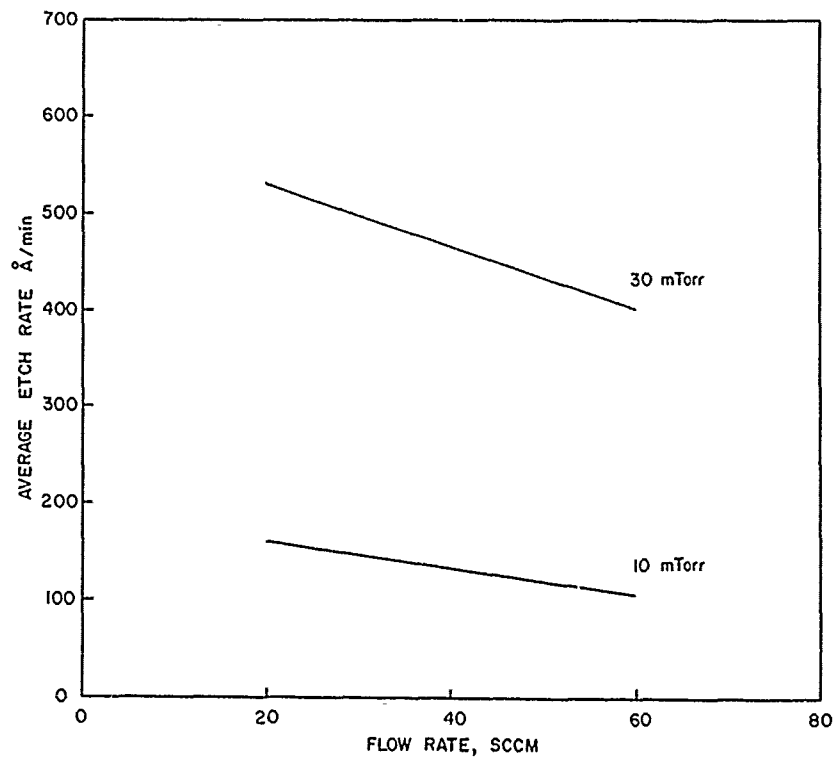


Figure 2. Etch rate vs. BCl_3 flow rate.

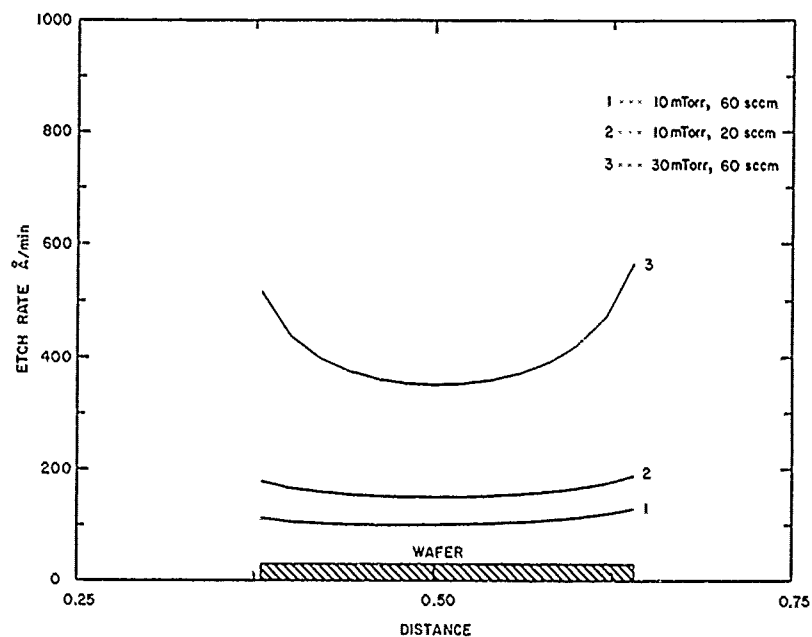


Figure 3. Etch rate uniformity across the wafer.

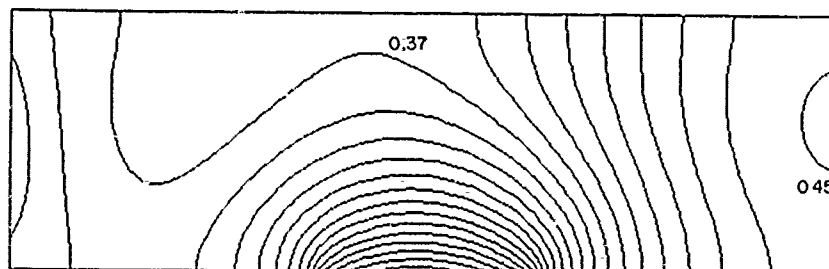


Figure 4. Contours of Cl atom mole fraction:
RIE, 10 mTorr and 20 sccm.

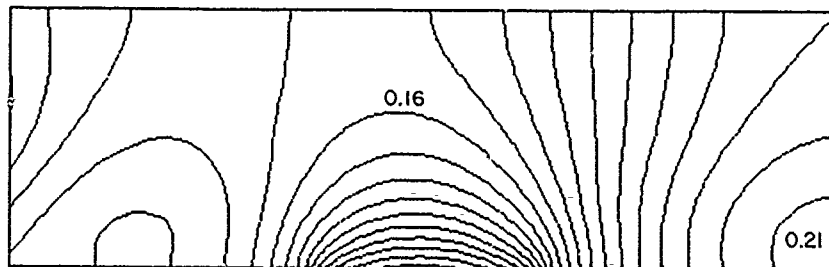


Figure 5. Contours of Cl atom mole fraction:
MIE, 10 mTorr and 20 sccm.

Conclusions

Process models are necessary to aid in the understanding of a complex process such as reactive ion etching. The model can be used to predict the effects of various process variables on etch rate and uniformity. In the present work, we have developed a model for the discharge chemistry. The predicted etch rate for boron trichloride reactive ion etching of GaAs compares favorably with previously reported experimental value. Also the model was used to show that the magnetron enhanced etching yields substantially higher etching rates than RIE. Three dimensional simulations will be performed in the future to predict uniformity and etching profiles across the entire wafer. In addition, work is in progress [12] to obtain information on electron and ion distributions and electron temperature, which is crucial to the modeling of dissociation kinetics.

Acknowledgement

This work was supported by the U.S. Army Electronic Technology and Devices Laboratory, Fort Monmouth, NJ under the SBIR program. The authors thank H. L. Grubin for his encouragement. One of the authors (MM) thanks Nara Meyyappan for introducing him to plasma etching problems, and Marc Fregeau and R. S. Krishnaswamy for many helpful discussions on the magnetron etching.

References

- [1] D. C. Hinson et al, Semiconductor International, 103, 10 (1983).
- [2] MRC-710 Series, Materials Research Corporation, Orangeburg, NY.
- [3] A. A. Bright et al., J. Appl. Phys., 62 (6), 2518 (1987); J. Vac. Sci. Technol. B, 7 (3), 1989 (1988); J. Vac. Sci. Technol. A, 6 (3), 1989 (1988).
- [4] R. J. Contolini and L. A. D'Asaro, J. Vac. Sci. Technol. B, 4 (3), 706 (1986).
- [5] D. B. Graves and K. F. Jensen, IEEE Trans. Plasma Sci., PS-14 (2), 78 (1986).
- [6] D. B. Graves, in the Proceedings of the Electrochemical Society Meeting, The Electrochemical Society, Oct. 1986.
- [7] H. Schlichting, Boundary-Layer Theory (McGraw-Hill, New York, 1968), p. 178.
- [8] K. Tokunaga et al, J. Electrochem. Soc., 128, 851 (1981).
- [9] W. R. Briley and H. McDonald, J. Comp. Physics, 24 (4), 372 (1977).
- [10] G. J. Sonek and M. Ballantyne, J. Vac. Sci. Technol. B 2 (4), 653 (1984).
- [11] L. I., D. C. Hinson, W. H. Class and R. L. Sandstrom, Appl. Phys. Lett, 44 (2), 185 (1984).
- [12] M. Meyyappan, J. P. Kreskovsky and T. R. Govindan, Glow Discharge Physics Through Solutions to the Moments of the Boltzmann Transport Equations, presented at the 2nd Topical Conference on Emerging Technologies and American Institute of Chemical Engineers Annual Meeting, San Francisco, Nov. 1989.

ETCHING OF GaAs ON AlGaAs IN RIE-MODE

GUDRUN KAUFEL AND ELFRIEDE OLANDER

Fraunhofer-Institut für Angewandte Festkörperphysik, Eckerstr.4,
D-7800 Freiburg, Fed. Rep. of Germany

ABSTRACT

Using MBE and MOCVD, High Electron Mobility Transistor (HEMT) structures were grown on two-inch GaAs wafers. The vertical structure included three GaAs layers and two thin (3nm) $\text{Al}_{0.3}\text{Ga}_{0.7}\text{As}$ etch stop layers to control precisely the depth of the etched recess and hence the threshold voltage of the devices.

The structure below the second etch stop layer depends on the particular device to be fabricated, but is irrelevant for the etching process.

The selective reactive ion etching of GaAs on AlGaAs is done by a Leybold MPE 3003 Plasma Etcher. The etch gas used is CF_2Cl_2 for GaAs and Ar for AlGaAs. The pressure lies between 30 μbar and 100 μbar and the self bias voltage between 47 V and 250 V.

The standard deviation for enhancement FETs is 12 mV for $V_t = +0.13$ V and for depletion FETs 18 mV for $V_t = -0.48$ V.

INTRODUCTION

Gate recess etching is used to fabricate high speed transistors in GaAs/AlGaAs heterostructures. This technology is desirable for producing devices with low source resistance. The etch depth of the recess can be defined by selective etching.

HEMT devices are ideal candidates for selective etch processes as the GaAs/AlGaAs interfaces provide convenient etch stop barriers.

The vertical structure of our devices contains two GaAs/AlGaAs hetero-interfaces. The gate of the depletion HEMT is deposited on the second GaAs layer, whereas the enhancement gate is deposited on the third GaAs layer. The AlGaAs layers act as etch stops.

EXPERIMENTAL

An all dry etch process was carried out in a commercial 13.56 MHz parallel plate Leybold (MPE 3003) reactor. In this reactor the wafers are placed on a 2" wafer-holder in a nitrogen purged load-lock. From here, the wafer-holder is transferred into the recipient where it is placed onto the lower electrode.

The background pressure in the etching chamber is 10^{-7} mbar. The etch gas enters the chamber through nozzles in the upper electrode and the flow of the gas is controlled by a MKS-flowmeter. The RF-power is applied to the lower electrode. The distance between the two electrodes is about five centimeters.

ETCHING

By varying to the etch conditions, we can produce anisotropic or isotropic etch profiles. Anisotropic etching means that the etch window coincide with the upper opening in the resist.

The first step of the etch process is the removal of the silicon nitride protection layer using CF_4 as etching gas.

The next step defines the etch trenches for the gates, and varies depending on whether D- or E-FETs are to be produced.

The D-FETs require only one etch step and a HCl dip for the removal of the AlGaAs layer. To avoid a short circuiting of the gate, the GaAs cap layer is etched isotropically with Freon 12 (CF_2Cl_2) at a pressure of 100 μbar . The undercut shown in Fig. 1 is about 50 nm.

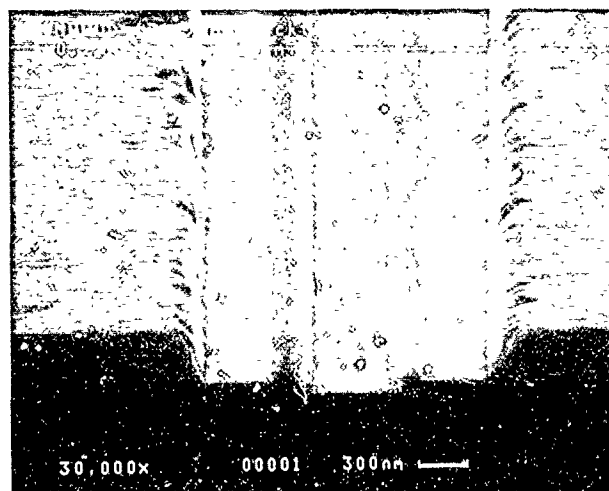


Fig. 1 0.2 μm recessed gate by RIE, demonstrating the undercutting of the GaAs cap layer with respect to the SiN layer.

In order to stop on the first AlGaAs layer, we have to choose low power and low voltage parameters. For RF-power values below 80 W, the selectivity of GaAs to AlGaAs is extremely high. Mild etching conditions are also desirable to keep the radiation damage as low as possible.

Etching of the E-FET is more complicated because the E-FET requires a multiple etch stop process. The first step includes the removal of the GaAs cap layer. Anisotropic etching is done using Freon 12 at 60 μbar and 102 V giving an etch rate of 360 nm/min. Under these conditions we achieved a good selectivity of GaAs to AlGaAs (Fig. 2).

Without the AlGaAs-stop layer the GaAs would be etched more than 400 nm in 80 seconds.

Although the thickness of the cap layer is only 30 nm we overetch by a factor of 10 in order to get the required undercutting of the trenches.

The undercut of the structure is a function of the etching time and pressure, and is demonstrated in Fig. 3 by varying the pressure at constant time.

In the next step the first AlGaAs-stop layer is removed. There are different methods to do this e.g. by etching with CF_2Cl_2 , by sputtering with Ar, or by removing the stop layer using a wet chemical etch.

The final step is to etch the GaAs layer under the first AlGaAs layer using CF_2Cl_2 , at 100 μbar , and 55 V.

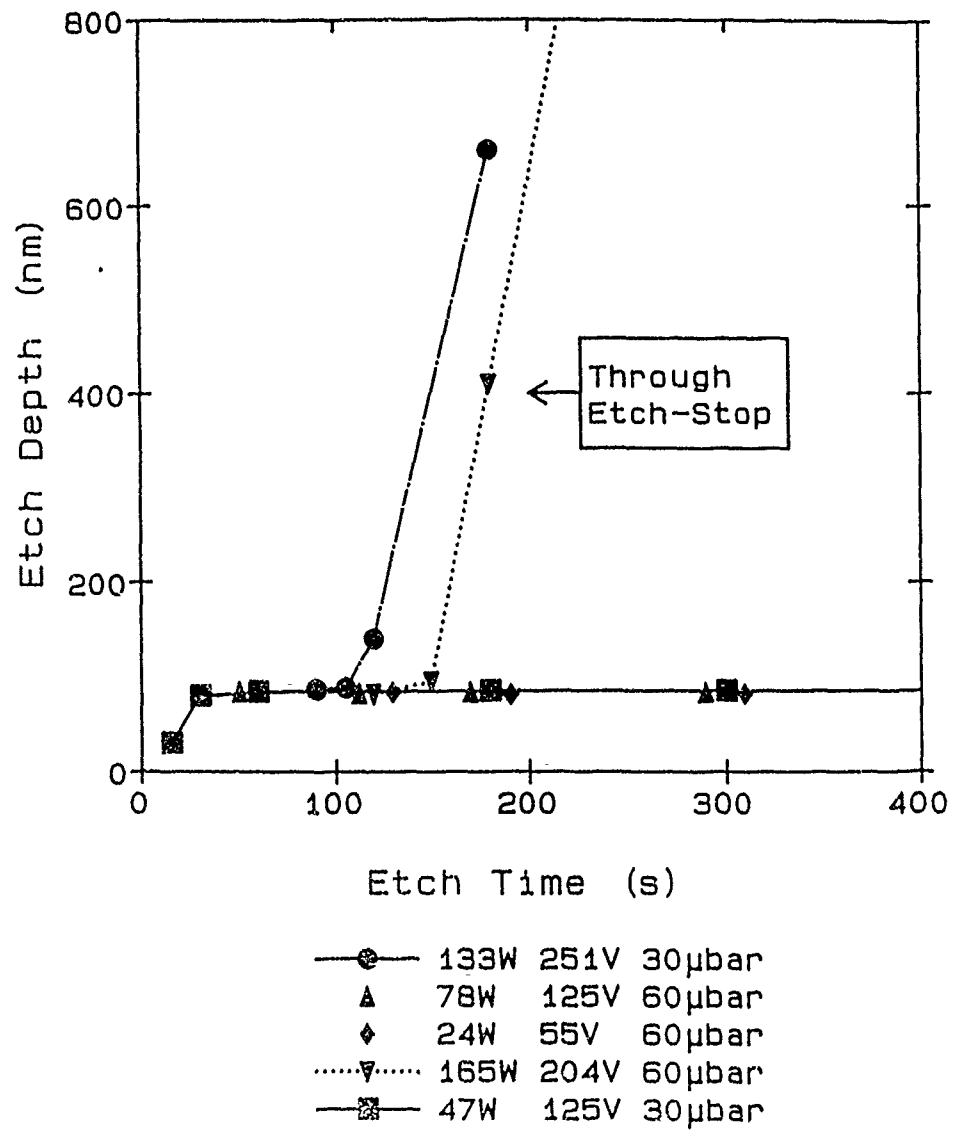
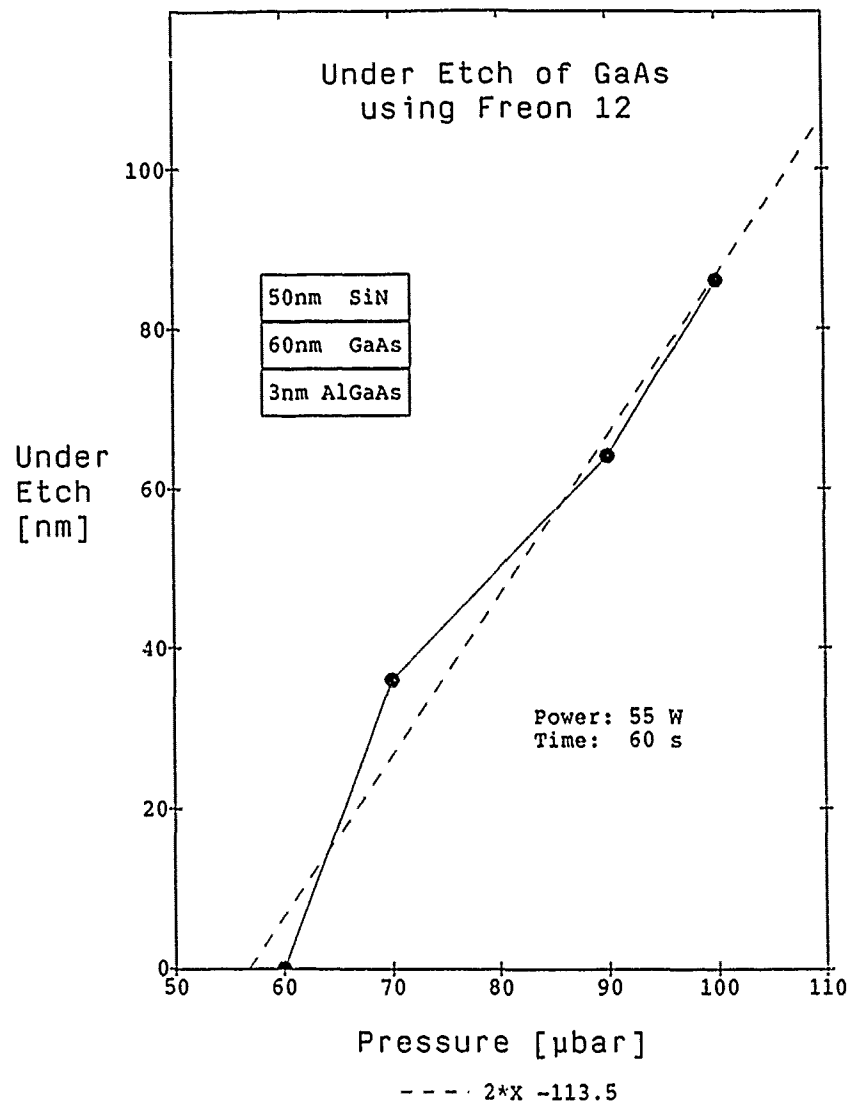


Fig. 2 Graph showing etch depth as a function of etch time for several etching conditions. For clarity, some symbols have been omitted from the curves particularly for etch times between 0 and 150 s.



Based on SEM pictures

Fig. 3 Graph showing the amount of underetching of GaAs (lateral etching) as a function of etch pressure.

RESULTS

After metallization and further processing the following results were obtained for our vertical HEMT structure. The average threshold voltages of D- and E-type devices (236 chips) were -0.48 V and $+0.13$ V respectively. The corresponding standard deviations in threshold voltage are 18 and 12 mV. Very high transconductance values were obtained: 388 mS/mm (std. dev. 8.1 mS/mm) for D-type and 485 mS/mm (12.6 mS/mm) for E-type device, both with $0.7\text{ }\mu\text{m}$ gate-length. For $0.5\text{ }\mu\text{m}$ E-type devices, the average transconductance was 560 mS/mm.

ACKNOWLEDGEMENT

The authors gratefully acknowledge Mr. Hornung and Mr. Grün for the measurements and Prof. Rupprecht, Mr. Jakobus, Mr. Patrick, Mr. Raynor, and Mr. Grille for their invaluable advice.

DOWNSTREAM ETCHING OF GaAs AND InP USING MOLECULAR CHLORINE AND CHLORINE RADICALS

DAVID G. LISHAN AND EVELYN L. HU

Department of Electrical and Computer Engineering, University of California, Santa Barbara, CA 93106

ABSTRACT

The temperature dependent etching of GaAs and InP using both molecular and remote plasma activated Cl_2 and HCl is examined. GaAs etches nearly three times faster in a remotely generated Cl_2 plasma than in a molecular Cl_2 environment with plasma off. The temperature dependence from room temperature to 250°C is similar for both cases. Significant etch rates of GaAs are observed for HCl remotely generated plasma even at room temperature ($\sim 1000 \text{ \AA}/\text{min}$). Although the etch rate for InP below 150°C is quite low for either Cl_2 or HCl, the relatively fast, temperature independent etch rate above this temperature is comparable to that of GaAs. The results are compared to RIE and a thermodynamic model.

INTRODUCTION

The formation vertical and angled structures in electronic and optoelectronic III-V compound devices has increasingly been carried out through a variety of directional, dry etching techniques. Typical dry etching techniques incorporate both a chemically reactive component with a superposed physical sputtering component to achieve high etch rates and control of profile. There has been increasing sensitivity to the damage that may be induced particularly by the sputtering component and realization that further knowledge of the purely chemical reactions is required both for damage-free etching and for the general preparation of surfaces for *in situ* processing[1-3]. This paper discusses the etching of GaAs and InP under the influence of thermally activated and remote plasma activated chlorine-containing radical beams. Our results indicate the potential for low damage etching using radical beams alone and highlight some important factors for achieving more efficient, ion enhanced etching.

We report etch rate versus temperature data for GaAs and InP in a well controlled, load-locked environment, using Cl_2 , HCl and the Cl^* radicals produced by these gases. The use of an HCl, rather than a Cl_2 remotely generated plasma, gives appreciable etch rates ($\sim 1000 \text{ \AA}/\text{min}$) even at room temperature. InP etching in HCl or Cl_2 remote plasmas shows a large activation energy of $\sim 55 \pm 15 \text{ kcal/mole}$ at low temperatures ($< 125^\circ\text{C}$), but suggests that substantial enhancements of etch rate (with or without ion assistance) are achievable by carrying out etching at modest temperatures of $\sim 150^\circ\text{C}$. Comparisons to RIE and thermodynamically predicted etching rates give insight into the mechanisms of chlorine based chemical etching.

EXPERIMENTAL

With considerations of low damage, we designed a dry etching system which is load-locked and achieves a typical base pressure of $\sim 5 \times 10^{-7}$ Torr. Radical beams are formed through the coupling of microwave power (via a McCaroll microwave cavity operating at 2.45 GHz) to the particular etch gases flowing through a quartz tube (Figure 1). The plasma region is approximately 25 cm from the sample with the end of the quartz tube extending to a point approximately two centimeters from the sample. The sample stage is temperature controlled and temperatures as high as 250°C can be obtained. Experiments were done with a microwave cavity power of 50 W for the "plasma on" condition while flowing 5 sccm of etching gas (chamber pressure $\sim 4 \times 10^{-4}$ Torr). Samples are either n-GaAs ($\sim 2 \times 10^{18} \text{ cm}^{-3} \text{ Si}$) or n-InP ($\sim 2 \times 10^{18} \text{ cm}^{-3} \text{ S}$) and received a brief pre-etch in 10% HCl to remove native oxides prior to chamber loading.

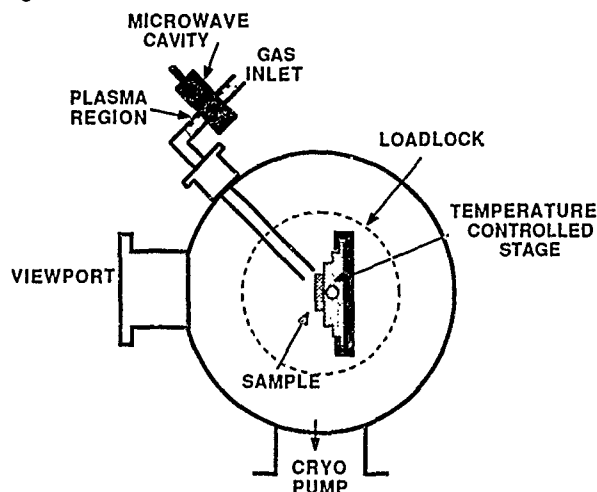


Figure 1. Schematic diagram of the apparatus used for remote plasma etching.

RESULTS AND DISCUSSION

GaAs etching with Cl_2 and HCl

Figure 2 shows the etch rate temperature dependence for GaAs by Cl_2 (plasma on and off conditions) and HCl (plasma on). The plasma off condition yielded no etching up to 250°C. Molecular chlorine (no plasma) yielded significantly high etch rates at relatively low temperatures ($\sim 800 \text{ Å/min}$ at $T = 100^\circ\text{C}$). Recent work carried out by Miyamoto et al. [4] shows similar GaAs etching of a few hundred Å/min at 100°C for 8×10^{-4} Torr Cl_2 . Miyamoto's data, in the 100-200°C temperature range give an activation energy of ~ 8 kcal/mole and our data from room temperature to $\sim 100^\circ\text{C}$ give a comparable activation energy of ~ 7 kcal/mole. We note that within experimental error and the difficulty in determination of the proper region of fit, our data is consistent with Miyamoto's. Identification of the proper region of fit is complicated by the smoothly varying form of the etch rate versus $1/T$ curve,

presence of several activation energies, corresponding to different rate limiting steps. Both Miyamota's data and ours show a range of temperatures of which the etch rate dependence on temperature is greatly reduced; in the case of Miyamoto's experiments, the etch rate is temperature-independent from 200°C to 400°C. Our etch rate versus temperature data flatten out towards $T > 175^\circ\text{C}$.

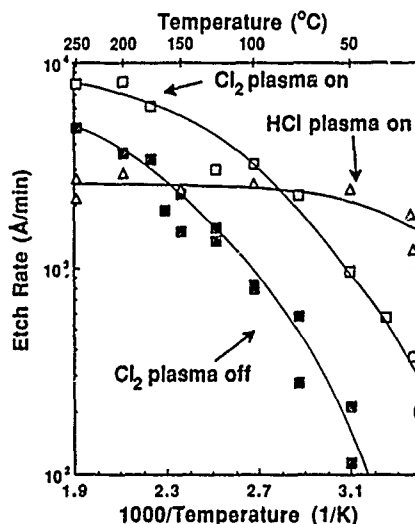


Figure 2. Etch rate vs reciprocal temperature for GaAs etched by Cl_2 and HCl.

Thus, molecular chlorine "cracks" upon adsorption to GaAs, and gas phase created Cl^* radicals are not necessary for etching. However, when gas phase Cl^* radicals are generated, the etch rate increases by a factor of nearly three and permits observation of room temperature etching ($\sim 300 \text{ Å/min}$). Previous work by Sugata [5] had remarked on the absence of etching at room temperature in the presence of ECR-generated chlorine radicals, although *in situ* Auger confirmed the presence of considerable chlorine adsorption. Later work by the same group [6] did observe room temperature etching GaAs by chlorine radicals at significantly reduced chlorine pressure and with a radical beam pre-clean of the substrate. For Cl^* radical etching, as with the reaction with molecular chlorine, we again see a change to an apparently lower activation energy at higher temperatures. The similarity in reaction mechanisms is manifested in the similarity between the curves for the plasma on and off cases. Etch results in the presence of a plasma (RIE) also show a strong temperature dependence but with an activation energy typically associated with the 11.4 kcal/mole desorption energy of GaCl_3 [7]. In our system, we believe that the temperature dependence and correspondingly lower activation energy arises from a rate limiting process other than GaCl_3 desorption and which may depend on Cl_2 adsorption/reaction dynamics. The data of Sugata, showing both no room temperature etching, even with the initiation of chlorine radicals, and an extraordinarily high activation energy ($\sim 500 \text{ kcal/mole}$), suggests that the ongoing competitive reactions with surface contaminants during etching may play the dominant role at low temperatures in determining the achievable etch rates [8].

From purely thermodynamic arguments, etch reactions in these pressure regimes should be temperature independent. McNevin [9] concluded that up to a saturation limit Cl_2 (a pressure related to the vapor pressure of GaCl_3) the etch reactions should be limited by the amount of Cl_2 present and not by the desorption of the GaCl_3 product. The saturation limit of chlorine is < 0.1 Torr at room temperature and increases with increasing temperature. Therefore, one would expect to observe temperature independent etching for studies carried out below those pressures, at or above room temperature.

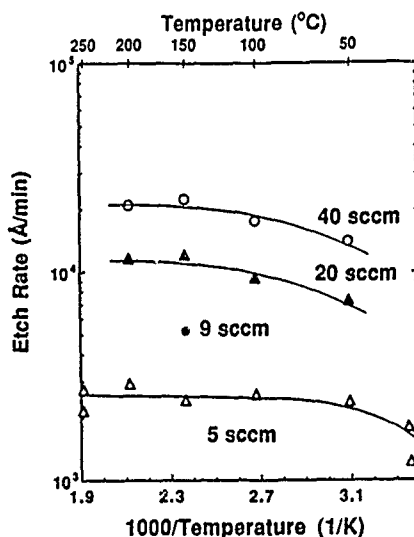


Figure 3. Etch rate vs reciprocal temperature for GaAs as a function of HCl flow rate.

In contrast to the behavior in Cl_2 , no etching of GaAs took place in HCl even at temperatures as high as 250°C unless a plasma was initiated. Curves of GaAs etching in HCl with the plasma on are shown in Figures 2 and 3. The sizable etch rates observed for remote plasma HCl even at room temperature (~ 1000 Å/min) are significantly different from those found with Cl_2 . Etch rates of GaAs with the HCl plasma on were largely temperature independent and remained independent over a wide pressure/flow regime. In this case, the lack of temperature dependence is consistent with McNevin's thermodynamic predictions. Assuming that desorption (or etching) of a steady state "contaminant" layer which is largely residual oxide is responsible for the temperature dependent etching that we observe for GaAs in Cl_2 , then the removal of that layer with HCl should yield temperature independent etching. Contour et al. [10] have used 0.1 Torr HCl at room temperature to perform an *in situ* clean of GaAs prior to MBE growth. *In situ* XPS confirmed the removal of oxide on the GaAs substrate, without etching of the substrate itself.

We might expect the surface morphology as a function of temperature to be markedly different for Cl_2 and HCl in that the transition from "rough" to "smooth" surfaces would occur at a lower temperature for HCl etching. Unfortunately the data from Nomarski photographs is ambiguous. However, in general, the substrate surfaces do tend to become smoother with increasing temperature.

InP Etching with Cl_2 and HCl

Figure 4 compares the etch rate in activated chlorine (plasma on) versus temperature for both GaAs and InP. The data for InP etching in Cl_2 differ from those for GaAs primarily by the threshold temperature for which etching is observed. Molecular Cl_2 also etches InP, apparently quite efficiently since the radical beam (plasma on) produces an etch rate only slightly faster than the molecular Cl_2 beam. In this case InCl_3 is less volatile than GaCl_3 , having an activation energy of ~ 38 kcal/mole [9]. The desorption of InCl_3 therefore limits InP etching at much lower Cl_2 pressures than for GaAs/ Cl_2 etching; McNevin's predicted Cl_2 saturation limit was 5×10^{-4} Torr at 225°C (and again drops sharply as temperature decreases). Our data in fact follow the thermodynamic prediction qualitatively well - a steeper curve of etch rate vs. $1/T$ at the lower temperatures, with no appreciable etching observed until $T = 150^\circ\text{C}$; thereafter, a much reduced temperature dependency is observed, as we become limited by chlorine flux rather than by InCl_3 desorption.

The etch rates of InP and GaAs are comparable at $T > 150^\circ\text{C}$. It has been observed [11] that RIE of GaAs and InP under identical conditions yields lower etch rates for InP and more poorly controlled sidewall anisotropy precisely because of the lower vapor pressure of the InCl_3 etch product. The work presented in this report suggests that more rapid etching of InP could be achieved at higher temperatures, even for the case of ion-enhanced etching. Either the directionality provided by the ion bombardment or the effect of sidewall masking by the etch product may result in fairly anisotropic etch profiles.

The comparison between GaAs and InP etched with HCl is made in Figure 5. Etching of InP in HCl shows similar behavior to etching in Cl_2 . The work by Contour et al. indicates that HCl fails to remove the oxide on InP. Since InP is unaffected by any "cleaning" properties of HCl (unlike the situation with GaAs) it should behave largely as it does for Cl_2 , with the low temperature behavior determined by a combined effect of surface contamination and InCl_3 desorption.

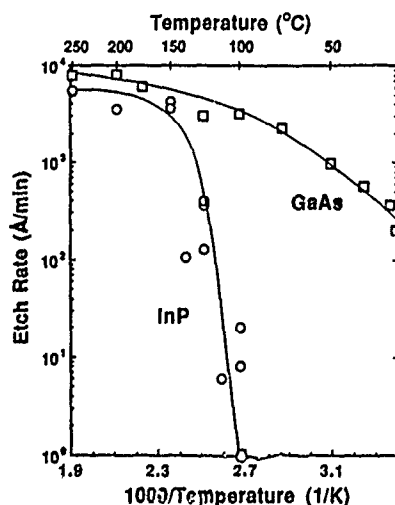


Figure 4: Etch rate vs reciprocal temperature for GaAs and InP etched by Cl_2 (plasma on).

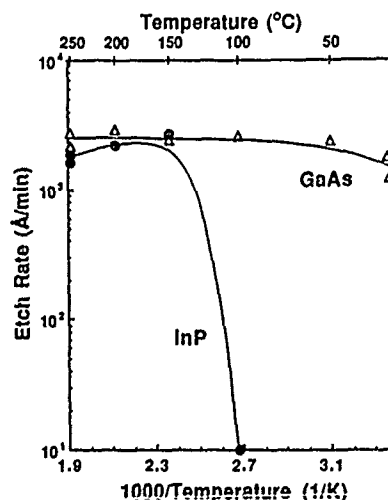


Figure 5: Etch rate vs reciprocal temperature for GaAs and InP etched by HCl (plasma on).

CONCLUSION

We note that in many of the current applications of dry etching, the most important criteria may be low damage, high chemical selectivity and controlled etching through thin (few hundred Å) layers, rather than a rapid etch rate. Where etching through thin layers, lateral etching of less than 100 Å may be tolerable. Our measurements of thermally activated and remote plasma activated plasma etching show that in a suitably clean, load-locked system, reasonably high etch rates of ~1000 Å/min are obtainable at low temperatures (~125°C) for InP, as well as GaAs. Where rapid, straight-walled etching is required, some ion-imposed directionality may be combined with etching at an elevated temperature to obtain substantial augmentation and improved anisotropy of InP etch rates.

The use of HCl in GaAs etching, which also effectively removes thin native oxide layers, in fact allows us to achieve rapid etch rates at room temperature, and has also allowed us to observe the temperature-independent, flux-limited etching behavior predicted by thermodynamic calculations. Finally, noting in Figures 4 and 5 the large disparity of etch rates between GaAs and InP at room temperature and nearly equi-rate etching at higher temperatures, we suggest that highly selective etches may be developed which could also be useful in passivation, etch and regrowth schemes. The capabilities of such an ion-less etch scheme for low damage, together with the etch enhancement at low temperatures, are apparent.

ACKNOWLEDGEMENTS

The authors would like to acknowledge helpful discussions with E.J. Caine and Jay Skidmore. This research was supported by DARPA and the NSF-supported Science and Technology Center, QUEST.

REFERENCES

- [1] H.-F. Wong, D.L. Green, T.Y. Liu, D.G. Lishan, M. Bellis, E.L. Hu, P.M. Petroff, P.O. Holtz, J.L. Merz, *J. Vac. Sci. Technol.* **B6**, 1906 (1988).
- [2] R. Cheung, S. Thoms, I. McIntyre, C.D.W. Wilkinson, S.P. Beaumont, *J. Vac. Sci. Technol.* **B6**, 1911 (1988).
- [3] K. Gamo, H. Miyake, Y. Yuba, S. Namba, H. Kasahara, H. Sawaragi, R. Aihara, *J. Vac. Sci. Technol.* **B6**, 2124 (1988).
- [4] H. Miyamoto, N. Furuhashi, H. Hoshino, A. Okamoto, K. Ohata, Gallium Arsenide and Related Compounds 1988, (Inst. of Phys. Conf. Series **96**, 1988), pp. 47.
- [5] S. Sugata, K. Asakawa, *Jap. Journ. Appl. Phys.* **23**, L564 (1984).
- [6] K. Asakawa, (private communication).
- [7] V.M. Donnelly, D.L. Flamm, C.W. Tu, and D.E. Ibbotson, *J. Electrochem Soc.* **129**, 2533 (1982).
- [8] M. Balooch, D.R. Olander, and W.J. Siekhaus, *J. Vac. Sci. Technol.* **B4**, 794 (1986).
- [9] S.C. McNeel, *J. Vac. Sci. Technol.* **B4**, 1216 (1986).
- [10] J.P. Contour, J. Massies, A. Saletes, M. Outrequin, F. Simondet, J.F. Rochette, *J. Vac. Sci. Technol.* **B5**, 730 (1987).
- [11] E.L. Hu, R.E. Howard, *Appl. Phys. Lett.* **37**, 1022 (1980).

HOLLOW COLD CATHODE ION SOURCE FOR REACTIVE ION-BEAM ETCHING

A.I. STOGNIJ AND V.V. TOKAREV

Institute of Solid State and Semiconductor Physics, the BSSR
Academy of Sciences, P.Brovka 17, Minsk 220726, USSR

ABSTRACT

A wide-aperture reactive gas ion source has been developed for various ion-beam processings in high vacuum ($p < 5 \times 10^{-2}$ Pa). The peculiar feature of the ion source is that two-stage self-maintained low-pressure discharge is used here as a plasma emitter. This provides high operating parameters of the source along with simple diode-type structure.

WIDE-APERTURE REACTIVE GAS ION SOURCE

Modern techniques of resolving scientific and technological problems in high vacuum using ion beams require an efficient gas discharge ion source, especially O_2 source or a source with O_2 addition, which can ensure beams with uniform density amounting to ~ 1 mA/cm² on the surface area of 100 cm² and over. The difficulties arising here are concerned first of all with the decomposition of electrodes which are heated in the course of chemical reactions proceeding on their surface in O_2 containing atmosphere. The removal of these electrodes from the ion source design leads to the rise of energy consumption for the generation of ions in the discharge and minimal pressure rise which finally decrease ion source efficiency on the whole.

We have developed a wide-aperture ion source in which a two-stage self-maintained low-pressure discharge is used as a plasma emitter [1,2], ensuring high ion source parameters without employing hot electrodes. To form the uniform plasma emission boundary the ion source has a constant polarity multipole magnet system located along the hollow cathode periphery just near the emission electrode. The general view of the source is shown in fig.1.

The source discharge chamber incorporates 60 mm high and 130 mm in diameter hollow cathode, closed from the ends, and a flat anode located symmetric about the cathode axis. An expendable insert with a central contracting hole 6 mm in diameter is located in the cathode end which faces anode.

Hollow cathode bottom end, which serves as an emission electrode, and an accelerating electrode form many-aperture flat ion beam contraction system. The collection of ions is executed through 800 coaxial pairs of holes. The holes are

2 mm high and 2.9 mm in diameter and they uniformly perforate each electrode on the surface 126 mm in diameter. The height of the acceleration spacing between the emission and the accelerating electrodes amounts to 2 mm.

All electrodes are made of stainless nonmagnetic steel, insulators are made of caprolon. The magnet system is located along the hollow cathode periphery just near the emission electrode. It contains 22 equally spaced Sm-Co magnets 6 mm high and 10 mm in diameter with a maximum magnetic flux density of 95 mT each. The like poles of these magnets are facing the cathode centre, their axes being perpendicular to the cathode axis. The magnet system is located within the cathode forced cooling flue to rule out the possibility of overheating.

Working gas is supplied into the ion source through the anode axial hole (2 mm in diameter) and is pumped out through the extraction system holes. The pressure in the beam drift region amounts to $\sim 10^{-2}$ Pa, inside the cathode cavity it amounts to $\sim 10^{-1}$ Pa, in the spacing between the anode and the cathode it amounts to ~ 1 Pa at a gas flow rate less than $3 \times 10^{-2} \text{ m}^3 \cdot \text{Pa/s}$ and vacuum facility efficiency of about $0.5 \text{ m}^3/\text{s}$.

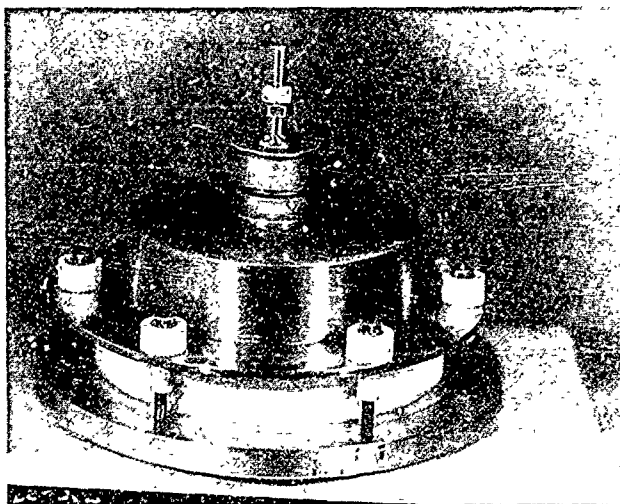


Fig.1 The general view of the ion source

Discharge is initiated by a short-time gas impulse after gas flow rate is set at a value above $0.9 \times 10^{-2} \text{ m}^3 \cdot \text{Pa/s}$ and $\sim 400 \text{ V}$ is applied between the anode and the cathode. The structure of gas discharge plasma includes equipotential cathode and anode parts (cascades). Cathode plasma is separated from the hollow cathode walls by the cathode potential drop layer of 220-260 V which thickness amounts to 4-6 mm. Anode plasma, which has a greater density adjoins anode and penetrates through a contracting hole into the hollow cathode

as an oval plasmoid with typical dimensions of 5-15 mm. Anode and cathode plasmas are separated by a double electric layer, the potential drop at which amounts to 40-60 V.

Bulk generation of charged particles in a cathode cascade is executed by secondary emission electrons from the cathode walls which are accelerated in the cathode potential drop layer and are oscillating in the cathode cavity. Ionization in the anode cascade is carried out by plasma electrons which gain the necessary energy in Langmuir oscillation fields. Langmuir oscillations are generated by the electron beam from the cathode cascade. Electrons are accelerated at the double layer when they migrate to the anode. Ions are collected into a beam both from the cathode plasma (40-50%) and from the anode plasma (50-60%). Ions from the anode plasma gain energy at the double layer and arrive at the emission boundary in the form of a divergencing flow. The existence of two groups of ions at the emission boundary ensures extraction efficiency up to 15% of the discharge current.

Ion source characteristics (with O_2 as a working gas) are presented at fig.2 for two gas flow rates, $Q = 10^{-2} m^3 \times Pa/s$ and $2.5 \times 10^{-2} m^3 \times Pa/s$.

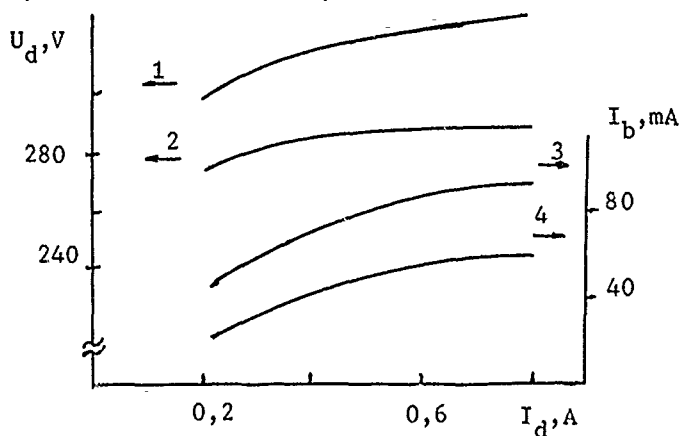


Fig.2 Ion source characteristics

Here 1 and 2 are V-I discharge characteristics, U_d - discharge voltage, I_d - discharge current, 3,4 - ion current dependences on I_d at $Q = 1.1 \times 10^{-2} m^3 \times Pa/s$ and accelerating voltage $U_{acc} = 4$ kV and 2 kV, respectively. Extraction efficiency decrease at $I_d < 0.4$ A and $I_d > 0.8$ A is explained in the first case by the localization of the anode cascade in the contracting hole and in the second case by the penetration of the anode plasma into the region of anode-cathode spacing. The outcome in both cases is hindering the ion transport from the anode cascade to the emission boundary. At $Q < 0.9 \times 10^{-2} m^3 \times Pa/s$ ion source operates unstable. Discharge voltage drops down to the level present at $Q = 2.4 \times 10^{-2} m^3 \times Pa/s$ and then

remains constant upon gas flow rate increase at a constant discharge current.

From the one hand, ion flux from the anode cascade increases ion source extraction efficiency, from the other hand, it is responsible for the decrease of plasma density profile down from the source axis to the periphery near emission boundary, which results in the nonuniform beam current density. Plasma density profile levelling along with the uniform sectioning of ion beam is achieved by inducing multipole magnetic field of constant polarity by the magnet system, disclosed in the description of the ion source design. The magnet system enables one to increase the life time of the oscillating electrons directly along the cathode periphery near the emission electrode by confining them in the magnetic field and without disbalancing discharge cascades. All this results in the formation of ion beam with \sqrt{L} -shaped current density profile. Current density value reaches 1 mA/cm^2 , its nonuniformity does not exceed $\pm 5\%$ on the area of 120 mm in diameter at $I_d \geq 0.8 \text{ A}$, $U_{el} \geq 2 \text{ keV}$, $Q = (1.2-2.4) \times 10^{-2} \text{ m}^3 \times \text{Pa/s}$ and at distances from accelerating electrode of $50 - 250 \text{ mm}$. Obtained with the three-electrode electrostatic energy analyzer ion energy straggling does not exceed 50 eV . Ion beam mass spectra show that it is composed of 65% of single charged O_2^+ ions, up to 25% of O^+ ions and some percent of multicharged ions and various impurity ions. Ion source life time exceeds 100 hours when it operates without noticeable deviations.

REFERENCES

- 1 A.I. Stognij, V.A. Nikitinskij, B.I. Zhuravlev, "Zhurnal Tekhnicheskoy fiziki" 1988, vol.59, No.5, pp.993-995, (USSR).
- 2 A.I. Stognij, V.V. Tokarev (to be published in "Pribery, tekhnika, experiment", 1990).

REACTIVE ION ETCHING OF In-BASED III-V SEMICONDUCTORS -COMPARISON OF Cl AND C₂H₆ CHEMISTRIES

S. J. PEARTON, U. K. CHAKRABARTI, F. A. BAIOCCHI AND W. S. HOBSON

AT&T Bell Laboratories, Murray Hill, NJ 07974

ABSTRACT

The reactive ion etching of InP, InGaAs and InAlAs in CCl₂F₂/O₂ or C₂H₆/H₂ discharges was investigated as a function of the plasma parameters pressure, power density, flow rate and relative composition. The etch rates of these materials are a factor of 3-5 times faster in CCl₂F₂/O₂ (~600-1000 Å · min⁻¹) compared to C₂H₆/H₂ (160-320 Å · min⁻¹). Significantly smoother morphologies are obtained with C₂H₆/H₂ etching provided the composition of the plasma is no more than 10 - 20% by volume of C₂H₆. At higher methane compositions, polymer formation increases leading to micromasking and rough surface morphologies. Sub-surface disorder is limited to <100 Å deep for both gas chemistries for plasma power densities of 0.85 W · cm⁻². The C₂H₆/H₂ mixture leaves an In-rich surface in all cases, but this surface is free of any residual contamination, whereas the CCl₂F₂/O₂ chemistry leaves chloro-fluorocarbon residues approximately 20-50 Å thick on the surface of all three In-based materials.

Introduction

The increasing importance of InP-based photonic and electronic devices requires the development of controlled methods for fabricating mesa-type structures. For small area devices wet chemical etching is simply unable to achieve the kind of anisotropic removal of material necessary to maintain the target dimensions. While there are beginning to appear some reports of simple devices fabricated using CH₄/H₂ dry etching^[1,2], work is still required to demonstrate that this gas mixture is completely acceptable as a replacement for Cl-based mixtures in etching InP and related compounds. In particular in laser structures it is often necessary to epitaxially regrow on the etched surface, while in heterojunction bipolar transistors ohmic contacts are fabricated after etching. Since either of these processes will be adversely affected by residues remaining after exposure to a reactive discharge, or by near-surface plasma-induced damage, it is necessary to thoroughly investigate the characteristics of InP, InGaAs and InAlAs surfaces after dry etching in organic-based discharges. In this paper we report a study of the dependence of etch rate of these materials on the pressure, power density, gas flow rate and relative composition of a C₂H₆/H₂ discharge, and measure the near-surface disorder induced using ion channeling and transmission electron microscopy. The surface stoichiometry was measured by Auger Electron Spectroscopy (AES) and X-ray Photoelectron Spectroscopy (XPS). In all cases we have compared the characteristics of C₂H₆/H₂ reactive ion etching with those of a more conventional gas mixture, Freon 12-oxygen (CCl₂F₂/O₂)^[3].

Experimental

A variety of samples were used in the work. The InP wafers were cut from Fe-doped, semi-insulating (>10⁷ Ω cm), (100) oriented crystals grown by the Liquid Encapsulated Czochralski (LEC) technique. Prior to patterning with photoresist they were etched in 5H₂SO₄:1H₂O₂:1H₂O for 5 mins to remove polish-induced damage that might affect the etch rate. The In_{0.53}Ga_{0.47}As and In_{0.52}Al_{0.48}As layers were grown lattice-matched to Fe-doped InP substrates within a barrel-geometry Organo-Metallic Chemical

Vapor Deposition (OMCVD) reactor operating at atmospheric pressure. The source chemicals used were trimethylgallium, trimethylindium and arsine, and the layers were nominally undoped with n-type carrier concentrations $\leq 10^{16} \text{ cm}^{-3}$.

For etch rate measurements the samples were selectively patterned with AZ1350J photoresist to give a variety of lines and spaces ranging from 1 – 50 μm in width. The mask openings were descummed by exposure to a 50W oxygen plasma for 3 min in a barrel reactor, and native oxide was removed by rinsing in $\text{NH}_4\text{OH}:\text{H}_2\text{O}$ immediately prior to loading in the RIE chamber. The etching was performed within a stainless steel, parallel plate reactor (Materials Research Corporation Model 51) with a 15 cm diameter powered lower electrode covered with a quartz plate. The total discharge pressure was varied 4 - 40 mTorr, the plasma power density from 0.4 - 1.3 $\text{W} \cdot \text{cm}^{-2}$, and the etch rate measured for times up to 12 min. The discharge compositions were also varied, from 5 - 60% C_2H_6 by volume in the $\text{C}_2\text{H}_6/\text{H}_2$ mixture, and from 25 - 95% CCl_2F_2 by volume in the $\text{CCl}_2\text{F}_2/\text{O}_2$ mixture.

Results

(a) Etch Rate Dependencies

Based on our past experience with etching other materials in $\text{CCl}_2\text{F}_2/\text{O}_2$ and $\text{C}_2\text{H}_6/\text{H}_2$ mixtures we used a set of standard conditions for most of the RIE treatments. The compositions were 19 $\text{CCl}_2\text{F}_2/1\text{O}_2$ and 2 $\text{C}_2\text{H}_6/18\text{H}_2$ respectively, at total gas flow rates of 20 sccm in each case, and a plasma power density of 0.85 $\text{W} \cdot \text{cm}^{-2}$, corresponding to self-biases on the cathode of 430V for $\text{C}_2\text{H}_6/\text{H}_2$ discharges and 445V for $\text{CCl}_2\text{F}_2/\text{O}_2$ plasmas. The total gas pressure in each case was 4 mTorr for standard etching runs.

Figure 1 shows the dependence of the etched feature depth on etching time for InP, InGaAs and InAlAs reactively ion etched in $\text{CCl}_2\text{F}_2/\text{O}_2$ or $\text{C}_2\text{H}_6/\text{H}_2$ under our standard conditions. There are three features to note. First, there is no delay between ignition of the discharge and the commencement of etching, which is sometimes observed with $\text{CCl}_2\text{F}_2/\text{O}_2$ RIE of AlGaAs and related materials. Second, the etched depth increases linearly with time up to 12 minutes. The crater depths were measured on triangular shaped openings in the mask, with sizes of either 5 μm or 50 μm on a side, and there were no significant differences in etched depth noted between the two. It is likely that in very small ($\leq 1 \mu\text{m}$) feature sizes that the etch rate would decrease with time because of the increasing difficulty of sweeping out the etch products. The third feature to note is that the etch rates are significantly higher for $\text{CCl}_2\text{F}_2/\text{O}_2$ discharges, which is consistent with past observations.

Figure 2 shows the dependence on plasma power density of the etch rates of InP, InGaAs and InAlAs in both types of discharge. For the $\text{CCl}_2\text{F}_2/\text{O}_2$ chemistry there is an essentially linear increase with increasing power density, while for the $\text{C}_2\text{H}_6/\text{H}_2$ chemistry the increase with power is initially very slow in the range 0.4 – 0.8 $\text{W} \cdot \text{cm}^{-2}$, and then shows a linear increase. This emphasises the role of ion sputtering in the etch mechanism using $\text{C}_2\text{H}_6/\text{H}_2$ because the purely chemical component of the etching is very small. Some degree of ion sputtering appears necessary either to increase the desorption rate of the etch products, principally the group III product, or to provide the energy necessary to promote the surface reactions to completion.

It has been previously established that the relative fraction of ethane and hydrogen in the discharge is a critical parameter in determining the etch rate of InP, GaAs and AlGaAs. It is reiterated by the results shown in Figure 3. The increase in etch rate we observe for C_2H_6 fractions up to 25% is presumably due to an increase in the active species concentration, whereas above 25% there appears to be a competition between polymer

deposition and etching, and the etch rate decreases with increasing ethane composition. At high C_2H_6 concentrations ($> 40\%$ by volume) a brown film could be observed on the photoresist mask, and there was a heavy polymeric coating around the reactor walls under these conditions. In contrast to the results for C_2H_6/H_2 RIE, the etch rate of all three materials shows a slow increase with increasing Freon 12 concentration until at a ratio of $0.75 CCl_2F_2$ to $0.25 O_2$ the rate rises in a super-linear fashion. This general trend would be expected as more active Cl species are supplied to the semiconductor surface, leading to a rapid increase in etch rate with increasing CCl_2F_2 composition. It is interesting to note that the etch rates of all three materials is actually greater for the C_2H_6/H_2 mixture at low values of C_2H_6 or CCl_2F_2 compositions.

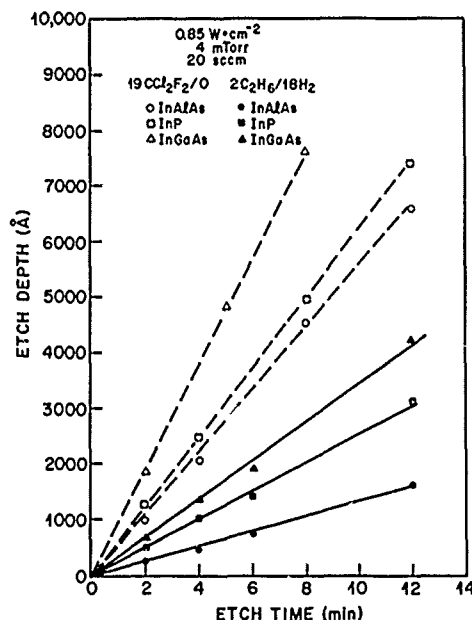


Figure 1. Etched depth in InP, InGaAs and InAlAs as a function of time in a $2C_2H_6:18H_2$ or $19CCl_2F_2:1O_2$ discharge, each at a pressure of 4 mTorr and a power density of $0.85 W \cdot cm^{-2}$.

In general we observed smooth etching for C_2H_6 concentrations less than 40%, and for total pressures less than approximately 25 mTorr. For higher pressures and larger ethane fractions the sidewalls showed increasing undercutting. Increasing the plasma power density also improved the etched surface morphology and anisotropy when holding the other discharge parameters constant. This is also consistent with the idea that ion bombardment plays an important role in the etch mechanism for C_2H_6/H_2 discharges. Under most conditions RIE of InP, InGaAs and InAlAs in CCl_2F_2/O_2 led to relatively rough surface morphologies, and severely overcut sidewalls.

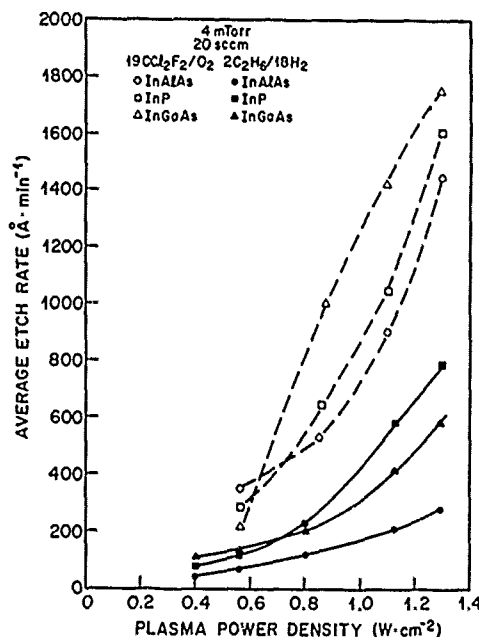


Figure 2. Average etch rate of InP, InGaAs and InAlAs in $2\text{C}_2\text{H}_6/18\text{H}_2$ or $19\text{CCl}_2\text{F}_2/1\text{O}_2$ discharges, as a function of the plasma power density.

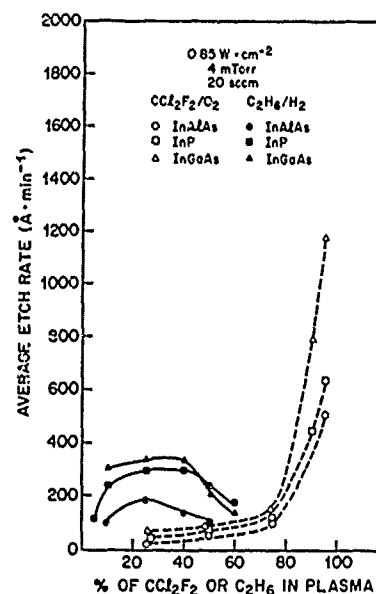


Figure 3. Average etch rate of InP, InGaAs and InAlAs as a function of gas composition in $\text{C}_2\text{H}_6/\text{H}_2$ or $\text{CCl}_2\text{F}_2/\text{O}_2$ ($0.85 \text{ W} \cdot \text{cm}^{-2}$, 4 mTorr) discharges.

(b) Structural Damage

The introduction of near-surface disorder by the RIE treatments was also investigated by glancing angle He^+ ion channeling. Figure 4 shows the relative intensity of backscattered 2 MeV He^+ ions in an aligned geometry from a control InP sample, and another sample etched in $2:18 \text{ C}_2\text{H}_6/\text{H}_2$ discharge ($0.85 \text{ W} \cdot \text{cm}^{-2}$, 4 mTorr, 20 sccm, 4 mins). The near-surface peak is a result of the presence of a native oxide and some surface reconstruction, and has a full-width-half maximum of $\sim 50 \text{ \AA}$ which is basically the resolution of the ion channeling measurement. After dry etching in $\text{C}_2\text{H}_6/\text{H}_2$ the damage peak extends to $\sim 300 \text{ \AA}$ and is a result of ion-induced disorder caused by energetic ions crossing the plasma sheath. Electrical compensation due to the introduction of point defects in the material is measurable to a depth of $\sim 1000 \text{ \AA}$, which is much greater than the projected range of 430 eV H^+ in InP. These would be the most energetic ions in the plasma, and would have the greatest range in the sample. The fact that the depth of point defect introduction is so deep has been ascribed to channeling of the bombarding ions in the near-surface region.^[5,6] This has been treated in more detail in a previous publication.^[6]

Layers of InAlAs etched in $\text{C}_2\text{H}_6/\text{H}_2$ under the same conditions as the InP just discussed did not show any evidence for the introduction of plasma-induced damage. The InAlAs therefore appears to be even more resistant to the introduction of damage than InP. For samples of InP and InAlAs etched in $\text{CCl}_2\text{F}_2/\text{O}_2$ we did not observe any disorder detectable by ion channeling, which implies if any damage was present it was contained

within $\sim 50 \text{ \AA}$ from the surface. This is consistent with the heavier mass of the fragment ions in this type of discharge in comparison to the light H^+ ions in the $\text{C}_2\text{H}_6/\text{H}_2$ plasma, and the consequent shallower damaged layer due to the energetic ions crossing the plasma sheath.

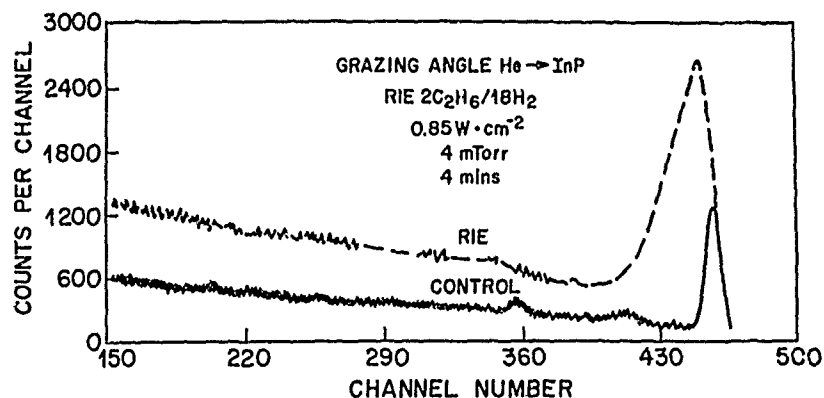


Figure 4. Ion channeling aligned spectra from control and reactively ion etched InP ($2\text{C}_2\text{H}_6/18\text{H}_2$, $0.85 \text{ W} \cdot \text{cm}^{-2}$, 4 mTorr, 4 mins).

(c) Surface chemistry

The composition and chemical bonding in the near-surface region after RIE in both mixtures was examined by AES and small area XPS. Figure 5 shows AES surface scans of an InP control sample, and samples etched for 4 min in either $19:1 \text{ CCl}_2\text{F}_2/\text{O}_2$ or $2:18 \text{ C}_2\text{H}_6/\text{H}_2$. There are several notable differences between the samples. First, after $\text{C}_2\text{H}_6/\text{H}_2$ the InP shows a deficiency in P in the near-surface region relative to the control sample or the one etched in $\text{CCl}_2\text{F}_2/\text{O}_2$. Second, the $\text{C}_2\text{H}_6/\text{H}_2$ chemistry appears to leave a much cleaner surface than $\text{CCl}_2\text{F}_2/\text{O}_2$. In the latter case Cl is detected, as well as a much higher C signal. By contrast, the sample etched in $\text{C}_2\text{H}_6/\text{H}_2$ appears to have even less C on the surface than the control. This is consistent with previous results showing that hydrogen-containing plasmas are very effective in removing carbon from semiconductor surfaces.^[7,9] The P deficiency after this type of etching is also expected because of the high probabilities for formation of PH_3 , and has been demonstrated by a number of authors.^[10-13]

The average elemental composition in the top 100 \AA of each sample, and for InP and InAlAs samples etched in the same way, was estimated and is reported in Table 1. The surface C concentration for the control samples or those etched in $\text{CCl}_2\text{F}_2/\text{O}_2$ varied from 40 to 45 atom percent, which is within the range expected for atmospheric contamination. The oxygen concentration in the near-surface region is clearly higher on the $\text{C}_2\text{H}_6/\text{H}_2$ etched samples, and this may be related to a higher chemical reactivity of these surfaces after the particular type of ion bombardment they incurred during the etch. Chlorine and in some cases fluorine contamination is evident for the material exposed to the $\text{CCl}_2\text{F}_2/\text{O}_2$ discharges.

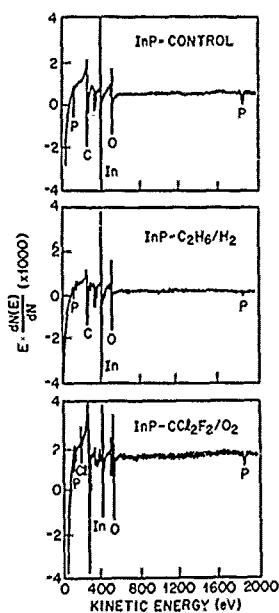


Figure 5. AES survey spectra from control and RIE InP samples etched either in $2\text{C}_2\text{H}_6/18\text{H}_2$ ($0.85 \text{ W} \cdot \text{cm}^{-2}$, 4 mTorr) or $19\text{CCl}_2\text{F}_2/1\text{O}_2$ ($0.85 \text{ W} \cdot \text{cm}^{-2}$, 4 mTorr).

Table 1. XPS elemental composition data measured from the top 100 Å of each sample and expressed in atomic percent units for the elements detected.

SAMPLE	C	O	F	Al	P	Cl	Ga	As	In
InP control	42.7	24.0	-	-	17.3	-	-	-	16.0
InP- $\text{C}_2\text{H}_6/\text{H}_2$	30.9	38.0	-	-	4.8	-	-	-	27.3
InP- $\text{CCl}_2\text{F}_2/\text{O}_2$	45.0	24.0	-	-	16.4	4.3	-	-	10.3
InGaAs-control	45.0	27.0	-	-	-	-	6.7	8.9	12.4
InGaAs- $\text{C}_2\text{H}_6/\text{H}_2$	34.0	37.0	-	-	-	-	6.4	13.0	9.6
InGaAs- $\text{CCl}_2\text{F}_2/\text{O}_2$	44.0	26.0	2.0	-	-	2.1	5.6	8.6	11.7
InAlAs-control	40.0	26.0	-	6.0	-	-	-	16.4	11.6
InAlAs- $\text{Cl}_2\text{H}_6/\text{H}_2$	20.5	49.5	-	17.7	-	-	-	6.9	5.4
InAlAs- $\text{CCl}_2\text{F}_2/\text{O}_2$	40.0	24.2	9.0	8.1	-	3.0	-	8.9	6.8

Etch Conditions : $2\text{C}_2\text{H}_6/18\text{H}_2$, $0.85 \text{ W} \cdot \text{cm}^{-2}$, 4 mTorr.

: $19\text{CCl}_2\text{F}_2/\text{O}_2$, $0.85 \text{ W} \cdot \text{cm}^{-2}$ 4 mTorr.

Summary and Conclusions

A comparison of the etching characteristics of C_2H_6/H_2 and CCl_2F_2/O_2 for InP, InGaAs and InAlAs yields the following main conclusions:

1. The etch rates of these materials under standard conditions are a factor of 3-5 higher for CCl_2F_2/O_2 relative to C_2H_6/H_2 . There is no delay in initiation of the etching upon ignition of the plasma for either mixture, and the maximum etch rates for the latter chemistry occurs at a concentration of 25% by volume in the discharge. Some degree of ion bombardment appears to be necessary for efficient desorption of the etch products for C_2H_6/H_2 RIE.

2. The etched surface morphology is smooth for InP, InGaAs and InAlAs for C_2H_6 compositions of $\leq 40\%$ in the C_2H_6/H_2 chemistry, while for CCl_2F_2/O_2 etching all of the materials show generally rough surfaces over the whole range of plasma parameters. No lattice disorder is detectable by ion channeling for CCl_2F_2/O_2 RIE even for high power density ($1.3 \text{ W} \cdot \text{cm}^{-2}$) discharges, but for C_2H_6/H_2 etching damage is detectable to $\sim 300 \text{ \AA}$ in InP under these conditions. InAlAs appears to be more damage-resistant than InP.

3. The C_2H_6/H_2 chemistry appears to leave an inherently cleaner surface on all three materials than CCl_2F_2/O_2 . There is less carbon remaining on the InP, InGaAs and InAlAs after C_2H_6/H_2 RIE than on the control samples, but more oxide is present. Chlorine-containing residues are detected on all three materials after CCl_2F_2/O_2 RIE.

References

- [1] D. Lecrosnier, L. Henry, A. LeCorre and C. Vaudry, *Electron. Lett.* 23 1254 (1987).
- [2] R. Cheung, S. Thomas, I. McIntyre, C. D. W. Wilkinson and S. P. Beamont, *J. Vac. Sci. Technol.* B5 1911 (1988).
- [3] E. L. Hu and R. E. Howard, *Appl. Phys. Lett.* 37 1022 (1980).
- [4] H. F. Wong, D. L. Green, T. Y. Liu, D. G. Lishan, M. Bellis, E. Hu, P. M. Petroff, P. O. Holtz and J. L. Merz, *J. Vac. Sci. Technol.* B6 1906 (1988).
- [5] S. J. Pearton, U. K. Chakrabarti and F. A. Baiocchi, *Appl. Phys. Lett.* (Oct. 16, 1989 issue).
- [6] Y. Kunitsuga, I. Suemune, Y. Tanaka, Y. Kan and M. Yamanishi, *J. Cryst. Growth* 95 91 (1989).
- [7] K. Asakawa and S. Augata, *J. Vac. Sci. Technol.* A4 677 (1986).
- [8] J. Saito, K. Nanbu, T. Ishikawa and K. Kondo, *J. Cryst. Growth* 95 322 (1989).
- [9] R. P. H. Chang, C.C. Chang and S. Darack, *J. Vac. Sci. Technol.* 20 45 (1982).
- [10] J. H. Thomas III, G. Kaganowicz and J. W. Robinson, *J. Electrochem. Soc.* 135 1201 (1988).
- [11] S. J. Fonash, *Solid-State Technol.* 28 150 (1985).
- [12] F. Proix, O. M'hamed and C. A. Sebenne, *J. Vac. Sci. Techn.* A6 199 (1988).

ELEVATED TEMPERATURE REACTIVE ION ETCHING OF GaAs AND AlGaAs in C_2H_6/H_2

S. J. PEARTON*, W. S. HOBSON* AND K. S. JONES**

*AT&T Bell Laboratories, 600 Mountain Ave., Murray Hill, NJ 07974

**University of Florida, Gainesville, FL 32611

ABSTRACT

The temperature dependence of etch rate, surface morphology and atomic composition, and depth of hydrogen passivation of Si dopants in n-type GaAs and AlGaAs has been measured for reactive ion etching in C_2H_6/H_2 . The etching of GaAs shows an increase of a factor of two between 150 and 250°C, decreasing at higher temperatures, while there is no temperature dependence for the etch rate of AlGaAs over the range 50-350°C. The As-to-Ga ratio in the near-surface region of GaAs remains unchanged over the whole temperature range investigated and there is no polymer deposition. The etched surface morphology is smooth for both GaAs and AlGaAs for all temperatures while the depth of Si dopant passivation by hydrogen shows an increase with increasing substrate temperature during the etching treatment.

INTRODUCTION

Recently a new gas chemistry for dry etching of III-V semiconductors, utilizing methane or ethane and hydrogen, has been introduced.⁽¹⁻³⁾ Most of the work to date has concentrated on etching of InP and InGaAs although smooth surface morphologies and controlled removal of GaAs has also been demonstrated.⁽⁴⁾ Because the use of C_2H_6/H_2 or CH_4/H_2 is relatively new, there is little information available on some of the fundamental properties of this chemistry. In general temperature has been one of the most neglected parameters in dry etching of III-V materials which is surprising in view of situations such as via-hole etching in which the sample is exposed to the plasma for a period of up to several hours with significant heating of the sample occurring. Since several etch mechanisms may be occurring simultaneously it is not usual to observe simple Arrhenius behavior for Cl-based dry etching of compound semiconductors.^(5,6)

In this paper we have examined the temperature dependence of etch rate, surface morphology and composition, and changes in the near-surface doping profile in n-type GaAs and AlGaAs reactively ion etched (RIE) in a C_2H_6/H_2 mixture. The dopant profiles after etching at various temperatures (50-350°C) were obtained from Hg-contact capacitance-voltage (C-V) measurements, and the surface composition by both Auger Electron Spectroscopy (AES) and X-ray Photoelectron Spectroscopy (XPS). The permeation of hydrogen into both GaAs and AlGaAs was obtained by substituting deuterium in the gas mixture and profiling for its presence using Secondary Ion Mass Spectrometry (SIMS) in a Cs^+ beam Cameca IMS 3f system.

Experimental

The GaAs wafers were either Si-doped ($n = 1 \times 10^{17} \text{ cm}^{-3}$) or undoped ($\rho = 1 \times 10^7 \Omega \text{ cm}$), each with (100) orientation. The $Al_{0.28}Ga_{0.72}As$ layers were grown on semi-insulating GaAs substrates by Metal Organic Chemical Vapor Deposition (MOCVD) using arsine, trimethylgallium and trimethylaluminum as the source chemicals. The AlAs mole fraction was measured by room temperature photoluminescence, and the Si doping level derived from a disilane source was obtained from C-V measurements. Some of the samples were deposited with 3000 Å of low temperature (275°C) Plasma Enhanced Chemical Vapor Deposition (PECVD) SiN_x . Photoresist (AZ 1350J) was then spun onto the samples and lithographically patterned after a hard bake at 90°C for 20 min. The resulting pattern contained a variety of different size shapes (lines, triangles and dots), and was transferred into the SiN_x by etching with a CF_4/O_2 plasma in a barrel reactor. Prior to RIE treatments the photoresist was removed using solvent cleaning, and after RIE the SiN_x was stripped off in buffered HF solution.

All of the dry etching was performed in a Model 51 Materials Research Corporation parallel plate system with a stainless steel chamber. The cathode was 6 inches in diameter and was covered

with a quartz cover plate. The samples were heat sunk to the cathode using heat conductive paste. All of the etching was performed for 4 mins using a mixture of 4:40 $C_2H_6:H_2$ at a total flow rate of 44 sccm and a total pressure of 4 mTorr. These conditions were chosen based on our past experience with this gas chemistry, and as reported by others it is necessary to dilute the ethane to approximately 10% by volume in order to minimize polymer deposition.⁽¹⁾ The cathode self-bias under these conditions was 390 V (power density $0.56 \text{ W} \cdot \text{cm}^{-2}$), and the reactor was pumped to $<5 \times 10^{-7}$ Torr prior to introduction of the gases through electronic mass flow controllers. After etching the samples were kept in a dry N_2 glove box until they could be transferred to the various measurement systems for analysis.

Results and Discussion

(a) Etch Rates

Figure 1 shows the temperature dependence of the etch rate of both GaAs and $Al_{0.28}Ga_{0.72}As$ in a $0.56 \text{ W} \cdot \text{cm}^{-2}$, 4 mTorr, 4 $C_2H_6:40H_2$ discharge. For GaAs the etch rate is constant up to 150°C , and then increases by a factor of two between 150 and 250°C . Above 250°C the etch rate decreases again, and by 350°C it is virtually at the same value as at 50°C . By sharp contrast the etch rate of AlGaAs is basically constant over the whole temperature range investigated. The results for GaAs are similar to those reported by Niggebrugge et. al.⁽¹⁾ for CH_4/H_2 RIE of InP. In the case of AlGaAs we do not appear to be desorption-limited at any temperature, while for GaAs the active hydrogen species may actually be desorbed from the material above 250°C before they have a change to react with the surface. This would imply that the presence of aluminum serves to reduce this desorption. The behavior for GaAs is non-Arrhenius and as mentioned earlier this has been reported previously for elevated temperature RIE of GaAs in BCl_3/Cl_2 and CCl_4 .^(5,6)

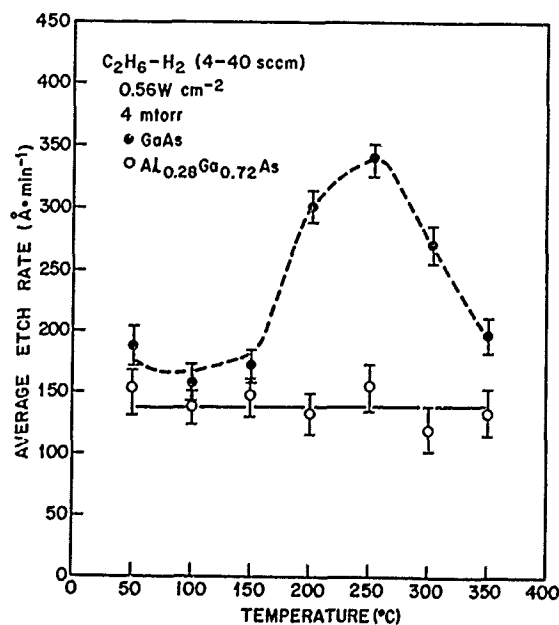


Figure 1 Average etch rate over a 4 min period for GaAs and AlGaAs reactively ion etched in a $4C_2H_6/40H_2$, 4 mTorr, $0.56 \text{ W} \cdot \text{cm}^{-2}$ discharge.

(b) Surface Morphology

The GaAs showed smooth surface morphologies for etching up to 350°C , where some waviness in the field of view of the SEM was apparent. The sidewalls were free of any obvious

deposits and were sloped slightly outwards for all the temperatures investigated. Similar results were obtained for AlGaAs, which is in sharp contrast to the rough-to-smooth-to-rough transitions observed for elevated temperature RIE of GaAs and AlGaAs in Cl_2 -based mixtures.

(c) Electrical Measurements

The deactivation of both shallow donor and acceptor dopants in GaAs and AlGaAs as a result of low power density hydrogen plasmas has been amply established.⁽⁷⁾ Figure 2 shows near-surface carrier profiles in GaAs etched in a $4\text{C}_2\text{H}_6:40\text{H}_2$, 4 mTorr, $0.56\text{W} \cdot \text{cm}^{-2}$ discharge, as a function of the sample temperature. All etches were for 4 min. From experiments with hydrogen-free RIE gas mixtures we have previously determined that ion-induced damage under our conditions is limited to $\leq 1500 \text{ \AA}$. Beyond this depth the reduction in carrier concentration is due to hydrogen passivation of the Si donors. The passivation depth increases with increasing etch temperature, due simply to the higher hydrogen diffusivity with temperature. An estimate of this diffusivity can be made as follows: (i) taking the etch rate data of Figure 1, the amount of material removed during the 4 min etch is calculated; (ii) this depth is subtracted from the passivation depth (which we take to be the depth at which the doping concentration is within $\frac{1}{2}$ of its bulk value), and the hydrogen diffusion coefficient, D , calculated from a simple \sqrt{Dt} relationship ($t = 4 \text{ min}$). Performing this analysis for each RIE temperature we find that the hydrogen diffusivity is thermally activated according to the relationship

$$D_H = 3.1 \times 10^{-5} \exp\left(-\frac{0.79\text{eV}}{KT}\right) \text{cm}^2 \cdot \text{s}^{-1} \quad (1)$$

This is in reasonable agreement with the results of Zavada et. al.⁽⁸⁾ using SIMS profiling of proton implanted GaAs. Other authors have reported activation energies for hydrogen diffusion ranging between 0.5 - 0.9 eV,⁽⁹⁻¹¹⁾ but it is apparent that a number of parameters such as plasma frequency, doping concentration in the GaAs, surface condition and hydrogen concentration both in the plasma and in the near-surface region of GaAs, can all affect the apparent hydrogen diffusivity.⁽¹²⁾

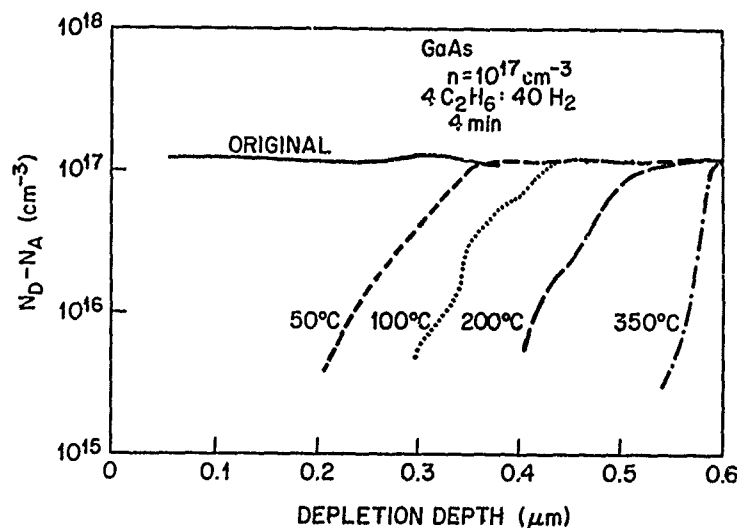


Figure 2 Near-surface carrier concentration profiles in n-type GaAs ($n = 10^{17}\text{cm}^{-3}$) before and after a 4 min RIE treatment in a $4/40 \text{ C}_2\text{H}_6/\text{H}_2$ discharge at temperatures between 50-350°C.

For AlGaAs the data is similar to that in GaAs, although the passivation depth in AlGaAs is slightly less, corresponding to a lower hydrogen diffusivity. Using the same analysis described above we found for $\text{Al}_{0.28}\text{Ga}_{0.72}\text{As}$ that D_H is given by

$$D_H = 1.8 \times 10^{-5} \exp\left(-\frac{0.85 \text{ eV}}{KT}\right) \text{ cm}^2 \cdot \text{S}^{-1} \quad (2)$$

To the best of our knowledge this is the first determination of an apparent hydrogen diffusion coefficient in AlGaAs.

It should be noted that the relationships derived above for hydrogen diffusion are accurate only if there is a one-to-one correspondence between the neutralized donor concentration and the hydrogen concentration. This is not always the case for low frequency hydrogen discharges. For rf frequencies however, this correspondence is found to hold. SIMS profiling of $\text{C}_2\text{H}_6/\text{D}_2$ RIE samples showed an excellent correlation between the total D concentration and the depth of carrier reduction.

(d) Surface Chemistry

Figure 3 shows AES surface scans of Ga, As, C and O on GaAs samples etched at four temperatures between 100-350°C. There are basically no differences in the surface compositions in any of these samples. Table 1 shows elemental composition data measured in the top 100 Å by XPS. There is no systematic variation in the compositions with RIE temperature. This is in sharp contrast to the results for Cl-based RIE of GaAs where significant differences are observed for elevated temperature etching. The $\text{C}_2\text{H}_6/\text{H}_2$ chemistry appears to have a wide temperature window in terms of reproducible etch rate and surface composition.

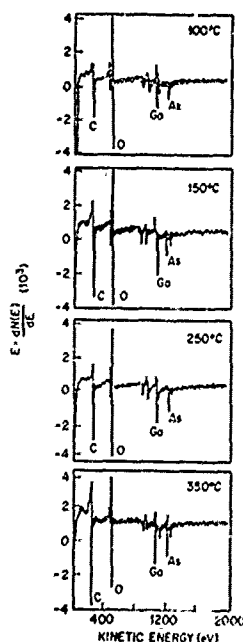


Figure 3 AES survey spectra from GaAs samples reactively ion etched for 4 min in a $0.56 \text{ W} \cdot \text{cm}^{-2}$, 4 mTorr, 4/40 $\text{C}_2\text{H}_6/\text{H}_2$ discharge, as a function of the sample temperature during the etch.

Table 1. XPS elemental composition data obtained from the top 100Å of GaAs samples etched for 4 min in a C_2H_6/H_2 discharge. The data are given in atomic percent units for the elements detected.

Etch Temperature (°C)	Elemental Composition (at. %)			
	C	O	Ga	As
100	29	38	21	12
150	37	30	20	13
200	36	29	20	15
250	26	35	23	16
300	37	30	20	13
350	41	28	18	13

In our samples the surface carbon concentrations varied from 26-41 atom percent, while approximately 30-50 atom percent C would be considered usual for atmospheric C on this type of sample. The high resolution C (1s) data show that the types of carbon species detected varied somewhat with the etch temperature. Our past experience with XPS of GaAs surfaces has shown that typical atmospheric contamination consists of hydrocarbon (C-C or C-H), ether/alcohol (C-OC or C-OH) and organic acid/ester (O = C-OC or O = C-OH) functionalities, with the hydrocarbon as the predominant species. The Ga and As are present as oxides (As_2O_3 , As_2O_5 and GaO_x) as well as being part of the bulk material. All of the samples are much cleaner in a chemical sense than GaAs etched under similar conditions in Cl-based mixtures where halocarbons, chlorides and oxides are present to a much more significant extent. We did only a limited amount of chemical analysis of the AlGaAs etched in C_2H_6/H_2 , but the surfaces on these samples also appeared to be similar to unetched control samples. There is always a debate about whether chemical analysis on samples exposed to the atmosphere are really all that useful, and indeed insight into the etch reactions require in-situ analysis after RIE. However from a practical viewpoint, samples will almost always be exposed to the ambient when subsequent processing takes place after RIE treatments. For this reason alone we believe our approach still yields useful information on the chemical nature of the surface. One interesting feature of the C_2H_6/H_2 RIE is that it does not appear to leave non-stoichiometric surfaces through preferential removal of As as arsine. This might have been expected by analogy with the situation with InP, where P is rapidly leached out by H-based plasmas.

Summary and Conclusions

The C_2H_6/H_2 mixture appears to give smooth, controlled etching of both GaAs and AlGaAs over a wide range of temperatures provided C_2H_6 is no more than about 15% by volume of the total flow rate. As observed by others with etching of In-based materials, concentrations of ethane or methane above ~15% lead to increasing polymer deposition on both the masked and unmasked areas. While the etch rates of GaAs and AlGaAs are low ($150-350 \text{ Å} \cdot \text{min}^{-1}$) under our conditions, these are appropriate for the etching of mesas in most field effect transistor structures. In conjunction with the smooth etching, the surface is chemically quite clean with no evidence of polymer formation or the creation of a non-stoichiometric region at the surface.

The passivation of donors in the n-type GaAs and AlGaAs by atomic hydrogen from the discharge is significant, and occurs over depths of $\sim 0.55\mu\text{m}$ for 4 min RIE treatments at 350°C . This does not appear to be a severe problem since past measurements have shown that the donors can be reactivated by annealing at approximately 400°C . This is compatible with ohmic contact alloying schemes, and therefore should not be a limiting factor with this etch chemistry.

REFERENCES

- [1] U. Niggebrugge, M. Klug and G. Garus, *Inst. Phys. Conf. Ser.* **79** 367 (1985).
- [2] N. Vojjdani and P. Parrens, *J. Vac. Sci. Techn.* **B5** 1591 (1987).
- [3] R. Cheung, S. Thomas, S. P. Beaumont, G. Doughty, V. Law and C. D. W. Wilkinson, *Electron. Lett* **23** 857 (1987).
- [4] R. Cheung, S. Thomas, J. McIntyre, C. D. W. Wilkinson and S. P. Beaumont, *J. Vac. Sci. Technol.* **B6** 1911 (1988).
- [5] R. J. Contolini, *J. Electrochem. Soc.* **135** 929 (1988).
- [6] R. H. Burton, R. A. Gottscho and G. Smolinsky, *Dry Etching for Microelectronics*, ed. R. A. Powell (Elsevier, NY 1984), Chapter 3.
- [7] See for example, S. J. Pearton, J. W. Corbett and T. S. Shi, *Appl. Phys. A.* **43** 153 (1987).
- [8] J. M. Zavada, H. A. Jenkinson, R. G. Sarkis and R. G. Wilson, *J. Appl. Phys.* **58** 3731 (1985).
- [9] S. J. Pearton, W. C. Dautremont-Smith, J. Chevallier, C. W. Tu and K. D. Cummings, *J. Appl. Phys.* **59** 2821 (1986).
- [10] E. M. Omeljanovsky, A. V. Kakhomov, A. J. Polyakov and A. V. Govorkov, *Proc. 5th Intl. Semi-insulating III-V Materials Conf. (Malmo Sweden 1988)* - to be published.
- [11] J. Chevallier and M. Aucouturier, *Ann. Rev. Mater. Sci.* **18** 265 (1988).
- [12] W. C. Dautremont-Smith, *Mat. Res. Soc. Symp. Proc.* **104** 385 (1988).

CHARACTERIZATION OF SIDEWALL RESIDUE FILM AND ATOMIC STRUCTURE OF THE TRENCH FORMED BY BCl_3/Cl_2 REACTIVE ION ETCHING

SUN JIN YUN,* YOUNG-JIN JEON,* AND JEONG Y. LEE**

*Electronics & Telecommunications Research Institute, Daedog Danji P.O. Box 8, Daejeon
302-606, Korea

**Korea Institute of Technology, Daedog Danji, Daejeon, 305-701, Korea

ABSTRACT

The silicon trench-etching in BCl_3/Cl_2 reactive ion etching plasma leads to the intrinsic bonding damage, the permeations of etching species and impurities into silicon substrates, and the deposition of residue film on trench sidewall. The contaminations and the damages in trench were investigated by using high resolution transmission electron microscopy (HRTEM), secondary ion mass spectrometry (SIMS), and x-ray photoelectron spectroscopy (XPS). The microstructure of the rounded bottom surface showed that the surface region was distorted by 2 - 6 atomic layers and the trench-etch was mainly limited by the physical sputtering-like mechanism. The damage in the silicon lattice consisted of prominent planar defects roughly confined to {110} and {111} planes. The thickness of sidewall residue film was 10 - 90 nm, which was thinner at deeper region of the trench, whereas that of residue film at the trench bottom was 1.5 - 3.5 nm. The SIMS results of no-patterned specimen presented that the permeation depths of boron and chlorine into the Si-substrate were about 40 and 20 nm, respectively. The presence of B_xCl_y and Cl-related Si chemical states was identified from XPS analysis of the residue film.

INTRODUCTION

Recently silicon trenches have been applied to device isolations and trench capacitors in very large scale integrated circuits [1,2]. Especially the reactive ion etching (RIE) [3,4] using BCl_3/Cl_2 plasma has been extensively studied because of a good controllability of trench shape and a high anisotropy. However, some problems exist in the trench etching of single crystalline silicon using RIE. The RIE exposures result in (i) intrinsic bonding damage, (ii) permeations of etching species and impurities into silicon substrates, and (iii) deposition of residue film on trench sidewall. Since these deformations would deteriorate the electrical performance of devices [5], and the post-RIE treatments are necessitated to eliminate damages and contaminations, it is required to characterize the residue film and the damaged layers of the etched specimens.

In this work, concerned with the trench formed by BCl_3/Cl_2 RIE, the microstructure of the etched surface of trench, the permeation profile of etching species into silicon substrate, and the thickness and the chemical state of residue film were characterized by using high resolution transmission electron microscopy (HRTEM), secondary ion mass spectrometry (SIMS), and x-ray photoelectron spectroscopy (XPS). From the microstructural analysis of the etched surface of trench bottom region, it was also suggested that the physical sputtering-like etching mechanism is predominant in this trench etching system.

EXPERIMENTAL

Etching

In this experiment, 5 inch n-type (about $5 \times 10^{15} \text{ cm}^{-3}$) silicon (100) wafers with 800 nm of chemical vapor deposited oxide was used. The oxide was patterned using photolithography and reactive ion etching in $\text{CHF}_3/\text{C}_2\text{F}_6$ plasma. Two kinds of specimens were made in accordance with the requirements of characterization techniques. One was the trench patterned specimen (I-type), in which the trenches have {110} sidewalls and {100} bottom surface. The trench widths were 0.8 - 1.5 μm . The other was 1 cm x 1 cm size square-patterned specimen (II-type) for SIMS and XPS study. The silicon trench etching was performed by the BCl_3/Cl_2 reactive ion etching, by two steps of (I) pre-etching of native oxide to prevent from

black silicon effect [6], with the conditions of $\text{BCl}_3/\text{Cl}_2 = 45 \text{ sccm}/10 \text{ sccm}$, $V_{\text{dc}} = -500 \text{ V}$, and etch time = 1 minute, (ii) the main silicon etching, with the conditions of $\text{BCl}_3/\text{Cl}_2 = 20 \text{ sccm}/60 \text{ sccm}$, $V_{\text{dc}} = -300 \text{ V}$, and etch time = 17 minutes. The main etching was carried out under the RF power density of 0.722 W/cm^2 and the chamber pressure of 150 mtorr . In the case of square-patterned specimens, the etching conditions were the same as those of the silicon trench etching, except for the etching time of the silicon etching step.

Characterizations

Cross-sectional transmission electron microscopy (XTEM) specimens were prepared by forming a sandwich with epoxy, followed by mechanical polishing and then argon ion milling in a specimen stage cooled by liquid nitrogen. High-resolution TEM image was taken in a $\langle 110 \rangle$ zone axis orientation with an objective aperture, which contained nine beams, on a JEOL JEM 2000EX microscope equipped with a pointed LaB_6 filament and operating at 200 keV .

In SIMS study, the samples were analyzed on Perkin-Elmer Model 6300 SIMS using Cs^+ primary ion bombardment with beam energy, 3 keV . The primary ions were impacted on the sample at an angle of 60° with respect to the surface normal, in order to obtain the reasonable depth resolution.

X-ray photoelectron spectra were obtained with VG ESCALAB Mk II instrument using Al K_α (1486.6 eV) x-ray source. The high resolution spectra of all regions of interest were recorded with 100 eV pass energy. The line structures of narrow scan spectra were resolved to characteristic component peaks by a least-squares fitting technique using Gaussian and Lorentzian functions [7]. Photoelectron spectra were acquired at two different electron emission angles, with respect to the surface, 30° and 70° , to alter the surface sensitivity.

RESULTS AND DISCUSSION

The SEM photograph in Fig. 1 shows the shapes of the 1.0 and $1.5 \mu\text{m}$ wide trenches of $4.4 \mu\text{m}$ depth obtained from the etching system described above. It was found that the trenches had rounded bottoms, and that the bottom of the trench with higher aspect ratio, i.e., $1.0 \mu\text{m}$ wide trench was more curved than that of $1.5 \mu\text{m}$ trench.

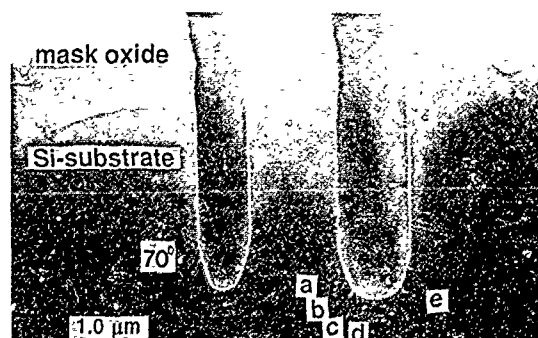


Figure 1. SEM photograph of 1.0 and $1.5 \mu\text{m}$ trenches formed by BCl_3/Cl_2 reactive ion etching.

The microstructure of silicon surface region was investigated by using high resolution electron microscopy, in order to characterize the etched surface of trench, and also to get informations about the etching mechanism. The as-etched surfaces of trench were observed with no further treatment, since any following processes, such as sidewall oxidation and polysilicon refill, would inevitably change the topmost surface state and the damaged structure of the near-surface region [8]. The microstructures of the surfaces along the trench bottom are shown in the high resolution XTEM micrographs of Fig. 2(a)-(e). The distortion of crystal orientation in the surface region of trench bottom seems to be induced by the energetic ion bombardments and removed by the succeeding etching. Therefore, the surface region of the trench bottom center with the largest etch rate is distorted by only 1-2 atomic layers as shown in Fig. 2(d). Generally the trench etching is considered to be proceeded by both physical sputter-like mechanism and chemical binding of reactive species on a silicon-surface site. The extreme case, mainly limited by the chemical binding mechanism, had been reported, in which the etching of (100) wafer had generated a V-groove trench so

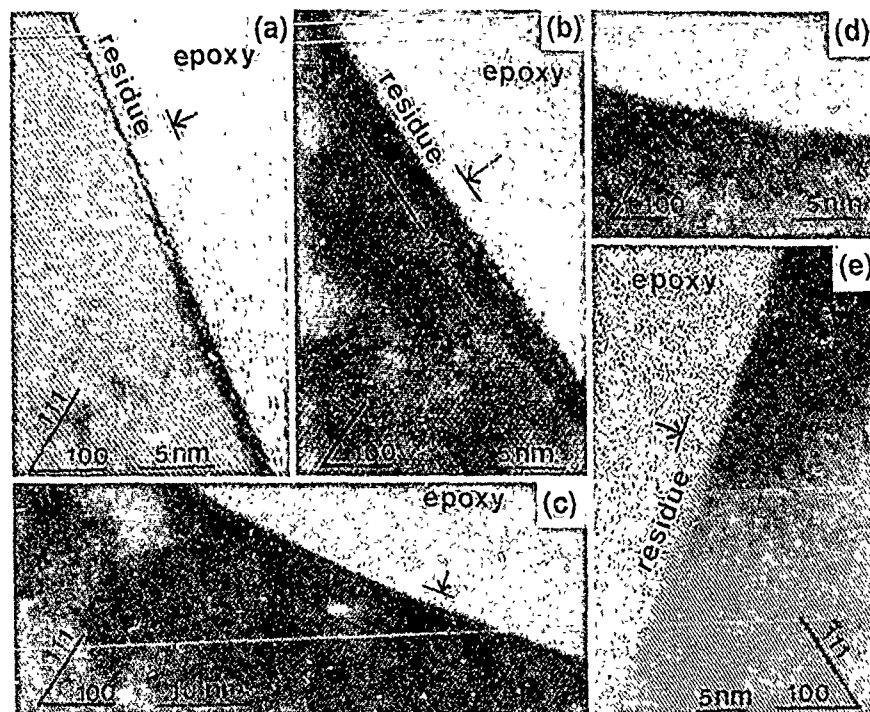


Figure 2. High resolution transmission electron micrograph. of the surfaces along the inner wall of 1.2 μm width trench. Micrographs in (a)-(e) are corresponded to a-e parts indicated in Figure 1, respectively.

that the V-groove had been two $\{111\}$ planes intersecting the $\{100\}$ at 54.47° [9]. However, the trenches in Fig. 1 have round bottoms roughly intersecting the $\{100\}$ at about 70° . Even though the $\{111\}$ plane was more severely distorted, about 5-6 atomic layers as shown in Fig. 2(b), most parts of the surfaces were not consistent with any low index crystallographic plane. These results in Figs. 1 and 2 implicate that the etching is limited by a physical sputtering-like mechanism of the surface atoms due to energetic ion bombardment rather than a chemical etching mechanism. Furthermore, we also found that the trench bottom became sharper as the etch time and the aspect ratio are increasing. These facts could be explained by two different ways. One is simply that the incidence angle of reactive ions for the vertical etching is largest in the center of bottom. The other is that the contribution of chemical etching is increasing as reducing the ion flux with trench depth, and the etch rate on $\{100\}$ plane is larger than that on $\{111\}$ plane since the ratio of the numbers of silicon atoms at $\{111\}$ and $\{100\}$, and the ratio of the numbers of available bonds on each surface are 1.15 and 1.59, respectively [9].

The low magnification TEM images of 1.2 μm width trench showed that the thicknesses of the trench sidewall residue films were close to 10 nm near the trench bottom (at about 4.0 μm deep region from the water surface), and 90 nm near the mask oxide. The reasons for which thicker layer is deposited at upper sidewall, are that the incidence angle of depositing species is greater and the deposition time is longer at upper region. The thickness of the residue film is known to be largely dependent on the plasma condition and the unmasked Si area [10,11]. The high resolution XTEM images presented that the residue films of the trench bottom region were 1.5 - 3.5 nm thick as indicated in Figs. 2(a) - (e), which are very thin compared with the residue film of trench sidewall. The thin residue films can be attributed to the sputtering by ion bombardments to the trench bottom region.

Figure 3(a) shows a typical area of 50-80 nm deep near-surface region at trench bottom with a high density of $\{111\}$ and $\{110\}$ defects. These strong contrasts are representative for a large stress field component perpendicular to the plane of the defects [12]. The damage

also consists of concentrated atomic defects (e.g., Si self-defects and impurities of the plasma constituents) [12]. The micrographs shown in Figs. 3(b), (c) and (d) presented the typical microstructures of the trench sidewall and the near surface region. The trench sidewall had the heavily damaged region of about several nm - 20 nm thickness, as shown in Figs. 3(b) and (c). The microstructure of the damaged region shows planar defects along $\{110\}$ plane and amorphized region, which seem to be due to the bombardments of scattered energetic ions. Tiny defects, roughly consistent with $\{113\}$ plane, were also generated in the near surface region of sidewall, as indicated in Fig. 3(d).

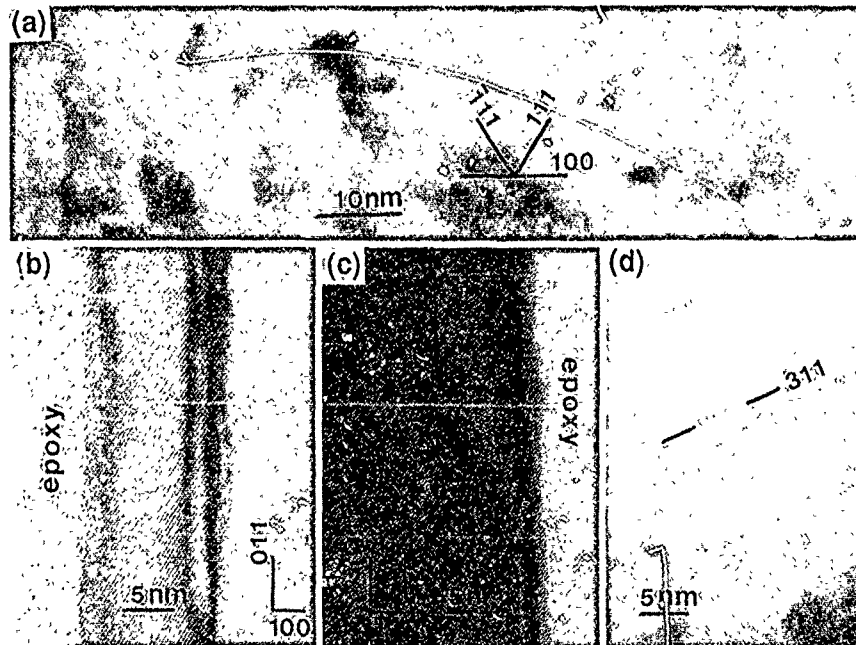


Figure 3. High resolution electron micrographs of (a) near surface region of trench bottom, (b) the trench sidewall, (c) the trench sidewall which shows the disappearing planar-defect and (d) the near surface region of the trench sidewall.

SIMS profiles in Fig. 4 represent the distribution of boron and chlorine incorporated into silicon substrate during RIE. As shown in Fig. 4(a), the SIMS profiles of I-type specimens with three different etch times, reveal nearly same behavior for both elements. This suggests the balance established between simultaneous processes of etching and etching-species permeation. The penetration depths of boron and chlorine into the silicon substrate were about 40 nm and 20 nm, respectively. The larger penetration depth of boron seems to be caused by the higher diffusivity than that of chlorine. The penetration depths obtained from the SIMS analysis seem not to be exaggerated by the surface roughness, since the SEM observations showed the mirror-like surfaces. In the SIMS profiles of boron and chlorine in the case of trench-patterned specimen (I-type) of Fig. 4(b), the difference between the penetration depths of two elements is severer than that in no-patterned specimen (II-type). In the SIMS analysis, the primary beam was exactly aligned parallel to the trenches in the sample, and a depth profiling of a whole field of trench cells was accomplished because of the lack of lateral resolution of the ion probe for direct analysis on a fraction of the wafer. By considering the angle of trench bottom to the surface, 70° in Fig. 1 and the difference in the penetration depths of two elements in Fig. 4(b), it can be suggested that the penetration of boron into substrate along the trench inner wall of bottom, is deeper as much as about 300 nm than that of chlorine. However the SIMS data of trench-patterned specimen, were subject to be exaggerated by redeposition of sputtered species, the reduction of the sputter rate at trench bottom, and the difference of sputter rate between residue film and silicon single crystal. Then we also obtained the SIMS profile after the cleaning, the

dry oxidation of surface (about 32 nm thick) in diffusion furnace at 900°C and the removal of oxidized silicon by dipping 10:1 HF solution. The SIMS profile showed that the specimen still retained boron with the concentration of $(3 - 10) \times 10^{17}$ atoms/cc and trace amount of chlorine. From these SIMS analyses, it is interesting to note that the observed penetration depths are generally much larger than those of expected on pure grounds of projected range estimates from ion implantation. The results could be ascribed to the recoil implantation from a thin deposited layer and the enhanced diffusion by a high inward flux of silicon-self interstitials induced by RIE [13].

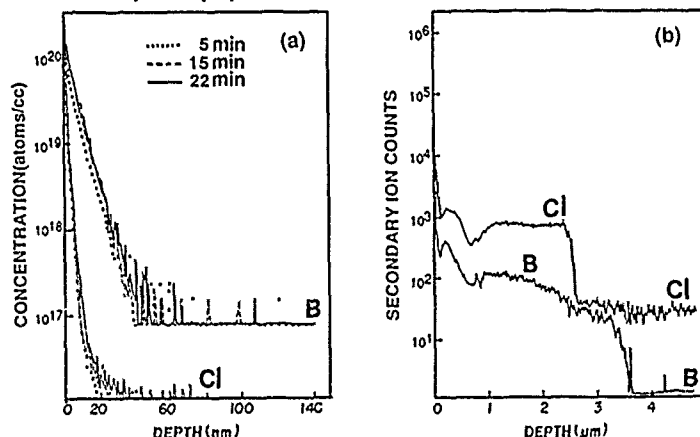


Figure 4. SIMS profiles of (a) blank-patterned specimens (II-type) of main etch time 5, 15, and 22 minutes, and (b) trench formed specimen (I-type) obtained from parallel sputtering to the trenches.

Although the residue film deposited on a flat silicon substrate may be different from those on trench sidewall, XPS study of II-type specimen can introduce the informations about the residue layer related to only Si etching, in which the redeposition caused by sputtered silicon and oxygen from silicon and mask oxide is ruled out. XPS survey spectra acquired with the take-off angle 30° , show that the residue film on Si-surface is mainly constituted of boron, chlorine, and air-contamination-induced carbon and oxygen. The small take-off angle configuration for photoelectron detection was used in order to increase the surface sensitivity. The B 1s and Cl 2p photoemission spectra were obtained by subtracting the energy loss peaks of Si 2s photoemission from the spectra of etched surface, because the peaks were severely overlapped with the energy loss peaks of Si 2s photoemission. The reference energy loss peaks of Si 2s photoemission had been obtained by using bare Si wafer. As shown in Fig. 5(a), we could find out peaks at binding energies 199.2 eV and 200.8 eV, and the trace of peaks in

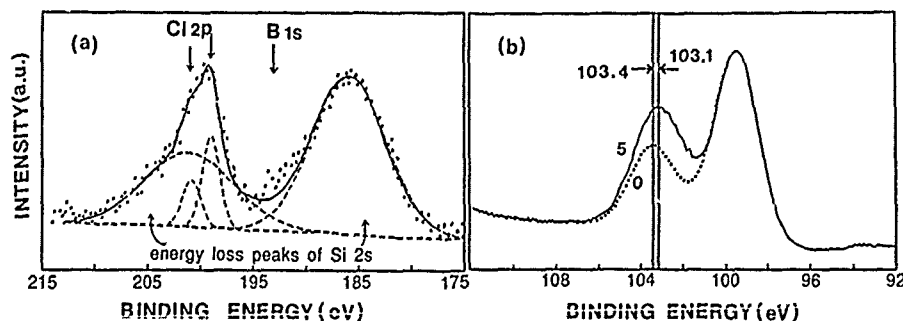


Figure 5. XPS spectra of (a) B 1s and Cl 2p photoemissions and (b) Si 2p photoemission, in which the take-off angle is 30° . The dashed curves and the solid line in (a) represent the various peak-fitted chemical components and the sum of all components, respectively. The numbers on peaks in (b) indicate the etch times.

191 - 193 eV region, except for the Si 2s energy loss peaks at 185.8 eV and 201.1 eV. These peaks were confirmed to be not abnormal photoemissions due to surface damage, by analyzing the Ar⁺-ion beam -etched Si surface. By the XPS analysis at different photoemission angle, 70°, it is also confirmed that the peaks at 199.2 eV and 200.8 eV were emitted from the overlayer on Si-substrate. The peaks at 199.2 eV and 200.8 eV are Cl 2p_{3/2} and Cl 2p_{1/2}, respectively. The small peaks at binding energy about 191 - 193 eV may be assigned to B 1s photoelectron peaks from B_xCl_y binding states. Since B 1s photoelectron has very small area sensitivity factor, the peak resolving into the different chemical components is not clear. Fig.5(b) represents the Si 2p photoemission spectra of silicon surfaces before etching and after 5 minutes-etching. Si 2p photoelectron spectrum from the specimen not exposed to plasma shows two peaks at 99.5 eV and 103.4 eV due to silicon substrate and oxidized silicon (SiO₂), respectively. In the case of specimen exposed to BCl₃/Cl₂ plasma, the peak maxima are found at 99.5 eV and 103.1 eV. The curve-fitting implicated the presence of additional peak at binding energy 102.5 eV, which could be assigned Cl-related chemical states of Si.

CONCLUSION

The damages and the contaminations induced by the trench etching of BCl₃/Cl₂ reactive ion plasma, were investigated by using HRTEM, SIMS, and XPS. The microstructures of the rounded bottom surface showed that the surface region was distorted by 2 - 6 atomic layers and the trench etching was mainly limited by the physical sputtering-like mechanism. The trench sidewall was heavily damaged and the damage in the silicon lattice consisted of prominent planar defects roughly confined to {111} and {110} planes, and partly {113} plane. The thickness of sidewall residue film was 10 - 90 nm, which was thinner at deeper region, whereas that of residue film at the trench bottom was 1.5 - 3.5 nm due to the ion-sputtering. The SIMS study of no-patterned specimens (II-type) showed that the permeation depths of boron and chlorine into the Si-substrate were about 40 and 20 nm, respectively. The SIMS profile of trench-patterned specimen (I-type) implicated that the permeation depth of boron was greater than that of no-patterned specimens. In the residue film, the presence of B_xCl_y and Cl-related chemical states was identified from XPS analysis.

ACKNOWLEDGEMENTS

This work is supported in part by Korea Telecommunications Authority and by the Korea Ministry of Science and Technology.

References

1. K. Sawada, H. Yamamoto, H. Ogawa, K. Yano, and T. Fujita, 1989 Symposium on VLSI Technology - Digest of Technical Papers, pp41 - 42; M. Sugiyama, T. Shimizu, H. Takemura, A. Yoshino, N. Oda, T. Tashiro, Y. Minato, Y. Takahashi, and M. Nakamae, *Ibid*, pp.59 - 60.
2. S. Banerjee, D. Coleman, Jr., W. Richardson, and A. Shah, *IEEE Trans. Electron Devices* **ED-35**, 108(1986).
3. J. W. Coburn, Plasma Etching and reactive ion etching (AVS Monograph Series, 1982).
4. S. Wolf and R. N. Tauber, Silicon Processing for the VLSI Era(Vol.1, Lattice Press, 1987) pp.539 - 585.
5. F. K. Moghadam and X.-C. Mu, *IEEE Trans. Electron Devices* **36**, 1602(1989).
6. I. W. Rangelow, P. Thoren, K. M. Jeli, R. Kassing, M. Engelhardt, and S. Schwarzl, *Microelectronic Engineering* **5**, 387(1986).
7. P. A. Sherwood, Practical Surface Analysis, Edited by D. Braggs and M. P. Seah(John Wiley & Sons, 1983) pp.445 - 474.
8. R. Sinclair, K. B. Kim, O. Shippou, and H. Iwasaki, *J. Electrochem. Soc.* **136**, 511(1989).
9. J. I. Ulacia F., C. J. Petti, and J. P. McVittie, *J. Electrochem. Soc., Solid State Sci. Technol.* **135**, 1521(1988).
10. M. Sato and Y. Arita, *J. Electrochem. Soc., Solid-State Sci. Technol.* **134**, 2856(1987).
11. G. S. Oehrlein, K. K. Chan, M. A. Jaso, and G. W. Rubloff, *J. Vac. Sci. Technol.* **A7**, 1030(1989).
12. H. P. Strunk, H. Cerva, and E. G. Mohr, *J. Electrochem. Soc., Solid State Sci. Technol.* **135**, 2876(1988).
13. P. K. Charvat, E. E. Krueger, and A. L. Ruoff, *J. Vac. Sci. Technol.* **B4**, 812(1986).

PART IX

Ablation

GENERATION OF BLIND VIA-HOLES FOR A HIGH DENSITY MULTI-CHIP-MODULE USING EXCIMER LASERS

FRIEDRICH G. BACHMANN

Siemens AG, Corporate Production and Logistics Department,
Otto-Hahn-Ring 6, D-8000 München 83, Fed. Rep. Germany

ABSTRACT

In recent years the on-chip delay has gone down much more rapidly than the signal delay in packaged circuits. As a consequence of this the packaging delay times have had to be reduced drastically, which means that a greater packaging density had to be implemented. A novel planar packaging technique, used in the new Siemens main frame computer 7500 H 90 has led to considerable progress in solving this problem. An essential part of this system is a multi-chip-module which can hold up to 144 bare chips. The carrier of these IC's is a 16-layer high density multilayer printed circuit board, which is fabricated in a sequential process. Inter-layer contacts are formed by 80 μm wide blind via-holes, which are generated by excimer-laser ablation of the dielectric. The process described in this paper shows that it is possible to produce blind via-holes with an aspect ratio of about one in an extremely reliable and reproducible way. This process is already being successfully run on a production line. It is to our best knowledge the first time excimer lasers have been used on a large-scale in an industrial environment.

INTRODUCTION

The laser is indispensable in industry for many production processes like cutting, drilling, scribing, welding and soldering. The CO_2 and the Nd:YAG laser are most widely used for applications of this kind. There are also numerous applications in printed circuit board (PCB) production [1]. In this field too, it is CO_2 and Nd:YAG lasers that are most widely used. In some cases, the doors have opened for the industrial use of argon-ion lasers and excimer lasers for PCB manufacture and the potential for further exploitation is by no means exhausted.

This paper describes the highly miniaturized multi-layer printed circuit board for the multi-chip-module in the new Siemens 7500 H 90 mainframe computer product and how it is manufactured, showing how essential the excimer is for the production process.

THE MICROWIRING PRINTED CIRCUIT BOARD

The signal delay time for chips has gone down much more rapidly than the delay times for the packaging. The consequence of this is that the evolution in computing speed of high-speed computers is restricted by the packaging techniques used (Fig. 1). The further development of packaging technology therefore became a prime objective for those developing high-performance computers. The packaging delay times had to be reduced

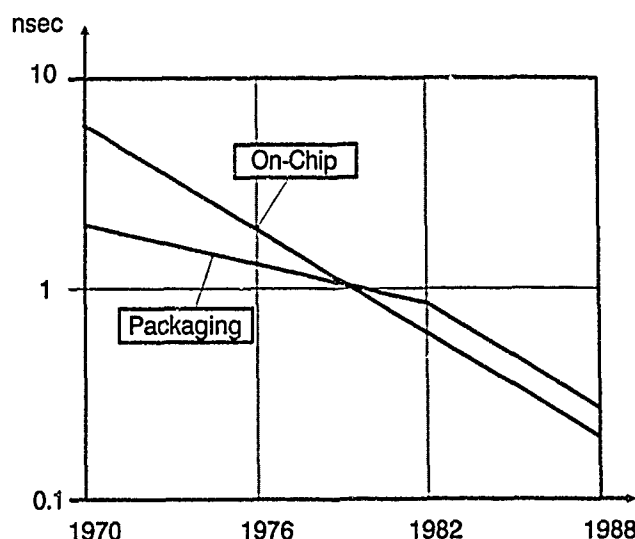


Fig. 1: Comparison of characteristic chip delay time and packaging delay time

drastically so that they could keep up with the chip delay time which was becoming increasingly shorter. This, in effect, meant that a greater packing density had to be implemented.

A novel planar packaging technique has lead to considerable progress in solving this problem [2]. A 28-layer back-panel wiring board accommodates a maximum of nine multi-chip-modules and a maximum of 216 connectors for cables and terminating impedances (Fig. 2). It is fitted to a frame which also supports the water-cooled heat sink.

The module connector with 1850 contacts, the multi-chip-module and the module cooling-plate (parts 1 to 3 in Fig. 2) form a unit which can be inserted into the main unit by means of a special tool (6). Fig. 3 clearly shows that either a LSI module with 320 leads or 9 MSI modules each with 52 leads can be accommodated in each of the 16 areas of the micro-wiring printed circuit board as "bare" IC's [4]. This means that a micro-wiring printed circuit board of this kind can accommodate between 16 (LSI) and 144 (MSI) chips. Fig. 4 shows the chip side of a printed circuit board of this kind [5]. The following sections of this paper will describe how these printed circuit boards are manufactured. As the specifications (Table I) show, blind vias 80 μm in diameter at a pitch of 0.5 mm have to be made in a 16-layer printed circuit board. It is intended that these blind vias will provide the through-contacting for neighboring layers. The excimer laser plays a major role in this process.

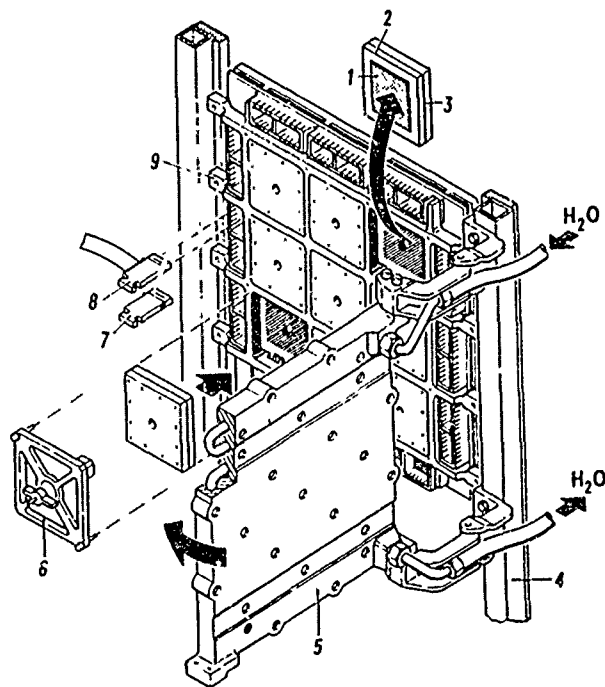


Fig. 2: Module side of the main board [2]
 (1) Connector, (2) Multi-chip-module, (3) Module heat sink,
 (4) Cabinet frame, (5) Cooling plate, (6) Insert-and-extract
 tool, (7) Terminating resistor packages, (8) Cable connector,
 (9) Aluminum frame

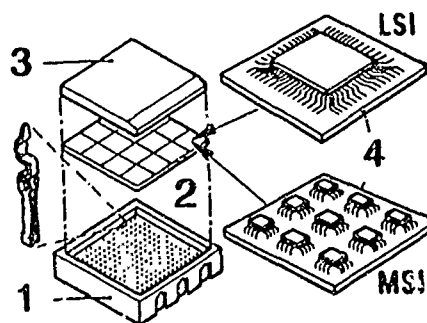


Fig. 3: Construction of a multi-chip module [3]
 (1) connector plate, (2) highly integrated printed circuit
 board, (3) cooling plate, (4) typical bonded chips

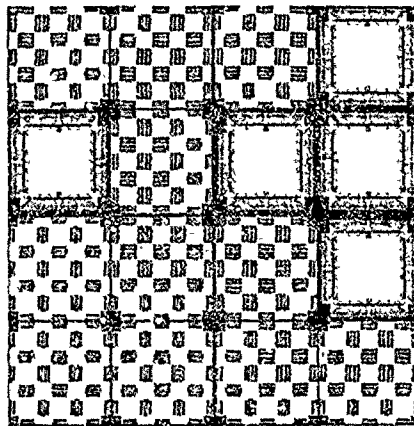


Fig. 4: Mounting layer for 5 LSI and 11x9 MSI chips [5]

MANUFACTURING THE MICRO-WIRING PRINTED CIRCUIT BOARD USING THE RELAMINATION TECHNIQUE [5]

A printed circuit board with the specifications given in Table I could not be implemented with conventional multi-layer printed circuit board techniques for the following reasons:

- The total through-contacting procedure, which would have been unavoidable if conventional multi-layer techniques were used, makes it difficult or even impossible to take tracks to the inner layers in the vicinity of the chips. For this reason, the only method that came into consideration from the outset was using highly miniaturized blind-via contacting to take the chip contacts to the interior of the printed circuit board.
- To solve the wiring problem using as few as possible internal signal layers it was necessary to find a substitute for (mechanically drilled) total through-contacting and to reduce the via diameter and the residual ring widths to values well below those used for conventional multi-layer techniques.

These requirements were met by using a novel relamination technique. In this technique layer $n+1$ is formed on top of an already up to layer n finished substrate (see below). The whole existing compound is "relaminated" several times. Relamination technology allows the realization of extremely fine interconnection patterns. On the other hand a priori one could say that a technique of this kind would have the following features:

- Long run-through time as it is a serial process
- Increased process reliability to ensure a satisfactory yield
- Need of full-coverage test techniques for each stage of production
- Need of repair procedures which can be used whenever necessary.

material	<ul style="list-style-type: none"> * glass-free dielectric, $\epsilon = 3.7$ * Cu-conductors 	
electrical data	<ul style="list-style-type: none"> * characteristic impedance $Z = (52,5 \pm 7,5) \Omega$ 	<ul style="list-style-type: none"> * cross talk 22,4 % max.
	<ul style="list-style-type: none"> * resistance $R = 13 \Omega/m$ 	<ul style="list-style-type: none"> * propagation time 6,4 ps/mm
design	<ul style="list-style-type: none"> * format: $\sim (100 \times 100) \text{ mm}^2$ * thickness: $\sim 2 \text{ mm}$ * layers: 16 * conductors: 80 μm wide 30 μm high * max. conductor length per signal layer: 30 m * via holes: \varnothing 80 μm 65 μm deep 30 000 vias max. between adjacent layers * grid: 500 μm 2 lines per channel 	
outer layers	<ul style="list-style-type: none"> * chip mounting layer SnPb fused, 16 chip mounting sites for TAB with 320 leads * connector layer Ni/Au, area connector with 1800 pins 	

Table I: Specifications of the micro wiring printed circuit board

An overview of most important stages in manufacturing a wiring layer is given in Fig. 5: Using adhesive resin, an 18 μm thick copper foil is attached to layer n which has been checked and, if necessary, repaired. The copper foil is then structured using photoresist and etching techniques to give 80 μm openings for the through contacts which electrically connect layer $(n+1)$ with layer n . After the photoresist foil has been removed, the resin in the 80 μm openings is exposed to the excimer-laser radiation and removed down to layer n (see next section). Copper is applied to the whole area, including the blind vias, using electroless plating followed by a galvanic process. This makes the electrical connection between the two vertically adjacent copper layers. In the course of several photoresist, galvanic and etching steps, the conducting lines for layer $(n+1)$ are built up. A temporary tin layer is used as etch-resist. After optical and electrical testing, and performing any repairs that may be necessary, the whole sequence described above is repeated for layer $(n+2)$.

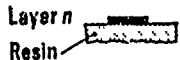



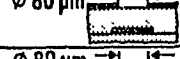




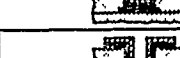
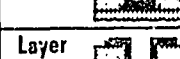
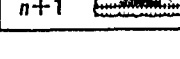
	Initial state: Layer n (signal or ground layer) completed. tested and repaired	
	Laminating (18 μm thick copper foil)	
	Photoimaging	Formation of up to 6000 blind holes between layer n and layer $n+1$
	Etching	
	Photoresist stripping	
	Laser drilling	
	Metal deposition (Cu)	
	Photoimaging	Pattern formation on layer $n+1$
	Metal deposition (Cu+Sn)	
	Photoresist stripping	
	Etching	
	Sn stripping	

Fig. 5: Schematic representation of the principal process steps for fabricating a microwiring substrate

THE EXCIMER LASER DRILLING PROCESS FOR BLIND-VIAS

To produce the blind via-holes, a technique which was capable of producing openings with a diameter of about 80 μm and an aspect ratio of about one had to be developed. Of course, there should only work at one plastic layer, the top one. The copper pad on the layer below should not suffer any damage. However, to guarantee through-contacts that are electrically and mechanically sound, the method had to produce absolutely clean via bases and ensure that the via walls were as near to the vertical as possible.

Because of the small bore-diameter and the condition that the contact area which is about 35 μm thick should suffer no damage, it was not possible to use conventional, mechanical drilling techniques. Drilling techniques using CO_2 -lasers had appeared in the literature [6]. For example, blind vias with diameters of about 200 μm have been drilled in epoxy resin foils (with glass-fiber reinforcement); because of the reflectivity of the underlying copper layer, the drilling process stops automatically. The technique, as the literature and our own experiments show, does not, however, meet the specified requirements. The walls slant and aspect ratios of about one or greater cannot be realized because of the isotropy of the melting and vaporization process and it is necessary to clean the via base

(e.g. with pumice [6] or plasma [7]). A further production disadvantage of the CO₂-laser drilling technique may well be the high demands made on the laser system with respect to pulse-to-pulse stability. Because a complete drilling action for one hole must be completed with one laser pulse, missing pulses or pulse energies which are too low mean that incomplete holes are produced. The holes must be redone [7] which decreases process reliability.

These are all reasons why a novel production technique was developed using excimer lasers to meet the requirements mentioned at the beginning of the paper. The basis of the technique is the well known process of "ablative photodecomposition" which was first mentioned in the literature in 1982 [8]. When materials, and in particular organic polymers, are exposed to laser light with sufficient photon energy and photon flux, they can undergo a transition to the gas phase with explosive suddenness. So sudden in fact that the thermal effect on the surrounding material is minimal. The reason for this is that, measured using time scale for decomposition or for the laser pulse, the energy transport to the neighboring material is negligible and so practically no warming occurs. UV lasers with pulse lengths in the nsec range are particularly well suited for this process. They give a high photon flux and photon energies which have the same order of magnitude as the binding energies. For organic polymers, the absorption length of light in the ultraviolet range is less than a micron so that extremely high energy densities can be achieved. On the other hand this means that the material is removed in a sequence of layers.

At present there is no complete agreement about the decomposition mechanism, i.e. the mechanism involved in material removal. However, it seems likely that both photochemical and photothermal mechanisms play a role [9,10], but depending on the material and the process conditions, one mechanism is more important than the other. The effects of heating on the surrounding material also depend on the conditions. This means that there may be difficulties when heterogeneous materials (e.g. materials with glass fiber reinforcement) are processed. This is not the case with our design. It may well be that different kinds of material have to be removed (acrylic resin, polyimides) but these materials will only be found as a sequence of homogeneous layers, one on top of the other. As the removal rate for both types of material are of the same order of magnitude, handling composite materials of this kind should not confront us with any unsurmountable problems.

The diagram in Fig. 6 shows the main stages of the process. The upper copper layer which carries the via pattern (see fig. 5) acts as a contact mask on the plastic layer to be processed. The UV light from the excimer laser will then decompose any parts of the surface not covered by the copper mask. The removal process stops automatically when the laser beam reaches the layer of copper below.

The variety of mechanisms could be seen in the results of a series of experiments, the object of which was to determine the optimal process parameters. It was important to ensure that the criteria mentioned above were largely met; under no circumstances whatsoever was damage to the copper layer permissible. First of all, the removal rates for a wide range of energy densities (0.1 to 2.0 J/cm²) were determined for three wavelengths, namely 308 nm (XeCl), 248 nm (KrF) and 193 nm (ArF). The pulse duration was about 20 nsec with minor variations due to the gas mixture used. Fig. 7 shows typical results for an epoxy adhesive and clearly indicates that KrF produces the optimal wavelength. The removal rates are maximal above a certain energy density and no damage to the copper layer occurs.

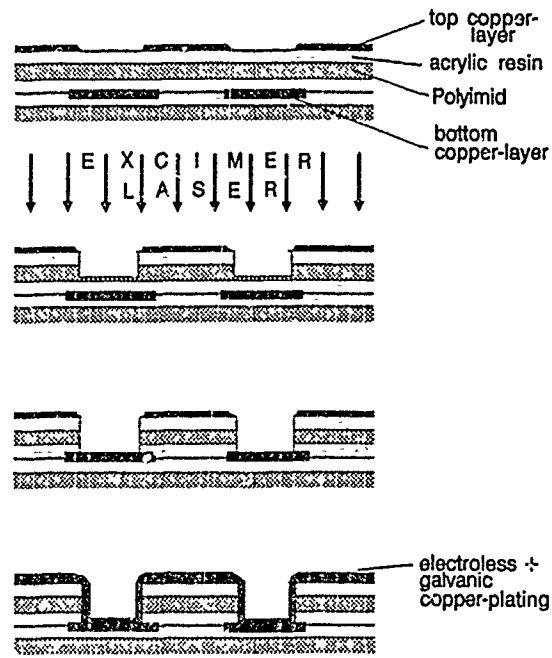


Fig. 6: Schematic representation showing the main stages in the laser drilling process

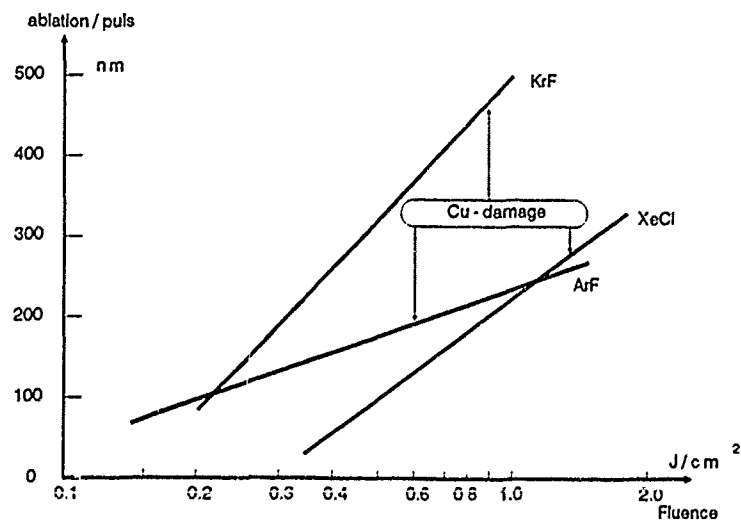


Fig. 7: Removal rates for an epoxy resin at different wavelengths

Both KrF and ArF produced straight via walls; the walls were practically vertical when ArF was used and with KrF the angle varies between 3° and 15° depending on the energy density. However when XeCl was used, wall rounding was observed, an indication that thermal effects were playing a major role in the removal process. Using an XeCl laser with a pulse duration of 60 nsec reduced the quality of the via walls.

Under the conditions that were finally selected, a KrF laser pulse was used to illuminate an area of about 15 mm^2 . Depending on the type of plastic used, each pulse removed a layer that was between 0.1 and $0.5 \mu\text{m}$ thick. This means that between 300 and 400 pulses would be required to produce a via; however as all the vias that are illuminated by the laser beam are processed simultaneously this means that, (assuming a $500 \mu\text{m}$ grid) a maximum of about 60 vias can be handled at the same time (see Fig. 8a). By using a meandering scan over the whole of the printed circuit board with overlapping laser pulses in overlapping tracks (see Fig. 8b) each via window then receives the number of pulses required to produce the complete via. As was mentioned previously, because the process parameters were selected so that the copper surface would suffer no damage, the process stops automatically when it reaches the next layer. This guarantees a high process reliability. Because of the integrating technique, the laser stability and the intensity distribution are not critical for the process.

Fig. 9 shows a scanning electron microscope photograph of a via that has been drilled away by a laser. The high positional accuracy of the removal procedure can be clearly seen. The traces of copper lying on the resin surface after etching are the unavoidable consequence of the treatment of the lower side of the copper foil. They cause fluting, or even columns, to form on the via wall. This is not a drawback as they provide better adhesion for the galvanic processing stage which follows. Fig. 10 is a cross-section through a copper-plated via lying between two layers and Fig. 11 is a cross-section through a completed micro-wiring board.

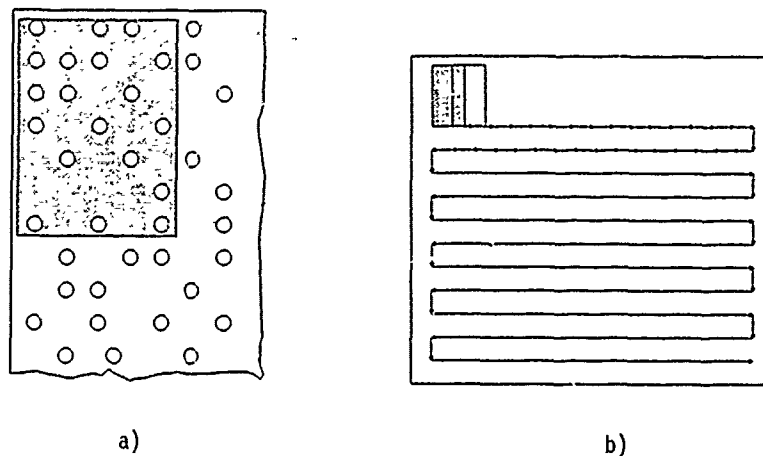


Fig. 8: Substrate illumination
 a) several vias with one pulse
 b) meandering scan over the entire substrate

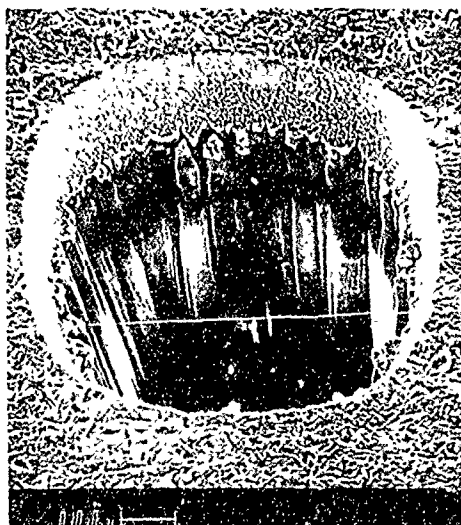


Fig. 9: SEM photograph of a laser drilled via

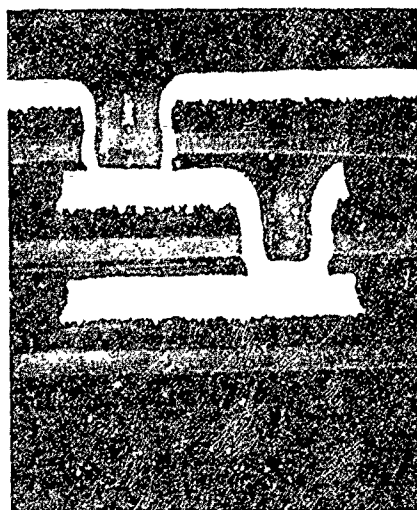


Fig 10: Cross section through
a copper plated via

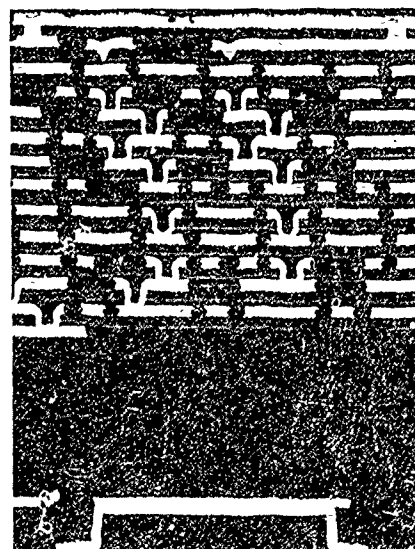


Fig. 11: Cross section through
a completed micro-
wiring board

USE OF THE TECHNIQUE IN PRODUCTION

The process described in this paper makes it possible to produce blind vias for through-contacting printed circuit boards in an extremely reliable way. Using excimer lasers in a production environment is entering into an area that, as yet, has been completely unexplored. First of all laboratory prototypes were used to check the essential selection criteria for the laser. Important aspects that had to be taken into account were the time between gas changes which should not be less than 8 hours (1 shift), and the interval between two window cleaning processes. The objective was to reach one cleaning a week (on a 3-shift basis). By using a cryogenic gas-cleaning system it was eventually possible to meet both criteria. Because the concept was entirely new, serviceability was a problem that had still to be solved - this was hardly a feature of excimer laser systems which up till now had almost exclusively been used in laboratories. The operating life of the thyatron and the electrodes (the most critical and most expensive components) had to be improved further. A few excimer laser companies are developing laser systems optimized for use in a production environment and some of these have already produced results in the form of actual products, which are available on the market place now.

Interatom, a Siemens subsidiary, developed a special machine for pilot production from the laboratory equipment for printed circuit board processing. By monitoring all important process functions (e.g. laser energy, laser-gas cleaning, table speed, table position, repetition rate etc.) by computer, faults could be detected immediately and the process stopped. This meant that destruction of the item being processed due to faults was almost impossible and the full effects of the process reliability which was mentioned previously were felt. The computer records details of each step in the process. To prevent contamination of the optics, counter-flow and extraction techniques were optimized. The meandering table-path was improved to reduce the acceleration and braking times as far as possible. This led to a 15% reduction in the processing time. The laser beam was passed through an inert gas environment to prevent the production of ozone. The process can be checked via a CCTV system.

After the pilot production plant had been run for about 1½ years, the production line was finally built (also by Interatom). A fully automatic conveyor-belt system carrying the items to be processed supplies the laser plant and takes the finished items away. Again, a host computer monitors the whole plant and records activity. Each printed circuit board is identified by a bar code. The production line has been designed so that servicing the excimer lasers presents no problems. If necessary, a defective laser can be replaced within an hour. The factory infrastructure supplies gas, suction facilities, cooling air and liquid nitrogen directly to the machines. The plant went into operation in August 1988, is now using 12 excimer lasers and is operating successfully on a 3-shift basis. This is the first time KrF-excimer lasers have been used on a large-scale in an industrial environment.

LITERATURE

1. A. Gemmler, T. Bolch, J.-L. Jostan :
Laser in der Leiterplattentechnik.
Galvanotechnik 79, 3447 (1988)
2. H. Wessely, W. Türk, K.-H. Schmidt, G. Nagel :
Computer Packaging.
Siemens Res. & Dev. Reports 17, 5, 234 (1988)
3. A. Krauter, J. Baumann, M. Becker :
Assembly Process for a New Micropackaging System.
Siemens Res. & Dev. Reports 17, 5, 254 (1988)
4. H. J. Hacke, H. H. Steckhan :
Micropack Packaging Technology.
Siemens Res. & Dev. Reports 17, 5, 227 (1988)
5. H. Brösamle, B. Brabetz, V. v. Ehrenstein, F. Bachmann
Technology for a Microwiring Substrate.
Siemens Res. & Dev. Reports 17, 5, 249 (1988)

H. Brösamle :
Technology for a Microwiring Substrate.
Proc. Conf. IEPC, Helsingör, June 13-15, 1988
Ed. by M. G. Fassini
6. F.-J. Hillebrand :
Laserbohren in organischem Leiterplatten-Material.
Feinwerktechnik & Meßtechnik 91, 56 (1983)
7. D. W. Korf :
Laser-Drilled Blind Vias Increase PCB Real Estate.
Electronic Packaging & Production Feb. 1987, p. 56
8. R. Srinivasan, W. J. Leigh :
Ablative Photodecomposition: Action of Far-Ultraviolet
(193 nm) Laser Radiation on Poly(ethylene terephthalat)
Films.
J. Am. Chem. Soc. 104, 6784 (1982)
9. V. Srinivasan, M. A. Smrtic, S. V. Babu :
Excimer Laser Etching of Polymers.
J. Appl. Phys. 59, 3961 (1986)
10. D. Dijkkamp, A. S. Goetz, T. Venkatesan, X. D. Wu :
Evidence for the Thermal Nature of Laser-Induced Polymer
Ablation.
Phys. Rev. Lett. 58, 2142 (1987)

LASER DEPOSITION AND PATTERNING OF HIGH-TEMPERATURE SUPERCONDUCTORS

D. BAUERLE, J. HEITZ, W. LUDORF, P. SCHWAB, AND X.Z. WANG
Angewandte Physik, Johannes-Kepler-Universität Linz, A-4040
Linz, Austria

ABSTRACT

Superconducting films of Y-Ba-Cu-O and Bi-Sr-Ca-Cu-O on (100) SrTiO₃ and (100) MgO substrates have been fabricated by reactive excimer-laser sputtering from ceramic targets. Film patterning by laser-induced reduction/metallization, oxidation, and ablation has been investigated.

1. INTRODUCTION

Among the large number of various different techniques employed in thin-film formation of high-temperature superconductors, laser sputtering is distinguished by a number of unique properties: it is fast, easy, inexpensive, permits great experimental versatility, and excellent control on the correct stoichiometry within the deposited film. Additionally, many applications of thin film and bulk high-temperature superconductors require proper surface patterning. Here, the laser techniques also offer many possibilities [1].

In this paper we report on the "in situ" fabrication of thin superconducting films of mainly Bi-Sr-Ca-Cu-O by reactive laser sputtering (Sect.2) and on laser-induced surface patterning by surface modifications (surface reduction, metallization, and oxidation) and by material ablation (Sects.3 and 4).

2. THIN FILM FORMATION BY LASER SPUTTERING

The main results on the deposition of thin films of different high temperature superconductors (HTS) by either reactive or non-reactive laser sputtering have been recently reviewed [1]. Subsequently, we will confine the further discussion on thin films of Y-Ba-Cu-O and Bi-Sr-Ca-Cu-O that have been produced by 308 nm XeCl and 248 nm KrF-excimer laser sputtering in O₂ atmosphere.

Y-Ba-Cu-O

Films of $\text{YBa}_2\text{Cu}_3\text{O}_{7-x}$ with thicknesses between 0.1 and 1.8 μm have been deposited mainly on (100) SrTiO_3 and (100) MgO substrates. The sputtering conditions employed and the film properties achieved were similar to those reported in the literature [1]. On the MgO substrates, in particular, zero resistance temperatures of up to 88 K have been achieved.

Bi-Sr-Ca-Cu-O

The first results in the in situ fabrication of superconducting films of Bi-Sr-Ca-Cu-O by reactive laser sputtering in O_2 atmosphere have been reported in [2]. These experiments were performed by means of 308 nm XeCl-excimer laser radiation and ceramic targets of nominal composition $\text{Bi}_{2.5}\text{Sr}_2\text{Ca}_2\text{Cu}_3\text{O}_y$. The substrate material employed was (100) MgO . A schematic diagram of a typical experimental setup used in such experiments has been shown in [1]. The XeCl-excimer laser employed had a pulse length of about 11 ns at FWHM and was operated at a pulse repetition rate of 20 Hz. The laser fluence at the surface of the target was, typically, about 1.5 J/cm^2 . For film deposition the temperature T_s , measured at the substrate holder, was varied between 800 and 824 $^\circ\text{C}$. At this latter temperature, melting of the film was frequently observed. The in-situ formation of superconducting films has been achieved in pure O_2 with a background pressure of 0.14 mbar. The average deposition rate was 0.16 $\text{\AA}/\text{pulse}$. Immediately following deposition, the reactor was filled with about 1 atmosphere of pure O_2 and cooled to room temperature within about 30 minutes. The film thicknesses prepared were, typically, 0.5 μm . With temperatures of $T_s \approx 821^\circ\text{C}$, the as-deposited films were grey to black with a smooth mirror-like appearance. Scanning-electron microscope (SEM) analyses revealed a strong dependence of surface morphology of films on oxygen pressure.

Figure 1 shows the film resistance as a function of temperature for a film deposited at $T_s = 821 \text{ K}$. The resistance behavior is metallic-like within the normal conductive state. At about 122 K, a clear drop in resistance, indicating a small amount of the 2223 superconducting phase, is observed. Zero

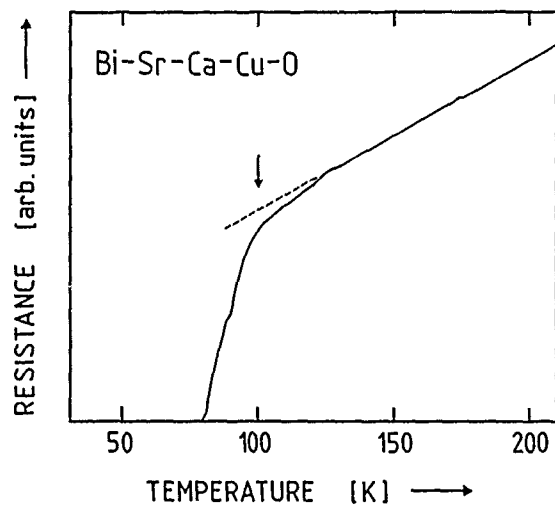


Fig. 1: Resistance of a 308 nm XeCl laser-deposited Bi-Sr-Ca-Cu-O film as a function of temperature. The onset to superconductivity as indicated by the arrow, is observed at around 100 K. Zero resistance was obtained at around $T_c(0) \approx 79$ K.

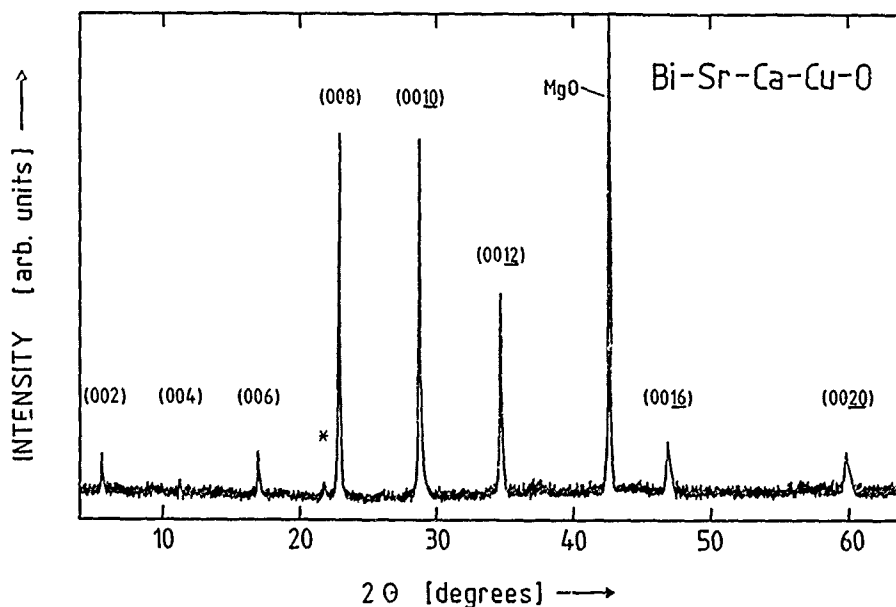


Fig. 2: X-ray diffraction pattern of a Bi-Sr-Ca-Cu-O film on a (100) MgO substrate. The film was deposited by 308 nm excimer-laser radiation at a substrate holder temperature of $T_s \approx 820^\circ\text{C}$ and an oxygen pressure of 0.14 mbar. The analysis of this pattern yields a c-axis of $c = 30.80 \pm 0.02$ Å that is characteristic of the 2212 phase. The asterisk marks a peak that indicates the presence of a small amount of the semiconducting phase ($c \approx 24.4$ Å).

resistance was found at around $T_c(\phi=0) \approx 79$ K. The zero magnetic field critical current density in this film, measured at 50 K, was $j_c(50K) \approx 10^4$ A/cm².

The microstructure of as-deposited films was investigated by X-ray diffraction. The very strong (00 ℓ) reflections seen in Fig. 2 indicate that the film is oriented with its c-axis normal to the (100) MgO substrate surface. The analysis of this pattern yields a lattice constant of $c = 30.80 \pm 0.02$ Å. The small peak marked by an asterisk indicates the presence of a small amount of a second phase, the semiconducting phase, with $c = 24.4$ Å. With films deposited at temperatures of $T_g < 817$ °C, the X-ray diffraction analyses reveal a mixed phase consisting of the 2212 phase and the semiconducting phase.

Similar results were obtained with KrF-laser radiation. Here, transition temperatures of $T_c(0) \approx 81$ K and critical current densities of $j_c(4.2K) \approx 2 \cdot 10^5$ A/cm² have been achieved.

3. SURFACE MODIFICATIONS

Laser-induced surface reduction, metallization, and oxidation has been investigated mainly for Y-Ba-Cu-O in the form of ceramic samples and thin films. The experiments were performed by employing 488 nm and 514.5 nm Ar⁺ laser radiation and hydrogen/oxygen pressures of $0 \leq p \leq 10$ bar. The experimental results achieved with thin films were qualitatively similar to those reported for ceramic samples [3,4]. However, for scans performed over, typically ten millimeters, the reproducibility of data was poor. This is related to the non-uniformity in film thicknesses on the one hand and the narrow parameter ranges where surface reduction/oxidation takes place without destruction or subsequent cracking of processed film areas on the other hand.

4. PATTERNING BY ABLATION

The ablation of thin films of Y-Ba-Cu-O on (100) SrTiO₃ and (100) MgO substrates and of Bi-Sr-Ca-Cu-O on (100) MgO substrates has been investigated by employing 249 nm KrF laser-light projection. Here, apertures of various diameters (0.3, 0.5, 0.7, 2, and 4 mm) were inserted into the beam path and imaged onto the film surface by employing a 10:1 reduction

optics. Ablation rates were measured as a function of incident laser fluence, ϕ , and laser beam spot diameter at the film surface, $2w$.

With both Y-Ba-Cu-O and Bi-Sr-Ca-Cu-O three characteristic regimes of laser-material interactions were observed: With low laser fluences of, typically, $\phi \approx 0.07 \text{ J/cm}^2$ the laser light causes film damage without significant ablation. With medium laser fluences of, typically, $\phi \approx 0.4 \text{ J/cm}^2$, non-stoichiometric inhomogeneous ablation takes place. With fluences exceeding 1 J/cm^2 , stoichiometric film ablation is observed. The transition between the different regimes depends on both the particular film composition and the type of substrate material.

Y-Ba-Cu-O

Figure 3 shows scanning electron micrographs of $\text{YBa}_2\text{Cu}_3\text{O}_7$ films on (100) MgO substrates irradiated in vacuum by 248 nm KrF laser light projection. The laser pulse repetition rate was 1 Hz. The circular area seen in Fig.3a occurs after irradiation with 50 laser pulses of $\phi \approx 0.12 \text{ J/cm}^2$. Under these conditions the film is damaged and becomes more transparent, but no significant ablation is observed. On the right-hand side of the picture irradiated and non-irradiated film regions are shown with larger magnification. A microprobe analysis reveals a depletion of Cu and, to a smaller extent, also of Ba with respect to Y. The increase in transparency results mainly from the loss of oxygen. Figure 3b shows a hole produced by a single laser pulse of fluence $\phi = 1.7 \text{ J/cm}^2$. With this fluence, ablation of the film is stoichiometric and almost homogeneous. Small inhomogeneities arise from light diffraction and, eventually, from large particles, fractions of which may remain within the hole. The hole shown in Fig.3b is surrounded by a torus whose structure is suggestive of film melting. The microanalysis of this region reveals a depletion of Cu. At constant laser fluence, the width of this damaged zone seems to increase with increasing laser pulse length and, with thick films, the number of pulses required for total film ablation.

Figure 4 shows the ablation rate for $\text{YBa}_2\text{Cu}_3\text{O}_7$ films on (100) MgO substrates as a function of laser fluence and for three different laser-beam spot sizes. Within the accuracy of the measurements, the ablation rate was independent of film

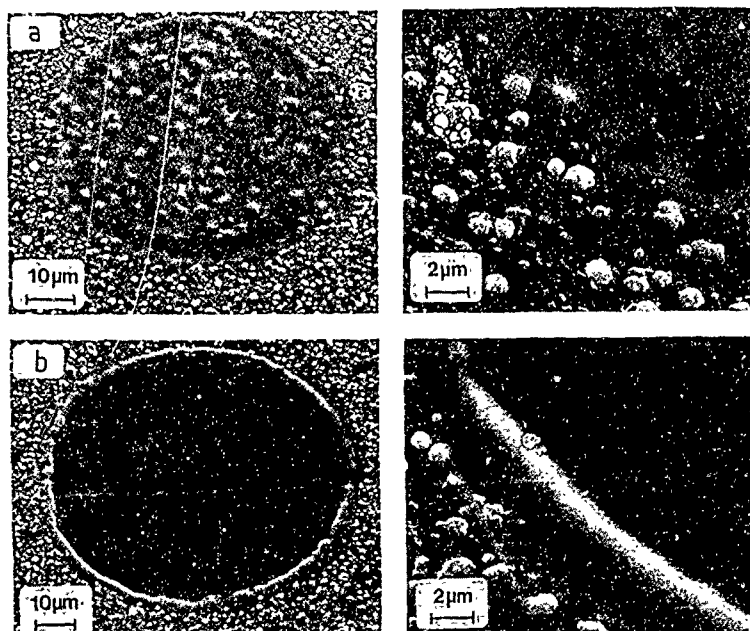


Fig. 3: $\text{YBa}_2\text{Cu}_3\text{O}_7$ films on (100) MgO substrates irradiated by 248 nm KrF-excimer laser radiation. The film thickness was about $1 \mu\text{m}$, and the laser spot diameter $2w = 70 \mu\text{m}$. Pictures on the right hand side show irradiated and non-irradiated regions in larger magnification.

a) regime of film damage ($\phi \approx 0.12 \text{ J/cm}^2$, 50 laser shots)

b) regime of stoichiometric ablation ($\phi \approx 1.7 \text{ J/cm}^2$, 5 laser shots)

thickness which was varied between 0.5 and $1.5 \mu\text{m}$. Each data point in Fig. 4 is an average of several single measurements. The error bars indicate the standard deviation. The characteristic regimes of laser light-material interaction are indicated. The regime where surface damage is observed starts at a fluence of $\phi_d \approx 0.04 \pm 0.01 \text{ J/cm}^2$. Then, with increasing ϕ , the transparency of films increases. For fluences in the regime $0.27 \pm 0.05 \text{ J/cm}^2 < \phi < 0.75 \pm 0.05 \text{ J/cm}^2$ non-stoichiometric ablation is observed. The material remaining within the hole shows a strong enrichment of Y with respect to Cu and Ba. For fluences $\phi_{th} > 0.75 \pm 0.05 \text{ J/cm}^2$ uniform

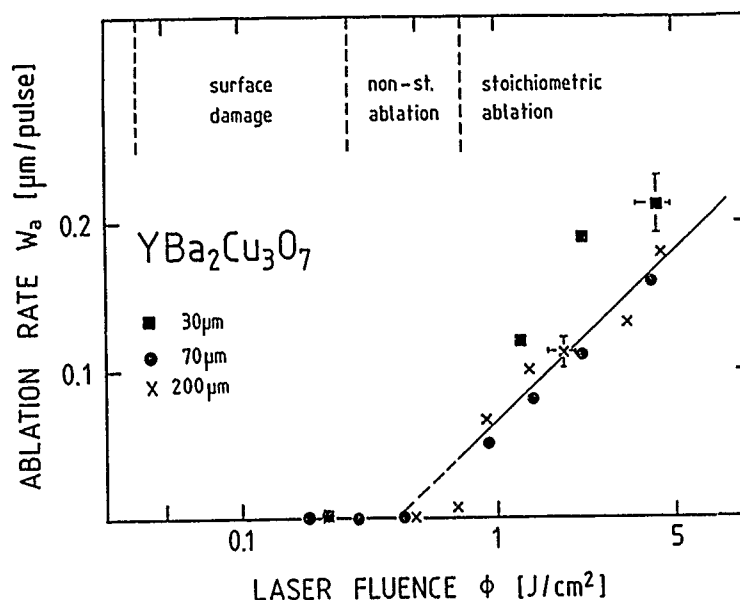


Fig. 4: Ablation rate for $\text{YBa}_2\text{Cu}_3\text{O}_7$ films on (100) MgO substrates as a function of 248 nm KrF-laser fluence. Here, the excimer-laser light was projected onto the thin film by employing a mechanical mask together with a 10:1 reduction optics. The laser beam spot sizes on the film surface, $2w$, are indicated by different symbols. Film thicknesses between 0.5 and 1.5 μm have been used.

ablation of films was observed. In this regime ablation is stoichiometric - within the accuracy of the microprobe analysis which was about $\pm 2\%$. The diameter of holes, d , is equal to the diameter of the laser spot, $2w$, with laser fluences $\phi < 2 \text{ J/cm}^2$, and becomes somewhat larger with higher fluences (for $\phi \approx 4.1 \text{ J/cm}^2$ and $2w = 30 \mu\text{m}$ we found $d \approx 36 \mu\text{m}$). In the regime of stoichiometric ablation which was investigated up to 4.5 J/cm^2 the etch depth increases linearly with the number of laser pulses (Fig. 5). The somewhat higher ablation rates observed with the $30 \mu\text{m}$ spot size are related to the shielding of the incident laser radiation which is less efficient with very small laser beam spot sizes. This effect has been investigated in more detail in [5,6]. The full and dashed curves included in Figures 4 and 5 are guides for the eyes.

Finally, we would like to mention that the characteristic thresholds for film damage/ablation are slightly lowered with films on (100) SrTiO_3 substrates.

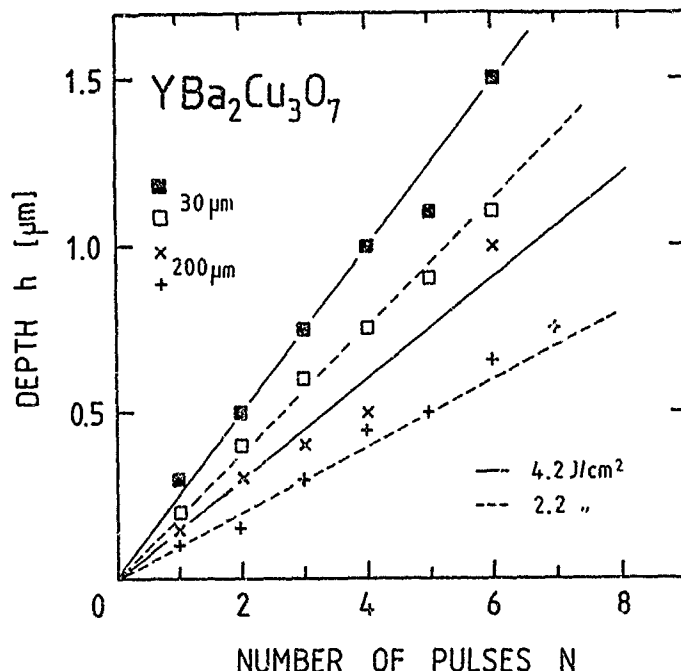


Fig. 5: Depth of holes in $\text{YBa}_2\text{Cu}_3\text{O}_7$ films on (100) MgO substrates as a function of the number of laser pulses for laser-beam spot diameters of $2w = 30 \mu\text{m}$ (\blacksquare 4.2 J/cm^2 , \square 2.2 J/cm^2) and $200 \mu\text{m}$ (\times 4.2 J/cm^2 , $+$ 2.2 J/cm^2).

Bi-Sr-Ca-Cu-O

Figure 6 shows the ablation rate for Bi-Sr-Ca-Cu-O films on (100) MgO substrates as a function of 248 nm KrF-laser fluence. The figure demonstrates that the ablation behavior is qualitatively very similar to that observed with $\text{YBa}_2\text{Cu}_3\text{O}_7$ films. The main differences are seen in the lowering of threshold fluences characteristic for the different regimes of material surface interactions. Non-stoichiometric ablation is observed within the regime $0.1 \pm 0.03 \text{ J/cm}^2 \leq \phi \leq 0.51 \pm 0.06 \text{ J/cm}^2$. Here, the material remaining within the hole shows mainly a loss of Bi. For fluences above $\phi_{\text{th}} > 0.51 \pm 0.06 \text{ J/cm}^2$, film ablation is uniform. Within the accuracy of the measurements, the ablation rates are the same for laser-beam spot diameters $2w \geq 50 \mu\text{m}$. Similarly to the case of Y-Ba-Cu-O, ablated regions are surrounded by a damaged zone.

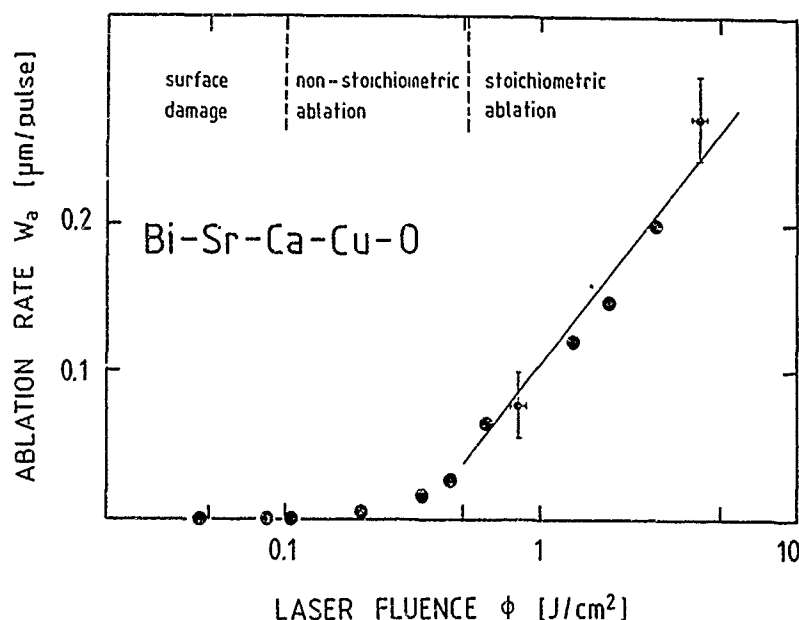


Fig. 6: Same as Fig. 4 but for Bi-Sr-Ca-Cu-O films.

Material damage

To further study the spatial extension of material damage during ablation by excimer-laser light projection, structures as shown in Fig. 7 have been produced. With such structures zero-resistance temperatures and critical current densities were measured for various widths of bridges, d_B . For $0.1 \mu\text{m}$ thick $\text{YBa}_2\text{Cu}_3\text{O}_7$ films on (100) SrTiO_3 substrates, the following results were obtained:

- The transition temperature, $T_c(0) \approx 92 \text{ K}$, remains unchanged as long as $d_B > 10 \mu\text{m}$.
- the critical current density, j_c , is decreased with respect to non-irradiated films. For the present example, projection patterning reduced the current density, measured at 77 K , from originally, typically, $3 \text{ to } 5 \cdot 10^6 \text{ A/cm}^2$ to about $1.5 \cdot 10^6 \text{ A/cm}^2$ ($d_B \approx 65 \mu\text{m}$). After post-annealing in oxygen this patterned film had a $j_c(77 \text{ K})$ of $2.7 \cdot 10^6 \text{ A/cm}^2$.
- in patterns with a width of $d_B < 10 \mu\text{m}$ no transition to the

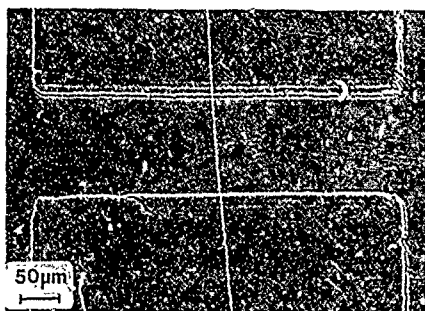


Fig. 7: $\text{YBa}_2\text{Cu}_3\text{O}_7$
film patterned by
248 nm KrF laser-
light projection.

superconducting state was observed. Post annealing of such small structures does not reveal superconductivity.

For Y-Ba-Cu-O and Bi-Sr-Ca-Cu-O films on (100) MgO substrates, the results were qualitatively the same. These investigations have revealed that patterning by excimer-laser light projection causes two types of film damage:

- An irreversibly damaged zone directly adjacent to the ablated region. This zone has a width of 2 to 8 μm , depending on the film thickness (the number of laser pulses for total film ablation).

- A zone in which the critical current density is decreased due to the loss of oxygen. In this zone the superconducting properties can be revealed by annealing in oxygen atmosphere.

It is not yet clear whether the film damage is caused by the diffraction of the laser light and/or by heat conduction. In the latter case it should be possible to reduce material damage by employing shorter laser pulses.

Summary

Excimer-laser sputtering permits the *in situ* fabrication of thin films of Bi-Sr-Ca-Cu-O. The zero resistance temperatures and critical current densities presently achieved are $T_c(0) \approx 81 \text{ K}$ and $j_c(4.2 \text{ K}) \approx 2 \cdot 10^5 \text{ A/cm}^2$. In thin films the reproducibility of laser-induced surface modifications (reduction, metallization, oxidation) can be improved only with films of excellent thickness uniformity. The threshold fluences

for stoichiometric ablation of $\text{YBa}_2\text{Cu}_3\text{O}_7$ and Bi-Sr-Ca-Cu-O films on (100) MgO substrates are $\phi_{\text{th}} > 0.75 \pm 0.05 \text{ J/cm}^2$ and $\phi_{\text{th}} \geq 0.51 \pm 0.06 \text{ J/cm}^2$ respectively. Projection patterning by ablation causes irreversible film damage in a 2 to 8 μm wide zone adjoining the ablated region. Otherwise, film damage can be annealed in oxygen.

ACKNOWLEDGEMENTS

We wish to thank Dr. L. Schultz for supplying us with a thin film of $\text{YBa}_2\text{Cu}_3\text{O}_7$ on a SrTiO_3 substrate. We are grateful to the "Fonds zur Förderung der wissenschaftlichen Forschung in Österreich" and the "Jubiläumsfonds der Österreichischen Nationalbank" for financial support.

REFERENCES

1. D. Bäuerle, Appl. Phys. A 48, 527 (1989).
2. W. Ludorf, X.Z. Wang, and D. Bäuerle, Appl. Phys. A 49, 221 (1989).
3. G. Liberts, M. Eyett, and D. Bäuerle, Appl. Phys. A 45, 313 (1988).
4. G. Liberts, M. Eyett and D. Bäuerle, Appl. Phys. A 46, 331 (1988).
5. M. Eyett and D. Bäuerle, Appl. Phys. Lett. 51, 2054 (1987).
6. D. Bäuerle, M. Eyett, U. Kolzer, R. Kullmer, P. Mogyrosi, and K. Piglmayer, in Laser- and Particle-Beam Chemical Processing for Microelectronics, eds. D.J. Ehrlich, G.S. Higashi, M.M. Oprysko (Materials Research Society 1988 Symposium Proceedings, Vol. 101) p. 411.

PRECURSORS TO THE PHOTO-ABLATION OF SODIUM TRISILICATE GLASS DUE TO UV EXCIMER IRRADIATION

P. A. ESCHBACH,* J. T. DICKINSON,* S. C. LANGFORD,* L. C. JENSEN,*
L. R. PEDERSON,** AND D. R. BAER**

* Washington State University, Pullman, WA 99164-2814

**Pacific Northwest Laboratory, Richland, WA 99352

ABSTRACT

On polished sodium trisilicate glass surfaces, a fairly distinct threshold in laser fluence is observed to commence ablative etching. An incubation or induction effect is also seen where a series of laser pulses is required to induce etching. In this paper we examine features of the charged particle emission over a broader range of fluences (in particular, at lower fluences) to identify those factors which control the onset of etching. Laser-free electron heating is proposed as a dominant mechanism.

INTRODUCTION

In previous work,¹ we examined the changes that occur in sodium trisilicate glass and the resulting plume products when the glass was irradiated with relatively high fluence (2.7 - 5.0 J/cm²) 248 nm excimer laser light. Irradiation at these high fluences produces high etch rates (typically 200 nm per laser pulse) accompanied by a visible near-surface plume composed of large quantities of electrons, positive ions (Na⁺, Si⁺, H⁺); neutral atoms (O, Na, Si); molecular NaO; and electronically excited Na atoms. Energetic ionic and excited neutral species in the plume indicate the presence of strong laser-plume interactions. At fluences ~2.7 J/cm² (which we define as an approximate threshold), a induction or incubation period involving bombardment of the surface with a few laser pulses was required to induce etching and plume formation.

In this paper we examine the interaction of 248 nm excimer radiation with sodium trisilicate glass at fluences below that required for the onset of plume formation and rapid surface etching, i.e., below about 2.7 J/cm², to identify those factors which control the onset of etching. We show that significant electron and Na⁺ emission is observed even at relatively low fluences. To within the sensitivity of our measurements, other charged and neutral species seen at fluences above the etching threshold were not observed at low fluences. Near-surface defect states appear to play an important role in the subthreshold emission processes. Increasing the near surface defect density by low energy (1 KeV) electron irradiation is shown to *lower* the threshold for plume formation and the onset of rapid etching. The manipulation of defect densities by particle irradiation and composition control may have important applications in ablative etching, laser ablation deposition, and the prevention of damage to optical materials.

EXPERIMENT

Details of the particle detection experiments are given in references 1-3. All of the laser experiments were conducted in a diffusion pumped, liquid nitrogen trapped vacuum chamber at a pressure of 10⁻⁵ Pa. Sample irradiation was performed with a Lambda Physik EMG203 excimer laser operating at 248 nm (KrF). The laser fluence was varied by inserting various filters in the beam. The beam energy was measured with a Gentec ED 500 joule meter. Charge particles were detected with an appropriately biased Channeltron electron multiplier (CEM), Galileo Electro-optics model 4039. When high particle currents were encountered, the CEM was operated in a "zero gain" mode, using the biased CEM front cone merely to collect the detected current. Ion identification was accomplished with a UTI 100C quadrupole mass spectrometer (QMS) with the ionizer removed. An electron beam for simultaneous bombardment of the glass surface was produced by a Varian Auger gun which provided a spot size of 1.5 mm diameter over an energy range of 500-3000 eV at currents in the range of 50-300 μ A.

Reflection electron energy loss spectra (REELS) of the sodium trisilicate glass was obtained in a different vacuum system, maintained at pressures < 10⁻⁶ Pa. The REELS data were

taken with PHI Model 15-255G double pass energy analyzer mounted concentrically with an electron gun operated at 300 eV and 10 nA. The spot diameter was 5-10 μm . Clean glass surfaces were obtained in the REELS system by in-situ fracture.

RESULTS AND DISCUSSION

Electron Emission. The highly energetic ionic and excited neutral particles accompanying etching at high fluences was attributed to inverse bremsstrahlung acceleration of electrons in the near-surface region of the vacuum, which results in ion acceleration by electrostatic attraction.¹ This process requires substantial electron and ion densities in this region during the early portion of the laser pulse; subsequent interactions with the laser pulse elevate both the electron and surface temperatures. In the context of the inverse bremsstrahlung model, the photoelectron and ion emission intensities play a crucial role in determining the onset of plume formation and rapid etching. The electron emission intensity vs laser fluence is shown in Fig. 1.

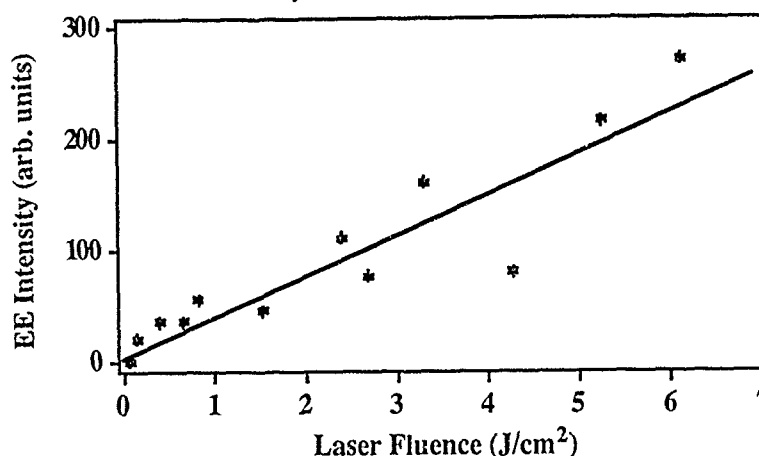


Fig. 1. The Electron Emission Intensity vs Laser Fluence. Note that it is linear, implying a single photon process.

Over a wide range of fluences, including those sufficient for plume formation, EE is a linear function of laser fluence. First order dependence of EE on laser fluence has also been observed during the laser irradiation of fused silica.⁴ Given the transparency of sodium trisilicate glass at 5 eV,⁵ this suggests that the emission is a single photon process involving mid-gap defect states. In our experiments, the EE intensity was quite stable from pulse to pulse, in contrast to other emissions (e.g., positive ion emission), suggesting that the observed EE at these fluences is not very sensitive to surface conditions. Further, the observed EE was a relatively strong function of laser repetition rate, falling markedly at rates above ~ 20 Hz. This dependence is likely due to depletion of filled traps which require times on the order of 50 ms to replenish. The simple first order process observed also suggests that overall charging of the surface was not very extensive; substantial charge transfer would be expected to introduce non-linear behavior.⁶

Positive Ion Emission (PIE). Positive ions are also emitted at fluences well below the threshold for plume formation and rapid etching. The low fluence positive ions were mass analyzed with a quadrupole mass spectrometer. Within our sensitivity, all PIE was mass 23, i.e., Na^+ . Estimates of E fields along the ion flight paths allow time-of-flight analyses which indicate that the ion energies are substantially less than 1 eV. This is in stark contrast to high fluence PIE which typically displayed energy distributions with peaks in excess of 10 eV. As noted above, we attribute this difference to inverse bremsstrahlung acceleration of electrons coupled with "wake-like" acceleration of positive ions towards the electrons moving away from the surface.

Plots of PIE Intensity (averages over 50 laser pulses) vs laser energy are shown in Figures 2a(log) and 2b (linear) intensity scales. Attempts to use simple first order heating and an Arrhenius equation⁷ for the PIE emission rate were unsuccessful in fitting the data over the full range of

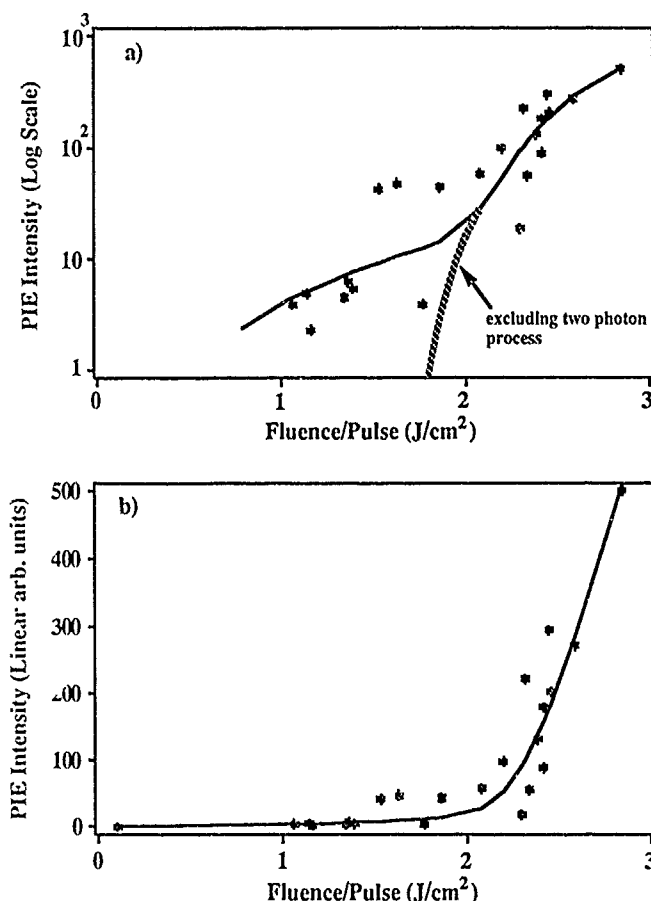


Fig.2 Positive Ion Emission Intensity vs laser fluence/pulse. a) log intensity scale, b) linear intensity scale. The solid lines represent a fit to equation 3. The hatched line indicates the consequences of discarding the first term $\sim f^2$.

fluences. At lower fluences, the data were consistent with a non-thermal, two photon process, i.e., $I_{PIE} \sim f^2$, where f is the fluence/pulse (Note that if we assume a "square wave" laser pulse, the photon flux F (photons/cm²/s) and the fluence/pulse, f , are proportional). Two photon excitations in this material would yield electronic states above the band gap; the emission of Na^+ under these conditions most likely involves electronic defects. Ohuchi et al.⁸ have proposed that electron stimulated desorption of Na^+ from sodium trisilicate glass involves a trapped hole precursor. Two photon production of related defects has been previously reported.^{9,10}

At higher fluences, the rapidly increasing PIE intensity is consistent with a heating mechanism consisting of *simultaneous* single photon-free electron release (from defects) accompanied by laser heating of the free electrons by the laser pulse itself. This is similar to multiphoton free electron production + heating proposed by Shen et al.¹¹ for the heating and damage of wide band gap, defect-free materials. An equation describing the temperature rise due to laser-free electron heating has been derived by Epifanov^{12,13} and is given by:

$$\frac{\partial T(r,t)}{\partial t} = \frac{C \cdot f^{1/2}(r,t)}{\rho c} n_c F^{3/2}(r,t)$$

1)

where C is a constant involving parameters of the material, r is the mass density of the glass, c the heat capacity, n_c the free electron density, and F is the photon flux (photons/cm²/s). For single photon-free electron generation, n_c would be proportional to $n_d F^2$ (or $n_d F$), where n_d is the density of defects capable of releasing electrons. Integrating this equation (assuming F constant and uniform over the interaction volume *during* the laser pulse), we obtain a temperature rise, ΔT , given by:

$$\Delta T = K_1 \cdot f^{5/2} + \frac{K_1^2}{1200} f^5 \quad (2)$$

Substituting this non-linear heating mechanism into an Arrhenius term and combining with the two photon emission process discussed above, we obtain for I_{PIE} the equation:

$$I_{PIE} = a_1 f^2 + a_2 \exp\left(-b / \left(K_1 \cdot f^{5/2} + \frac{K_1^2}{1200} \cdot f^5\right)\right) \quad (3)$$

where a_1 , a_2 , b , and K_1 are adjustable parameters.

The solid lines in both Fig. 2a and 2b are generated from a non-linear least squares fit to the raw data using this equation. The hatched line shows the effect of ignoring the first term ($\sim f^2$) of this equation. Although there is considerable scatter, the overall fit is quite reasonable. In addition, when we take PIE data with the full gain of the Channeltron electron multiplier at fluences as low as 0.1 J/cm², we continue to find a strongly non-linear intensity vs. fluence dependence, consistent with this equation. The significant influence of the second term coincides with the very beginning of the onset of plume formation and etching of the glass surface in what appears to be somewhat like an avalanche. In fact, no avalanche (usually attributed to electron multiplication) is required for this PIE behavior; the higher order heating is sufficient to explain the rapid rise in PIE with fluence. We therefore propose that the dominating factor for these strong laser surface interactions is the free carrier density, n_c . n_c , in turn is directly related to the density of defects serving as sources for single photon generated free electrons, consistent with the observed first order electron emission results (Fig. 1).

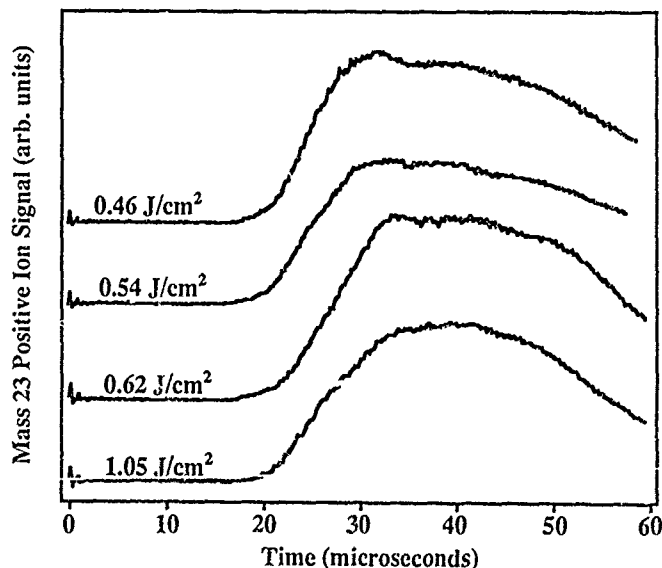


Fig. 3. Mass 23 (Na⁺) positive ion signals vs time for different fluences (0.46 - 1.05 J/cm²). The laser pulse struck the surface at $t = 0$.

Further evidence for these two mechanisms involves the time-of-flights of the PIE at low fluence. Until one approaches the threshold fluence, the time interval between the laser pulse and the arrival of the ions at the detector were insensitive to laser fluence. Fig. 3 shows the mass 23 PIE signal vs time (through the QMS) for for different fluences between 0.4 J/cm^2 to 1.05 J/cm^2 , where most of the ion flight path was in near zero E field.

Little difference in flight times are seen; such behavior is inconsistent with a thermal emission mechanism, which would yield energy distributions dependent on surface temperature and would therefore depend on laser fluence. The Na^+ emission mechanism at low fluences thus appears to be photoelectronic in nature rather than thermal, and is further support for the non-thermal first term in eq. 3.

Once the surface has been irradiated at high fluences to induce etching and plume formation, a plume could be maintained at lower fluences (e.g., $\sim 0.7 F_{\text{threshold}}$). At fluences barely above the threshold for plume formation, the decrease in PIE noted above was still observed, but was eventually followed by a dramatic increase in PIE accompanied by plume formation and the onset of rapid etching. Immediately below the threshold, the onset of plume formation often required thousands of shots with little PIE. At higher fluences ($> 2.7 \text{ J/cm}^2$),¹ we observed a similar but much shorter pre-treatment for plume formation. In each case, this induction period is apparently required to produce the accumulation of damage in the form of near-surface defects. We have recently determined that in the range of fluences near threshold and higher, there is also copious negative ion emission which appears to be principally an oxygen containing ion (O^- or OH^-) and has many characteristics of the PIE in terms of fluence dependence.

Effect of Electron Irradiation on PIE. To investigate if electron beam induced states are capable of promoting strong interactions of 248 nm with the glass, we examined the effect of simultaneous and sequential electron and laser irradiation. In Fig. 4 we show the effect of simultaneous electron and laser irradiation on PIE at a laser fluence well below the etching

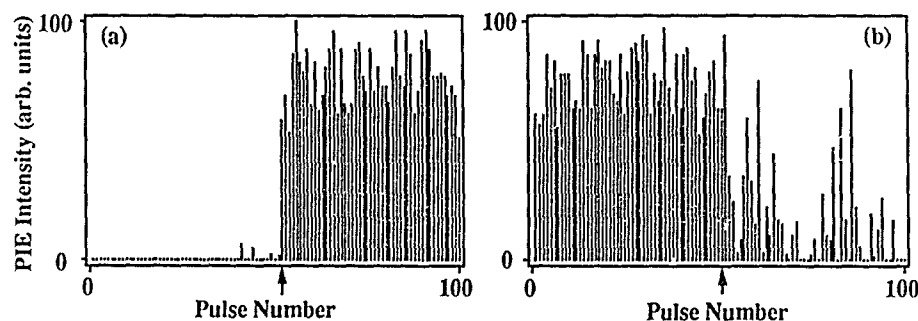


Fig. 4. Peak PIE due to successive laser pulses with and without simultaneous electron irradiation at 1.5 keV. In (a) the electron current density at the interaction region is initially zero and is raised to $\sim 3 \text{ A/cm}^2$ at the arrow. In (b), the electron current density is initially $\sim 3 \text{ A/cm}^2$ and is reduced to zero at the arrow.

threshold. In Fig. 4(a), the electron beam is initially off and is turned on midway through the sequence of pulses. The effect of the electron beam is an immediate increase in PIE emission. A visible plume, signaling the onset of rapid etching, accompanied the rise in PIE. In Fig. 4(b), the electron beam is initially on and is turned off midway through the sequence. The intense PIE during electron irradiation decays over several laser pulses. This decay indicates that the electron irradiation not only shortens the induction time for the onset of etching, but also lowers the etching threshold. Electron irradiation apparently results in the efficient production of states which enhance PIE and plume formation, presumably by increasing the absorption at 248 nm and increasing n_c . As discussed elsewhere,³ electron irradiation combined with laser irradiation may prove useful for a variety of surface modification and deposition processes.

Reflection Electron Energy Loss Spectroscopy (REELS). REELS measurements were made to identify possible surface states which might participate in the emission processes. The consequences of electron bombardment of the surface could also be analyzed. Three REELS spectra are shown in Fig. 5 for 0, 5, and 10 minutes of exposure time. The REELS data taken at 0 min. after in situ fracture show no states in the -2 to -6 eV energy range. (The energy zero is defined by the elastic peak.) Following five minutes of electron beam exposure, peaks appear in the range of -2 to -6 eV. These peaks were very well defined after ten minutes of electron beam exposure. These results suggest that absorption sites for 5 eV photons are produced by damaging the surface. The build-up (as beam exposure time increases) of electron energy loss peaks in the range from -2 to -6 eV suggests that defects are created by electron or ion beams. These shallow electronic levels which may be responsible for light absorption and electron emission at low laser fluences are associated with surface and/or defect states. REELS studies on amorphous SiO_2 films show loss peaks at 3.5, 5.1, and 7.2 eV which are attributed to a metastable surface phase of nearly monoxide stoichiometry.¹⁴ These energy losses are close to surface levels seen on pure Si (where the electron affinity of silicon is 4.2 eV and the band gap is 1.1 eV), suggesting that the levels responsible are indeed within 5 eV of the vacuum level and capable of participating in photostimulated electron emission.

The creation of E' centers by excimer laser irradiation at 5 eV has been observed by Stahis and Kastner¹⁵ in high purity amorphous silicon dioxide (Suprasil and Suprasil W) with electron paramagnetic resonance (EPR) techniques. Absorption of light in photoinduced E' centers would be consistent with the observed delay in the onset of laser etching seen on polished surfaces.

These filled states are possible sources for the free electrons created in the near surface region which couple with the laser light as discussed above. Collisions of the electrons within the first few tenths of microns of the glass surface would eventually elevate the temperature to the softening or melting point of the glass at high fluences, resulting in the hydrodynamic type sputtering observed.¹

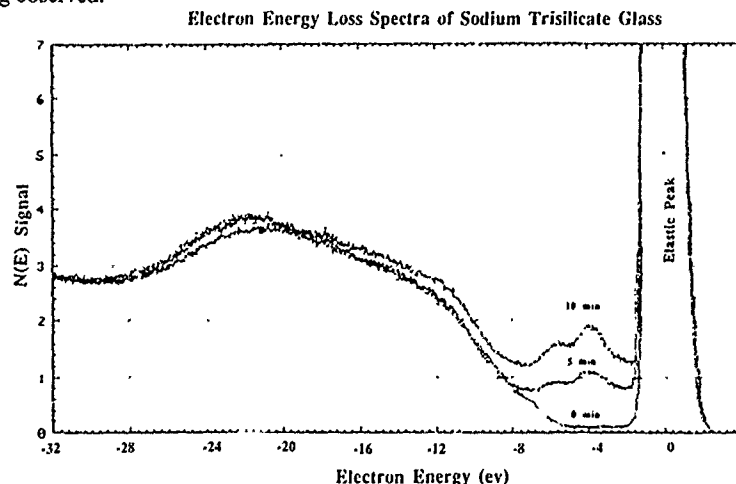


Fig. 5. Electron Energy Loss Spectra of sodium trisilicate glass.

Surface Roughness. At higher fluences, increased absorption of energy in the near surface region could also be due to an enhancement caused by surface roughness. While polished glass requires twenty or more pulses to induce etching at 2.7 J/cm^2 , unpolished glass etches immediately upon irradiation with the laser. Wood¹⁶ has noted that electric field concentrations at scratches increase as the index of refraction squared; thus, the corresponding energy density at a crack is enhanced by the fourth power of the refraction index. The real part of the refraction index for sodium trisilicate is very near three halves which yields an energy density enhancement of five at a crack. In previous work,¹ we noted that after ten pulses at high fluence, polished sodium trisilicate glass displays fracture craters. These craters on the polished glass could enhance the energy

density causing more damage to the surface until the surface was rough. Thus, surface roughening may also play a significant role in the onset and extent of etching of silica based glasses.

CONCLUSION

We have presented measurements of the pre-threshold charged particle emission from 248 nm laser bombardment of sodium trisilicate glass and indicate that electron emission and simultaneous laser-free electron heating are the dominating mechanisms for subsequent release of large quantities of material including charged species, neutrals, and eventually ejecta. We showed that creating defects with another radiations source, namely an electron beam,³ can greatly reduce the laser intensity required to begin etching the glass surfaces. Extension of these concepts to other inorganic targets is now in progress.

ACKNOWLEDGMENTS

The authors wish to thank Brad Pate, Washington State University, for helpful discussions. The WSU portion of this work was supported by the Office of Naval Research under Contract N00014-87-K-0514, the National Science Foundation under Grant DMR 8601281, and the Washington Technology Center. The PNL activities were supported by the U. S. Department of Energy (BES-DMS) and through internal Exploratory Research of the Molecular Science Research Center under Contract DE-AC06-76RL0-1830.

REFERENCES

1. P. A. Eschbach, J. T. Dickinson, S. C. Langford, and L. R. Pederson, *J. Vac. Sci. Technol.* **A7**(5), 2943 (1989).
2. P. A. Eschbach, J. T. Dickinson, and L. R. Pederson, *MRS Symp. Proc.* **129**, 385-392 (1989).
3. J. T. Dickinson, S. C. Langford, L. C. Jensen, P. A. Eschbach, L. R. Pederson, and D. R. Baer, submitted to *J. Appl. Phys.*
4. G. Tetite, P. Agnostini, G. Boiziau, J. P. Vigouroux, C. Le Gressus, and J. P. Duraud, *Optics Comm.* **53**, 189 (1985).
5. A. Miotello and F. Toigo, *Nucl. Instru. Methods Phys. Res.* **B32**, 258 (1988).
6. T. L. Gilton and J. P. Cowin, "Laser Induced Electron Emission: Space Charge and Electron Acceleration," conference presentation, ACS National Meeting 1988, L.A.
7. R. W. Dreyfus, "Are Laser-Ablated Monolayers Accurately Characterized by Their Ion Emission?," in *Microbeam Analysis 1989*, P. E. Russell, Ed., San Francisco Press, Inc., San Francisco, pp. 261-263 (1989).
8. F. Ohuchi and P. H. Holloway, *J. Vac. Sci. Technol.* **20**, 863 (1982).
9. T. E. Tsai, D. L. Griscom, and E. J. Friebele, *Phys. Rev. Lett.* **61**, 444 (1988).
10. R. A. B. Devine, *Phys. Rev. Lett.* **62**, 340 (1989).
11. X. A. Shen, S. C. Jones, and P. Braunlich, *Phys. Rev. Lett.* **62**, 2711 (1989).
12. A. S. Epifanov, *Sov. Phys. JETP* **40**, 897 (1975).
13. S. C. Jones, P. Braunlich, R. T. Casper, X. A. Shen, and P. Kelly, *Optical Engineering* (1989).
14. J. E. Rowe, *Appl. Phys. Lett.* **25**, 576 (1974).
15. J. H. Stahis, M.A. Kestner, *Phys. Rev. B*, **29**(12), 7079 (1984).
16. R. M. Wood, in *Laser Damage in Optical Materials*, Adam Hilger, ed. pp. 5-7, (1986)

ULTRAFAST IMAGING OF ULTRAVIOLET LASER ABLATION AND ETCHING OF POLYMETHYL METHACRYLATE.

Bodil Braren, R. Srinivasan, Kelly G. Casey, and Mildred Yeh,
IBM, T. J. Watson Research Center
Yorktown Heights, NY 10598

ABSTRACT

Ablation and etching of the surface of polymethyl methacrylate (=PMMA) by pulses of 248 nm laser radiation ~ 20 ns full width at half maximum (FWHM) have been probed by pulses of visible laser radiation (596 nm; < 1 ns FWHM). The results were recorded photographically in real time with a set time delay between the 248 nm ablation pulse and the 596 nm probe pulse.

Modification of the surface structure of the polymer at a fluence ~ 3 J/cm² is first visible at 12 ns and appears to be complete in ~ 60 ns. The first manifestation of the ablation does not occur until the UV pulse is over and consists of a nearly transparent shock-wave that has an initial velocity of 6×10^4 cm/sec. Solid material from the ablated zone begins to leave the surface at $\sim 150 - 200$ ns and reaches a maximum in intensity at $6 \mu\text{s}$, continuing for $\sim 20 \mu\text{s}$. The average velocity of the solid material, which is probably a low molecular weight polymer of PMMA, is 1.5×10^4 cm/sec.

The conclusion to be drawn from the present work is that the signal measured by photoacoustic detectors does not coincide with the bulk of the material leaving the surface.

INTRODUCTION

Two studies^{1,2} over the past year have shown that short (~ 1 ns) pulses in the visible spectrum can be used to probe the course of the ultraviolet laser ablation of tissue¹ or a polymer (polyimide).² In these pioneering investigations, the samples were viewed from only one optical perspective and the span of time was limited to either the width of the UV pulse² or to times that were long (microseconds) in relation to it.¹ We show that probing the surface of a sample of polymethyl methacrylate (=PMMA) during ablation along more than one perspective and over a

time span that extended from the start of the UV pulse to many tens of microseconds following its conclusion provides a more complete picture of the stages in the decomposition, ablation, and etching of the surface of this polymer by a UV laser pulse. Improved imaging techniques have been used recently by Kim *et al.*³ to study the interaction of a 77 ps pulse of 532 nm laser radiation with PMMA while probing with part of the same pulse at various delay times. Although the mechanism of the interaction between the photons and the polymer in this instance is viewed³ as being different from the interaction of a UV laser pulse of longer duration with the same polymer, common features of that study and this one are also mentioned here.

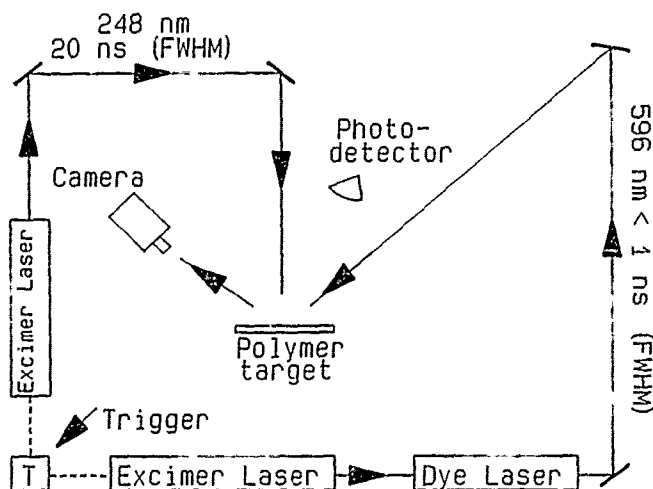


Figure 1. Schematic Diagram of Experiment. When the probe beam was moved to illuminate the polymer surface at a glancing angle, the camera was also moved so that it was parallel to the surface on the opposite side.

The apparatus that was used is shown schematically in Fig. 1. Of the two excimer lasers, one (Lambda-Physik EMG 201) produced 248 nm pulses of ~ 20 ns FWHM which were used to ablate the polymer. The second excimer laser (Lambda-Physik 201MSC), which was electrically coupled to the first by an electronic trigger (Philips Pulse Generator PM 5716), pumped a dye laser (Lambda-Physik FL 4000 T) which produced pulses of < 1 ns FWHM at 596 nm. The delay between the ablation and probe pulses was measured for each pulse by a photodiode which was monitored by a Tektronix 2467 Oscilloscope. The viewing of the polymer surface was by a standard photographic camera (Hasselblad 500C) which was fitted with a Rodenstock-Heligon lens ($f.l. = 25$ mm) to provide a recorded magnification of 15-20 X. A band-pass filter which transmitted from 560 to 640 nm limited the wavelength range of the photographic image. The sample of PMMA used was 0.73 mm thick and was polished on both sides. When the probe beam was in-

clined to the polymer surface at an angle of 30° - 45° , interference fringes were seen in the reflected beam which were useful in observing the changes not only in the area undergoing ablation, but also in the atmosphere above and around it. All experiments were carried out in air using only single pulses and a fresh surface of the polymer for each exposure. Problems due to the conditioning or "incubation" of the surface were avoided by the use of a relatively high fluence of the laser to cause ablation.

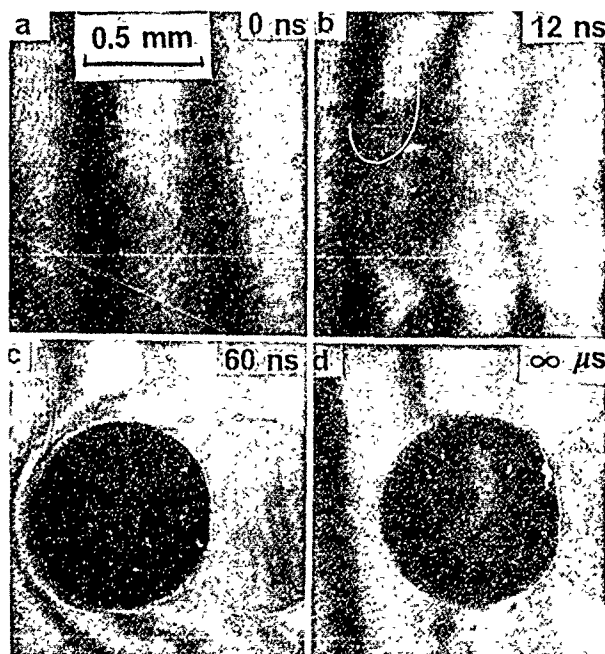


Figure 2. Pictures of PMMA surface during one UV (248 nm; 20 ns FWHM) ablation pulse. Probe beam and camera were positioned as in Fig. 1.

Figure 2 shows a series of photographs of the surface of PMMA which were taken at various time intervals following the start of the UV pulse of 56.4 MW/cm^2 (2.82 J/cm^2). The irradiated area is seen to "blacken" which can be attributed to the scattering and/or absorption of the visible light away from the camera. In turn, this shows that in as little as 12 ns after the start of the UV pulse, physical and/or chemical changes start to occur in the polymer. The blackening also leads to reduced transmission of the visible light through the sample as shown by the shadow of the UV exposed area on the back, inner surface of the PMMA. The exposed area reaches a maximum darkness at about 60 ns which is at the end of the UV pulse of $\sim 20 \text{ ns}$ FWHM, which could be explained by the change in UV transmission reported by two groups.^{4,5} When the probe beam il-

illuminated the polymer at a glancing angle (Fig. 3) and the camera viewed the ablation process in profile with the probe beam behind the plume, the first manifestation of the ablation is at 60 ns and consists of a nearly transparent shock-wave that has an initial velocity of 6×10^4 cm/sec. In successive frames, the shock-wave is seen to expand hemispherically, but its velocity does not follow the $t^{0.4}$ relationship that was seen by Kim *et al.*³ using visible, 54 Gw/cm² pulses. The best fit of the present data corresponded to an exponent of 0.76 ± 0.06 . The shock-wave can be seen as a ring, as in their work, when the camera is at an angle of 30° to the surface. The expanding gases behind it may explain the temporary disruption of the interference fringes around the ablated area in Figs. 2b and 2c. The fringes are completely restored at the end of the ablation process (Fig. 2d).

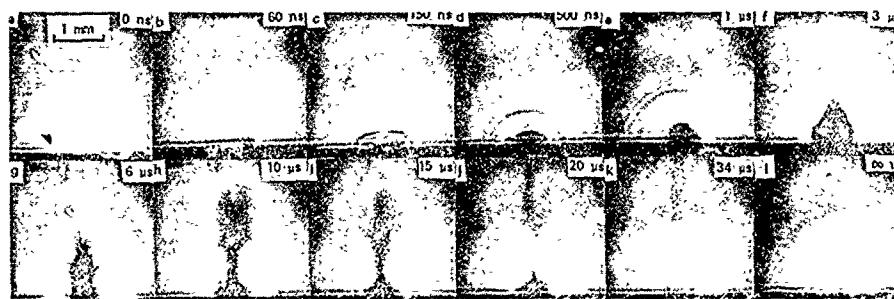


Figure 3. Ablation of PMMA by one UV (248 nm) pulse seen in profile. The horizontal line at the bottom of each frame is the edge of the polymer film. The ablating pulse was directed normal to the surface, i.e. vertically downwards. The probe beam was almost parallel to the surface and illuminated the plume from behind. The camera was nearly in line with the probe beam.

Solid material i.e., debris, from the ablated zone does not begin to leave the surface until the UV pulse is over (Fig. 3(e)-(l)), as also observed by Puliafito *et al.*¹ in the case of tissue ablation with 248 nm (nanosecond) pulses. When the focus was optimized, the motion of the debris above the polymer surface could be resolved to $12 \mu\text{m}$. The ejection of solid material continued well into tens of microseconds, the bulk of the material being ejected at an average velocity of 1.5×10^4 cm/sec. This velocity is in line with values which were estimated from time-of-flight measurements on PMMA (in a vacuum; pyroelectric detector)⁶ and other polymers (in a vacuum; mass spectrometric detection).⁷ Careful examination of Fig. 3(e)-(g) shows that the ejected polymer is made up of fine particles. From earlier work⁸ it is known that the principal product of the ablation of PMMA (Mol. Wt. $\sim 10^6$) with 248 nm pulses is a polymer of low molecular weight ($\bar{M}_n = 2500$) while volatile products such as the monomer amount to less than a few per cent.

The most surprising conclusion to be drawn from the present work is that the bulk of the material leaving the surface does not need to coincide with the decomposition of the polymer as measured by photoacoustic measurements⁹ but can follow it slowly.

ACKNOWLEDGEMENTS

The authors are indebted to Carmen A. Puliafito, P. Simon, and Dana D. Dlott for providing preprints of their work.

REFERENCES

1. C. A. Puliafito, D. Stern, R. R. Krueger and E. R. Mandel, Arch. of Ophth., 105, 1255 (1987).
2. P. Simon, Appl. Phys., B 48, 253 (1989).
3. H. Kim, J. C. Postlewaite, T. Zyung, and D. D. Dlott, J. Appl. Phys., 64, 2955 (1988).
4. G. M. Davis and M. C. Gower, J. Appl. Phys., 61, 2090 (1987).
5. S. Kuper and M. Stuke, Appl. Phys., B 44, 199 (1987).
6. P. E. Dyer and R. Srinivasan, J. Appl. Phys., 66, 2608 (1989).
7. S. G. Hansen, J. Appl. Phys., 66, 1411 (1989).
8. R. Srinivasan, B. Braren, R. W. Dreyfus, L. Hadel, and D. E. Seeger, J. Opt. Soc., A3, 785 (1986).
9. P. E. Dyer and R. Srinivasan, J. Appl. Phys., 48, 445 (1986).

Low Temperature Laser Physical Vapor Deposition of Multilayered Thin Films

N. Biunno, J. Krishnaswamy, S. Sharan, L. Ganapathi, and J. Narayan
Department of Materials Science and Engineer, North Carolina State University, P.O. Box
7916, Raleigh, NC 27695

Abstract

We have investigated the formation of various multilayer thin films by the laser physical vapor deposition technique. A multi stage target holder was constructed to perform all process steps in-situ; target/substrate cleaning, deposition, and annealing. The laser physical vapor deposition technique offers many advantages over conventional physical vapor techniques, such as, lower substrate temperature, microstructural control, and very low contamination levels. Film thickness can be controlled from near atomic to micron dimensions. A layer-by-layer (two dimensional) growth can be achieved, resulting in nonequilibrium structures. The films were analyzed using cross-section and high resolution transmission electron microscopy (TEM). The significant reduction in substrate temperature for the formation of high quality multilayer and epitaxial films opens up many new areas of applications requiring reduced thermal-budget processing.

1. Introduction

Thin film technology now has a dominant role in many industries, and particularly in the microelectronics industry. This is reflected in the enormous volume of literature on the subjects of new techniques for thin film processing and characterization. Thin films range widely in applications, hard coatings for machine tooling, reflecting and antireflecting coatings for optical mirrors and lenses, active and passive layers in semiconductor devices, etc. More recently ultrathin films of uniform and precisely controlled thickness in the range of 1 - 10 nm have come to be important both scientifically in the branch of solid-state physics as well as in the technology of very large scale integrated (VLSI) circuit design.

Laser physical vapor deposition (LPVD) is a rapidly emerging technique for the deposition of thin films. LPVD offers many advantages over conventional physical vapor deposition techniques. The LPVD technique can produce energetic (10 to 100 eV) ionized and excited vapor species which can enhance the surface mobility and crystallization process and thus lower the growth temperature.¹ Undesirable impurities are minimized since the substrate is at a low temperature (<400°C) and the heating of the sputter target occurs in a spatially selective region inside the vacuum chamber. The process is fully compatible with high-vacuum since the laser beam is generated outside the vacuum system. LPVD also provides instantaneous control of the ablation process and the film thickness from near atomic to micron dimensions by choosing appropriate laser parameters. The forward directed nature of the LPVD process can provide better step coverage in applications such as metal contact formation in holes smaller than $1\mu\text{m}^2$ for VLSI circuit design. Laser physical vapor deposition of films with properties comparable to those made by conventional techniques have been previously reported.²

In this work we present results of sequential deposition of multilayered thin films of carbon and tungsten, titanium nitride and carbide, and high T_c superconductor compounds. We also combine the process of laser atomic cleaning of silicon substrates and the initial stages of epitaxial growth of germanium.

2. Experimental

For the multilayer deposition of carbon and tungsten a beam deflection technique was used as shown in figure 1. The (100) silicon substrates were mounted on a molybdenum face plate resistance heater. To deposit W/C composite films a graphite block and a thick sheet of tungsten foil (99.9%) were mounted together side by side on the target holder. A pulse XeCl excimer laser (wavelength 308 nm, pulse duration 40×10^{-9} s, repetition rate 1Hz) was used to ablate the targets. A laser mirror mounted on a 2 axis angular translation stage was used to translate the beam rapidly between the two targets. The 2 cm diameter laser beam (0.3 joule per pulse) was focused onto the targets with an energy density of 4 to 5 Jcm⁻² at a 45° angle of incidence.

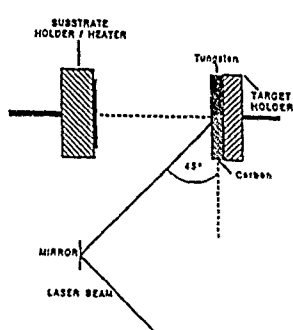


Figure 1. Diagram of the target/substrate holder for the beam deflection technique.

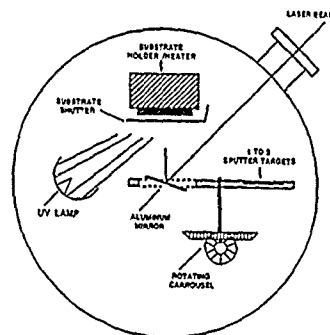


Figure 2. Diagram of the target/substrate holder for the sequential processing technique.

The TiN/TiC, Y₁₂₃/La₁₂₃, and Ge films, were deposited using a multi-target sequential processing technique as shown in figure 2. A rotating target holder was designed to hold four 3 cm diameter targets or three targets and a mirror to direct the laser to the substrate. The (100) silicon substrates for titanium nitride and carbide, and germanium, or (100) YSZr and (100) LaAlO₃ substrates for high T_c superconductor were also mounted on the molybdenum face plate resistance heater. A stainless steel shutter plate was used to shield the substrate during pulsed laser preconditioning of the targets and mirror.

The (100) silicon substrates (0.5 Ωcm, B doped) were precleaned in hydrofluoric acid for 30 seconds and dried using ultrapure dry nitrogen. The substrates were then mounted on the heater and prebaked at 400°C alone with the vacuum chamber bakeout at 200°C to a base pressure of 2×10^{-7} torr using a turbomolecular pump. A KrF excimer laser beam (wavelength 248 nm, pulse duration 20×10^{-9} s, repetition rate 5 - 10 Hz) was used to ablate the targets. With the shutter covering the substrate, the ablation surface area of the targets were scan first at a low energy density. The 3 cm² laser beam, at 0.3 joule, was focused to an energy density of 1 to 2 Jcm⁻² depending on the target. A multi-step scan (5 pulses per step) over the target surface was performed to remove any surface contaminants on the targets prior to deposition. The mirror surface was cleaned in a similar manner at an energy density of 0.75 Jcm⁻². The

laser beam was then directed onto the Si substrate at an energy density of 1 to 1.3 Jcm⁻² using the same multi-step scan over the area used for deposition (4 to 6 cm²). Previous experiments have shown that pulsed laser irradiation of silicon at this energy density and temperature causes the near surface region of the substrate to melt but not ablate.³ The melted layer then regrows from the underlying substrate by means of a liquid phase epitaxial regrowth. The contaminants oxygen and carbon are either desorbed from the surface during irradiation or undergo redistribution by means of liquid-phase diffusion during the time the surface region is molten. For the epitaxial germanium films only half of the deposition area was precleaned so that a comparison could be made between the laser cleaned and original regions.

The substrates, (100)YSZ (yttrium stabilize zirconium and (100)La AlO₃ (lanthanum aluminide) used for high Tc superconductor multilayer films were precleaned in the solvents acetone and methanol. The two targets used to form multiple layers were YBa₂Cu₃O_{7-x} and LaBa₂Cu₃O_{7-x}. The vacuum chamber was initially pumped down to 1 x 10⁻⁶ torr and then backfilled, the pressure set to 200 mtorr, with oxygen flowing at 175 sccm. The substrate temperature was held at 650°C with negligible heating of the targets. The target to substrate distance was set at 4 cm. The energy density was in the range 2.3-2.7 Jcm⁻² and pulse rate was less than one per second. After the deposition, the oxygen pressure was raised to 760 torr and the substrates were slowly cooled to room temperature.

Germanium was deposited using an energy density ranging from 3.5 to 6 Jcm⁻² and 2500 pulses per deposition over a 4 cm² area of the substrate. The substrate temperature was held at 400°C during the cleaning process and deposition. The deposition rate was found to be 0.04 Å per pulse for 3.5 Jcm⁻² and 0.4 Å per pulse for 6 Jcm⁻². For energy densities greater than 4 Jcm⁻² the films contained particulates of 1 to 10µm in diameter with a number density ranging from 10⁵ to 10⁶ cm⁻².⁴ At energy density below 4 Jcm⁻² the particulate size was less than a micron the density of which was in the range of 10³ to 10⁴ cm⁻².

Detailed cross-section high resolution transmission electron microscopy (HRTEM) and X-ray diffraction were used to investigate film microstructure and epitaxial relationships. Chemical analysis was performed using Rutherford backscattering/channeling spectroscopy (RBS) and Auger electron spectroscopy (AES).

3. Discussion

3.1 Tungsten/Carbon on (100)Silicon

Thin films of tungsten and carbon are being investigated as a possible multilayer optical coating for X-Ray mirrors. The layer thickness and microstructure quality must be maintained. Laser PVD of these coating presents many advantages over existing coating techniques, such as lower deposition temperature for sensitive substrates, localized target heating, and very fine control over microstructure and thickness of the films. Also the energetic beam is expected to result in enhanced surface mobility and increased density of the films.

Figure 3(a) shows a cross-sectional micrograph of a multilayer tungsten/carbon film on a (100) silicon substrate. The RBS spectrum of figure 3(b) shows the tungsten peaks for the first three layers. The tungsten peaks from layers further in are not distinguishable due to the spread in energy of the backscattered ion signal deeper into the film.

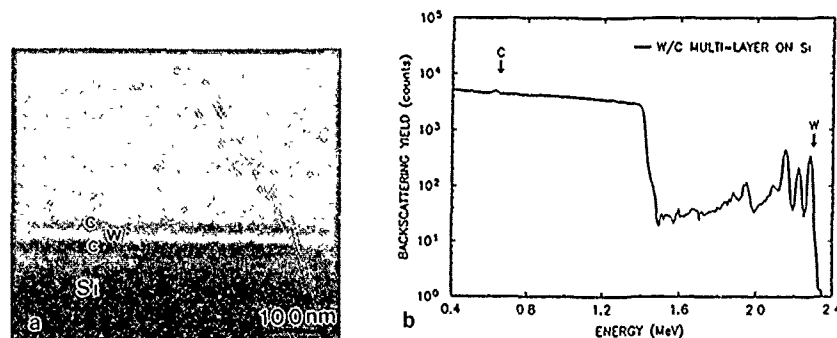


Figure 3(a) TEM cross-section of a multilayer carbon/tungsten deposition at 400°C and 4 Jcm^{-2} . (b) RBS spectrum of the multilayer film showing the tungsten peaks for the first three layers.

This multilayer film was deposited using a beam deflection technique because the laserbeam can be quickly translated from one target to the other (less than a second for a manual controlled system). Localized target heating is minimum and does not cause cross contamination. The deposition consisted of 7 tungsten layers and 6 carbon layers at 200 pulses per layer. The energy density for both targets was 4 Jcm^{-2} . The average layer thickness was 220 \AA for tungsten and 180 \AA for carbon. The total thickness of the deposited multilayer was 2600 \AA which gives a deposition flux of $\sim 1\text{ \AA}$ per pulse. It should be noted that the deposition flux depends on the laser beam intensity, its spatial and temporal profile, the overall shape of the laser beam, the energy density, the amount of beam focusing, and the distance between the target and substrate.⁵ All of these parameters are readily available or can be determined experimentally. By scanning the laser beam over the target and/or translating the substrate in the proper increments film uniformity and depth can be precisely controlled.

3.2 Titanium Nitride/Titanium Carbide on (100) Silicon

Titanium nitride and carbide coatings have found numerous applications in view of their excellent corrosion and erosion resistance, relative inertness, high hardness and desirable optical and electronic properties.⁶ Multilayer films of TiN and TiC are being investigated to take advantage of their mechanical properties. TiC is slightly harder than TiN, but TiN is more ductile than TiC.

Polycrystalline films grown by conventional chemical vapor deposition (CVD) and physical vapor deposition (PVD) methods are affected by growth parameters such as substrate temperature, gas pressure and flow ratio, target and substrate biasing. Polycrystalline TiN and TiC films grown by conventional methods tend to grow often with columnar grains, where faster diffusion along grain boundaries make them susceptible to environmental effects. We have recently developed a laser ablation method to deposit polycrystalline films at or near room temperature.⁷ Figure 4 shows a cross-section TEM view of a multilayer film formation of TiN/TiC/TiN on a (100)silicon substrate deposited at 400°C . The approximate layer thickness

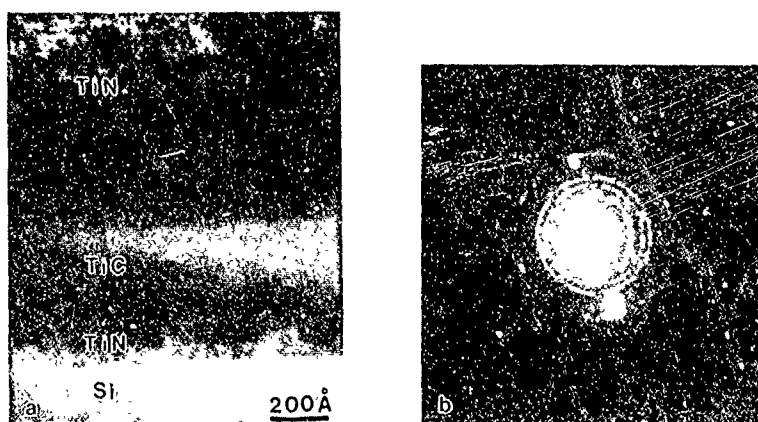


Figure 4 (a) TEM cross-section of a TiN(1000 Å)/TiC(1000 Å)/TiN(200 Å)/(100)Si multilayer film deposited at 400° C and 5 Jcm⁻². (b) Corresponding selected area diffraction pattern.

are TiN(1000 Å)/TiC(1000 Å)/TiN (200 Å) which gives an average deposition flux 0.5 Å for TiN and 0.3 Å for TiC. Using the new generation of high pulse rate excimer lasers, deposition rate of up to 1 to 10 μm per hour can be achieved in a 6 cm² area. The distinguishing feature of these films are lower substrate temperature, lower impurity content, and the equiaxed nature of the grain structure. The polycrystalline films are very dense with an average grain size of 100 Å which remained approximately constant with deposition temperatures from 25 to 600°C. We are currently investigating a process where titanium can be deposited on a laser cleaned silicon surface and then laser annealed⁸ to form an intermediate titanium silicide layer. This can be followed by a TiN deposition to form a diffusion barrier and a low resistive metal contact for VSLI technology.

3.3 Textured Multilayer La₁₂₃ and Y₁₂₃ Thin Films

Targets of semiconducting and/or superconducting (La/Y)₁₂₃ compounds were prepared by standard ceramic routes reported in literature for the preparation of high T_c materials starting from the respective metal carbonates and/or oxides. As semiconducting properties in the La₁₂₃ compounds are observed around oxygen contents of 7, we have investigated the semiconductor / superconductor superlattice of La₁₂₃ / Y₁₂₃. A semiconducting La₁₂₃ film of about 1000 Å thickness was first deposited on (100) LaAlO₃ which was followed by another 1000 Å thick superconducting Y₁₂₃ film. The time for the change of the bulk target through the rotation of the carousel was less than 3 seconds. High resolution X-ray diffraction pattern of this film is shown in figure 5(a). We clearly observed two different sets (001) reflections corresponding to the La₁₂₃ as well as Y₁₂₃ layers. These results clearly demonstrate the textured growth of superlattice La₁₂₃/Y₁₂₃ films.

Long period structures and intergrowth structures of the layered high-T_c materials have been suggested to improve the T_c of these new materials.⁹ We have investigated the superlattices of superconducting La₁₂₃ and Y₁₂₃ with varying modulations. We have made superlattices with a calculated modulation of 120 Å and 300 Å by alternately depositing the thin

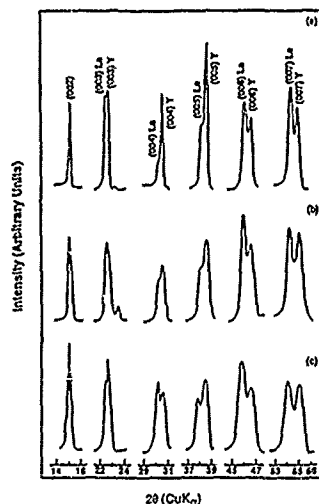


Figure 5 X-Ray diffraction spectrum of the (00L) planes of the multilayer Y_{123}/La_{123} film showing textured growth in the (00L) direction. (a) $Y_{123}(1000 \text{ Å})/La_{123}(1000 \text{ Å})/(100)LaAlO_3$. (b) $Y_{123}(120 \text{ Å})/La_{123}(120 \text{ Å})/\dots 8 \text{ layer}\dots/(100)YSZr$. (c) $Y_{123}(300 \text{ Å})/La_{123}(300 \text{ Å})/\dots 6 \text{ layers}\dots/(100)YSZr$.

films of orthorhombic La_{123} and Y_{123} . The textured growth of the superlattices is not hindered by the 3 sec delay in rotating targets. We clearly see the separate identity of the La_{123} and Y_{123} unit cells in the X-ray diffraction patterns (see Fig.5(b) and (c)) for all the superlattice structures in the form of separate set of (100) reflections. However, we observe gradual broadening of the X-ray peaks as the modulation length is decreased, probably due to the decreased dimensions of the film along the c-axis. Thus, it is clear that controlled growth of superlattice structures of La_{123}/Y_{123} is possible. These superlattice films exhibited a $T_c(\text{zero}) = 85 \text{ K}$ and further investigations are under process to study the decreasing modulation lengths.

3.4 Initial stages of Ge nucleation

The studies on the initial stages of epitaxial growth in various heteroepitaxial systems, are expected to shed light on fundamental aspects of crystal growth¹⁰ particularly two-dimensional versus three dimensional growth. For low misfit systems ($f < 1.5\%$), the growth of the epilayer can occur layer by layer (two-dimensional) growth. However, the growth in large misfit systems normally proceeds by island (three-dimensional growth). The initial stages of the growth of Ge films deposited on laser pre-irradiated and non-irradiated Si substrates (mismatch = 4%) by laser physical vapor deposition has been studied using high-resolution TEM.

The samples were studied using a JEOL 200CX electron microscope. The microscope has a spherical aberration coefficient $C_s = 1.4 \text{ mm}$ and a point to point resolution of 2.6 Å . The electron beam was parallel to the $[110]$ direction. Figure 6 shows a high resolution electron micrograph of the Ge islands formed on a laser pre-irradiated section of the (100)Si substrate. The island size varies from 80 Å to 120 Å . The Ge island growth epitaxial to the Si substrate can be clearly seen in figure 7 which is a higher magnification micrograph of one of the islands

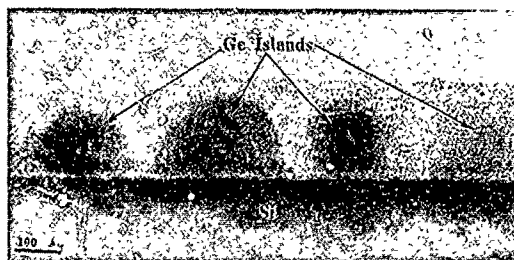


Figure 6 High-resolution electron micrograph of Ge islands grown on the laser pre-irradiated part of an Si substrate. The imaging direction is $[110]$.

in figure 6. The interface between the Ge islands and Si substrate is quite smooth. The native oxide present on the Si surface has been almost completely removed on the pre-irradiated section of the Si substrate using the KrF laser. Most of the islands have two dimensional defects like stacking faults, twins and microtwins.

Figure 8 shows a high resolution electron micrograph containing Ge islands on an area of the Si substrate with was not pre-cleaned. It is clear from the micrograph that the native oxide layer at the Si surface has not been removed. The Ge islands grow on the oxide layer and occasionally we find some Ge islands are epitaxial with the Si substrate. This could occur if there are some local interruptions in the oxide layer leading to an epitaxial growth or the energetic Ge vapor pulse beam could be initiating the nucleation through the oxide layer. It is clear from a comparison of the micrographs of Ge islands grown on pre-irradiated and



Figure 7 High-resolution TEM micrograph of one of the Ge islands shown in figure 6.

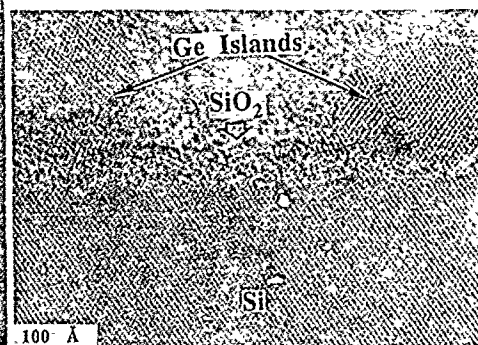


Figure 8 High-resolution TEM micrograph of Ge and native oxide layer on an area not pre-irradiated.

unirradiated Si portions of the substrate, that there is removal of the native oxide layer due to laser pre-irradiation. The cleanliness produced by laser irradiation of the Si substrate which depends on the oxygen partial pressure in the chamber leads to a better epitaxial growth of Ge.

LASER PATTERNING AND ELECTRICAL PROPERTIES OF SUBMICRON LINES OF Y-Ba-Cu-O

J. P. ZHENG, Q. Y. YING, H. S. KIM, D. BHATTACHARYA, D. T. SHAW AND
H.S. KWOK

State University of New York at Buffalo, Institute on Superconductivity, Bonner Hall,
Amherst, NY 14260

ABSTRACT

0.6 μm -wide lines of high T_c Y-Ba-Cu-O have been fabricated by direct laser writing on mirror-like thin films which were grown by laser deposition without post annealing. Laser ablation etching had no effect on the T_c and J_c until the lines were $< 1 \mu\text{m}$ wide. The 0.6 μm -wide strip showed some degradation of T_c and J_c . The critical current densities for these patterned lines were measured to be $\sim 5 \times 10^6 \text{ A/cm}^2$ at 50 K.

INTRODUCTION

Since the discovery of high T_c superconductors, there has been a tremendous effort to grow quality thin films of these materials by various techniques [1-4]. Currently, thin films of such materials can be made with very large critical current densities. Because of the interest in developing these films into devices, patterning of these films is important. High-resolution patterning of these films is pursued for two reasons. First, it is used to fabricate high T_c devices such as superconducting quantum interference devices (SQUID) [5], transmission lines [6], microwave [7] and optical [8] detectors and so on. Second, such studies can lead to some insight into the physical phenomena of these superconducting materials on the micro scale.

Superconducting films have been patterned by various methods. These include ion beam lithography [9,10], electron beam lithography [11], conventional chemical etching [12] and laser etching [13-16]. Unfortunately, in most cases, involving wet lithography, high temperature post-annealing of the films are often necessary. The surface morphology of the resulting patterned films is rough and usually shows percolation of microcrystals on the surface due to this high temperature.

On the other hand, thin films have been deposited which are superconducting without post-annealing [1,2]. There is clearly a need for patterning these smooth as deposited films by dry techniques such as plasma etching and laser ablation [17,18] which do not require further annealing. We have investigated the use of laser dry etching for the patterning of as-deposited superconducting Y-Ba-Cu-O thin films on various substrates. Lines as narrow as 0.6 μm have been fabricated on the in situ laser-deposited thin films with high critical current densities.

EXPERIMENTAL

The thin films were deposited on $\text{ZrO}_2(100)$ and $\text{MgO}(100)$ substrates. The substrate surface was prepared by ultrasonic cleaning in trichloroethylene, acetone, methanol and de-ionized water. The deposition was carried out in a vacuum chamber with a base pressure of $\sim 10^{-6}$ Torr. An ArF excimer laser with 193 nm wavelength was focused on a rotating Y-Ba-Cu-O superconducting target. A flowing oxygen atmosphere of 5 mTorr was maintained in the chamber during the deposition. The laser was operated at 10 Hz with an intensity of $\sim 3 \text{ J/cm}^2$ and a spot size of $1 \times 3 \text{ mm}^2$. The substrate was heated to a temperature of about 620°C - 660°C and mounted at $\sim 10 \text{ cm}$ above the target. The deposition time was 15 min for a 0.27- μm -thick film. After deposition, the film was cooled to room temperature over a period of 1 h in a 100 Torr O_2 atmosphere.

The laser patterning system is shown in Fig. 1. A frequency doubled single-mode cw Q-switched Nd:YAG laser was used. The laser pulse had a duration of 80 ns and a variable repetition rate of 1-10,000 Hz. The laser beam was focused to a diameter of 1

μm by an optical microscope objective. A video monitor was used to display the pattern simultaneously. A 10X eyepiece and a 40X objective lens with a numerical aperture of 0.7 were used. Two computer-controlled stepper motors were employed to translate the film on the sample holder. The laser intensity was adjusted to slightly above the ablation threshold of 2 J/cm^2 . The laser was highly attenuated to produce such fluences. Typically, only $20 \mu\text{W}$ of the 532 nm output power was used.

At a laser repetition rate of 1000 Hz, the maximum scanning rate of the system was 0.5 mm/sec and was limited by the laser repetition rate. It was found that a N_2 gas jet over the sample played a very important role in producing good results. The N_2 stream carried away the particles which were evaporated by the laser beam to prevent re-deposition on both the surface of the film and micro-objective lens.

RESULTS

To characterize the patterning system, as well as the superconducting films, superconducting microstrips in the range of $87 \mu\text{m}$ width were produced with a length of $100 \mu\text{m}$. Fig. 2 shows the scanning electron microscope (SEM) picture of a patterned $\text{YBa}_2\text{Cu}_3\text{O}_{7-x}$ superconducting film. The edge was quite sharp to within $0.1 \mu\text{m}$.

The electrical properties were measured by the standard four-probe method. No further annealing was necessary after the patterning. Fig. 3 shows curves of the resistance as a function of temperature for MgO (100) substrate with different linewidths. The substrate temperature was about 660°C . The original film showed an onset of 90 K and a zero resistance at 87.7 K . After patterning, the $T_c(R=0)$ decreased by less than 2 K for the $87\text{-}3.5 \mu\text{m}$ lines. However, for the $0.8 \mu\text{m}$ line, T_c decreased to 81 K. The suppression of T_c for the submicrometer lines is very similar to the results obtained with ion beam lithography [10]. It is probably due to the finite grain size of the Y-Ba-Cu-O film, and not the result of chemical degradation [19].

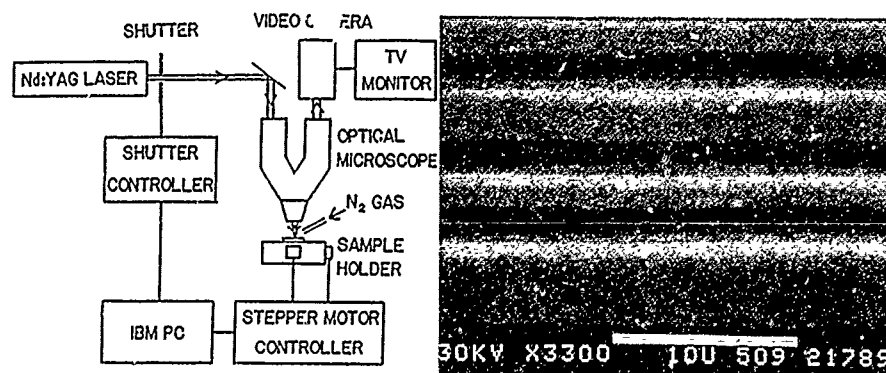


Fig. 1 Schematic diagram of the laser patterning systems.

Fig. 2 Photographs of the patterned Y-Ba-Cu-O films.

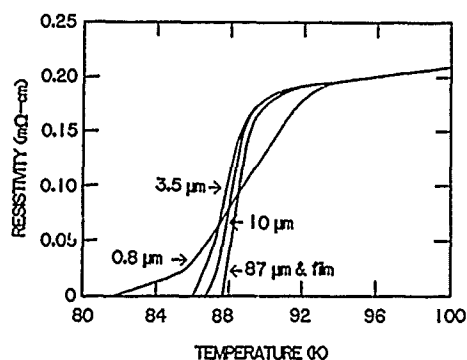


Fig. 3 Temperature dependence of the resistivity of a Y-Ba-Cu-O film on MgO(100). The 87 μm line and film results are indistinguishable.

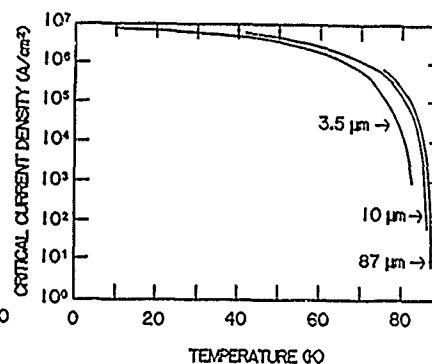


Fig. 4 Critical current densities dependence on the temperature for YBCO on MgO for various linewidths.

The critical current J_c was defined as the current at which the voltage between the voltage probes was less than $1 \mu\text{V}$, the resolution limit of the measurement system. Fig. 4 shows the critical current densities as a function of temperature for the 3.5–87 μm lines on MgO. The limiting J_c was $5 \times 10^6 \text{ A/cm}^2$ at 50 K. This value is quite good compared with other results. However the J_c decreased significantly for a 0.8 μm line.

When the substrate temperature was decreased to about 620°C , similar results for the superconducting transition were observed for various linewidths on $\text{ZrO}_2(100)$ as shown in Fig. 5. However the critical current densities of this sample were at least 10 times lower than the one with higher substrate temperatures. For the 0.6 μm line, the J_c

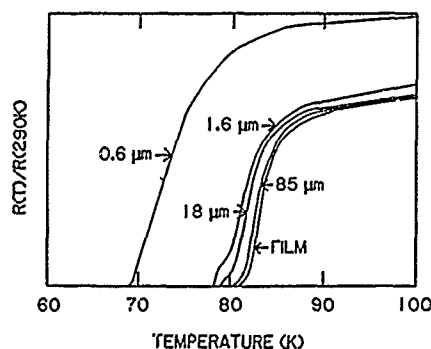


Fig. 5 Temperature dependence of resistance for superconducting lines on ZrO_2 .

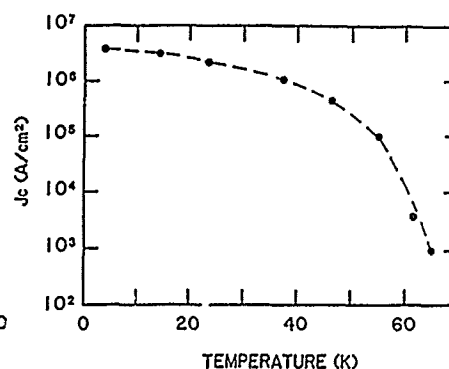


Fig. 6 Critical current densities dependence on the temperature for the finest 0.6 μm microstrip on ZrO_2 .

was lower compared with the one of wider lines since the T_c decreased to 69 K from 81 K of the original film. However the J_c remained the same for all pattern lines at low temperature (2 K). Fig. 6 shows the critical current densities as a function of temperature for the finest 0.6 μm line.

It was found that the grain size of the Y-Ba-Cu-O film increased with increased substrate temperature during deposition. The superconducting properties will start to degrade when the linewidth approaches the dimension of the grains. Thus the grain boundaries are believed to play an important role in the ultimate size of the device patterned. The observation is consistent with the results of the critical current density on the submicrometer lines.

Compared with the cw Ar ion laser [16], it can be seen that the cw Q-switched Nd:YAG laser produces much better results. A power level of 0.5 W was needed for "ablation" with the Ar ion laser. Under such high laser power, the entire microstrips would be heated to high temperatures. These high temperatures may lead to oxygen loss and degradation of the superconducting properties. In the present work, average laser powers of $\sim 20 \mu\text{W}$ were used. No significant heating and decomposition was observed. No post annealing was necessary. This was confirmed by an energy dispersive X-ray (EDAX) analysis of the microstrip.

To optimize the laser repetition rate, the thermal diffusion time for both Y-Ba-Cu-O thin film and substrate was measured by the pulse photothermal radiometry (PPTR) technique [20]. It was found that the thermal diffusion times are $\sim 2 \mu\text{s}$ and $\sim 200 \mu\text{s}$ for a 0.1 μm Y-Ba-Cu-O thin film and for bare MgO substrate at room temperature, respectively. To avoid the thermal accumulation, the time interval between two pulses should be longer than the thermal diffusion time. On other hand, the maximum scanning rate of the system was limited by the laser repetition rate. So the optimal laser repetition rate for this application is about 1 kHz.

CONCLUSIONS

Laser etching is a quick, simple process for patterning the as-deposited Y-Ba-Cu-O films. It does not require any masking or chemical processing. No post-annealing is necessary whatsoever. Lines as narrow as 0.6 μm were fabricated by a cw Q-switched Nd:YAG laser. The surface of the patterned film remained as smooth as the original film. The patterned lines on our best quality film showed a J_c of $5.5 \times 10^9 \text{ A/cm}^2$ at 50 K and 10^7 A/cm^2 at 10K. These patterned lines have been successfully applied to the study of optical nonthermal response in the high T_c films [8].

This research was supported partially by the New York State Institute on Superconductivity. HSK is a NSF Presidential Young Investigator.

REFERENCES

1. X.D. Wu, D. Dijkkamp, S.B. Ogale, A. Inam, E.W. Chase, P.F. Miceli, C.C. Chang, J.M. Tarascon, and T. Venkatesan, *Appl. Phys. Lett.*, **51**, 861 (1987).
2. S. Witanachchi, H.S. Kwok, X.W. Wang, and D.T. Shaw, *Appl. Phys. Lett.*, **53**, 234 (1988).
3. P. Chaudhari, R.H. Koch, R.B. Laibowitz, T.R. McGuire, and R.J. Gambino, *Phys. Rev. Lett.*, **58**, 2684 (1987).
4. M. Hong, S.H. Liou, J. Kwo, and B.A. Davidson, *Appl. Phys. Lett.*, **51**, 694 (1988).
5. R.H. Koch, C.P. Umbach, G.J. Clark, P. Chaudhari, and R.B. Laibowitz, *Appl. Phys. Lett.*, **51**, 200 (1987).

6. D.R. Dykaar, J.M. Chwalek, J.F. Whitaker, R. Sobolewski, T.Y. Hsiang, and A. Mourou, in *Superconductivity and Its Applications*, p231, ed. H.S. Kwok and D.T. Shaw, (Elsevier, New York) 1988.
7. J. Konopka, R. Sobolewski, A. Konopka, and S.J. Lewandowski, *Appl. Phys. Lett.*, **53**, 796 (1988).
8. H.S. Kwok, J.P. Zheng, Q.Y. Ying, and R. Rao, *Appl. Phys. Lett.*, **54**, 2473 (1989).
9. S. Natsui, N. Takado, H. Tsuge, and K. Asakawa, *Appl. Phys. Lett.*, **52**, 69 (1988).
10. T. Tsuge, S. Matsui, N. Matsukura, Y. Kojima, and Y. Wada, *Jpn. J. Appl. Phys.*, **27**, L2237 (1988).
11. J.V. Maantese, A.B. Catalan, A.H. Hamdi, A.L. Micheli, and K.K. Studer-Rabeller, *Appl. Phys. Lett.*, **53**, 526 (1988).
12. I. Shih and C.X. Qiu, *Appl. Phys. Lett.*, **52**, 1523 (1988).
13. A. Inam, X.D. Wu, T. Venkatesan, S.B. Ogale, C.C. Chang, and D. Dijkamp, *Appl. Phys. Lett.*, **51**, 1112 (1987).
14. A. Gupta and G. Koren, *Appl. Phys. Lett.*, **52**, 665 (1988).
15. J. Mannhart, M. Scheuermann, C.C. Tsuei, M.M. Oprysko, C.C. Chi, C.P. Umbach, R.H. Koch, and C. Millor, *Appl. Phys. Lett.*, **52**, 1271 (1988).
16. R.G. Humphreys, J.S. Satchell, N.G. Chew, and J.A. Edwards, *Appl. Phys. Lett.*, **54**, 75 (1988).
17. B.M. McWilliams, J.S. Satchell, F. Mitlitsky, R.A. Hyde, and L.L. Wood, *Appl. Phys. Lett.*, **43**, 946 (1983).
18. D.V. Podlesnik, H.H. Gilgen, and R.M. Osgood, Jr., *Appl. Phys. Lett.*, **48**, 496 (1986).
19. M.F. Yan, R.L. Barns, H.M. O'Bryan, Jr., P.K. Gallagher, R.C. Sherwood, and S. Jin, *Appl. Phys. Lett.*, **51**, 532, (1987).
20. A.C. Tam, *Infrared Phys.*, **25**, 305 (1985).

Author Index

- Akita, K., 211
 Allen, Susan D., 85
 Anderson, G.W., 371
 Anderson, W.T., 261
 Andreshak, Joseph C., 267
 Asai, T., 91
 Auvert, Geoffroy, 155
 Avouris, Ph., 201
 Bachmann, Friedrich G., 161, 439
 Baer, D.R., 463
 Baiocchi, F.A., 417
 Baseman, Robert J., 267, 319
 Batchelor, D., 147
 Bäuerle, D., 451
 Bedair, S.M., 377
 Bhattacharya, D., 485
 Bialy, S., 103
 Bittenson, S.N., 79
 Biunno, N., 477
 Bozso, F., 201
 Braren, Bodil, 471
 Brewer, P.D., 289
 Bronner, Gary B., 339
 Buggeln, R.C., 395
 Cacouris, T., 121
 Carey, Paul G., 241
 Casey, Kelly G., 471
 Chakrabarti, U.K., 417
 Chayahara, A., 301
 Chin, B.H., 217
 Choi, Jin-O, 39
 Chong, P.J., 91
 Christou, A., 261, 371
 Cole, H.S., 61
 Comita, Paul B., 21, 73
 Datta, Saswati, 103
 Davidson, J.L., 129
 Davis, J.L., 261
 Dickinson, J.T., 463
 Dowben, P.A., 103
 Economou, N.P., 79
 Edwards, Jr., D., 79
 Ehrlich, D.J., 79
 Eridon, J.M., 261
 Eschbach, P.A., 463
 Esrom, Hilmar, 109, 189
 Ethimiopoulos, T., 261
 Fogarassy, Eric, 281
 Foulon, Francois, 281
 Freedman, Andrew, 381, 389
 Gamo, Kenji, 223
 Ganapathi, L., 477
 Goorsky, M.S., 351
 Gossett, C.R., 261
 Grider, D.T., 147
 Gupta, Arunava, 319
 Haarer, D., 307
 Haba, Belgacem, 319
 Hails, J.E., 357
 Hanabusa, Mitsugu, 135
 Hara, M., 255
 Harriott, L.R., 217
 Hatzopoulos, Z., 261
 Heitz, J., 451
 Herman, Irving P., 331
 Hess, P., 27
 Hewak, D.W., 97
 Hidaka, H., 211
 Hill, H., 357
 Hobson, W.S., 417, 425
 Höfflinger, B., 365
 Hu, Evelyn L., 407
 Hussey, Brian W., 319
 Hutton, Richard S., 3
 Ikeda, Masashi, 135
 Irvine, Stuart J.C., 357
 Izquierdo, R., 141
 Jensen, J.E., 289
 Jensen, L.C., 463
 Jeon, Young-Jin, 431
 Jerominek, H., 97
 John, P., 129, 181
 Jones, K.S., 425
 Jubber, M., 129
 Kaufel, Gudrun, 401
 Kawai, S., 91
 Kim, H.S., 485
 Kim, Yoon-Gi, 103
 Kirch, S.J., 229
 Kiriakidis, G., 261
 Klumpp, A., 273
 Kobayashi, A., 91
 Kodas, Toivo T., 73
 Kogelschatz, Ulrich, 189
 Kosugi, Toshihiko, 223
 Krishnaswamy, J., 477
 Kudumas, M., 261
 Kuech, T.F., 351
 Kwok, H.S., 485

- Langford, S.C., 463
 Lavoie, C., 141
 Lee, Jeong Y., 431
 Lin, Jian-Yang, 85
 Lishan, David G., 407
 Littlejohn, M.A., 147
 Liu, H., 377
 Liu, Y.S., 61
 Lu, Y.F., 301
 Ludorf, W., 451
 Matz, R., 307
 McCarthy, Anthony M., 241
 Meiler, J., 307
 Meunier, M., 141
 Meyyappan, M., 395
 Michelakis, C., 261
 Miller, R.W., 103
 Minamisono, T., 301
 Moore, J.A., 39
 Morgan, D.V., 261
 Müller, Heinrich G., 169
 Mullin, J.B., 357
 Murahara, M., 33, 295
 Nalamasu, Omkaram, 3
 Namba, Susumu, 223, 301
 Narayan, J., 477
 Neudeck, G.W., 365
 Ninomiya, K., 235
 Nishimatsu, S., 235
 Nowak, R., 27
 Odeh, I.M., 181
 Okoshi, M., 33
 Okuhira, H., 235
 Olander, Elfriede, 401
 Olson, G.L., 289
 Osgood, Jr., R.M., 121
 Öztürk, M.C., 147
 Papanicolaou, N.A., 371
 Pashmakoff, B.I., 313
 Pauleau, Yves, 155
 Pearton, S.J., 417, 425
 Pederson, L.R., 463
 Pitt, A.D., 257
 Potemski, R., 351
 Price, Jr., Peter E., 73
 Qayyum, A., 181
 Rager, Berthold, 161
 Ramdani, J., 377
 Roberts, J.C., 377
 Roberts, P.G., 129
 Rothschild, M., 79
 Russell, P., 147
 Russell, S.D., 325
 Sameshima, T., 255
 Sanda, H., 301
 Satou, M., 301
 Savova, Evdokia B., 313
 Scarmozzino, R., 121
 Schuler, Siegfried, 169
 Schwab, P., 451
 Sedlacek, J.H.C., 79
 Seeger, D.E., 229
 Sexton, D.A., 325
 Sharan, S., 477
 Shaver, D.C., 79
 Shaw, D.T., 485
 Shirakawa, K., 295
 Siffert, Paul, 281
 Sigmon, Thomas W., 241
 Sigmund, H., 273
 Slaoui, Abdelilah, 281
 Spencer, J.T., 103
 Springholz, G., 273
 Srinivasan, R., 471
 Steinfeld, J.I., 175
 Stinespring, Charter D., 381, 389
 Stognij, A.I., 413
 Strongin, Daniel R., 21
 Sugimoto, Y., 211
 Takahashi, Jun-Ichi, 53
 Takai, M., 301
 Taneya, M., 211
 Tang, Hua, 331
 Taylor, Gary N., 3
 Temkin, H., 217
 Thompson, P.E., 261
 Tokarev, V.V., 413
 Tonneau, Didier, 155
 Toyoda, K., 33
 Tyndall, George W., 47
 Urisu, Tsuneo, 53
 Usui, S., 255
 Utsumi, Yuichi, 53
 Wahl, Georg, 109
 Wang, X.Z., 451
 Wang, Y.L., 217
 Weiner, Kurt H., 241
 Wilson, J.I.B., 129, 181
 Wortman, J.J., 147
 Xu, Xin, 175
 Xu, Zheng, 223
 Yeh, Mildred, 471
 Ying, Q.Y., 485
 Yonekawa, M., 295
 Yun, Sun Jin, 431
 Zheng, J.P., 485
 Zhong, Y., 147
 Zinck, J.J., 289
 Zingg, René P., 365

Subject Index

- ablation of
 - carbon, 477
 - PMMA, 471
 - polyimide, acrylic resin, 439
 - sodium trisilicate glass, 463
 - superconductor, 477, 485
 - tungsten, 477
- activation energy, dimethyl aluminum hydride decomposition, 121
- adhesion, improvement of, 235
- adsorption, of carbon precursors on Si, 229
- alloy, a-Si:C:H, 181
- aluminum
 - deposition from
 - dimethyl aluminum hydride, 21, 135
 - trimethyl aluminum, 21
 - diethyl aluminum chloride, 351
 - dimethyl aluminum hydride, 21, 121, 135
 - gallium alloy, 351
- annealing, laser, 261
- atomic beam, Cl, 389
- cadmium
 - dimethyl, 381
 - cadmium, 357
 - etching, 289
 - telluride, 357, 381
 - etching, 289
- carbon, deposition, 229
- by laser sputtering, 477
- carbonyl
 - chromium hexacarbonyl, 27
 - cobalt, 79
- carrier generation, transient conductance measurements, 255
- chemical vapor deposition
 - ion beam, 223
 - laser, 27, 73, 79, 85, 91, 155, 161, 175, 235, 377, 381
 - selective rapid thermal, 147
 - tungsten on Ti-ion irradiated SiO₂, 235
- chromium
 - deposition from Cr(CO)₆, 27
 - etching, 47
 - film composition, 27
- cobalt
 - deposition from Co₂(CO)₈, 79
 - etching, 47
- contact
 - ohmic, 261
 - Schottky, 223
- copper
 - chloride, 331
 - deposition from copper formate, 169
 - etching, 47, 331
- curing of
 - polyimide using Ar⁺ laser, 97
 - SiO₂:TiO₂ precursors using Ar⁺ laser, 97
- decomposition
 - aluminum, metalorganics, 21
 - of palladium acetate, 109
 - by VUV, 189
 - PMMA by UV, 39
- deposition
 - Al, 121
 - aluminum, 21
 - Au, 129
 - carbon, 229
 - Co, 79
 - copper, 169
 - Ge, 147
 - gold from Me₂Au(hfac), 73
 - ion beam, 229
 - of
 - SiO₂ from polysiloxane, 273
 - superconductors by laser sputtering, 451, 477, 485
 - Pd, 319
 - from palladium acetate, 189
 - polysiloxane, 273
 - silicon, 201
 - nitride, 201
 - oxinitride, 201
 - titanium from TiCl₄, 141
 - tungsten, 155, 161
 - from WF₆, 235
- desorption, laser induced, 47
- dissociation, disilane and ammonia on silicon, 201

- doping
 - laser, 241, 255
 - phosphorous into silicon, 281
 - Zn, Se in GaAs, 377
- electron beam, 201, 211
- epitaxy
 - CdTe, 381
 - on GaAs, 357
 - doped GaAs, 377
 - $\text{Ge}_x\text{Si}_{1-x}$ on Si, 241
 - $\text{In}_x\text{Ga}_{1-x}\text{As}$ on GaAs, 241
 - MBE of GaAs, laser assisted, 371
 - selective silicon, 339
 - Si, 365
- etching
 - ablative, 463, 471
 - Au^+ implanted Mn-Zn ferrite, 301
 - doping dependence of Si etching, 53
 - electron beam, 211
 - GaAs and InP, 407
 - Ge-Sb-S, 313
 - III-V semiconductors, 417
 - InP, 217
 - ion-beam induced Cl_2 etching on InP, 217
 - laser, 301
 - etching of ferrite by KOH, 319
 - mechanism of
 - Br_2 excimer laser etching of transition metals, 47
 - Cu etching by chlorine, 331
 - methyl radical etching of Te, Cd, CdTe, 289
 - of
 - GaAs
 - by BCl_3 , simulation, 395
 - by Cl_2 , electron beam induced, 211
 - with CF_2Cl_2 , 401
 - InP by HCl, HBr, Cl_2 , 307
 - photolysed teflon by $\text{B}(\text{CH}_3)_3$, 33
 - Si, SiO_2 using synchrotron radiation, 53
 - silicon by $\text{C}_2\text{F}_5\text{Cl}$, 325
 - reactive ion
 - beam, 413
 - magnetron, 395
 - of GaAs and GaAlAs, 401
 - remote Cl_2 plasma, 407
- RIE
 - in
 - BCl_3 , Cl_2 , 431
 - C_2 , 417
 - $\text{CCl}_2\text{F}_2\text{-O}_2$, 417
 - $\text{C}_2\text{H}_6\text{-H}_2$, 425
 - of
 - GaAs, and GaAlAs, 425
 - InP, InGaAs, InAlAs, 425
 - trenches, 431
 - silicon-carbide, 295
 - transition metals, 47
- excimer
 - KrF, 141
 - laser, 109, 261, 471, 485
 - ArF, 33, 91, 161, 175, 273, 281, 307, 381, 439
 - KrF, 27, 47, 439, 463
 - sputtering, 451
 - Xe, 189
 - XeCl, 241, 261, 371, 451
- ferrite
 - manganese-zinc, 319
 - Mn-Zn, 301
- gallium
 - aluminum
 - alloy, 351
 - arsenide, 211
 - etching, 425
 - MOCVD, 401
 - arsenide
 - contacts, 223, 261
 - epitaxy, 371
 - etching, 211, 389, 395, 407, 425
 - MOCVD, 401
 - oxidation, 211
 - diethyl gallium chloride, 351
 - nitride, deposition, 91
- germane, pyrolysis, 147
- germanium
 - amorphous films with Sb and S, 313
 - deposition from GeH_4 , 147
- glass, sodium trisilicate, 463
- gold
 - $\text{CH}_4\text{Au}(\text{C}_2\text{H}_5)_3\text{P}$, 129
 - laser deposition from $\text{Me}_2\text{Au}(\text{hfac})$, 73
 - LCVD using copper vapor laser, 319
- hollow cold cathode ion source, 413

- indium
 - aluminum arsenide, etching, 417
 - gallium arsenide, etching, 417
 - phosphide, etching, 217, 307, 407, 417
- ion beam, 223
- focused, 217, 229
- iron
 - deposition from $\text{Fe}(\text{CO})_5$, 175
 - etching, 47
- laser
 - Ar^+ , 97, 129, 155
 - frequency doubled, 181, 357
 - cleaning of Si surfaces, 477
 - copper vapor, 319
 - doping, 241, 255
 - doubled Nd:YAG, 485
 - Nd:YAG, 169
 - sputtering, 451, 477, 485
- lithography
 - excimer projection, 307
 - submicron, 3
- melting, laser, of
 - Al, 73, 267
 - Si, 241, 255, 281
- metalorganic
 - (π -allyl)(π -cyclopentadienyl) palladium, 103
 - Cd alkyl, 357
 - $\text{CH}_3\text{Au}(\text{C}_2\text{H}_5)_3\text{P}$, 129
 - copper formate, 169
 - dimethyl
 - cadmium, 381
 - tellurium, 381
 - zinc, 377
 - dimethylaluminum hydride (DMAH), 21, 121, 135
 - Engelhard gold ink, 319
 - $\text{Me}_2\text{Au}(\text{hfac})$, 73
 - palladium acetate, 109, 319
 - silver neodeconate, 319
 - Te alkyl, 357
 - trimethylaluminum (TMA), 21
 - trimethylgallium, 91
- molecular beam, Cl_2 , 389
- multi-chip module, 61, 439
- nanosecond thermal processing (NTP), 241
- nickel, etching, 47
- nucleation, 27, 91
- optical interconnects, 97
- palladium, deposition, 189
 - from acetate, 319
 - on
 - Al_2O_3 from acetate, 109
 - polyimide
 - from acetate, 61
 - polyetherimide, 103
- passivation, hydrogen, 425
- photoluminescence,
 - $\text{Al}_x\text{Ga}_{1-x}\text{As}$, 351
- photolysis
 - (π -allyl)(π -cyclopentadienyl) palladium, 103
 - Cl_3F by excimer laser, 295
 - $\text{Co}_2(\text{Co})_8$, 79
 - dimethyl aluminum hydride, 135
 - of Cd and Te alkyls, 357
 - polymer, 3
 - structural changes in
 - Ge-Sb-S films, 313
 - surface, 175
 - teflon, 33
 - TiCl_4 , 141
 - trimethylgallium, 91
- photo-oxidation, 181
- planarization, laser, effect of substrate heating, 267
- plasma emitter, 413
- plating
 - electroless, 61, 109, 189
 - electrolytic, 61
- PMMA
 - ablation, 471
 - micropores in UV-irradiated, 39
- polishing, chemomechanical, 365
- polyimide
 - ablation, 439
 - laser curing, 97
- polymer, ablation, 439
- polymerization, of TEOS with O_2 , N_2O by UV, 273
- polysiloxane, 273
- printed circuit board, multilayer, 439
- pyrolysis
 - germane, 147
 - gold metalorganic, 129
 - palladium acetate, 319
 - PF_5 , 281
- quantum well, 351
- reflectance, time-resolved, 73
- reflectivity, time resolved, 357

- selenium, hydrogen selenide, 377
- silicide, refractory metal, 261
- silicon
 - amorphous silicon
 - deposition, 201
 - carbide, etching, 295
 - carbon amorphous alloy, 181
 - dioxide
 - deposition, 97, 201
 - etching, 53
 - nitride, deposition, 201
 - oxinitride, deposition, 201
 - etching, 53, 325
- superconductor
 - deposition by laser
 - sputtering, 451, 477, 485
 - Y-Ba-Cu-O, 485
 - Bi-Sr-Ca-Cu-O, 451
- synchrotron radiation, 53
- teflon, etching, 33
- tellurium
 - diethyl tellurium, 357
 - dimethyl, 381
 - etching, 289
- titanium
 - deposition from titanium
 - tetrachloride, 141
 - dioxide, deposition, 97
 - etching, 47
 - tetrachloride, surface reaction, 3
- transistor
 - CMOS, stacked, 365
 - dual-gate, 365
 - for 3-D DRAM, 339
 - HEMT, 261, 401
 - MOSFET, submicron, 241
 - narrow base bipolar, 241
 - polycrystalline silicon
 - thin film, 255
- tungsten
 - amorphous, 161
 - deposition
 - by laser sputtering, 477
 - from
 - W(CO)₆, WCl₆, 161
 - WF₆, 85, 155, 223, 235
 - on GaAs, 223
- via, laser drilling, 439
- zinc, dimethyl, 377

MATERIALS RESEARCH SOCIETY SYMPOSIUM PROCEEDINGS

ISSN 0272 - 9172

- Volume 1—Laser and Electron-Beam Solid Interactions and Materials Processing, J. F. Gibbons, L. D. Hess, T. W. Sigmon, 1981, ISBN 0-444-00595-1
- Volume 2—Defects in Semiconductors, J. Narayan, T. Y. Tan, 1981, ISBN 0-444-00596-X
- Volume 3—Nuclear and Electron Resonance Spectroscopies Applied to Materials Science, E. N. Kaufmann, G. K. Shenoy, 1981, ISBN 0-444-00597-8
- Volume 4—Laser and Electron-Beam Interactions with Solids, B. R. Appleton, G. K. Celler, 1982, ISBN 0-444-00693-1
- Volume 5—Grain Boundaries in Semiconductors, H. J. Leamy, G. E. Pike, C. H. Seager, 1982, ISBN 0-444-00697-4
- Volume 6—Scientific Basis for Nuclear Waste Management IV, S. V. Topp, 1982, ISBN 0-444-00699-0
- Volume 7—Metastable Materials Formation by Ion Implantation, S. T. Picraux, W. J. Choyke, 1982, ISBN 0-444-00692-3
- Volume 8—Rapidly Solidified Amorphous and Crystalline Alloys, B. H. Kear, B. C. Giessen, M. Cohen, 1982, ISBN 0-444-00698-2
- Volume 9—Materials Processing in the Reduced Gravity Environment of Space, G. E. Rindone, 1982, ISBN 0-444-00691-5
- Volume 10—Thin Films and Interfaces, P. S. Ho, K.-N. Tu, 1982, ISBN 0-444-00774-1
- Volume 11—Scientific Basis for Nuclear Waste Management V, W. Lutze, 1982, ISBN 0-444-00725-3
- Volume 12—In Situ Composites IV, F. D. Lemkey, H. E. Cline, M. McLean, 1982, ISBN 0-444-00726-1
- Volume 13—Laser-Solid Interactions and Transient Thermal Processing of Materials, J. Narayan, W. L. Brown, R. A. Lemons, 1983, ISBN 0-444-00788-1
- Volume 14—Defects in Semiconductors II, S. Mahajan, J. W. Corbett, 1983, ISBN 0-444-00812-8
- Volume 15—Scientific Basis for Nuclear Waste Management VI, D. G. Brookins, 1983, ISBN 0-444-00780-6
- Volume 16—Nuclear Radiation Detector Materials, E. E. Haller, H. W. Kraner, W. A. Higinbotham, 1983, ISBN 0-444-00787-3
- Volume 17—Laser Diagnostics and Photochemical Processing for Semiconductor Devices, R. M. Osgood, S. R. J. Brueck, H. R. Schlossberg, 1983, ISBN 0-444-00782-2
- Volume 18—Interfaces and Contacts, R. Ludeke, K. Rose, 1983, ISBN 0-444-00820-9
- Volume 19—Alloy Phase Diagrams, L. H. Bennett, T. B. Massalski, B. C. Giessen, 1983, ISBN 0-444-00809-8
- Volume 20—Intercalated Graphite, M. S. Dresselhaus, G. Dresselhaus, J. E. Fischer, M. J. Moran, 1983, ISBN 0-444-00781-4
- Volume 21—Phase Transformations in Solids, T. Tsakalakos, 1984, ISBN 0-444-00901-9
- Volume 22—High Pressure in Science and Technology, C. Homan, R. K. MacCrone, E. Whalley, 1984, ISBN 0-444-00932-9 (3 part set)
- Volume 23—Energy Beam-Solid Interactions and Transient Thermal Processing, J. C. C. Fan, N. M. Johnson, 1984, ISBN 0-444-00903-5
- Volume 24—Defect Properties and Processing of High-Technology Nonmetallic Materials, J. H. Crawford, Jr., Y. Chen, W. A. Sibley, 1984, ISBN 0-444-00904-3
- Volume 25—Thin Films and Interfaces II, J. E. E. Baglin, D. R. Campbell, W. K. Chu, 1984, ISBN 0-444-00905-1

MATERIALS RESEARCH SOCIETY SYMPOSIUM PROCEEDINGS

- Volume 26—Scientific Basis for Nuclear Waste Management VII, G. L. McVay, 1984, ISBN 0-444-00906-X
- Volume 27—Ion Implantation and Ion Beam Processing of Materials, G. K. Hubler, O. W. Holland, C. R. Clayton, C. W. White, 1984, ISBN 0-444-00869-1
- Volume 28—Rapidly Solidified Metastable Materials, B. H. Kear, B. C. Giessen, 1984, ISBN 0-444-00935-3
- Volume 29—Laser-Controlled Chemical Processing of Surfaces, A. W. Johnson, D. J. Ehrlich, H. R. Schlossberg, 1984, ISBN 0-444-00894-2
- Volume 30—Plasma Processing and Synthesis of Materials, J. Szekeley, D. Apelian, 1984, ISBN 0-444-00895-0
- Volume 31—Electron Microscopy of Materials, W. Krakow, D. A. Smith, L. W. Hobbs, 1984, ISBN 0-444-00898-7
- Volume 32—Better Ceramics Through Chemistry, C. J. Brinker, D. E. Clark, D. R. Ulrich, 1984, ISBN 0-444-00898-5
- Volume 33—Comparison of Thin Film Transistor and SOI Technologies, H. W. Lam, M. J. Thompson, 1984, ISBN 0-444-00899-3
- Volume 34—Physical Metallurgy of Cast Iron, H. Fredriksson, M. Hillerts, 1985, ISBN 0-444-00938-8
- Volume 35—Energy Beam-Solid Interactions and Transient Thermal Processing/1984, D. K. Biegelsen, G. A. Rozgonyi, C. V. Shank, 1985, ISBN 0-931837-00-6
- Volume 36—Impurity Diffusion and Gettering in Silicon, R. B. Fair, C. W. Pearce, J. Washburn, 1985, ISBN 0-931837-01-4
- Volume 37—Layered Structures, Epitaxy, and Interfaces, J. M. Gibson, L. R. Dawson, 1985, ISBN 0-931837-02-2
- Volume 38—Plasma Synthesis and Etching of Electronic Materials, R. P. H. Chang, B. Abeles, 1985, ISBN 0-931837-03-0
- Volume 39—High-Temperature Ordered Intermetallic Alloys, C. C. Koch, C. T. Liu, N. S. Stoloff, 1985, ISBN 0-931837-04-9
- Volume 40—Electronic Packaging Materials Science, E. A. Gies, N. Tu, D. R. Uhlmann, 1985, ISBN 0-931837-05-7
- Volume 41—Advanced Photon and Particle Techniques for the Characterization of Defects in Solids, J. B. Roberto, R. W. Caletner, M. C. Wittels, 1985, ISBN 0-931837-06-5
- Volume 42—Very High Strength Cement-Based Materials, J. F. Young, 1985, ISBN 0-931837-07-3
- Volume 43—Fly Ash and Coal Conversion By-Products: Characterization, Utilization, and Disposal I, G. J. McCarthy, R. J. Lauf, 1985, ISBN 0-931837-08-1
- Volume 44—Scientific Basis for Nuclear Waste Management VIII, C. M. Jantzen, J. A. Stone, R. C. Ewing, 1985, ISBN 0-931837-09-X
- Volume 45—Ion Beam Processes in Advanced Electronic Materials and Device Technology, B. R. Appleton, F. H. Eisen, T. W. Sigmon, 1985, ISBN 0-931837-10-3
- Volume 46—Microscopic Identification of Electronic Defects in Semiconductors, N. M. Johnson, S. G. Bishop, G. D. Watkins, 1985, ISBN 0-931837-11-1
- Volume 47—Thin Films: The Relationship of Structure to Properties, C. R. Aita, K. S. Sreeharsha, 1985, ISBN 0-931837-12-X
- Volume 48—Applied Materials Characterization, W. Katz, P. Williams, 1985, ISBN 0-931837-13-8
- Volume 49—Materials Issues in Applications of Amorphous Silicon Technology, D. Adler, A. Madan, M. J. Thompson, 1985, ISBN 0-931837-14-6

MATERIALS RESEARCH SOCIETY SYMPOSIUM PROCEEDINGS

- Volume 50—Scientific Basis for Nuclear Waste Management IX, L. O. Werme, 1986, ISBN 0-931837-15-4
- Volume 51—Beam-Solid Interactions and Phase Transformations, H. Kurz, G. L. Olson, J. M. Poate, 1986, ISBN 0-931837-16-2
- Volume 52—Rapid Thermal Processing, T. O. Sedgwick, T. E. Seidel, B.-Y. Tsaur, 1986, ISBN 0-931837-17-0
- Volume 53—Semiconductor-on-Insulator and Thin Film Transistor Technology, A. Chiang, M. W. Geis, L. Pfeiffer, 1986, ISBN 0-931837-18-9
- Volume 54—Thin Films—Interfaces and Phenomena, R. J. Nemanich, P. S. Ho, S. S. Lau, 1986, ISBN 0-931837-19-7
- Volume 55—Biomedical Materials, J. M. Williams, M. F. Nichols, W. Zingg, 1986, ISBN 0-931837-20-0
- Volume 56—Layered Structures and Epitaxy, J. M. Gibson, G. C. Osbourn, R. M. Tromp, 1986, ISBN 0-931837-21-9
- Volume 57—Phase Transitions in Condensed Systems—Experiments and Theory, G. S. Cargill III, F. Spaepen, K.-N. Tu, 1987, ISBN 0-931837-22-7
- Volume 58—Rapidly Solidified Alloys and Their Mechanical and Magnetic Properties, B. C. Giessen, D. E. Polk, A. I. Taub, 1986, ISBN 0-931837-23-5
- Volume 59—Oxygen, Carbon, Hydrogen, and Nitrogen in Crystalline Silicon, J. C. Mikkelsen, jr., S. J. Pearton, J. W. Corbett, S. J. Pennycook, 1986, ISBN 0-931837-24-3
- Volume 60—Defect Properties and Processing of High-Technology Nonmetallic Materials, Y. Chen, W. D. Kingery, R. J. Stokes, 1986, ISBN 0-931837-25-1
- Volume 61—Defects in Glasses, F. L. Galeener, D. L. Griscom, M. J. Weber, 1986, ISBN 0-931837-26-X
- Volume 62—Materials Problem Solving with the Transmission Electron Microscope, L. W. Hobbs, K. H. Westmacott, D. B. Williams, 1986, ISBN 0-931837-27-8
- Volume 63—Computer-Based Microscopic Description of the Structure and Properties of Materials, J. Broughton, W. Krakow, S. T. Pantelides, 1986, ISBN 0-931837-28-6
- Volume 64—Cement-Based Composites, Strain Rate Effects on Fracture, S. Mindess, S. P. Shah, 1986, ISBN 0-931837-29-4
- Volume 65—Fly Ash and Coal Conversion By-Products: Characterization, Utilization and Disposal II, G. J. McCarthy, F. P. Glasser, D. M. Roy, 1986, ISBN 0-931837-30-8
- Volume 66—Frontiers in Materials Education, L. W. Hobbs, G. L. Liedl, 1986, ISBN 0-931837-31-6
- Volume 67—Heteroepitaxy on Silicon, J. C. C. Fan, J. M. Poate, 1986, ISBN 0-931837-33-2
- Volume 68—Plasma Processing, J. W. Coburn, R. A. Gottscho, D. W. Hess, 1986, ISBN 0-931837-34-0
- Volume 69—Materials Characterization, N. W. Cheung, M.-A. Nicolet, 1986, ISBN 0-931837-35-9
- Volume 70—Materials Issues in Amorphous-Semiconductor Technology, D. Adler, Y. Hamakawa, A. Madan, 1986, ISBN 0-931837-36-7
- Volume 71—Materials Issues in Silicon Integrated Circuit Processing, M. Wittmer, J. Stimmell, M. Strathman, 1986, ISBN 0-931837-37-5
- Volume 72—Electronic Packaging Materials Science II, K. A. Jackson, R. C. Pohanka, D. R. Uhlmann, D. R. Ulrich, 1986, ISBN 0-931837-38-3
- Volume 73—Better Ceramics Through Chemistry II, C. J. Brinker, D. E. Clark, D. R. Ulrich, 1986, ISBN 0-931837-39-1
- Volume 74—Beam-Solid Interactions and Transient Processes, M. O. Thompson, S. T. Picraux, J. S. Williams, 1987, ISBN 0-931837-40-5

MATERIALS RESEARCH SOCIETY SYMPOSIUM PROCEEDINGS

- Volume 75—Photon, Beam and Plasma Stimulated Chemical Processes at Surfaces, V. M. Donnelly, I. P. Herman, M. Hirose, 1987, ISBN 0-931837-41-3
- Volume 76—Science and Technology of Microfabrication, R. E. Howard, E. L. Hu, S. Namba, S. Pang, 1987, ISBN 0-931837-42-1
- Volume 77—Interfaces, Superlattices, and Thin Films, J. D. Dow, I. K. Schuller, 1987, ISBN 0-931837-56-1
- Volume 78—Advances in Structural Ceramics, P. F. Becher, M. V. Swain, S. Sōmiya, 1987, ISBN 0-931837-43-X
- Volume 79—Scattering, Deformation and Fracture in Polymers, G. D. Wignall, B. Crist, T. P. Russell, E. L. Thomas, 1987, ISBN 0-931837-44-8
- Volume 80—Science and Technology of Rapidly Quenched Alloys, M. Tenhover, W. L. Johnson, L. E. Tanner, 1987, ISBN 0-931837-45-6
- Volume 81—High-Temperature Ordered Intermetallic Alloys, II, N. S. Stoloff, C. C. Koch, C. T. Liu, O. Izumi, 1987, ISBN 0-931837-46-4
- Volume 82—Characterization of Defects in Materials, R. W. Siegel, J. R. Weertman, R. Sinclair, 1987, ISBN 0-931837-47-2
- Volume 83—Physical and Chemical Properties of Thin Metal Overlayers and Alloy Surfaces, D. M. Zehner, D. W. Goodman, 1987, ISBN 0-931837-48-0
- Volume 84—Scientific Basis for Nuclear Waste Management X, J. K. Bates, W. B. Seefeldt, 1987, ISBN 0-931837-49-9
- Volume 85—Microstructural Development During the Hydration of Cement, L. Struble, P. Brown, 1987, ISBN 0-931837-50-2
- Volume 86—Fly Ash and Coal Conversion By-Products Characterization, Utilization and Disposal III, G. J. McCarthy, F. P. Glasser, D. M. Roy, S. Diamond, 1987, ISBN 0-931837-51-0
- Volume 87—Materials Processing in the Reduced Gravity Environment of Space, R. H. Doremus, P. C. Nordine, 1987, ISBN 0-931837-52-9
- Volume 88—Optical Fiber Materials and Properties, S. R. Nagel, J. W. Fleming, G. Sigel, D. A. Thompson, 1987, ISBN 0-931837-53-7
- Volume 89—Diluted Magnetic (Semimagnetic) Semiconductors, R. L. Aggarwal, J. K. Furdyna, S. von Molnar, 1987, ISBN 0-931837-54-5
- Volume 90—Materials for Infrared Detectors and Sources, R. F. C. Farrow, J. F. Schetzina, J. T. Cheung, 1987, ISBN 0-931837-55-3
- Volume 91—Heteroepitaxy on Silicon II, J. C. C. Fan, J. M. Phillips, B.-Y. Tsaur, 1987, ISBN 0-931837-58-8
- Volume 92—Rapid Thermal Processing of Electronic Materials, S. R. Wilson, R. A. Powell, D. E. Davies, 1987, ISBN 0-931837-59-6
- Volume 93—Materials Modification and Growth Using Ion Beams, U. Gibson, A. E. White, P. P. Pronko, 1987, ISBN 0-931837-60-X
- Volume 94—Initial Stages of Epitaxial Growth, R. Hull, J. M. Gibson, David A. Smith, 1987, ISBN 0-931837-61-8
- Volume 95—Amorphous Silicon Semiconductors—Pure and Hydrogenated, A. Madan, M. Thompson, D. Adler, Y. Hamakawa, 1987, ISBN 0-931837-62-6
- Volume 96—Permanent Magnet Materials, S. G. Sankar, J. F. Herbst, N. C. Koon, 1987, ISBN 0-931837-63-4
- Volume 97—Novel Refractory Semiconductors, D. Emin, T. Aselage, C. Wood, 1987, ISBN 0-931837-64-2
- Volume 98—Plasma Processing and Synthesis of Materials, D. Apelian, J. Szekely, 1987, ISBN 0-931837-65-0

MATERIALS RESEARCH SOCIETY SYMPOSIUM PROCEEDINGS

- Volume 99—High-Temperature Superconductors, M. B. Brodsky, R. C. Dynes, K. Kitazawa, H. L. Tuller, 1988, ISBN 0-931837-67-7
- Volume 100—Fundamentals of Beam-Solid Interactions and Transient Thermal Processing, M. J. Aziz, L. E. Rehn, B. Stritzker, 1988, ISBN 0-931827-68-5
- Volume 101—Laser and Particle-Beam Chemical Processing for Microelectronics, D.J. Ehrlich, G.S. Higashi, M.M. Oprysko, 1988, ISBN 0-931837-69-3
- Volume 102—Epitaxy of Semiconductor Layered Structures, R. T. Tung, L. R. Dawson, R. L. Gunshor, 1988, ISBN 0-931837-70-7
- Volume 103—Multilayers: Synthesis, Properties, and Nonelectronic Applications, T. W. Barbee Jr., F. Spaepen, L. Greer, 1988, ISBN 0-931837-71-5
- Volume 104—Defects in Electronic Materials, M. Stavola, S. J. Pearton, G. Davies, 1988, ISBN 0-931837-72-3
- Volume 105—SiO₂ and Its Interfaces, G. Lucovsky, S. T. Pantelides, 1988, ISBN 0-931837-73-1
- Volume 106—Polysilicon Films and Interfaces, C.Y. Wong, C.V. Thompson, K-N. Tu, 1988, ISBN 0-931837-74-X
- Volume 107—Silicon-on-Insulator and Buried Metals in Semiconductors, J. C. Sturm, C. K. Chen, L. Pfeiffer, P. L. F. Hemment, 1988, ISBN 0-931837-75-8
- Volume 108—Electronic Packaging Materials Science II, R. C. Sundahl, R. Jaccodine, K. A. Jackson, 1988, ISBN 0-931837-76-6
- Volume 109—Nonlinear Optical Properties of Polymers, A. J. Heeger, J. Orenstein, D. R. Ulrich, 1988, ISBN 0-931837-77-4
- Volume 110—Biomedical Materials and Devices, J. S. Hanker, B. L. Giammara, 1988, ISBN 0-931837-78-2
- Volume 111—Microstructure and Properties of Catalysts, M. M. J. Treacy, J. M. Thomas, J. M. White, 1988, ISBN 0-931837-79-0
- Volume 112—Scientific Basis for Nuclear Waste Management XI, M. J. Apted, R. E. Westerman, 1988, ISBN 0-931837-80-4
- Volume 113—Fly Ash and Coal Conversion By-Products: Characterization, Utilization, and Disposal IV, G. J. McCarthy, D. M. Roy, F. P. Glasser, R. T. Hemmings, 1988, ISBN 0-931837-81-2
- Volume 114—Bonding in Cementitious Composites, S. Mindess, S. P. Shah, 1988, ISBN 0-931837-82-0
- Volume 115—Specimen Preparation for Transmission Electron Microscopy of Materials, J. C. Bravman, R. Anderson, M. L. McDonald, 1988, ISBN 0-931837-83-9
- Volume 116—Heteroepitaxy on Silicon: Fundamentals, Structures, and Devices, H.K. Choi, H. Ishiwara, R. Hull, R.J. Nemanich, 1988, ISBN: 0-931837-86-3
- Volume 117—Process Diagnostics: Materials, Combustion, Fusion, K. Hays, A.C. Eckbreth, G.A. Campbell, 1988, ISBN: 0-931837-87-1
- Volume 118—Amorphous Silicon Technology, A. Madan, M.J. Thompson, P.C. Taylor, P.G. LeComber, Y. Hamakawa, 1988, ISBN: 0-931837-88-X
- Volume 119—Adhesion in Solids, D.M. Mattox, C. Batich, J.E.E. Baglin, R.J. Gottschall, 1988, ISBN: 0-931837-89-8
- Volume 120—High-Temperature/High-Performance Composites, F.D. Lemkey, A.G. Evans, S.G. Fishman, J.R. Strife, 1988, ISBN: 0-931837-90-1
- Volume 121—Better Ceramics Through Chemistry III, C.J. Brinker, D.E. Clark, D.R. Ulrich, 1988, ISBN: 0-931837-91-X

MATERIALS RESEARCH SOCIETY SYMPOSIUM PROCEEDINGS

- Volume 122—Interfacial Structure, Properties, and Design, M.H. Yoo, W.A.T. Clark, C.L. Briant, 1988, ISBN: 0-931837-92-8
- Volume 123—Materials Issues in Art and Archaeology, E.V. Sayre, P. Vandiver, J. Druzik, C. Stevenson, 1988, ISBN: 0-931837-93-6
- Volume 124—Microwave-Processing of Materials, M.H. Brooks, I.J. Chabinsky, W.H. Sutton, 1988, ISBN: 0-931837-94-4
- Volume 125—Materials Stability and Environmental Degradation, A. Barkatt, L.R. Smith, E. Verink, 1988, ISBN: 0-931837-95-2
- Volume 126—Advanced Surface Processes for Optoelectronics, S. Bernasek, T. Venkatesan, H. Temkin, 1988, ISBN: 0-931837-96-0
- Volume 127—Scientific Basis for Nuclear Waste Management XII, W. Lutze, R.C. Ewing, 1989, ISBN: 0-931837-97-9
- Volume 128—Processing and Characterization of Materials Using Ion Beams, L.E. Rehn, J. Greene, F.A. Smidt, 1989, ISBN: 1-55899-001-1
- Volume 129—Laser and Particle-Beam Modification of Chemical Processes on Surfaces, A.W. Johnson, G.L. Loper, T.W. Sigmon, 1989, ISBN: 1-55899-002-X
- Volume 130—Thin Films: Stresses and Mechanical Properties, J.C. Bravman, W.D. Nix, D.M. Barnett, D.A. Smith, 1989, ISBN: 1-55899-003-8
- Volume 131—Chemical Perspectives of Microelectronic Materials, M.E. Gross, J. Jasinski, J.T. Yates, Jr., 1989, ISBN: 1-55899-004-6
- Volume 132—Multicomponent Ultrafine Microstructures, L.E. McCandlish, B.H. Kear, D.E. Polk, and R.W. Siegel, 1989, ISBN: 1-55899-005-4
- Volume 133—High Temperature Ordered Intermetallic Alloys III, C.T. Liu, A.I. Taub, N.S. Stoloff, C.C. Koch, 1989, ISBN: 1-55899-006-2
- Volume 134—The Materials Science and Engineering of Rigid-Rod Polymers, W.W. Adams, R.K. Eby, D.E. McLemore, 1989, ISBN: 1-55899-007-0
- Volume 135—Solid State Ionics, G. Nazri, R.A. Huggins, D.F. Shriver, 1989, ISBN: 1-55899-008-9
- Volume 136—Fly Ash and Coal Conversion By-Products: Characterization, Utilization and Disposal V, R.T. Hemmings, E.E. Berry, G.J. McCarthy, F.P. Glasser, 1989, ISBN: 1-55899-009-7
- Volume 137—Pore Structure and Permeability of Cementitious Materials, L.R. Roberts, J.P. Skalny, 1989, ISBN: 1-55899-010-0
- Volume 138—Characterization of the Structure and Chemistry of Defects in Materials, B.C. Larson, M. Ruhle, D.N. Seidman, 1989, ISBN: 1-55899-011-9
- Volume 139—High Resolution Microscopy of Materials, W. Krakow, F.A. Ponce, D.J. Smith, 1989, ISBN: 1-55899-012-7
- Volume 140—New Materials Approaches to Tribology: Theory and Applications, L.E. Pope, L. Fehrenbacher, W.O. Winer, 1989, ISBN: 1-55899-013-5
- Volume 141—Atomic Scale Calculations in Materials Science, J. Tersoff, D. Vanderbilt, V. Vitek, 1989, ISBN: 1-55899-014-3
- Volume 142—Nondestructive Monitoring of Materials Properties, J. Holbrook, J. Bussiere, 1989, ISBN: 1-55899-015-1
- Volume 143—Synchrotron Radiation in Materials Research, R. Clarke, J. Gland, J.H. Weaver, 1989, ISBN: 1-55899-016-X
- Volume 144—Advances in Materials, Processing and Devices in III-V Compound Semiconductors, D.K. Sadana, L. Eastman, R. Dupuis, 1989, ISBN: 1-55899-017-8

Recent Materials Research Society Proceedings listed in the front.

MATERIALS RESEARCH SOCIETY CONFERENCE PROCEEDINGS

Tungsten and Other Refractory Metals for VLSI Applications, Robert S. Blewer, 1986; ISSN 0886-7860; ISBN 0-931837-32-4

Tungsten and Other Refractory Metals for VLSI Applications II, Eliot K. Broadbent, 1987; ISSN 0886-7860; ISBN 0-931837-66-9

Ternary and Multinary Compounds, Satyen K. Deb, Alex Zunger, 1987; ISBN 0-931837-57-X

Tungsten and Other Refractory Metals for VLSI Applications III, Victor A. Wells, 1988; ISSN 0886-7860; ISBN 0-931837-84-7

Atomic and Molecular Processing of Electronic and Ceramic Materials: Preparation, Characterization and Properties, Ilhan A. Aksay, Gary L. McVay, Thomas G. Stoebe, J.F. Wager, 1988; ISBN 0-931837-85-5

Materials Futures: Strategies and Opportunities, R. Byron Pipes, U.S. Organizing Committee, Rune Lagneborg, Swedish Organizing Committee, 1988; ISBN 1-55899-000-3

Tungsten and Other Refractory Metals for VLSI Applications IV, Robert S. Blewer, Carol M. McConica, 1989; ISSN 0886-7860; ISBN 0-931837-98-7

Tungsten and Other Advanced Metals for VLSI/ULSI Applications V, S. Simon Wong, Seiji Furukawa, 1990; ISSN 1048-0854; ISBN 1-55899-086-2

High Energy and Heavy Ion Beams in Materials Analysis, Joseph R. Tesmer, Carl J. Maggiore, Michael Nastasi, J. Charles Barbour, James W. Mayer, 1990; ISBN 1-55899-091-7

Physical Metallurgy of Cast Iron IV, Goro Ohira, Takaji Kusakawa, Eisuke Niyama, 1990; ISBN 1-55899-090-9